
Conference on Physics of Fundamental Interactions
Experiment

$\beta\beta(2\nu)$ Decay of ^{100}Mo to the First Excited 0^+ State of $^{100}\text{Ru}^*$

L. De Braeckeleeer¹⁾, **, M. Hornish¹⁾, ***, A. S. Barabash²⁾, ****, and V. I. Umatov²⁾, *****

Received March 21, 2001

Abstract—The rate of the double-beta $\beta\beta(2\nu)$ decay of ^{100}Mo to the first 0^+ excited state in ^{100}Ru is measured by a $\gamma\gamma$ -coincidence technique in which two HPGe detectors are used to detect the two γ rays ($E_{\gamma 1} = 590.76$ keV and $E_{\gamma 2} = 539.53$ keV) from the daughter nucleus ^{100}Ru as it deexcites to the ground state via the transition sequence $0^+ \rightarrow 2^+ \rightarrow 0^+$. In contrast to all previous $\beta\beta$ -decay experiments, this technique provides data that are essentially background-free. By using a 1.05-kg isotopically enriched (98.4%) disk of ^{100}Mo , 22 coincidence events (with the background estimated at 2.5 events) are detected in 440 d of measuring time, which translates into a half-life time of $[5.9_{-1.1}^{+1.7}(\text{stat.}) \pm 0.6(\text{syst.})] \times 10^{20}$ yr.

© 2002 MAIK “Nauka/Interperiodica”.

1. INTRODUCTION

Although the main interest in studying double-beta ($\beta\beta$) decay is currently related to the neutrinoless mode ($0\nu\beta\beta$) because of its potential for discovering elementary-particle physics beyond the Standard Model, considerable efforts are underway to investigate the ordinary allowed second-order weak decay ($2\nu\beta\beta$ decay) [1–4]. Accumulation of experimental information on $2\nu\beta\beta$ processes (transitions to ground and excited states) promotes a better understanding of the nuclear part of $\beta\beta$ decay and allows one to check theoretical schemes of nuclear-matrix-element calculations for the two-neutrino mode, as well as for the neutrinoless one. It is very important to note that, within models based on the quasiparticle random-phase approximation (QRPA), nuclear matrix elements depend differently on the particle-particle strength parameter g_{pp} for ground-state transitions and transitions to excited states [3, 5]. Therefore, the decay to excited states probes different aspects of the computational method.

$0\nu\beta\beta$ transitions to excited states of daughter nuclei have a very important experimental signature: in addition to the two electrons of fixed energy, there are one ($0^+ \rightarrow 2_1^+$ transition) or two ($0^+ \rightarrow 0_1^+$

transition) γ rays that again have strictly fixed energy. If one can perform an experiment such that all decay products are detected with a high efficiency and with a good energy resolution, then the experimental background can be totally suppressed, even for massive detectors (~ 1 t) and long measurement times (~ 10 yr).

The idea of detecting the $2\nu\beta\beta(0^+ \rightarrow 0_1^+)$ decay of ^{100}Mo [6] initiated experiments to seek this decay by using enriched molybdenum samples and γ -ray detectors operated in a single mode. In the experiment of [7] using 310 g of ^{100}Mo and a surface-based 100-cm³ HPGe detector, only a lower limit was obtained for the half-life: $T_{1/2} > 4.2 \times 10^{19}$ yr. Afterward, this decay mode was positively identified by using about 1 kg of ^{100}Mo and a low-background 114-cm³ HPGe detector located in the Soudan mine in Minnesota (2090-mwe depth); the result was $T_{1/2} = (6.1_{-1.1}^{+1.8}) \times 10^{20}$ yr [8, 9]. At approximately the same time (the measurement started half a year after the beginning of the measurement in the Soudan mine), an experiment with another 1-kg sample of ^{100}Mo using a 100-cm³ HPGe detector was performed in the Modane Underground Laboratory (4800-mwe depth) [10]. However, only a lower limit was obtained because the measuring time was not sufficiently long (a factor of about 4 shorter in comparison with the 415.43 d of [8]) and, in addition, a rather high level of background was experienced in this experiment (a factor of about 2 larger in comparison with [8]). A new positive result for the $2\nu\beta\beta(0^+ \rightarrow 0_1^+)$ decay of ^{100}Mo was obtained in [11]. This experiment was again performed in the Modane Underground Laboratory. A set of ^{100}Mo enriched metal-powder samples were

*This article was submitted by the authors in English.

¹⁾The Department of Physics, Duke University and Triangle Universities Nuclear Laboratory, Durham, North Carolina, 27708-0308 USA.

²⁾Institute of Theoretical and Experimental Physics, Bol'shaya Chermushkinskaya ul. 25, Moscow, 117218 Russia.

** e-mail: ludwigdb@tunl.tunl.duke.edu

*** e-mail: hornish@duke.edu

**** e-mail: alexander.barabash@itep.ru

***** e-mail: vladimir.umatov@itep.ru

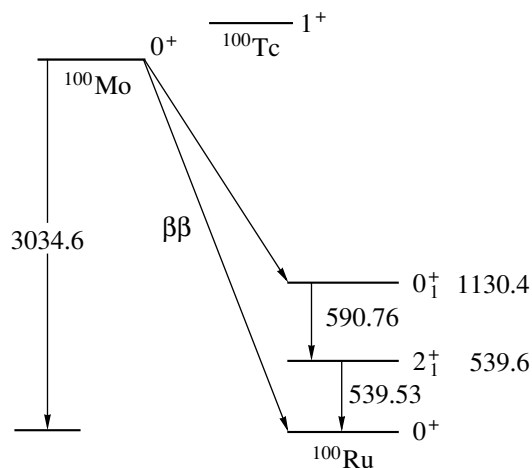


Fig. 1. $\beta\beta$ -decay and γ -decay schemes for ^{100}Mo (energy in keV).

measured by using low-background HPGe detectors. Data from 17 measurements were analyzed and a half-life of $T_{1/2} = (9.3^{+2.8}_{-1.7}) \times 10^{20}$ yr was deduced from the summed γ -ray spectrum, with an additional systematic error estimated at approximately 15%. When the spectrum of [8] is added to the one of [11], one obtains $T_{1/2} = (7.6^{+1.8}_{-1.1}) \times 10^{20}$ yr [11], also with a 15% systematic error.

2. APPARATUS AND METHODS

The present article reports on a new positive result for the $2\nu\beta\beta(0^+ \rightarrow 0^+)$ decay of ^{100}Mo using a novel method with two HPGe detectors in a coincidence scheme. The previous experiments focused on very low background detection systems. This was achieved by building the detectors from low-radioactivity materials and by operating the experiments in underground laboratories, which offer an efficient shielding against the cosmic-ray-induced background. An alternative approach to background reduction is to employ a coincidence technique, in which two separate detectors simultaneously detect the two emitted γ rays from the $2\nu\beta\beta(0^+ \rightarrow 0^+)$ decay of ^{100}Mo with $E_{\gamma 1} = 590.76$ keV and $E_{\gamma 2} = 539.53$ keV (Fig. 1). This approach was accomplished for the first time by using two HPGe detectors (8.5-cm diameter, 5-cm width, 1.8-keV FWHM energy resolution at 1.33 MeV, and 0.7-keV resolution at 0.122 MeV) in coincidence in the present study. A disk sample of molybdenum was sandwiched between these two γ -ray detectors, which were inserted into a NaI annulus (56-cm length, 35.6-cm diameter with a 12.5-cm hole along the axis of symmetry) that acted as an active veto. Plastic plates (10-cm thickness)

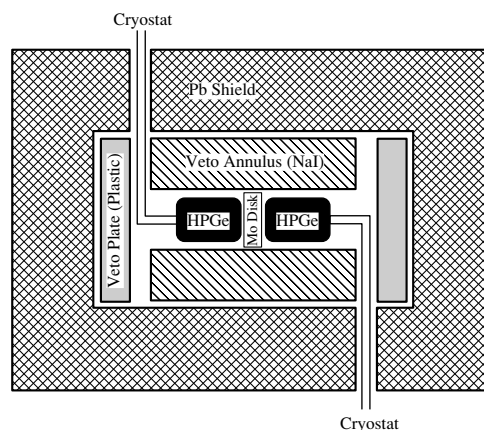


Fig. 2. Experimental apparatus including a ^{100}Mo sample, HPGe detectors, active shielding (veto), and passive shielding (Pb).

on either side of the apparatus acted as a veto for the regions that are not covered with the NaI annulus. The entire apparatus was surrounded by a passive shielding made from lead bricks (Fig. 2). The experiment was conducted inside the Low-Background Counting Facility of the Triangle Universities Nuclear Laboratory (TUNL), a well-shielded room located in the basement of the Physics Department of Duke University.

In order to calculate the half-life of a given decay, it is necessary to understand and to determine the efficiency of our $\gamma\gamma$ -coincidence apparatus. To accomplish this, a ^{102}Rh source was produced at TUNL by (p, n) activation of a natural Ru target. This source was then used to measure the probability for detecting the full energy of both γ rays. ^{102m}Rh was chosen because it emits two γ rays having similar energies and the same angular distribution as the γ rays emitted in the $\beta\beta$ decay of ^{100}Mo . In addition, the lifetime of 206 d is quite convenient, and it decays to the first excited 0^+ state of the daughter nucleus via electron capture only; this implies no radiation from annihilation or bremsstrahlung and makes the measurement of the efficiency very simple. The source was used to measure the coincidence efficiency of the apparatus as a function of the radial distance from the center of the detectors. The source was also surrounded by disks of molybdenum to simulate the attenuation of the γ rays in the actual molybdenum sample. The efficiency ε was averaged over the entire volume of the sample and was determined to be $\varepsilon = (0.22 \pm 0.02)\%$. The coincidence efficiency was also studied with a Monte Carlo simulation. This calculation included the effects of extended geometry, the attenuation of the γ rays in the sample, the full-energy peak efficiency of the germanium detectors, and the

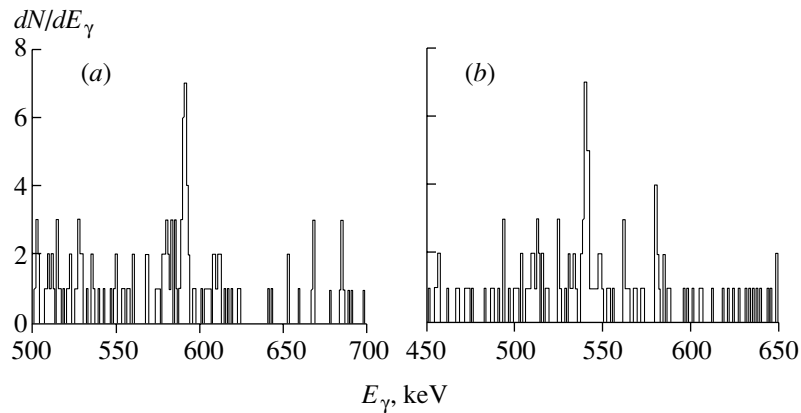


Fig. 3. γ -ray spectra in coincidence with (a) 540 ± 2.5 keV and (b) 591 ± 2.5 keV. Note the 22 coincidence events (540 keV–591 keV) in 440 d of measuring time.

strongly anisotropic angular correlation between the γ rays.

3. RESULTS AND ANALYSIS

A ^{100}Mo sample (1.05-kg mass, 10.6-cm diameter, 1.1-cm thickness, 98.4% enrichment) has been studied for 440 d. Twenty-two 539.6-keV to 590.8-keV coincidence events were detected, and Fig. 3 shows the γ -ray spectra in coincidence with (a) 540 ± 2.5 keV and (b) 591 ± 2.5 keV. A measurement of the background rate yields 2.5 events per 5 keV. From these data, the half-life with respect to the $\beta\beta$ decay of ^{100}Mo to the first excited 0^+ state of ^{100}Ru can be determined. After subtraction of the background, one obtains a half-life of $[5.9_{-1.1}^{+1.7}(\text{stat.}) \pm 0.6(\text{syst.})] \times 10^{20}$ yr.

Before our result obtained above ground can be compared with the previous results for ^{100}Mo measured underground, one must investigate the possibility of whether (or not) the signal observed in our ^{100}Mo $\beta\beta$ -decay experiment, or at least part of it, is due to $^{100}\text{Mo}(p, n)$ or $^{100}\text{Mo}(n, \gamma)$ reactions (or both). The reactions $^{100}\text{Mo}(p, n)$ to bound states in ^{100}Tc will produce, after prompt γ -ray deexcitation, the ground state of ^{100}Tc . The latter has a half-life of 15.8 s and a 5.7% branching ratio for the transition to the 0_1^+ state of ^{100}Ru , which decays to the ground state by emitting two γ rays (540 and 591 keV). It is worth noting that our NaI veto does not act against this process due to the 15.8-s half-life of the ^{100}Tc ground state. One way to estimate the magnitude of the process $^{100}\text{Mo}(p, n)$ is to seek very similar $^{95}\text{Mo}(p, n)$ reactions. ^{95}Mo is an abundant isotope: 16% of natural molybdenum. One sample, a disk of natural molybdenum (1-kg mass, 10-cm diameter, 0.965-cm thickness, 9.6% ^{100}Mo), has been stored in

the apparatus and investigated for 180 d. The production of the isomer ($1/2^-$, half-life time of 61 d) of ^{95}Tc can proceed via the (p, n) reaction on ^{95}Mo and is very practical for our purpose. This element decays with large branching ratios to two excited states: 38% to the 786.2-keV state and 30% to the 1039.3-keV state. In both cases, these states decay to the first excited state at 204 keV with a branching ratio of 78 and 89%, respectively. Moreover, the first excited state has a short lifetime of 0.75 ns. One hundred eighty days worth of data with the natural molybdenum sample were analyzed, and no such coincidence events were detected. Thus, it can be concluded that a proton background does not contribute to the $\beta\beta$ signal. Another potential source of background is neutrons, which could contribute via neutron capture in the $^{100}\text{Mo}(n, \gamma)$ reaction. The decay of ^{101}Mo yields some γ rays with energies very close to the ones of interest in the $\beta\beta$ decay of ^{100}Mo . However, this neutron-capture process should also produce other γ rays in coincidence with a 10^5 higher probability. Since these γ rays have not been observed in our experiment, this possible background is completely ruled out.

The present experimental method is incapable of distinguishing between $2\nu\beta\beta$ and $0\nu\beta\beta$ decay because the energy of the two electrons is not measured. In addition, the best present limit on the $0\nu\beta\beta$ decay of ^{100}Mo to the first 0^+ excited state of ^{100}Ru is not sufficiently stringent ($>6 \times 10^{20}$ yr [12]). Nevertheless, $\beta\beta$ transitions of ^{100}Mo to the ground state of ^{100}Ru indicate that our experiment observes the $2\nu\beta\beta$ mode instead of the neutrinoless one. The experimental limit on the $0\nu\beta\beta$ decay of ^{100}Mo to the 0^+ ground state of ^{100}Ru is $T_{1/2}^{0\nu} > 5.2 \times 10^{22}$ yr [13]. Taking into account the fact that the phase-space factor is much smaller for the transition to the excited state, one can

expect that the contribution of $0\nu\beta\beta$ events in our set of data is negligible. Thus, it is safe to conclude that we do indeed see the $2\nu\beta\beta$ decay of ^{100}Mo to the 0^+ excited state of ^{100}Ru . An additional confirmation of this conclusion can be seen in the quite good agreement between our experimental result and the theoretical predictions for this decay (see below).

One can compare the derived value with the theoretical predictions that were obtained by using QRPA-based models (5.4×10^{19} – 1.3×10^{20} yr [14], 2.1×10^{21} yr [15], and 10^{21} yr [16]) and pseudo-SU(3) models (1.5×10^{21} yr [17]). It should be mentioned that the present accuracy of theoretical predictions is directly related to the accuracy of nuclear-matrix-element calculations and usually is a factor of about 4 for the half-life (factor of about 2 for nuclear matrix elements). Thus, there is reasonable agreement between experimental and theoretical values of the half-life.

Recently, the half-life for the $2\nu\beta\beta(0^+ \rightarrow 0_1^+)$ transition of ^{100}Mo was estimated by using the so-called single-state-dominance hypothesis (SSDH) [18, 19] and a recent result for the electron-capture (EC) transition $^{100}\text{Tc} \rightarrow ^{100}\text{Mo}$ [20]: $T_{1/2}^{2\nu}(0^+ \rightarrow 0_1^+) = 4.45 \times 10^{20}$ yr [21] (with an accuracy of $\pm 50\%$ because of this accuracy of the EC transition [20]). If, in the future, the accuracy of the EC transition can be improved, then a comparison between experimental and estimated values will provide the possibility of checking the SSDH.

4. CONCLUSION

In summary, a new and independent confirmation of the $\beta\beta$ decay of ^{100}Mo to the first excited 0^+ state of ^{100}Ru has been obtained by using the novel method of $\gamma\gamma$ -coincidence detection above ground with HPGe detectors. Our result for the half-life of $T_{1/2} = [5.9_{-1.1}^{+1.7}(\text{stat.}) \pm 0.6(\text{syst.})] \times 10^{20}$ yr with respect to this decay is consistent with previous measurements [8, 11].

ACKNOWLEDGMENTS

This work was supported in part by the U.S. Department of Energy, Office of High Energy and Nuclear Physics, grant no. DE-FG02-97ER41033.

REFERENCES

1. M. Moe and P. Vogel, *Annu. Rev. Nucl. Part. Sci.* **44**, 247 (1994).
2. H. V. Klapdor-Kleingrothaus and A. Staudt, *Non-accelerator Particle Physics* (Institute of Physics Publ., Bristol, 1995).
3. J. Suhonen and O. Civitarese, *Phys. Rep.* **300**, 123 (1998).
4. A. Faessler and F. Šimkovic, *J. Phys. G* **24**, 2139 (1998).
5. M. Aunola and J. Suhonen, *Nucl. Phys. A* **602**, 133 (1996).
6. A. S. Barabash, *Pis'ma Zh. Éksp. Teor. Fiz.* **51**, 181 (1990) [*JETP Lett.* **51**, 207 (1990)].
7. A. S. Barabash, A. V. Kopylov, and V. I. Cherehovskiy, *Phys. Lett. B* **249**, 186 (1990).
8. A. S. Barabash *et al.*, *Phys. Lett. B* **345**, 408 (1995).
9. A. S. Barabash *et al.*, in *XXVI Rencontre de Moriond* (Editions Frontières, Gif-sur-Yvette, 1991), p. 77.
10. D. Blum *et al.*, *Phys. Lett. B* **275**, 506 (1992).
11. A. S. Barabash *et al.*, *Yad. Fiz.* **62**, 2211 (1999) [*Phys. At. Nucl.* **62**, 2039 (1999)].
12. D. Dassié *et al.*, *Phys. Rev. D* **51**, 2090 (1995).
13. H. Ejiri *et al.*, *Nucl. Phys. A* **611**, 85 (1996).
14. J. Suhonen, *Yad. Fiz.* **61**, 1286 (1998) [*Phys. At. Nucl.* **61**, 1186 (1998)].
15. S. Stoica and I. Mihut, *Nucl. Phys. A* **602**, 197 (1996).
16. A. Griffiths and P. Vogel, *Phys. Rev. C* **46**, 181 (1992).
17. J. G. Hirsch *et al.*, *Phys. Rev. C* **51**, 2252 (1995).
18. J. Abad *et al.*, *An. Fis., Ser. A* **80**, 9 (1984).
19. O. Civitarese and J. Suhonen, *Nucl. Phys. A* **653**, 321 (1999).
20. A. Garcia *et al.*, *Phys. Rev. C* **47**, 2910 (1993).
21. F. Šimkovic, P. Domin, and S. V. Semenov, in *Proceedings of International Workshop "NANPINO 2000;"* nucl-th/0006084.

Conference on Physics of Fundamental Interactions Experiment

Search for the Double-Beta Decay of ^{130}Te to Excited States in $^{130}\text{Xe}^*$

A. S. Barabash**, **F. Hubert¹⁾**, **Ph. Hubert¹⁾**, and **V. I. Umatov**

Institute of Theoretical and Experimental Physics, Bol'shaya Cheremushkinskaya ul. 25, Moscow, 117218 Russia

Received March 21, 2001

Abstract—Experimental limits on the half-lives with respect to the $(0\nu + 2\nu)$ double-beta decay of ^{130}Te to excited states in ^{130}Xe are obtained by using low-background HPGe detectors. At a 90% C.L., they are 1.6×10^{21} , 2.7×10^{21} , and 2.3×10^{21} yr for transitions to the 2_1^+ , 2_2^+ , and 0_1^+ levels, respectively.

© 2002 MAIK “Nauka/Interperiodica”.

1. INTRODUCTION

The main interest in double-beta decay is connected with the neutrinoless mode ($0\nu\beta\beta$) as a probe for physics beyond the Standard Model of electroweak interactions. Its existence is connected with fundamental aspects of particle physics—i.e., the lepton-number nonconservation, the existence and nature of the neutrino mass, the existence of right-handed currents in the electroweak interaction, the existence of a massless Goldstone boson, Majoron, supersymmetry, etc.

To date, only lower limits on the half-lives ($T_{1/2}^{0\nu}$) of various nuclei have been obtained experimentally. These limits are used to deduce upper limits on the Majorana neutrino mass, the right-handed-current admixture parameter, the Majoron–Majorana neutrino coupling constant, etc. (see, for instance, [1–4]). One particular source of uncertainty in the above analysis is the evaluation of nuclear matrix elements appearing in the theoretical expressions for these fundamental observables.

In connection with $0\nu\beta\beta$ decay, the detection of double-beta decay accompanied by the emission of two neutrinos ($2\nu\beta\beta$), which is an allowed process of second order in the Standard Model, enables an experimental determination of nuclear matrix elements involved in the double-beta-decay processes. This in turn leads to the development of theoretical schemes for nuclear-matrix-element calculations, in connection with both $2\nu\beta\beta$ decays and $0\nu\beta\beta$ decays. More precise calculations of nuclear matrix elements allow a more unambiguous extraction of the values of the relevant $0\nu\beta\beta$ observables mentioned above.

Double-beta decay can proceed through transitions to the ground state and to various excited states of the daughter nuclide. Studies of the latter transitions allow one to obtain supplementary information about $\beta\beta$ decay. Because of lower transition energies, the probabilities for $\beta\beta$ -decay transitions to excited states are substantially suppressed in relation to transitions to the ground state. But as was shown [5], by using low-background facilities utilizing HPGe detectors, $2\nu\beta\beta$ decay to the 0_1^+ level in the daughter nucleus can be detected for ^{100}Mo , ^{96}Zr , and ^{150}Nd . In this case, the energies involved in the $\beta\beta$ transitions are comparatively high (1903, 2202, and 2627 keV, respectively), and the expected half-lives are on the order of 10^{20} – 10^{21} yr. The required sensitivity was reached only for ^{100}Mo , and the transition was detected in three experiments [6–8] with a half-life lying within $(6\text{--}9) \times 10^{20}$ yr. Recently, additional isotopes, ^{82}Se , ^{130}Te , ^{116}Cd , and ^{76}Ge , also became of interest to studies of the $2\nu\beta\beta$ decay to the 0_1^+ level (for an overview, see [9]).

Theoretical estimates of the $2\nu\beta\beta$ decay to a 2^+ excited state revealed that, for a few nuclei (^{82}Se , ^{96}Zr , ^{100}Mo , ^{130}Te), the half-lives can be about 10^{22} – 10^{23} yr [4]. This would mean that the detection of such decays will become possible in the near future by using the present and new installations.

It is very important to note that, within models based on quasiparticle random-phase approximation, the behavior of nuclear matrix elements with the parameter g_{pp} is completely different for transitions to the ground and to excited (2^+ and 0^+) states [4, 10]. This is why the decay to excited states and the decay to the ground states may probe different aspects of the computational method. Therefore, searches for $\beta\beta$ transitions to excited states are of particular interest in itself.

*This article was submitted by the authors in English.

¹⁾Centre d'Etudes Nucléaires, IN2P3-CNRS et Université de Bordeaux, France.

**e-mail: alexander.barabash@itep.ru

Table 1. Information about TeO₂ powder measurements (sample gives the weight of the TeO₂ powder, HPGe is the volume of a Ge detector, η is the ¹³⁰Te content of a sample, and t is the time of counting)

Sample, g	HPGe, cm ³	η , %	t , h
721.4	400	89.4	567.2
711.0	380	89.4	1192.7
698.0	380	89.4	385.8
587.8	380	89.4	666.0
1004.2	400	34.49	475.4

In this article, we present the results of an experimental investigation into the $\beta\beta$ decay of ¹³⁰Te to the excited states in ¹³⁰Xe. The decay scheme for the ¹³⁰Te–¹³⁰I–¹³⁰Xe triplet is shown in Fig. 1. A search for $\beta\beta$ transitions of ¹³⁰Te to excited states in ¹³⁰Xe was carried out by using a germanium detector to seek γ -ray lines corresponding to the decay scheme.

2. EXPERIMENTAL

The experimental work has been performed in the Modane Underground Laboratory (depth of 4800 mwe). A set of TeO₂ powder samples with tellurium either enriched in ¹³⁰Te or natural was investigated by using two low-background HPGe detectors of volume 380 and 400 cm³. Both Ge spectrometers were composed of p -type crystals. For each HPGe detector, the cryostat, the endcap, and the main mechanical parts were made of very pure Al–Si alloy. The cryostat had a J -type geometry to shield the crystal from radioactive impurities in the Dewar. The passive shielding for each detector was similar and consisted of 4 cm of Roman time lead and 3–10 cm of OFHC copper inside 15 cm of ordinary lead. To remove ²²²Rn gas, one of the main sources of

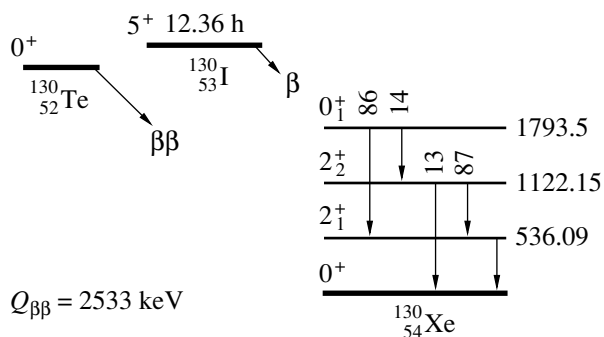


Fig. 1. Scheme of ¹³⁰Te decay. Energies of levels are given in keV, while relative intensities of γ rays are given in percent.

Table 2. Detection efficiencies (%) for γ rays from investigated excited states for each TeO₂ powder measurement

Sample, g	2 ₁ ⁺	2 ₂ ⁺		0 ₁ ⁺	
	536.1	536.1	586.1	536.1	1257.4
721.4	4.51	3.32	3.21	3.76	2.10
711.0	3.91	2.98	2.84	3.35	1.86
698.0	3.88	2.96	2.88	3.34	1.85
587.8	3.76	2.86	2.74	3.16	1.74
1004.2	3.81	2.89	2.80	3.23	1.90
$A(10^{21} \text{ yr})$	22.1	16.7	16.1	18.8	10.5

Note: Here, we present the weight of a TeO₂ sample, the parameters of excited states, and the energies of γ rays specified for each excited state. The last row shows quantities A (see main body of the text).

background, a special effort was made to minimize the free space near the detector. In addition, the passive shielding was enclosed in an aluminum box flushed with high-purity nitrogen.

The electronics used consisted of currently available spectrometric amplifiers and a 8192-channel ADC. The energy calibration was adjusted to cover the energy range from 50 keV to 3.5 MeV for all detectors. The energy resolution was 1.8–2.0 keV for the 1332-keV line of ⁶⁰Co. The electronics

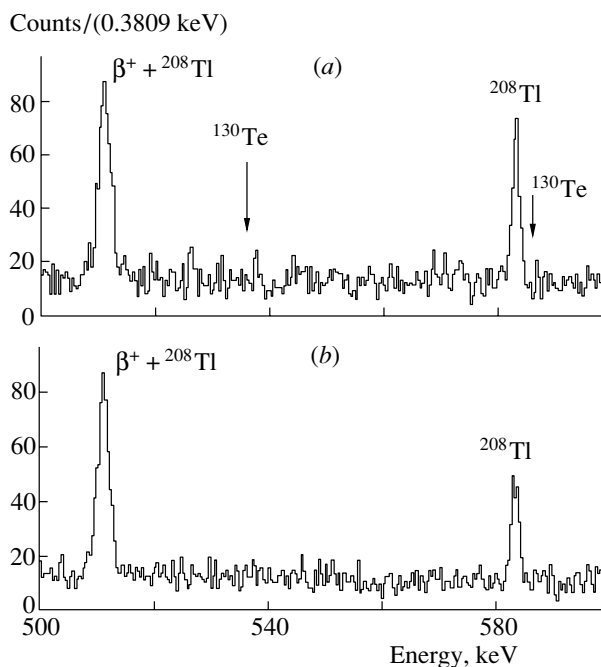


Fig. 2. (a) Total γ -ray spectrum in the energy range 500–600 keV and (b) background spectrum for the same time of measurement.

Table 3. Theoretical and experimental results for the $\beta\beta$ decay of ^{130}Te

Transition	$(T_{1/2}^{2\nu})_{\text{calc.}}$, yr [4]	$(T_{1/2}^{0\nu+2\nu})_{\text{exp.}}$, 10^{21} yr	
		our study	other studies
$0^+ \rightarrow 0_{\text{g.s.}}^+$	$2.6 \times 10^{20} - 2.7 \times 10^{21}$		0.8 ^a [11] 2.7 ^a [12]
$0^+ \rightarrow 2_1^+$	$3.0 \times 10^{22} - 2.8 \times 10^{24}$	> 1.6	> 2.8 [13] > 97 ^b [14]
$0^+ \rightarrow 2_2^+$	$2.0 \times 10^{25} - 1.0 \times 10^{28}$	> 2.7	—
$0^+ \rightarrow 0_1^+$	$5.1 \times 10^{22} - 1.39 \times 10^{23}$ ^c	> 2.3	> 25 ^b [14]

Note: All limits are given at a 90% C.L. (a) Geochemical experiment, (b) only the 0ν decay mode, and (c) corrected values (see main body of the text).

was stable during the experiment owing to constant conditions in the laboratory (temperature of 23°C, hygrometric degree of 50%). A daily check on the apparatus ensured that the counting rate was statistically constant.

The samples of TeO_2 powder were put into delrin Marinelli boxes surrounding the HPGe detector. Table 1 presents details of these measurements. The most intensive γ rays from the decay scheme (Fig. 1) were used for our analysis—i.e., the 536.1-keV γ ray for the 2_1^+ level, the 536.1-keV and the 586.1-keV γ ray for the 2_2^+ level, and the 536.1-keV and the 1257.4-keV γ ray for the 0_1^+ level. The detection efficiencies for photopeaks corresponding to the above γ rays are given in Table 2. The efficiencies were computed with the aid of the CERN Monte Carlo code GEANT 3.21. Special calibration measurements with radioactive sources and powders containing well-known ^{226}Ra activities confirmed that the accuracy of these efficiencies was about 10% for each detector.

3. ANALYSIS AND RESULTS

To analyze the $2\nu\beta\beta$ decay of ^{130}Te to excited states in ^{130}Xe , we considered the sum of all spectra. The contribution of the $\beta\beta$ decay of ^{130}Te to the peak corresponding to a specific excited state is given by

$$N_{\text{peak}} = \frac{\sum_i N_i t_i \varepsilon_i \ln 2}{T_{1/2}} = \frac{A}{T_{1/2}},$$

where summation is performed over all measurements, N_i is the number of ^{130}Te atoms to expose, t_i is the counting time, ε_i is the peak-detection efficiency, and $T_{1/2}$ is the half-life with respect to the transition being investigated. The quantities A , which characterize the contributions to the peaks under study, are given in Table 2.

The total spectra for two specific energy ranges and the corresponding background spectra (for 3287 h) are shown in Figs. 2a and 3a and in Figs. 2b and 3b, respectively. As can be seen, there are no statistically significant peaks at the points in question. The lower half-life limits reported in Table 3 were calculated by using the likelihood-function technique described in [15, 16]. Available data on the $\beta\beta$ decay of ^{130}Te from other experimental studies and theoretical estimates are also presented in Table 3.

Our limits on $\beta\beta$ transitions of ^{130}Te to excited states of a daughter nucleus are valid for the 0ν and 2ν decay modes. As one can see from Table 3, our results

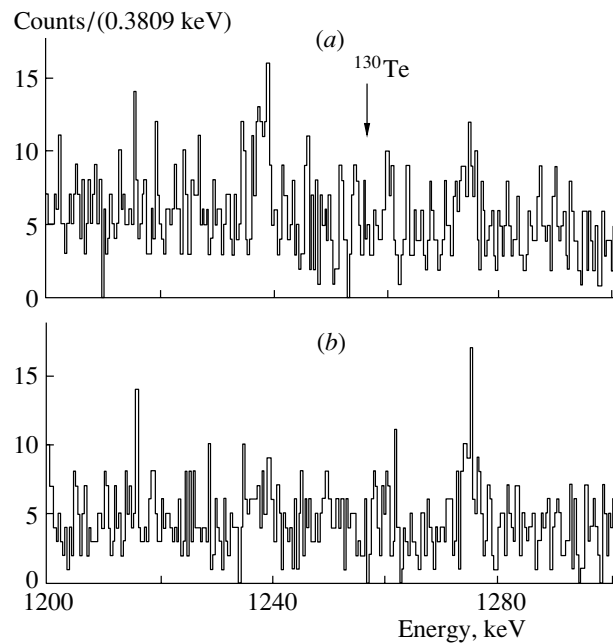


Fig. 3. Total γ -ray spectrum in the energy range 1200–1300 keV (a). Background spectrum for the same time of measurement is shown below (b).

on the transitions to the 2_2^+ (0ν and 2ν modes) and 0_1^+ (2ν mode) levels of ^{130}Xe were obtained for the first time. Here, it is worth mentioning that the theoretical half-lives for $2\nu\beta\beta$ decay to the 0_1^+ level from [4] are less than those in Table 3 by a factor of about 200. This is related to the error value of $4.6 \times 10^{-20} \text{ yr}^{-1}$ in the phase-space factor as given in [4]. The corrected value is $2.35 \times 10^{-22} \text{ yr}^{-1}$ [17]. Using the new phase-space factor and the nuclear matrix elements from [4], we recalculated the half-lives and presented them in Table 3.

The sensitivity of such experiments could be still increased to about 10^{23} yr by using larger Ge crystals ($800\text{--}1000 \text{ cm}^3$) with a lower background and by investigating $5\text{--}10 \text{ kg}$ of ^{130}Te for a few years. In that case, there is the possibility of detecting the $2\nu\beta\beta$ decay of ^{130}Te to the 0_1^+ level and, maybe, to the 2_1^+ level of ^{130}Xe .

ACKNOWLEDGMENTS

We are grateful to the Modane Underground Laboratory staff for their technical assistance in running the experiment and to Prof. Jouni Suhonen (University of Jyväskylä, Finland) for a stimulating discussion on phase-space factors. We are also indebted to Michael Hornish (Duke University, USA) for his comments.

REFERENCES

1. H. V. Klapdor-Kleingrothaus, Nucl. Phys. B (Proc. Suppl.) **77**, 357 (1999).
2. A. Faessler and F. Šimcovic, J. Phys. G **24**, 2139 (1998).
3. P. Vogel, nucl-th/0005020.
4. J. Suhonen and O. Civitarese, Phys. Rep. **300**, 123 (1998).
5. A. S. Barabash, Pis'ma Zh. Éksp. Teor. Fiz. **51**, 181 (1990) [JETP Lett. **51**, 207 (1990)].
6. A. S. Barabash *et al.*, Phys. Lett. B **345**, 408 (1995).
7. A. S. Barabash *et al.*, Yad. Fiz. **62**, 2211 (1999) [Phys. At. Nucl. **62**, 2039 (1999)].
8. L. De Braekeleer *et al.*, Yad. Fiz. **63**, 1288 (2000) [Phys. At. Nucl. **63**, 1214 (2000)].
9. A. S. Barabash, Czech. J. Phys. **50**, 447 (2000).
10. M. Aunola and J. Suhonen, Nucl. Phys. A **602**, 133 (1996).
11. O. K. Manuel, J. Phys. G **17**, 221 (1991).
12. T. Bernatowicz *et al.*, Phys. Rev. C **47**, 806 (1993).
13. E. Bellotti *et al.*, Europhys. Lett. **3**, 889 (1987).
14. A. Alessandrello *et al.*, Phys. Lett. B **486**, 13 (2000).
15. A. S. Barabash *et al.*, J. Phys. G **22**, 487 (1996).
16. A. S. Barabash *et al.*, Nucl. Phys. A **604**, 115 (1996).
17. J. Suhonen, private communication.

Conference on Physics of Fundamental Interactions Experiment

Research Program for the Nuclotron

A. I. Malakhov*

Joint Institute for Nuclear Research, Dubna, Moscow oblast, 141980 Russia

Received March 21, 2001; in final form, June 26, 2001

Abstract—Information is given about experiments at the accelerator complex of the Laboratory of High Energies (LHE) at the Joint Institute for Nuclear Research (JINR, Dubna) and about projects for this facility. The projects were developed by collaborations, groups, and divisions of the LHE, as well as of other JINR laboratories and of institutes from the countries that are JINR members and from some other countries. © 2002 MAIK “Nauka/Interperiodica”.

INTRODUCTION

The research program of the Laboratory of High Energies (LHE) at the Joint Institute for Nuclear Research (JINR, Dubna) for its own accelerator facility is now focused on investigations into the interactions of relativistic nuclei in the energy range from a few hundred MeV to a few GeV per nucleon. These investigations are aimed at seeking manifestations of quark–gluon degrees of freedom in nuclei and asymptotic laws for nuclear matter at high collision energies and at establishing the spin structure of extremely light nuclei [1]. Experiments along these lines are performed with the aid of a synchrophasotron–nuclotron accelerator complex.

In recent years, the implementation of the research program in question has been relying on the nuclotron to an ever greater extent—as a matter of fact, the synchrophasotron is used only in investigations with a polarized deuteron beam. In the near future, it is planned to obtain a polarized beam at the nuclotron as well.

1. DEVELOPMENT OF THE ACCELERATOR COMPLEX

The LHE accelerator complex is the main device for generating protons, polarized deuterons (as well as neutrons and protons), and multiply charged ions in the energy region extending to 6 GeV per nucleon. The layout of the JINR LHE accelerator complex is displayed in Fig. 1.

The nuclotron was created on the basis of a unique technology of superconducting magnetic systems that were proposed and investigated in the LHE [2].

Before 1999, we used only the internal beam of the nuclotron for physical experiments. At the end

of 1999, an extracted beam of the nuclotron was obtained with the aid of a slow-beam-extraction system developed on the basis of superconducting units. Some parameters of synchrophasotron and nuclotron beams are listed in the table.

The main lines of development of the nuclotron complex within the next few years are the following: (i) the completion of work devoted to transporting the beam extracted from the nuclotron to the large experimental hall housing the experimental facilities to be used; (ii) the creation of the injecting complex (this involves manufacturing sources of ions, partly reconstructing the linear accelerator, and evolving a booster); and (iii) the production of cryogenic power-supply units, as well as cryogenic systems for diagnostics and control.

There are also a program of the first experiments with an extracted beam of the nuclotron and a long-term program of investigations. Two facilities (STRELA and SKAN-2) were used for physics investigations in the first runs of the nuclotron with the extracted beam. Concurrently, experiments in the internal beam of the nuclotron are being continued.

1.1. First Experiments at the Nuclotron

1.1.1. First experiments with an extracted beam of the nuclotron

The STRELA experiment (see Fig. 2) is aimed at studying the spin-dependent component of the nucleon scattering amplitude in the charge-exchange process $np \rightarrow pn$ in a deuteron beam extracted from the nuclotron. It is planned to measure the cross section for the production of two protons at a low momentum transfer in dp interactions at primary deuteron momenta in the range between 3.0 and 4.0 GeV/c.

*e-mail: malakhov@lhe.jinr.ru

Some parameters of synchrophasotron and nuclotron beams

Beam	Intensity, particle/spill			
	Synchro- phasotron	Nuclotron		
		available	planned	
			after an upgrade of the sources	with a booster
p	4×10^{12}	2×10^{10}	10^{11}	10^{13}
d	10^{12}	2×10^{10}	5×10^{10}	10^{13}
${}^4\text{He}$	5×10^{10}	8×10^8	5×10^9	2×10^{12}
${}^7\text{Li}$	2×10^9		2×10^{10}	5×10^{12}
${}^{12}\text{C}$	10^9	10^8	7×10^9	2×10^{12}
${}^{20}\text{Ne}$	10^4		10^8	5×10^9
${}^{24}\text{Mg}$	5×10^6	4×10^6	3×10^8	5×10^{11}
${}^{32}\text{S}$	10^3		10^8	10^{10}
${}^{40}\text{Ar}$			3×10^7	2×10^9
${}^{56}\text{Fe}$				10^{11}
${}^{84}\text{Kr}$		10^3	2×10^7	5×10^8
${}^{96}\text{Mo}$				10^{10}
${}^{131}\text{Xe}$			10^7	2×10^8
${}^{181}\text{Ta}$				10^8
${}^{209}\text{Bi}$			3×10^6	10^8
${}^{238}\text{U}$				10^8
n	10^{10}		10^8	10^9
$n \uparrow$	10^6		10^6	5×10^7
$d \uparrow$	2×10^9		10^9	5×10^{10}
t	10^9		10^6	10^{10}
Energy (A GeV)	4.5	5.2	6.0	

The possibility of obtaining additional information about the amplitude of the elementary charge-exchange reaction $np \rightarrow pn$ with the aid of the charge-exchange process $dp \rightarrow (pp)n$ from experiments with unpolarized deuterons was indicated by Migdal and Pomeranchuk [3, 4].

Within the impulse approximation, the charge-exchange process $np \rightarrow pn$ and the reaction $dp \rightarrow (pp)n$ —that is, charge exchange on a deuteron (see Fig. 3), which is the simplest nucleus—represent the simplest version of these two processes. In the first case, both spin orientations are allowed, whereas, in the second case, the reaction at a small scattering angle (the two protons move in the forward direction at a low relative momentum) can proceed, in accordance

with the Pauli exclusion principle, only if the spin of the scattered proton is flipped. At zero momentum transfer, the differential cross section for the reaction $dp \rightarrow (pp)n$ is determined by the spin-flip part of the amplitude for the charge-exchange process $np \rightarrow pn$.

The SKAN-2 facility is intended for studying the proton-formation length in $d + A_T \rightarrow p_1(0^\circ) + p_2(0^\circ) + \dots$ reactions.

Information from the STRELA and SKAN-2 facilities, which is now being analyzed, was obtained in the nuclotron run of March 2000 with an extracted deuteron beam. Preliminary results concerning the separation of two-proton and one-proton events at the STRELA facility is presented in Fig. 4.

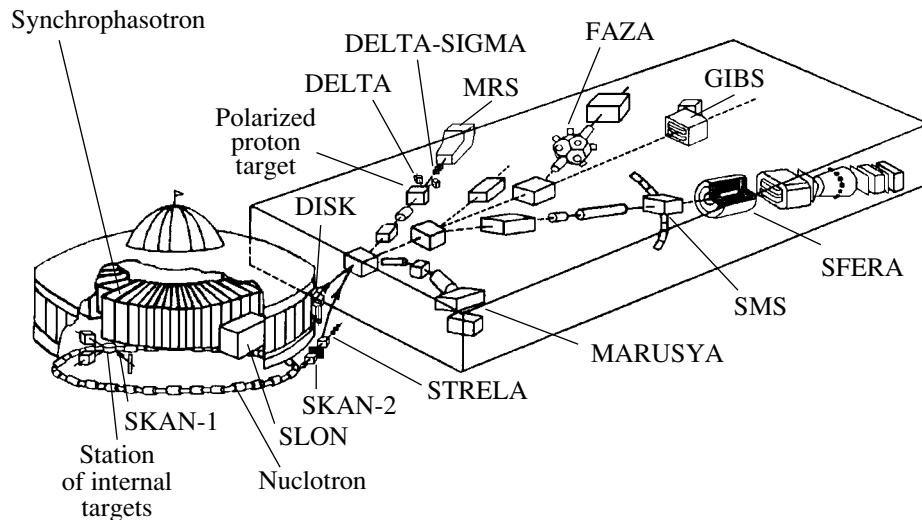


Fig. 1. Layout of the JINR LHE accelerator complex.

1.1.2. Experiments in an internal beam

The fragmentation of the target into two cumulative protons is now being studied with the aid of the SKAN-1 facility in the internal beam of the nuclotron (Fig. 5).

The experiment is aimed at measuring the transverse dimensions of the region of nucleus–nucleus interactions. Use is being made of the method of measuring correlations between cumulative protons emitted with low relative momenta. Correlations between protons emitted into the angular interval between 106° and 112° in the laboratory frame are being studied in $d + C \rightarrow p + p + \dots$ and $d + Cu \rightarrow p + p + \dots$ ($p_d = 2 A$ GeV) reactions.

These measurements yield approximately equal radii for dC and dCu interactions: $r_{dC} = 3.0^{+0.5}_{-0.4}$ fm and $r_{dCu} = 2.6^{+0.8}_{-0.7}$ fm [5].

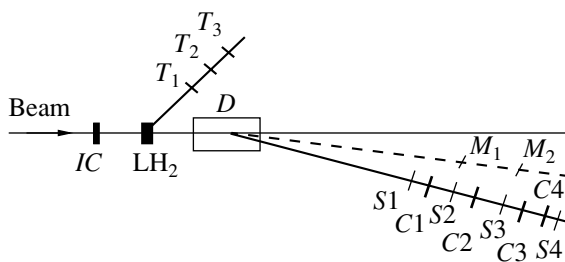


Fig. 2. Layout of the STRELA facility: (IC) ionization chamber, (LH₂) liquid-hydrogen target, (D) analyzing magnet, (T₁–T₃, M₁, M₂) scintillation monitors, (C1–C4) Cherenkov counters, and (S1–S4) scintillation counters.

These investigations will be continued with different projectiles and targets.

A group from the MARUSYA collaboration has begun studying the yield of secondary fragments from the interaction of the internal beam of the nuclotron with heavy targets. By using a thin semiconductor detector, this group obtained a good separation of secondary fragments of very low energies between 2 and 25 MeV from $d + Au$ interactions at a deuteron energy of 1.044 GeV (see Fig. 6).

These data are now under analysis and will be used to study the effect of the total disintegration of nuclei. This is facilitated by a low energy of secondary fragments.

1.2. Program of Long-Term Investigations at the Nuclotron

Presently, there are 12 facilities for fundamental investigations at the nuclotron. These are the

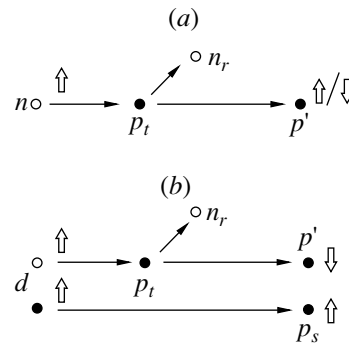


Fig. 3. Elementary charge-exchange reactions (a) $np \rightarrow pn$ and (b) $dp \rightarrow (pp)n$. Double arrows indicate the directions of the nucleon spins.

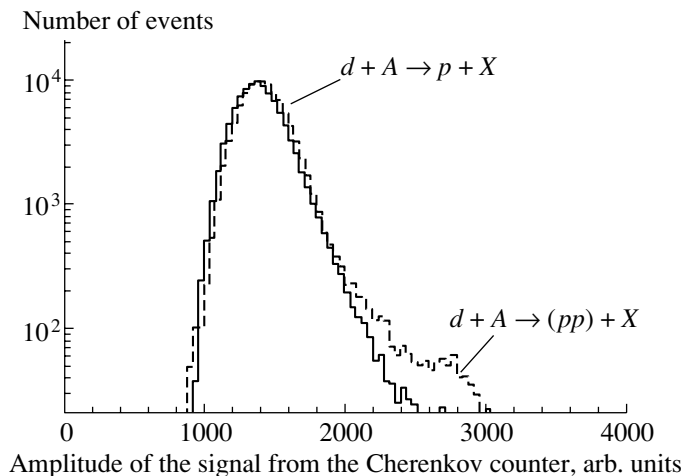


Fig. 4. Preliminary results of the STRELA experiment aimed at separating two-proton and one-proton events ($p_d = 4.5 \text{ GeV}/c$).

SFERA, GIBS, FAZA, DELTA-SIGMA, DELTA, DISK, SMS, MARUSYA, SKAN-1, SKAN-2, STRELA, and SLON facilities. It is also planned to use facilities based on the Medium Resolution Spectrometer (MRS) from Los Alamos (USA).

The research program for these facilities is briefly surveyed in the present section.

1.2.1. Experiments with relativistic nuclei

SFERA project. The main objective of the SFERA project (Fig. 7) is to study the fragmentation of relativistic nuclei in nearly 4π geometry.

With the forward detector of the SFERA facility, some new results were obtained at the synchrophasotron. For example, the inclusive cross sections for deuteron fragmentation into cumulative π^- mesons on a nuclear target have been measured, and the relevant cross section has been investigated as a function of the atomic mass A of the target nucleus. The best description of these data was obtained under the assumption that the pion-formation length is $l_\pi = 3 \pm 1 \text{ fm}$ [6] (Fig. 8).

The research program for the SFERA facility includes (i) investigation of the multiparticle production of cumulative particles in 4π geometry, (ii) investigation of nuclear excitations in charge-exchange reactions, (iii) investigation of formation of η nuclei, and (iv) investigation of the tensor analyzing power for the production of cumulative hadrons.

GIBS project. The GIBS facility is a magnetic spectrometer based on a streamer chamber of dimensions $1.9 \times 0.8 \times 0.6 \text{ m}$. The GIBS collaboration obtained interesting results at the synchrophasotron.

One of these concerns the expansion of the volume from which narrow dipions are emitted in MgMg interactions. Podgoretskiĭ proposed an interference method for measuring the velocity and dimensions of the source [7]. This method makes it possible to obtain a direct piece of experimental evidence for the time dependence of the pion-generation volume. This proof was first obtained with the GIBS facility at the LHE for central MgMg interactions at $4.4 \text{ GeV}/c$ [8]. From relevant experimental data, it can be seen that pions from different sections of the kinematical spectrum are emitted from different source elements moving relative to one another (see Fig. 9).

The GIBS collaboration plans to study, at the nuclotron, the ($t, {}^3\text{He}$) charge-exchange reaction on carbon and magnesium by using a tritium beam of momentum in the range between 2.2 and $3.0 A \text{ GeV}/c$.

Another experiment will be devoted to studying the production of hypernuclei with momenta of a few GeV/c —this is possible because hypernuclei decay within distances of 20 to 30 cm from the production vertex. Hypernuclear interactions with various absorbers will be studied in this way. In the case of the hypertriton, the method makes it possible to estimate the binding energy of the Λ particle involved.

FAZA project. The objective of this project is to study the mechanism of nuclear multifragmentation occurring in nucleus–nucleus interactions at intermediate and high energies.

Some experiments have been performed with proton and alpha-particle beams of the synchrophasotron by using the FAZA spectrometer, which is characterized by a 4π coverage. Among the results obtained, the main one is the following: a cold spectator of

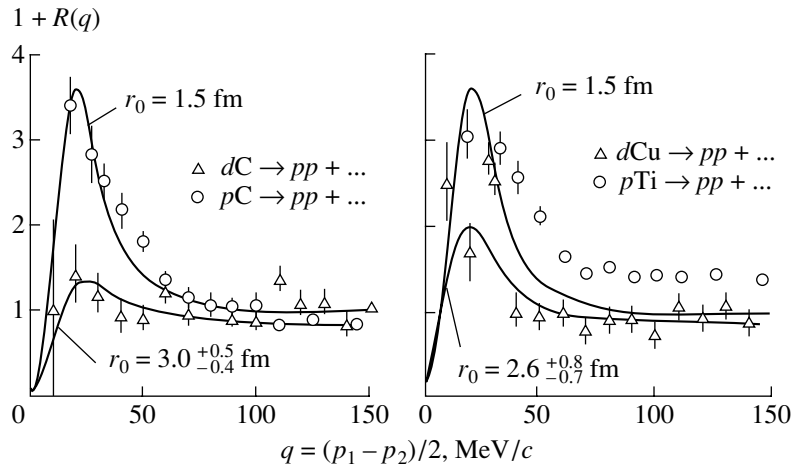


Fig. 5. Correlation function for cumulative protons emitted with a low relative momentum q for (left panel) dC and (right panel) dCu interactions at $E/A = 2$ GeV for $\theta = 109^\circ$.

the target expands prior to emitting fragments. As a result, its density appears to be about one-third of a normal density [9]. This effect can be explained as an observation of a liquid–gas phase transition in nuclear matter (see Fig. 10).

The research program of the FAZA collaboration at the nuclotron is aimed at pursuing further investigations into the mechanism of fragment emission in nonsymmetric nucleus–nucleus collisions. From these investigations, one would expect the following important results: new data on the time of decay of the systems being studied as a function of the excitation energy and the mass of the projectile nucleus and data on the evolution of the decay mechanism from a purely thermal multifragmentation to a more intricate mechanism as the projectile mass increases.

MARUSYA project. The project MARUSYA is aimed at studying the transition regime corresponding to the situation where nucleonic degrees of freedom give way to quark–gluon degrees of freedom in nuclei. This will be done by exploring hadron production in relativistic nuclear collisions. Presently, the facility is fully prepared for operation in an extracted beam of the nuclotron (see Fig. 11).

SMS project. The project is devoted to studying leading particles from proton–nucleus interactions by using the experimental facility referred to as the Scintillation Magnetic Spectrometer (SMS) and developed at Moscow State University. The objective is to reveal the mechanism of strong interaction in the energy region extending up to 10 GeV. The facility represents a one-arm magnetic spectrometer whose spectrometric component has changeable geometry [10].

1.2.2. Experiments with polarized beams

Investigation of polarization effects in collisions of relativistic nuclei at the SFERA facility.

The main objective of this project is to study the spin structure of the deuteron at short internucleon distances by using hadronic probes and spin effects in hadron scattering at an energy of about a few GeV.

The tensor analyzing power A_{yy} for cumulative pion production in $d\uparrow + {}^{12}\text{C} \rightarrow \pi^- (0, 135, 178 \text{ mrad}) + \dots$ reactions was measured with the SFERA facility in a beam of deuterons having a tensor polarization and coming from a synchrotron. The experiment was focused on a cumulative

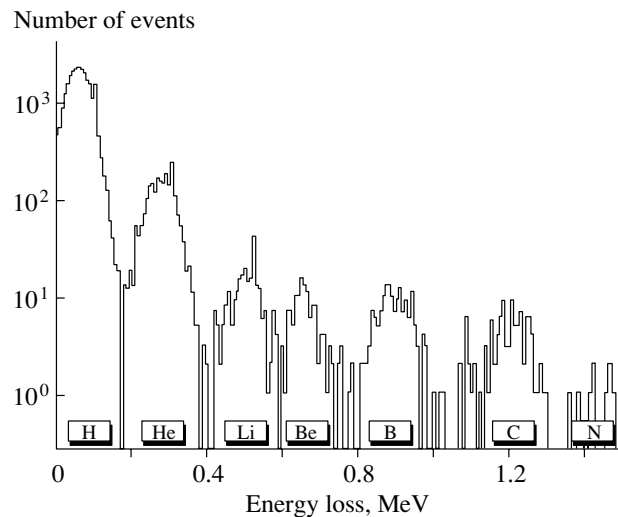


Fig. 6. Separation of secondary fragments for $d + Au$ interactions at a deuteron energy of 1.044 GeV.

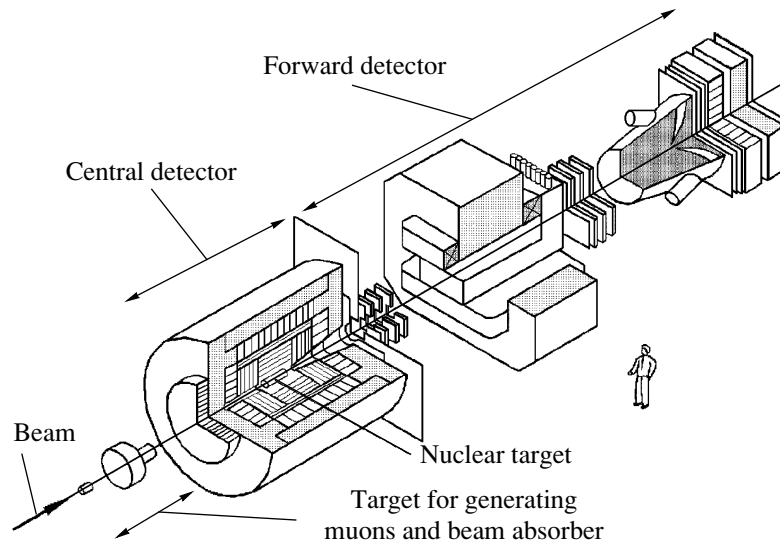


Fig. 7. Layout of the SFERA facility.

production of pions that are formed beyond the kinematics of nucleon–nucleon collisions (see Fig. 12).

The measured values of A_{yy} do not comply with the results of our calculations within the impulse approximation that were based on the $NN \rightarrow \pi NN$ transition and which were performed with allowance for the internal motion of nucleons in the deuteron [11].

The investigations will be continued at the nuclotron as soon as a polarized beam of sufficient intensity is obtained.

DELTA-SIGMA project. New results for the np -spin-dependent difference of the total cross sections, $\Delta\sigma_L(np)$, at kinetic energies of the neutron beam

between 1.2 and 3.4 GeV (Fig. 13) were obtained at the DELTA-SIGMA facility.

A quasimonochromatic beam of neutrons was obtained from accelerated deuterons that were extracted

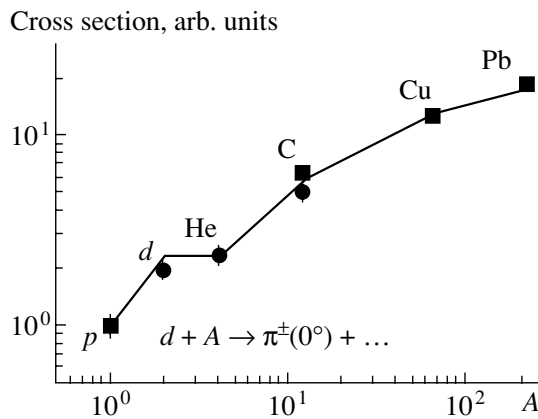


Fig. 8. Cross section for the production of cumulative pions as a function of the atomic number A of target nuclei ($0.9 < x_c < 1.7$).

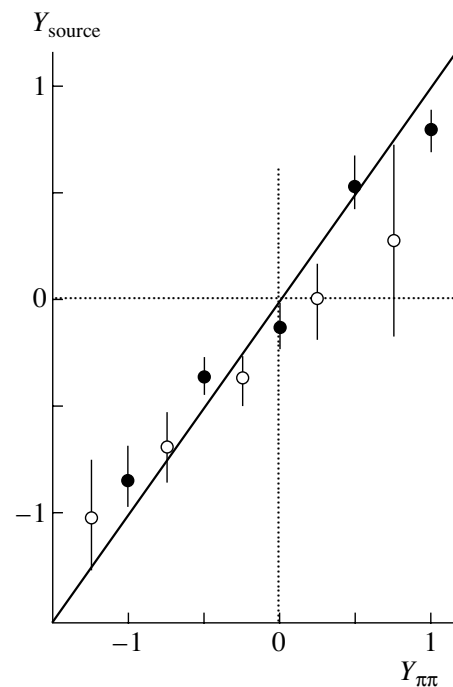


Fig. 9. Correlation between the rapidities of the elements of the source emitting pions, Y_{source} , and the rapidities of dipions, $Y_{\pi\pi}$, in (open circles) the longitudinal and (closed circles) the transverse direction with respect to the reaction axis in the rest frame of the $MgMg$ colliding system.

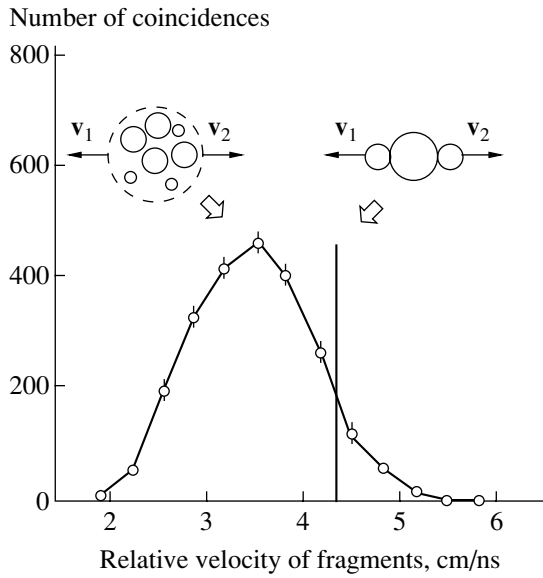


Fig. 10. Distribution of the relative velocities of coinciding fragments in α + Au interactions according to the measurements at correlation angles in the range 150° – 180° . The vertical straight-line segment indicates the expected position of the maximum for the case where fragments are emitted from the nuclear surface. The experimental distribution is shifted toward smaller velocities that correspond to the volume distribution for an expanded system.

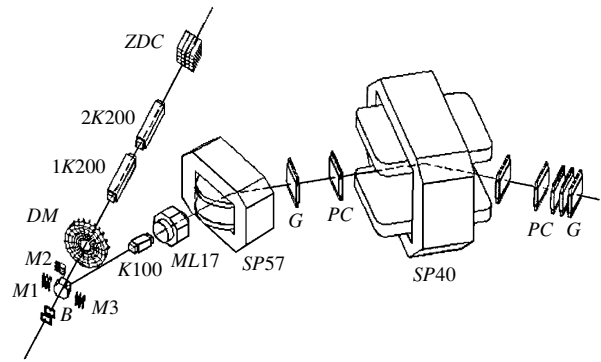


Fig. 11. Layout of the MARUSYA facility: (M1–M3) beam-monitoring system, (1K200, 2K200, K100, ML17) magnetic lenses, (SP57, SP40) dipole magnets, (B) system surrounding the target, (PC) proportional chambers, (G) scintillation hodoscope, (DM) multiplicity detector, and (ZDC) hadronic calorimeter.

from the synchrotron and which had a vector polarization. The neutrons passed through a large polarized proton beam. The quantity $\Delta\sigma_L(np)$ was measured as the difference of the total np cross sections for parallel and antiparallel polarizations of the beam and the target. A fast decrease in $\Delta\sigma_L(np)$ with increasing energy was observed above 1 GeV [12].

In order to complete measurements concerning the energy dependence of $\Delta\sigma_L(np)$, it is necessary to measure this quantity at 1.4, 1.6, 2.0, and 3.17 GeV. It is also necessary to measure $\Delta\sigma_T(np)$ for the case of transverse polarizations of the neutron beam and target protons. It is planned to continue these experiments at the nuclotron.

MRS project. It is planned to use the medium resolution spectrometer (MRS) from Los Alamos (USA) at our accelerator complex. This became possible after the agreement of scientific cooperation between the Los Alamos National Laboratory, the Institute for Nuclear Research (Russian Academy of Sciences), and the Joint Institute for Nuclear Research was signed. The relevant research program includes (i) investigation of spin effects in multiparticle systems, (ii) investigation of the strange content of the nucleon, and (iii) investigation of the production of cumulative particles by using a polarized deuteron beam.

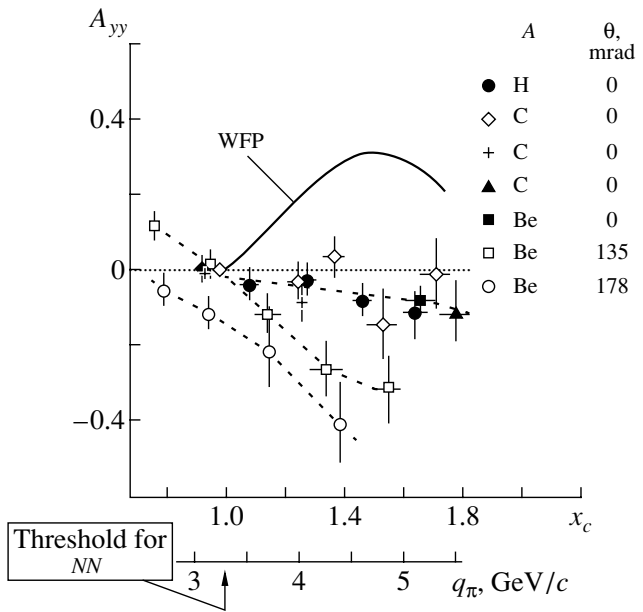


Fig. 12. Tensor analyzing power A_{yy} as a function of the cumulative number x_c (or the pion momentum q_π) for $d\uparrow(4.5 A \text{ GeV}/c) + A \rightarrow \pi^-(0, 135, 178 \text{ mrad}) + \dots$ reactions (WFP is the wave function for the Paris potential).

1.2.3. Investigation of asymptotic laws in relativistic nuclear physics

Principles of symmetry and similarity were used to obtain an analytic expression for the inclusive cross section for the production of particles, nuclear fragments, and antinuclei in relativistic nuclear collisions

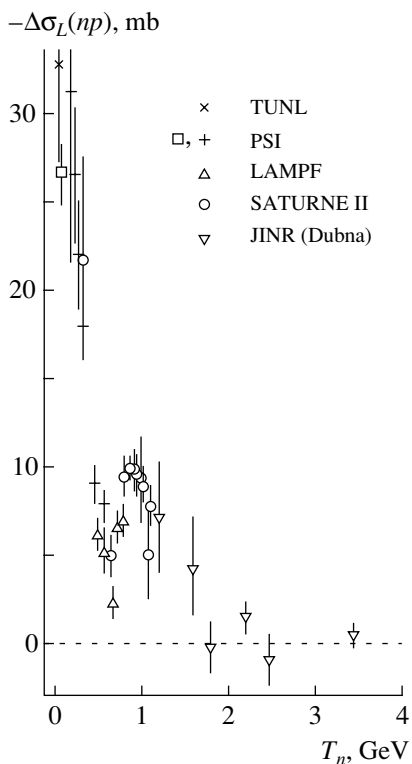


Fig. 13. Energy dependence of $\Delta\sigma_L(np)$.

in the central rapidity region ($y = 0$). The results are in agreement with available experimental data. It is shown that the effective number of nucleons that take part in nuclear interactions decreases with increasing energy and that the cross section tends to a constant that takes identical values for particles and for antiparticles. An analysis of the results obtained makes it possible to predict the asymptotic behavior of the cross section for the production of particles, nuclear fragments, and antinuclei [13, 14]. One of such predictions in the region extending from the energies of the accelerator complex in Dubna to the energies of the LHC at CERN is displayed in Fig. 14.

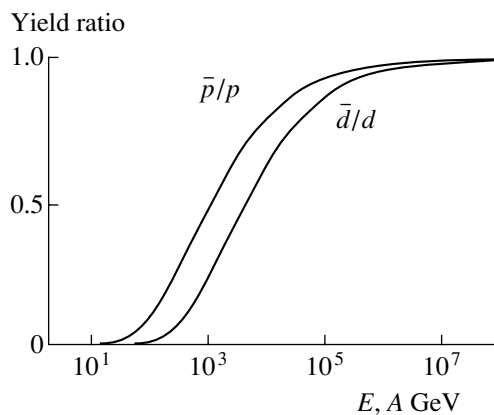


Fig. 14. Predicted ratios of the yields of particles and antiparticles in nucleus–nucleus interactions versus the laboratory collision energy.

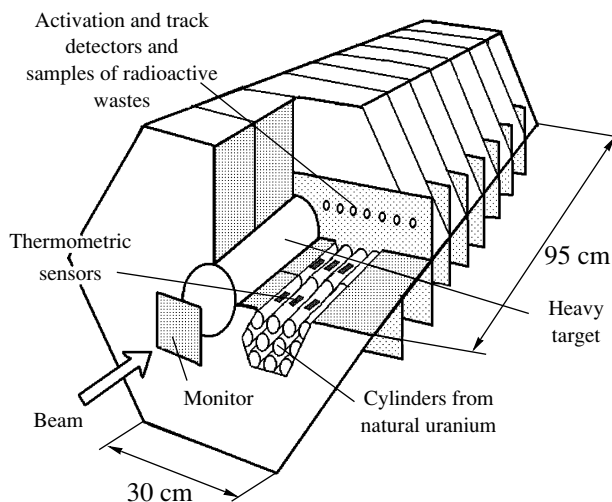


Fig. 15. Layout of the facility developed within the ENERGY–TRANSMUTATION project for studying various aspects of the electronuclear method for the generation of energy and for the transmutation of radioactive wastes.

2. APPLIED INVESTIGATIONS

The synchrotron was employed for applied investigations that will be continued at the nuclotron with heavier ions.

These investigations include the following lines: (i) radiobiology and cosmic medicine [15], (ii) the effect of nuclear beams on microelectronics components, (iii) transmutation of radioactive wastes [16], (iv) problems associated with the electronuclear method for the generation of energy (Fig. 15) [17], and the use of a carbon beam for cancer therapy.

3. CONCLUSION

A vast program of investigations with relativistic nuclei, polarized deuterons, and polarized neutrons has been prepared and is being implemented at the Laboratory of High Energies at JINR. Physicists from Russia and from other countries that are both JINR members and guests are actively participating in the implementation of this program. New prospects for investigations into the realms of relativistic nuclear physics are being unveiled in connection with the creation of particle and ion beams extracted from the nuclotron.

ACKNOWLEDGMENTS

I am grateful to heads of the projects at the accelerator complex of the Laboratory of High Energy Physics at JINR for placing relevant information at my disposal.

This work was supported by the Russian Foundation for Basic Research (project nos. 00-02-16528a, 00-02-16580, and 00-15-96737).

REFERENCES

1. *Research Program of the Laboratory of High Energies, 99-266*, Ed. by A. M. Baldin *et al.* (Dubna, 1999).
2. A. D. Kovalenko, in *Proceedings of the International Symposium "The 50th Anniversary of the Discovery of Phase Stability Principle," Dubna, 1994*, Ed. by A. M. Baldin *et al.* (Dubna, 1996), p. 44.
3. A. B. Migdal, *Zh. Éksp. Teor. Fiz.* **28**, 3 (1955) [*Sov. Phys. JETP* **1**, 2 (1955)].
4. I. Ya. Pomeranchuk, *Dokl. Akad. Nauk SSSR* **78**, 249 (1951).
5. Yu. S. Anisimov *et al.*, *JINR Rapid Commun.*, No. 5(91)-98, 25 (1998).
6. Yu. S. Anisimov *et al.*, *Yad. Fiz.* **60**, 1070 (1997) [*Phys. At. Nucl.* **60**, 957 (1997)].
7. M. I. Podgoretskiĭ, *Fiz. Élem. Chastits At. Yadra* **20**, 628 (1989) [*Sov. J. Part. Nucl.* **20**, 266 (1989)].
8. M. Kh. Anikina *et al.*, *Phys. Lett. B* **397**, 30 (1997).
9. V. A. Karnaukhov, Preprint No. P1-99-193, OIYaF (Joint Inst. for Nuclear Research, Dubna, 1999).
10. L. I. Belzer *et al.*, Preprint No. P1-87-591, OIYaF (Joint Inst. for Nuclear Research, Dubna, 1987).
11. S. Afanasiev *et al.*, *Phys. Lett. B* **445**, 14 (1998).
12. V. I. Sharov *et al.*, *Eur. Phys. J. C* **13**, 255 (2000).
13. A. M. Baldin and A. I. Malakhov, *JINR Rapid Commun.*, No. 1(87)-98, 5 (1998).
14. A. I. Malakhov, in *Proceedings of the 29th International Conference on High Energy Physics, Vancouver, Canada, 1998*, Ed. by Alan Astbury *et al.* (World Sci., Singapore, 1998), Vol. II, p. 1497.
15. G. N. Timoshenko *et al.*, Preprint No. E16-99-47, OIYaF (Joint Inst. for Nuclear Research, Dubna, 1999).
16. R. Brandt, Preprint No. E1-99-251, OIYaF (Joint Inst. for Nuclear Research, Dubna, 1999).
17. Ts. Tumendelger *et al.*, Preprint No. P1-99-247, OIYaF (Joint Inst. for Nuclear Research, Dubna, 1999).

Translated by A. Isaakyan

Conference on Physics of Fundamental Interactions Experiment

Polarization Experiments with the SPIN Setup at the ITEP Synchrotron

I. G. Alekseev, P. E. Budkovsky, V. P. Kanavets*, L. I. Koroleva, B. V. Morozov,
V. M. Nesterov, V. V. Ryltsov, D. N. Svirida, A. D. Sulimov, V. V. Zhurkin,
Yu. A. Beloglazov¹⁾, A. I. Kovalev¹⁾, S. P. Kruglov¹⁾, D. V. Novinsky¹⁾, V. A. Shchedrov¹⁾,
V. V. Sumachev¹⁾, V. Yu. Trautman¹⁾, N. A. Bazhanov²⁾, and E. I. Bunyatova²⁾

*Institute of Theoretical and Experimental Physics,
Bol'shaya Chermushkinskaya ul. 25, Moscow, 117218 Russia*

Received March 21, 2001

Abstract—New experimental data on the spin-rotation parameters A and R measured for elastic $\pi^\pm p$ scattering in the resonance region and on the asymmetry in pC scattering at primary momenta in the range 1.35–2.02 GeV/ c , as well as in quasielastic proton scattering on nuclei in the same momentum range, are summarized. All these data were recently obtained by using the proton synchrotron installed at the Institute of Theoretical and Experimental Physics (ITEP, Moscow). The spectrum and features of seven isospin-3/2 baryon resonances that form a peak in the total cross section at a c.m. energy of 1.9 GeV are analyzed on the basis of new data on the parameters A and R , and the results of this analysis are presented. The experiments surveyed in this article were performed by a collaboration of researchers from ITEP and the Petersburg Nuclear Physics Institute (PNPI, Gatchina), the ITEP–PNPI collaboration.

© 2002 MAIK “Nauka/Interperiodica”.

1. INTRODUCTION

In recent years, experiments at the SPIN facility that were devoted to measuring the spin-rotation parameters in elastic pion–proton scattering at energies in the resonance region, as well as allied experiments measuring the analyzing power in proton–carbon scattering, have been implemented by a collaboration that includes experimentalists from the Institute of Theoretical and Experimental Physics (ITEP, Moscow) and the Petersburg Nuclear Physics Institute (PNPI, Gatchina) and which is referred to in the following as the ITEP–PNPI collaboration. The main objective of these studies was to deduce information necessary for unambiguously reconstructing amplitudes for pion–nucleon scattering and, hence, the undistorted spectrum and features of baryon resonance consisting of light quarks.

The interval of primary momenta accessible to the SPIN facility is 0.8–2.1 GeV/ c . According to the Particle Data Group (PDG) [1], about 65% of the resonances known to date are concentrated in this region; also, this is the region where the total and elastic-scattering cross sections as functions of

energies display peaks at 1.7 GeV (π^-p), 1.9 GeV (π^+p), and 2.2 GeV (π^+p) in the c.m. frame. The partial-wave analyses (PWA) KH80, KA84 [2], and CMB80 [3], which form the basis of modern experimental baryon spectroscopy, reveal that the first two of these peaks are due to clusters of, respectively, six and seven nearly degenerate baryon resonances.

Physical interest in measuring polarization observables is motivated by some features of the experimental baryon spectrum that defy any attempt at explaining them within the constituent quark model. By way of example, we indicate that, although a major part of known resonances fits in the multiplet classification scheme following from the quark model that employs the $SU(6) \otimes O(3)$ basis of state functions [4], it is hardly possible to account for the observation of negative-parity resonances at the 1.9-GeV peak. The very fact of the existence of resonance clusters featuring parity doublets is inexplicable within this model. At the same time, there are general theoretical approaches that claim to be capable of explaining resonance clusters and parity doublets. For example, clusters are expected in the dual resonance model [5], whereas parity doublets are predicted on the basis of the straight-line character of baryon Regge trajectories [6]. It is also feasible that parity doublets arise owing to the chiral symmetry of strong interaction [7]. The problem of missing resonances—that is, of a deficit in observed resonances in relation to

¹⁾Petersburg Nuclear Physics Institute, Russian Academy of Sciences, Gatchina, 188350 Russia.

²⁾Joint Institute for Nuclear Research, Dubna, Moscow oblast, 141980 Russia.

*e-mail: vadim.kanavets@itep.ru

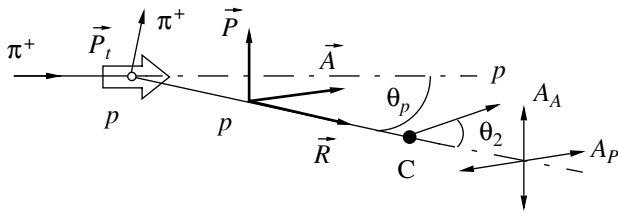


Fig. 1. Schematic representation of an experiment aimed at measuring the spin-rotation parameters: (\vec{P}_t) initial target-proton polarization vector in the A experiment; (C) nuclei of carbon scatterer; and (A_A , A_P) asymmetries corresponding to, respectively, the spin-rotation parameter A and the normal polarization P .

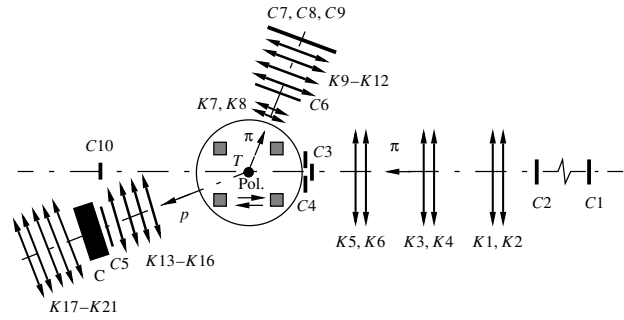


Fig. 2. Layout of the SPIN setup: (T) polarized proton target in a superconducting solenoid, ($C1-C10$) system of trigger counters, ($K1-K21$) coordinate detectors, and (C) carbon scatterer.

the predictions of the quark model—which concerns primarily the excitation peak at 2.2 GeV, is also of interest. Finally, there is the important question of the possible existence of hybrid resonances of the ($qqqg$) type. According to currently prevalent concepts, the lowest hybrid states can be expected in the regions around the peaks at 1.7 GeV (P_{11} , P_{13} waves) and at 1.9 GeV (P_{31} , P_{33} , F_{35} waves) [8].

Despite obvious physical interest, the experimental basis of PWA in the resonance region at momentum values in excess of 0.75 GeV/ c is insufficient for unambiguously reconstructing relevant amplitudes. In contrast to the region below 0.75 GeV/ c , where information about all independent observables of pion-nucleon scattering was obtained owing primarily to efforts of research groups from PNPI and LAMPF, the region of momenta above 0.75 GeV/ c has not yet received adequate study: only the total and differential cross sections and the normal polarization have been measured prior to the present experiments. As a result, the predictions of different PWAs for spin-rotation parameters (A , R) showed a wide scatter in some kinematical regions. Moreover, four of the thirteen resonances that form the clusters at 1.7 and 1.9 GeV were not found by more recent analyses of the group from the University of Virginia [9]. Finally, a theoretical analysis based on the formalism of zeros of transverse amplitudes [10] reveals that, in the absence of information about the spin-rotation parameters, there can arise discrete ambiguities of the type considered by Barrelet; the latter in turn can lead to the mixing of partial-wave amplitudes, distortions of resonance parameters, and even to spurious resonances [11].

Thus, our experimental program is aimed predominantly at (i) verifying the existing PWAs by measuring independent variables (spin-rotation parameters) that are not contained in their experimental basis and (ii) revealing and eliminating the discrete ambiguities of the PWAs.

2. EXPERIMENTAL SETUP

2.1. Layout of the Experimental Setup

Figure 1 shows the layout of the experimental setup intended for measuring spin-rotation parameters. The experiment consisted in measuring the direction of the recoil-proton polarization vector with the aid of scattering on carbon at a known polarization of target protons. In other words, we measured the angle of polarization-vector rotation in the scattering plane. In the present experiment, we adopted the geometry of an A experiment, where the vector of target polarization is aligned with the pion-beam axis. In this case, the transverse component of the recoil-proton polarization in the scattering plane is $P_t \cdot A$, while the component along the recoil-proton momentum is $P_t \cdot R$, where P_t is the target polarization. The polarization component along the normal to the scattering plane is equal to the normal-polarization parameter P . The horizontal (vertical) component of the recoil-proton polarization vector is determined by measuring the vertical (horizontal) asymmetry of proton scattering on carbon. Because of parity conservation in strong interactions, the cross section for scattering on carbon is independent of the longitudinal polarization. In the geometry of the A experiment, the second spin-rotation parameter R cannot therefore be measured directly by studying scattering in a polarimeter, but its absolute value can be found from the relation

$$A^2 + R^2 + P^2 = 1, \quad (1)$$

which is valid for elastic pion-nucleon scattering [12].

A polarized proton target in a superconducting solenoid, a carbon polarimeter, blocks of wire coordinate detectors for determining the trajectories of incident and scattered pions and recoil protons, a triggering system, and a system for measuring time of flight for identifying beam particles are basic elements of the facility used (Fig. 2). The facility is arranged

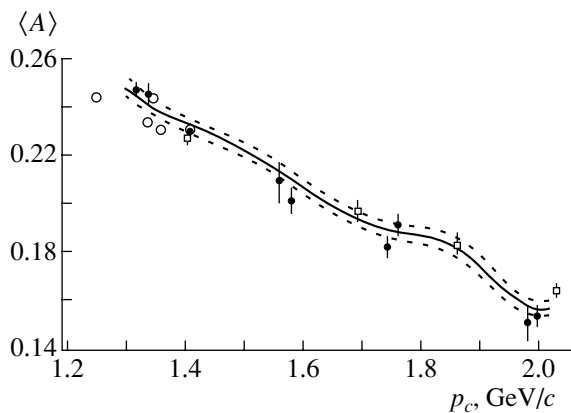


Fig. 3. Mean analyzing power for proton–carbon scattering as a function of the proton momentum p_c at the scatterer center. The solid curve, together with the error corridor bounded by the dashed curves, represents the parametrization from [14]. The experimental data were borrowed from (open circles) [15] [LAMPF(85)], (open boxes) [16] [SACLAY(95)], and (closed circles) [14] [ITEP(98)].

at the universal two-step magneto-optical channel of the ITEP accelerator, which ensures the extraction of charged pions and of protons in the momentum interval 0.8–2.1 GeV/ c with resolution $\Delta p/p = \pm 1.8\%$. In the region of the target, the horizontal and the vertical dimension of the beam (FWHM) are both about 30 mm.

2.2. Target

We employed a dynamically polarizable proton target characterized by a horizontal orientation of the polarization vector [13]. A magnetic field of strength 2.5 T was generated by a pair of superconducting Helmholtz coils. The frequency of polarization pumping was 70 GHz. Propanediol ($C_3H_8O_2$) with an admixture of Cr^V was used for an operating substance. The fraction of hydrogen in the target was about 10%. The operating substance of the target was enclosed in a container having the shape of a vertical cylinder of height 30 mm and diameter 30 mm. The degree of proton polarization in the target was 0.7–0.8 at a temperature of 0.55 K, which was maintained with the aid of a cryostat employing the evacuation of 3He vapors. The error in measuring the polarization did not exceed ± 0.02 . The polarization was reversed every day.

2.3. Polarimeter

In the last runs of measurements, we employed a one-layer polarimeter based on wire chambers that features a graphite scatterer of thickness 36.5 g/ cm^2 .

The choice of polarimeter configuration and of scatterer thickness was a tool for studying in detail various versions of polarimeter in a beam of polarized protons. Since a low rate of counting of useful events is the main problem in experiments devoted to double scattering, the requirements on the polarimeter involved achieving the maximum possible figure of merit and measuring its analyzing power to a high precision.

2.4. Analyzing Power of the Polarimeter

The systematic errors in the measured parameters depend substantially on the accuracy to which we know the analyzing power of the polarimeter and on the level of its spurious asymmetries. In view of this, we have performed a calibrating experiment devoted to measuring the analyzing power of the polarimeter in a beam of polarized protons that was obtained by making protons of the internal beam of the accelerator scatter on internal targets from polyethylene and carbon [14]. In the interval 1.35–2.02 GeV/ c , we have studied, for a carbon scatterer, the analyzing power as a function of the scattering angle and the scatterer thickness. The data obtained at 170 experimental points agree with other available results in the interval where the former and the latter overlap. For scatterer thicknesses in the range 19–40 g/ cm^2 , the analyzing power exhibits but a weak thickness dependence; this makes it possible to parametrize, to a sufficiently high degree of precision, this analyzing power as a function of the proton momentum determined at the scatterer center and of the scattering angle. The mean values of the analyzing power, together with the corridor of errors, are shown in Fig. 3 versus the proton momentum, along with available experimental data.

The spurious asymmetry of the polarimeter was measured in a pion beam. It proved to be small (0.0026 ± 0.0014), so that it cannot introduce significant errors in the sought parameters.

2.5. Polarization in Quasielastic Scattering

Along with the data on the analyzing power of the polarimeter, we have obtained information about the polarization of protons in quasielastic scattering on carbon and beryllium nuclei for scattering at an angle of 10.5° in the laboratory frame (in kinematics corresponding to elastic scattering). The results (Fig. 4) agree with the LAMPF [18] and JINR [20] data, but they contradict the Saclay data [17]. The polarization in quasielastic scattering is about 70% of the polarization in elastic proton–proton scattering. These results comply with the expectations based on the relativistic model [21], which takes into account nuclear-matter-induced modification to the proton wave function.

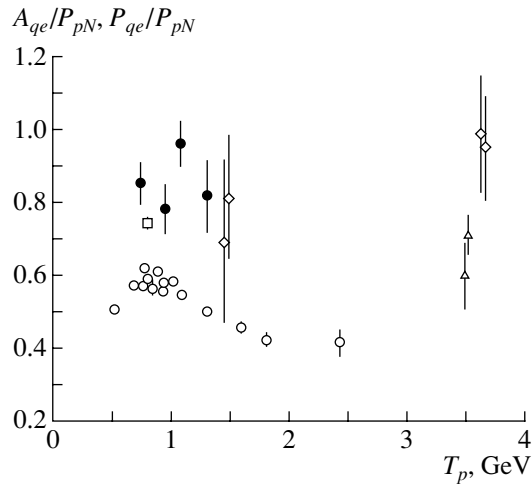


Fig. 4. Experimentally determined ratios of (open symbols) the analyzing power A_{qe} and (closed circles) the normal polarization P_{qe} in quasielastic proton–carbon scattering to the mean polarization in proton–nucleon scattering versus the kinetic energy T_p of polarized protons: (open circles) BYSTR(84) [17], (open boxes) MCGILL(84) [18], (open triangles) OHMOPI(90) [19], (open diamonds) JINR(97) [20], and (closed circles) ITEP(98)[14].

3. DATA PROCESSING

3.1. Selection of Events Involving Elastic Scattering on the Protons of the Polarized Target

The contribution of events involving quasielastic scattering on unpolarized protons bound in the nuclei of polarized-target matter was an important source of systematic errors in measuring polarization parameters. Coplanarity and kinematical correlations between the pion scattering angle and the recoil-proton scattering angle are used to suppress this background. In processing the last series of the measurements, we employed a unified χ^2 criterion that takes into account both these relationships. The specific form of the relevant functional is

$$\chi^2 = (\Delta\theta/\sigma_\theta)^2 + (\Delta\varphi/\sigma_\varphi)^2, \quad (2)$$

where $\Delta\varphi$ and $\Delta\theta$ are angles that take into account deviations from the kinematics of elastic scattering, while σ_φ and σ_θ are widths of the corresponding distributions according to a Monte Carlo simulation. Figure 5 shows the distribution of events with respect to χ^2 for a polarized and a carbon target. If a cut on χ^2 is chosen in the interval 5–8, the background is 6–8%, the corresponding loss of useful statistics being 5–15%.

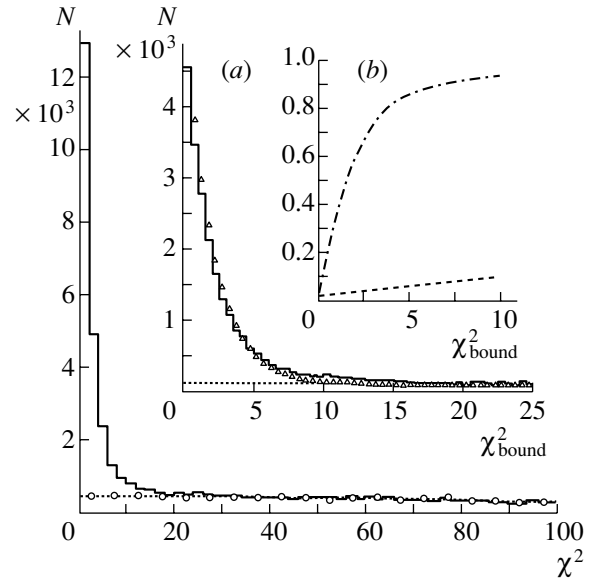


Fig. 5. χ^2 distribution for elastic and quasielastic events [the quantity χ^2 was computed according to expression (2)]: (histograms) distribution for a polarized target, (open circles) distribution for a carbon target, (dotted curves) fit to the quasielastic-scattering background, and (open triangle) theoretical χ^2 distribution. The insets show (a) the same distribution on an enlarged scale and (b) results that characterize (dash-dotted curve) the yield of useful events and (dashed curve) the magnitude of the relative background versus the boundary of the cut on χ^2 .

3.2. Selection of Secondary-Scattering Events

In the polarimeter, we selected single-track events in which the polar scattering angle was not smaller than 3° and for which the geometry of the chambers allows any values of the azimuthal scattering angle. In various series of the measurements, useful statistics of double-scattering events were 5000 to 16 000.

3.3. Determination of Polarization Parameters

The maximum-likelihood method was used to determine the polarization parameters from the azimuthal asymmetry of recoil-proton scattering in the polarimeter. For the parameters to be found, we have chosen A and P . The parameter R was determined from relation (1). In the likelihood function, we

Table 1

p , GeV/ c	Elastic scattering	$\theta_{c.m.}$, deg	References
1.00	π^+p, π^-p	157–168	Unpublished
1.43	π^+p	125–135	[22]
1.62	π^+p, π^-p	120–135	[23]

took into account the magnitude and the sign of the target polarization, the fraction of the quasielastic background and its polarization, the analyzing power of the polarimeter, and the change suffered by the proton-spin direction as the proton travels between the points of the first and the second scattering events in the magnetic field of the solenoid. The polarization of the quasielastic-scattering background was taken to be 0.7 ± 0.1 of the polarization in elastic $\pi^\pm p$ scattering—this relation is similar to the relation between the polarizations in quasielastic pC and elastic pp scattering. The results of the fit were virtually independent of the assumption on the sign of the parameter R .

3.4. Estimates of Systematic Errors

The main contribution to the systematic errors (normalization) in the parameters A , R , and P comes from the uncertainty in the analyzing power of the polarimeter (not more than 4%). The systematic errors may also be due to the uncertainty in the target polarization, the instrumental asymmetry of the polarimeter, and the uncertainty in the estimated polarization of the quasielastic-scattering background. The contribution of the small instrumental asymmetry of the polarimeter to the errors in the spin-rotation parameters is suppressed by periodically reversing the sign of the target polarization, so that it leads to a negligibly small correction. For example, the contribution to the instrumental asymmetry to the error in the parameter P does not exceed 0.02. The effect of uncertainties in the polarization of the quasielastic-scattering background was estimated by processing data at zero polarization and the polarization equal to that in elastic scattering. The contributions of these uncertainties to the spin-rotation parameters A and R proved to be negligible, while their contribution to the parameter P was less than 0.04. The total estimate of systematic errors was $\Delta_{\text{sys}} < \Delta_{\text{stat}}/3$ at $\Delta_{\text{stat}} = 0.15\text{--}0.20$.

4. RESULTS

All experiments that we have performed were implemented in the geometry of the A experiment. Data on the parameters A , P , and $|R|$ were obtained simultaneously. The kinematical intervals studied here are listed in Table 1. The results of the measurements are displayed in Fig. 6 and in Table 2.

In π^+p scattering, our data on the parameter P agree satisfactorily both with the world-averaged results and with the predictions of all PWAs at 1.00, 1.43, and 1.62 GeV/ c . This indicates that there are no grave systematic errors in our measurements. Data on the parameter A clearly discriminate between the

predictions of the different PWAs. They are consistent with the solutions of the SM90 and SM99 analyses performed by the group from the University of Virginia and are in sharp contradiction with the KH80, KA84, and CMB PWAs at 1.43 and 1.62 GeV/ c .

In π^-p scattering, the results for the parameter P comply well both with all PWAs and with precise experimental data on asymmetry that were obtained at the ITEP SPIN facility in the early 1990s [28]. There are only discrepancies with the results of the SM99 analysis at 1.00 GeV/ c . The value of the parameter A at 1.62 GeV/ c is compatible with the results of all analyses. At 1.00 GeV/ c , data on this parameter are consistent with the KH80 and SM99 analyses and are in sharp contradiction with the CMB and SM90 analyses.

5. ANALYSIS OF THE SPECTRUM AND PROPERTIES OF ISOSPIN-3/2 BARYON RESONANCES AROUND 1.9 GeV

5.1. Formalism of Zeros of Transverse Amplitudes

The elastic-scattering matrix for pion–nucleon interaction has the form

$$M = g + ih(\boldsymbol{\sigma} \cdot \mathbf{n}), \quad (3)$$

where \mathbf{n} is the normal to the scattering plane, $\boldsymbol{\sigma}$ is the Pauli matrix, and g and h are complex amplitudes. The transverse amplitudes f^+ and f^- are defined as

$$f^+ = g + ih, \quad f^- = g - ih. \quad (4)$$

The squared moduli of the transverse amplitudes yield the probability of scattering for a proton whose polarization vector is parallel or antiparallel to the normal to scattering plane. The relevant observables are expressed in terms of f^+ and f^- as

$$d\sigma/d\Omega = |f^+|^2 + |f^-|^2, \quad (5)$$

$$P \cdot d\sigma/d\Omega = |f^+|^2 - |f^-|^2,$$

$$A/2 \cdot d\sigma/d\Omega = \text{Re}(f^+ f^{-*}) \sin(\theta_{\text{c.m.}} - \theta_{\text{lab}})$$

$$- \text{Im}(f^+ f^{-*}) \cos(\theta_{\text{c.m.}} - \theta_{\text{lab}}),$$

$$R/2 \cdot d\sigma/d\Omega = \text{Re}(f^+ f^{-*}) \cos(\theta_{\text{c.m.}} - \theta_{\text{lab}})$$

$$+ \text{Im}(f^+ f^{-*}) \sin(\theta_{\text{c.m.}} - \theta_{\text{lab}}),$$

where $\theta_{\text{c.m.}}$ and θ_{lab} are the scattering angles for the recoil proton in the c.m. and in the laboratory frame. From expressions (5), it is obvious that the cross section and polarization make it possible to find only the moduli of the transverse amplitudes. In order to determine their relative phase, it is necessary to measure the spin-rotation parameters.

It is well known that the amplitudes g and h can be represented as expansions in partial-wave amplitudes—that is, in the form of a polynomial in

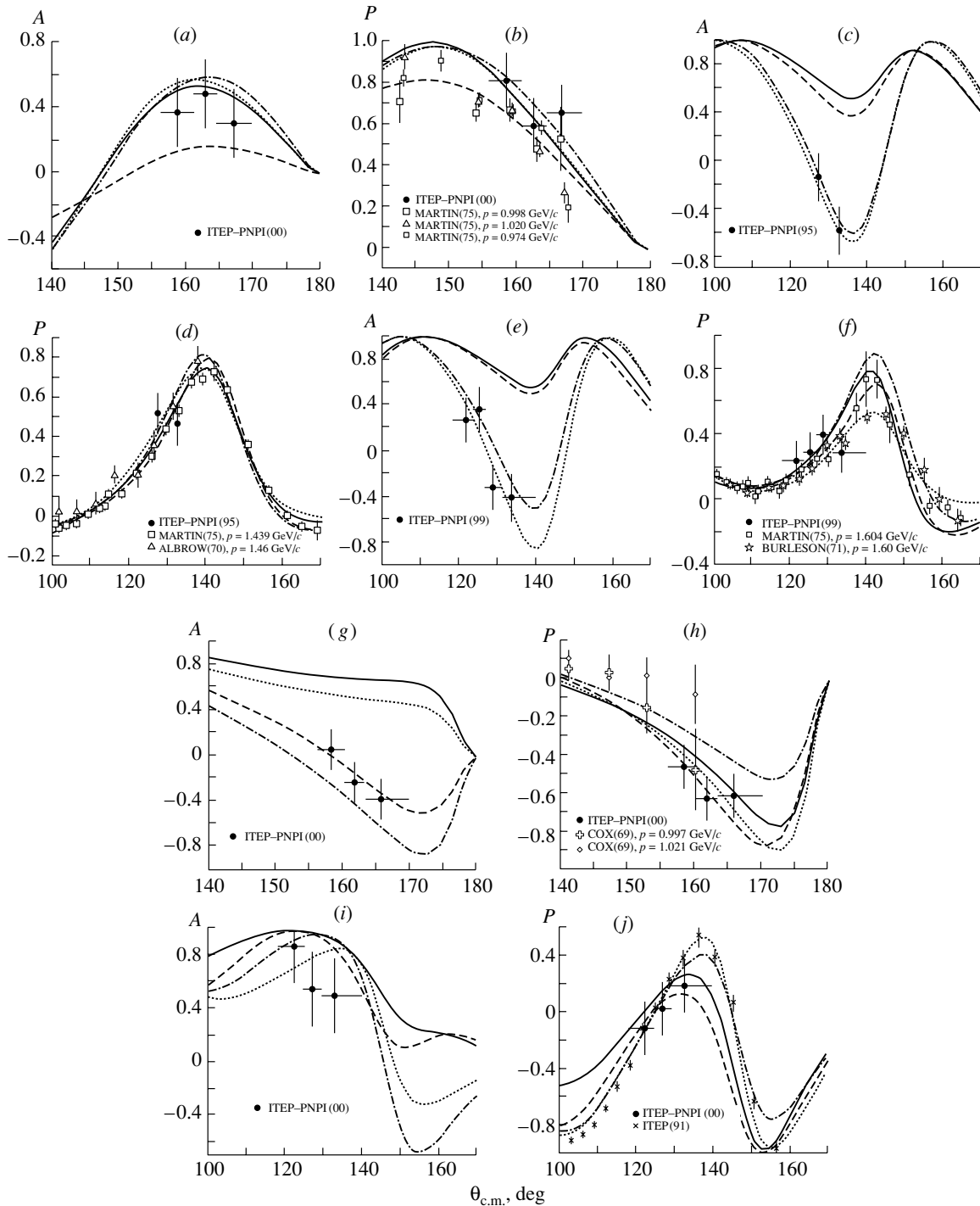


Fig. 6. Spin-rotation parameter A and the normal polarization P in elastic $\pi^\pm p$ scattering versus the c.m. scattering angle $\theta_{c.m.}$: (a, b) $\pi^+ p$ interaction at 1.00 GeV/c, (c, d) $\pi^+ p$ interaction at 1.43 GeV/c, (e, f) $\pi^+ p$ interaction at 1.62 GeV/c, (g, h) $\pi^- p$ interaction at 1.00 GeV/c, and (i, j) $\pi^- p$ interaction at 1.62 GeV/c. The results of the CMB [3], the KH80 [2], the SM90 [9], and the SM99 [9] PWA are represented by, respectively, the solid, the dashed, the dotted, and the dash-dotted curve. The experimental data were borrowed from [24] [MARTIN(75)], [25] [ALBROW(70)], [26] [BURLESON(71)], [27] [COX(69)], [28] [ITEP(91)], [22] [ITEP-PNPI(95)], and [23] [ITEP-PNPI(99)]. Also displayed here are our present results [ITEP-PNPI(00)].

$\cos \theta_{c.m.}$ and $\sin \theta_{c.m.}$. It is convenient to introduce the variable $\omega = \exp(i\theta_{c.m.})$ [10], in which case we have $\cos \theta_{c.m.} = (\omega + \omega^{-1})/2$ and $\sin \theta_{c.m.} = (\omega - \omega^{-1})/2i$. It follows that the amplitudes f^+ and f^- are

Table 2. Spin-rotation and polarization parameters for elastic $\pi^\pm p$ scattering at momenta of 1.00, 1.43, and 1.62 GeV/ c

Elastic scattering Momentum, GeV/ c	Interval of angles $\theta_{c.m.}$, deg	Mean angle $\theta_{c.m.}$, deg	P	A	$ R $
$\pi^+ p$ 1.00	156.0–161.0	158.7	0.81 ± 0.13	0.37 ± 0.22	0.45 ± 0.30
	161.0–164.7	162.8	0.59 ± 0.14	0.49 ± 0.22	0.64 ± 0.21
	164.7–170.0	167.0	0.66 ± 0.13	0.30 ± 0.21	0.69 ± 0.16
$\pi^- p$ 1.00	156.0–160.1	158.4	-0.46 ± 0.11	0.07 ± 0.18	0.89 ± 0.06
	160.1–163.4	161.8	-0.63 ± 0.12	-0.22 ± 0.18	0.75 ± 0.11
	163.4–170.0	165.8	-0.61 ± 0.12	-0.37 ± 0.18	0.70 ± 0.14
$\pi^+ p$ 1.43		127.2	0.52 ± 0.10	-0.14 ± 0.20	0.84 ± 0.07
		132.5	0.47 ± 0.11	-0.58 ± 0.20	0.67 ± 0.19
$\pi^+ p$ 1.62	118.0–123.5	121.7	0.24 ± 0.12	0.27 ± 0.18	0.93 ± 0.06
	123.5–127.0	125.2	0.30 ± 0.12	0.36 ± 0.20	0.88 ± 0.09
	127.0–131.0	128.8	0.40 ± 0.13	-0.32 ± 0.20	0.86 ± 0.10
$\pi^- p$ 1.62	118.0–124.8	122.3	-0.11 ± 0.19	0.88 ± 0.28	0.46 ± 0.54
	124.8–129.4	127.0	0.03 ± 0.19	0.56 ± 0.28	0.83 ± 0.19
	129.4–140.0	132.8	0.19 ± 0.20	0.51 ± 0.29	0.84 ± 0.18

represented as polynomials in ω and that their roots occur in the complex plane of ω . At a fixed energy, the set of the roots of the polynomials (zeros of the amplitudes) determines completely the results of a PWA, in just the same way as the conventionally used set of partial-wave amplitudes does. The physical region in the complex plane of ω is represented as a unit circle, since $|\omega| = 1$ at real values of $\theta_{c.m.}$. The zeros of the amplitudes as functions of energy generate continuous trajectories. At the points where the trajectories of the zeros intersect the physical region, the polarization takes the value of +1 or -1, while the spin-rotation parameters vanish. Such points are referred to as critical ones. The discrete transformation $\omega_i \rightarrow 1/\omega_i^*$ of any root—it is referred to as the Barellet conjugation—conserves the moduli of the transverse amplitudes, leaving the cross section and polarization unchanged; that is, it does not disturb correspondence between the analysis and experimental basis. Figure 7 shows the trajectories of the zeros of the $\pi^+ p$ amplitudes from the KH80 and SM90 analyses. It can be seen that the trajectory of the zero at an angle of about 140° is off the circle for the former and within it for the latter analysis. This is precisely a manifestation of what is referred to as a discrete ambiguity in a partial-wave analysis.

5.2. Correction of Analyses

The application of the Barellet transformation to the trajectory of a zero between two critical points

makes it possible to introduce corrections in the existing analyses in order to render their results consistent with experimental data on the spin-rotation parameters. The correction of the KH80, KA84, and CMB analyses that was performed for $\pi^+ p$ scattering [29] led to solutions that comply well with

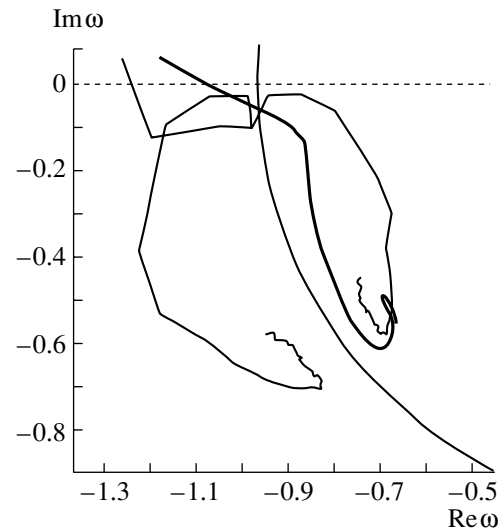


Fig. 7. Trajectories of the zeros of the transverse $\pi^+ p$ amplitudes in the complex plane of ω for the KH80 PWA [2] at angles between 120° and 180° in the original form (off the unit circle) and in the Barellet conjugate form (within it). The unit circle $|\omega| = 1$ is represented here by a smooth curve. The thick curve shows the trajectory for the SM90 PWA [9].

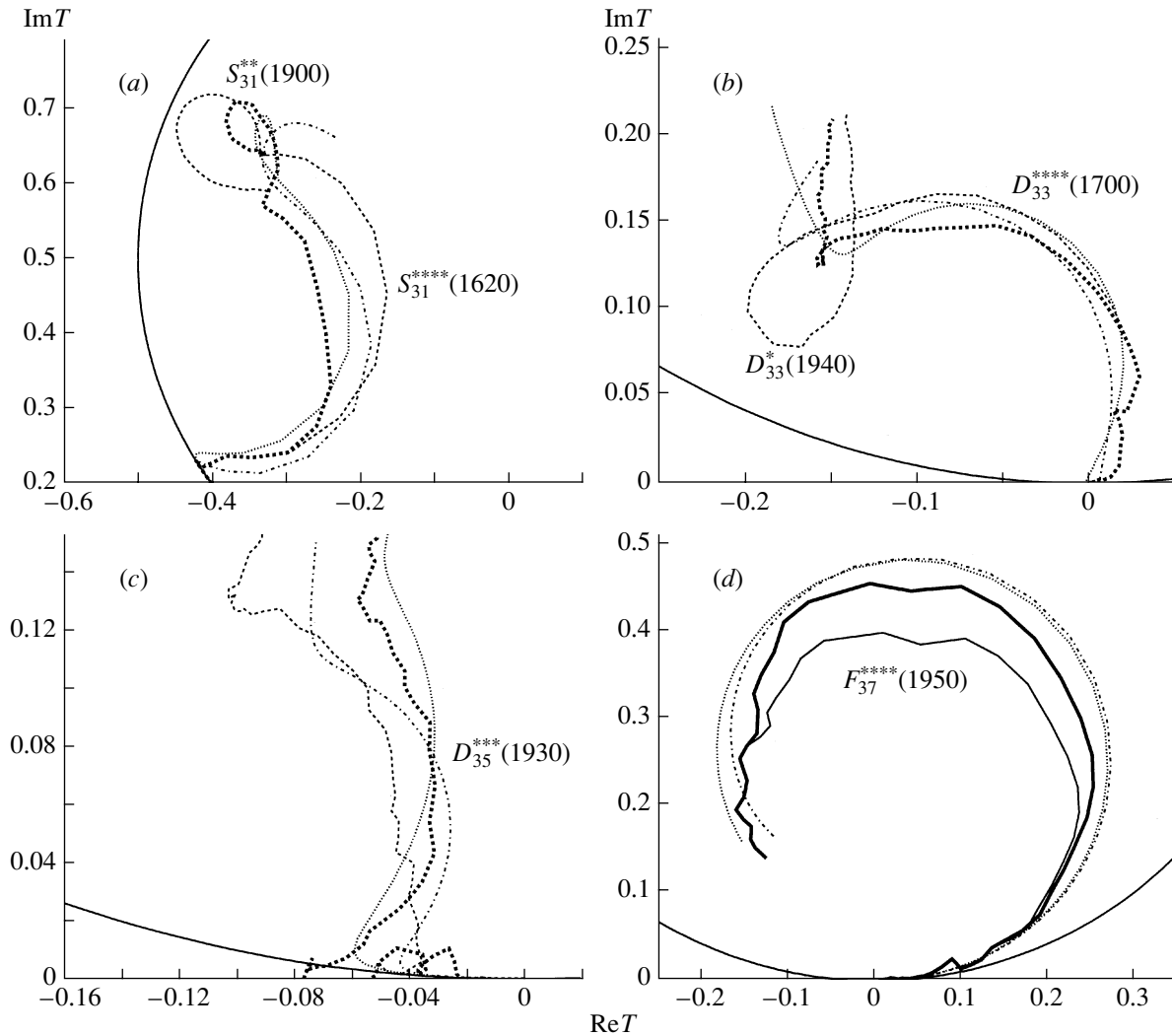


Fig. 8. Argand diagrams for some partial waves: (a) S_{31} , (b) D_{33} , (c) D_{35} , and (d) F_{37} (T is a partial-wave amplitude). The predictions of the KH80 [2], the KH80-C [29], the SM90 [9], the SM99 [9], the CMB [3], and the CMB-C [29] PWA are represented, respectively, by the thin dashed, the thick dashed, the dotted, the dash-dotted, the thin solid, and the thick solid curve.

data on the spin-rotation parameters. This gives sufficient grounds to state that a wrong branch of solutions was chosen in the original analyses. Figure 8 shows the Argand diagrams for some partial waves. It can be seen that the correction (KH80-C, CMB-C) improves considerably the agreement for partial-wave amplitudes between all the existing analyses. At the same time, the $D_{33}^*(1940)$ resonance disappears, while the elasticity factor for the $S_{31}^{**}(1900)$ resonance decreases, its identification concurrently becoming less reliable. The parameters of the $D_{35}^{***}(1930)$, $F_{35}^{****}(1905)$, and $F_{37}^{****}(1950)$ resonances change only slightly. A quantitative analysis involving a determination of the pole resonance parameters [11] confirms these conclusions.

6. CONCLUSION

An observation of discrete ambiguities in PWAs for π^+p scattering at 1.43 and 1.62 GeV/c and for π^-p scattering at 1.00 GeV/c and a clear-cut choice of correct branches of solutions are important results of our measurements and data analysis. At the same time, satisfactory agreement of our results for A and R with the predictions of partial-wave analyses (apart from discrete ambiguities) indicates that, although the experimental basis of modern PWAs does not contain information about these independent parameters, such analyses are capable of reconstructing amplitudes to a sufficiently high degree of precision.

The analyses of π^+p scattering that are based on the formalism of zeros of the transverse amplitudes lead to results suggesting that the rating of

the $S_{31}(1900)$ resonance should be lowered and that it should be excluded from the summary table of baryons that is presented by the Particle Data Group. Since 1998, this has already been done in the issues of the *Review of Particle Physics*.

The problem of negative-parity resonances in the region around 1.9 GeV, which are not expected, within quark models, to occur there, has been partly solved since the $D_{33}(1940)$ resonance has not been confirmed and since the $S_{31}(1900)$ resonance is not presently considered as that which has been established conclusively. At the same time, $D_{35}^{***}(1930)$ remains the only reliably established resonance that does not fit well in the quark model. It belongs to the third level of excitation [possibly, it enters into $(56, 1_3^-)$ supermultiplet], and its mass must be greater by 200 MeV.

The problem of parity doublets in the regions around the peaks at 1.7 GeV (a pole at $\text{Re} = 1665$ MeV and $\text{Im} = -55$ MeV) and at 1.9 GeV [pair of $D_{35}(1930)$ and $F_{35}(1905)$] remains open.

ACKNOWLEDGMENTS

We are indebted to the ITEP accelerator staff for ensuring excellent conditions for our work with the beam and to the personnel of the Cryogenic Laboratory for proving us with liquid nitrogen and helium.

This work was supported in part by the Russian Foundation for Basic Research (project nos. 99-02-16635 and 00-15-96545) and by the Russian State Scientific and Technological Program Fundamental Nuclear Physics.

REFERENCES

- Particle Data Group, *Eur. Phys. J. C* **15**, 1 (2000).
- G. Hohler, *Handbook of Pion-Nucleon Scattering*, Physics Data, No. 12-1 (Fachinformationzentrum, Karlsruhe, 1979).
- R. E. Cutkosky *et al.*, *Phys. Rev. D* **20**, 2839 (1979).
- N. Isgur and G. Karl, *Phys. Rev. D* **18**, 4187 (1978); **19**, 2653 (1979); **20**, 1191 (1979); A. J. G. Hey and R. L. Kelly, *Phys. Rep.* **96**, 71 (1983).
- S. Mandelstam, *Phys. Rep. C* **13**, 260 (1974).
- A. B. Kaĭdalov, *Proceedings of the 17th Physics School of Institute of Theoretical and Experimental Physics "Physics of Resonances," Moscow, 1987* (unpublished).
- S. Weinberg, *Rev. Mod. Phys.* **46**, 255 (1974); H. Pagels, *Phys. Rep.* **16**, 219 (1975).
- D. V. Bugg, *πN Newsletter* **15**, 319 (1999).
- R. A. Arndt *et al.*, *Phys. Rev. C* **52**, 2120 (1995); nucl-th/9807087; <http://said.phys.vt.edu/>
- E. Barrelet, *Nuovo Cimento A* **8**, 331 (1972).
- D. N. Svirida, Doctoral Dissertation in Physics and Mathematics (Inst. Teor. Éksp. Fiz., Moscow, 1998).
- S. M. Bilen'kiĭ, L. I. Lapidus, and R. M. Ryndin, *Usp. Fiz. Nauk* **84**, 243 (1964) [*Sov. Phys. Usp.* **7**, 721 (1965)].
- É. I. Bunyatova *et al.*, Preprint No. 1191, LIYaF (Inst. of Nuclear Physics, Leningrad, 1986).
- I. G. Alekseev *et al.*, *Yad. Fiz.* **62**, 2194 (1999) [*Phys. At. Nucl.* **62**, 2024 (1999)]; I. G. Alekseev *et al.*, *Nucl. Instrum. Methods Phys. Res. A* **434**, 254 (1999).
- M. W. McNaughton *et al.*, *Nucl. Instrum. Methods Phys. Res. A* **241**, 435 (1985).
- N. E. Cheung *et al.*, *Nucl. Instrum. Methods Phys. Res. A* **363**, 561 (1995).
- J. Bystrickiy *et al.*, *Lett. Nuovo Cimento* **40**, 466 (1984).
- J. A. McGill *et al.*, *Phys. Lett. B* **134B**, 157 (1984).
- C. Ohmori *et al.*, *Phys. Lett. B* **234**, 29 (1990).
- E. V. Anoshina *et al.*, *Yad. Fiz.* **60**, 283 (1997) [*Phys. At. Nucl.* **60**, 224 (1997)].
- C. J. Horowitz and M. J. Iqbal, *Phys. Rev. C* **33**, 2059 (1986).
- V. V. Abaev *et al.*, *Yad. Fiz.* **58**, 1635 (1995) [*Phys. At. Nucl.* **58**, 1542 (1995)]; I. G. Alekseev *et al.*, *Phys. Lett. B* **351**, 585 (1995).
- I. G. Alekseev *et al.*, Preprint No. 22-00, ITÉF (Inst. of Theoretical and Experimental Physics, Moscow, 2000); *Phys. Lett. B* **485**, 32 (2000).
- J. E. Martin *et al.*, *Nucl. Phys. B* **89**, 253 (1975).
- M. G. Albrow *et al.*, *Nucl. Phys. B* **25**, 9 (1971).
- G. R. Burleson *et al.*, *Phys. Rev. Lett.* **26**, 338 (1971).
- C. R. Cox *et al.*, *Phys. Rev.* **184**, 1453 (1969).
- I. G. Alekseev *et al.*, *Nucl. Phys. B* **348**, 257 (1991).
- I. G. Alekseev *et al.*, in *Proceedings of VI Workshop on High Energy Spin Physics, Protvino, 1996*, p. 80; V. P. Kanavets *et al.*, in *Proceedings of PANIC-96, Williamsburg, 1996*, p. 545; I. G. Alekseev *et al.*, *Phys. Rev. C* **55**, 2049 (1997).

Translated by A. Isaakyan

Conference on Physics of Fundamental Interactions
Experiment

**Spectra of Fast π^+ Mesons from the $\pi^- A \rightarrow \pi^+ X$
Reaction on Oxygen and Lithium Nuclei at 0.59 GeV**

**B. M. Abramov, L. Álvarez-Ruso¹⁾, Yu. A. Borodin, S. A. Bulychjov,
I. A. Dukhovskoy, A. I. Khanov, A. P. Krutenkova*, V. V. Kulikov, M. A. Matsuk,
I. A. Radkevich, A. I. Sutormin, E. N. Turdakina, and M. J. Vicente Vacas¹⁾**

Institute of Theoretical and Experimental Physics, Bol'shaya Cheremushkinskaya ul. 25, Moscow, 117218 Russia

Received March 21, 2001

Abstract—The spectra of fast π^+ mesons from the $\pi^- A \rightarrow \pi^+ X$ reaction on $A = {}^6\text{Li}$, ${}^7\text{Li}$, and ${}^{16}\text{O}$ nuclei at a primary momentum of $p_0 = 0.72 \text{ GeV}/c$ ($T_0 = 0.59 \text{ GeV}$) are measured at emission-angle values in the range $\vartheta = 0^\circ - 14^\circ$. The results obtained in this way are compared with experimental data taken in other studies at lower energies and with the results of model calculations. The energy dependence of the cross sections and of shadowing effects is analyzed for the reactions in question that occur on lithium isotopes.

© 2002 MAIK “Nauka/Interperiodica”.

1. INTRODUCTION

Interest in pion double charge exchange (PDCX) on nuclei is motivated by the following remarkable feature of this process: it proceeds on at least two identical nucleons. This feature makes it possible to use PDCX to study both the structure of nuclei (excitation of doubly isobar-analog transitions and searches for exotic nuclear states) in exclusive reactions and the dynamics of particle interactions with nuclei in inclusive reactions (for an overview, see, for example, [1, 2]). Inclusive PDCX reactions at primary kinetic energies in the range $T_0 = 0.12 - 0.27 \text{ GeV}$ were investigated in detail, predominantly in experiments at the LAMPF meson factory (see [3, 4] and references therein). The mechanism of two sequential single charge exchanges (SSCX) suffered by a pion in a nucleus is a commonly accepted model for analyzing experimental data on PDCX at energies of up to 0.5 GeV (see, for example [5]), which are characteristic of meson factories. Naturally, the SSCX amplitude is related to the square of the amplitude for single charge exchange on a free nucleon, and the energy dependence of SSCX reflects the energy dependence of charge exchange on a free nucleon. It is well known that, in the region $T_0 = 0.6 - 1.3 \text{ GeV}$, the cross section for charge exchange on free nucleons decreases sharply with increasing energy. Therefore, a strong decrease in the PDCX cross section is expected in the SSCX model at these energies [6]. In the experiments

reported in [7, 8], the 3-m spectrometer installed at the Institute of Theoretical and Experimental Physics (ITEP, Moscow) was used to measure the cross section for the inclusive reactions

$$\pi^- {}^{16}\text{O} \rightarrow \pi^+ X. \quad (1)$$

These measurements, which were performed in the range of T_0 between 0.6 and 1.1 GeV, revealed evidence for an anomalously weak decrease in the PDCX cross section with energy in relation to its sharp decrease in the SSCX model [9]. This observation motivated the appearance of a new approach to the PDCX problem at high energies (see [10, 11]). In describing the PDCX process within this approach, it is necessary to take into account, in the Glauber pattern of pion–nucleus scattering, not only elastic rescatterings (that is, the SSCX mechanism) but also inelastic rescatterings. As was shown in [10], the contribution of inelastic Glauber rescattering is dominant at energies in excess of 1 GeV. This conclusion was based on a theoretical analysis of the behavior of the inclusive cross section for a pure PDCX process occurring in the forward direction (that is, without the inclusion of the production of an extra pion), the high-energy section of the spectrum for reaction (1) corresponding to this in experiments.

In the present study, the spectra of fast positive pions from the interaction of negative pions with oxygen and lithium nuclei at $T_0 = 0.59 \text{ GeV}$ have been measured over a momentum interval broader than that in [7]. This makes it possible to perform a detailed comparison of our results with available data on inclusive PDCX on nuclei. The experimental data are also compared with the results of Monte Carlo

¹⁾Universidad de Valencia, Av. Dr. Moliner 50, E-46100 Burjassot, Valencia, Spain.

*e-mail: krutenkova@vxitep.itep.ru

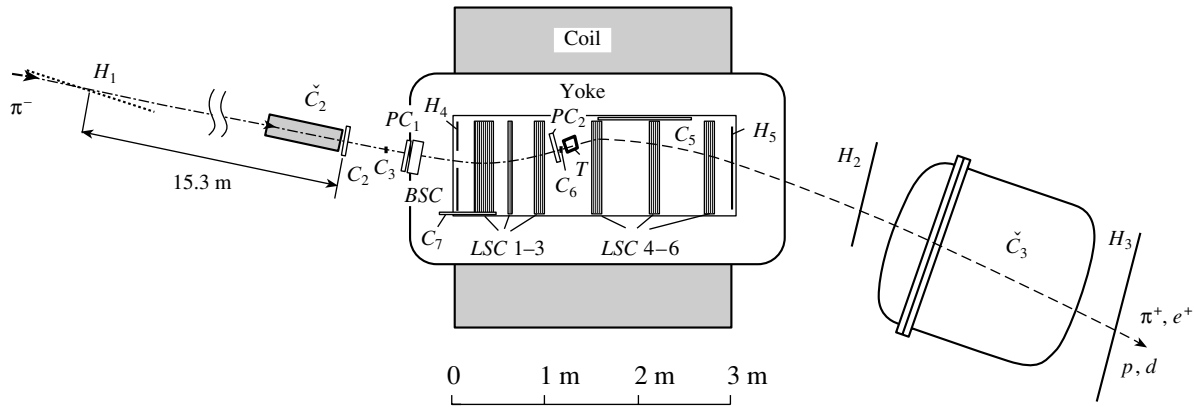


Fig. 1. Layout of the experimental setup used.

calculations within the cascade model, where, for the first time, we take into account the effect of nuclear-medium polarization.

2. DESCRIPTION OF THE EXPERIMENT

Our objective was to measure the energy spectra of positive pions from the reaction

$$\pi^- A \rightarrow \pi^+ X, \quad (2)$$

where $A = {}^6\text{Li}$, ${}^7\text{Li}$, and ${}^{16}\text{O}$, at a primary pion momentum of $p_0 = 0.72 \text{ GeV}/c$ and scattering angles of $\vartheta = 0^\circ - 14^\circ$ in the range $\Delta T \equiv T_0 - T = 0 - 250 \text{ MeV}$, where T is the kinetic energy of the final pion. We note that the interval $\Delta T \leq m_\pi = 140 \text{ MeV}$ corresponds to the region of a pure PDCX process,

where the production of an extra pion in the reaction is forbidden kinematically.

The experiment, which was performed at the 3-m ITEP spectrometer, employed spark chambers arranged in a magnetic field. The layout of the facility used is depicted in Fig. 1. A beam of negative pions passed through the H_1 , C_2 , and C_3 scintillation counters; the PC_1 and PC_2 proportional chambers; and the BSC and LSC 1–3 spark chambers and was focused onto the target T . The C_6 counter in front of the target was used only during the adjustment of the beam. The H_1 hodoscope, which consisted of 24 scintillation counters and which was positioned at the intermediate focus of the beam channel, made it possible to determine the momentum of a beam pion with a precision of $\pm 0.3\%$, the momentum spread of the beam, $\Delta p/p$, being about 5%. For target materials, we employed H_2O , D_2O , enriched ${}^6\text{Li}$ (90.4% of ${}^6\text{Li}$ and 9.6% ${}^7\text{Li}$) and ${}^7\text{Li}$ (natural mixture of isotopes: 7.5% ${}^6\text{Li}$ and 92.5% ${}^7\text{Li}$), which completely filled thin-wall steel containers that had the shape of a cylinder 9.5 cm in length and 8 cm in diameter. The targets attached to a rotatable device were periodically replaced with the aid of it, one by another. Particles from

$$\pi^- A \rightarrow (e^+, \pi^+, p, d) X \quad (3)$$

reactions that were emitted from the target passed through the LSC 4–6 spark chambers and were recorded by the scintillation counters of the H_5 , H_2 , and H_3 hodoscopes. A considerable part of beam particles that suffered no interaction entered the veto counter C_5 . The Cherenkov counters \check{C}_2 (a beam one) and \check{C}_3 (a wide-aperture one) [12] served to suppress the background from electrons and positrons, respectively. We measured the time of flight over the base of about 6 m between the counters C_2 and H_3 (seven counters of total area $1.1 \times 0.7 \text{ m}^2$). The error of the measurements was about 0.8 ns, whereas the

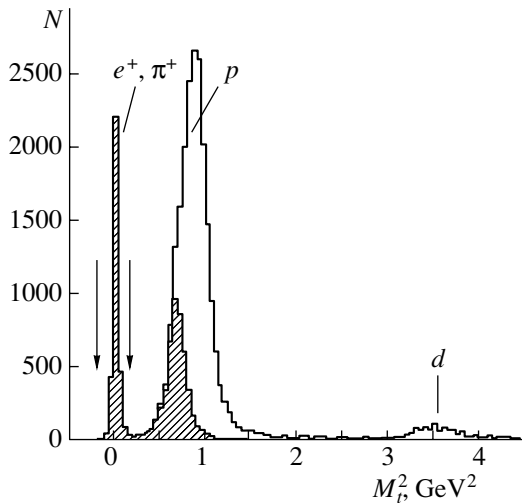


Fig. 2. Distribution of events with respect to the squared mass of a particle from $\pi^- A \rightarrow (e^+, \pi^+, p, d) X$ reactions. The shaded histogram corresponds to the S_π trigger (see main body of the text).

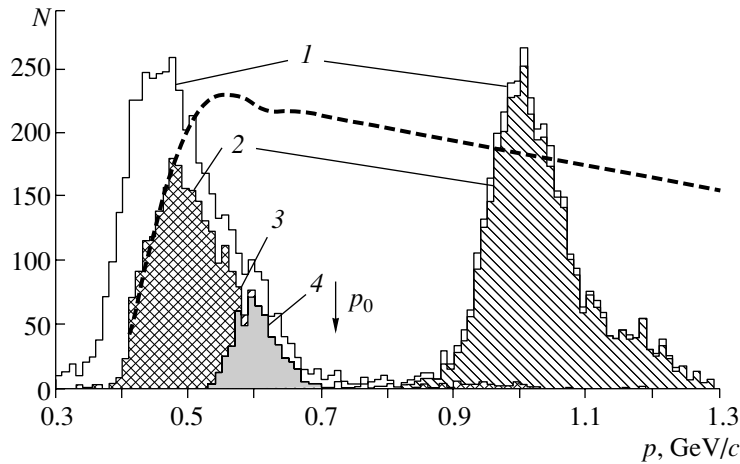


Fig. 3. Distribution of events with respect to the momentum of the emitted particle. Histograms 1, 2, 3, and 4 illustrate the successive steps of selection of PDCX events. The curve represents the geometric efficiency of the facility in relative units.

difference of the times of flight between the pions and the fastest protons from reaction (3) was ~ 4.3 ns (for forward emitted protons from the reaction $\pi^- p \rightarrow p\pi^-$, this difference amounted to about 7.0 ns). The trigger that we used was determined by the formula

$$S_\pi = (H_1 C_2 C_3 \bar{C}_2) \bar{C}_5 (H_5 H_3 \bar{C}_3) (C_2 H_3)_{t\pi}. \quad (4)$$

A $(C_2 H_3)_{t\pi}$ coincidence selected events where the time of flight was close to that of the pions, whereby we achieved a considerable suppression of the contribution from events of reaction (3) that involve the emission of protons. Unsuppressed protonic events were used, in particular, in comparing, with the Monte Carlo calculations, various characteristic distributions that are generated by particles emitted in reactions (3). Protons from reactions (3) were also recorded by the trigger that was intended for studying backward quasielastic $\pi^- p$ scattering on nuclei (see, for example, [13]) and which operated along with S_π , the counters H_4 and C_7 serving to separate a backward scattered negative pion. For a detailed description of the facility used, the interested reader is referred to [14].

Tracks of particles from events selected by the trigger were photographed. Information fixed on a photofilm was read out by the ITEP PSP-2 automatic scanning device. The geometric reconstruction of events was performed, and the results were analyzed.

With the S_π trigger, we obtained, in all, more than 35 000 photographs and processed them. A major part of these contained the background from beam interaction with the body of the magnet. In order to single out the inclusive PDCX reaction, we successively selected (i) events having tracks in the LSC 4–6 chambers; (ii) events for which the trajectories of positively charged particles passed near the

spark chamber and intersected the plane of the H_3 hodoscope; (iii) events for which the square of the mass of a particle emitted from the target (it was determined from its momentum and time of flight), M_t^2 , was constrained by the region indicated by the arrows in Fig. 2 [this corresponds to pion emission—that is, to the observation of reaction (2)]; and (iv) events of the pure PDCX process (that is, events occurring in the kinematical region $\Delta T = 0$ –140 MeV).

For the H_2O , D_2O , 6Li , and 7Li targets, the total numbers of events of reaction (2) were, respectively, 707 (162), 1020 (207), 530 (88), and 507 (102)

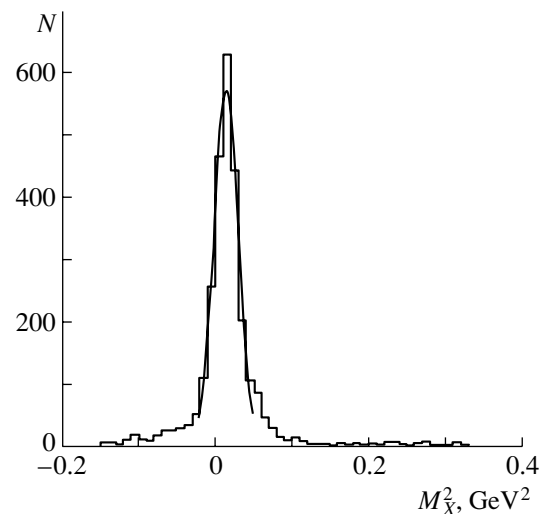


Fig. 4. Distribution of events featuring a backward scattered pion with respect to the square of the missing mass for the $\pi^- p \rightarrow pX$ reaction on the H_2O target. The curve represents the results of a fit for $-0.02 \leq M_X^2 \leq 0.04$ GeV^2 in terms of a Gaussian function characterized by $\sigma = 0.016$ GeV^2 .

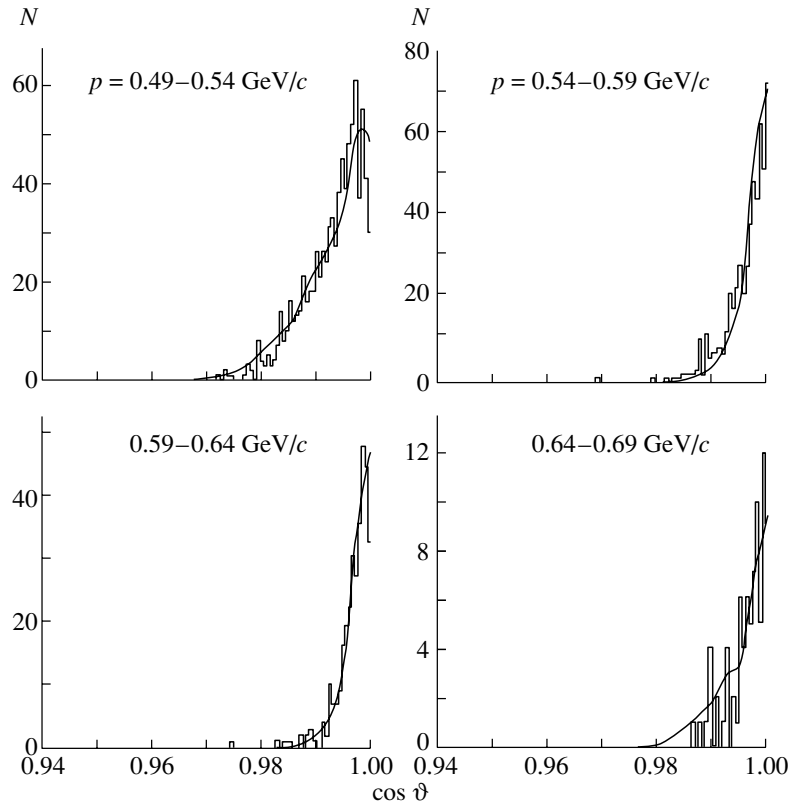


Fig. 5. Angular distributions of events in $\pi^- A \rightarrow \pi^+ X$ reactions for various ranges of the momenta of emitted positive pions. The curves represent the geometric efficiency of the facility according to Monte Carlo calculations for a uniform distribution of the cross section with respect to $\cos\theta$.

(indicated parenthetically are the numbers of PDCX events).

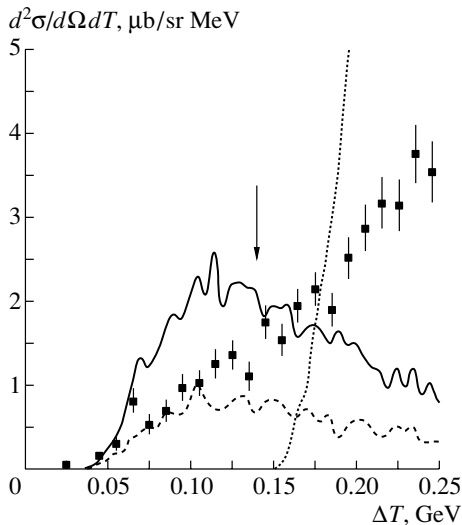


Fig. 6. Double-differential cross section for the reaction $\pi^- A \rightarrow \pi^+ X$ ($A = \text{H}_2\text{O} + \text{D}_2\text{O}$) as a function of ΔT at $T_0 = 0.59$ GeV. The curves represent the results of the calculations performed on the basis of the model proposed in [9] (see main body of the text). The fluctuations in the calculations (here and in Fig. 7) are due to insufficient statistics in calculations by the Monte Carlo method.

The subsequent steps of this selection are also illustrated in Fig. 3, which displays the distributions of events with respect to the momentum of the emitted particle. Two groups of particles within the momentum acceptance of the facility (curve) are protons (at higher momenta) and pions. Their clear-cut separation in Fig. 3 is ensured by the use of $(C_2H_3)_t\pi$ coincidences, which eliminate protons of relatively lower momenta (left boundary of the proton peak). Histograms 1, 2, 3, and 4 in Fig. 3 correspond to events selected according to items (i), (ii), (iii), and (iv) (histograms 2 and 3 for pions coincide). A distinct separation of pion and proton events in the time of flight (see Fig. 2) ensures a low level (less than 5%) of the proton background to PDCX events (see histogram 4 in Fig. 3). It should be noted that the left boundary of histogram 4—it is due to the constraint $\Delta T < 140$ MeV—is smeared in this distribution, largely because of the beam momentum acceptance. The total resolution of the facility in ΔT (about 8 MeV) was determined from the width of the peak associated with backward $\pi^- p$ elastic scattering on a water target (see Fig. 4).

As to the positron background, its sources are the following: (a) $e^- A \rightarrow \gamma X \rightarrow e^+ X'$ reactions (bremsstrahlung from electrons and photon con-

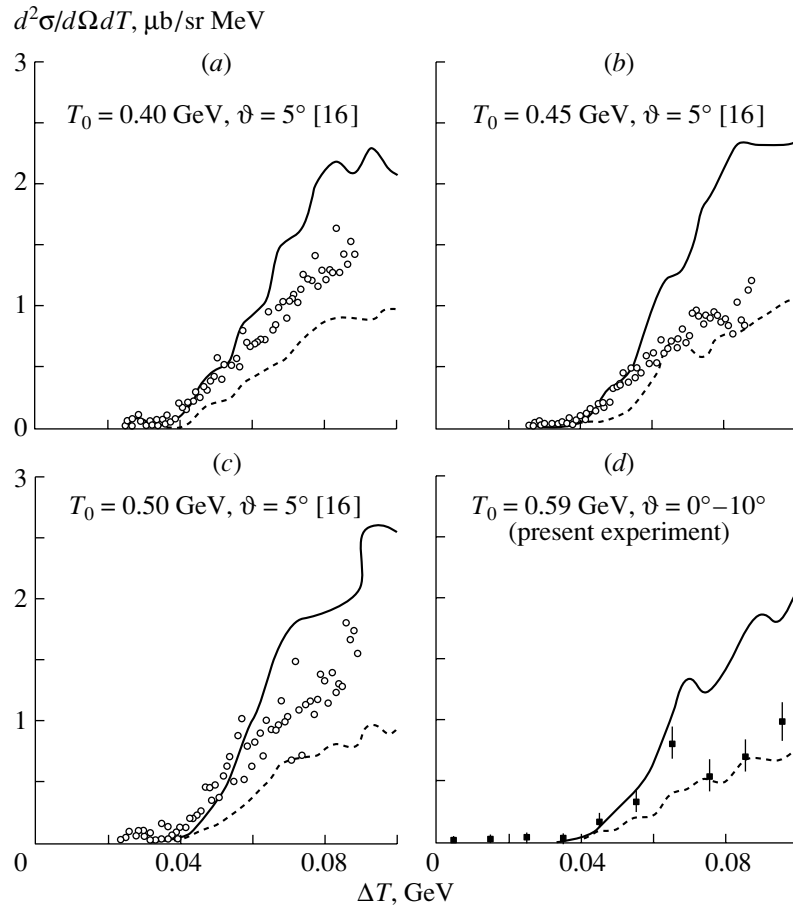


Fig. 7. Double-differential cross sections for (a–c) $\pi^{+16}\text{O} \rightarrow \pi^- X$ and (d) $\pi^{-16}\text{O} \rightarrow \pi^+ X$ reactions versus ΔT [$\Delta T = T_0 - T$, where $T_0(T)$ is the kinetic energy of a beam (forward emitted) pion] at various energies. The results of the calculations performed on the basis of the model proposed in [9] by assuming the SSCX mechanism with (without) allowance for the effect of nuclear-medium polarization are shown by the dashed (solid) curve.

version in a target material) induced by a 10% admixture of electrons in the π^- beam (the yield of positrons at $\vartheta \approx 0^\circ$ is approximately two orders of magnitude greater than the PDCX yield) and (b) $\pi^- A \rightarrow \pi^0 X \rightarrow e^+ X'$ reactions, whose background (about 30% of PDCX) was estimated by eliminating the Cherenkov counter \check{C}_3 from the trigger and by recording its signal in collecting a small individual data sample.

The use of the Cherenkov counters \check{C}_2 and \check{C}_3 made it possible to suppress both sources of positron background almost completely.

That the angular distributions of events of reaction (2) for various intervals of momenta of incident π^+ mesons (some of these intervals are presented in Fig. 5) comply well with the results of our Monte Carlo calculation of the geometric efficiency of the facility (under the assumption that the cross section is isotropic) suggests a rather weak angular dependence of the measured cross section.

3. RESULTS

The double-differential cross sections for the inclusive reaction (2) were calculated by the formula

$$\frac{d^2\sigma}{d\Omega dT} = \frac{N}{(\rho l/A)N_A N_0 \Delta\Omega \delta T k}, \quad (5)$$

where N is number of PDCX events in the interval $\delta T = 10$ MeV; A is the target mass number; ρl is the target thickness in g/cm^2 ; N_A is Avogadro's number; N_0 is the negative-pion flux as determined by the coincidences of the counters H_1 , C_2 , C_3 , and \check{C}_2 ; $\Delta\Omega$ is the solid angle covered by the facility acceptance; and k is a coefficient that is equal to 0.55 ± 0.06 or 0.57 ± 0.06 for H_2O (D_2O) or ${}^6,{}^7\text{Li}$, respectively, and which takes into account corrections to the cross section for the presence of a lepton admixture in the beam (0.83), for pion absorption in the target (0.92 and 0.97) and in materials of the equipment (0.96), for pion decays in the spectrometer (0.94), for the halo of the beam at the entrance of the target (0.84), and

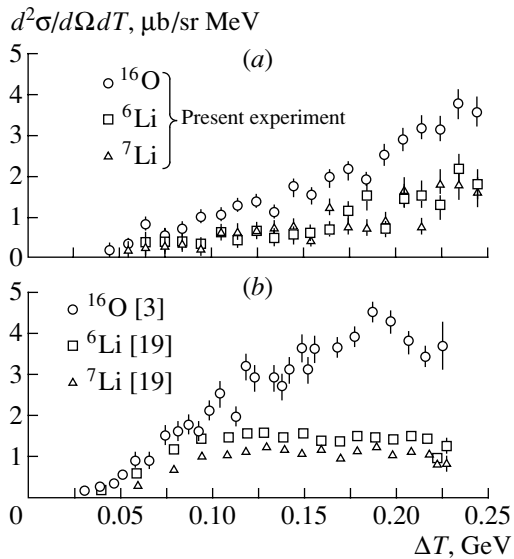


Fig. 8. Double-differential cross sections for $\pi^- A \rightarrow \pi^+ X$ reactions versus ΔT at (a) $T_0 = 0.59$ GeV for $\vartheta = 0^\circ$ – 14° and (b) $T_0 = 0.24$ GeV for $\vartheta = 25^\circ$.

for spurious actuations of the Cherenkov counter \tilde{C}_3 (0.94).

In order to test the correctness of our procedure for measuring the cross section for reaction (2), we determined the cross sections for backward elastic pion–proton scattering in the angular range $\cos\vartheta = 0.86$ – 0.99 . To a precision higher than 10%, these cross sections proved to be in agreement with the data of partial-wave analysis reported in [15].

The ΔT dependence of $d^2\sigma/d\Omega dT$ for the process occurring on ^{16}O at $T_0 = 0.59$ GeV was obtained by averaging the cross sections that were found for H_2O and D_2O and which comply well with each other within the statistical errors. This dependence is in reasonably good agreement with the spectrum obtained previously in [7]. From Fig. 6, one can see that, in the interval of ΔT between 0.03 and 0.25 GeV, the cross section steadily grows, showing no special features near the threshold for the reaction involving the production of an extra pion (the threshold is indicated by the arrow). The solid curve in Fig. 6 represents the PDCX contribution to the cross section for reaction (1) according to the calculations performed for the SSCX mechanism on the basis of the model that was proposed in [9] and which was intended for describing the set of processes induced by pion–nucleus interaction. In these calculations, we took into account the Fermi motion of nucleons, the Pauli exclusion principle, and absorptive effects. It can be seen that the results of the calculations exceed considerably the measured cross section; a similar excess is also observed for the inclusive spectra [16] at

the lower energies of $T_0 = 0.4$ – 0.5 GeV for $\pi^+ {}^{16}\text{O} \rightarrow \pi^- X$ reactions (see Fig. 7).

It is worth noting here that the results obtained by calculating the cross sections for the exclusive reactions $\pi^+ {}^{14}\text{C} \rightarrow \pi^- {}^{14}\text{O}$ and $\pi^+ {}^{18}\text{O} \rightarrow \pi^- {}^{18}\text{Ne}$ within Glauber theory [6] without free parameters are also in excess of the cross sections measured at $T_0 = 300$ – 525 MeV [17]. Oset and Strottman [6] and Oset *et al.* [18] were able to fit the results of their calculations with data from [17] upon taking into account a renormalization of the amplitude for pion charge exchange on a nucleon, this renormalization being interpreted as an effect of nuclear-medium polarization. The inclusion of this effect in calculating the PDCX contribution to the cross section for reaction (1) (dashed curve in Fig. 6) reduces substantially the cross-section value. Such a renormalization also leads to the reduction of the calculated cross section displayed in Fig. 7 (dashed versus solid curve).

From Fig. 6, one can also see that the calculated cross section for the reaction leading to the production of an extra pion (dotted curve) grows sharply from the threshold, considerably exceeding the measured cross section. This discrepancy may probably be due to overly rough approximations embedded in the model behind the computational procedure. An adequate parametrization of the cross sections cannot be constructed here in view of the paucity of experimental data on the differential cross sections for the production of an extra pion.

On average, the differential cross section that we measured for ${}^6\text{Li}$ proved to be about one-half as large as the cross section for ${}^{16}\text{O}$, but it does not differ, within the errors, from the cross section for ${}^7\text{Li}$ (see Fig. 8a). This is the point where our data differ substantially from the results presented in [19] at $T_0 = 0.24$ GeV (see Fig. 8b)—there, the cross section measured for ${}^7\text{Li}$ is smaller than that for ${}^6\text{Li}$ nearly by a factor of 1.5. We recall that the PDCX reaction studied here proceeds on two intranuclear protons, neutrons having only a shadowing effect. This shadowing effect is much more pronounced at the energy of $T_0 = 0.24$ GeV than at the energy of our experiment ($T_0 = 0.59$ GeV), since the cross section for $\pi^- n$ interaction is one order of magnitude larger at $T_0 = 0.24$ GeV.

4. CONCLUSION

The spectra of fast π^+ mesons from the $\pi^- A \rightarrow \pi^+ X$ reactions on $A = {}^6\text{Li}$, ${}^7\text{Li}$, and ${}^{16}\text{O}$ nuclei at a primary momentum of $p_0 = 0.72$ GeV/c ($T_0 = 0.59$ GeV) have been measured for $\vartheta = 0^\circ$ – 14° in the range $\Delta T = 0$ – 250 MeV. The results have been analyzed and compared with experimental data

obtained at lower energies. Calculations performed on the basis of the model proposed in [9] have yielded results exceeding the cross sections obtained here. The agreement with the experimental data is noticeably improved upon taking into account the effect of nuclear-medium polarization. The spectrum in the region of the production of an extra pion has not yet been reproduced. The shape of the π^+ spectrum measured in our experiment for the ^{16}O target at $T_0 = 0.59$ GeV complies with the shape of the π^- spectrum [16] for $\pi^{+16}\text{O} \rightarrow \pi^- X$ reactions at $T_0 = 0.40, 0.45,$ and 0.50 GeV. The distinction between the cross sections for ^6Li and ^7Li vanishes at higher energies in accordance with the decrease in the total cross section for $\pi^- n$ interactions above the Δ -isobar region.

ACKNOWLEDGMENTS

We are indebted to A.L. Williams for placing at our disposal tables of the cross sections from the experiment reported in [16]. The help of the personnel of the 3-m spectrometer and the ITEP accelerator in conducting the experiment is gratefully acknowledged. We also thank our colleagues from the PSP-2 group.

This work was supported in part by the Russian Foundation for Basic Research (project nos. 98-02-17179 and 00-15-96545).

REFERENCES

1. H. Clement, Prog. Part. Nucl. Phys. **29**, 175 (1992).

2. M. B. Johnson and C. L. Morris, Annu. Rev. Nucl. Part. Sci. **43**, 165 (1993).
3. S. A. Wood *et al.*, Phys. Rev. C **46**, 1903 (1992).
4. M. Yuly *et al.*, Phys. Rev. C **55**, 1848 (1997).
5. *Pion Nucleus Double Charge Exchange*, Ed. by W. R. Gibbs and M. J. Leitch (World Sci., Singapore, 1990).
6. E. Oset and D. Strottman, Phys. Rev. Lett. **70**, 146 (1993).
7. B. M. Abramov *et al.*, Yad. Fiz. **59**, 399 (1996) [Phys. At. Nucl. **59**, 376 (1996)].
8. B. M. Abramov *et al.*, Few-Body Syst., Suppl. **9**, 237 (1995).
9. M. J. Vicente Vacas, M. Kh. Khankhasayev, and S. G. Mashnik, nucl-th/9412023.
10. A. B. Kaidalov and A. P. Krutenkova, Yad. Fiz. **60**, 1334 (1997) [Phys. At. Nucl. **60**, 1206 (1997)].
11. A. B. Kaidalov and A. P. Krutenkova, J. Phys. G **27**, 893 (2001).
12. B. M. Abramov *et al.*, Nucl. Instrum. Methods Phys. Res. A **248**, 203 (1986).
13. B. M. Abramov *et al.*, Pis'ma Zh. Éksp. Teor. Fiz. **71**, 524 (2000) [JETP Lett. **71**, 359 (2000)].
14. B. M. Abramov *et al.*, Nucl. Phys. A **372**, 301 (1981).
15. R. A. Arndt *et al.*, Phys. Rev. C **52**, 2120 (1995).
16. R. G. Burleson, in *Pion Nucleus Double Charge Exchange*, Ed. by W. R. Gibbs and M. J. Leitch (World Sci., Singapore, 1990), p. 79.
17. A. L. Williams *et al.*, Phys. Lett. B **216**, 11 (1989).
18. E. Oset, D. Strottman, H. Tok, and J. Navarro, Phys. Rev. C **48**, 2395 (1993).
19. P. A. M. Gram, in *Pion-Nucleus Physics: Future Directions and New Facilities at LAMPF*, Ed. by R. J. Peterson and D. D. Strottman (American Inst. of Physics, New York, 1988), p. 79.

Translated by A. Isaakyan

Conference on Physics of Fundamental Interactions
Experiment

**Measurement of the Differential Cross Sections for π^-p
Charge-Exchange Scattering in the Region of the Low-Lying
 P_{11} , S_{11} , and D_{13} Resonances**

I. V. Lopatin

Petersburg Nuclear Physics Institute, Russian Academy of Sciences, Gatchina, 188350 Russia

Received March 21, 2001

Abstract—The differential cross sections for the reaction $\pi^-p \rightarrow \pi^0n$ were measured for scattering angles in the backward hemisphere. The experiment was performed by using the pion channel of the synchrocyclotron installed at the Petersburg Nuclear Physics Institute (PNPI, Gatchina), the momenta of incident pions being varied in the range between 456 and 710 MeV/ c . The measurements were performed by recording the recoil neutron in coincidence with one of the photons from the decay process $\pi^0 \rightarrow 2\gamma$. The experimental facility used is described, and the results of the measurements are presented. These new results are characterized by a statistical accuracy higher than that of all results published previously and are in better agreement with the predictions of the partial-wave analysis (SM-95 version) performed by a group from Virginia Polytechnic Institute. © 2002 MAIK “Nauka/Interperiodica”.

1. INTRODUCTION

The present article reports the results of an experiment performed by using the pion channel of the Synchrocyclotron installed at the Petersburg Nuclear Physics Institute (PNPI, Gatchina). The full list of the authors who participated in this experiment can be found in the PNPI preprint [1].

Together with elastic $\pi^\pm p$ scattering, the process of charge-exchange π^-p scattering ($\pi^-p \rightarrow \pi^0n$) belongs to the group of three basic processes that furnish the main body of information about the spectroscopy of nonstrange baryons (in other words, pion–nucleon resonances). The features of these resonances (masses, widths, decay modes) are of great importance. Precise knowledge of them would allow a multiparameter test of available quark models that is aimed at choosing the most realistic of these. Unfortunately, the present-day accuracy to which the features in question have been determined is insufficiently high; moreover, the existence of some resonances has not yet been established conclusively. The reason behind this situation is twofold: on one hand, the procedures for a partial-wave analysis used to extract the features of resonances from experimental data are imperfect; on the other hand, the quality of these experimental data is insufficiently high.

An analysis of the currently prevalent experimental situation reveals that, in the region of the low-lying pion–nucleon resonances $P_{11}(1440)$, $S_{11}(1535)$, and $D_{13}(1520)$, quite a rich database has been created for

elastic π^+p and π^-p scattering owing predominantly to the studies performed at PNPI [2], at the Los Alamos meson factory (USA) [3], and at the Rutherford Laboratory (United Kingdom) [4]. However, the quality of data on charge-exchange π^-p scattering leaves much to be desired. This especially concerns relevant differential cross sections—in the range of incident-pion energies between 100 and 600 MeV, data on them are scanty, some of these data being far from reliable.

2. EXPERIMENTAL FACILITY

The experiment was performed by using the pion channel of the PNPI synchrocyclotron at incident-pion energies in the range between 337 and 585 MeV, the corresponding momentum values being 456 and 710 MeV/ c . The layout of the experimental facility is shown in Fig. 1. As basic elements, the facility includes a liquid-hydrogen target, neutron detectors, a deflecting magnet (which prevents beam pions from hitting the neutron detectors used), and γ detectors of two types.

The experiment detected recoil neutrons in coincidence with one of the photons from neutral-pion decay. For this, the neutron and γ detectors were arranged at angles approximately corresponding to the kinematics of the reaction $\pi^-p \rightarrow \pi^0n$ (in the subsequent decay of the product π^0 mesons, the photons are emitted predominantly in the direction of π^0 -meson emission). The layout of the equipment

(see Fig. 1) was intended for recording the process of charge-exchange π^-p scattering into the backward hemisphere, in which case the recoil neutron goes in the forward direction, while the photons originating from π^0 -meson decay travel predominantly in the backward direction. In the c.m. frame, the range of angles that is specified by the arrangement of the neutron detectors is that between 155° and 180° .

Presented immediately below is a detailed description of individual units of the facility.

The experiment employed a safe vacuum-type liquid-hydrogen target [5] preliminarily cooled by means of a nitrogen vessel. The angle open for detecting emitted particles was 270° . The hydrogen container had the shape of a vertical cylinder of height 12 cm and diameter 10 cm, its wall thickness being $100 \mu\text{m}$ of aluminum. Hydrogen was liquefied by cooling the container with cold gaseous helium. The outer window of the vacuum casing was manufactured from Mylar $200 \mu\text{m}$ thick. The temperature (and, hence, the density) of liquid hydrogen was monitored throughout the experimental time by measuring the resistance of a calibrated germanium diode and the pressure of vapors over the surface of the liquid. The density of liquid hydrogen was $0.0740 \pm 0.0004 \text{ g/cm}^3$.

The neutron detectors were designed and manufactured at the University of California at Los Angeles [6]. Each detector consisted of scintillation blocks tightly adjacent to one another that had dimensions of $25.4 \times 25.4 \times 8.9 \text{ cm}^3$ (length \times height \times width), each block being viewed by two phototubes. The scintillator length of 25.4 cm ensured the neutron-detection efficiency ε_n at a level not poorer than 0.2. The efficiency value was previously determined in the United States [7]. The distance from the target center to the entrance of the detector was 475 cm, and the angular acceptance of each detector was 3.14° ($\pm 1.57^\circ$ from the detector axis). An anticoincidence counter that rejected triggering from charged particles was arranged in front of each neutron detector; the anticoincidence counters were manufactured at the University of California at Los Angeles, the thickness of plastic scintillators being 3 mm.

In order to prevent the incident-pion beam from hitting the neutron detectors, a dedicated deflecting magnet was placed in between the target and these detectors. This magnet generated a field of strength up to 0.8 T in a gap of width 23 cm (the diameter of the pole was 73 cm), ensuring the deflection of the beam through an angle of about 20° . The scintillation counter $S4$ was arranged on the trajectory of the deflected pion beam. This veto counter (together with the counter $S3$ positioned on the beam axis immediately downstream of the target) served to

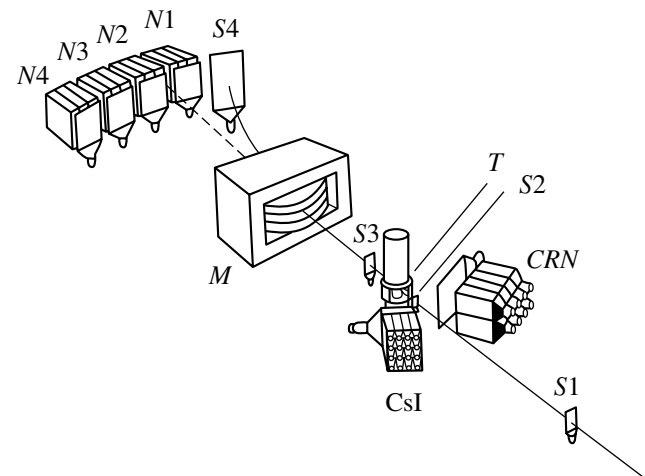


Fig. 1. Layout of the experimental facility used to measure the differential cross sections for charge-exchange π^-p scattering: ($S1$, $S2$) monitoring counters, ($S3$, $S4$) beam veto counters, ($N1$ – $N4$) neutron detectors, (M) Magnet deflecting the incident pion beam, (T) liquid-hydrogen target, (CsI) γ detector consisting of 16 $\text{CsI}(\text{Na})$ crystals, and (CRN) Cherenkov spectrometer consisting of eight blocks from lead glass. Anticoincidence counters are arranged in front of the neutron and γ detectors.

reduce the number of spurious triggerings due to the background counting of photons and neutrons in the neutron detectors.

Two types of total-absorption electromagnetic calorimeters were used in the experiment to record photons from π^0 -meson decays. The first included eight Cherenkov spectrometers from SF-5 lead-glass blocks. Each block had dimensions of $15 \times 15 \times 35 \text{ cm}^3$ (the last dimension, thickness, corresponded to 13.8 radiation-length units) and was viewed by a phototube glued directly to the end face of this block. The other calorimeter consisted of 16 $\text{CsI}(\text{Na})$ crystals arranged as a 4×4 assembly, the dimensions of an individual crystal being $6 \times 6 \times 30 \text{ cm}^3$. The crystal thickness corresponded to 16.2 radiation-length units. Anticoincidence counters were placed in front of each of the two γ detectors. These counters served to reject cases where it was a charged particle emitted from the target and not a photon that hit the detector.

An important feature peculiar to this experiment was that it employed γ detectors of different types positioned on the different sides of the beam axis. Since the neutron detectors $N1$ and $N2$ were also placed on the different sides of the beam axis symmetrically with respect to it, there arose the possibility of measuring the cross section for scattering at the same angle by using the different types of γ detectors, whereby we

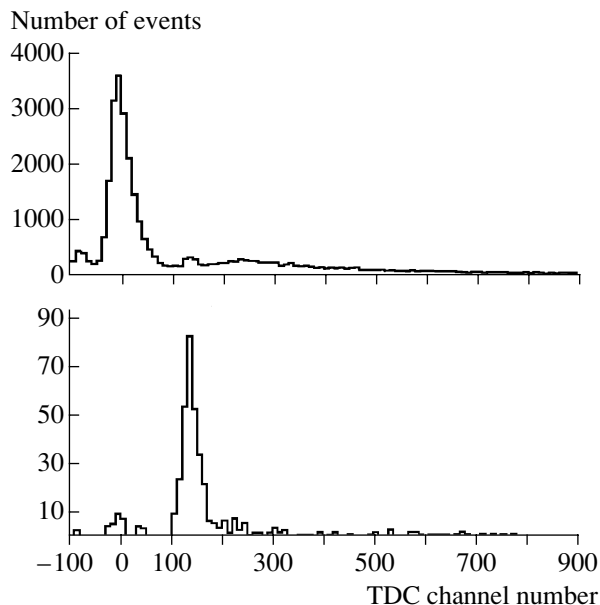


Fig. 2. Time-of-flight spectra of the neutrons (upper histogram) prior to and (lower histogram) following the introduction of $n\gamma$ coincidences. The number of a channel of the time-to-digital converter (TDC) is plotted along the abscissa. The time channel widths was 0.05 ns.

were able to study the influence of possible disregarded systematic effects.

3. EXPERIMENTAL PROCEDURE

As was indicated in the preceding section, the differential cross sections for charge-exchange π^-p scattering are measured in the present experiment by simultaneously detecting the recoil neutron and one of the photons. In order to ensure, however, the possibility of using, in data processing, various cuts on energy, $n\gamma$ coincidences were introduced not at the stage of trigger formation but at the subsequent stage of data processing.

In the course of this experiment, the entire body of information coming from the detectors (the amplitude spectra from the neutron and γ detectors, time-of-flight spectra from the neutron detectors, numbers of counts from the monitoring counters and from the anticoincidence counters) was recorded in the random-access memory of a PC. After the accumulation of 100 events, a buffer was formed and recorded on a hard disk. The time of accumulation of one buffer was varied from 2 to 10 s, its actual value being dependent on the incident-pion momentum and on the beam intensity. In all, we collected 20 000 to 40 000 buffers in dealing with the hydrogen-filled target and approximately half of this number for the empty target. The total time of data-sample accumulation at a single

momentum value was 50 h ($p_\pi = 456$ MeV/c) to 120 h ($p_\pi = 710$ MeV/c).

The amplitude spectra associated with the passage of cosmic-ray muons¹⁾ through the γ detectors were recorded simultaneously with data acquisition in order to check the stability of the amplitude channels of all γ detectors. The positions of the peaks in these spectra were periodically monitored, and the required corrections were introduced if there arose some random drifts.

In the course of subsequent data processing, the number of events due to the reaction being studied was determined from an analysis of the time-of-flight spectra measured over a flight base of about 5 m between the monitoring counter $S2$ and the actuated neutron detector. First, we performed (upon the relevant renormalization of monitoring numbers) a channel-by-channel subtraction of the spectra obtained in measurements with the hydrogen-filled and the empty target. This made it possible to eliminate the contribution of the charge-exchange reaction occurring on a material of the scintillator of the $S2$ counter, on aluminum walls of the container, and on the entrance Mylar diaphragm of the target. Thus, the resulting spectrum contained only events of pion interaction with hydrogen. An example of such a spectrum is represented by the upper histogram in Fig. 2, where we plotted the number of events along the ordinate and the number of a channel of the time-to-digital converter (TDC) along the abscissa. The spectrum is seen to be dominated by a strong peak²⁾ associated with photons from the decay process $\pi^0 \rightarrow 2\gamma$ that hit the detector, recoil neutrons from the reaction $\pi^-p \rightarrow \pi^0n$ manifesting themselves as a modest enhancement (in the region of the 130th channel) above the pedestal that is associated with neutrons from pion-production reactions ($\pi^-p \rightarrow \pi^0\pi^0n$, $\pi^+\pi^-n$, etc.) and with a general neutron background in the experimental hall of the accelerator.

The lower histogram in Fig. 2 demonstrates that the separation of “useful” events (that is, events due to the reaction $\pi^-p \rightarrow \pi^0n$) is facilitated upon introducing the requirement of $n\gamma$ coincidences: the photon peak and the pedestal are substantially suppressed, while the component generated by the reaction $\pi^-p \rightarrow \pi^0n$, which is studied here, becomes quite distinct.³⁾ It is the number of events under the corresponding peak—we denote it by N_{event} —that

¹⁾These muons were detected in pauses of 10 ms between two successive accelerator spills.

²⁾For the sake of convenience, the peak position was chosen for a reference point of the histograms.

³⁾It should be emphasized that different scales along the ordinate are chosen for the upper and the lower histogram.

is used below to calculate the absolute value of the differential cross section.

It is worth noting here that the number N_{event} may also include events due to the radiative-capture reaction $\pi^- p \rightarrow \gamma n$. The time-of-flight criterion cannot distinguish between neutrons from the charge-exchange process (in the formulas given below, we denote it by “cex”) from neutrons from the radiative-capture reaction (“rex”)—the positions of the corresponding neutron peaks are separated by 0.2 to 0.3 ns. In a further treatment of the data that come from the present experiment, it is therefore necessary to subtract the contribution of the radiative-capture reaction; that is, the differential cross sections for charge-exchange $\pi^- p$ scattering must be calculated with the number $N_{\text{ev}}^{\text{cex}} = N_{\text{ev}} - N_{\text{ev}}^{\text{rex}}$.

The formula for calculating the required differential cross sections in the c.m. frame has the form

$$\frac{d\sigma}{d\Omega} = \frac{N_{\text{ev}}^{\text{cex}}}{N_{\pi} N_p \Delta\Omega_n^{\text{lab}} J_n \varepsilon_n F_{\gamma}}. \quad (1)$$

The number N_{π} of pions that traversed the operating volume of the target and which actuated the facility was determined on the basis of the recorded number of coincidences of the monitoring counters $S1$ and $S2$ that was corrected for percentage of alien particles (electrons and muons) in the beam.

The number of protons in the target is given by $N_p = N_A \rho t_{\text{eff}}$, where N_A is Avogadro’s number, ρ is the liquid-hydrogen density corresponding to the measured (in the course of the experiment) temperature of the target operating volume, and t_{eff} is the effective target thickness calculated with allowance for the radius of the cylindrical container of hydrogen and for the dimensions of the monitoring counter $S2$.

The solid angle $\Delta\Omega_n^{\text{lab}}$ covered by the neutron detector is determined by the geometry of the experiment and, for a distance of 488 cm between the target center and the midpoint of the detector, is 2.85×10^{-3} sr.

The values of the neutron-detector efficiency ε_n were taken from [7], where they were measured with the aid of tagged neutrons from the reaction $\pi^- d \rightarrow nn$. In the neutron-energy range $E_n = 83\text{--}290$ MeV, which was explored in that study, the energy dependence of the efficiency in question was described there by the expression

$$\varepsilon_n(E_n) = 1 - e^{-\lambda(E_n)L},$$

where $\lambda(E_n)$ is the neutron-detection efficiency per centimeter of the scintillator traversed and L is the thickness of the scintillation block. For three neutron detection thresholds of 2, 5, and 15 MeV, the efficiency of neutron detectors was determined to within $\pm 3.5\%$.

The neutron Jacobian J_n is determined exclusively by the kinematics of the process being studied, ranging here between 0.43 and 0.49, its specific value being dependent on the incident-pion momentum and on the recoil-neutron emission angle.

The coefficient F_{γ} , which is hereafter referred to as the angular acceptance, indicates, among all photons that originate from the decays of neutral pions kinematically conjugate with recoil neutrons hitting a given neutron detector, the fraction that is recorded by the γ detector. In order to calculate F_{γ} , the experiment was simulated by the Monte Carlo method. In these calculations, we took precisely into account the actual geometry of the experiment, including the design of the γ detectors and the possible interaction of neutrons and photons emitted from the hydrogen container with the structural elements of the target and of the detectors. Since the anticoincidence counter situated in front of a γ detector could be triggered by the conversion of photons in the scintillator of this counter that were emitted from the target or by the conversion of annihilation photons that escaped from the γ detector in the opposite direction, our simulation procedure allowed for the probability of such spurious actuations. In the calculations, we employed the spatial features of the pion beam (its dimensions and angular divergence) that were measured previously and took into account the momentum distribution of particles in the beam. For the chosen geometry of the experiment, the coefficient F_{γ} ranged between 0.2 and 0.4, its specific value being dependent on the angle at which the neutron detector was arranged.

To conclude this section, we revisit the definition of the number $N_{\text{ev}}^{\text{cex}}$. It can easily be shown that this number can be represented as

$$N_{\text{event}}^{\text{cex}} \quad (2)$$

$$= \frac{N_{\text{event}}}{1 + (F_{\gamma}^{\text{rex}}/F_{\gamma}^{\text{cex}})(J_n^{\text{rex}}/J_n^{\text{cex}})(1/R)} = N_{\text{event}} K,$$

where

$$R = \left(\frac{d\sigma}{d\Omega}\right)^{\text{cex}} \bigg/ \left(\frac{d\sigma}{d\Omega}\right)^{\text{rex}}$$

is the so-called Panofsky ratio. In the ensuing calculations, we used R values that were computed on the basis of partial-wave analyses of pion–nucleon scattering [8] and of pion photoproduction [9]. The possible error in the R values obtained in this way can be estimated by comparing them with those measured experimentally at a few points for which such measurements were performed. Usually, $R > 1$ (for the scattering angles being investigated, the ratio R takes values between 3 and 30, depending on the incident-pion momentum), but this is compensated to a considerable extent by the fact that the angular

acceptance F_γ^{cex} for the charge-exchange reaction is considerably smaller than the angular acceptance F_γ^{rex} for the radiative-capture reaction (this is because, in the case of the reaction $\pi^-p \rightarrow \pi^0n$, photons from pion decay have a broad angular distribution, whereas the photon produced in the reaction $\pi^-p \rightarrow \gamma n$ travels in a specific direction). As a result, the contribution of the radiative-capture reaction proves to be quite large for specific combinations of neutron and γ detectors. By way of example, we indicate that, in the case where neutrons hitting the $N3$ or the $N4$ detector are recorded in coincidence with photons hitting the Cherenkov spectrometer CRN , the denominator in formula (2) proves to be close to 2 (that is, $N_{\text{event}}^{\text{cex}} \approx N_{\text{event}}/2 \approx N_{\text{event}}^{\text{rex}}$) in the momentum range 500–600 MeV/c, where the cross section for the charge-exchange reaction is minimal for scattering at large angles. At the same time, we note that the contribution of the radiative-capture reaction vanishes if one records $N1 + \text{CsI}$ and $N2 + CRN$ coincidences since, in this case, the relative disposition of the neutron detector and γ detectors does not fit the kinematics of the reaction $\pi^-p \rightarrow \gamma n$, so that the photons from this reaction that are kinematically conjugate with the recorded neutrons merely miss the γ detector.

It is necessary to introduce some corrections in the quantity $d\sigma/d\Omega$ obtained with the aid of formula (1). We now consider this issue at greater length.

The number of particles that have traversed, throughout the experimental time, the target volume singled out by the monitoring counter $S2$ is determined by the number of $S1 \cdot S2$ coincidences; however, it is necessary to introduce a correction for the presence of muons and electrons in the pion beam. The composition of the beam was comprehensively studied in [10], where it was shown experimentally that the concentration of electrons increases with decreasing momentum of particles in the beam, changing from 4.5% at 625 MeV/c to 20% at 450 MeV/c. More recently, the composition of the beam was measured in the course of experiments reported in [11] and devoted to the energy calibration of γ detectors by using electrons of various energies. The results obtained in this way comply well with the beam composition presented in [10]. As to the admixture of muons in the beam, it is less significant: according to [10], it is about 4% at 570 MeV/c and $(8.0 \pm 1.3)\%$ at 400 MeV/c.

Taking the above into account, we have

$$N_\pi = N_{\text{beam}} - N_e - N_\mu = N_{\text{beam}}(1 - \alpha_1), \quad (3)$$

where the correction term is given by $\alpha_1 = (N_e + N_\mu)/N_{\text{beam}}$.

In addition, a small fraction of pions recorded by the monitoring counter $S2$ decay on the path between this counter and the target. Assuming that, on average, this decay proceeds within the base of 25 cm between the $S2$ counter and the target center, we estimate the relevant correction α_2 at 0.7% for 710 MeV/c and at 1.0% for 456 MeV/c.

Yet another correction is associated with the periodic time structure of the proton beam at the outlet of the accelerator, where particle microbunches of duration about 10 ns are separated by intervals of 75 ns. Accordingly, secondary-particle beams generated by the primary beam have a similar time structure. At a particle flux of 10^6 s^{-1} in the pion channel, there is a nonzero probability that two pions from two successive microbunches hit the hydrogen target. If the second of these pions undergoes interaction in the target, inducing the charge-exchange reaction, this useful event will be rejected provided that the beam veto counter actuated by the preceding pion has a pulse duration commensurate with the separation of microbunches, which is about 75 ns (see above).

The corresponding correction α_3 was calculated on the basis of the Poisson distribution. By way of example, we indicate that, at a momentum of 456 MeV/c, the calculated value of this correction is $\alpha_3 = 0.1$. At this momentum value, we additionally performed a dedicated test experiment at an accelerator intensity reduced by a factor of 2; needless to say, the suppression of useful events that is due to the effect being considered must be less pronounced in that case. Upon introducing the calculated corrections, the cross-section values obtained in the test experiment at the reduced multiplicity and in the basic experiment at full intensity were in agreement within 5%. This gives sufficient grounds to state that, at a momentum of 456 MeV/c, the systematic error in determining the cross sections that is introduced by the correction being discussed does not exceed 5%; that is, $\alpha_3 = 0.1 \pm 0.05$. In other words, the quantity α_3 itself is known to within $\pm 50\%$.

With allowance for all the aforementioned corrections, expression (1) takes the form

$$\frac{d\sigma}{d\Omega} = \frac{N_{\text{event}}^{\text{cex}}}{N_{\text{beam}} N_p \Delta\Omega_n^{\text{lab}} J_n \varepsilon_n F_\gamma} \quad (4)$$

$$\times \frac{1}{(1 - \alpha_1)(1 - \alpha_2)(1 - \alpha_3)}.$$

4. RESULTS

The measurements were performed at the pion channel of the PNPI synchrophasotron for nine values of the incident-pion momentum. These were 456, 490, 573, 614, 655, 681.5, 685, 697.5, and

Differential cross sections for charge-exchange $\pi^- p$ scattering that are obtained in the present study [both the statistical and the systematic error (respectively, first and second error) are quoted for each cross-section value]

p , MeV/ c	$d\sigma/d\Omega$, mb/sr			
	$N1 + \text{CsI}$	$N2 + \text{CRN}$	$N3 + \text{CRN}$	$N4 + \text{CRN}$
	$\theta^{\text{c.m.}} = 175^\circ$		$\theta^{\text{c.m.}} = 166^\circ$	$\theta^{\text{c.m.}} = 157^\circ$
456	$0.326 \pm 0.024 \pm 0.023$	$0.388 \pm 0.016 \pm 0.032$	$0.339 \pm 0.010 \pm 0.023$	$0.305 \pm 0.008 \pm 0.020$
490	$0.117 \pm 0.016 \pm 0.013$	$0.097 \pm 0.012 \pm 0.011$	$0.101 \pm 0.006 \pm 0.011$	$0.113 \pm 0.005 \pm 0.012$
573	$0.065 \pm 0.011 \pm 0.010$	$0.067 \pm 0.008 \pm 0.011$	$0.066 \pm 0.003 \pm 0.010$	$0.055 \pm 0.003 \pm 0.008$
614	$0.277 \pm 0.015 \pm 0.018$	$0.244 \pm 0.013 \pm 0.020$	$0.207 \pm 0.007 \pm 0.014$	$0.162 \pm 0.006 \pm 0.011$
655	$0.491 \pm 0.013 \pm 0.021$	$0.506 \pm 0.011 \pm 0.033$	$0.447 \pm 0.007 \pm 0.022$	$0.339 \pm 0.006 \pm 0.015$
681.5	$0.641 \pm 0.012 \pm 0.027$	$0.684 \pm 0.014 \pm 0.045$	$0.581 \pm 0.007 \pm 0.029$	$0.475 \pm 0.007 \pm 0.020$
685	$0.662 \pm 0.016 \pm 0.028$	$0.714 \pm 0.014 \pm 0.047$	$0.601 \pm 0.009 \pm 0.030$	$0.489 \pm 0.008 \pm 0.021$
697.5	$0.686 \pm 0.018 \pm 0.033$	$0.712 \pm 0.015 \pm 0.049$	$0.617 \pm 0.009 \pm 0.033$	$0.534 \pm 0.008 \pm 0.026$
710	$0.642 \pm 0.017 \pm 0.031$	$0.697 \pm 0.015 \pm 0.048$	$0.600 \pm 0.010 \pm 0.032$	$0.529 \pm 0.009 \pm 0.025$

710 MeV/ c . The absolute values of the particle momenta in the beam were known to within $\pm 0.5\%$ from the previous measurements reported in [10]. The total momentum acceptance (FWHM of the respective distribution) was 6%. The particle flux through the monitoring counter $S2$ changed from $1.5 \times 10^5 \text{s}^{-1}$ at 710 MeV/ c to $3.5 \times 10^5 \text{s}^{-1}$ at 450 MeV/ c , the $S2$ counter capturing about 70% of the total particle flux in the beam.

The results are compiled in the table, which quotes, for each value of the differential cross section, both the statistical and the systematic error (respectively, first and second error value).

The systematic errors stemmed predominantly from (i) the uncertainty in determining the density of liquid hydrogen in the target (estimated above at 0.7%); (ii) the uncertainty in determining the neutron-detector efficiency (3.5%); (iii) uncertainty in determining the admixture of electrons and muons in the pion beam [the coefficient α_1 in (4) was 3 to 1%, depending on the momentum value]; (iv) the uncertainties in determining the angles at which the neutron detectors, the calorimeter from CsI crystals, and the Cherenkov spectrometer are arranged with respect to the beam axis ($\pm 0.2^\circ$, $\pm 0.1^\circ$, and $\pm 0.5^\circ$, respectively), the corresponding total error in calculating the angular acceptance being 0.5 and 5% (the specific value of this error depends on the combination of the neutron and γ detectors that is being considered); (v) the uncertainty in subtracting the contribution of the radiative-capture reaction (for the $N3 + \text{CRN}$ and $N4 + \text{CRN}$ combinations, it amounts to 15% for a momentum value of 573 MeV/ c , at which the radiative-capture cross section becomes

commensurate with the cross section for charge-exchange reaction, and decreases to a few percent at lower and at higher momenta; for the $N1 + \text{CsI}$ and $N2 + \text{CRN}$ combinations, the contribution of the radiative-capture reaction vanishes); and (vi) the uncertainty in determining the correction α_3 for the suppression of useful events because of the presence of beam particles in two successive microbunches (in the preceding section, this uncertainty was estimated at $\pm 50\%$ of the correction value itself; this yields the error of 1 to 7% in determining the cross section, the specific value being dependent on the beam intensity).

The total systematic error was calculated as the square root of the sum of the squares of the above six components. For the majority of the momentum values, it is at a level of 5 to 10%, and only at 490 and 573 MeV/ c , where the contribution of the radiative-capture reaction appears to be significant, does the total systematic error become as large as 13–16%.

For the c.m. scattering angle of 175° , we display two sets of the results, that obtained with the Cherenkov spectrometers used as γ detectors and that obtained with the calorimeter of CsI(Na) crystals. As was mentioned above, the neutron detectors conjugate to these two γ detectors were arranged at identical angles on the two sides of the beam axis. A comparison of the cross sections as obtained for the same scattering angle but with the different γ detectors can make it possible to assess additional systematic effects overlooked in data processing. We can state that, in the majority of the cases, the difference of the two cross-section values does not exceed 10%; only for the lowest two momentum values does this difference become as large as 20%. At some

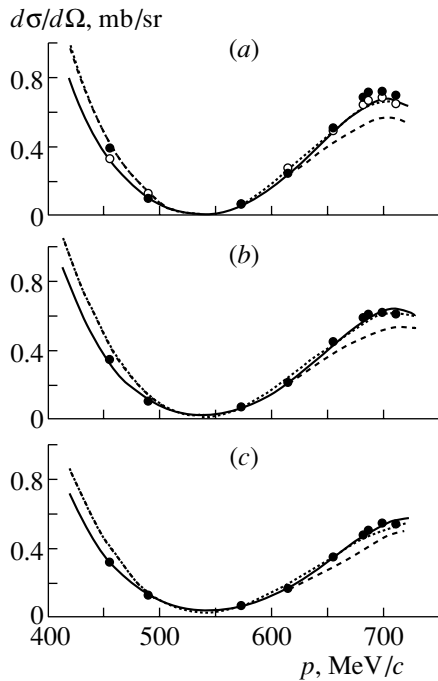


Fig. 3. Experimental results for the $\pi^-p \rightarrow \pi^0n$ differential cross sections at the scattering angles of $\theta^{c.m.} =$ (a) 175° , (b) 166° , and (c) 157° : (closed circles) results obtained with the aid of the Cherenkov spectrometers and (open circles) results obtained with the aid of the CsI(Na) crystals. The dashed, dotted, and solid curves represent the predictions of respectively the KH-80 [12], the PNPI-94 [13], and the SM-95 [8] partial-wave analysis.

momentum values, the difference in question is beyond the statistical errors, but it never exceeds two standard deviations. At the same time, this discrepancy cannot be associated with the systematic errors discussed above, because these could lead to a regular bias of one series of the results (obtained with the Cherenkov spectrometers) with respect to the other series (obtained with the CsI crystals), but, in fact, this is not observed. In all probability, there are some other errors of yet unknown nature.

Our data on the differential cross sections for the charge-exchange reaction⁴⁾ are displayed in Fig. 3, along with the predictions of three partial-wave analyses (KH-80 [12], PNPI-94 [13], SM-95 [8]). It can be seen that, over the entire momentum interval being studied, the new experimental results comply well with the data from the SM-95 partial-wave analysis, but they deviate significantly from the predictions of the KH-80 analysis. This fact can have far-reaching consequences since all features of the pion-nucleon resonances from the tables of the Particle Data Group were obtained on the basis of precisely

⁴⁾The statistical errors of the measurements are within the dimensions of the points.

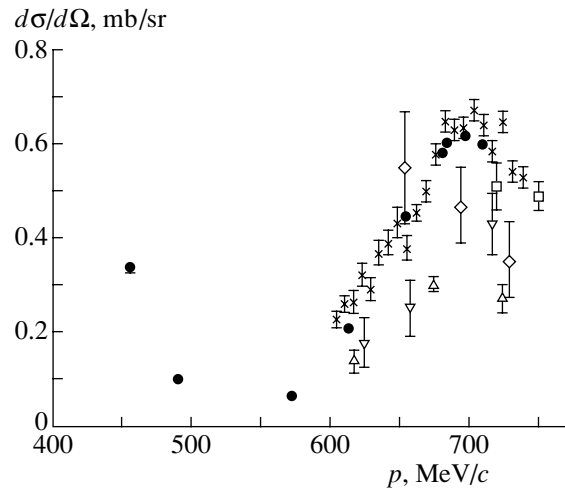


Fig. 4. Differential cross sections for the reaction $\pi^-p \rightarrow \pi^0n$ at the scattering angle of $\theta^{c.m.} = 166^\circ$ according to our data (closed circles), along with results of other experiments (open symbols): (∇) [14], (\square) [15], (\diamond) [16], (\times) [17], and (\triangle) [18].

the KH-80 partial-wave analysis. As a matter of fact, the discrepancy between the new experimental data obtained in the present study and the predictions of the KH-80 analysis suggests that the results of that analysis are not quite correct and should be revised.

In order to illustrate the significance of what our new results introduce in the world database of the charge-exchange reaction, the differential cross sections that we obtained for the scattering angle of $\theta^{c.m.} = 166^\circ$ are shown in Fig. 4, along with the results of those scanty measurements that were performed previously (it should be recalled that all those experiments were performed 25 or even more years ago). It can be seen that there have been no measurements at momenta below 600 MeV/c and that the results of our study in this region are the only source of experimental information about the cross sections for charge-exchange backward scattering. In the region of higher momenta, there is only one consistent set of data that were reported in [17] and which are in satisfactory agreement with our data, especially if one considers that the systematic error therein as estimated by the authors of [17] themselves is 11 to 14%. The remaining results of earlier experiments in Fig. 4 are fragmentary and are characterized by much greater errors.

As can be seen, the PNPI results have a higher statistical accuracy than all previous experiments. Moreover, they cast some doubt on the majority of previous results, which were used as a basis in the partial-wave analyses of pion-proton scattering.

ACKNOWLEDGMENTS

The participants of the experiment are indebted to the Accelerator Department of the PNPI for ensuring the stable operation of the accelerator for periods spanning many days and to the Computer Systems Department of the High Energy Physics Division for the reliable operation of central computer facilities. Special thanks are due to L.D. Malakhov, A.V. Shvedchikov, and Yu.A. Beloglazov for their help in the maintenance of the liquid-hydrogen target and to V.A. Volchenkov for assistance in calculating the features of the pion channel. We are also grateful to our colleagues from abroad—Prof. B.M.K. Nefkens from the University of California at Los Angeles (USA), who provided the experiment with neutron detectors and with part of the fast electronics; Prof. M.E. Sadler from the Abilene Christian University (USA), who placed the qVt measuring instrument and fast discriminators at our disposal; and Prof. J. Julien (France), who extended his aid in the use of Cherenkov γ detectors based on lead glass.

This work was supported by the Russian State Program Fundamental Nuclear Physics, Russian Foundation for Basic Research (project no. 99-02-17500), and a joint grant (no. 00-02-04008) from the Russian Foundation for Basic Research and Deutsche Forschungs Gemeinschaft.

REFERENCES

1. I. V. Lopatin *et al.*, Preprint PIYaF-2363 (Gatchina, 2000).
2. S. P. Kruglov, πN Newsletter, No. 4, 14 (1991).
3. M. E. Sadler, in *Proceedings of International Conference on Mesons and Nuclei at Intermediate Energies, Dubna, 1994* (World Sci., Singapore, 1994), p. 3.
4. J. F. Martin *et al.*, Nucl. Phys. B **89**, 253 (1975).
5. S. P. Kruglov *et al.*, Prib. Tekh. Éksp., No. 6, 23 (1997).
6. J. A. Wightman, B. M. K. Nefkens, *et al.*, Nucl. Instrum. Methods Phys. Res. A **275**, 281 (1989).
7. R. S. Kessler, B. M. K. Nefkens, *et al.*, Nucl. Instrum. Methods Phys. Res. A **275**, 285 (1989).
8. R. A. Arndt *et al.*, Phys. Rev. C **52**, 2120 (1995).
9. R. A. Arndt *et al.*, Phys. Rev. C **53**, 430 (1996).
10. V. P. Koptev *et al.*, Preprint LIYaF-196 (Leningrad, 1975).
11. I. V. Lopatin *et al.*, Preprint PIYaF-2268 (Gatchina, 1998).
12. G. Höhler, *Handbook of Pion–Nucleon Scattering, Physics Data, No. 12-1* (Fachinformationzentrum, Karlsruhe, 1979).
13. V. V. Abaev and S. P. Kruglov, Z. Phys. A **352**, 85 (1995).
14. C. B. Chiu *et al.*, Phys. Rev. **156**, 1415 (1967).
15. E. Hyman *et al.*, Phys. Rev. **165**, 1437 (1968).
16. F. Bulos *et al.*, Phys. Rev. **187**, 1827 (1969).
17. N. C. Debenham *et al.*, Phys. Rev. D **12**, 2545 (1975).
18. R. M. Brown *et al.*, Nucl. Phys. B **117**, 12 (1976).

Translated by A. Isaakyan

Conference on Physics of Fundamental Interactions Experiment

Search for T Violation in the Decays $K^+ \rightarrow \pi^0 \mu^+ \nu$ and $K^+ \rightarrow \mu^+ \nu \gamma^*$

Yu. G. Kudenko

*Institute for Nuclear Research, Russian Academy of Sciences,
pr. Shestidesyatletiya Oktyabrya 7a, Moscow, 117312 Russia*

Received March 21, 2001; in final form, June 4, 2001

Abstract—Recent advances in a search for a T -violating transverse muon polarization in the decays $K^+ \rightarrow \pi^0 \mu^+ \nu$ and $K^+ \rightarrow \mu^+ \nu \gamma$ in the on-going E246 experiment at KEK are reported. Future prospects in polarization measurements are also discussed. © 2002 MAIK “Nauka/Interperiodica”.

1. INTRODUCTION

Measurement of the transverse muon polarization P_T in the decays $K^+ \rightarrow \pi^0 \mu^+ \nu$ ($K_{\mu 3}$) and $K^+ \rightarrow \mu^+ \nu \gamma$ ($K_{\mu 2\gamma}$) can provide important clues to new physics beyond the Standard Model (SM). In $K_{\mu 3}$ decay, P_T is the T -odd observable $\mathbf{s}_\mu \cdot [\mathbf{p}_\pi \times \mathbf{p}_\mu]$ determined by the π^0 momentum \mathbf{p}_π and the muon momentum \mathbf{p}_μ and spin \mathbf{s}_μ . In the case of $K_{\mu 2\gamma}$ decay, P_T is proportional to $\mathbf{s}_\mu \cdot [\mathbf{q} \times \mathbf{p}_\mu]$, where \mathbf{q} is the photon momentum. These observables are very small in the SM [1], but they are interesting probes of non-SM CP -violation mechanisms [2–4], where P_T could be as large as 10^{-3} in either $K_{\mu 3}$ or $K_{\mu 2\gamma}$.

Whether CP or T is violated or not, a nonvanishing P_T in both decays can be induced by electromagnetic final-state interactions (FSI). The value of P_T due to FSI is expected to be about 4×10^{-6} for $K_{\mu 3}$ decay [5, 6]—i.e., much smaller than the expected non-SM effects. On the contrary, for $K_{\mu 2\gamma}$ decay, FSI can induce an average $P_T \lesssim 10^{-3}$ [7]. In this decay, P_T due to FSI depends on the axial-vector form factor F_A and the vector form factor F_V . Moreover, P_T varies significantly over the Dalitz plot, reaching a maximum value at a high muon energy—i.e., in the region of high sensitivity to T -violating parameters [3].

For $K_{\mu 3}$ decay, the most general invariant amplitude is

$$M_{K_{\mu 3}} = -\frac{G_F}{\sqrt{2}} V_{us} \frac{1}{\sqrt{2}} \left[(p_K + p_\pi)_\lambda f_+(t) + (p_K - p_\pi)_\lambda f_-(t) \right] \bar{u}(p_\mu) \gamma_\lambda (1 + \gamma_5) v(p_\nu), \quad (1)$$

where G_F is the Fermi constant; V_{us} is the Kobayashi–Maskawa matrix element; p_K , p_π , p_μ , and p_ν are, respectively, the kaon, the pion, the muon, and the antineutrino momentum; and $t = (p_K - p_\pi)^2$ is

the square of the momentum transfer to the lepton pair. In the K^+ c.m. frame, P_T can be expressed as a function of the muon and pion energies,

$$P_T \cong \text{Im}(\xi) \left(\frac{m_\mu}{m_K} \right) \frac{|\mathbf{p}_\mu|}{E_\mu + |\mathbf{p}_\mu| \mathbf{n}_\mu \cdot \mathbf{n}_\nu - m_\mu^2/m_K} = \text{Im}(\xi) \cdot \Phi, \quad (2)$$

where $\xi(t) = f_-(t)/f_+(t)$; m_μ and m_K are, respectively, the muon and the kaon mass; \mathbf{n}_ν and \mathbf{n}_μ are unit vectors along the neutrino and the muon momentum, respectively; and $\Phi \simeq 0.3$ is a kinematical factor. In the case of T invariance, the parameter ξ must be real-valued; i.e., a nonvanishing $\text{Im}(\xi)$ would signal a violation of T invariance. The value of $\text{Im}(\xi)$ depends on the choice of model. In the case of models featuring nonstandard scalar interactions, it is proportional to the imaginary part of the scalar coupling constants, and measurement of P_T is a very efficient tool for constraining these models (multi-Higgs, leptoquark, minimal SUSY with R -parity violation). In the minimal three-Higgs-doublet model, the indirect limits on P_T that were obtained from measurements of the neutron dipole moment and $B \rightarrow X\tau\nu$ and $b \rightarrow s\gamma$ decays are updated in [8].

In the decay $K^+ \rightarrow \mu^+ \nu \gamma$, the T -violating polarization is sensitive to new pseudoscalar, vector, and axial-vector interactions. It can arise from the interference between the tree-level amplitude in the SM and the new CP -violating amplitudes. The polarization can be as large as 10^{-2} – 10^{-3} in models involving left–right symmetry, multi-Higgs bosons, SUSY, and leptoquarks [3]. As was shown in [4], it is important to study both decays because of existing correlations between T -violating polarizations that could allow one to distinguish new sources of CP violation if $P_T \neq 0$ in one or both decays or to set new constraints on new CP phases if $P_T = 0$.

*This article was submitted by the author in English.

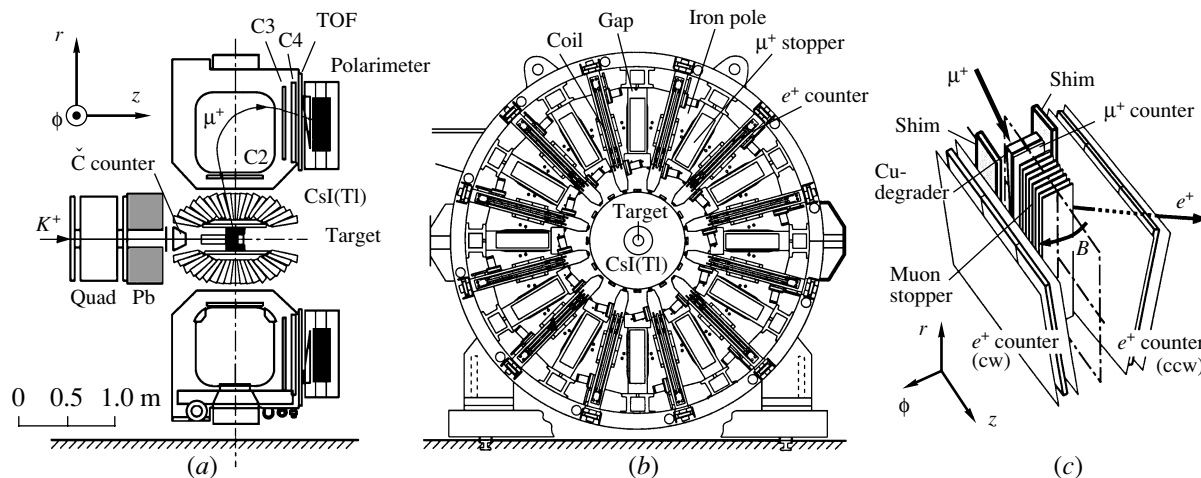


Fig. 1. Layout of the KEK E246 detector: (a) side view, (b) end view, and (c) one sector of the polarimeter.

2. DESCRIPTION OF THE DETECTOR

Figure 1 shows the E246 setup. A separated 660-MeV/ c K^+ beam ($\pi/K \simeq 6$) is produced at the 12-GeV KEK proton synchrotron with a typical intensity of 3.0×10^5 kaons per 0.6-s spill duration with a repetition of 3 s. A Cherenkov counter with a multiplicity trigger distinguished positive kaons from positive pions. The kaons were then moderated in a BeO degrader and stopped in a target made from 256 scintillating fibers located at the center of a 12-sector superconducting toroidal spectrometer. A $K_{\mu 3}^+$ event was identified by analyzing μ^+ with the spectrometer and detecting π^0 with a CsI(Tl) photon detector consisting of 768 modules [9]. In the CsI(Tl) barrel, there were twelve holes for muons to pass into the magnet. Since the solid-angle coverage of the CsI(Tl) was only 75% of 4π , π^0 was identified not only as two photons (2γ) giving a π^0 invariant mass ($M_{\gamma\gamma}$) but also as one photon (1γ) with an energy greater than 70 MeV, which preserved directional information about parent π^0 . Charged particles from the target were tracked by means of multiwire proportional chambers at the entrance (C2) and exit (C3 and C4) of each magnet sector, along with the target and a scintillation ring hodoscope [10] around the target. The momentum resolution ($\sigma_p = 2.6$ MeV/ c at 205 MeV/ c) was adequate to remove the predominant background of the decay $K^+ \rightarrow \pi^+\pi^0$ ($K_{\pi 2}$). Positrons from $K^+ \rightarrow \pi^0 e^+\nu$ in the relevant momentum region 100–190 MeV/ c were rejected by the time of flight. The $K^+ \rightarrow \pi^+\pi^0\pi^0$ background was negligible because π^+ stopped in the Cu degrader and could not reach the polarimeter. Muons entering the polarimeter (Fig. 1c) were degraded by a Cu block and stopped in a stack of pure Al plates. Positron

counters involving three layers of plastic scintillators were located between the magnet gaps. The time spectra of e^+ were recorded by multistop TDCs up to 20 μ s. The background associated with the beam was suppressed by a veto counter system surrounding the beam region.

The transverse polarization P_T is directed in a screw sense around the beam axis and generates the asymmetry $A_T = [N_{cw} - N_{ccw}]/[N_{cw} + N_{ccw}] \approx [N_{cw}/N_{ccw} - 1]/2$ in the counting rate between clockwise (cw) and counterclockwise (ccw) emitted positrons. Here, N_{cw} and N_{ccw} are the sums of cw and ccw positron counts over all 12 sectors. The sign of P_T of events featuring forward-going π^0 is opposite to that of events featuring backward-going π^0 . This allows one to take a double ratio of these two types of events, which is of importance for reducing a major part of systematic errors. The quantity P_T is related to A_T by the equation $A_T = \alpha f P_T$, where α is the analyzing power of the polarimeter and f is the average angular attenuation factor.

3. $K^+ \rightarrow \pi^0 \mu^+ \nu$

3.1. Analysis

The experimental data were analyzed by two groups independently using a so-called “blind” approach. Each analysis selected $K_{\mu 3}$ events in the μ^+ momentum range 100–190 MeV/ c , which removes $K_{\pi 2}$ decays. The majority of muons from pion decay in-flight into $K_{\pi 2}$ were rejected by using the χ^2 cut in tracking. For 2γ events, π^0 was identified by a $\gamma\gamma$ coincidence in CsI and by applying a cut on the pion invariant mass. $K_{e 3}$ events, which also satisfied these requirements, were removed by the time of flight. $K_{\mu 3}$ events from in-flight kaon decays in the

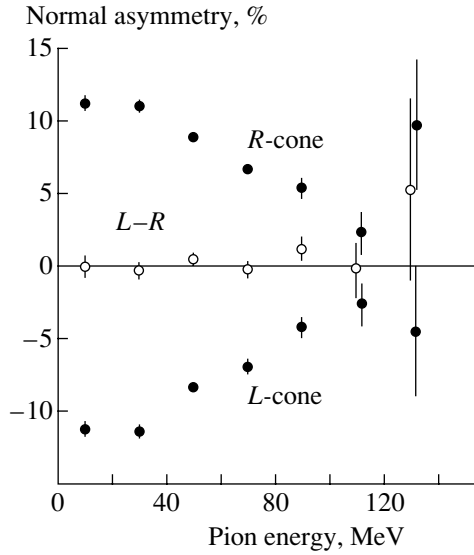


Fig. 2. Normal asymmetry measured for two-photon $K_{\mu 3}$ events. The R cone shows events where the pion moves into the right hemisphere relative to median plane of a given magnet sector, while the L cone includes events where the pion moves into the left hemisphere. Open circles represent the difference of the R and L normal asymmetries.

target were rejected by applying a cut on the kaon decay time: the time difference between kaon stop and decay should be more than 2 ns. “Good” $K_{\mu 3}$ events were separated into two classes: forward (fwd) events, where the angle between π^0 and beam directions (z axis) was less than 70° , and backward (bwd) events, where the angle between π^0 and beam directions was more than 110° .

The signal was extracted by integrating the time spectrum of positrons from $\mu^+ \rightarrow e^+ \nu \bar{\nu}$ decays of muons stopped in the polarimeter after subtracting the background. A null asymmetry check ($A_0 = [(N_{cw}/N_{ccw})_{fwd+bwd} - 1]/2$ for fwd + bwd events) performed in each analysis did not show a significant spurious asymmetry. After that, T -violating asymmetry

$$A_T = \frac{1}{4} \left[\frac{(N_{cw}/N_{ccw})_{fwd}}{(N_{cw}/N_{ccw})_{bwd}} - 1 \right] \quad (3)$$

was obtained by using a combination of both analyses as described in [11].

The detector sensitivity to muon polarization (analyzing power α) can be obtained from a measurement of the normal muon polarization P_N , which is the in-plane component of the muon polarization normal to the muon momentum. The polarization P_N is the T -even observable $\mathbf{s}_\mu \cdot [\mathbf{p}_\mu \times (\mathbf{p}_\pi \times \mathbf{p}_\mu)]$. The value of P_N averaged over the accepted part of the $K_{\mu 3}$ Dalitz plot is about 0.6 and can be measured if

the accepted events are separated into two classes: events where the pion moves into the left hemisphere with respect to the median plane of a given magnet sector and events where the pion moves into the right hemisphere. The values of P_N for these two classes should be of the same magnitude but opposite in sign. In addition, P_N decreases with increasing pion energy. The results are presented in Fig. 2. The value of $\alpha \simeq 0.2$ was extracted from this measurement. The difference between the L and R normal asymmetries is consistent with zero, and this is also a good test of the detector azimuthal symmetry.

The main systematic contributions to P_T come from the presence of two large components of the muon in-plane polarization: P_L , which is parallel to the muon momentum, and P_N ($P_T \ll P_{N,L} \lesssim 1$). A major part of their contribution is canceled by the azimuthal symmetry of the detector and by the fwd/bwd ratio. The largest systematic errors are due to the misalignment of the polarimeter, the asymmetry of the magnetic-field distribution, and the asymmetric kaon stopping distribution. The fwd/bwd ratio dramatically reduces these contributions. The total systematic error of P_T is 0.9×10^{-3} [11], which is significantly lower than the statistical error.

3.2. Results

After the analysis of data taken in 1996 and 1997, we selected about 3.9×10^6 good fwd + bwd $K_{\mu 3}$ events. The value obtained for P_T was $-0.0042 \pm 0.0049(\text{stat.}) \pm 0.0009(\text{syst.})$ and $\text{Im}(\xi) = -0.013 \pm 0.016(\text{stat.}) \pm 0.003(\text{syst.})$ [11]. The analysis of the 1998 data was recently completed. The results obtained in both analyses are consistent and both show zero transverse muon polarization [12]. The dependence of A_T on the pion energy for forward- and backward-going pions (2γ events) is shown in Fig. 3. The statistical error of P_T of the combined 1996–1998 result is expected to be about 3×10^{-3} (1σ level), which corresponds to $\delta \text{Im}(\xi) \sim 1.1 \times 10^{-2}$. The systematic error is three times smaller than the statistical one.

4. $K^+ \rightarrow \mu^+ \nu \gamma$

4.1. Analysis

A key problem in extracting $K^+ \rightarrow \mu^+ \nu \gamma$ events is the presence of the intense background from $K_{\mu 3}$ decays when only one photon from the π^0 decay was detected and the second disappeared in one of 12 holes in the CsI calorimeter. However, due to the precise measurement of the muon momentum and the photon energy and direction, the kinematics of

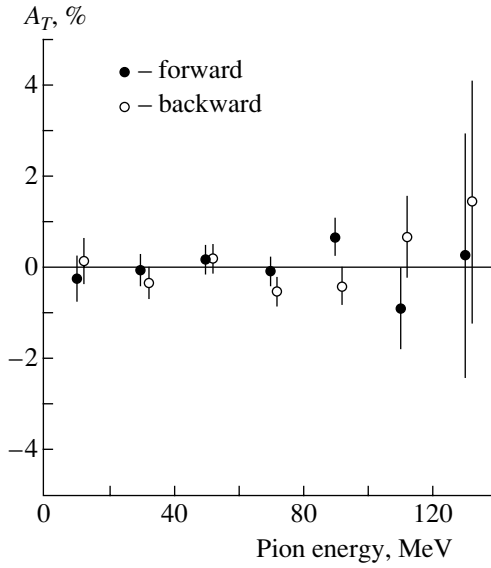


Fig. 3. T -odd muon asymmetry as a function of the pion kinetic energy for forward- and backward-going π^0 according to one analysis of 1998 data.

$K_{\mu 3}$ and $K_{\mu 2\gamma}$ decays could be reconstructed completely. Kinematical parameters such as the missing mass squared M_{miss}^2 , the angle between the muon and photon momenta, $\theta_{\mu\gamma}$, and the neutrino momentum p_ν can be efficiently used to suppress the $K_{\mu 3}$ background. The missing mass squared for 1γ events is

$$M_{\text{miss}}^2 = E_{\text{miss}}^2 - \mathbf{p}_{\text{miss}}^2 = (M_K - E_\mu - E_\gamma)^2 - (\mathbf{p}_K - \mathbf{p}_\mu - \mathbf{q})^2. \quad (4)$$

For $K_{\mu 2\gamma}$ events, the neutrino is the only missing particle; therefore, $\mathbf{p}_\nu = \mathbf{p}_{\text{miss}}$, $E_\nu = E_{\text{miss}}$, and $M_{\text{miss}}^2 = E_\nu^2 - \mathbf{p}_\nu^2 = 0$. The missing mass squared M_{miss}^2 in $K_{\mu 3}$ events is distributed over a wide range with the maximum of the broad peak at about $20000 \text{ MeV}^2/c^4$. The best suppression of $K_{\mu 3}$ events is achieved for the cut $|M_{\text{miss}}^2| \lesssim 5000 \text{ MeV}^2/c^4$. A cut additional to the M_{miss}^2 cut is that on $\mathbf{p}_\nu = -(\mathbf{p}_\mu + \mathbf{p}_\gamma)$. Other cuts are that on the muon momentum, $\mathbf{p}_\mu \lesssim 195 \text{ MeV}/c$, and $\theta_{\mu\gamma} \lesssim 75^\circ$. The neutrino momentum of 1γ events that was reconstructed after imposing the M_{miss}^2 , $\theta_{\mu\gamma}$, and \mathbf{p}_μ cuts and accepting events with $E_\gamma > 50 \text{ MeV}$ is given in Fig. 4. The peak at $p_\nu \sim 220 \text{ MeV}/c$ corresponds to $K_{\mu 2\gamma}$ events. In the region $p_\nu > 200 \text{ MeV}/c$, the contamination of the $K_{\mu 3}$ events is estimated to be not higher than 20%. Accepted $K_{\mu 2\gamma}$ events are concentrated in the Dalitz plot region where the inner-bremsstrahlung (IB) term dominates and where the normal polarization of the muon in the decay plane, P_N , is about 0.2. It is interesting that P_N in $K_{\mu 2\gamma}$ and $K_{\mu 3}$ events have the opposite

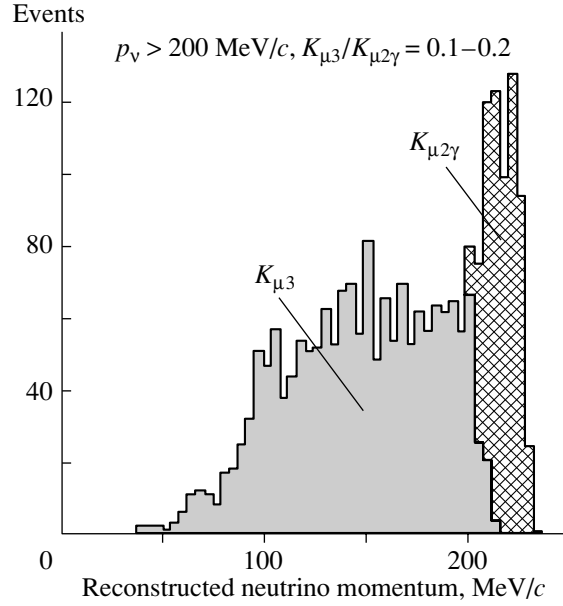


Fig. 4. Momentum of the missing particle of 1γ events after applying the cuts $|M_{\text{miss}}^2| \lesssim 5000 \text{ MeV}^2/c^4$, $\mathbf{p}_\mu \lesssim 195 \text{ MeV}/c$, and $E_\gamma > 50 \text{ MeV}$. The distribution with a dominant contribution from $K_{\mu 2\gamma}$ decay is obtained after applying the additional cut $\theta_{\mu\gamma} \lesssim 75^\circ$. $K_{\mu 3}$ events were selected by applying the criterion $\theta_{\mu\gamma} \gtrsim 75^\circ$.

signs. This provides another test of $K_{\mu 2\gamma}$ events and shows the detector sensitivity to polarization measurements in $K_{\mu 2\gamma}$ decay. For the data accumulated in 1998, the values obtained for normal asymmetries for left and right cones were $A_N^L = (-4.89 \pm 0.2) \times 10^{-2}$ and $A_N^R = (4.36 \pm 0.2) \times 10^{-2}$. The analogous values for $K_{\mu 2\gamma}$ events are $A_N^L = (0.64 \pm 1.16) \times 10^{-2}$ and $A_N^R = (-2.05 \pm 1.16) \times 10^{-2}$. All these results are in agreement with the expected polarization values, although the statistical errors are overly large in $K_{\mu 2\gamma}$ decay to support a more definitive conclusion.

4.2. Results

From the data accumulated by E246 between 1996 and 2000, about $(2-3) \times 10^5$ “good” $K_{\mu 2\gamma}$ events are estimated to be extracted. The final sensitivity to T -odd muon polarization in $K_{\mu 2\gamma}$ decay is expected to be at a level of 1.5×10^{-2} . The analysis is in progress.

5. FUTURE PROSPECTS

The final E246 sensitivity to P_T in $K_{\mu 3}$ is expected to be about 2×10^{-3} , which corresponds to $\delta \text{Im}(\xi)$ of about 7×10^{-3} . Since statistics mainly determine the

sensitivity, the detector still has an ability to improve the sensitivity at least by a factor of 2 for a more intense kaon beam.

New planned experiments will reach higher sensitivity in measuring both $K_{\mu 3}$ and $K_{\mu 2\gamma}$ decays. The proposed E923 experiment at BNL [13] is designed to use in-flight K^+ decays. A cylindrical active polarimeter around the kaon beam and an electromagnetic calorimeter will be used to reconstruct $K_{\mu 3}$ decays and suppress the background. The detector acceptance to $K_{\mu 3}$ events is about 2.5×10^{-5} per 2-GeV/c kaons. The advantage of the in-flight experiment is thus a relatively high detector acceptance. The statistical sensitivity (1σ level) to P_T in this experiment will be about 1.3×10^{-4} , which corresponds to $\delta \text{Im}(\xi) = 7 \times 10^{-4}$. In this experiment, a sensitivity of $\leq 10^{-3}$ can be also obtained for P_T in $K_{\mu 2\gamma}$ decay.

A new approach to measure the T -odd polarization in $K_{\mu 3}$ and $K_{\mu 2\gamma}$ with a statistical sensitivity to P_T at a 1σ level of about 10^{-4} by using stopped kaons was proposed in [14]. The virtue of this experiment is a high-resolution measurement of π^0 (momentum resolution of about 1 to 2%), which will allow an almost complete suppression of $K_{\pi 2}$ decay. Another important detector element is an active muon polarimeter that provides higher sensitivity to the muon polarization and a more efficient background suppression than a passive polarimeter by means of a complete measurement of the muon track, muon stopping point, and both energy and direction of the positron from muon decay. A calorimeter and an additional highly efficient photon veto system around the polarimeter cover nearly a 4π solid angle. This experiment can be performed in a low-energy separated kaon beam at JHF [15].

6. CONCLUSION

The status of measurements of T -violating muon polarization in the decays $K^+ \rightarrow \pi^0 \mu^+ \nu$ and $K^+ \rightarrow$

$\mu^+ \nu \gamma$ and future prospects have been outlined. These measurements with a sensitivity to P_T at a level of 10^{-3} – 10^{-4} could be a good test of nonstandard sources of CP violation.

ACKNOWLEDGMENTS

This work was supported by the Russian Foundation for Basic Research (project no. 99-02-17814).

REFERENCES

1. E. Golovich and G. Valencia, Phys. Rev. D **40**, 112 (1989).
2. G. Garisto and G. Kane, Phys. Rev. D **44**, 2038 (1991); M. Fabbrichesi and F. Vissani, Phys. Rev. D **55**, 5334 (1997); G.-H. Wu and J. N. Ng, Phys. Lett. B **392**, 93 (1997).
3. G. Bélanger and C. Q. Geng, Phys. Rev. D **44**, 2789 (1991).
4. M. Kobayashi, T.-T. Lin, and Y. Okada, Prog. Theor. Phys. **95**, 361 (1996).
5. A. R. Zhitnitskiĭ, Yad. Fiz. **31**, 1024 (1980) [Sov. J. Nucl. Phys. **31**, 529 (1980)].
6. V. P. Efrosinin *et al.*, Phys. Lett. B **493**, 293 (2000); hep-ph/0008199.
7. V. P. Efrosinin and Yu. G. Kudenko, Yad. Fiz. **62**, 1054 (1999) [Phys. At. Nucl. **62**, 987 (1999)].
8. M. V. Diwan and Hong Ma, hep-ex/0101003.
9. A. D. Dementjev *et al.*, Nucl. Instrum. Methods Phys. Res. A **440**, 151 (2000).
10. A. P. Ivashkin *et al.*, Nucl. Instrum. Methods Phys. Res. A **394**, 321 (1997).
11. M. Abe *et al.*, Phys. Rev. Lett. **83**, 4253 (1999).
12. M. Aoki, in *Proceedings of the 30th International Conference on High Energy Physics, Osaka, Japan, 2000*.
13. M. V. Diwan *et al.*, AGS Experiment Proposal 923 (1996).
14. Yu. G. Kudenko and A. N. Khotjantsev, Yad. Fiz. **63**, 890 (2000) [Phys. At. Nucl. **63**, 820 (2000)].
15. *Proceedings of the International Workshop on JHF Science, 1998*, Ed. by J. Chiba, M. Furusaka, H. Miyatake, and S. Sawada, Vols. I–III, KEK Proc. 98-5, Aug. 1998.

Conference on Physics of Fundamental Interactions
Experiment

**Measurement of $D^{*\pm}$ Diffractive Cross Sections
in Photoproduction at HERA***

I. A. Korzhavina^{1),}**
(for the ZEUS Collaboration)

Received January 23, 2001

Abstract—The first measurement of the cross sections for $D^{*\pm}$ -meson diffractive photoproduction was performed with the ZEUS detector at the HERA ep collider by using an integrated luminosity of 38 pb^{-1} . The measurement was performed for photon–proton c.m. energies in the range $130 < W < 280 \text{ GeV}$ and photon virtualities in the region $Q^2 < 1 \text{ GeV}^2$. The product $D^{*\pm}$ mesons were reconstructed for $p_T^{D^*} > 2 \text{ GeV}$ and $-1.5 < \eta^{D^*} < 1.5$ from the decay channel $D^{*+} \rightarrow D^0 \pi_s^+$ with $D^0 \rightarrow K^- \pi^+$ (+ c.c.). The diffractive component was selected for $0.001 < x_{\mathbf{P}} < 0.018$. The measured cross section in this kinematical range is $\sigma_{ep \rightarrow e' D^* X p'}^{\text{diff}} = 0.74 \pm 0.21(\text{stat.})_{-0.18}^{+0.27}(\text{syst.}) \pm 0.16(\text{p.diss.}) \text{ nb}$ (ZEUS preliminary). The measured integrated and differential cross sections are compared with theoretical expectations.

© 2002 MAIK “Nauka/Interperiodica”.

1. INTRODUCTION

Charm-production processes are those that proceed mainly through gluon-initiated hard subprocesses and are perturbatively calculable. Thus, the diffractive production of charmed mesons can provide new tests of the partonic structure of diffractive interactions—in particular, of their gluon component.

Over the years of HERA collider operation, the integrated and differential cross sections for inclusive charm production have been measured in kinematical ranges where an effective signal separation from suppressed backgrounds could be achieved [1, 2]. The measured cross sections for photoproduction (PhP) and deep-inelastic scattering (DIS) processes were compared with various next-to-leading (NLO) calculations within perturbative QCD (pQCD). DIS data were found to be in good agreement with the calculations. The calculated PhP cross sections are smaller than the measured ones, especially in the forward (proton) direction.

As for diffractive charm production, there are only preliminary results on diffractive dissociation in DIS, measured with $D^{*\pm}$ mesons [3, 4]. Here, we present preliminary results from ZEUS measurements of the cross sections for the diffractive photoproduction of

$D^{*\pm}(2010)$ mesons²⁾ for Pomeron fractional momentum in the range $0.001 < x_{\mathbf{P}} < 0.018$ at energies $130 < W < 280 \text{ GeV}$ in the photon–proton c.m. frame and at photon virtualities $Q^2 < 1 \text{ GeV}^2$. D^* mesons were reconstructed through the decay channel $D^{*+} \rightarrow D^0 \pi_s^+ \rightarrow (K^- \pi^+) \pi_s^+$ (and c.c.) in the restricted kinematical region specified by the inequalities $p_T^{D^*} > 2 \text{ GeV}$ and $|\eta^{D^*}| < 1.5$. Here, $p_T^{D^*}$ is the transverse momentum of the product D^* meson, and $\eta^{D^*} = -\ln(\tan(\theta/2))$ is its pseudorapidity, defined in terms of the D^* polar angle θ with respect to the proton-beam direction.

The measurements were performed at the HERA collider with the ZEUS detector, whose detailed description can be found elsewhere [5]. The data were taken throughout 1996 and 1997, when HERA collided positron and proton beams with energies of 27.5 and 820 GeV, respectively. An integrated luminosity of 38 pb^{-1} was used for this measurement. Charged particles were measured in the central tracking detector (CTD) [6]. The uranium-scintillator sampling calorimeter (CAL) [7] was used to detect the scattered electron and to measure global energy values. The luminosity was determined from the rate of the bremsstrahlung process $e^+ p \rightarrow e^+ \gamma p$, where the photon was measured by a lead scintillator calorimeter [8].

*This article was submitted by the author in English.

¹⁾Institute of Nuclear Physics, Moscow State University, Vorob'evy gory, Moscow, 119899 Russia.

** e-mail: irina@mail.desy.de

²⁾In the following, $D^{*\pm}(2010)$ will be referred to simply as D^* .

2. KINEMATICS OF DIFFRACTIVE PHOTOPRODUCTION

We consider diffractive photoproduction in ep scattering at HERA,

$$e(e) + p(p) \rightarrow e'(e') + X + p'(p'),$$

where the four momenta of the particles involved are indicated in parentheses. A collision occurs at the squared positron–proton c.m. energy $s = (e + p)^2$ and a photon virtuality $Q^2 = -q^2$, where $q = e - e'$. The squared photon–proton c.m. energy $W^2 = (p + q)^2$ is defined for this reaction. One may consider that the interaction proceeds through a photon–Pomeron (\mathbf{P}) scattering,

$$\gamma(q) + \mathbf{P}(P_{\mathbf{P}}) \rightarrow X,$$

where $P_{\mathbf{P}} = p - p'$. This process is described by the invariant mass M_X of the hadronic system X produced by photon dissociation, and the proton-momentum fraction

$$x_{\mathbf{P}} = \frac{P_{\mathbf{P}} \cdot q}{p \cdot q} \simeq \frac{M_X^2}{W^2}$$

carried away by the Pomeron.

The variables W , M_X , and $x_{\mathbf{P}}$ were reconstructed from the final hadronic system measured by energy-flow objects (EFO) [9] made from tracks detected by the CTD and from energy depositions in the CAL cells. The Jacquet–Blondel formula [10]

$$W_{\text{JB}} = \sqrt{2E_p \sum_i (E - P_z)_i}$$

was used to reconstruct W . Here, E_p is the proton beam energy. The invariant mass of the diffractively produced system, M_X , was calculated by the formula

$$M_X^2 = \left(\sum_i E_i \right)^2 - \left(\sum_i P_{x_i} \right)^2 - \left(\sum_i P_{y_i} \right)^2 - \left(\sum_i P_{z_i} \right)^2.$$

The sums in both equations are taken over the energies E_i and momenta P_i of all EFOs. To select the W range, W_{JB} was calculated with calorimeter cell depositions only so as to be consistent with the inclusive-charm-photoproduction analysis [1]. Measured values were corrected to the true ones by factors determined from Monte Carlo simulations of diffraction as the average ratios of reconstructed-to-generated values. All variables were reconstructed to a precision higher than 15%.

3. EVENT SELECTION AND D^* RECONSTRUCTION

Event-selection and D^* -reconstruction procedures are described in detail elsewhere [1]. Here, a short description is given.

Photoproduction events were selected by requiring that no scattered positron be identified in the CAL [11] and that the photon–proton c.m. energy W be between 130 and 280 GeV. Under these conditions, the photon virtuality Q^2 is limited to values less than 1 GeV². The corresponding median Q^2 was estimated from a Monte Carlo simulation to be about 3×10^{-4} GeV². The product D^* mesons were reconstructed through the decay channel $D^* \rightarrow (D^0 \rightarrow K\pi)\pi_s$ by combining candidates from charged tracks measured by the CTD. For the reconstruction, “right-charge” track combinations defined for $(K\pi)$ with two tracks of opposite charges and with π_s that has a charge that is opposite to that of the K meson in $(K\pi)$ were accepted as long as the combination of the invariant masses $\Delta M = M(K\pi\pi_s) - M(K\pi)$ and $M(K\pi)$ were within wide mass windows around the nominal values of $\Delta M = M(D^*) - M(D^0)$ and $M(D^0)$ [12]. To determine the number of D^* mesons in the signal, the combinatorial background was simulated by “wrong-charge” track combinations and subtracted after a normalization to the “right-charge” distribution in the range $0.15 < \Delta M < 0.17$ GeV. “Wrong-charge” combinations were defined for $(K\pi)$ with two tracks of the same charge and with π_s of an opposite charge. The measurements were performed in the pseudorapidity range $-1.5 < \eta^{D^*} < 1.5$, where the CTD acceptance is high. The kinematical region in $p_T^{D^*}$ was limited to $2 < p_T^{D^*} < 8$ GeV.

The Monte Carlo event samples used for this analysis were prepared with the RAPGAP [13], PYTHIA [14], and HERWIG [15] generators. Diffractive interactions were simulated within the resolved Pomeron model [16] with $\beta(1 - \beta)$ or the H1 FIT2 [17] parametrizations for the initial parton distributions in the Pomeron. Here, β is the Pomeron momentum fraction carried by a parton that couples to the Pomeron and which participates in hard interaction. The MRSG [18] and GRV-G HO [19] parametrizations were used for the proton and the photon structure functions, respectively, in simulating nondiffractive interactions. The fragmentation of the generated partons (parton-shower evolution and hadronization) was simulated according to the LUND model [20] in using RAPGAP or PYTHIA simulations. The HERWIG generator models the hadronization process with a cluster hadronization model. The Monte Carlo events were processed through the standard ZEUS detector and trigger

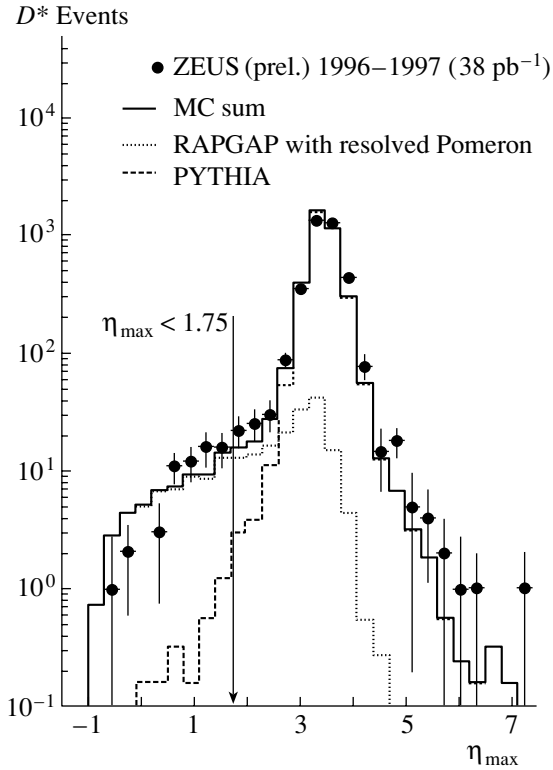


Fig. 1. Comparison of the measured η_{\max} distribution (points) with the sum of the diffractive and non-diffractive Monte Carlo distributions (solid histogram) for events with D^* mesons. D^* candidates were selected in the kinematical region specified by the conditions $Q^2 < 1 \text{ GeV}^2$, $130 < W < 280 \text{ GeV}$, $p_T^{D^*} > 2 \text{ GeV}$, and $|\eta^{D^*}| < 1.5$. The sums of diffractive resolved Pomeron RAPGAP Monte Carlo (dotted histogram) and non-diffractive Monte Carlo (dashed histogram) events were normalized to the data.

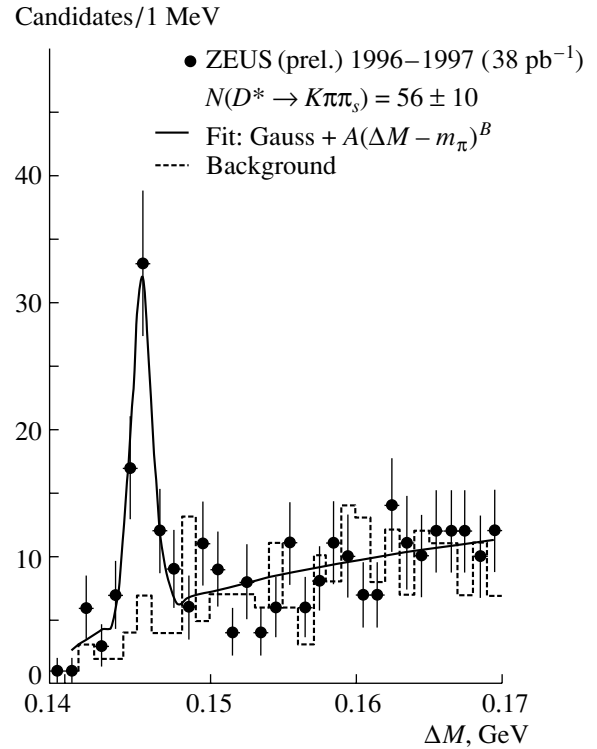


Fig. 2. ΔM distribution for the D^* -diffractive-photoproduction reaction with $D^* \rightarrow (D^0 \rightarrow K\pi)\pi_s$ for $Q^2 < 1 \text{ GeV}^2$, $130 < W < 280 \text{ GeV}$, and $0.001 < x_P < 0.018$. The kinematical region of the measurements is specified by the inequalities $p_T^{D^*} > 2 \text{ GeV}$ and $|\eta^{D^*}| < 1.5$. The points are for the right-charge combinations, and the dashed histogram is for the wrong-charge combinations from the D^0 -signal region (1.80–1.92 GeV). The solid curve represents the result of a fit to the sum of a Gaussian function and the functional form $A(\Delta M - m_\pi)^B$.

simulation codes and through the same event reconstruction package as that used for data processing. The shapes of Monte Carlo and data distributions were found to be in reasonable agreement within statistical errors.

Diffractive events were identified by a large rapidity gap (LRG) between the scattered proton that escaped detection through the beam pipe and the hadronic system X produced by the dissociated photon. LRG events were sought by using the η_{\max} method, for which η_{\max} was defined as the pseudorapidity of the most forward EFO with energy greater than 400 MeV. Figure 1 presents the η_{\max} distribution for all photoproduced D^* mesons reconstructed within the signal range $0.143 < M(K\pi\pi_s) - M(K\pi) < 0.148 \text{ GeV}$ and $1.80 < M(K\pi) < 1.92 \text{ GeV}$ after the combinatorial-background subtraction. This distribution shows two structures. The plateaulike structure at $\eta_{\max} \lesssim 2$ is populated predominantly by LRG events, while the wide peaklike structure around

$\eta_{\max} \sim 3.5$ originates from nondiffractive events and has an exponential falloff toward lower values of η_{\max} . From a comparison of the data points and the sum of simulated diffractive and nondiffractive event distributions normalized to the data, a cutoff of $\eta_{\max} = 1.75$ was chosen as a compromise between the magnitudes of the diffractive signal and the nondiffractive background. The nondiffractive background fractions for subtraction were estimated from the Monte Carlo-to-data distribution ratios by using nondiffractive Monte Carlo simulations.

In using the η_{\max} method for diffractive-event selection, one needs to take into account the following properties of the method. The measurement of rapidities by the CAL is limited to the edge of the forward beam hole of the CAL. Thus, the proton dissociative events, $ep \rightarrow e'XN$, can satisfy the requirement $\eta_{\max} < 1.75$ if the proton dissociative hadronic system N has an invariant mass that is sufficiently

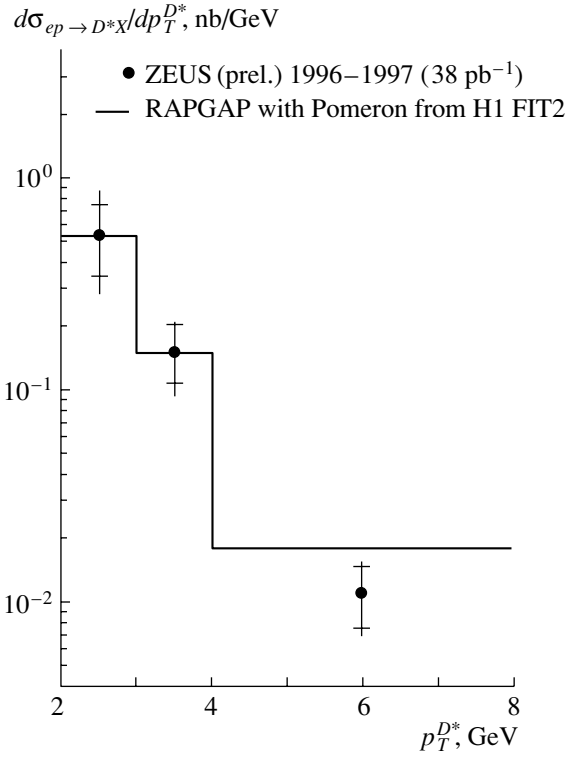


Fig. 3. Differential cross section $d\sigma/dp_T^{D^*}$ (points) for the diffractive-photoproduction reaction $ep \rightarrow e'D^*Xp'$ for $Q^2 < 1 \text{ GeV}^2$, $130 < W < 280 \text{ GeV}$, and $0.001 < x_{\mathbf{P}} < 0.018$. The kinematical region of the measurements is specified by the inequalities $p_T^{D^*} > 2 \text{ GeV}$ and $|\eta^{D^*}| < 1.5$. The inner bars show statistical errors, while the outer bars correspond to statistical and systematic errors added in quadrature. The data are compared with the distributions of the RAPGAP Monte Carlo diffractive events simulated within the resolved-Pomeron model with the H1 FIT2 Pomeron parametrization (histogram). The Monte Carlo distribution was normalized to have the same area as the data distribution.

small to pass undetected through the forward beam pipe. It was found earlier that the proton dissociation contribution comprises 0.31 ± 0.15 [21]. The measured cross sections were corrected for this value. A cut in η_{max} correlates with the range of accessible values of $x_{\mathbf{P}}$; $\eta_{\text{max}} < 1.75$ constrains it to be in the region $x_{\mathbf{P}} < 0.018$. In addition, a limited acceptance restricts it to be in the region $x_{\mathbf{P}} > 0.001$.

After the above selection and the “wrong-charge” background subtraction, a signal of 56 ± 10 diffractively photoproduced D^* mesons was found in the ΔM distribution (Fig. 2).

4. CROSS SECTIONS

The cross section for inclusive D^* production is given by

$$\sigma_{ep \rightarrow D^*X} = \frac{N_{D^*}^{\text{corr}}}{\mathcal{L} \cdot B_{D^* \rightarrow (D^0 \rightarrow K\pi)\pi}},$$

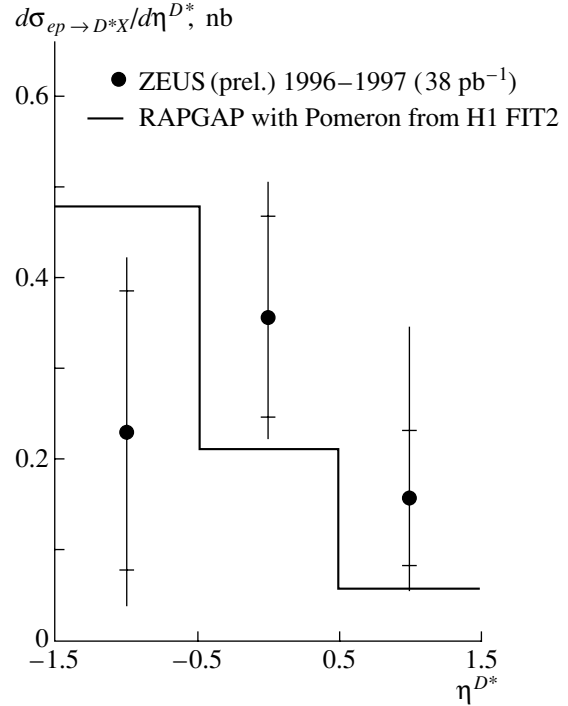


Fig. 4. Differential cross section $d\sigma/d\eta^{D^*}$ (points) for the diffractive-photoproduction reaction $ep \rightarrow e'D^*Xp'$ for $Q^2 < 1 \text{ GeV}^2$, $130 < W < 280 \text{ GeV}$, and $0.001 < x_{\mathbf{P}} < 0.018$. The kinematical region of the measurements is specified by the inequalities $p_T^{D^*} > 2 \text{ GeV}$ and $|\eta^{D^*}| < 1.5$. The inner bars show statistical errors, while the outer bars correspond to statistical and systematic errors added in quadrature. The data are compared with the distributions of the RAPGAP Monte Carlo diffractive events simulated within the resolved-Pomeron model with the H1 FIT2 Pomeron parametrization (histogram). The Monte Carlo distribution was normalized to have the same area as the data distribution.

where $N_{D^*}^{\text{corr}}$ is the number of observed D^* mesons corrected for the acceptance, $\mathcal{L} = 38.0 \pm 0.6 \text{ pb}^{-1}$ is the integrated luminosity, and $B_{D^* \rightarrow (D^0 \rightarrow K\pi)\pi} = 0.0263 \pm 0.0010$ is the combined branching ratio for the decay $D^* \rightarrow (D^0 \rightarrow K^+\pi^-)\pi_s$ [12]. Acceptance corrections were calculated by using the RAPGAP Monte Carlo sample.

The total cross section for D^* diffractive photoproduction in the kinematical region specified by the inequalities $Q^2 < 1 \text{ GeV}^2$, $130 < W < 280 \text{ GeV}$, $p_T^{D^*} > 2 \text{ GeV}$, $|\eta^{D^*}| < 1.5$, and $0.001 < x_{\mathbf{P}} < 0.018$ was measured to be $\sigma_{ep \rightarrow e'D^*Xp'}^{\text{diff}} = 0.74 \pm 0.21(\text{stat.})_{-0.18}^{+0.27}(\text{syst.}) \pm 0.16(\text{p.diss.}) \text{ nb}$ (ZEUS preliminary). The last error is due to the uncertainty in the proton-dissociative-background subtraction. Other sources of systematic uncertainties due to analysis and detector features were studied, and their effect on the cross section was estimated. The largest

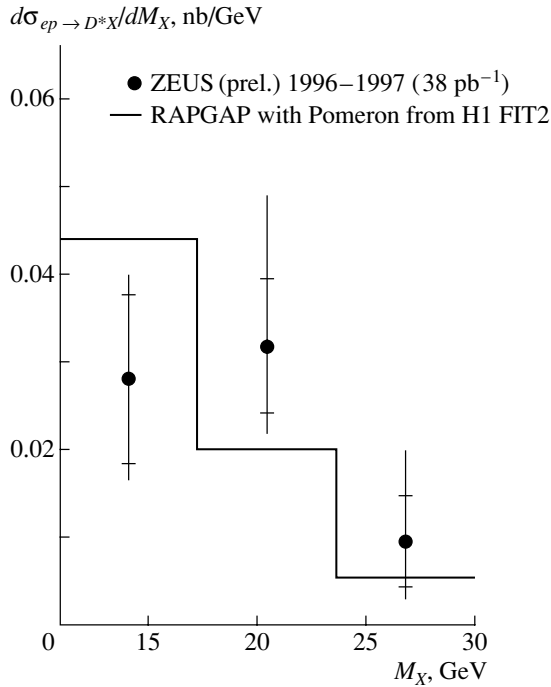


Fig. 5. Differential cross section $d\sigma/dM_X$ (dots) for the diffractive-photoproduction reaction $ep \rightarrow e'D^*Xp'$ for $Q^2 < 1 \text{ GeV}^2$, $130 < W < 280 \text{ GeV}$, and $0.001 < x_P < 0.018$. The kinematical region of the measurements is specified by the inequalities $p_T^{D^*} > 2 \text{ GeV}$ and $|\eta^{D^*}| < 1.5$. The inner bars show statistical errors, while the outer bars correspond to statistical and systematic errors added in quadrature. The data are compared with the distributions of the RAPGAP Monte Carlo diffractive events simulated within the resolved Pomeron model with the H1 FIT2 Pomeron parametrization (histogram). The Monte Carlo distribution was normalized to have the same area as the data distribution.

contributions to the systematic error came from the uncertainty in the CAL energy scale ($+12.0\%$, -4.8%), the signal-determination procedure ($+16.4\%$, -14.5%), the selection of diffractive events ($+11.3\%$, -8.0%), and the acceptance-correction calculations ($+26.5\%$, -16.9%). The overall normalization uncertainties due to the error in the luminosity value ($\pm 1.7\%$) and in the D^{*-} and D^{0-} decay branching ratios ($\pm 3.8\%$) were not included in the systematic error quoted above. All of the systematic uncertainties were added in quadrature to determine the overall systematic uncertainty of $+35.6\%$, -24.1% . The summation of the systematic uncertainties was also performed for each bin of the differential distributions.

The measured cross section for D^* diffractive photoproduction, while only a fraction of the total diffractive contribution, amounts to about 4% of the cross section for inclusive D^* photoproduction, $\sigma_{ep \rightarrow D^*X} = 18.9 \pm 1.2(\text{stat.})_{-0.8}^{+1.8}(\text{syst.}) \text{ nb}$ [1], in the

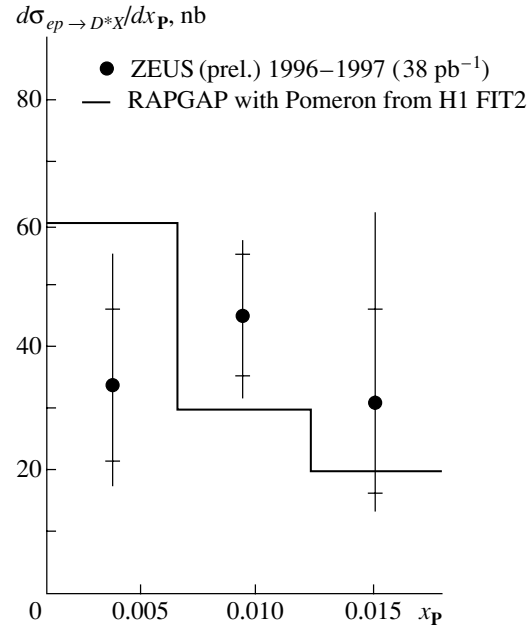


Fig. 6. Differential cross section $d\sigma/dx_P$ (dots) for the diffractive-photoproduction reaction $ep \rightarrow e'D^*Xp'$ for $Q^2 < 1 \text{ GeV}^2$, $130 < W < 280 \text{ GeV}$, and $0.001 < x_P < 0.018$. The kinematical region of the measurements is specified by the inequalities $p_T^{D^*} > 2 \text{ GeV}$ and $|\eta^{D^*}| < 1.5$. The inner bars show statistical errors, while the outer bars correspond to statistical and systematic errors added in quadrature. The data are compared with the distributions of the RAPGAP Monte Carlo diffractive events simulated within the resolved-Pomeron model with the H1 FIT2 Pomeron parametrization (histogram). The Monte Carlo distribution was normalized to have the same area as the data distribution.

same kinematical region. This fraction indicates that diffractive charm production is not suppressed as much as some early models predicted [22].

Measurements were compared with resolved-Pomeron-model expectations [16] calculated with the RAPGAP Monte Carlo code in the same kinematical region. The parton distributions in the Pomeron were parametrized by using a fit to the HERA data [17] of the H1 collaboration (H1 FIT2). Only the boson-gluon fusion (BGF) mechanism of charm production was taken into account. The leading-order RAPGAP Monte Carlo simulation with the H1 FIT2 Pomeron parametrization predicts 1.42 nb for the cross section for D^* diffractive photoproduction in the same kinematical region [23].

The differential cross sections $d\sigma/dp_T^{D^*}$, $d\sigma/d\eta^{D^*}$, $d\sigma/dM_X$, and $d\sigma/dx_P$ are presented in Figs. 3–6. All of the above-mentioned systematic uncertainties were added in quadratures to statistical errors (inner error bars) in each bin to calculate the total error (outer error bars), both of which are shown in Figs. 3–6.

The measured differential cross sections (Figs. 3–6), when compared to the ones of the resolved-Pomeron model that were calculated with the aid of the RAPGAP Monte Carlo code show reasonable agreement in shape with the theoretical expectations with allowance for the measurement errors. The cross section $d\sigma/dp_T^{D^*}$ agrees well, while the other three distributions are shifted somewhat toward larger values with respect to the predictions.

5. SUMMARY AND CONCLUSIONS

The first measurement of diffractive D^* photoproduction has been performed with the ZEUS detector at HERA with a luminosity of 38 pb^{-1} . The preliminary results are reported here. The total cross section for D^* diffractive photoproduction in the kinematical region specified by the inequalities $Q^2 < 1 \text{ GeV}^2$, $130 < W < 280 \text{ GeV}$, $p_T^{D^*} > 2 \text{ GeV}$, $|\eta^{D^*}| < 1.5$, and $0.001 < x_P < 0.018$ has been measured to be $\sigma_{ep \rightarrow e'D^*Xp'}^{\text{diff}} = 0.74 \pm 0.21(\text{stat.})_{-0.18}^{+0.27}(\text{syst.}) \pm 0.16(\text{p.diss.}) \text{ nb}$ (ZEUS preliminary). The leading-order calculations within the resolved Pomeron model predict 1.42 nb for this cross section. The differential-cross-section shapes for $d\sigma/dp_T^{D^*}$, $d\sigma/d\eta^{D^*}$, $d\sigma/dM_X$, and $d\sigma/dx_P$ show reasonable agreement with the resolved-Pomeron model with allowance for the measurement errors.

ACKNOWLEDGMENTS

We would like to thank the DESY Directorate for their strong support and encouragement. The remarkable achievements of the HERA machine group were of crucial importance for this study and are greatly appreciated. We would like to thank H. Jung for stimulating discussions and help in the use of the RAPGAP Monte Carlo generator.

REFERENCES

1. ZEUS Collab. (M. Derrick *et al.*), Phys. Lett. B **349**, 225 (1995); ZEUS Collab. (J. Breitweg *et al.*), Phys. Lett. B **401**, 192 (1997); **407**, 402 (1997); Eur. Phys. J. C **6**, 67 (1999); **12**, 35 (2000).
2. H1 Collab. (S. Aid *et al.*), Nucl. Phys. B **472**, 32 (1996); Z. Phys. C **72**, 593 (1996); H1 Collab. (C. Adloff *et al.*), Nucl. Phys. B **545**, 21 (1999).
3. ZEUS Collab., in *Proceedings of the International Europhysics Conference on High Energy Physics, Jerusalem, Israel, 1997*, Paper No. 645; in *Proceedings of the International Europhysics Conference on High Energy Physics, Tampere, Finland, 1999*, Paper No. 527; in *Proceedings of the 8th International Workshop on Deep-Inelastic Scattering (DIS-2000), Liverpool, England, 2000*; in *Proceedings of the XXX International Conference on*

- High Energy Physics, Osaka, Japan, 2000*, Paper no. 874.
4. H1 Collab., in *Proceedings of the 28th International Conference on High Energy Physics, Warsaw, Poland, 1996*, pa02-60; in *Proceedings of the 29th International Conference on High Energy Physics (ICHEP-98), Vancouver, Canada, 1998* (Paper no. 558); in *Proceedings of the 8th International Workshop on Deep-Inelastic Scattering (DIS-2000), Liverpool, England, 2000*.
5. ZEUS Collab. (M. Derrick *et al.*), Phys. Lett. B **293**, 465 (1992); ZEUS Collab. (Ed. by U. Holm), The ZEUS detector: Status Report (unpublished), DESY (1993); available on <http://www.zeus.desy.de/bluebook.html>.
6. N. Harnew *et al.*, Nucl. Instrum. Methods Phys. Res. A **279**, 290 (1989); B. Foster *et al.*, Nucl. Phys. B (Proc. Suppl.) **32**, 181 (1993); Nucl. Instrum. Methods Phys. Res. A **338**, 254 (1994).
7. M. Derrick *et al.*, Nucl. Instrum. Methods Phys. Res. A **309**, 77 (1991); A. Andresen *et al.*, Nucl. Instrum. Methods Phys. Res. A **309**, 101 (1991); A. Caldwell *et al.*, Nucl. Instrum. Methods Phys. Res. A **321**, 356 (1992); A. Bernstein *et al.*, Nucl. Instrum. Methods Phys. Res. A **336**, 23 (1993).
8. J. Andrusków *et al.*, DESY 92-066 (1992); ZEUS Collab. (J. Breitweg *et al.*), Z. Phys. C **63**, 391 (1994).
9. ZEUS Collab. (M. Derrick *et al.*), Eur. Phys. J. C **1**, 81 (1998); **6**, 43 (1999); G. Briskin, PhD Thesis (University of Tel Aviv, 1998).
10. F. Jacquet and A. Blondel, in *Proceedings of the Study for an ep Facility for Europe, 1979*, DESY 79-48, p. 391.
11. ZEUS Collab. (M. Derrick *et al.*), Phys. Lett. B **322**, 287 (1994).
12. Particle Data Group (C. Caso *et al.*), Eur. Phys. J. C **3**, 1 (1998).
13. H. Jung, Comput. Phys. Commun. **86**, 147 (1995).
14. T. Sjöstrand, Comput. Phys. Commun. **82**, 74 (1994).
15. G. Marchesini *et al.*, Comput. Phys. Commun. **67**, 465 (1992).
16. G. Ingelman and P. Schlein, Phys. Lett. B **152B**, 256 (1985); A. Donnachie and P. V. Landshoff, Nucl. Phys. B **303**, 634 (1988).
17. H1 Collab. (C. Adloff *et al.*), Z. Phys. C **76**, 613 (1997).
18. A. D. Martin, W. J. Stirling, and R. G. Roberts, Phys. Lett. B **354**, 155 (1995).
19. M. Glück, E. Reya, and A. Vogt, Phys. Rev. D **46**, 1973 (1992).
20. T. Sjöstrand, Comput. Phys. Commun. **39**, 347 (1986); T. Sjöstrand and M. Bengtsson, Comput. Phys. Commun. **43**, 367 (1987).
21. ZEUS Collab. (M. Derrick *et al.*), Z. Phys. C **70**, 391 (1996).
22. N. N. Nikolaev and B. G. Zakharov, Z. Phys. C **53**, 331 (1992).
23. H. Jung, private communication.

Conference on Physics of Fundamental Interactions
Experiment

Toward Improving the Accuracy of Testing the Equivalence of the Inertial and the Gravitational Mass under Terrestrial Conditions

**S. M. Kalebin, V. S. Artamonov, D. A. Liakin, G. V. Rukolaine,
I. L. Karpikhin, S. V. Barabin, and V. V. Kononov**

*Institute of Theoretical and Experimental Physics, Bol'shaya
Cheremushkinskaya ul. 25, Moscow, 117218 Russia*

Received March 21, 2001

Abstract—An experiment aimed at testing the equivalence of the inertial and the gravitational mass is considered in which use is made of a facility including a vacuum chamber with two coupled oscillators (a pendulum and dynamical damper that form a vibrational system featuring two degrees of freedom) and falling onto the Sun. The layout of the facility and its basic parameters are presented. The pendulum and the dynamical damper have the same natural frequency, which is equal to the frequency of their rotation about the Sun. This frequency is dependent on the date of the experiment and can be calculated on the basis of the time equation. In the proposed facility, the amplitude of oscillations of the damper is 1.2×10^{-5} rad, which is much greater than the value of 10^{-7} rad previously achieved in the experiment that tested the equivalence principle to the highest precision of about 10^{-12} . This precision can be considerably improved. The result is presented that was obtained from a measurement during the solar eclipse in Moscow on August 11, 1999.

© 2002 MAIK “Nauka/Interperiodica”.

1. INTRODUCTION

The concept of the mass of a body has a double meaning. On one hand, it determines the inertial properties of this body (Newton's second law); on the other hand, it is the source of gravitational forces (Newton's third law). This duality is reflected in the terms “inertial mass” $m^{(i)}$ and “gravitational mass” $m^{(g)}$. An experimental test of the equivalence of these masses is of fundamental importance for confirming Einstein's general theory of relativity.

In the majority of the most precise experiments, use is made of a torsional pendulum, with weights from different materials (“1” and “2”) being placed at the ends of its arm. The experiments consist in investigating the dimensionless quantity

$$\Delta = \left(\frac{m^{(g)}}{m^{(i)}} \right)_1 - \left(\frac{m^{(g)}}{m^{(i)}} \right)_2$$

for the situation where the bodies fall onto the Earth or onto the Sun. In the first case (falling onto the Earth), the sought torque T_E is static and is given by

$$T_E = m^{(i)} l \Omega^2 R \Delta \sin \varphi \cos \varphi,$$

where l is the arm length, Ω is the angular velocity of Earth's rotation, R is the radius of the Earth, and φ is the latitude of the place where this experiment is

performed. In the second case, the torque is variable, its amplitude T_D being

$$T_D \approx 0.62 [\text{cm s}^{-2}] m^{(i)} l \Delta,$$

where 0.62 cm s^{-2} is the acceleration due to the Sun's gravitational attraction.

An experiment where use is made of bodies falling onto the Earth was first proposed and implemented by Eötvös *et al.* [1], while the analogous experiment to study falling onto the Sun was proposed by the authors of [2].

The literature devoted to the test of the equivalence principle is quite extensive. A considerable number of more recent publications were initiated by the study reported in [3], where the hypothesis of the fifth force was put forth on the basis of an analysis of the data presented in [1].

The most accurate test of the equivalence principle was performed in [4], where the quantity Δ was estimated to a precision of about 10^{-12} .

In the present study, we discuss a way to improve considerably the accuracy of this estimate under terrestrial conditions. A preliminary report is given on the experimental facility that is being developed at the Institute of Theoretical and Experimental Physics (ITEP, Moscow) and which is intended for this purpose. Specialists from the All-Russia Research Institute for Electronic Mechanics (ARRIEM) are taking part in its fabrication.

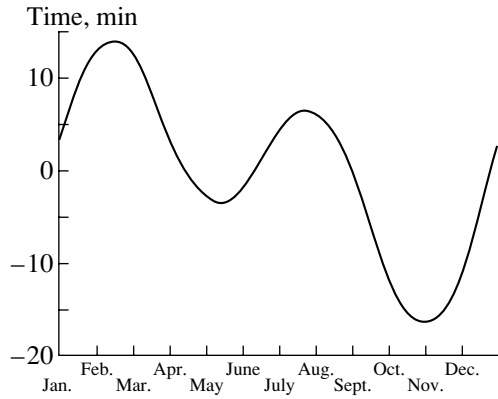


Fig. 1. Graph of the time equation.

2. WAY TO IMPROVE THE ACCURACY OF THE TEST OF THE EQUIVALENCE PRINCIPLE

The proposed experiment for testing the equivalence principle employs a device having a vacuum chamber equipped with two coupled torsional pendulums and falling onto the Sun. The device is suspended in space with the aid of a magnetic field and rotates at an angular velocity ω that is maintained with a high precision. The coupled torsional pendulums form a vibrational system having two degrees of freedom; each taken separately (that is, in an uncoupled state) has the same natural frequency ω_0 , the period τ_0 of the system being given by

$$\tau_0 = 2\pi \sqrt{\frac{32IL}{E\pi d^4}},$$

where L is the length of the pendulum thread, d is the thread diameter, I is the moment of inertia, and E is the shear modulus of the thread material [1.5×10^{12} g/(cm s²) for tungsten]. One (large) pendulum has a moment of inertia I_1 ; in order to generate the required variable torque from the Sun, there are two identical weights from different materials at the ends of its arm. The other (small) pendulum from the same material has a moment of inertia $I_2 \ll I_1$, a weight at the end of its thread being much lighter than the weights of the massive pendulum. If the equivalence principle were violated, the effect of the Sun on the weights of the massive pendulum would excite small-amplitude oscillations of frequency ω_0 ; in the steady-state regime, there would concurrently arise oscillations of the lighter pendulum in antiphase, their amplitude being much larger. The oscillations of the massive pendulum would then be damped by the oscillations of the lighter pendulum and could in principle disappear completely despite the effect of the sought torque on the massive pendulum. In this case, the oscillations of the lighter pendulum in antiphase become very large. In the theory of oscillators, this

remarkable phenomenon is commonly referred to as an antiresonance, while the small pendulum is called a dynamical damper. In the experiment being discussed, this property of the oscillations of a dynamical damper is used to improve the sensitivity of searches for sought oscillations. In contrast to conventional applications of an oscillating system with two degrees of freedom in many technical devices, the proposed experiment would employ it, figuratively speaking, in an “inverted” form. Under the antiresonance condition, the angular velocity of the dynamical damper is given by

$$\omega = -\Omega_u \sin \varphi + \sqrt{\Omega_u^2 \sin^2 \varphi + \omega_0^2 - \Omega_u^2},$$

where Ω_u is the angular velocity of the Earth with respect to the Sun (it depends on the date of experiment), while the period T can be found from the time equation (Fig. 1)

$$T = (1440 - \eta) \text{ min},$$

$$\eta = 7.6 \sin 0.986^\circ (n - 4) - 9.8 \sin 1.973^\circ (n - 81),$$

where n is the ordinal number of the day in a year from January 1. The numerical value of η can be found in the astronomical calendar.

If the accuracy of the experiment is sufficiently high, the resonance frequency ω_0 can be fixed for a specific date of the experiment in accordance with the time equation; for another date, the torsional pendulum will automatically be off the resonance. If the measuring procedure is invariable, the manifestation of the sought oscillations will become different, which will be a clear signal of their existence. The condition

$$\delta\omega < |\omega_0 - \omega|,$$

where $\delta\omega = \omega_0/Q$ is the half-width of the resonance and Q is its quality factor, is satisfied in this experiment. From this inequality, it follows that the sought oscillations induced by the Sun can be separated in frequency from the background oscillations associated with the rotation about the Earth.

Krylov [5] performed a calculation of steady-state forced oscillations for a stabilizer of ship rolling. The formulas that he obtained are applicable to oscillations of a torsional pendulum and a dynamical damper, the former and the latter playing, respectively, the role of a ship and the role of the stabilizer of rolling. In the antiresonance regime, the amplitude A_Γ of sought forced steady-state oscillations of the dynamical damper will be

$$A_\Gamma = \frac{T_D \tau_1 \tau_2}{4I_1} \left[\left(1 + \frac{I_2 \omega_0^2 \tau_1 \tau_2}{4I_1} \right)^2 + \frac{I_2^2 \omega_0^2 \tau_1^2}{4I_1^2} \right]^{-1/2},$$

where $\tau_1 = \tau_2 = \tau = 2Q/\omega_0$ is the relaxation time for the pendulum and the dynamical damper and I_1 and I_2 are their moments of inertia.

Parameters of coupled oscillators

	Pendulum	Damper
Thread length, L	250 cm	53 cm
Thread diameter, d	5×10^{-3} cm	5×10^{-4} cm
Arm length, l	15 cm	4 cm
Mass of weights, m	600 g	4 g
Moment of inertia, I	1.35×10^5 g cm ²	64 g cm ²
Resonance frequency, ω_0	1.7×10^{-3} rad/s	1.7×10^{-3} rad/s
Relaxation time, τ	10^5 s	10^5 s
Quality factor, Q	85	85
Resonance half-width, $\delta\omega$	2×10^{-5} rad/s	2×10^{-5} rad/s

The damper-induced enhancement of the amplitude A_M of pendulum oscillations is

$$\frac{A_\Gamma}{A_M} = Q.$$

We note that, in an experiment without a dynamical damper, the amplitude of the pendulum, A_M , due to the sought torque T_D is equal to the resonance value A_r :

$$A_r = \frac{T_D \tau_1}{2I_1 \omega_0}.$$

If the experiment features a damper and if the condition $I_2 \omega_0^2 \tau_1 \tau_2 (4I_1) \gg 1$ is satisfied, the increase in this amplitude is

$$\frac{A_\Gamma}{A_r} = \frac{I_1}{I_2 Q}.$$

The precision that can be achieved in the experiment is restricted by thermal noise causing the deflection angle $\delta\Theta$ [6],

$$\delta\Theta = \left(\frac{1}{\omega_0}\right)^2 \sqrt{\frac{6kT^0}{I_2 \tau_2 t}},$$

where k is the Boltzmann constant, T^0 is the absolute temperature, and t is the measurement time.

The estimated parameters of the apparatus are presented in the table. For the experiment performed in February, the time equation yields $\Omega_u = 7.345 \times 10^{-5}$ rad/s (the period is equal to 24 h – 14.3 min = 8.5542×10^4 s). At the measurement time of $t = 6 \times 10^5$ s, the condition $t \gg \tau$ is satisfied, and the forced pendulum oscillations in question can be considered to be steady-state.

For the value of $\Delta = 10^{-12}$ and the parameters of the pendulum and the dynamical damper from the table, we obtain

$$T_D = 2.8 \times 10^{-9} \text{ g cm}^2/\text{s}^2,$$

$$\omega = 1.636 \times 10^{-3} \text{ rad/s},$$

$$\omega_0 - \omega = 6.4 \times 10^{-5} \text{ rad/s},$$

$$A_\Gamma = 1.2 \times 10^{-5} \text{ rad},$$

$$\frac{A_\Gamma}{A_M} = 85,$$

$$\frac{A_\Gamma}{A_r} = 24.8,$$

$$\delta\Theta \approx 8.8 \times 10^{-8} \text{ rad}.$$

From a comparison of the above value of A_Γ with the value of 10^{-7} rad reported in [4], we conclude that the accuracy of testing the equivalence principle can be considerably improved. In order to isolate the effect, use is made of the Fourier analysis of oscillations of the main pendulum and dynamical damper. At $\Delta = 10^{-12}$, the amplitude of the sought oscillations of the dynamical damper will be greater than the amplitude of the main pendulum by the factor A_Γ/A_M .

3. EXPERIMENTAL FACILITY

The layout of the experimental facility for testing the equivalence principle is shown in Fig. 2. The device is suspended in space with the aid of an electromagnet (5) (see [7]) and, through a flexible link (3), is rotated with a frequency $\omega \approx 1.636 \times 10^{-3}$ rad/s (the period is about 1 h) with respect to the Earth by an electric motor (1), which is controlled by an electronic device (2). The rotation is monitored by a laser and recording electronics (11), as well as by 36 mirrors (12). Upon the switching of the electromagnet on and a smooth increase in the current through it, the experimental facility of weight about 150 kg is gently lifted from the support (not shown in the figure) and is

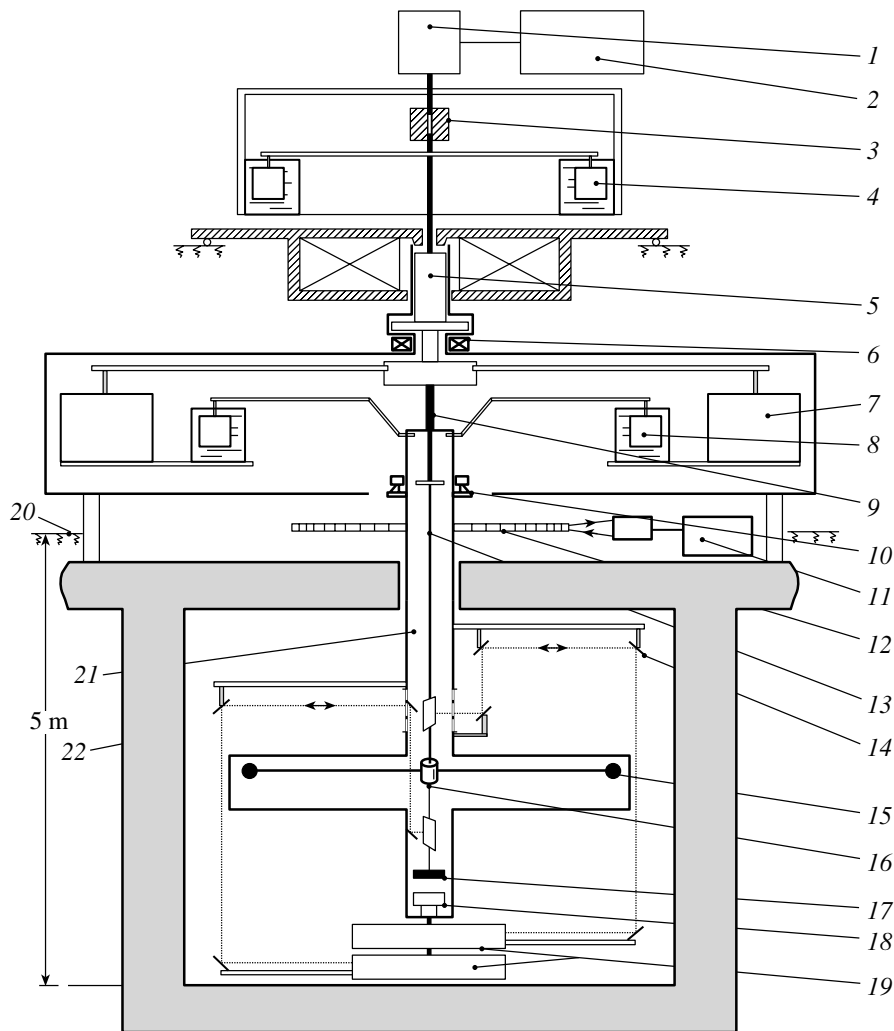


Fig. 2. Layout of the experimental facility: (1) electric motor, (2) electronic control for the electric motor, (3) flexible link between the electric motor and the experimental facility, (4) damper of the experimental facility, (5) magnetic suspension device, (6) coils for generating a rotating magnetic field, (7) weight of the experimental facility, (8) damper of the vacuum chamber, (9) thread for suspending the vacuum chamber, (10) magnet for damping pendulum oscillations, (11) laser and electronics for measuring the rotation, (12) 36 mirrors mounted on the device for measuring the rotation, (13) tungsten thread of the torsional pendulum, (14) mirrors for measuring the oscillations of the pendulum and dynamical damper, (15) weight of the torsional pendulum, (16) tungsten thread of the dynamical damper, (17) weight of the dynamical damper, (18) adsorption vacuum pump, (19) autocollimators, (20) Earth's surface, (21) vacuum chamber, and (22) concrete walls of the basement.

suspended at a current of about 120 mA in the space at a given altitude.

The laboratory room formed by four weights (7) of about 30 kg each (only two of them are shown in the figure) that rotates at a constant speed, its moment of inertia being about 2×10^8 g cm², is the main structural part of the facility. In the rotating laboratory room, background perturbations (including seismic perturbations) are suppressed by the magnetic suspension device and the damper (4). In the laboratory room, a vacuum chamber (21) is suspended with a thread (9) about 3 mm in diameter; in turn, two coupled oscillators (13) and (16) are suspended within

the vacuum chamber. In the laboratory room, the background oscillations of the vacuum chamber are suppressed by the damper (8). Prior to the beginning of the experiment, the chamber is evacuated, and an adsorption pump (18) is used in the course of the experiment to maintain a vacuum at the required level of 10^{-5} torr. The initial torsional oscillations of the pendulum and the dynamical damper are forced to relax by the rotating magnetic field with the aid of a follow-up system (not shown in the figure), while pendulum oscillations are suppressed by a magnetic damper (10).

In the facility, the sought oscillations are measured

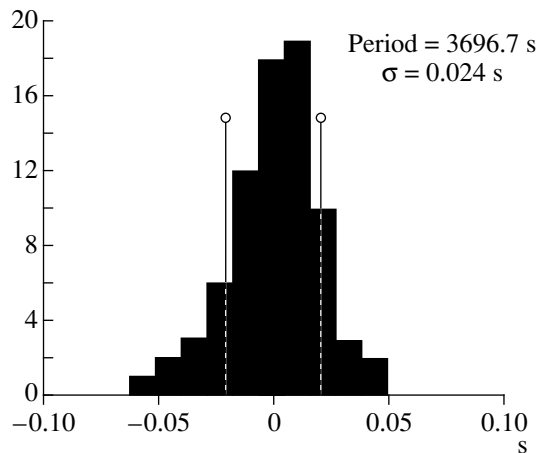


Fig. 3. Experimental histogram of deviations of the periods of facility rotation from its average value.

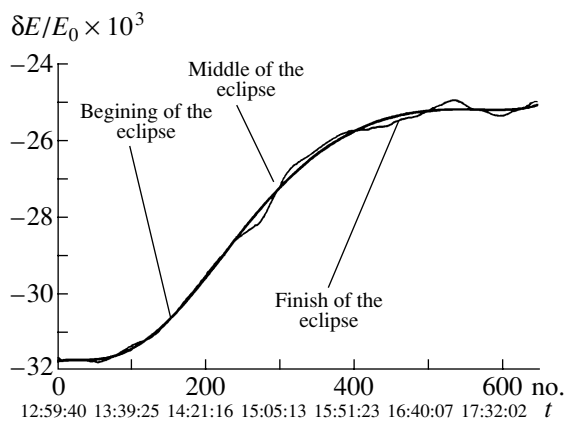


Fig. 4. Relative energy loss per revolution in inertial free rotation of bodies suspended in space with the aid of magnetic field during the solar eclipse in Moscow on August 11 (the symbol "no." stands for the ordinal number of a period, while the symbol t stands for time of its detection.).

by autocollimators (19) that are attached to the rotating vacuum chamber. Information is transferred in a contactless way through the infrared channel. The light beams of autocollimators are incident on the mirror of the pendulum and of the dynamical damper from opposite sides; owing to this, the effect of background chamber oscillations decreases in the difference of their readings. Therewith the amplitude of the sought oscillations of the dynamical damper undergoes virtually no changes, since, in the antiresonance regime, it is much greater than the amplitude of oscillations of the torsional pendulum. In the experimental facility, the dynamical damper, which is a sensitive detector of the sought oscillations, is thereby shielded from background oscillations (including seismic oscillations) by the magnetic suspension de-

vice, the damper of the laboratory room, the damper of the vacuum chamber, and the damper of pendulum oscillations.

For the experimental facility to be rotated in such a way that the relative deviation of its period was less than the attained value of about 6×10^{-6} (see Fig. 3), two versions of driver are investigated. The first employs a step-type motor with a reduction of 2×10^6 , while the second relies on an electronically controlled special motor developed in ARRIEM.

4. CONCLUSIONS

The proposed experiment is advantageous in that the accuracy can be improved by using (1) heavy (a few hundred kilograms) bodies that are suspended in space with the aid of a magnetic field and which can freely rotate with a period of one hour; (2) the resonance enhancement of the sought oscillations; (3) an oscillatory system with two degrees of freedom and special features of oscillations of coupled oscillators; (4) a multistep damping of background oscillations, whose effect can be reduced owing to a special detection of the sought oscillations; and (5) the time equation for test measurements.

As a result, it becomes possible to investigate, with an improved precision, the following fundamental problems of gravitation: the dependence of gravitational interaction on the material of the substance, the effect of screening, the interaction of ordinary matter with dark matter, and so on.

We note that the use of the experimental features indicated above gives impetus to the development of the technique of physical experiments aimed at revealing and analyzing weak physical interactions. In this context, we would like to mention the circumstance that may be of interest.

In 2000, there appeared the study of Qian-shen Wang *et al.* [8], who discussed the experiment that was performed during the solar eclipse in March 1997 and which revealed an unusual variation in the acceleration due to the gravitational attraction of the Earth. In connection with this observation, they put forth the assumption that the gravitational field is screened. This highlights the need for precision measurements that would seek the possible new properties of the gravitational interaction. We therefore deem it advisable to recall the experiment performed at the facility in question with a magnetic suspension of bodies of weight about 120 kg that were executing inertial free rotation in a suspended state during the solar eclipse in Moscow on August 11, 1999 [9]. The results are presented in Fig. 4. The graph depicts the time variation of the ratio $\delta E/E_0$, where δE is the rotational-energy loss per revolution and E_0 is the initial rotational energy. In the case of ordinary

damping of rotation, the graph would have the form of a straight line (exponential damping). In all probability, the observed shape of the curve is associated with a magnetic hysteresis and with the rotation of the magnetization vector in the magnetic field of the suspension device as the horizontal inclination of Earth's surface changes owing to tidal forces; however, we cannot rule out the possible existence of a new phenomenon in gravitational interaction.

ACKNOWLEDGMENTS

We are grateful to L.B. Okun, Yu.G. Abov, G.A. Lobov, A.L. Suvorov, V.Ya. Averbukh, V.E. Remezov, V.V. Shichkov, É.M. Khromenko, and P.V. Mokrov for their interest in this study.

This work was supported by the Russian Foundation for Basic Research (project no. 95-02-03534-a).

REFERENCES

1. R. V. Eötvös, D. Pekár, and E. Fekete, *Ann. Phys. (Leipzig)* **68**, 11 (1922).
2. R. G. Roll, R. Krotkov, and R. H. Dicke, *Ann. Phys. (N.Y.)* **26**, 442 (1964).
3. E. Fischbach, D. Sudarsky, A. Szafer, *et al.*, *Phys. Rev. Lett.* **56**, 3 (1986).
4. V. B. Braginskii and V. I. Panov, *Zh. Éksp. Teor. Fiz.* **61**, 873 (1971) [*Sov. Phys. JETP* **34**, 463 (1972)].
5. A. N. Krylov, *On Some Differential Equations of Mathematical Physics Having Application in Technical Problems* (Akad. Nauk SSSR, Moscow, 1949).
6. E. G. Adelberger *et al.*, *Phys. Rev. D* **42**, 3267 (1990).
7. S. M. Kalebin, G. V. Rukolaine, A. N. Polozov, *et al.*, *Nucl. Instrum. Methods Phys. Res. A* **267**, 35 (1988).
8. Qian-shen Wang, Chuan-zhen Wu, Hong-gang Guo, *et al.*, *Phys. Rev. D* **62**, 041101(R) (2000).
9. S. M. Kalebin, V. S. Artamonov, D. A. Lyakin, *et al.*, *Scientific Session of Moscow Engineering Physics Institute: Collection of Scientific Works* (Moscow, 2000), Vol. 7, p. 25.

Translated by A. Isaakyan

Conference on Physics of Fundamental Interactions Theory

Low-Energy γp Scattering and Determination of Proton Polarizabilities*

P. S. Baranov, A. I. L'vov, V. A. Petrun'kin, and L. N. Shtarkov**

Lebedev Institute of Physics, Russian Academy of Sciences, Leninskii pr. 53, Moscow, 117924 Russia

Received March 21, 2001

Abstract—For the first time, an analysis of all experimental data on the differential cross section for elastic γp scattering at photon energies below 150 MeV is performed in order to determine the electric (α_p) and magnetic (β_p) polarizabilities of the proton. A fit to these data with two free parameters α_p and β_p embedded into the theoretical cross section obtained on the basis of finite-energy s -channel dispersion relations gives the following world-average values of the proton polarizabilities: $\alpha_p = 11.7 \pm 0.8$ (stat. + syst.) ± 0.7 (model), $\beta_p = 2.3 \pm 0.9$ (stat. + syst.) ± 0.7 (model) in units of 10^{-4} fm^3 . The first error is combined—it takes into account the statistical and systematic errors in the experimental cross sections—while the second error comes from the theoretical uncertainties in the dispersion-theory cross sections. © 2002 MAIK “Nauka/Interperiodica”.

1. INTRODUCTION

The electromagnetic polarizabilities of the proton are structure parameters that characterize the ability of a particle to be deformed under the effect of an external electromagnetic field. A convenient tool for studying the polarizability phenomenon is provided by γp scattering at low energies, in which case the wavelength of the photon is larger than the proton size.

Experimental studies of γp scattering started in the mid-1950s [1–7], but the proton polarizabilities α_p and β_p were extracted from experimental cross sections for the first time only in [4, 7]. New experimental results [8–11] on γp scattering and new determinations of α_p and β_p were published only in the 1990s. In those new studies, however, statistical and systematic errors in the experimental values of proton polarizabilities were quite sizable.

This short report presents some results of our analysis concerning the compatibility of all world data on elastic γp scattering at photon energies below 150 MeV. The proton polarizabilities α_p and β_p and their world-average values are determined from different data sets and their combinations, and the compatibility of different data is estimated on the basis of the statistical criterion χ^2/N_f . Uncertainties in the polarizabilities coming from the theoretical-model cross sections are also estimated.

*This article was submitted by the authors in English.

**e-mail: shtarkov@x4u.lpi.ruhep.ru

2. ANALYSIS OF DATA

All experimental data on the differential cross section for elastic γp scattering at photon energies below 150 MeV from FIAN, MAMI, SAL, and other centers are split into two sets: 46 early data points of 1955 to 1974 [2–7] and 48 recent data points of the 1990s [8–11]. In our analysis, we consider that the authors of [6–8] later introduced significant corrections in their data. We do not use data from [1], since the systematic uncertainty is not given there.

A compilation of all those data (with corrections) and a description of the calculations of the theoretical cross section on the basis of dispersion relations that is used to fit the data points are given in [12, 13].

2.1. Statistical Method of Analysis

An important point of our analysis consists in combining statistical and systematic experimental errors in a special way that was proposed in [14]. The functional χ^2 used in fitting the experimental cross sections is written as

$$\chi^2 = \sum_{j=1}^N \left\{ \sum_{i=1}^{n_j} \left(\frac{k_j \sigma_{ij}^{\text{expt}} - \sigma_{ij}^{\text{theor}}(\alpha_p, \beta_p)}{k_j \Delta \sigma_{ij}^{\text{expt}}} \right)^2 + \left(\frac{k_j - 1}{k_j \delta_j} \right)^2 \right\},$$

where N is the total number of experiments, j is the experiment number, n_j is the number of points in the j th experiment, i is the point number, $\sigma_{ij}^{\text{expt}}$ and $\sigma_{ij}^{\text{theor}}(\alpha, \beta)$ are the experimental and theoretical

Table 1. Proton polarizabilities extracted from [2–11]

Exper.	Ref.	n	α_p	β_p	$\alpha_p + \beta_p$	χ^2/N_f	P , %
Oxl58	[2]	4	17.0 ± 8.1	-6.7 ± 3.7	10.2 ± 9.2	4.2/2	12
Hym59	[3]	12	13.9 ± 5.6	-4.7 ± 7.2	9.2 ± 6.1	0.6/10	100
Gol60	[4]	5	10.1 ± 7.8	9.0 ± 5.0	19.1 ± 10.2	2.3/3	52
Ber60	[5]	2	11.4 ± 2.9	2.6 ± 2.9	–	0.7/1	41
Fri67	[6]	16	14.2 ± 4.0	5.6 ± 4.2	19.8 ± 4.3	2.4/14	100
Bar74	[7]	7	11.4 ± 1.4	-4.7 ± 2.5	6.7 ± 3.3	8.0/5	15
Fed91	[8]	16	13.7 ± 3.7	2.1 ± 3.1	15.9 ± 4.4	17/14	24
Zie92	[9]	2	10.0 ± 1.4	4.0 ± 1.4	–	0.1/1	73
Hal93	[10]	12	9.1 ± 1.7	3.7 ± 1.5	12.7 ± 2.0	5.9/10	82
Mac95	[11]	18	12.2 ± 1.7	3.3 ± 1.8	15.5 ± 3.1	7.4/16	97
M95tag	[11]	8	18.3 ± 5.7	13.2 ± 7.2	31.5 ± 12.3	2.2/6	90

Note: The polarizabilities are given in units of 10^{-4} fm^3 ; n is the number of experimental points; χ^2/N_f shows the values of chi squared and the number of degrees of freedom; and P is the probability for the shown values of χ^2/N_f . The errors take into account both statistical and systematic uncertainties in the experimental cross sections. The last line refers to the tagged-photon subset of the experiment reported in [11].

cross sections taken at the photon energy ω_i and the scattering angle θ_i , $\Delta\sigma_{ij}^{\text{expt}}$ is the statistical error at an individual point, δ_j is the systematic error for the j th experiment, k_j is a normalization factor to be found for the j th experiment, and α_p and β_p are the proton polarizabilities to be found.

With this functional, fitting the combined data of N experiments leads to some nontrivial consequences: (a) before averaging, the values of $\sigma_{ij}^{\text{expt}}$ are corrected for each experiment on the scale of systematic errors δ_j ; (b) the final averaged values of the polarizabilities α_p and β_p are calculated from the corrected values of $\sigma_{ij}^{\text{expt}}$; (c) the final errors $\Delta\alpha_p$ and $\Delta\beta_p$ automatically take into account both statistical and systematic errors of the measurements; (d) the final value of χ^2 shows the compatibility of all measured points with the dispersion-theory version used; and (e) as a by-product, the N normalization (correcting) factors k_j are calculated.

2.2. Polarizabilities from Separate Experiments

The first step in our analysis consists in separate fits to experimental data from each of the studies quoted above. Since the data from [5, 9] are taken at a fixed angle, two polarizabilities cannot be found, and we fit those data using fixed $\alpha_p + \beta_p = 14.0 \pm 0.5$ calculated from a dispersion sum rule [13].

The results in Table 1 show that (1) all individual experiments are in agreement with the dispersion theory used, (2) errors (statistical plus systematic) in the

extracted polarizabilities are rather large, and (3) the individual extracted values of α_p and β_p are approximately consistent within 2 to 3 standard deviations. All that means the possibility of using differential cross sections measured in [2–11] in a combined fit.

It is interesting to note that the tagged-photon subset of data from [11] results in rather large errors in the extracted polarizabilities (see the last line in Table 1). Therefore, traditional experiments with the bremsstrahlung photon spectrum still have a certain advantage for determining α_p and β_p over tagged-photon experiments, at least at the present level of statistical errors in the measured cross sections.

2.3. Polarizabilities from Groups of Experiments

The second step in our analysis consisted in fitting two groups of data, the early 46 points and the recent 48 points. After that, a global fit to all 94 points was performed.

The corresponding world-average polarizabilities are shown in Table 2. In this table, the low values of χ^2/N_f demonstrate satisfactory agreement inside the group of early experiments, inside the group of recent experiments, and between the early and recent experiments. The early and the recent experiments have virtually the same level of errors; by combining of all the experiments results, we therefore reduce the errors. At present, the results given in the bottom line are the most objective world-average values of the proton polarizabilities.

Table 2. Final world-average values of the proton polarizabilities

Expt.	Refs.	n	α_p	β_p	$\alpha_p + \beta_p$	$\alpha_p - \beta_p$	χ^2/N_f
Early	[2–7]	46	12.8 ± 1.1	-0.3 ± 1.6	12.5 ± 2.2	13.0 ± 1.7	33/44
Recent	[8–11]	48	10.8 ± 1.0	3.2 ± 1.0	14.0 ± 1.6	7.7 ± 1.2	33/46
All	[2–11]	94	11.7 ± 0.8	2.3 ± 0.9	14.0 ± 1.3	9.5 ± 1.0	73/92

Note: The polarizabilities were separately extracted (three lines) from early data, recent data, and all data. The units are 10^{-4} fm^3 ; n is the number of experimental points; χ^2/N_f shows the values of chi squared and the number of degrees of freedom. The errors take into account both statistical and systematic uncertainties in the experimental cross sections.

Table 3. Polarizability uncertainties from the model dependence of the theory

	Changes	$\Delta\alpha_p$	$\Delta\beta_p$	$\Delta(\alpha_p + \beta_p)$	$\Delta(\alpha_p - \beta_p)$
a	SAID \rightarrow HDT	-0.44 (-0.19)	-0.08 (+0.03)	-0.51 (-0.16)	-0.36 (-0.22)
b	$M_{1+} \rightarrow +2\%$	+0.18 (+0.07)	-0.11 (-0.04)	+0.06 (+0.03)	+0.29 (+0.11)
c	$M_1 = 500 \rightarrow 700 \text{ MeV}$	-0.35 (-0.20)	+0.53 (+0.24)	+0.19 (+0.04)	-0.88 (-0.44)
d	$ g_{\pi NN}F_{\pi\gamma\gamma} \rightarrow +4\%$	-0.14 (-0.09)	+0.10 (+0.07)	-0.04 (-0.02)	-0.24 (-0.16)
e	$\gamma_{\pi}^{(\text{non-}\pi^0)} = 5.5 \rightarrow 7.3$	+0.40 (+0.18)	-0.45 (-0.15)	-0.05 (+0.03)	+0.84 (+0.32)
Total model uncertainty		0.72 (0.34)	0.72 (0.29)	0.56 (0.17)	1.33 (0.62)

Note: Uncertainties are in units of 10^{-4} fm^3 . The values without parentheses were obtained for the energy region below 150 MeV, while the values in parentheses are for the energy region below 100 MeV. The sources of uncertainties are the following: (a) the pion-photoproduction amplitudes near the threshold, (b) the resonance pion-photoproduction amplitude M_{1+} , (c) the σ -meson mass, (d) the pion coupling constants, (e) the non- π^0 -exchange background.

2.4. Model Uncertainties in Polarizabilities

The third step in our analysis consisted in varying model parameters in the theoretical cross section obtained on the basis of the finite-energy s -channel dispersion relations and in estimating model errors in the extracted values of α_p and β_p . The most important contributions to the model errors are shown in Table 3 for $\omega < 150 \text{ MeV}$ and for $\omega < 100 \text{ MeV}$ (in parentheses).

Summing the contributions in quadrature, we get the total model errors:

$$\Delta\alpha_p^{\text{mod}} \approx \Delta\beta_p^{\text{mod}} \approx 0.7 \quad \text{at } \omega < 150 \text{ MeV}$$

$$(\Delta\alpha_p^{\text{mod}} \approx \Delta\beta_p^{\text{mod}} \approx 0.3 \quad \text{at } \omega < 100 \text{ MeV}).$$

It can be seen that the calculated model errors are comparable with the experimental ones (cf. Table 2). All the theoretical model errors would be much lower if the energy region under consideration were below

100 MeV (see the values in parentheses). Unfortunately, there are presently insufficient data points in this low-energy region.

3. SUMMARY AND CONCLUSION

An analysis of world data on γp elastic scattering below 150 MeV has been performed on the basis of finite-energy s -channel dispersion relations and with allowance for both statistical and systematic errors. All the data have been shown to be statistically compatible. The earlier data set and the recent-data set have virtually the same level of errors, and they have been combined in order to extract more reliable average values for the proton polarizabilities. Taking the values of α_p and β_p from Table 2 for the case of all data and adding the model errors, we get the world-average values of the proton polarizabilities:

$$\alpha_p = 11.7 \pm 0.8 \text{ (stat. + syst.)} \pm 0.7 \text{ (model)},$$

$$\beta_p = 2.3 \pm 0.9 \text{ (stat. + syst.)} \pm 0.7 \text{ (model)}.$$

It should be emphasized that these values were obtained without a theoretical constraint on their sum. Instead, the experimental value of the sum

$$\alpha_p + \beta_p = 14.0 \pm 1.3 \text{ (stat. + syst.)} \pm 0.6 \text{ (model)}$$

is found to be in agreement with the theoretical sum-rule prediction [13]. The values determined for α_p and β_p and for the sum $\alpha_p + \beta_p$ seem the most precise and the most reliable average values for the proton polarizabilities.

The above values might be recommended for a general use and for publications of the Particle Data Group (PDG). The current proton-polarizability values given by the PDG are based on the results of only three recent experiments [8–10]; moreover, they were obtained at the fixed value of $\alpha_p + \beta_p = 14.2 \pm 0.5$ in order to reduce actual experimental errors.

At present, experimental and model errors in the polarizabilities are comparable. In order to reduce both kinds of errors, it is necessary to perform new measurements of the differential cross section for γp scattering with statistical and systematic errors of about 1 to 2%, preferably in the energy region below 100 MeV, where the model errors are significantly lower.

ACKNOWLEDGMENTS

This work was supported in part by the Russian Foundation for Basic Research (project nos. 96-02-17590 and 97-02-71019 INTAS-a).

REFERENCES

1. B. B. Govorkov *et al.*, Dokl. Akad. Nauk SSSR **111**, 988 (1956) [Sov. Phys. Dokl. **1**, 735 (1957)].
2. C. Oxley and V. Telegdi, Phys. Rev. **100**, 435 (1955); Nuovo Cimento **4**, Suppl. 2, 953 (1956); C. Oxley, Phys. Rev. **110**, 733 (1958).
3. L. Hyman *et al.*, Phys. Rev. Lett. **3**, 93 (1959).
4. V. I. Goldansky *et al.*, Nucl. Phys. **18**, 473 (1960).
5. G. Bernardini *et al.*, Nuovo Cimento **18**, 1203 (1960).
6. G. Pugh *et al.*, Phys. Rev. **105**, 982 (1957); MIT Summer Study, 555 (1967); D. Frish, private communication (1967).
7. P. S. Baranov *et al.*, Phys. Lett. B **52B**, 122 (1974).
8. F. J. Federspiel *et al.*, Phys. Rev. Lett. **67**, 1511 (1991); A. M. Nathan, private communication (1993).
9. A. Zieger *et al.*, Phys. Lett. B **278**, 34 (1992).
10. E. L. Hallin *et al.*, Phys. Rev. C **48**, 1497 (1993).
11. B. E. MacGibbon *et al.*, Phys. Rev. C **52**, 2097 (1995).
12. P. S. Baranov *et al.*, Preprint No. 50, FIRAN [Lebedev Institute of Physics, Russian Academy of Sciences, Moscow, 1999]; Fiz. Élem. Chastits At. Yadra **32**, 699 (2001) [Phys. Part. Nucl. **32**, 376 (2001)].
13. A. Lvov, V. Petrun'kin, and M. Schumacher, Phys. Rev. C **55**, 359 (1997).
14. P. S. Baranov *et al.*, Yad. Fiz. **5**, 1221 (1967) [Sov. J. Nucl. Phys. **5**, 873 (1967)].

Conference on Physics of Fundamental Interactions Theory

Proton-Polarizability Contribution to the Hyperfine Splitting in Hydrogen*

R. N. Faustov^{1), **} and A. P. Martynenko^{2), ***}

Received March 7, 2001; in final form, May 30, 2001

Abstract—The contribution of the proton polarizability to the hyperfine splitting in hydrogen is evaluated on the basis of modern experimental and theoretical results on the proton polarized structure functions. The value of this correction is 1.4 ppm. © 2002 MAIK “Nauka/Interperiodica”.

For many years, investigation of the hyperfine splitting (HFS) of the hydrogen-atom ground state has been considered as an important test of quantum electrodynamics (QED). The experimental value of the hyperfine splitting in hydrogen was obtained with a very high precision [1]:

$$\Delta E_{\text{HFS}}^{\text{exp}} = 1420405.7517667(9) \text{ kHz.} \quad (1)$$

The corresponding theoretical expression for the hyperfine splitting in hydrogen can be presently written in the form [2]

$$\Delta E_{\text{HFS}}^{\text{th}} = E_{\text{F}}(1 + \delta^{\text{QED}} + \delta^{\text{S}} + \delta^{\text{P}}), \quad (2)$$

$$E_{\text{F}} = \frac{8}{3}\alpha^4 \frac{\mu_p m_p^2 m_e^2}{(m_p + m_e)^3},$$

where μ_p is the proton magnetic moment and m_e and m_p are the masses of the electron and the proton, respectively. The calculation of various corrections to E_{F} has a long history. The modern status in the theory of hydrogenic atoms was presented in detail in [3]. The quantity δ^{QED} stands for the contribution of higher order QED effects. The corrections δ^{S} and δ^{P} take into account the influence of strong interaction, while δ^{S} describes the effects of proton finite-size and recoil contribution; δ^{P} is the correction due to the proton polarizability. The basic uncertainty in the theoretical result (2) is associated with this term.

The main contribution to δ^{P} is determined by the two-photon diagrams in Fig. 1. The corresponding amplitudes of virtual Compton scattering on a proton

can be expressed in terms of the nucleon polarized structure functions $G_1(\nu, Q^2)$ and $G_2(\nu, Q^2)$. The inelastic contribution of the diagrams in Figs. 1a and 1b can be represented in the form [3–8]

$$\Delta E_{\text{HFS}}^{\text{P}} = \frac{Z\alpha m_e}{2\pi m_p(1 + \kappa)} E_{\text{F}}(\Delta_1 + \Delta_2) \quad (3)$$

$$= (\delta_1^{\text{P}} + \delta_2^{\text{P}}) E_{\text{F}} = \delta^{\text{P}} E_{\text{F}},$$

$$\Delta_1 = \int_0^{\infty} \frac{dQ^2}{Q^2} \left\{ \frac{9}{4} F_2^2(Q^2) \right. \quad (4)$$

$$\left. - 4m_p^3 \int_{\nu_{\text{th}}}^{\infty} \frac{d\nu}{\nu} \beta_1 \left(\frac{\nu^2}{Q^2} \right) G_1(\nu, Q^2) \right\},$$

$$\Delta_2 = -12m_p^2 \int_0^{\infty} \frac{dQ^2}{Q^2} \int_{\nu_{\text{thr}}}^{\infty} d\nu \beta_2 \left(\frac{\nu^2}{Q^2} \right) G_2(\nu, Q^2), \quad (5)$$

where ν_{thr} determines the pion–nucleon threshold,

$$\nu_{\text{thr}} = m_{\pi} + \frac{m_{\pi}^2 + Q^2}{2m_p}, \quad (6)$$

and the functions $\beta_{1,2}$ are given by

$$\beta_1(\theta) = 3\theta - 2\theta^2 - 2(2 - \theta)\sqrt{\theta(\theta + 1)}, \quad (7)$$

$$\beta_2(\theta) = 1 + 2\theta - 2\sqrt{\theta(\theta + 1)}, \quad \theta = \nu^2/Q^2. \quad (8)$$

Further, $F_2(Q^2)$ is the Pauli form factor for the proton, and κ is the proton anomalous magnetic moment ($\kappa = 1.792847386(63)$ [9]). For many years, there have not been sufficient experimental data and theoretical information about proton spin-dependent structure functions. Therefore, previous investigations of the contribution $\Delta E_{\text{HFS}}^{\text{P}}$ contain only estimates of the proton polarizability effects, $\delta^{\text{P}} \sim 1$ – 2 ppm, or the calculation of the main resonance contributions [6–8, 10]. A theoretical bound on the

*This article was submitted by the authors in English.

¹⁾Scientific Council for the Interdisciplinary Problem Cybernetics, Russian Academy of Sciences, ul. Vavilova 40, Moscow, 117967 Russia.

²⁾Department of Theoretical Physics, Samara State University, ul. Akademika Pavlova 1, Samara, 443011 Russia.

** e-mail: faustov@theory.npi.msu.su

*** e-mail: mart@info.ssu.samara.ru

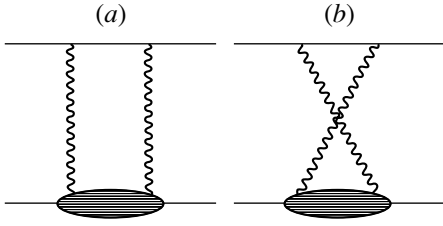


Fig. 1. Feynman diagrams for the proton-polarizability correction to the hyperfine splitting in hydrogen.

proton-polarizability contribution is $|\delta^P| \leq 4$ ppm. As was noted in [3], the problem of the proton-polarizability contribution requires a new investigation, which would take into account more recent experimental data on the spin structure of the nucleon.

The polarized structure functions $g_1(\nu, Q^2)$ and $g_2(\nu, Q^2)$ appear in the antisymmetric part of hadronic tensor $W_{\mu\nu}$, describing deep-inelastic lepton-nucleon scattering [11]:

$$W_{\mu\nu} = W_{\mu\nu}^{[S]} + W_{\mu\nu}^{[A]}, \quad (9)$$

$$W_{\mu\nu}^{[S]} = \left(-g_{\mu\nu} + \frac{q_\mu q_\nu}{q^2} \right) W_1(\nu, Q^2) \quad (10)$$

$$+ \left(P_\mu - \frac{P \cdot q}{q^2} q_\mu \right) \left(P_\nu - \frac{P \cdot q}{q^2} q_\nu \right) \frac{W_2(\nu, Q^2)}{m_p^2},$$

$$W_{\mu\nu}^{[A]} = \epsilon_{\mu\nu\alpha\beta} q^\alpha \left\{ S^\beta \frac{g_1(\nu, Q^2)}{P \cdot q} \quad (11)$$

$$+ [(P \cdot q)S^\beta - (S \cdot q)P^\beta] \frac{g_2(\nu, Q^2)}{(P \cdot q)^2} \right\}.$$

Here, $\epsilon_{\mu\nu\alpha\beta}$ is the totally antisymmetric tensor in four dimensions; $g_1(\nu, Q^2) = m_p^2 \nu G_1(\nu, Q^2)$ and $g_2(\nu, Q^2) = m_p \nu^2 G_2(\nu, Q^2)$; P is the nucleon 4-momentum; $x = Q^2/2m_p\nu$ is the Bjorken variable; S is the proton spin 4-vector normalized as $S^2 = -1$; and $q^2 = -Q^2$ is the square of the four-momentum transfer. The invariant quantity $P \cdot q$ is related to the energy transfer ν in the proton rest frame as $P \cdot q = m_p\nu$. The invariant mass of the electroproduced hadronic system, W , is then given by $W^2 = m_p^2 + 2m_p\nu - Q^2 = m_p^2 + Q^2(1/x - 1)$. Here, W_1 and W_2 are the structure functions for unpolarized scattering. In the regime of deep-inelastic scattering, the invariant mass W must be greater than that of any resonance in the nucleon. The threshold between the resonance region and the deep-inelastic region is not well defined, but it is usually taken to be about $W^2 = 4$.

The hadronic tensor $W_{\mu\nu}$ is proportional to the imaginary part of the off-shell Compton amplitude for the forward scattering of virtual photons on nucleons:

$\gamma^* N \rightarrow \gamma^* N$. The photon-nucleon interaction depends on the photon and on the nucleon polarization. This gives four independent helicity amplitudes of the form $M_{ab;cd}$, with a, b, c , and d specifying the helicities of the photon and the nucleon initial and final states:

$$M_{1,1/2;1,1/2}, \quad M_{1,-1/2;1,-1/2}, \quad M_{0,1/2;0,1/2}, \\ M_{1,1/2;0,-1/2}.$$

Their degrees of freedom correspond to four structure functions W_1, W_2, g_1 , and g_2 . All other possible combinations of the initial and the final photon and nucleon helicities are related to the above by the time reversal and the parity transformation.

The proton spin structure functions can be measured in the inelastic scattering of polarized electrons on polarized protons. Recent improvements in polarized lepton beams and targets made it possible to perform ever more accurate measurements of the nucleon polarized structure functions $g_{1,2}$ in experiments at SLAC, CERN, and DESY [12–19]. The spin-dependent structure functions can be expressed in terms of virtual photon-absorption cross sections as [11]

$$g_1(\nu, Q^2) = \frac{m_p \cdot K}{8\pi^2 \alpha (1 + Q^2/\nu^2)} \left[\sigma_{1/2}(\nu, Q^2) \quad (12) \right. \\ \left. - \sigma_{3/2}(\nu, Q^2) + \frac{2\sqrt{Q^2}}{\nu} \sigma_{TL}(\nu, Q^2) \right],$$

$$g_2(\nu, Q^2) = \frac{m_p \cdot K}{8\pi^2 \alpha (1 + Q^2/\nu^2)} \left[-\sigma_{1/2}(\nu, Q^2) \quad (13) \right. \\ \left. + \sigma_{3/2}(\nu, Q^2) + \frac{2\nu}{\sqrt{Q^2}} \sigma_{TL}(\nu, Q^2) \right],$$

where $K = \nu - Q^2/2m_p$ is the Hand kinematical flux factor for virtual photons; $\sigma_{1/2}$ and $\sigma_{3/2}$ are the virtual photoabsorption transverse cross sections for the total helicity of, respectively, 1/2 and 3/2 between the photon and the nucleon; and σ_{TL} is the term taking into account the interference between the transverse and longitudinal photon-nucleon amplitude. In this study, we calculate the contribution ΔE_{HFS}^P on the basis of modern experimental data on the structure functions $g_{1,2}(\nu, Q^2)$ and theoretical predictions on the cross sections $\sigma_{1/2,3/2,TL}$.

To obtain correction (3) in the resonance region ($W^2 \leq 4 \text{ GeV}^2$), we use the Breit-Wigner parametrization for the photoabsorption cross sections in (12) and (13), which was suggested in [20–26]. There are many baryon resonances that contribute to the photon-absorption cross sections. We take into account only five important resonances:

$P_{33}(1232)$, $S_{11}(1535)$, $D_{13}(1520)$, $P_{11}(1440)$, and $F_{15}(1680)$. Considering the one-pion decay channel of the resonances, we can recast the absorption cross sections $\sigma_{1/2}$ and $\sigma_{3/2}$ into the form [23, 27]

$$\sigma_{1/2,3/2} = \left(\frac{k_R}{k}\right)^2 \frac{W^2 \Gamma_\gamma \Gamma_{R \rightarrow N\pi}}{(W^2 - M_R^2)^2 + W^2 \Gamma_{\text{tot}}^2} \quad (14)$$

$$\times \frac{4m_p}{M_R \Gamma_R} |A_{1/2,3/2}|^2,$$

where $A_{1/2,3/2}$ are transverse electromagnetic helicity amplitudes,

$$\Gamma_\gamma = \Gamma_R \left(\frac{k}{k_R}\right)^{j_1} \left(\frac{k_R^2 + X^2}{k^2 + X^2}\right)^{j_2}, \quad (15)$$

$$X = 0.3 \text{ GeV}.$$

The resonance parameters Γ_R , M_R , j_1 , j_2 , and Γ_{tot} were taken from [9, 28]. In accordance with [22, 24, 28], the parametrization of the one-pion decay width is

$$\Gamma_{R \rightarrow N\pi}(q) = \Gamma_R \frac{M_R}{M} \left(\frac{q}{q_R}\right)^3 \left(\frac{q_R^2 + C^2}{q^2 + C^2}\right)^2, \quad (16)$$

$$C = 0.3 \text{ GeV},$$

for $P_{33}(1232)$ and

$$\Gamma_{R \rightarrow N\pi}(q) = \Gamma_R \left(\frac{q}{q_R}\right)^{2l+1} \left(\frac{q_R^2 + \delta^2}{q^2 + \delta^2}\right)^{l+1} \quad (17)$$

for $D_{13}(1520)$, $P_{11}(1440)$, and $F_{15}(1680)$; l is the pion angular momentum, and $\delta^2 = (M_R - m_p - m_\pi)^2 + \Gamma_R^2/4$. Here, q (k) and q_R (k_R) denote the momenta of the resonances with masses M and M_R , respectively, in the pion (photon) c.m. frame. In the case of $S_{11}(1535)$ we take into account πN and ηN decay modes [24, 28],

$$\Gamma_{R \rightarrow \pi, \eta} = \frac{q_{\pi, \eta}}{q} b_{\pi, \eta} \Gamma_R \frac{q_{\pi, \eta}^2 + C_{\pi, \eta}^2}{q^2 + C_{\pi, \eta}^2}, \quad (18)$$

where $b_{\pi, \eta}$ is the $\pi(\eta)$ branching ratio.

The cross section σ_{TL} is determined by an expression that is similar to (14), but which contains $(S_{1/2}^* A_{1/2} + A_{1/2}^* S_{1/2})$ [12]. The helicity amplitudes $A_{1/2}$ and $A_{3/2}$ and the longitudinal amplitude $S_{1/2}$ as functions of Q^2 were calculated on the basis of the constituent quark model in [29–34]. In the real-photon limit $Q^2 = 0$, we take the corresponding resonance amplitudes from [9]. For the Δ -isobar amplitudes $A_{1/2}(Q^2)$ and $A_{3/2}(Q^2)$, we used the relations obtained in [35]. The helicity amplitudes of the other resonances were taken from [31–34]. We have considered the Roper resonance $P_{11}(1440)$ as an ordinary qqq state [36]. As follows from the predictions of the quark model, the helicity amplitudes, which may be suppressed at $Q^2 = 0$, become

dominant very fast with increasing Q^2 . This can be seen from Figs. 2 and 3, where we also show experimental data of the E143 collaboration at two fixed momentum-transfer points: $Q^2 = 0.5 \text{ GeV}^2$ and $Q^2 = 1.2 \text{ GeV}^2$. Our results for the structure function $g_1(\nu, Q^2)$ in Fig. 2, which are in qualitative agreement with [27] and experimental data, show that Breit–Wigner five-resonance parametrization of the photon cross sections and the constituent quark model provide a good description of the proton polarized structure functions in the resonance region. The existing discrepancy between the predictions of this model for $g_{1,2}(\nu, Q^2)$ and experimental data, which is clearly seen in Fig. 2b, requires a further improvement in constructing the spin-dependent structure functions. This may be implemented by considering the contributions of other baryon resonances in the large- W region [$S_{31}(1620)$, $F_{37}(1950)$, $D_{33}(1700)$, $P_{13}(1720)$, $F_{35}(1905)$] and taking into account various decay modes for such states [27]. The Gerasimov–Drell–Hern sum rule [37]

$$-\frac{\kappa^2}{4m_p^2} = \frac{1}{8\pi^2\alpha} \int_{\nu_{\text{th}}}^{\infty} \frac{d\nu}{\nu} [\sigma_{1/2}(\nu, 0) - \sigma_{3/2}(\nu, 0)] \quad (19)$$

is valid to a high precision [27]. The second part of (4) gives an especially large negative contribution to the correction δ_1^P in the region of small Q^2 , where the contribution of the Δ isobar is dominant. With increasing Q^2 , its value decreases and the total correction δ_1^P is positive.

Our calculation of the contribution ΔE_{HFS}^P in the region of deep-inelastic scattering ($W^2 \geq 4 \text{ GeV}^2$) is based on experimental data from [12–19]. All data, including the SMC data at $Q^2 \leq 1 \text{ GeV}^2$, were fitted in terms of the parametrization

$$g_1(x, Q^2) = a_1 x^{a_2} (1 + a_3 x + a_4 x^2) \quad (20)$$

$$\times [1 + a_5 f(Q^2)] F_1(x, Q^2),$$

where $x = Q^2/2m_p\nu$ is the Bjorken scaling variable and $F_1 = W_1 m_p$. Fitted coefficients and various models for the form of the Q^2 dependence can be found in [12, 19]. In Fig. 4, the experimental data and the parametrization in the form (20) for the ratio g_1/F_1 are presented at two different points Q^2 . A numerical integration in (4) was performed with the function $f(Q^2) = -\ln Q^2$ (fit IV), corresponding to perturbative-QCD behavior. The coefficient function is $f(Q^2) = 0$ in the case of fit I. We have extrapolated relation (20) to the region near $Q^2 = 0$. The second part of the correction δ^P in (5) for the nonresonance

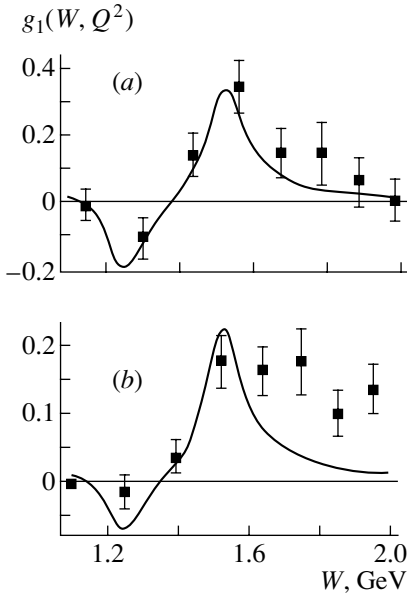


Fig. 2. Proton structure function $g_1(W, Q^2)$ at $Q^2 =$ (a) 0.5 and (b) 1.2 GeV^2 in the resonance region. The experimental data were taken from [12].

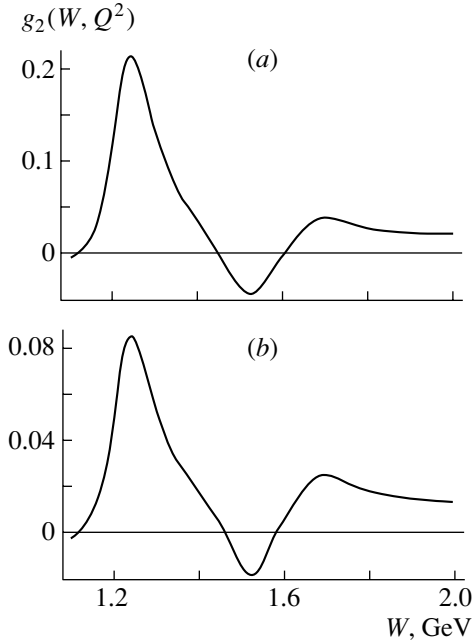


Fig. 3. Proton structure function $g_2(W, Q^2)$ at $Q^2 =$ (a) 0.5 and (b) 1.2 GeV^2 in the resonance region.

region was calculated by means of the Wandzura–Wilczek relation between the spin structure functions $g_1(x, Q^2)$ and $g_2(x, Q^2)$:

$$g_2^{\text{WW}}(x, Q^2) = -g_1(x, Q^2) + \int_x^1 g_1(t, Q^2) \frac{dt}{t}, \quad (21)$$

$$g_2^{\text{WW}} \approx g_2.$$

Higher twist terms contribute to $g_2(x, Q^2)$ as well, but they are so small that, when the transverse asymmetry A_\perp has not been measured or when it is not known sufficiently well, $g_2 = g_2^{\text{WW}}$ is often used. The values of contributions δ_1^P and δ_2^P and of the total contribution δ^P that are obtained after a numerical integration over the resonance and nonresonance regions are as follows:

$$\delta_{1,\text{res}}^P = 0.93 \text{ ppm}, \quad \delta_{1,\text{nonres}}^P = 0.86 \text{ ppm}, \quad (22)$$

$$\delta_1^P = 1.79 \text{ ppm},$$

$$\delta_{2,\text{res}}^P = -0.42 \text{ ppm}, \quad \delta_{2,\text{nonres}}^P = -0.01 \text{ ppm}, \quad (23)$$

$$\delta_2^P = -0.43 \text{ ppm},$$

$$\delta^P = \delta_1^P + \delta_2^P = 1.4 \pm 0.6 \text{ ppm}, \quad (24)$$

where the error indicated in expression (24) is determined by two main factors associated with the polarized structure functions: uncertainty in the experimental data in the nonresonance region and the possible contribution of other baryonic resonances to the functions $g_{1,2}(\nu, Q^2)$. The second error was estimated by means of the results of integration in (4) and (5) for various intervals of Q^2 and W and for possible modification of the spin-dependent structure functions in the resonance region $W \geq 1.5 \text{ GeV}$ due to changing the Breit–Wigner parametrization (14). The first part of the error in (24) is associated with statistical and systematic errors in the experimental data from [12].

The difference between the experimental value (1) and the theoretical result $\Delta E_{\text{HFS}}^{\text{th}} = 1420399.3(1.6) \text{ kHz}$ without the proton-polarizability contribution can be represented in the form [2, 3, 38, 39]

$$\frac{\Delta E_{\text{HFS}}^{\text{exp}} - \Delta E_{\text{HFS}}^{\text{th}}}{E_{\text{F}}} = 4.5(1.1) \text{ ppm}. \quad (25)$$

As was indicated in [2, 3, 38], the main sources of uncertainty in this difference are the inaccuracy of the proton-form-factor parametrization (dipole fit, etc.) and contradictory experimental data on the proton radius. The proton-polarizability correction δ^P calculated here makes the contribution in (24) of the proper sign and order of magnitude to the difference (25). A further improvement of this calculation is associated with new experimental and theoretical investigation of the internal structure of the light-quark baryons [40], with new more accurate measurements of the proton polarized structure functions, and with the use of QCD-based methods for calculating spin-dependent structure functions [41, 42]. A more detailed consideration of the structure functions $g_{1,2}(\nu, Q^2)$ in the resonance region, with

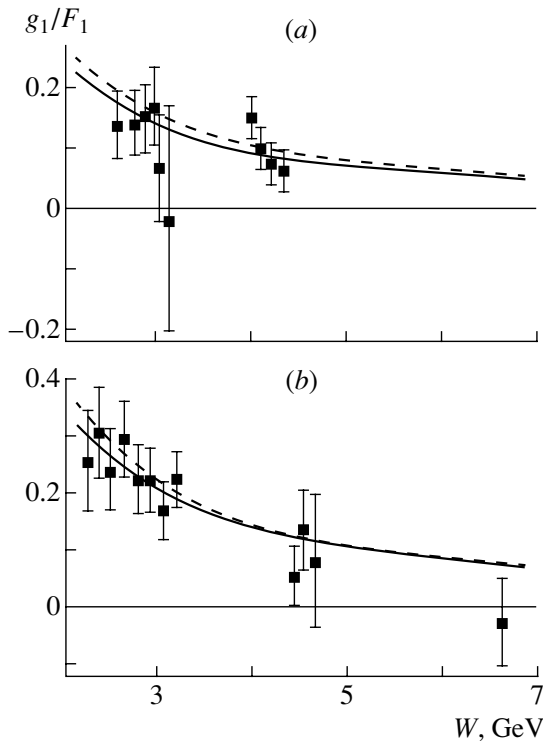


Fig. 4. Ratio $g_1(W, Q^2)/F_1(W, Q^2)$ as a function of W for the proton at $Q^2 = (a) 0.7$ and $(b) 1.2 \text{ GeV}^2$ in the region of deep-inelastic scattering [12]. The dashed and solid curves represent the results of fits I and IV, respectively.

allowance for the contributions of some other baryonic resonances and additional decay channels, is also required.

ACKNOWLEDGMENTS

We are grateful to M.I. Eides, S.G. Karshenboim, I.B. Khriplovich, V.A. Petrun'kin, and R.A. Sen'kov for stimulating discussions.

The work was supported by the Russian Foundation for Basic Research (project no. 00-02-17771) and the program Universities of Russia—Fundamental Research (project no. 990192).

REFERENCES

1. H. Hellwig, R. F. C. Vessot, M. W. Levine, *et al.*, IEEE Trans. Instrum. Meas. **19**, 200 (1970).
2. V. V. Dvoeglazov, Yu. N. Tuykhtyaev, and R. N. Faustov, Fiz. Élem. Chastiits At. Yadra **25**, 144 (1994) [Phys. Part. Nucl. **25**, 58 (1994)].
3. M. I. Eides, H. Grotch, and V. A. Shelyuto, Phys. Rep. **342**, 62 (2001).
4. C. K. Iddings and P. M. Platzman, Phys. Rev. **115**, 919 (1959).

5. S. D. Drell and J. D. Sullivan, Phys. Rev. **154**, 1477 (1967).
6. A. Verganalakis and D. Zwanziger, Nuovo Cimento A **39**, 613 (1965).
7. F. Guerin, Nuovo Cimento A **50**, 1 (1967).
8. G. M. Zinov'ev, B. V. Struminskii, R. N. Faustov, and V. L. Chernyak, Yad. Fiz. **11**, 1284 (1970) [Sov. J. Nucl. Phys. **11**, 715 (1970)].
9. Particle Data Group, Eur. Phys. J. C **15**, 1 (2000).
10. R. N. Faustov, A. P. Martynenko, and V. A. Saleev, Yad. Fiz. **62**, 2280 (1999) [Phys. At. Nucl. **62**, 2099 (1999)].
11. R. P. Feynman, *Photon-Hadron Interactions* (Benjamin, Reading, 1972; Mir, Moscow, 1975); F. E. Close, *An Introduction to Quarks and Partons* (Academic, London, 1979; Mir, Moscow, 1972).
12. K. Abe, T. Akagi, P. L. Anthony, *et al.*, Phys. Rev. D **58**, 112003 (1998).
13. K. Abe *et al.*, Phys. Rev. Lett. **78**, 815 (1997).
14. P. L. Anthony *et al.*, Phys. Lett. B **458**, 529 (1999).
15. G. S. Mitchell, Preprint SLAC-PUB-8104 (1999).
16. D. Adams *et al.*, Phys. Rev. D **56**, 5330 (1997).
17. D. Adeva *et al.*, Phys. Rev. D **60**, 072004 (1999).
18. V. W. Hughes, Preprint CERN-PPE/95-178 (1995); C. Aidala, A. Deshpande, and V. Hughes, in *Proceedings of the Workshop on Polarized Protons at High Energies—Accelerator Challenges and Physics Opportunities, 1999*, DESY-PROC-1999-03, p. 248.
19. R. D. Erbacher, SLAC-Report-546 (1999).
20. R. L. Walker, Phys. Rev. **182**, 1729 (1969).
21. R. A. Arndt, R. L. Workman, Z. Li, *et al.*, Phys. Rev. C **42**, 1864 (1990).
22. S. Teis, W. Cassing, M. Effenberger, *et al.*, Z. Phys. A **356**, 421 (1997).
23. M. Effenberger, A. Hombach, S. Teis, *et al.*, Nucl. Phys. A **613**, 353 (1997).
24. B. Krusche, J. Ahrens, G. Anton, *et al.*, Phys. Rev. Lett. **74**, 3736 (1995).
25. N. Bianchi, V. Muccifora, E. Sanctis, *et al.*, Phys. Rev. C **54**, 1688 (1996).
26. D. Drechsel, O. Hanstein, S. S. Kamalov, *et al.*, Nucl. Phys. A **645**, 145 (1999).
27. Y.-B. Dong, Eur. Phys. J. A **1**, 347 (1998).
28. M. Effenberger, A. Hombach, S. Teis, *et al.*, Nucl. Phys. A **614**, 501 (1997).
29. Z. Li and Y.-B. Dong, Phys. Rev. D **54**, 4301 (1996).
30. R. Koniuk and N. Isgur, Phys. Rev. D **21**, 1868 (1980).
31. F. E. Close and Z. Li, Phys. Rev. D **42**, 2194 (1990); **42**, 2207 (1990).
32. S. Capstick, Phys. Rev. D **46**, 1965 (1992); **46**, 2864 (1992).
33. Zhenping Li, V. Burkert, and Zhujun Li, Phys. Rev. D **46**, 70 (1992).
34. M. Warns, W. Pfeil, and H. Rollnik, Phys. Rev. D **42**, 2215 (1990).
35. C. E. Carlson and N. C. Mukhopadhyay, Preprint RPI-98-N126; WM-98-105; hep-ph/9804356.

36. A. P. Martynenko, *Yad. Fiz.* **54**, 809 (1991) [*Sov. J. Nucl. Phys.* **54**, 488 (1991)]; *Yad. Fiz.* **58**, 2054 (1995) [*Phys. At. Nucl.* **58**, 1943 (1995)].
37. S. B. Gerasimov, *Yad. Fiz.* **2**, 598 (1965) [*Sov. J. Nucl. Phys.* **2**, 430 (1966)]; S. D. Drell and A. C. Hern, *Phys. Rev. Lett.* **16**, 908 (1966).
38. G. T. Bodwin and D. R. Yennie, *Phys. Rev. D* **37**, 498 (1988).
39. S. G. Karshenboim, *Phys. Lett. A* **225**, 97 (1997).
40. V. Burkert, *Nucl. Phys. A* **623**, 59 (1997).
41. G. Altarelli, R. D. Ball, S. Forte, *et al.*, *Nucl. Phys. B* **496**, 337 (1997).
42. M. Hirai, S. Kumano, and M. Miyama, *Comput. Phys. Commun.* **108**, 38 (1998).

Conference on Physics of Fundamental Interactions
Theory

Magnetic Moment of a Two-Particle Bound State in Quantum Electrodynamics

A. P. Martynenko^{1),*} and R. N. Faustov^{2),**}

Received March 7, 2001; in final form, August 23, 2001

Abstract—A quasipotential method for calculating relativistic and radiative corrections to the magnetic moment of a two-particle bound state is formulated for particles of arbitrary spin. It is shown that the expression for the g factors of bound particles involve $O(\alpha^2)$ terms depending on the particle spin. Numerical values are obtained for the g factors of the electron in the hydrogen atom and in deuterium.

© 2002 MAIK “Nauka/Interperiodica”.

In quantum electrodynamics (QED), investigation of the electromagnetic properties of hydrogen-like atoms and ions is one of the basic problems in the theory of two-particle bound states. The calculation of the g factors for bound-state particles has been verified experimentally for a long time [1, 2]. The g factors measured for the electron in hydrogen, deuterium, and helium ($^4\text{He}^+$) are in good agreement with theoretical results. In recent years, the range of the experimental investigations of hydrogen-like ions has been considerably extended [3, 4]. These experiments stimulate new theoretical calculations of various contributions to the g factors of bound particles [5–7]. At present, the most precise measurements of the g factor have been performed for the electron in the carbon hydrogen-like ion $^{12}\text{C}^{5+}$ ($Z = 6$) [3, 4, 7]:

$$g_e^{\text{expt}}(^{12}\text{C}^{5+}) = 2.0010415964(8)(6)(40). \quad (1)$$

Here, the statistical error, the systematic error, and the uncertainties associated with the electron mass (8, 6, and 40, respectively) are indicated consecutively in parentheses. Theoretical investigations of the electromagnetic properties of hydrogen-like atoms showed [8–14] that the gyromagnetic factors of bound particles can be represented in the form of the expansion

$$g(\text{H atom}) = 2 + \Delta g_{\text{rel}} + \Delta g_{\text{rad}} + \Delta g_{\text{rec}} + \dots \quad (2)$$

The relativistic corrections Δg_{rel} , the radiative corrections Δg_{rad} , and the recoil corrections Δg_{rec}

were calculated to orders $\alpha^3(m/M)$ and $\alpha^2(m/M)^2$ inclusive (here, α is the fine-structure constant and m/M is the ratio of the electron mass to the mass of the nucleus) [8, 9] by using the quasipotential method for spin-1/2 particles forming the bound system. The ellipsis in (2) stands for other possible terms that can appear in the expression for the g factor.

At the same time, experiments studying deuterium and hydrogen-like ions, where the nuclei have various spins, require constructing methods for calculating g factors for the case of an arbitrary spin. Eides and Grotch [15] proposed a method for calculating corrections to gyromagnetic factors on the basis of the Bargmann–Michel–Telegdi equation [16] and concluded that these corrections are independent of the value of the constituent spins. In the present study, a quasipotential method for calculating the magnetic moment of the bound state formed by two particles of arbitrary-spin is formulated in the one-photon approximation. By using this method, we further calculate the leading contributions of orders $O(\alpha^2)$ and $O(\alpha^3)$ to relation (2) (see figure).

Over a long period of time, the interaction of massive particles of arbitrary spin with an electromagnetic field has been investigated on the basis of various approaches [17–27], but the relevant problem has not yet been solved conclusively. It was shown in [18–20] that, in the tree approximation, particles of arbitrary spin must have the gyromagnetic factor of $g = 2$. For a particle of spin s , the matrix element of the electromagnetic current is generally determined in terms of $2s + 1$ form factors (charge, magnetic, quadrupole, and so on). In investigating the magnetic moments of the simplest atomic systems, we can restrict ourselves to form factors of lowest multipole orders that determine the electric-charge and magnetic-moment distributions. The matrix element

¹⁾Samara State University, ul. Akademika Pavlova 1, Samara, 443011 Russia.

²⁾Scientific Council for the Interdisciplinary Problem Cybernetics, Russian Academy of Sciences, ul. Vavilova 40, Moscow, 117967 Russia.

* e-mail: mart@info.ssu.samara.ru

** e-mail: faustov@theory.npi.msu.su

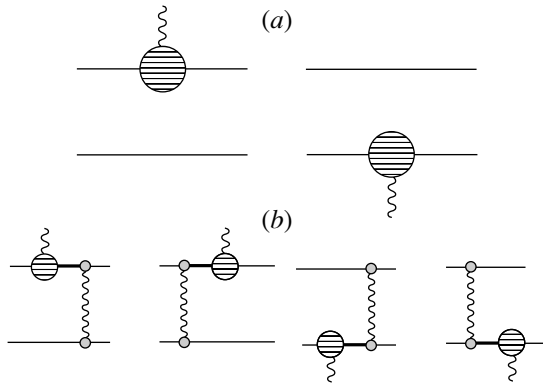


Fig. 1. Generalized two-particle vertex function Γ_μ : (a) $\Gamma_\mu^{(0)}$ and (b) $\Gamma_\mu^{(1)}$ (here, thick lines represent the negative-frequency part of the particle propagator).

J_μ of the electromagnetic-current operator between states characterized by the momenta p and q can be written in the form

$$J_\mu = \bar{U}(p) \left\{ \Gamma_\mu F_1^D + \frac{1}{2m} \Sigma_{\mu\nu} k^\nu F_2^P \right\} U(q), \quad (3)$$

where $k^\nu = (p - q)^\nu$; m is the particle mass; and F_1^D and F_2^P are, respectively, the Dirac and the Pauli form factor. The wave function $U(p)$ for a particle of arbitrary spin [it appears in Eq. (3)] can be represented in the form [26, 27]

$$U = \begin{pmatrix} \xi \\ \eta \end{pmatrix} = \begin{pmatrix} \xi_{\beta_1 \beta_2 \dots \beta_p}^{\alpha_1 \alpha_2 \dots \alpha_p} \\ \eta_{\dot{\alpha}_1 \dot{\alpha}_2 \dots \dot{\alpha}_p}^{\beta_1 \beta_2 \dots \beta_p} \end{pmatrix}, \quad p + q = 2s, \quad (4)$$

where the spin tensors ξ and η are symmetric in superscripts and subscripts individually. For a particle of half-integer spin, we have $p = s + 1/2$ and $q = s - 1/2$; for a particle of integral spin, $p = q = s$. The Lorentz transformation for the spinors ξ and η has the form [27, 28]

$$\xi = e^{\Sigma \cdot \phi / 2} \xi_0, \quad \eta = e^{-\Sigma \cdot \phi / 2} \eta_0, \quad (5)$$

where ξ_0 is the spinor in the rest frame, the direction of the vector ϕ coincides with the particle velocity \mathbf{v} , $\tanh \phi = v$, and the generator Σ of the Lorentz transformation has the form

$$\Sigma = \sum_{i=1}^p \sigma_i - \sum_{i=p+1}^{p+q} \sigma_i. \quad (6)$$

The matrix σ_i acts on the index i of the spinor ξ_0 in the following way:

$$\sigma_i \xi_0 = (\sigma_i)_{\alpha_i \beta_i} (\xi_0)_{\dots \beta_i \dots} \quad (7)$$

The components of the antisymmetric tensor $\Sigma_{\mu\nu}$ in (3) are the generators of boosts and rotations [27, 28]; that is,

$$\Sigma_{n0} = \begin{pmatrix} \Sigma_n & 0 \\ 0 & -\Sigma_n \end{pmatrix}, \quad (8)$$

$$\Sigma_{mn} = -2i \epsilon_{mnk} \begin{pmatrix} s_k & 0 \\ 0 & s_k \end{pmatrix},$$

$$\mathbf{s} = \frac{1}{2} \sum_{i=1}^{2s} \sigma_i.$$

In the standard representation that is introduced by analogy with the case of a spin of 1/2, the wave function (4) for a free particle to terms of order $(v/c)^2$ has the form

$$U(p) = \begin{pmatrix} \left[1 + \frac{(\boldsymbol{\Sigma} \cdot \mathbf{p})^2}{8m^2} \right] \xi_0 \\ \frac{\boldsymbol{\Sigma} \cdot \mathbf{p}}{2m} \xi_0 \end{pmatrix}. \quad (9)$$

The magnetic moment of the bound state of two particles of arbitrary spin is given by [8, 9]

$$\mathcal{M} = -\frac{i}{2} \left[\frac{\partial}{\partial \Delta} \times \langle \mathbf{K}_A | \mathbf{J}(0) | \mathbf{K}_B \rangle \right], \quad (10)$$

$$\Delta = \mathbf{K}_A - \mathbf{K}_B,$$

where the matrix element of the electromagnetic-current operator between bound states can be written as

$$\langle \mathbf{K}_A | J_\mu(0) | \mathbf{K}_B \rangle = \int \frac{d\mathbf{p}_1 d\mathbf{p}_2}{(2\pi)^3} \delta(\mathbf{p}_1 + \mathbf{p}_2 - \mathbf{K}_A) \quad (11)$$

$$\times \Psi_{\mathbf{K}_A}^*(\mathbf{p}) \Gamma_\mu(\mathbf{p}, \mathbf{q}, E_A, E_B) \\ \times \Psi_{\mathbf{K}_B}(\mathbf{q}) \delta(\mathbf{q}_1 + \mathbf{q}_2 - \mathbf{K}_B) \frac{d\mathbf{q}_1 d\mathbf{q}_2}{(2\pi)^3};$$

that is, it is expressed in terms of the wave functions $\Psi_{\mathbf{K}_B}(\mathbf{p})$ for the bound system and the generalized vertex function Γ_μ , which is shown in the figure. The vertex function Γ_μ is expressed in terms of the five-point function

$$R_\mu = \langle 0 | \psi_1(t, \mathbf{x}_1) \psi_2(t, \mathbf{x}_2) \\ \times J_\mu(0) \bar{\psi}_1(\tau, \mathbf{y}_1) \bar{\psi}_2(\tau, \mathbf{y}_2) | 0 \rangle, \quad (12)$$

which is projected onto positive-frequency states. Specifically, we have

$$\Gamma_\mu = G^{-1} R_\mu^{(+)} G^{-1}, \quad R_\mu^{(+)} = U_1^* U_2^* R_\mu U_1 U_2, \quad (13)$$

where G is the two-particle Green's function and $\psi(t, \mathbf{x})$ is the Heisenberg field operator of the particle. Since we study a loosely bound two-particle system, all of the quantities Γ , R , and G^{-1} can be expanded in the perturbation-theory series

$$\Gamma = \Gamma^{(0)} + \Gamma^{(1)} + \dots, \quad (14)$$

$$R = R_0 + R_1 + \dots, \quad G^{-1} = G_0^{-1} - V_1 - \dots,$$

$$\Gamma^{(0)} = G_0^{-1} R_0 G_0^{-1}, \quad (15)$$

$$\Gamma^{(1)} = G_0^{-1} R_1 G_0^{-1} - V_1 G_0 \Gamma^{(0)} \\ - \Gamma^{(0)} G_0 V_1, \dots, \quad (16)$$

where G_0 is the Green's function for two noninteracting particles and V_1 is the quasipotential for the one-photon interaction [see Eq. (19)].

It was shown in [29] that, upon the transition from the rest frame to the frame moving at the momentum \mathbf{K}_B , the wave function $\Psi_{\mathbf{K}_B}(\mathbf{p})$ for the system consisting of two particles with the spins s_1 and s_2 transforms as

$$\delta(\mathbf{p}_1 + \mathbf{p}_2 - \mathbf{K}_B)\Psi_{\mathbf{K}_B}(\mathbf{p}) \quad (17)$$

$$= D_1^{s_1}(R_W)D_2^{s_2}(R_W)\sqrt{\frac{\epsilon_1^\circ\epsilon_2^\circ M}{\epsilon_1\epsilon_2 E}}\Psi_0(\mathbf{p}^\circ)\delta(\mathbf{p}_1^\circ + \mathbf{p}_2^\circ),$$

where $D^s(R)$ stands for the rotation matrices and R_W is the Wigner rotation that is related to the Lorentz transformation $\Lambda_{\mathbf{K}_B}$: $(E_B, \mathbf{K}_B) = \Lambda_{\mathbf{K}_B}(M, 0)$; $(\epsilon, \mathbf{p}) = \Lambda(\epsilon^\circ, \mathbf{p}^\circ)$, $E_B = \sqrt{M^2 + \mathbf{K}_B^2}$, $\epsilon(\mathbf{p}) = \sqrt{\mathbf{p}^2 + m^2}$. The exact expression for the rotation matrix has the form [9]

$$D^s(R_W) = S^{-1}(\mathbf{p})S(\mathbf{K}_B)S(\mathbf{p}^\circ), \quad (18)$$

where $S(\mathbf{p})$ is the matrix of the Lorentz transformation of the spinor wave function (4). In the rest frame of the bound state, the quasipotential wave function $\Psi_0(\mathbf{p}^\circ)$ satisfies the quasipotential equation [30]

$$G_0^{-1}\Psi \equiv \left(\frac{b^2}{2\mu_R} - \frac{\mathbf{p}^{\circ 2}}{2\mu_R} \right) \Psi_0(\mathbf{p}^\circ) \quad (19)$$

$$= \int V(\mathbf{p}^\circ, \mathbf{q}^\circ, M)\Psi_0(\mathbf{q}^\circ)\frac{d\mathbf{q}^\circ}{(2\pi)^3},$$

where the relativistic reduced mass is given by

$$\mu_R = \frac{E_1 E_2}{M} = \frac{M^4 - (m_1^2 - m_2^2)^2}{4M^3},$$

$$E_{1,2} = \frac{M^2 - m_{2,1}^2 + m_{1,2}^2}{2M},$$

with $M = E_1 + E_2$ being the bound-state mass, while

$$b^2(M) = \frac{[M^2 - (m_1 + m_2)^2][M^2 - (m_1 - m_2)^2]}{4M^2}.$$

In the nonrelativistic limit, Eq. (19) reduces to the Schrödinger equation with the Coulomb potential. The functions D^s (18) can be obtained in an approximate form by using expressions (5):

$$D^s(R_W) \approx 1 + \frac{\mathbf{p}^{\circ 2} - (\boldsymbol{\Sigma} \cdot \mathbf{p}^\circ)(\boldsymbol{\Sigma} \cdot \mathbf{p}^\circ)}{4m^2} \quad (20)$$

$$+ \frac{\mathbf{K}_B^2 - (\boldsymbol{\Sigma} \cdot \mathbf{K}_B)(\boldsymbol{\Sigma} \cdot \mathbf{K}_B)}{4M^2}$$

$$+ \frac{\mathbf{p}^\circ \cdot \mathbf{K}_B - (\boldsymbol{\Sigma} \cdot \mathbf{p}^\circ)(\boldsymbol{\Sigma} \cdot \mathbf{K}_B)}{4mM}.$$

The main contribution to the vertex function Γ_μ is represented by the diagram in Fig. 1a. In the Breit frame, it has the form

$$\mathbf{\Gamma}^{(0)}(\mathbf{p}, \mathbf{q}) = \bar{U}_1(p_1)e_1 \left\{ \mathbf{\Gamma}_1 + \frac{i\kappa_1}{m_1} [\mathbf{S}_1 \times \boldsymbol{\Delta}] \right\} \quad (21)$$

$$\times U_1(q_1)\delta(\mathbf{p}_2 - \mathbf{q}_2) + (1 \leftrightarrow 2),$$

$$\mathbf{S}_1 = \begin{pmatrix} \mathbf{s}_1 & 0 \\ 0 & \mathbf{s}_1 \end{pmatrix}, \quad \boldsymbol{\Delta} = \mathbf{p}_1 - \mathbf{q}_1,$$

where $F_{1,2}^D(0) = e_{1,2}$, $F_{1,2}^P(0) = e_{1,2}\kappa_{1,2}$ ($\kappa_{1,2}$ are the anomalous magnetic moments of particles), and the matrix

$$\mathbf{\Gamma} = \begin{pmatrix} 0 & \boldsymbol{\Sigma} \\ -\boldsymbol{\Sigma} & 0 \end{pmatrix} \quad (22)$$

is a natural generalization of the Dirac γ matrix for the spin of 1/2 in the standard representation. In order to simplify the individual terms in (21), it is convenient to use the commutation relations [27]

$$[\boldsymbol{\Sigma}_i, \boldsymbol{\Sigma}_j] = 4i\epsilon_{ijk}s_k, \quad [\boldsymbol{\Sigma}_i, s_j] = i\epsilon_{ijk}\Sigma_k. \quad (23)$$

In order to construct the vertex function $\mathbf{\Gamma}^{(0)}(\mathbf{p}, \mathbf{q})$ with allowance for terms of order $(v/c)^2$, we use the explicit form of the wave function (9), transforming the individual terms of the matrix element in (21) with the aid of the equation of motion for the spinors $U(p)$. Taking into account the factor $\delta(\mathbf{p}_2 - \mathbf{q}_2)$, we obtain

$$\bar{U}_1(\mathbf{p}_1)(\mathbf{p}_1 + \mathbf{q}_1)U_1(\mathbf{q}_1) \quad (24)$$

$$= 2\mathbf{p}^\circ - \frac{\epsilon_2}{M}\boldsymbol{\Delta} + \frac{i\mathbf{p}^\circ(\mathbf{S}_1 \cdot [\mathbf{p}^\circ \times \boldsymbol{\Delta}])}{m_1^2},$$

$$\bar{U}_1(\mathbf{p}_1)[\epsilon_1(\mathbf{p}_1) - \epsilon_1(\mathbf{q}_1)]\mathcal{A}_1 U_1(\mathbf{q}_1) \quad (25)$$

$$= -\frac{2\mathbf{p}^\circ \cdot \boldsymbol{\Delta}}{m_1^2}i[\mathbf{S}_1 \times \mathbf{p}^\circ],$$

$$\bar{U}_1(\mathbf{p}_1)[\mathbf{S}_1 \times \boldsymbol{\Delta}]U_1(\mathbf{q}_1) \quad (26)$$

$$= [\mathbf{S}_1 \times \boldsymbol{\Delta}] - \frac{1}{2m_1^2} \{ \mathbf{p}^\circ(\mathbf{S}_1 \cdot [\mathbf{p}^\circ \times \boldsymbol{\Delta}])$$

$$+ [\mathbf{p}^\circ \times \mathbf{S}_1](\mathbf{p}^\circ \cdot \boldsymbol{\Delta}) \}.$$

The effects in the vertex function Γ_μ that are associated with the fact that the particles being considered are bound are represented by the diagram in Fig. 1b. The expression that corresponds to this diagram and which takes into account the iterative terms of the quasipotential approach can be written in the convenient form [8, 9]

$$\mathbf{\Gamma}^{(1)}(\mathbf{p}, \mathbf{q}) = U_1^*(\mathbf{p}_1)U_2^*(\mathbf{p}_2)\frac{e_1}{2m_1} \quad (27)$$

$$\times \{ \mathcal{A}_1\Lambda_1^{(-)}(\mathbf{p}'_1)\mathcal{B}_1\mathcal{B}_2\hat{V}(\mathbf{q}_2 - \mathbf{p}_2)$$

$$\begin{aligned}
& + \mathcal{B}_1 \mathcal{B}_2 \hat{V}(\mathbf{p}_2 - \mathbf{q}_2) \Lambda_1^{(-)}(\mathbf{q}'_1) \mathcal{A}_1 \} \\
& \times U_1(\mathbf{q}_1) U_2(\mathbf{q}_2) + (1 \leftrightarrow 2), \\
\hat{V}(\mathbf{k}) = & \mathcal{B}_1 \mathcal{B}_2 \left\{ \left(1 + \frac{\kappa_1}{2m_1} \mathbf{\Gamma}_1 \cdot \mathbf{k} \right) \right. \\
& \times \left(1 - \frac{\kappa_2}{2m_2} \mathbf{\Gamma}_2 \cdot \mathbf{k} \right) - \left(\mathcal{A}_1 + \frac{\kappa_1}{m_1} \mathcal{B}_1 i [\mathbf{S}_1 \times \mathbf{k}] \right) \\
& \left. \times \left(\mathcal{A}_2 - \frac{\kappa_2}{m_2} \mathcal{B}_2 i [\mathbf{S}_2 \times \mathbf{K}] \right) \right\} \frac{e_1 e_2}{k^2},
\end{aligned} \quad (28)$$

where $\Lambda^-(\mathbf{p}) \approx (1 - \mathcal{B})/2 - \mathcal{A} \cdot \mathbf{p}/2m$ is the single-particle operator of projection onto negative-frequency states, $\mathbf{p}'_1 = \mathbf{p}_1 - \mathbf{\Delta}$, and $\mathbf{q}'_1 = \mathbf{q}_1 + \mathbf{\Delta}$. As in (22), the matrices $\mathcal{A}_{1,2}$ and $\mathcal{B}_{1,2}$ are natural generalizations of $\alpha_{1,2}$, $\beta_{1,2}$ in the case of spin-1/2 particles:

$$\mathcal{A} = \begin{pmatrix} 0 & \mathbf{\Sigma} \\ \mathbf{\Sigma} & 0 \end{pmatrix}, \quad \mathcal{B} = \begin{pmatrix} I & 0 \\ 0 & -I \end{pmatrix}. \quad (29)$$

Apart from terms of order $(v/c)^2$, both terms of the potential (28) contribute to the magnetic moment of the system. By substituting (27), (28), and (9) into (11) and calculating the derivative with respect to $\mathbf{\Delta}$ in (10), we obtain

$$\begin{aligned}
\mathcal{M} = & \frac{1}{(2\pi)^3} \int d\mathbf{p} \Psi_0^*(\mathbf{p}) \frac{e_1}{2\epsilon_1(\mathbf{p})} \\
& \times \left\{ 2(1 + \kappa_1) \mathbf{s}_1 [1 + N_1 + N_2] \right. \\
& + (1 + 4\kappa_1) \frac{[\mathbf{p} \times [\mathbf{s}_1 \times \mathbf{p}]]}{2m_1^2} \\
& + (1 + \kappa_2) \frac{[\mathbf{p} \times [\mathbf{s}_2 \times \mathbf{p}]]}{m_1 m_2} \frac{\mathbf{\Sigma}_1^2}{3} - \frac{\epsilon_2(\mathbf{p})}{M} \\
& \left. \times \left[1 + N_1 + N_2 + \frac{(M - \epsilon_1 - \epsilon_2) \mathbf{\Sigma}_1^2}{m_2} \frac{1}{3} \right] i \left[\mathbf{p} \times \frac{\partial}{\partial \mathbf{p}} \right] \right\}
\end{aligned} \quad (30)$$

$$K_{s_2} = \frac{\langle \mathbf{\Sigma}_2^2 \rangle}{3} = \begin{cases} 4s_2/3, & s_2 \text{ being an integral nuclear spin} \\ (4s_2 + 1)/3, & s_2 \text{ being a half-integer nuclear spin,} \end{cases}$$

so that the g factors for the electron and the nucleus in the bound state are given by

$$\begin{aligned}
g_e^{(\text{bound})} = & g_e \left\{ 1 - \frac{m_2^2 (Z\alpha)^2}{3(m_1 + m_2)^2} \left[1 - \frac{3\kappa_1}{2(1 + \kappa_1)} \right. \right. \\
& - \frac{3}{2} (1 - K_{s_1}) - \frac{3}{2} \frac{m_1^2}{m_2^2} \left(1 - K_{s_2} - \frac{2}{3} ZK_{s_2} \right) \\
& \left. \left. + \frac{m_1}{2(m_1 + m_2)(1 + \kappa_1)} \left(1 + Z \frac{m_1}{m_2} \right) \right] \right\}, \\
g_N^{(\text{bound})} = & g_N \left\{ 1 - \frac{m_1^2 (Z\alpha)^2}{3(m_1 + m_2)^2} \left[1 - \frac{3\kappa_2}{2(1 + \kappa_2)} \right. \right.
\end{aligned} \quad (35)$$

$$\begin{aligned}
& + \frac{1}{2M} \left[\mathbf{p} \times \left[\mathbf{p} \times \left(\frac{\mathbf{s}_1}{m_1} - \frac{\mathbf{s}_2}{m_2} \right) \right] \right] \Bigg\} \\
& \times \Psi_0(\mathbf{p}) + (1 \leftrightarrow 2),
\end{aligned}$$

where

$$N_i = \frac{\mathbf{p}^2 - (\mathbf{\Sigma}_i \cdot \mathbf{p})(\mathbf{\Sigma}_i \cdot \mathbf{p})}{2m_i^2}. \quad (31)$$

For S states, expression (30) is significantly simplified to become

$$\mathcal{M} = \frac{1}{2} g_1^{(\text{bound})} \frac{e_1}{m_1} \langle \mathbf{s}_1 \rangle + \frac{1}{2} g_2^{(\text{bound})} \frac{e_2}{m_2} \langle \mathbf{s}_2 \rangle, \quad (32)$$

where the g factors of bound particles are given by

$$\begin{aligned}
g_1^{(\text{bound})} = & g_1 \left\{ 1 - \frac{\langle \mathbf{p}^2 \rangle}{3m_1^2} \left[1 - \frac{3\kappa_1}{2(1 + \kappa_1)} \right] \right. \\
& + \frac{\langle \mathbf{p}^2 \rangle}{2m_1^2} \left[1 - \frac{\langle \mathbf{\Sigma}_1^2 \rangle}{3} + \frac{m_1^2}{m_2^2} \left(1 - \frac{\langle \mathbf{\Sigma}_2^2 \rangle}{3} \right) \right] \\
& + \frac{e_2 \langle \mathbf{p}^2 \rangle \langle \mathbf{\Sigma}_2^2 \rangle}{e_1 3m_2^2} \frac{1}{3} - \frac{\langle \mathbf{p}^2 \rangle}{(1 + \kappa_1) 6m_1(m_1 + m_2)} \\
& \left. \times \left(1 - \frac{e_2 m_1}{e_1 m_2} \right) \right\},
\end{aligned} \quad (33)$$

$$g_2^{(\text{bound})} = g_1^{(\text{bound})} (1 \leftrightarrow 2), \quad g_{1,2}/2 = 1 + \kappa_{1,2}.$$

For a hydrogen-like ion (here, 1 and 2 stand for the electron and the nucleus, respectively), we have $e_1 = -e$, $e_2 = Ze$, $\langle \mathbf{p}^2 \rangle = m_1^2 m_2^2 (Z\alpha)^2 / (m_1 + m_2)^2$, $g_e/2 = 1 + \kappa_1$, $g_N/2 = 1 + \kappa_2$, and

$$K_{s_1} = \frac{\langle \mathbf{\Sigma}_1^2 \rangle}{3} = 1, \quad (34)$$

$$\begin{aligned}
& - \frac{3}{2} (1 - K_{s_2}) - \frac{3}{2} \frac{m_2^2}{m_1^2} (1 - K_{s_1} - \frac{2}{3Z} K_{s_1}) \\
& + \frac{m_2}{2(m_1 + m_2)(1 + \kappa_2)} \left(1 + \frac{m_2}{Zm_1} \right) \Bigg\}.
\end{aligned} \quad (36)$$

Here, we have retained the factors K_{s_1} and K_{s_2} in the general form in order to demonstrate the symmetry of relations (35) and (36) under the interchange $1 \leftrightarrow 2$. Expressions (35) and (36), which were obtained on the basis of the diagrams in Figs. 1a and 1b, involve $O(\alpha^2)$ and $O(\alpha^3)$ corrections, which are due to effects of particle binding. We recall that the interaction of particles in the bound state was considered

in the one-photon approximation. In the case being considered, $O(\alpha^3)$ corrections arise upon taking into account quasipotential terms that are proportional to the anomalous magnetic moments κ_1 and κ_2 of the particles. Relations (30), (35), and (36) generalize the expressions for the magnetic moment of a hydrogen-like atom and for the gyromagnetic factors for spin-1/2 particles from [8, 9] to the case of particles of arbitrary spin. The expression for the magnetic moment in (30) involves terms corresponding to the interaction of free nonrelativistic pointlike charged particles with an external electromagnetic field and some corrections to these terms for the effects of particle binding. Among these corrections, which are quadratic in the spin operator Σ (terms proportional to N_i), those that are determined by the transformation properties of the spinors ξ and η (5) can be interpreted as relativistic corrections for a particle of spin s . Other corrections associated with the general structure of the matrix element of the current J_μ in (3) stem from the dipole interaction. As follows from (35) and (36), our calculations show that the $O(\alpha^2)$ terms in expressions for $g_e^{(\text{bound})}$ and $g_N^{(\text{bound})}$ depend on the spin of the second particle, nucleus, in contrast to the results presented in [15], where there is no such dependence. The g factors for the electron in the hydrogen atom, deuterium, and tritium and their ratios are of importance from the experimental point of view [1].

The experimental value of the ratio g_e^H/g_e^D was obtained in [13] to a high precision. It is

$$r^{\text{expt}} = \left[\frac{g_e^H}{g_e^D} \right]^{\text{expt}} = 1 + 7.22(3) \times 10^{-9}. \quad (37)$$

The theoretical expression for this ratio follows from (35):

$$r^{\text{th}} = \left[\frac{g_e^H}{g_e^D} \right]^{\text{th}} = 1 + \alpha^2 \left[\frac{1}{4} \frac{m_1}{m_2} - \frac{25}{72} \frac{m_1^2}{m_2^2} - \frac{\alpha}{\pi} \left(\frac{m_1}{24m_2} - \frac{1}{16} \frac{m_1^2}{m_2^2} \right) \right]. \quad (38)$$

The numerical value of the expression in (38) is $r^{\text{th}} = 1 + 7.237 \times 10^{-9}$, which is in good agreement with the experimental result in (37).

The problem of constructing a relativistic description of the interaction of a massive particle of arbitrary spin with an electromagnetic field has been studied for a long time [17–25], but, at the moment, it is far from being conclusively solved. It is well known that, if the minimal-interaction principle is used in relativistic equations for particles of spin $s \geq 1$, there arise difficulties of a fundamental character [17–27]. In the nonrelativistic limit, different relativistic wave equations for a particle of spin s lead to different equations of the Pauli type. As was mentioned above, Eides

and Grotch [15] proposed a method for calculating the contributions of various orders to the magnetic moment of a loosely bound system on the basis of the relativistic semiclassical equation of motion for a spin. The Hamiltonian that was constructed in [15] on the basis of this equation describes the interaction of a particle of arbitrary spin with an external electromagnetic field and leads to spin-independent g factors for bound-state particles. The Bargmann–Michel–Telegdi equation is approximate: it is linear in the spin of a particle and in the field $F_{\mu\nu}$ whose coordinate dependence is disregarded. In the case where a particle of spin s is in a bound state in a uniform external electromagnetic field, the terms that are omitted in the approximation of the Bargmann–Michel–Telegdi equation can contribute to the g factors for bound particles. In this study, the method proposed in [26, 27] to describe the interaction of a particle of arbitrary spin with an electromagnetic field is used to calculate nuclear-spin-dependent contributions to the g factors for the bound particles of a hydrogen-like ion. New (in relation to the results presented in [8]) contributions in expressions (35), (36), and (38) are due to the replacement of the ordinary boost generators α for spin-1/2 particles by the operators in (29). Thus, our approach to describing the interaction of a particle of arbitrary spin with an electromagnetic field is based on the use of the matrix element of the electromagnetic current (11) and on the Lorentz transformation (5) of the spinor wave functions ξ and η . We have obtained additional spin-dependent terms in the g factors for bound particles [see (33)]. They arise upon taking into account, in the particle-interaction operator, terms that are nonlinear in the spin operator Σ . The Hamiltonian obtained in [15] does not involve such $O((v/c)^2)$ nonlinear terms for particles of arbitrary spin s . Effects quadratic in the operator Σ that appear in the interaction operator of particles of arbitrary spin were investigated in [26, 27]. A term of the $(\Sigma \cdot \mathbf{q})^2$ type can be represented as the sum of a contact and a quadrupole term:

$$\Sigma_i \Sigma_j q_i q_j = \frac{1}{3} \mathbf{q}^2 \Sigma_i \Sigma_i + \left(q_i q_j - \frac{1}{3} \mathbf{q}^2 \delta_{ij} \right) \Sigma_i \Sigma_j. \quad (39)$$

The contact term contributes to the energy spectrum of the system, while the quadrupole term determines the correction to the quadrupole moment of the nucleus. The results that we obtained here for the contributions to the gyromagnetic factors of particles are determined by the contact terms of interaction (39). For spin-1/2 particles, these terms correctly reproduce the well-known result that was independently obtained within the various approximations in [8, 10, 11, 22]. The numerical value of the correction to r^{th} associated with the spin of the deuteron, for

which we have $I = 1$, $Z = 1$, and $m = 2m_2$ (m_2 is the proton mass), is $\Delta r^{\text{th}} = 5\alpha^2 m_1^2 / 72m_2^2 = 0.001 \times 10^{-9}$; as follows from (37), it is currently within the experimental errors. The corrections in (35) and (36) that are associated with the spin of the nucleus also depend on Z and N (the latter being the number of nucleons in the nucleus). Although these corrections grow in proportion to Z^3 with increasing Z , an increase in the number N of nucleons in the nucleus leads to the inverse effect. Because of this, the numerical value of these corrections is currently beyond the experimental accuracy for ions of the $^{12}\text{C}^{5+}$ type of nonzero spin ($I \neq 0$). For the carbon ion $^{12}\text{C}^{5+}$ itself, the spin is $I = 0$; therefore, $K_I = 0$, and the corresponding spin correction vanishes. At present, the g factors for the electron have been measured in the oxygen and sulfur ions ($^{16}\text{O}^{7+}$ and $^{32}\text{S}^{14+}$ [4]), whose nuclei also have zero spin $I = 0$. In our opinion, it would be interesting to measure, by means of Penning traps [3, 4], the g factors of particles for ions such that their spin is nonzero ($I \neq 0$), on one hand, and the ratio Z^3/N^2 would be as great as possible, on the other hand. This may be, for example, the $^{59}\text{Co}^{26+}$ ion, for which $I = 7/2$ and $Z^3/N^2 \approx 5.65$, while the spin-dependent correction in (35) is 0.1×10^{-9} . As was indicated in the report presented by Quint [4], measurement of the g factor for a bound electron to a precision higher than 10^{-9} will become possible in the near future.

ACKNOWLEDGMENTS

We are grateful to I.B. Khriplovich for critical comments and interest in this study, to V.M. Shabaev and W. Quint for information about new experimental data on g factors for bound particles, and to S.G. Karshenboim for an enlightening discussion on the problem of the magnetic moments of bound states.

This work was supported in part by the Russian Foundation for Basic Research (project no. 00-02-17771) and by the program Universities of Russia—Basic Research (project no. 990192).

REFERENCES

1. P. J. Mohr and B. N. Taylor, *Rev. Mod. Phys.* **72**, 351 (2000).
2. T. Beier, *Phys. Rep.* **339**, 79 (2000).
3. N. Hermanspahn, H. Haffner, H.-J. Kluge, *et al.*, *Phys. Rev. Lett.* **84**, 427 (2000).
4. W. Quint, *Invited Talk at 2nd Workshop on Frontier Tests of Quantum Electrodynamics and Physics of the Vacuum "QED 2000", Trieste, Italy, 2000*.
5. V. M. Shabaev, *Can. J. Phys.* **76**, 907 (1998).
6. S. G. Karshenboim, *Phys. Lett. A* **266**, 380 (2000).
7. A. Czarnecki, K. Melnikov, and A. Yelkhovsky, *Phys. Rev. A* **63**, 012509 (2001).
8. R. N. Faustov, *Phys. Lett. B* **33B**, 422 (1970).
9. R. N. Faustov, *Nuovo Cimento A* **69**, 37 (1970).
10. H. Grotch, *Phys. Rev. Lett.* **24**, 39 (1970).
11. H. Grotch and R. A. Hegstrom, *Phys. Rev. A* **4**, 59 (1971).
12. S. A. Blundell, K. T. Cheng, and J. Sapirstein, *Phys. Rev. A* **55**, 1857 (1997).
13. F. G. Walther, W. D. Phillips, and D. Kleppner, *Phys. Rev. Lett.* **28**, 1159 (1972).
14. H. Persson, S. Salomonson, P. Sunnergren, and I. Lindgren, *Phys. Rev. A* **56**, R2499 (1997); T. Beier, I. Lindgren, H. Persson, *et al.*, *Phys. Rev. A* **62**, 032510 (2000).
15. M. I. Eides and H. Grotch, *Ann. Phys. (N.Y.)* **260**, 191 (1997).
16. V. B. Berestetskii, E. M. Lifshitz, and L. P. Pitaevskii, *Quantum Electrodynamics* (Nauka, Moscow, 1989; Pergamon, Oxford, 1982).
17. L. P. S. Singh and C. R. Hagen, *Phys. Rev. D* **9**, 898 (1974); **9**, 910 (1974).
18. S. Weinberg, in *Lectures on Elementary Particles and Quantum Field Theory*, Ed. by S. Deser, M. Grisaru, and H. Pendleton (MIT Press, Cambridge, 1970).
19. I. B. Khriplovich, *Zh. Éksp. Teor. Fiz.* **96**, 385 (1989) [*Sov. Phys. JETP* **69**, 217 (1989)].
20. S. Ferrara, M. Poratti, and V. L. Telegdi, *Phys. Rev. D* **46**, 3529 (1992).
21. S. D. Brodsky and J. R. Primack, *Ann. Phys. (N.Y.)* **52**, 315 (1969).
22. F. E. Close and H. Osborn, *Phys. Lett. B* **34B**, 400 (1971).
23. V. I. Fushich and A. G. Nikitin, *Symmetry of Equations of Quantum Mechanics* (Nauka, Moscow, 1990).
24. S. Deser, V. Pascalutsa, and A. Waldron, *Phys. Rev. D* **62**, 105031 (2000).
25. Yu. M. Zinoviev, in *Proceedings of the XVII Seminar on High Energy Physics and Field Theory, Protvino, 1994*, p. 189.
26. I. B. Khriplovich, A. I. Milstein, and R. A. Sen'kov, *Zh. Éksp. Teor. Fiz.* **111**, 1935 (1997) [*JETP* **84**, 1054 (1997)].
27. A. A. Pomeranskiĭ and I. B. Khriplovich, *Zh. Éksp. Teor. Fiz.* **113**, 1537 (1998) [*JETP* **86**, 839 (1998)].
28. Yu. B. Rumer and A. I. Fet, *Theory of Groups and Quantum Fields* (Nauka, Moscow, 1977).
29. R. N. Faustov, *Ann. Phys. (N.Y.)* **78**, 176 (1973).
30. A. P. Martynenko and R. N. Faustov, *Theor. Math. Phys.* **64**, 765 (1985).

Translated by A. Isaakyan

**Conference on Physics of Fundamental Interactions
Theory**

**Lepton-Pair Production by a Neutrino
in an External Electromagnetic Field**

A. V. Kuznetsov*, **N. V. Mikheev****, and **D. A. Rumyantsev*****

Yaroslavl State University, ul. Sovetskaya 14, Yaroslavl, 150000 Russia

Received March 7, 2001

Abstract—Lepton-pair production by a neutrino in an external electromagnetic field is investigated within the Standard Model. For the probability of this process, a comparatively simple exact expression is derived that is convenient for a numerical analysis. © 2002 MAIK “Nauka/Interperiodica”.

Presently, the well-established fact that a medium has a profound impact on quantum processes occurring in it stimulates an ever growing interest in the physics of elementary particles in a medium, especially in connection with possible astrophysical applications. By a medium, we mean here not only dense matter but also an intense electromagnetic field, which, in astrophysical objects, can attain the Schwinger critical value of $B_e = m_e^2/e \simeq 4.41 \times 10^{13}$ G or even significantly exceed it.¹⁾ At the same time, the situation is possible where, for a relativistic particle moving in a relatively weak electromagnetic field, $F < B_e$ ($F = E$ or B), the so-called dynamical field parameter $e(p_\alpha F_{\alpha\beta} F_{\beta\sigma} p_\sigma)^{1/2}$ (here, p_α is the particle 4-momentum, and $F_{\alpha\beta}$ is the strength tensor of the electromagnetic field) can prove to be the greatest dimensional parameter of the problem. In the rest frame of this particle, the field can then considerably exceed the critical value and can be very close to a crossed field. Thus, a calculation in a crossed field is of interest in and of itself. A technique for computations in such a field was developed by Nikishov and Ritus (see, for example, [1]).

There are processes—in particular, lepton-pair production by a neutrino, $\nu \rightarrow \nu \ell^- \ell^+$ ($\ell = e, \mu, \tau$)—that are forbidden in a vacuum, but which become possible in an intense electromagnetic field. We note that, by virtue of the special kinematical features of a charged particle in an electromagnetic field, a $\ell^- \ell^+$ pair can have a total spacelike momentum of rather large magnitude, whence it follows that,

for ultrarelativistic neutrinos, the process becomes purely diagonal in the neutrino flavor and insensitive to the neutrino mass and to mixing in the lepton sector.

Investigation of the production of electron–positron pairs by a neutrino in the crossed-field limit has a rather long history [2–6]. Even in the first of the studies quoted immediately above ([2]), a correct dependence of the leading contribution to the probability of the process on the dimensionless dynamical parameter χ [the parameter χ is given by $\chi^2 = e^2(p_\alpha F_{\alpha\beta} F_{\beta\sigma} p_\sigma)/m_e^6 \equiv e^2(pFFp)/m_e^6$, where p_α is the 4-momentum of the primary neutrino and m_e is the electron mass] was found in the leading-logarithm approximation (the result was proportional to $\chi^2 \ln \chi$), but the numerical factor was erroneous there. More recent studies were devoted to refining the common factor in the expression for the probability and to computing postlogarithmic corrections, which may prove to be of importance at not overly large values of $\ln \chi$.

From the very formulation of the problem, it follows that we are dealing here solely with an ultrarelativistic neutrino, which, owing to a chiral character of its interaction within the Standard Model, can exist only in a state having a left-hand circular polarization, this being so even if its mass is nonzero. This statement remains in force even if we assume that the neutrino has exotic properties that, under certain physical conditions, could lead to depolarization effects (which have not yet been observed). The disregard of the fact that, in nature, there are no unpolarized ultrarelativistic neutrinos fluxes often led to the appearance of the erroneous factor of 1/2 in expressions for the probabilities of processes involving neutrinos in the initial state, this being due to unphysical averaging over its polarizations (see, for example, [7, 8]).

* e-mail: avkuzn@uniyar.ac.ru

** e-mail: mikheev@yars.free.net

*** e-mail: rda@uniyar.ac.ru

¹⁾In this article, we use a natural system of units where $\hbar = c = 1$ and the pseudo-Euclidean metric with a (+ – – –) signature.

Table 1. Constants K and Δ appearing in expression (1) according to various studies

		K	Δ
Choban, Ivanov	1969 [2]	$\frac{29}{1024\pi}$	—
Borisov <i>et al.</i>	1983 [3]	1	$-2 \ln 2 - \frac{389}{384} + \frac{9}{128} \frac{g_V^2 - g_A^2}{g_V^2 + g_A^2}$
Knizhnikov <i>et al.</i>	1984 [4]	$\frac{9}{16} \frac{E_\nu}{m_e}$	—
Borisov <i>et al.</i>	1993 [5]	$\frac{1}{2}$	$+\frac{5}{4}$
Kuznetsov, Mikheev	1997 [6]	1	$-\frac{29}{24}$
Borisov, Zamorin	1999 [8]	$\frac{1}{2}$	$-\frac{29}{24}$

The results that the authors of the studies quoted above obtained for the probability of the process $\nu \rightarrow \nu e^- e^+$ in a crossed field show significant distinctions. In their recent study, Borisov and Zamorin [8], who considered the massive-neutrino decay $\nu_i \rightarrow \nu_j e^- e^+$ ($m_i > m_j + 2m_e$) in an external field, also compared various formulas for the probability of the process and asserted that the results are consistent; however, we do not think so.

Let us explore this point in greater detail. In the limit $\chi \gg 1$, the probability of the process can be represented in the form

$$W(\nu \rightarrow \nu e^- e^+) \quad (1)$$

$$= KW_0 \chi^2 \left(\ln \chi - \frac{1}{2} \ln 3 - \gamma_E + \Delta \right),$$

where

$$W_0 = \frac{G_F^2 (g_V^2 + g_A^2) m_e^6}{27\pi^3 E_\nu}, \quad (2)$$

$\gamma_E = 0.577\dots$ is the Euler constant, and g_V and g_A are constants in the effective local Lagrangian for neutrino–electron interaction [see Eq. (3) below]. The constants K and Δ appearing in expression (1) were calculated by various authors (see table). By way of example, we indicate that the calculation in [2, 8] took into account electron–neutrino interaction only through a W boson. In order to compare formula (1) with the results obtained in those studies, it is necessary to set, in it, $g_V = g_A = 1$ for the calculations from [2] and $g_V = g_A = |U_{ei} U_{e3}|$ for the calculation from [8]. That the factor m_e/E_ν was lost in the formulas for the probability in [4] is a physical (rather than a numerical) error, since this violates the relativistic invariance of the quantity wE .

As has already been indicated, formula (1) for the probability describes a very particular case of $\ln \chi \gg 1$. In a number of physics problems, a situation can be realized, however, where the dynamical field parameter takes moderately large values, so that $\chi \gg 1$, but $\ln \chi \sim 1$. In this case, the crossed-field approximation is applicable, but the aforementioned condition $\ln \chi \gg 1$ is not satisfied, with the result that, in expression (1), it is necessary to take into account higher order terms in the expansion in inverse powers of the parameter χ . The formulas presented in the aforementioned studies for arbitrary values of χ involve cumbersome multidimensional integrals and are therefore inconvenient for an analysis.

Thus, the problem of calculating the probability of the production of a lepton (electron–positron or muon) pair by a neutrino in a crossed field at an arbitrary value of the parameter χ is of considerable importance. At the same time, an analysis of the production of $e^- e^+$ and $\mu^- \mu^+$ pairs by a neutrino would be, in a sense, incomplete without considering processes featuring the production of $e^- \mu^+$ and $e^+ \mu^-$ pairs via the standard μ -decay interaction, because the latter processes are less suppressed kinematically than the production of a $\mu^- \mu^+$ pair. Here, we present a rather simple expression that we found for the probability of the process $\nu_i \rightarrow \nu_j \bar{\ell}_n \ell_m^+$ and which is convenient for a numerical analysis.

We will consider the case of relatively low momentum transfers, $|q^2| \ll m_W^2$. The weak neutrino–lepton interaction can then be described in the local limit by the general effective Lagrangian

$$\mathcal{L} = \frac{G_F}{\sqrt{2}} [\bar{\ell}_n \gamma_\alpha (g_V + g_A \gamma_5) \ell_m] \quad (3)$$

$$\times [\bar{\nu}_j \gamma^\alpha (1 + \gamma_5) \nu_i],$$

where g_V and g_A are, respectively, the vector and the axial-vector electroweak coupling constants,

$$g_V = U_{in} U_{jm}^* - \frac{1}{2} \delta_{ij} \delta_{nm} (1 - 4 \sin^2 \theta_W),$$

$$g_A = U_{in} U_{jm}^* - \frac{1}{2} \delta_{ij} \delta_{nm}.$$

Here, the subscripts i and j label pure neutrino mass states, and U_{in} are elements of the neutrino mixing matrix in the lepton sector. As has already been indicated, the effects of mixing in the lepton sector are irrelevant to the process that we consider here in an external field. Since $U_{in} = \delta_{in}$ if mixing is disregarded, the expressions for the coupling constants in Lagrangian (3) can be represented in a convenient form for each specific process being considered. We quote these results immediately below:

In the case where both Z - and W -boson exchanges contribute,

$$\nu_e \rightarrow \nu_e e^- e^+, \quad \nu_\mu \rightarrow \nu_\mu \mu^- \mu^+, \quad (4)$$

$$g_V = 1/2 + 2 \sin^2 \theta_W, \quad g_A = 1/2.$$

For processes featuring only Z -boson exchanges,

$$\nu_\mu \rightarrow \nu_\mu e^- e^+, \quad \nu_e \rightarrow \nu_e \mu^- \mu^+, \quad (5)$$

$$g_V = -1/2 + 2 \sin^2 \theta_W, \quad g_A = -1/2.$$

For processes of inverse μ decay, which are mediated only by a W boson,

$$\nu_\mu \rightarrow \nu_\mu e^- e^+, \quad \nu_e \rightarrow \nu_e \mu^- \mu^+, \quad (6)$$

$$g_V = 1, \quad g_A = 1.$$

We have used a standard computational technique employing exact solutions to the Dirac equation for the electron and the muon in a crossed field [1]. Omitting the details of the calculations, we present the result for the probability of the process $\nu \rightarrow \nu \ell_1 \bar{\ell}_2$ in the form of a double integral involving the Airy function:

$$W(\nu \rightarrow \nu \ell_1 \bar{\ell}_2) \quad (7)$$

$$= \frac{G_F^2 (g_V^2 + g_A^2) m_1^3 m_2^3 \chi^2}{54 \pi^4 E_\nu} \int_{-1}^1 du \int_0^1 x dx z \Phi(z)$$

$$\times \left\{ \frac{3 + x^2}{(1 - u^2)(1 - x)} + \frac{3}{8} (1 - 3x) \right.$$

$$+ \frac{9(1 - \lambda^2)u}{16\lambda y} \left(1 + x + 2 \frac{1 - x}{x} \ln(1 - x) \right)$$

$$+ \frac{9(1 - \lambda^2)^2(1 - u^2)}{64\lambda^2 y^2} \left(1 + 4 \frac{1 - x}{x} \ln(1 - x) \right)$$

$$\left. + \frac{9(1 - \lambda)^2(5 + x)}{16\lambda y} + \frac{9}{4} \frac{g_A^2}{g_V^2 + g_A^2} \frac{5 + x}{y} \right\}$$

$$+ \frac{3}{4} \frac{g_V g_A}{g_V^2 + g_A^2} \frac{1 - \lambda^2}{\lambda y} \frac{3 - x^2}{1 - x} \Big\}.$$

For the process being considered, it is convenient to define the dynamical parameter χ as $\chi^2 = e^2 = (pFFp)/m_1^3 m_2^3$, where m_1 and m_2 are the charged-lepton masses. In addition, we have introduced the following notation in expression (7):

$$y = \frac{1 + \lambda^2}{2\lambda} + u \frac{1 - \lambda^2}{2\lambda},$$

$$z = y \left(\frac{4}{\chi(1 - u^2)(1 - x)} \right)^{2/3}, \quad \lambda = \frac{m_2}{m_1},$$

and $\Phi(z)$ is the Airy function defined as

$$\Phi(z) = \int_0^\infty dt \cos \left(zt + \frac{t^3}{3} \right).$$

It is interesting to analyze the properties of formula (7) with respect to the charge-conjugation operation, which, in the case being considered, consists in the substitutions $m_1 \leftrightarrow m_2$ ($\lambda \rightarrow 1/\lambda$) and $u \rightarrow -u$ (the variable u derives from integration with respect to the momenta of the lepton pair, and its sign is reversed upon the interchange of the leptons involved). It can easily be seen that, under this operation, all terms in (7) are invariant, with the exception of the last one, which involves the product $g_V g_A$ changing sign. Since this term is also P -odd, CP symmetry holds, as might have been expected.

Expression (7) for the probability can further be recast into a form that involves a one-dimensional integral and which is more convenient for a numerical analysis, but, in the general case of $m_1 \neq m_2$, the resulting formula is very cumbersome and is not presented here for this reason. At identical values of the lepton masses ($m_1 = m_2 = m_\ell$)—that is, for the processes in (4) and (5)—the probability can be represented in a comparatively simple form involving a one-dimensional integral. Specifically, we have

$$W(\nu \rightarrow \nu \ell^- \ell^+) \quad (8)$$

$$= \frac{G_F^2 (g_V^2 + g_A^2) m_\ell^6 \chi^2}{27 \pi^4 E_\nu} \int_0^1 u^2 du \tau \Phi(\tau)$$

$$\times \left\{ \frac{4}{1 - u^2} \left(2L(u) - \frac{29}{24} \right) - \frac{15}{2} L(u) - \frac{47}{48} \right.$$

$$+ \frac{1}{8} (1 + (1 - u^2)L(u)) \left(33 - \frac{47}{4} (1 - u^2) \right)$$

$$\left. + \frac{9}{16} \frac{g_A^2}{g_V^2 + g_A^2} \left[48L(u) + 2 - (1 + (1 - u^2)L(u)) \right] \right\}$$

$$\times (28 - 3(1 - u^2)) \Big] \Big\},$$

where $\chi^2 = e^2(pFFp)/m_\ell^6$,

$$\tau = \left(\frac{4}{\chi(1-u^2)} \right)^{2/3}, \quad L(u) = \frac{1}{2u} \ln \frac{1+u}{1-u}.$$

In the case of $\chi \ll 1$, it immediately follows from formula (8) that the expression for the probability can be represented in the form

$$W(\chi \ll 1) = \frac{3\sqrt{6}G_F^2 m_\ell^6}{(16\pi)^3 E_\nu} \quad (9)$$

$$\times (3g_V^2 + 13g_A^2)\chi^4 \exp\left(-\frac{8}{3\chi}\right),$$

which involves the well-known exponential suppression and which is consistent with the corresponding expression from [5].

In the case of $\chi \gg 1$, expression (8) straightforwardly leads to formula (1), where $K = 1$ and $\Delta = -29/24$, in agreement with the result presented in [6].

From formula (7), one can also derive an approximate formula for the probability of the process $\nu \rightarrow \nu \ell_1 \bar{\ell}_2$ for $m_1 \neq m_2$. The result is

$$W(\chi \gg 1) = \frac{G_F^2 (g_V^2 + g_A^2) m_1^3 m_2^3 \chi^2}{27\pi^3 E_\nu} \quad (10)$$

$$\times \left\{ \ln \chi - \frac{1}{2} \ln 3 - \gamma_E - \frac{29}{24} + \frac{3}{2} \frac{g_V g_A}{g_V^2 + g_A^2} \ln \frac{m_1}{m_2} \right\}.$$

An attempt at refining formula (1) and at finding, from expression (8), the next term of the expansion in inverse powers of the parameter χ revealed [9] that, in the region of moderately large values of χ , the correction term of order $\chi^{-2/3}$ tends to impair the description of the behavior of the probability. An analysis shows that this term ($\sim \chi^{-2/3}$) has the meaning of a correction proper only for $\chi \gtrsim 10^5$. From the figures presented in [9], it can also be seen that, at any value of χ , the probability computed by the exact formula (8) is greater than the approximate value

given by (1) [by way of example, we indicate that, at $\chi = 20$, it is greater by a factor of about 1.5—at smaller values of χ , the approximate formula (1) is inapplicable].

Thus, we see that, at moderately large values of the parameter χ , it is reasonable to employ our exact formula (8) in performing a detailed analysis of the probability of lepton-pair production by a neutrino in an external electromagnetic field.

ACKNOWLEDGMENTS

We are grateful to A.V. Borisov for an enlightening discussion that stimulated us to perform this investigation.

This work was supported in part by the Ministry of the Russian Federation for Higher Education (project no. E00-11.0-5) and by the Russian Foundation for Basic Research (project no. 01-02-17334).

REFERENCES

1. V. I. Ritus, *Tr. Fiz. Inst. Akad. Nauk SSSR* **111**, 5 (1979); A. I. Nikishov, *Tr. Fiz. Inst. Akad. Nauk SSSR* **111**, 152 (1979).
2. É. A. Choban and A. N. Ivanov, *Zh. Éksp. Teor. Fiz.* **56**, 194 (1969) [*Sov. Phys. JETP* **29**, 109 (1969)].
3. A. V. Borisov, V. Ch. Zhukovskii, and B. A. Lysov, *Izv. Vyssh. Uchebn. Zaved., Fiz.*, No. 8, 30 (1983).
4. M. Yu. Knizhnikov and A. V. Tatarintsev, *Vestn. Mosk. Univ., Ser. 3: Fiz., Astron.* **25** (3), 26 (1984).
5. A. V. Borisov, A. I. Ternov, and V. Ch. Zhukovsky, *Phys. Lett. B* **318**, 489 (1993).
6. A. V. Kuznetsov and N. V. Mikheev, *Phys. Lett. B* **394**, 123 (1997); A. V. Kuznetsov and N. V. Mikheev, *Yad. Fiz.* **60**, 2038 (1997) [*Phys. At. Nucl.* **60**, 1865 (1997)].
7. V. V. Skobelev, *Zh. Éksp. Teor. Fiz.* **108**, 3 (1995) [*JETP* **81**, 1 (1995)].
8. A. V. Borisov and N. B. Zamorin, *Yad. Fiz.* **62**, 1647 (1999) [*Phys. At. Nucl.* **62**, 1543 (1999)].
9. A. V. Kuznetsov, N. V. Mikheev, and D. A. Rummyantsev, *Mod. Phys. Lett. A* **15**, 573 (2000).

Translated by A. Isaakyan

Conference on Physics of Fundamental Interactions Theory

Z' -Boson Decays as a Test of the Four-Color Symmetry of Quarks and Leptons

A. V. Povarov* and **A. D. Smirnov****

Yaroslavl State University, ul. Sovetskaya 14, Yaroslavl, 150000 Russia

Received March 7, 2001

Abstract—The quark and leptonic widths of the Z' boson that arises from four-color quark–lepton symmetry are calculated and compared with the predictions of the E_6 and the left–right (LR) model. It is shown that this four-color symmetry leads to a specific relation of the type $(v'_q + a'_q)/(v'_l + a'_l) = (t_{15})_q/(t_{15})_l = -1/3$ between the vector and axial coupling constants for Z' -boson interaction with quarks and leptons. Calculations with allowance for the four-color symmetry in question yield leptonic widths of the Z' boson that are considerably greater than those predicted within the E_6 and the LR model and result in a relatively small hadronic-to-leptonic width ratio. Since these features are associated with the four-color symmetry, their observation would suggest its manifestation in Z' -boson decays.
© 2002 MAIK “Nauka/Interperiodica”.

Searches for and analysis of possible symmetries higher than that of the Standard Model—such as supersymmetries and left–right (LR) symmetry—represent one of the lines of investigations in elementary-particle physics. As an example of such symmetries, we consider here a four-color symmetry of quarks and leptons that belongs to the Pati–Salam type [1] and which can indeed exist in nature. Minimally combined with the Standard Model on the basis of the $SU_V(4) \times SU_L(2) \times U_R(1)$ group, the four-color symmetry in question {the resulting model is referred to as that of minimal quark–lepton symmetry (MQLS) or the MQLS model [2, 3]} leads to the prediction of two vector leptoquarks V^\pm of charge $\pm 2/3$ and an additional neutral Z' boson. Controlling the interactions of these new particles with quarks and leptons, the four-color symmetry can manifest itself via some features of processes involving quarks and leptons. A theoretical analysis of such features is of interest for revealing the possible experimental signals from four-color symmetry.

On the basis of the MQLS model, we analyze here the fermionic decays of the Z' boson induced by the four-color symmetry in order to reveal possible manifestations of four-color quark–lepton symmetry in these decays. We compare our results with those produced by other models also predicting an extra Z' boson like the E_6 and the LR model (for an overview, see [4]).

The interaction of Z and Z' bosons with the corresponding neutral currents can be represented in the form

$$\begin{aligned} \mathcal{L}_{\text{NC}}^{\text{gauge}} &= -eZ_\mu J_\mu^Z - \frac{e}{c_W} Z'_\mu J_\mu^{Z'} \\ &= -eZ_{1\mu} J_\mu^{Z_1} - \frac{e}{c_W} Z_{2\mu} J_\mu^{Z_2}, \end{aligned} \quad (1)$$

where $c_W = \cos \theta_W$, θ_W being the Weinberg angle; Z_μ and Z'_μ are mass eigenstates that are superpositions of the standard field $Z_{1\mu}$ and the extra field $Z_{2\mu}$; and the currents

$$\begin{aligned} J_\mu^{Z_1} &= \bar{f} \gamma_\mu (v_f^{Z_1} + a_f^{Z_1} \gamma_5) f, \\ J_\mu^{Z_2} &= \bar{f} \gamma_\mu (v_f^{Z_2} + a_f^{Z_2} \gamma_5) f \end{aligned} \quad (2)$$

are, respectively, the usual neutral current of the Standard Model (here, $v_f^{Z_1}$ and $a_f^{Z_1}$ are the vector and axial Z -boson coupling constants within the Standard Model) and the extra neutral current specified by the model being considered.

Within the MQLS model, the coupling constants for Z' -boson interaction with up ($a = 1$) and down ($a = 2$) fermions f_a take the form (hereafter, we neglect the small Z – Z' mixing that is present within the model)

$$v'_{f_a} \approx v_{f_a}^{Z_2} = \frac{1}{s_S \sqrt{1 - s_W^2 - s_S^2}} \quad (3)$$

$$\times \left[c_W^2 \sqrt{\frac{2}{3}} (t_{15})_f - \left(Q_{f_a} - \frac{(\tau_3)_{aa}}{4} \right) s_S^2 \right],$$

* e-mail: povarov@univ.uniyar.ac.ru

** e-mail: asmirnov@univ.uniyar.ac.ru

Table 1. Vector and axial fermionic coupling constants of the Z' boson within the MQLS model

f	a'_f	v'_f
ν	$\frac{s_S}{4\sqrt{1-s_W^2-s_S^2}}$	$\frac{-2c_W^2+s_S^2}{4s_S\sqrt{1-s_W^2-s_S^2}}$
e	$-\frac{s_S}{4\sqrt{1-s_W^2-s_S^2}}$	$\frac{-2c_W^2+3s_S^2}{4s_S\sqrt{1-s_W^2-s_S^2}}$
u	$\frac{s_S}{4\sqrt{1-s_W^2-s_S^2}}$	$\frac{2c_W^2-5s_S^2}{12s_S\sqrt{1-s_W^2-s_S^2}}$
d	$-\frac{s_S}{4\sqrt{1-s_W^2-s_S^2}}$	$\frac{2c_W^2+s_S^2}{12s_S\sqrt{1-s_W^2-s_S^2}}$

$$a'_{f_a} \approx a_{f_a}^{Z_2} = \frac{s_S}{\sqrt{1-s_W^2-s_S^2}} \frac{(\tau_3)_{aa}}{4}, \quad (4)$$

where $s_S = \sin \theta_S$, θ_S being the strong-mixing angle introduced in the model; t_{15} is the 15th generator of the $SU_V(4)$ group; τ_3 is the third Pauli matrix; and Q_{f_a} is the electric charge of the fermion in units of the proton charge. The parameter s_S^2 is controlled by the ratio of the coupling constants for electromagnetic and strong interaction and is associated with the scale M_C of the breakdown of $SU(4)$ symmetry. Provided that the four-color symmetry is a primary symmetry, a lower limit on M_C is determined by experimental data and can be $M_C \sim 10-10^3$ TeV [5–9], in which case, $s_S^2 \sim 0.08-0.14$. At $M_C \sim 10^9$ TeV, which corresponds to the scale of M_C within the Grand Unified theories, $s_S^2 \sim 0.25$.

An extra Z' boson also arises in other models involving an additional $U(1)'$ factor at the scale of the Standard Model, with the interaction of the Z'

boson with fermions carrying an imprint of the primary symmetry of the model. The fermionic coupling constants of the Z' boson within the MQLS model are presented in Table 1 versus the parameter s_S^2 . For the sake of comparison, the analogous constants predicted by the E_6 and the LR model [4, 10–12] are quoted in Table 2 versus β and α_{LR} , respectively. In the E_6 model, the angle β determines the orientation of the $U(1)'$ generator in the E_6 group space and satisfies the condition $0 \leq \beta \leq \pi$. Within the LR model, $\alpha_{LR} = \sqrt{k^2 c_W^2 / s_W^2 - 1}$, where $k = g_R / g_L$ is the ratio of the gauge coupling constants for the $SU_L(2)$ and $SU_R(2)$ groups, which usually varies in the range $1/\sqrt{2} < \alpha_{LR} < 3$.

In order to compare the coupling constants, we introduce the ratio

$$P_L^{ql} \equiv P_L^q / P_L^l = \frac{v'_q + a'_q}{v'_l + a'_l},$$

where $P_L^f = (v'_f + a'_f) / (2a'_e)$ is a generalization of the parameter P_L^q from [10]. Within the MQLS model, this ratio is equal to the ratio of the eigenvalues of the 15th generator of the $SU_V(4)$ color group for quarks and leptons:

$$P_L^{ql} \equiv \frac{v'_q + a'_q}{v'_l + a'_l} = \frac{(t_{15})_q}{(t_{15})_l} = -\frac{1}{3}. \quad (5)$$

This result is a direct consequence of four-color symmetry. Within the E_6 model, this ratio can take any value, depending on $\cos \beta$. Within the LR model, it is also equal to $-1/3$, but this is not, strictly speaking, a model prediction but a result of the use of the actual quark and lepton charges.

A comparison of the absolute values of the fermionic coupling constants of the Z' boson reveals that the predictions of the MQLS model for them differ from those of the E_6 and the LR model. The largest distinctions are observed for the vector leptonic constant. In Fig. 1, the vector leptonic coupling constant v'_e within the MQLS model is displayed as a function of s_S^2 . It can easily be seen that, at $M_C \sim 10-10^3$ TeV (that is, at $s_S^2 \sim 0.08-0.14$), the MQLS model predicts relatively large absolute values of the vector leptonic coupling constant (from -1.6 to -1.0); at the same time, the analogous results within the E_6 and the LR model are predicted to fall between -0.5 and 0.5 , the specific value being dependent on the model parameters. Thus, the absolute value of the vector leptonic coupling constant v'_e is 2 to 3 times greater in the MQLS model than in the E_6 and the LR model.

This leads to the corresponding distinctions between the leptonic widths. At $m_f^2 / m_{Z'}^2 \ll 1$, the

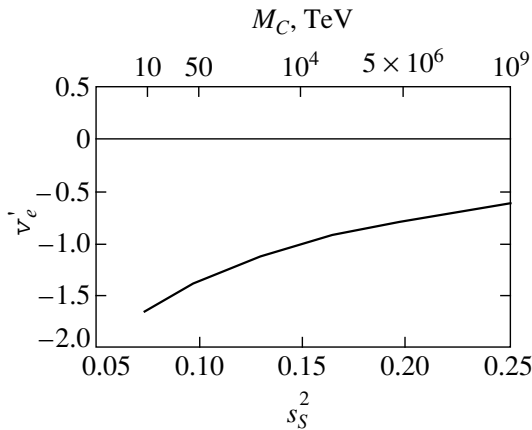


Fig. 1. Vector leptonic coupling constant v'_e of the Z' boson within the MQLS model as a function of s_S^2 and of the scale M_C of the breakdown of four-color symmetry.

Table 2. Vector and axial fermionic coupling constants of the Z' boson within the E_6 and the LR model

f	a'_f	v'_f	a'_f	v'_f
ν	$\frac{3 \cos \beta}{4\sqrt{6}} + \frac{\sqrt{10} \sin \beta}{24}$	$\frac{3 \cos \beta}{4\sqrt{6}} + \frac{\sqrt{10} \sin \beta}{24}$	$\frac{1}{4\alpha_{LR}}$	$\frac{1}{4\alpha_{LR}}$
e	$\frac{\cos \beta}{2\sqrt{6}} + \frac{\sqrt{10} \sin \beta}{12}$	$\frac{\cos \beta}{\sqrt{6}}$	$\frac{\alpha_{LR}}{4}$	$\frac{1}{2\alpha_{LR}} - \frac{\alpha_{LR}}{4}$
u	$-\frac{\cos \beta}{2\sqrt{6}} + \frac{\sqrt{10} \sin \beta}{12}$	0	$-\frac{\alpha_{LR}}{4}$	$-\frac{1}{6\alpha_{LR}} + \frac{\alpha_{LR}}{4}$
d	$\frac{\cos \beta}{2\sqrt{6}} + \frac{\sqrt{10} \sin \beta}{12}$	$-\frac{\cos \beta}{\sqrt{6}}$	$\frac{\alpha_{LR}}{4}$	$-\frac{1}{6\alpha_{LR}} - \frac{\alpha_{LR}}{4}$

width of the Z' boson with respect to decay into a fermion pair has the form

$$\Gamma(Z' \rightarrow f\bar{f}) = \Gamma_{f\bar{f}} = N_f M_{Z'} \frac{\alpha}{3c_W^2} (v_f'^2 + a_f'^2),$$

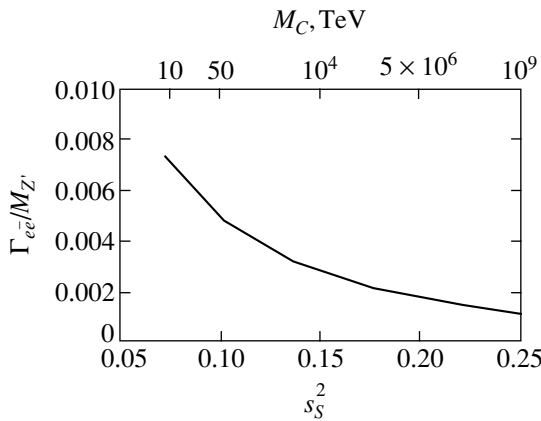


Fig. 2. Leptonic width of the Z' boson, $\Gamma_{e\bar{e}}/M_{Z'}$, within the MQLS model as a function of s_S^2 and of the scale M_C of the breakdown of four-color symmetry.

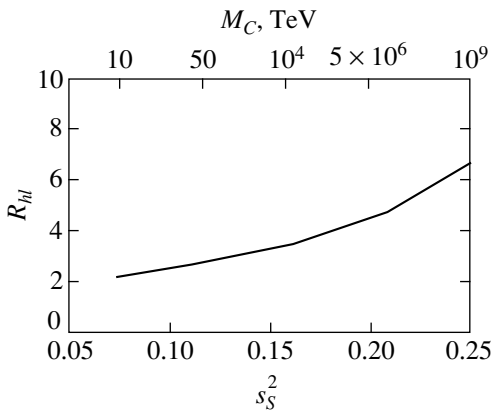


Fig. 3. Hadronic-to-leptonic width ratio R_{hl} for the Z' -boson as a function of s_S^2 and of the scale M_C of the breakdown of four-color symmetry.

where N_f is the color index [$N_f = 1$ (3) for $f = l$ (q)].

In Fig. 2, the leptonic-decay width $\Gamma_{e\bar{e}}$ of the Z' boson within the MQLS model is displayed (in units of the Z' -boson mass $M_{Z'}$) as a function of s_S^2 . For $s_S^2 = 0.08-0.14$, it amounts to $0.007-0.003$ of $M_{Z'}$, while, in the E_6 and the LR model, we have $\Gamma_{e\bar{e}}/M_{Z'} < 0.001$ and $\Gamma_{e\bar{e}}/M_{Z'} < 0.003$, respectively.

Finally, a considerable distinction is predicted for the hadronic-to-leptonic width ratio $R_{hl} = \sum_q \Gamma_{q\bar{q}}/\Gamma_{l\bar{l}}$ as well. The s_S^2 dependence of R_{hl} within the MQLS model is shown in Fig. 3, where one can see that, for $s_S^2 \sim 0.08-0.14$, this ratio is about 2 to 3; at the same time, $R_{hl} > 9$ in the E_6 model and $R_{hl} > 7$ in the LR model.

Thus, we can see that, in the case where the mass scale at which four-color symmetry is broken is modest ($M_C \sim 10-10^3$ TeV), the predictions of the MQLS model for Z' -boson decays differ considerably from the corresponding predictions of the E_6 and the LR model. In particular, the four-color symmetry leads to the specific ratio (5) for the fermionic coupling constants; it predicts a two- to threefold increase in the vector leptonic constant with respect to the E_6 and the LR model, relatively large leptonic widths, and a small hadronic-to-leptonic width ratio. These features are caused by the Z' -boson interaction (1)–(4) with fermions, which is induced by the four-color symmetry of quarks and leptons. An experimental observation of these features could be treated as a manifestation of this particular symmetry in Z' -boson decays.

ACKNOWLEDGMENTS

This work was supported in part by the Program Universities of Russia—Fundamental Research (project no. 02.01.25) and by the Russian Foundation for Basic Research (project no. 00-02-17883).

REFERENCES

1. J. C. Pati and A. Salam, Phys. Rev. D **10**, 275 (1974).
2. A. D. Smirnov, Phys. Lett. B **346**, 297 (1995).
3. A. D. Smirnov, Yad. Fiz. **58**, 2252 (1995) [Phys. At. Nucl. **58**, 2137 (1995)].
4. A. Leike, Phys. Rep. **317**, 143 (1999).
5. A. Blumhofer and B. Lampe, Eur. Phys. J. C **7**, 141 (1999).
6. G. Valencia and S. Willenbrock, Phys. Rev. D **50**, 6843 (1994).
7. R. R. Volkas, Phys. Rev. D **53**, 2681 (1996).
8. A. V. Kuznetsov and N. V. Mikheev, Phys. Lett. B **329**, 295 (1994).
9. A. V. Kuznetsov and N. V. Mikheev, Yad. Fiz. **58**, 2228 (1995) [Phys. At. Nucl. **58**, 2113 (1995)].
10. F. del Aguila and M. Cvetič, Phys. Rev. D **50**, 3158 (1994).
11. F. del Aguila, M. Cvetič, and P. Langacker, Phys. Rev. D **52**, 37 (1995).
12. A. A. Pankov, Yad. Fiz. **57**, 472 (1994) [Phys. At. Nucl. **57**, 444 (1994)].

Translated by O. Chernavskaya

**Conference on Physics of Fundamental Interactions
Theory**

Higgs Bosons in the Simplest SUSY Models*

R. B. Nevzorov, K. A. Ter-Martirosyan, and M. A. Trusov

*Institute of Theoretical and Experimental Physics, Bol'shaya
Cheremushkinskaya ul. 25, Moscow, 117218 Russia*

Received May 15, 2001; in final form, September 13, 2001

Abstract—Nowadays, in the MSSM, the moderate values of $\tan\beta$ are almost excluded by the LEP II lower bound on the mass of the lightest Higgs boson. In the next-to-minimal supersymmetric standard model (NMSSM), the theoretical upper bound on it increases and reaches a maximal value in the limit of strong Yukawa coupling, where all solutions to renormalization-group equations are concentrated near the quasifixed point. For a calculation of the Higgs boson spectrum, the perturbation-theory method can be applied. We investigate the particle spectrum within the modified NMSSM, which leads to the self-consistent solution in the limit of strong Yukawa coupling. This model allows one to get $m_h \sim 125$ GeV at $\tan\beta \geq 1.9$. In the model under investigation, the mass of the lightest Higgs boson does not exceed 130.5 ± 3.5 GeV. The upper bound on the mass of the lightest CP -even Higgs boson in more complicated supersymmetric models is also discussed. © 2002 MAIK “Nauka/Interperiodica”.

1. INTRODUCTION

Last year, there was great progress in Higgs boson searches. The experimental lower bound on the Higgs boson mass in the Standard Model (SM) increased from 95.2 [1] to 113.3 GeV [2]. At the same time, the upper bound that comes from an analysis of radiative corrections to the electroweak observables decreased to 210 GeV [2]. Thus, the allowed region of the Higgs boson mass in the SM has shrunk drastically. Moreover, a few additional $b\bar{b}$ events were observed at LEP II [3]. They can be interpreted as a signal of the production of a Higgs boson with mass 115 GeV in e^+e^- annihilation. This Higgs boson mass does not agree with the theoretical lower bound in the SM following from the stability of the physical vacuum up to the Planck scale of $M_{\text{Pl}} \approx 2.4 \times 10^{18}$ GeV [4–7].

The simplest supersymmetric (SUSY) extension of the SM is the minimal supersymmetric standard model (MSSM). Its Higgs sector includes two doublets H_1 and H_2 . Each of them, after spontaneous symmetry breaking, acquires a nonzero vacuum expectation value, v_1 and v_2 , respectively. Instead of them, the sum of their squares $v^2 = v_1^2 + v_2^2$ and the value of $\tan\beta = v_2/v_1$ are usually used.

An important feature of SUSY models is the existence of a light Higgs boson in the CP -even Higgs sector. The upper bound on its mass strongly depends on the value of $\tan\beta$. At the tree level, the mass of the lightest Higgs boson does not exceed [8] the Z -boson mass: $m_h \leq M_Z |\cos 2\beta|$. Loop corrections from the t

quark and its superpartners significantly increase the upper bound on m_h :

$$m_h \leq \sqrt{M_Z^2 \cos^2 2\beta + \Delta}, \quad (1)$$

where, in the one-loop approximation, Δ is given by

$$\Delta \approx \frac{3}{2\pi^2} \frac{m_t^4}{v^2} \left[\ln \frac{M_S^2}{m_t^2} + \frac{X_t^2}{M_S^2} \left(1 - \frac{X_t^2}{12M_S^2} \right) \right]. \quad (2)$$

Here, m_t is the running t -quark mass at the electroweak scale (at $q = M_t^{\text{pole}} = 174$ GeV, M_t^{pole} is the t -quark pole mass); X_t is the stop mixing parameter; and M_S is the SUSY breaking scale, which is expressed in terms of the stop masses $m_{\tilde{t}_1}$ and $m_{\tilde{t}_2}$: $M_S = \sqrt{m_{\tilde{t}_1} m_{\tilde{t}_2}}$. The one-loop corrections (2) attain a maximum value at $X_t = \pm\sqrt{6}M_S$. These corrections are proportional to m_t^4 and depend logarithmically on the SUSY breaking scale M_S . They are almost insensitive to the choice of $\tan\beta$. The absolute value of Δ is of order M_Z^2 . The one-loop and two-loop corrections to the mass of the lightest Higgs boson were calculated and analyzed in [9] and [10], respectively. The upper bound on the mass of the lightest Higgs boson grows with increasing $\tan\beta$ and $\ln(M_S^2/m_t^2)$ and, for large $\tan\beta$ ($\tan\beta \gg 1$), reaches 125–128 GeV. In [6], the bounds on the mass of the Higgs boson in the SM and the MSSM were compared.

However, large values of $\tan\beta$ are undesirable for two reasons. The first of these is proton decay. If one assumes that electroweak and strong interactions are embedded in SUSY Grand Unified Theory (GUT)

*This article was submitted by the authors in English.

at high energies, then an overly fast proton decay is induced owing to $d = 5$ operators. The major decay mode is $p \rightarrow \bar{\nu}K^+$. In this case, the proton lifetime τ_p is inversely proportional to $\tan^2 \beta$. When $\tan \beta$ is large enough, the proton lifetime calculated within SUSY GUT models contradicts an experimental constraint on it. Another problem of the large- $\tan \beta$ scenario concerns flavor-changing neutral currents. The $b \rightarrow s\gamma$ branching ratio increases with $\tan \beta$ as $\text{Br}(b \rightarrow s\gamma) \sim \tan^2 \beta$. Thus, values of $\tan \beta$ much greater than unity ($\tan \beta \gtrsim 40$) lead to unacceptable large flavor-changing transitions.

In the case of moderate values of $\tan \beta$ ($\tan \beta \lesssim 5$), the b -quark and τ -lepton Yukawa coupling constants are small and one can get an analytic solution to one-loop renormalization-group equations [11]. For the t -quark Yukawa coupling constant $h_t(t)$ and the gauge coupling constants $g_i(t)$, the analytic solution has the form

$$Y_t(t) = \frac{E(t)/(6F(t))}{(1 + 1/[6Y_t(0)F(t)])}, \quad (3)$$

$$\tilde{\alpha}_i(t) = \frac{\tilde{\alpha}_i(0)}{1 + b_i \tilde{\alpha}_i(0)t},$$

$$E(t) = \left[\frac{\tilde{\alpha}_3(t)}{\tilde{\alpha}_3(0)} \right]^{16/9} \left[\frac{\tilde{\alpha}_2(t)}{\tilde{\alpha}_2(0)} \right]^{-3} \left[\frac{\tilde{\alpha}_1(t)}{\tilde{\alpha}_1(0)} \right]^{-13/99},$$

$$F(t) = \int_0^t E(\tau) d\tau,$$

where $Y_t(t) = (h_t(t)/(4\pi))^2$ and $\tilde{\alpha}_i(t) = (g_i(t)/(4\pi))^2$. The index i varies from 1 to 3, which corresponds to $U(1)$, $SU(2)$, and $SU(3)$ gauge couplings. The coefficients b_i of the one-loop beta functions of $\tilde{\alpha}_i(t)$ are $b_1 = 33/5$, $b_2 = 1$, and $b_3 = -3$. The initial conditions $Y_t(0)$ and $\tilde{\alpha}_i(0)$ for the MSSM renormalization-group equations are usually set at the Grand Unification scale $M_X \approx 3 \times 10^{16}$ GeV, where all gauge coupling constants coincide. The variable t is defined in a conventional way; that is, $t = \ln(M_X^2/q^2)$.

Substituting the numerical values of the gauge coupling constants, one finds that, at the electroweak scale, the second term in the denominator of the expression describing the evolution of $Y_t(t)$ is approximately equal to $[10h_t^2(0)]^{-1}$. If $h_t^2(0) \geq 1$, the dependence of the t -quark Yukawa coupling constant on its initial value $Y_t(0)$ disappears and all solutions are concentrated near the quasifixed point [12]:

$$Y_{\text{QFP}}(t_0) = \frac{E(t_0)}{6F(t_0)}, \quad (4)$$

where $t_0 = 2 \ln(M_X/M_t^{\text{pole}}) \approx 65$. Together with $Y_t(t)$, the trilinear scalar coupling of the Higgs boson

doublet H_2 to stops, $A_t(t)$, and some combination of their masses, $\mathfrak{M}_t^2(t) = m_Q^2 + m_U^2 + m_2^2$, are also driven to the infrared quasifixed points. In the vicinity of these points, $A_t(t)$ is proportional to the universal gaugino mass $M_{1/2}$ at the scale M_X and $\mathfrak{M}_t^2(t) \sim M_{1/2}^2$. Although the solutions to the MSSM renormalization-group equations achieve quasifixed points only for infinite values of $Y_t(0)$, the deviations from them at the electroweak scale are determined by the ratio $1/[6F(t_0)Y_t(0)]$, which is quite small if $h_t^2(0) \geq 1$.

The behavior of solutions to the MSSM renormalization-group equations near the quasifixed point at $\tan \beta \sim 1$ and the particle spectrum were studied by many authors [13–15]. It was shown that, in the vicinity of this point, the b - τ Yukawa coupling unification is realized [13]. The value of $\tan \beta$ that corresponds to the quasifixed-point regime was calculated in some recent publications (see [15–17]). It was restricted to be between 1.3 and 1.8. Such comparatively low values of $\tan \beta$ yield a more stringent bound on the mass of the lightest Higgs boson in the MSSM. Thus, it does not exceed 94 ± 5 GeV [15, 16]. The resulting theoretical bound on m_h has to be compared with the lower experimental one in the SM since it was computed for the SUSY breaking scale M_S on the order of 1 TeV, where all other Higgs bosons and superparticles are rather heavy. A straightforward comparison shows that the quasifixed-point scenario and a considerable part of the MSSM parameter space are almost excluded by LEP II data, which stimulates a theoretical analysis of the Higgs sector in nonminimal SUSY models.

In this article, the spectrum of Higgs bosons in the next-to-minimal supersymmetric standard model (NMSSM) is reviewed. The mass of the lightest Higgs boson in the NMSSM attains a maximum value in the limit of strong Yukawa coupling, where the Yukawa coupling constants are much larger than the gauge ones. All SUSY models contain a large number of free parameters, which is the main obstacle in the way of their investigations. For example, each SUSY model includes three or four independent SUSY breaking constants, which determine the SUSY particle spectrum. Nevertheless, in the limit of strong Yukawa coupling, solutions to the renormalization-group equations are focused near the quasifixed point, which simplifies the analysis. We propose a modification of the NMSSM that allows one to get $m_h \sim 125$ GeV for moderate values of $\tan \beta$ and to study the Higgs boson spectrum of the model. In the last part, the mass of the lightest Higgs boson in more complicated SUSY models is considered.

2. HIGGS SECTOR OF THE NMSSM

2.1. μ Problem and Parameters of the NMSSM

The simplest extension of the MSSM is the NMSSM. Historically, the NMSSM was suggested as a solution to the μ problem in the supergravity (SUGRA) models [18]. In addition to observable superfields, these models contain a “hidden” sector where local supersymmetry is broken. In the superstring-inspired SUGRA models, the “hidden” sector always includes the singlet dilaton S and moduli T_m superfields. They appear in the four-dimensional theory as a result of compactification of extra dimensions. The full superpotential of SUGRA models can be represented as an expansion in powers of observable superfields,

$$W = \hat{W}_0(S, T_m) + \mu(S, T_m)(\hat{H}_1 \hat{H}_2) + h_t(S, T_i)(\hat{Q} \hat{H}_2) \hat{U}_R^c + \dots, \quad (5)$$

where $\hat{W}_0(S, T_m)$ is the superpotential of the hidden sector. From the expansion in (5), it is obvious that the parameter μ should be on the order of the Planck scale because that is the only scale characterizing the hidden (gravity) sector of the theory. On the other hand, if $\mu \sim M_{\text{Pl}}$, then the Higgs doublets get huge positive masses $m_{H_1, H_2}^2 \simeq \mu^2 \simeq M_{\text{Pl}}^2$ and electroweak-symmetry breaking does not occur at all.

In the NMSSM, a new singlet superfield Y is introduced. By definition, the superpotential of this model is invariant with respect to the Z_3 discrete transformations [19]. The Z_3 symmetry usually arises in the superstring-inspired models in which all observable superfields are massless in the exact supersymmetry limit. The term $\mu(\hat{H}_1 \hat{H}_2)$ does not satisfy the last requirement. Therefore, it must be eliminated from the NMSSM superpotential. Instead of it, there arises the sum of two terms [18–20],

$$W_h = \lambda \hat{Y}(\hat{H}_1 \hat{H}_2) + \frac{\varkappa}{3} \hat{Y}^3. \quad (6)$$

After electroweak-symmetry breaking, the singlet field Y acquires a nonzero vacuum expectation value ($\langle Y \rangle = y/\sqrt{2}$) and the effective μ term ($\mu = \lambda y/\sqrt{2}$) is generated.

The NMSSM superpotential contains a lot of Yukawa couplings. But at the moderate values of $\tan \beta$, all of them are small and can be neglected, with the exception of h_t , λ , and \varkappa . In addition to the Yukawa couplings, the Lagrangian of the NMSSM contains a large number of soft SUSY breaking parameters. Each of the scalar and gaugino fields has a soft mass (m_i and M_i , respectively). Each of the Yukawa couplings corresponds to the trilinear scalar coupling A_i in the full Lagrangian. The number of these unknown parameters can be considerably

reduced if one assumes the universality of the soft SUSY breaking terms at the scale M_X . Thus, only three independent dimensional parameters are left: the universal gaugino mass $M_{1/2}$, the universal scalar mass m_0 , and the universal trilinear coupling of scalar fields A . Naturally, universal soft SUSY breaking terms appear in the minimal supergravity model [21] and in the simplest models deduced from the superstring theories [22]. The universal parameters of soft supersymmetry breaking determined at the Grand Unification scale have to be considered as boundary conditions for the renormalization-group equations that describe the evolution of all fundamental couplings up to electroweak scale or SUSY breaking scale. A complete set of the NMSSM renormalization-group equations can be found in [23, 24].

2.2. CP-Even Higgs Boson Spectrum

The Higgs sector of the NMSSM includes six massive states. Three of them are CP -even fields, two are CP -odd fields, and one is a charged field. The determinants of the mass matrices of the CP -odd and charged Higgs bosons are equal to zero. This corresponds to the appearance of two Goldstone bosons,

$$\eta^0 = \sqrt{2} \sin \beta \operatorname{Im} H_2^0 + \sqrt{2} \cos \beta \operatorname{Im} H_1^0, \quad (7)$$

$$\eta^+ = \sin \beta H_2^+ + \cos \beta (H_1^-)^*,$$

which are swallowed up by the massive vector W^\pm and Z bosons during the spontaneous breaking of $SU(2) \otimes U(1)$ symmetry. For this reason, the masses of neutral CP -odd bosons and charged boson are easily calculated.

In the CP -even Higgs sector, the situation is more complicated. The CP -even states arise as the result of mixing of the real parts of the neutral components of two Higgs doublets with the real part of the field Y . The determinant of their mass matrix does not vanish, and one has to diagonalize the 3×3 mass matrix in order to calculate its eigenvalues. Instead of $\operatorname{Re} H_1^0$, $\operatorname{Re} H_2^0$, and $\operatorname{Re} Y$, it is much more convenient to consider their linear combinations

$$\chi_1 = \sqrt{2} \cos \beta \operatorname{Re} H_1^0 + \sqrt{2} \sin \beta \operatorname{Re} H_2^0, \quad (8)$$

$$\chi_2 = -\sqrt{2} \sin \beta \operatorname{Re} H_1^0 + \sqrt{2} \cos \beta \operatorname{Re} H_2^0,$$

$$\chi_3 = \sqrt{2} \operatorname{Re} Y.$$

In basis (8), the mass matrix of CP -even Higgs fields can be simply written in the symmetric form (see [25])

$$M_{ij}^2 = \begin{pmatrix} \frac{\partial^2 V}{\partial v^2} & \frac{1}{v} \frac{\partial^2 V}{\partial v \partial \beta} & \frac{\partial^2 V}{\partial v \partial y} \\ \frac{1}{v} \frac{\partial^2 V}{\partial v \partial \beta} & \frac{1}{v^2} \frac{\partial^2 V}{\partial \beta^2} & \frac{1}{v} \frac{\partial^2 V}{\partial y \partial \beta} \\ \frac{\partial^2 V}{\partial v \partial y} & \frac{1}{v} \frac{\partial^2 V}{\partial y \partial \beta} & \frac{\partial^2 V}{\partial y^2} \end{pmatrix}, \quad (9)$$

where $V(v_1, v_2, y)$ is the effective potential of the NMSSM Higgs sector,

$$\begin{aligned} V(H_1, H_2, Y) = & m_1^2 |H_1|^2 + m_2^2 |H_2|^2 + m_y^2 |Y|^2 \\ & + \left(\lambda A_\lambda (H_1 H_2) Y + \frac{\kappa}{3} A_\kappa Y^3 \right. \\ & \left. + \lambda \kappa (H_1 H_2) (Y^*)^2 + \text{h.c.} \right) \\ & + \lambda^2 |h_1 H_2|^2 + \lambda^2 |H_2|^2 |Y|^2 \\ & + \lambda^2 |H_1|^2 |Y|^2 + \kappa^2 |Y|^4 + \frac{g'^2}{8} (|H_1|^2 - |H_2|^2)^2 \\ & + \frac{g^2}{8} (H_1^+ \sigma H_1 + H_2^+ \sigma H_2)^2 + \Delta V. \end{aligned} \quad (10)$$

Here, $\Delta V(H_1, H_2, Y)$ is the sum of loop corrections to the effective potential, and g and g' are the gauge constants of the $SU(2)$ and $U(1)$ interactions, respectively ($g_1 = \sqrt{5/3} g'$).

It is well known that the minimum eigenvalue of a matrix does not exceed its minimum diagonal element. Thus, the mass of the lightest CP -even Higgs boson is always smaller than

$$\begin{aligned} m_h^2 &\leq M_{11}^2 = \frac{\partial^2 V}{\partial v^2} \\ &= \frac{\lambda^2}{2} v^2 \sin^2 2\beta + M_Z^2 \cos^2 2\beta + \Delta. \end{aligned} \quad (11)$$

On the right-hand side of inequality (11), Δ is the contribution of loop corrections to the Higgs boson potential. Expression (11) was obtained in the tree-level approximation ($\Delta = 0$) in [20]. The contribution of loop corrections to the upper bound on the lightest Higgs boson mass in the NMSSM is almost the same as in the minimal SUSY model. In particular, in order to calculate the corrections from the t quark and its superpartners, one has to replace the parameter μ in the corresponding formulas of the MSSM by $\lambda y/\sqrt{2}$. The Higgs boson sector of the NMSSM and loop corrections to it were studied in [24–26]. Let us also remark that the upper bound on m_h in the NMSSM was compared (see [7]) with theoretical bounds in the SM and in its minimal SUSY extension.

The calculation of the CP -even Higgs spectrum is simplified in the most interesting realistic case where all superparticles are heavy ($M_S \gg M_Z$). In this case, the contributions of new particles to the electroweak observables are suppressed as $(M_Z/M_S)^2$ (see, for example, [27]). On the other hand, the prediction for the values of the strong coupling constant at the electroweak scale $\alpha_3(M_Z)$ that can be obtained from the gauge coupling unification [28] is improved with increasing of the supersymmetry breaking scale M_S . For $M_S \simeq 1$ TeV, it becomes close to $\alpha_3(M_Z) = 0.118(3)$ which has been found independently from the analysis of the experimental data [29]. Also it should be noted that the lightest Higgs boson mass reaches its maximal value in the SUSY models for $M_S \sim 1\text{--}3$ TeV.

In the limit being considered, the mass matrix (9) has a hierarchical structure and can be represented as a sum of two matrices [25]:

$$M_{ij}^2 = \begin{pmatrix} E_1^2 & 0 & 0 \\ 0 & E_2^2 & 0 \\ 0 & 0 & E_3^2 \end{pmatrix} + \begin{pmatrix} V_{11} & V_{12} & V_{13} \\ V_{21} & V_{22} & V_{23} \\ V_{31} & V_{32} & V_{33} \end{pmatrix}. \quad (12)$$

The first matrix is diagonal with $E_1^2 = 0$ and $E_{2,3}^2 \sim M_S^2$. The matrix elements V_{11} , V_{22} , V_{33} , and $V_{12} = V_{21}$ are of order M_Z^2 . The other matrix elements that correspond to mixing of χ_1 and χ_2 with χ_3 are

$$V_{13} = V_{31} = \lambda v X_1, \quad V_{23} = V_{32} = \lambda v X_2, \quad (13)$$

where $X_1 \sim X_2 \sim M_S$.

Considering the ratio $M_Z^2/E_{2,3}^2$ as a small parameter, it is easy to diagonalize the mass matrix (12) by means of usual quantum-mechanical perturbation theory. For the Higgs boson masses, it yields

$$m_S^2 \approx E_3^2 + V_{33} + \lambda^2 v^2 \frac{X_1^2}{E_3^2} + \lambda^2 v^2 \frac{X_2^2}{E_3^2 - E_2^2}, \quad (14)$$

$$m_H^2 \approx E_2^2 + V_{22} + \lambda^2 v^2 \frac{X_2^2}{E_2^2 - E_3^2},$$

$$m_h^2 \approx \frac{\lambda^2}{2} v^2 \sin^2 2\beta + M_Z^2 \cos^2 2\beta + \Delta - \lambda^2 v^2 \frac{X_1^2}{E_3^2}.$$

The explicit expressions for the E_i^2 and V_{ij} can be found in [25]. For the sake of simplicity, we restrict our consideration to the first order of perturbation theory and neglect matrix element V_{12} because its contribution to m_i^2 is of order M_Z^4/M_S^2 .

Perturbation theory becomes inapplicable when $|E_2^2 - E_3^2| \sim \lambda v X_2$. However, the mass matrix (12) can be easily diagonalized even in this case. In order to do this, one should choose the basis where the matrix element M_{23} is zero. After that, in the new

basis, the Higgs boson masses can be computed using ordinary perturbation theory.

The first three terms in the last relation in (14) reproduce the upper bound on the lightest Higgs boson mass in the NMSSM. Their sum is equal to V_{11} in our notation. The last term in this expression makes a negative contribution to m_h . Even when the ratio M_Z^2/M_S^2 goes to zero, it does not vanish. Thus, in the NMSSM, the mass of the lightest CP -even Higgs boson can be considerably less than its upper bound [25].

2.3. Renormalization of the Yukawa Couplings and Soft SUSY Breaking Terms

According to inequality (11), the upper bound on m_h rises when λ increases and the value of $\tan\beta$ diminishes. For $\tan\beta \gg 1$, the value of $\sin 2\beta$ goes to zero and the upper bound on the lightest Higgs boson mass in the NMSSM coincides with that in the minimal SUSY model. With decreasing $\tan\beta$, the t -quark Yukawa coupling at the electroweak scale $h_t(t_0)$ grows. An analysis of solutions to the NMSSM renormalization-group equations reveals that a growth of the Yukawa coupling constants at the electroweak scale entails an increase in them at the Grand Unification scale. As a result, the upper bound on the lightest Higgs boson mass in the NMSSM reaches its maximum value in the limit of strong Yukawa coupling, where the Yukawa coupling constants are much larger than the gauge ones at the scale M_X .

The renormalization of the NMSSM coupling constants in the strong Yukawa coupling limit has been studied in [30, 31]. In the case under consideration, the Yukawa coupling constants are attracted toward a Hill-type effective (quasifixed) line ($\varkappa = 0$) or surface ($\varkappa \neq 0$) which restricts the allowed regions of h_t , λ , and \varkappa . Outside this range, the solutions to renormalization-group equations blow up before the Grand Unification scale M_X and perturbation theory becomes invalid at $q^2 \sim M_X^2$. While the values of the Yukawa couplings at the scale M_X grow, the region where all solutions are concentrated shrinks and $h_t^2(0)$, $\lambda^2(0)$, and $\varkappa^2(0)$ are focused near the quasifixed points [30]. These points appear as a result of intersection of the quasifixed line or surface with the invariant (fixed) line. The latter connects the stable fixed point in the strong Yukawa coupling regime [32] with the infrared fixed point of the NMSSM renormalization-group equations [33]. The properties of invariant lines and surfaces were reviewed in detail in [5, 34].

When the values of Yukawa couplings tend to quasifixed points, the trilinear scalar couplings $A_i(t)$

and some combinations of scalar particle masses, $\mathfrak{M}_i^2(t)$, where

$$\begin{aligned} \mathfrak{M}_t^2(t) &= m_2^2(t) + m_Q^2(t) + m_U^2(t), \\ \mathfrak{M}_\lambda^2(t) &= m_1^2(t) + m_2^2(t) + m_y^2(t), \\ \mathfrak{M}_\varkappa^2(t) &= 3m_y^2(t), \end{aligned} \tag{15}$$

become insensitive to their initial values A and $3m_0^2$ at the scale M_X [31]. For the universal boundary conditions, one has

$$\begin{aligned} A_i(t) &= e_i(t)A + f_i(t)M_{1/2}, \\ m_i^2(t) &= a_i(t)m_0^2 + b_i(t)M_{1/2}^2 \\ &\quad + c_i(t)AM_{1/2} + d_i(t)A^2. \end{aligned} \tag{16}$$

The functions $e_i(t)$, $f_i(t)$, $a_i(t)$, $b_i(t)$, $c_i(t)$, and $d_i(t)$ remain unknown since an analytic solution to the NMSSM renormalization-group equations has not yet been found. While the Yukawa coupling constants tend to infinity, the values of functions $e_i(t_0)$, $c_i(t_0)$, and $d_i(t_0)$ vanish. This means that the solutions of renormalization-group equations go to the quasifixed points too. In the vicinity of the quasifixed points, $A_i(t)$ are proportional to $M_{1/2}$ and $\mathfrak{M}_i^2(t) \sim M_{1/2}^2$.

3. PARTICLE SPECTRUM IN THE MODIFIED NMSSM

3.1. Modified NMSSM

The fundamental parameters of the NMSSM at the Grand Unification scale have to be adjusted in such a way as to satisfy the minimization conditions for the effective Higgs boson potential:

$$\begin{aligned} \frac{\partial V(v_1, v_2, y)}{\partial v_1} = 0, \quad \frac{\partial V(v_1, v_2, y)}{\partial v_2} = 0, \\ \frac{\partial V(v_1, v_2, y)}{\partial y} = 0. \end{aligned} \tag{17}$$

Since the vacuum expectation value v is known, they can be used for the calculation of A , m_0 , and $M_{1/2}$. But in the strong Yukawa coupling limit, it is impossible to get the real solution of nonlinear algebraic equations (17). Thus, although the recent investigations [35, 36] reveal that the upper bound on the mass of the lightest Higgs boson in the NMSSM is larger than that in the MSSM by 7–10 GeV, the self-consistent solution cannot be obtained in that region of the NMSSM parameter space which we consider here. Such a solution to Eqs. (17) appears for $\lambda^2(0), \varkappa^2(0) \leq 0.1$ if the upper bound on m_h is identical to that in the minimal SUSY model.

Moreover, three degenerate vacuum configurations arise owing to Z_3 symmetry. After a phase transition at the electroweak scale, the Universe is filled

by three degenerate phases. The regions with different phases are separated from each other by domain walls. The cosmological observations do not confirm the existence of such domain walls. The domain structure of the vacuum is destroyed if the discrete Z_3 symmetry of the NMSSM Lagrangian disappears. An attempt at obtaining Z_3 symmetry breaking by means of operators of dimension $d = 5$ was made in [37]. It was shown that their introduction leads to quadratic divergences in the two-loop approximation, i.e., to the emergence of the hierarchy problem. As a result, the vacuum expectation value of Y turns out to be on the order of 10^{11} GeV.

Thus, in order to avoid the domain wall problem and obtain the self-consistent solution in the limit of strong Yukawa coupling, one has to modify the NMSSM. The simplest way is to introduce the bilinear terms $\mu(\hat{H}_1\hat{H}_2)$ and $\mu'\hat{Y}^2$ in the superpotential which are not forbidden by electroweak symmetry. At the same time, one can omit the coupling \varkappa , which allows one to simplify the analysis of the modified NMSSM (MNSSM). In this case ($\varkappa = 0$), the upper bound on the lightest Higgs boson mass reaches its maximum value. Neglecting all the Yukawa constants except for h_t and λ , one obtains the following expression for the MNSSM superpotential [38]:

$$W_{\text{MNSSM}} = \mu(\hat{H}_1\hat{H}_2) + \mu'\hat{Y}^2 + \lambda\hat{Y}(\hat{H}_1\hat{H}_2) + h_t(\hat{H}_2\hat{Q})\hat{U}_R^C. \quad (18)$$

The bilinear terms in the superpotential (18) break the Z_3 symmetry, and the domain walls do not arise, because the degenerate vacua do not exist. The introduction of the parameter μ permits us to obtain the self-consistent solution of algebraic equations (17) for $h_t^2(0)$, $\lambda^2(0) \gg g_i^2(0)$. In the SUGRA models, the bilinear terms may be generated due to the additional terms $[Z(H_1H_2) + Z'Y^2 + \text{h.c.}]$ in the Kähler potential [39, 40] or due to nonrenormalizable interaction of the Higgs doublet superfields with the hidden sector ones [40, 41].

The effective Higgs boson potential of MNSSM can be written as the sum

$$V(H_1, H_2, Y) = \mu_1^2|H_1|^2 + \mu_2^2|H_2|^2 + \mu_y^2|Y|^2 + \left[\mu_3^2(H_1H_2) + \mu_4^2Y^2 + \lambda A_\lambda Y(H_1H_2) + \lambda\mu'Y^*(H_1H_2) + \lambda\mu Y(|H_1|^2 + |H_2|^2) + \text{h.c.} \right] + \lambda^2|(H_1H_2)|^2 + \lambda^2Y^2(|H_1|^2 + |H_2|^2) + \frac{g'^2}{8}(|H_2|^2 - |H_1|^2)^2 + \frac{g^2}{8}(H_1^+\sigma H_1 + H_2^+\sigma H_2)^2 + \Delta V(H_1, H_2, Y), \quad (19)$$

where the parameters μ_i^2 are expressed via the soft SUSY breaking terms as follows:

$$\mu_1^2 = m_1^2 + \mu^2, \quad \mu_2^2 = m_2^2 + \mu^2, \quad \mu_y^2 = m_y^2 + \mu'^2, \\ \mu_3^2 = B\mu, \quad \mu_4^2 = \frac{1}{2}B'\mu'.$$

The μ terms in the superpotential (18) lead to the appearance of bilinear scalar couplings B and B' in the effective potential of the Higgs fields. They arise as the result of the soft supersymmetry breaking. The values of B and B' depend on the mechanism of the μ and μ' generation. For a minimal choice of the fundamental parameters, all soft scalar masses and all bilinear scalar couplings should be set equal at the scale M_X :

$$m_1^2(M_X) = m_2^2(M_X) = m_y^2(M_X) = m_0^2, \\ B(M_X) = B'(M_X) = B_0.$$

Thus, in addition to the parameters of the SM, the MNSSM contains seven independent ones:

$$\lambda, \mu, \mu', A, B_0, m_0^2, M_{1/2}.$$

3.2. Method of the Analysis

Although the parameter space of the model being considered is enlarged, it is possible to deduce some predictions for the Higgs boson spectrum in the strong Yukawa coupling limit. It is reasonable to start our analysis from the quasifixed point of MNSSM [30],

$$\rho_t^{\text{QFP}}(t_0) = 0.803, \quad \rho_{A_t}^{\text{QFP}}(t_0) = 1.77, \quad (20) \\ \rho_{\mathfrak{M}_t^2}^{\text{QFP}}(t_0) = 6.09, \\ \rho_\lambda^{\text{QFP}}(t_0) = 0.224, \quad \rho_{A_\lambda}^{\text{QFP}}(t_0) = -0.42, \\ \rho_{\mathfrak{M}_\lambda^2}^{\text{QFP}}(t_0) = -2.28,$$

because all solutions to renormalization-group equations are concentrated in the vicinity of it at $h_t^2(0)$, $\lambda^2(0) \gg g_i^2(0)$. In relations (20), the following notation is used: $\rho_{t,\lambda}(t) = Y_{t,\lambda}(t)/\tilde{\alpha}_3(t)$, $Y_t = h_t^2(t)/(4\pi)^2$, $Y_\lambda(t) = \lambda^2(t)/(4\pi)^2$, $\rho_{A_t,\lambda} = A_{t,\lambda}/M_{1/2}$, and $\rho_{\mathfrak{M}_{t,\lambda}^2} = \mathfrak{M}_{t,\lambda}^2/M_{1/2}^2$.

For given $\rho_t(t_0)$ (20), the value of $\tan\beta$ can be extracted from the equation that relates the running t -quark mass $m_t(M_t^{\text{pole}})$ to $h_t(t_0)$:

$$m_t(M_t^{\text{pole}}) = \frac{1}{\sqrt{2}}h_t(M_t^{\text{pole}})v \sin\beta. \quad (21)$$

We substitute, into the expression on the left-hand side of Eq. (21), the value of the running t -quark mass $m_t(M_t^{\text{pole}}) = 165 \pm 5$ GeV calculated in the \overline{MS} scheme [42]. The uncertainty in $m_t(M_t^{\text{pole}})$ is

determined by the experimental error with which the t -quark pole mass is measured: $M_t^{\text{pole}} = 174.3 \pm 5.1$ GeV [43]. In the infrared-quasifixed-point regime, which corresponds to the maximum allowed values of $h_t^2(0)$ and $\lambda^2(0)$ [we take $h_t^2(0) = \lambda^2(0) = 10$], we obtain $\tan \beta \approx 1.88$ for $m_t(M_t^{\text{pole}}) = 165$ GeV [38].

At the first step of our analysis, the supersymmetry-breaking scale is also fixed by means of the condition $M_3(1000 \text{ GeV}) = 1000 \text{ GeV}$, where M_3 is the gluino mass. This condition permits us to calculate immediately the universal gaugino mass at the Grand Unification scale. It ensures that the superparticles are much heavier than the observable ones.

Next, we use Eqs. (17), which define the minimum of the Higgs boson potential of the NMSSM, to restrict the allowed region of the parameter space. Instead of μ , it is more convenient to introduce $\mu_{\text{eff}} = \mu + \lambda y / \sqrt{2}$. After some transformations, we then obtain

$$\mu_{\text{eff}}^2 = \frac{m_1^2 - m_2^2 \tan^2 \beta + \Delta_Z}{\tan^2 \beta - 1} - \frac{1}{2} M_Z^2, \quad (22)$$

$$\sin 2\beta = \frac{-2(B\mu + \lambda y X_2 / \cos 2\beta)}{m_1^2 + m_2^2 + 2\mu_{\text{eff}}^2 + \lambda^2 v^2 / 2 + \Delta_\beta},$$

$$y(m_y^2 + \mu'^2 + B'\mu') = \frac{\lambda}{2} v^2 X_1 - \Delta_y,$$

where Δ_i are the contributions of loop corrections and

$$X_1 = \frac{1}{\sqrt{2}} (2\mu_{\text{eff}} + (\mu' + A_\lambda) \sin 2\beta),$$

$$X_2 = \frac{1}{\sqrt{2}} (\mu' + A_\lambda) \cos 2\beta.$$

As the values of v and $\tan \beta$ are known, one can find from Eqs. (22) the vacuum expectation value y and parameters B_0 and μ_{eff} . In the numerical analysis, we take into account only the loop corrections from t quark and its superpartners, because they give a leading contribution. Therefore, Δ_i are the functions of μ_{eff} and do not depend on B_0 and y . From the first equation in (22), the absolute value of μ_{eff} is calculated. The sign of μ_{eff} is not determined and should be considered as a free parameter. The bilinear scalar coupling B_0 and vacuum expectation value y are computed from the two other equations in (22). The last of them indicates that the value of y is on the order of $\lambda v^2 / M_S$ and is much smaller than v if the superparticles are sufficiently heavy.

Since μ_{eff} , B_0 , and y have been found, we investigate the dependence of the Higgs boson spectrum on A , m_0 , and μ' using relations (16). For the masses of CP -odd states, one can obtain the exact analytic result

$$m_{A_1, A_2}^2 = \frac{1}{2} \left(m_A^2 + m_B^2 \right) \quad (23)$$

$$\pm \sqrt{(m_A^2 - m_B^2)^2 + 4 \left(\frac{\lambda v}{\sqrt{2}} (\mu' + A_\lambda) + \Delta_0 \right)^2},$$

$$m_A^2 = m_1^2 + m_2^2 + 2\mu_{\text{eff}}^2 + \frac{\lambda^2}{2} v^2 + \Delta_A,$$

$$m_B^2 = m_y^2 + \mu'^2 - B'\mu' + \frac{\lambda^2}{2} v^2 + \Delta_3.$$

The mass matrix of the CP -even Higgs sector has a hierarchical structure and can be written in the form (12) with

$$E_2^2 = m_1^2 + m_2^2 + 2\mu_{\text{eff}}^2, \quad (24)$$

$$E_3^2 = m_y^2 + \mu'^2 + B'\mu',$$

$$V_{11} = M_Z^2 \cos^2 2\beta + \frac{1}{2} \lambda^2 v^2 \sin^2 2\beta + \Delta_{11},$$

$$V_{12} = V_{21} = \left(\frac{1}{4} \lambda^2 v^2 - \frac{1}{2} M_Z^2 \right) \sin 4\beta + \Delta_{12},$$

$$V_{22} = M_Z^2 \sin^2 2\beta + \frac{1}{2} \lambda^2 v^2 \cos^2 2\beta + \Delta_A + \Delta_{22},$$

$$V_{13} = V_{31} = \lambda v X_1 + \Delta_{13},$$

$$V_{23} = V_{32} = \lambda v X_2 + \Delta_{23},$$

$$V_{33} = \frac{1}{2} \lambda^2 v^2 + \Delta_{33}.$$

In formulas (23) and (24), $\Delta_0, \Delta_3, \Delta_A$, and Δ_{ij} ($\Delta_{11} = \Delta$) are loop corrections to the CP -odd and CP -even mass matrices. The mass matrix of CP -even Higgs sector can be diagonalized, and the expressions for the masses of the CP -odd states (23) can be simplified by using the perturbation theory of quantum mechanics. In the leading order of perturbation theory, the masses of the heavy Higgs bosons are $m_H^2 \approx E_2^2$, $m_S^2 \approx E_3^2$, $m_{A_1}^2 \approx m_B^2$, and $m_{A_2}^2 \approx m_A^2$, while the first-order perturbation corrections have a form similar to that in Eq. (14).

3.3. Numerical Results

The results of the numerical analysis of the particle spectrum near the MNSSM quasifixed point are presented in Figs. 1–3. There are two regions of the MNSSM parameter space. In one of them, the mass of the lightest CP -even Higgs boson is larger than the upper bound on m_h in the MSSM (see Figs. 1a and 2a), whereas, in the other region, it is smaller (see Figs. 1b and 2b). As follows from relations (14), the lightest Higgs boson mass in the NMSSM and in its modification attains its upper bound when V_{13} (or X_1) goes to zero. In the MNSSM, this happens if

$$\mu' = -\frac{2\mu_{\text{eff}}}{\sin 2\beta} - A_\lambda - \frac{\sqrt{2}\Delta_{13}}{\lambda v \sin 2\beta}. \quad (25)$$

Thus, m_h is larger in that part of the parameter space where the signs of μ and μ' are opposite. If μ' tends to

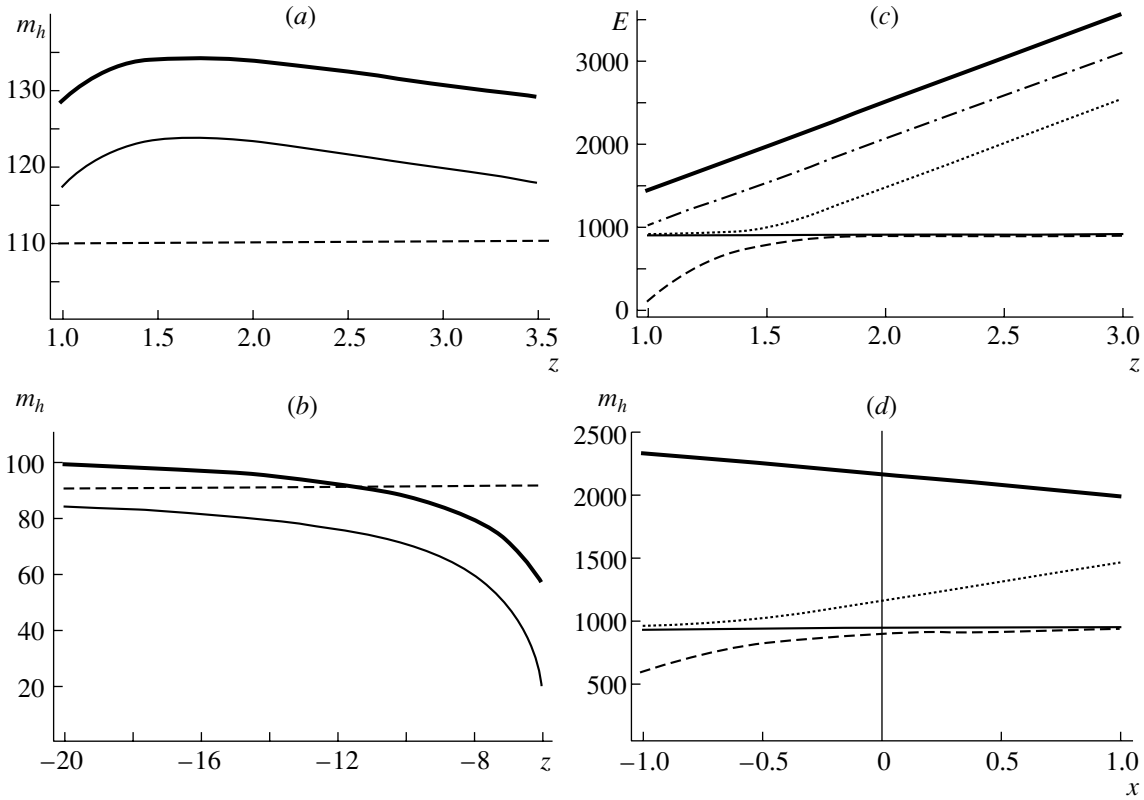


Fig. 1. Particle spectrum (in GeV) in the MNSSM as a function of $z = \mu'/(1 \text{ TeV})$ and $x = A/M_{1/2}$ for $h_t^2(0) = \lambda^2(0) = 10$, $m_0^2 = 0$, $M_3 = 1 \text{ TeV}$, and $\mu_{\text{eff}} < 0$. The thick and thin curves (a and b) correspond to the lightest Higgs boson mass calculated in the one- and the two-loop approximation, respectively. The thick and thin curves (c and d) reproduce the dependence of CP -even Higgs boson masses m_S and m_H on z and x , while the dotted and dashed curves represent the CP -odd Higgs boson masses m_{A_1} and m_{A_2} as functions of these parameters. The dash-dotted curve (c) corresponds to the mass of the heaviest neutralino.

infinity, then the singlet CP -odd and CP -even fields get huge masses and their contribution to the effective potential of the Higgs bosons vanishes because of the decoupling property. In the considered limit, the lightest Higgs boson mass is the same as in the minimal SUSY model.

It is necessary to emphasize that the one-loop and even two-loop corrections give an appreciable contribution to the mass of the lightest CP -even Higgs boson. Thus, the two-loop corrections [10] reduce its mass approximately by 10 GeV. They nearly compensate the growth of the lightest Higgs boson mass with increasing SUSY breaking scale M_S which arises because of one-loop corrections. Due to loop corrections, the values of m_h for $\mu_{\text{eff}} > 0$ and $\mu_{\text{eff}} < 0$ become different. The contribution of loop corrections Δ grows with increasing stop mixing parameter $X_t = A_t + \mu_{\text{eff}}/\tan\beta$. Since near the quasifixed point $A_t < 0$ [see (20)], the absolute value of X_t is larger if $\mu_{\text{eff}} < 0$.

As the part of the parameter space where μ_{eff} and μ' have the same signs is almost excluded by Higgs

search data from LEP II, we investigate the particle spectrum in the case when the signs of μ_{eff} and μ' are opposite. In the most interesting region, where the lightest Higgs boson mass is close to its upper bound, the value of μ' is considerably larger than μ_{eff} and M_S [see (25)]. Moreover, the product $B'\mu'$ is positive. Indeed, from the second relation of the system in (22), which defines the minimum of the MNSSM Higgs boson potential (19), it follows that the bilinear scalar coupling B and μ have different signs. As a consequence, near the maximum of the curves in Figs. 1a and 2a, the sign of B' coincides with the sign of μ' .

It means that the heaviest particle in the MNSSM is the CP -even Higgs boson that corresponds to the neutral field Y . Its mass is $m_S^2 > \mu'^2$ and is substantially larger than the scale of supersymmetry breaking. As one can see from Figs. 1c and 2c, the mass of the other heavy CP -even Higgs boson m_H is almost insensitive to the value of μ' since $m_S^2 \gg m_H^2$. The masses of CP -odd states are always smaller than μ'^2 . If the value of μ' grows, the mass of the heaviest

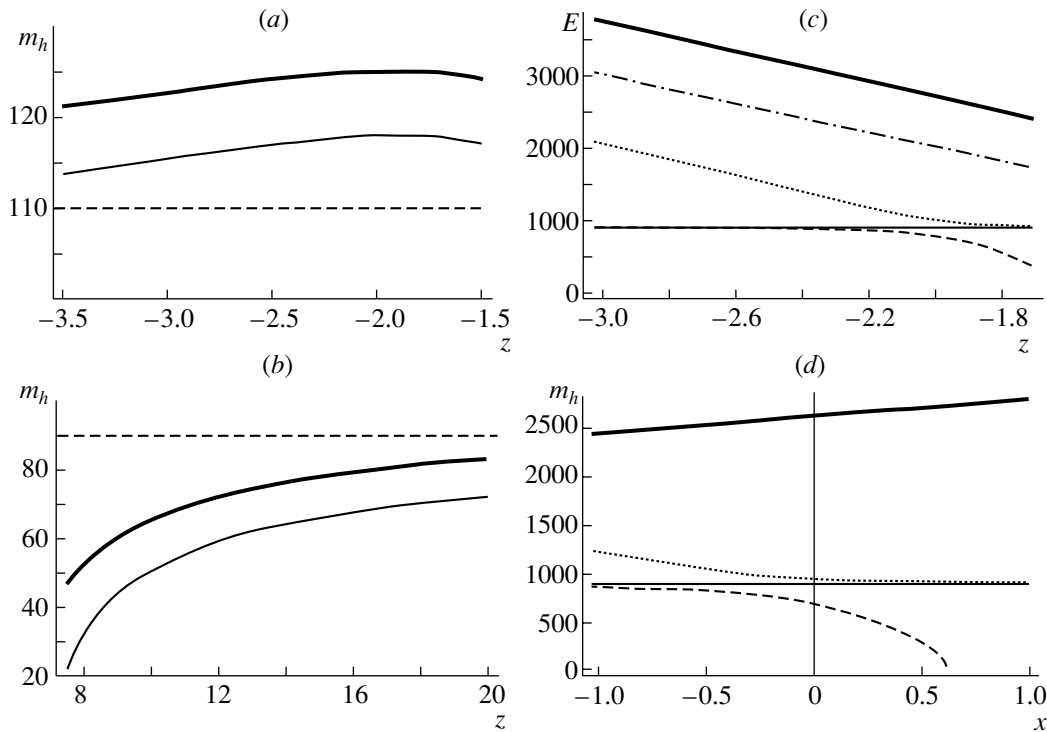


Fig. 2. Particle spectrum (in GeV) in the MNSSM as a function of $z = \mu'/1 \text{ TeV}$ and $x = A/M_{1/2}$ for $h_t^2(0) = \lambda^2(0) = 10$, $m_0^2 = 0$, $M_3 = 1 \text{ TeV}$, and $\mu_{\text{eff}} > 0$. The notation is identical to that in Fig. 1.

CP -odd state $m_{A_1}^2$ increases too as $m_{A_1}^2 \sim \mu'^2$. As the value of μ' decreases, the mass m_{A_2} of the lightest CP -odd boson decreases and appears to be on the order of the electroweak scale for $\mu' \sim B'$. At given values of μ' , a lower constraint on μ' appears that comes from the requirement $m_{A_2}^2 > 0$. However, even if the mass of the lightest CP -odd state is on the order of M_Z , it will be quite difficult to observe it in future experiments because the main contribution to its wave function gives the CP -odd component of the singlet field Y . The heaviest fermion in the MNSSM is the neutralino ($m_{\tilde{\chi}_5}$) which is a superpartner of the scalar field Y . Its mass is proportional to μ' . The remaining masses of the neutralinos ($m_{\tilde{\chi}_i}$), the charginos ($m_{\tilde{\chi}_i^\pm}$), the squarks, and the sleptons do not depend on μ' .

The spectrum of new fermion states, squarks, and sleptons is also insensitive to the choice of the parameter A , since near the quasifixed point (20), the dependence of scalar masses m_i^2 and trilinear scalar couplings A_i on it disappears. For this reason, the lightest CP -even Higgs boson mass is almost independent of A . Nevertheless, the dependence of the heavy Higgs boson spectrum on the universal trilinear scalar coupling A is conserved. This occurs because the bilinear scalar coupling B' is proportional to A .

The dependence of the Higgs boson masses on the parameter A for $m_0 = 0$ is presented in Figs. 1d and 2d.

Although we set $m_0 = 0$ everywhere in Figs. 1 and 2, the qualitative pattern of the particle spectrum does not change if the universal soft scalar mass varies from zero to $M_{1/2}^2$. It should be noted that the masses of the squarks, the sleptons, the heavy Higgs bosons, the heavy charginos, and the neutralinos grow with increasing m_0 , while the spectrum of the lightest particles remains unchanged.

Up to now, the particle spectrum in the quasifixed-point regime, which corresponds to the initial values of the Yukawa couplings $h_t^2(0) = \lambda^2(0) = 10$, has been studied. In the vicinity of the quasifixed point (20) for $m_t(M_t^{\text{pole}}) = 165 \text{ GeV}$ and $M_3 \leq 2 \text{ TeV}$, the lightest Higgs boson mass does not exceed 127 GeV. The results presented in the table point out that the qualitative pattern of the MNSSM particle spectrum does not change even if $h_t^2(0) \gg \lambda^2(0)$ or $h_t^2(0) \ll \lambda^2(0)$ as long as the Yukawa couplings are much larger than the gauge ones at the scale M_X . The masses of the Higgs bosons and the masses of the superpartners of the observable particles were calculated there for the values of μ' computed by formula (25) and $A = m_0 = 0$. At the same time, one can see from the table that the numerical value of the lightest

Table 1. Spectrum of the superparticles and Higgs bosons for $m_t(174 \text{ GeV}) = 165 \text{ GeV}$ and $A = m_0 = 0$ and for different initial values of $h_t^2(0)$ and $\lambda^2(0)$ (all mass parameters are given in GeV)

	$\mu_{\text{eff}} < 0$			$\mu_{\text{eff}} > 0$		
$\lambda^2(0)$	2	10	10	2	10	10
$h_t^2(0)$	10	10	2	10	10	2
$M_{1/2}$	-392.8	-392.8	-392.8	-392.8	-392.8	-392.8
$\tan \beta$	1.736	1.883	2.439	1.736	1.883	2.439
μ_{eff}	-771.4	-727.8	-641.8	772.4	728.6	642.3
B_0	622.5	1008.0	886.2	-988.1	-1629.1	-1583.3
y	-0.0014	-0.0015	-0.0012	-0.0003	-0.0004	-0.0005
$\mu'(t_0)$	1693.9	1671.5	1749.8	-1941.4	-1899.8	-1943.1
$m_h(t_0)$	123.6	134.1	137.6	112.4	125.0	131.2
(one-loop)						
$m_h(t_0)$	113.0	124.4	127.8	105.5	118.4	123.6
(two-loop)						
$M_3(1 \text{ TeV})$	1000	1000	1000	1000	1000	1000
$m_{\tilde{t}_1}(1 \text{ TeV})$	891.6	890.2	890.5	837.0	840.6	853.5
$m_{\tilde{t}_2}(1 \text{ TeV})$	622.2	630.3	648.5	693.8	695.1	696.4
$m_H(1 \text{ TeV})$	961.0	896.2	758.5	963.3	898.5	761.1
$m_S(1 \text{ TeV})$	1999.8	2147.4	2187.2	2405.3	2623.4	2663.8
$m_{A_1}(1 \text{ TeV})$	1374.8	1123.2	1294.0	1390.6	953.9	965.1
$m_{A_2}(1 \text{ TeV})$	949.8	857.6	735.6	951.6	704.3	674.3
$m_{\tilde{\chi}_1}(t_0)$	160.1	160.0	159.9	164.6	164.6	164.4
$m_{\tilde{\chi}_2}(t_0)$	311.9	311.1	309.4	328.1	327.8	326.4
$ m_{\tilde{\chi}_3}(1 \text{ TeV}) $	795.8	753.7	665.8	797.2	755.1	668.1
$ m_{\tilde{\chi}_4}(1 \text{ TeV}) $	807.8	764.7	677.1	800.9	755.9	666.7
$ m_{\tilde{\chi}_5}(1 \text{ TeV}) $	1711.2	1700.7	1790.0	1960.7	1931.8	1986.5
$m_{\tilde{\chi}_1^\pm}(t_0)$	311.6	310.7	309.0	328.1	327.8	326.4
$m_{\tilde{\chi}_2^\pm}(1 \text{ TeV})$	806.0	763.3	676.7	800.4	757.0	669.0

Higgs boson mass is raised from 105–113 GeV for $\lambda^2(0) = 2$ to 118–128 GeV for $\lambda^2(0) = 10$.

Therefore, at the last stage of our analysis, we investigate the dependence of the upper bound on m_h on the choice of the Yukawa couplings at the Grand Unification scale. For each $h_t^2(t_0)$, we find the value of $\tan \beta$ using relation (21) and choose $\lambda^2(t_0)$ and μ' so that the lightest Higgs boson mass attains its upper bound. The resulting curve $m_h(\tan \beta)$ is

plotted in Fig. 3, where the upper bound on m_h in the MSSM as a function of $\tan \beta$ is also presented. The two bounds are very close for large $\tan \beta$ ($\tan \beta \gg 1$). The curve $m_h(\tan \beta)$ in the MNSSM reaches its maximum at $\tan \beta = 2.2$ – 2.4 , which corresponds to the limit of strong Yukawa coupling. The numerical analysis reveals that the mass of the lightest CP -even Higgs boson in the NMSSM is always smaller than $130.5 \pm 3.5 \text{ GeV}$, where the uncertainty is mainly due to the error in the t -quark mass.

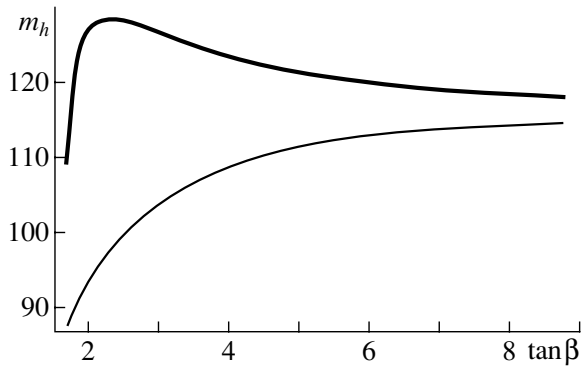


Fig. 3. Upper bound on the lightest Higgs boson mass (in GeV) in the (lower curve) MSSM and (upper curve) MNSSM as a function of $\tan \beta$ for $M_3 = 2$ TeV.

4. FINAL REMARKS AND CONCLUSIONS

We have argued that the upper bound on the lightest Higgs boson mass in the NMSSM attains its maximal value in the strong Yukawa coupling limit. In the limit being considered, all solutions of renormalization-group equations are gathered near the quasifixed points. If the scale of supersymmetry breaking is much larger than the electroweak one, perturbation theory can be used to calculate the Higgs boson masses. Even for $M_S \gg M_Z$, however, the mass of the lightest CP -even Higgs boson in the NMSSM is appreciably smaller than its upper bound in the dominant part of the parameter space. Moreover, the self-consistent solution does not exist in the limit of strong Yukawa coupling within the NMSSM with a minimal set of fundamental parameters. In addition, the Z_3 symmetry of the NMSSM superpotential leads to the domain-wall problem.

We have suggested such a modification of the NMSSM that allows one to get the self-consistent solution in the strong Yukawa coupling limit and at the same time to avoid the domain-wall problem. The superpotential of MNSSM includes the bilinear terms which break the Z_3 symmetry. We have studied the spectrum of the Higgs bosons in the MNSSM. The qualitative pattern of the particle spectrum is most sensitive to the choice of two parameters: μ' and M_S . The limit $\mu' \gg M_S$, where the CP -even and CP -odd scalar fields become very heavy, corresponds to the minimal SUSY model. In the most interesting region of the parameter space, where the mass of the lightest Higgs boson is larger than that in the MSSM, the Higgs boson mass matrix has a hierarchical structure and can be diagonalized by using the method of perturbation theory. The heaviest particle in this region of the MNSSM parameters is the CP -even Higgs boson corresponding to the neutral scalar field Y and the heaviest fermion is \tilde{Y} , which is the

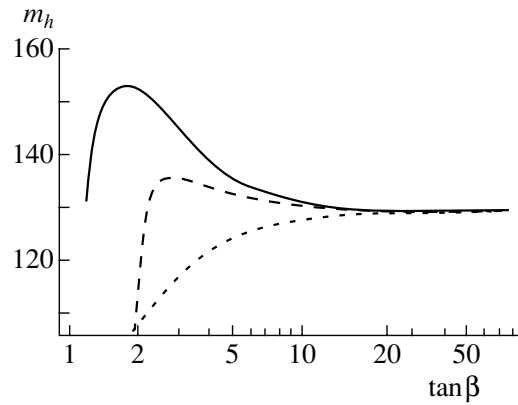


Fig. 4. Upper bound on the mass of the lightest Higgs boson (in GeV) in the NMSSM (solid and long-dashed curves) and in the MSSM (short-dashed curve) as a function of $\tan \beta$. The solid curve is the upper bound on m_h in the NMSSM with four additional $5 + \bar{5}$ multiplets, while the long-dashed curve is that in the ordinary NMSSM (see [36]).

superpartner of the singlet field Y . The lightest Higgs boson mass in the model under consideration may reach 127 GeV even for the comparatively low value of $\tan \beta \approx 1.9$ and does not exceed 130.5 ± 3.5 GeV.

The resulting upper bound on the mass of the lightest CP -even Higgs boson is not an absolute one in the SUSY models. For instance, the upper bound on m_h increases if new $5 + \bar{5}$ supermultiplets appear in the NMSSM at the SUSY breaking scale. These multiplets change the evolution of gauge coupling constants. Their values at the intermediate scale grow if the number of new supermultiplets increases. For this reason, the allowed region of the Yukawa couplings at the electroweak scale is expanded. This leads to the growth of the upper bound on m_h with increasing number of $5 + \bar{5}$ supermultiplets (see Fig. 4). The investigations performed in [36] showed that the introduction of four or five $5 + \bar{5}$ supermultiplets increases the theoretical bound on the mass of the lightest Higgs boson up to 155 GeV. If more than five multiplets are introduced at the SUSY breaking scale, then the gauge coupling constants blow up before the Grand Unification scale and perturbation theory is not valid at $q^2 \sim M_X^2$.

Recently, the upper bound on the lightest Higgs boson mass in more complicated SUSY models has been analyzed [44–47]. In particular, in addition to the gauge singlet superfield, three $SU(2)$ triplets \hat{T}_i with different hypercharges can be introduced in the Higgs boson superpotential:

$$W_{\text{Higgs}} = \lambda \hat{Y}(\hat{H}_1 \hat{H}_2) + \lambda_1(\hat{H}_1 \hat{T}_0 \hat{H}_2) + \chi_1(\hat{H}_1 \hat{T}_1 \hat{H}_1) + \chi_2(\hat{H}_2 \hat{T}_1 \hat{H}_2) + \dots \quad (26)$$

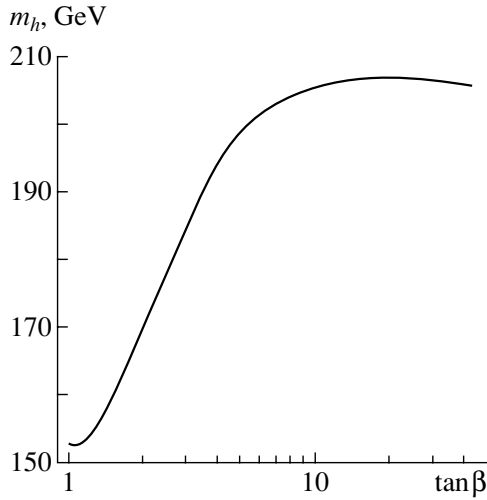


Fig. 5. Theoretical upper bound on the lightest Higgs boson mass in the SUSY model, which contains singlet and three $SU(2)$ triplet fields in the Higgs sector and four $3 + \bar{3}$ color multiplets, as a function of $\tan\beta$ for $\lambda_1 = 0$ (see [45]).

As a result, the expression for the upper bound on m_h changes to become

$$m_h^2 \leq M_Z^2 \cos^2 2\beta + \left[\left(\frac{\lambda^2}{2} + \frac{\lambda_1^2}{4} \right) \sin^2 2\beta + 2\chi_1^2 \cos^4 \beta + 2\chi_2^2 \sin^4 \beta \right] v^2 + \Delta. \quad (27)$$

The appearance of triplet superfields destroys the gauge-coupling-constant unification at high energies. In order to restore the unification scheme of the electroweak and strong interactions, one has to add several $SU(3)$ multiplets, for example, four $3 + \bar{3}$, that do not participate in the $SU(2) \otimes U(1)$ interactions. A numerical analysis [45, 46] reveals that the unification of gauge couplings then occurs at the scale $\tilde{M}_X \sim 10^{17}$ GeV. As one can see from Fig. 5 (see also [45]), the upper bound on the mass of the lightest Higgs boson mass grows with increasing $\tan\beta$ and, for $\tan\beta \gg 1$, can be approximately equal to 190 GeV [46].

Also the upper bound on m_h is raised if a fourth generation of the quarks and leptons exists in the MSSM [47]. However, no evidence for the existence of the fourth generation in the SM or the MSSM has been found so far. Moreover, new particles make considerable contributions to electroweak observables, which upsets the agreement between theoretical predictions and the results of experimental measurements. Thus, the growth of the upper bound on the lightest Higgs boson mass in the supersymmetric

models is usually accompanied by a substantial increase in the number of particles that may be considered as the main drawback of these models.

ACKNOWLEDGMENTS

We are grateful to D.I. Kazakov, L.B. Okun, and M.I. Vysotsky for stimulating discussions. R.B. Nevzorov thanks Istituto Nazionale di Fisica Nucleare (Sezione di Ferrara), where a considerable part of this investigation was performed, for their hospitality.

This work was supported by the Russian Foundation for Basic Research (project nos. 00-15-96786 and 00-15-96562).

REFERENCES

1. E. Gross, in *Proceedings of International Europhysics Conference on High-Energy Physics, Tampere, 1999*, p. 144.
2. P. Igo-Kemenes, in *Proceedings of XXX International Conference on High-Energy Physics, Osaka, 2000* (in press).
3. R. Barate *et al.*, Phys. Lett. B **495**, 1 (2000); G. Abbiendi *et al.*, Phys. Lett. B **499**, 38 (2001).
4. N. Cabibbo, L. Maiani, G. Parisi, and R. Petronzio, Nucl. Phys. B **158**, 295 (1979); M. A. Beg, C. Panagiotakopoulos, and A. Sirlin, Phys. Rev. Lett. **52**, 883 (1984); M. Lindner, Z. Phys. C **31**, 295 (1986); M. Sher, Phys. Rep. **179**, 273 (1989); M. Lindner, M. Sher, and H. W. Zaglauer, Phys. Lett. B **228**, 139 (1989); C. Ford, D. R. T. Jones, P. W. Stephenson, and M. B. Einhorn, Nucl. Phys. B **395**, 17 (1993); M. Sher, Phys. Lett. B **317**, 159 (1993); **331**, 448 (1994); G. Altarelli and G. Isidori, Phys. Lett. B **337**, 141 (1994); T. Hambye and K. Reisselmann, Phys. Rev. D **55**, 7255 (1997).
5. B. Schrempp and M. Wimmer, Prog. Part. Nucl. Phys. **37**, 1 (1996).
6. N. V. Krasnikov and S. Pokorski, Phys. Lett. B **288**, 184 (1992); J. A. Casas, J. R. Espinosa, and M. Quiros, Phys. Lett. B **342**, 171 (1995); P. Q. Hung and G. Isidori, Phys. Lett. B **402**, 122 (1997); D. I. Kazakov, Phys. Rep. **320**, 187 (1999).
7. M. A. Diaz, T. A. ter Veldhuis, and T. J. Weiler, Phys. Rev. D **54**, 5855 (1996).
8. K. Inoue, A. Kakuto, H. Komatsu, and S. Takeshita, Prog. Theor. Phys. **67**, 1889 (1982); R. Flores and M. Sher, Ann. Phys. (N.Y.) **148**, 95 (1983).
9. H. E. Haber and R. Hempfling, Phys. Rev. Lett. **66**, 1815 (1991); Y. Okada, M. Yamaguchi, and T. Yanagida, Prog. Theor. Phys. **85**, 1 (1991); J. Ellis, G. Ridolfi, and F. Zwirner, Phys. Lett. B **257**, 83 (1991); **262**, 477 (1991); R. Barbieri, M. Frigeni, and F. Caravaglios, Phys. Lett. B **258**, 167 (1991); Y. Okada, M. Yamaguchi, and T. Yanagida, Phys. Lett. B **262**, 54 (1991); M. Drees and M. Nojiri, Phys. Rev. D **45**, 2482 (1992); D. M. Pierce, A. Papadopoulos, and S. Johnson, Phys. Rev. Lett. **68**, 3678 (1992); P. H. Chankowski, S. Pokorski, and

- J. Rosiek, Phys. Lett. B **274**, 191 (1992); H. E. Haber and R. Hempfling, Phys. Rev. D **48**, 4280 (1993); P. H. Chankowski, S. Pokorski, and J. Rosiek, Nucl. Phys. B **423**, 437 (1994); A. Yamada, Z. Phys. C **61**, 247 (1994); A. Dabelstein, Z. Phys. C **67**, 495 (1995); D. M. Pierce, J. A. Bagger, K. Matchev, and R. Zhang, Nucl. Phys. B **491**, 3 (1997); D. I. Kazakov *et al.*, Nucl. Phys. B **498**, 3 (1997).
10. J. R. Espinosa and M. Quiros, Phys. Lett. B **266**, 389 (1991); R. Hempfling and A. H. Hoang, Phys. Lett. B **331**, 99 (1994); M. Carena, J. R. Espinosa, M. Quiros, and C. E. M. Wagner, Phys. Lett. B **355**, 209 (1995); J. A. Casas, J. R. Espinosa, M. Quiros, and A. Riotto, Nucl. Phys. B **436**, 3 (1995); M. Carena, M. Quiros, and C. E. M. Wagner, Nucl. Phys. B **461**, 407 (1996); H. E. Haber, R. Hempfling, and A. H. Hoang, Z. Phys. C **75**, 539 (1997); S. Heinemeyer, W. Hollik, and G. Weiglein, Phys. Rev. D **58**, 091701 (1998); Phys. Lett. B **440**, 296 (1998); **455**, 179 (1999); R. Zhang, Phys. Lett. B **447**, 89 (1999);
 11. L. E. Ibáñez and C. López, Phys. Lett. B **126B**, 54 (1983); Nucl. Phys. B **233**, 511 (1984); W. De Boer, R. Ehret, and D. I. Kazakov, Z. Phys. C **67**, 647 (1995).
 12. C. T. Hill, Phys. Rev. D **24**, 691 (1981); C. T. Hill, C. N. Leung, and S. Rao, Nucl. Phys. B **262**, 517 (1985).
 13. V. Barger, M. S. Berger, P. Ohmann, and R. J. N. Phillips, Phys. Lett. B **314**, 351 (1993); W. A. Bardeen, M. Carena, S. Pokorski, and C. E. M. Wagner, Phys. Lett. B **320**, 110 (1994); V. Barger, M. S. Berger, and P. Ohmann, Phys. Rev. D **49**, 4908 (1994); S. A. Abel and B. C. Allanach, Phys. Lett. B **431**, 339 (1998).
 14. M. Carena, M. Olechowski, S. Pokorski, and C. E. M. Wagner, Nucl. Phys. B **419**, 213 (1994); M. Carena and C. E. M. Wagner, Nucl. Phys. B **452**, 45 (1995); S. A. Abel and B. C. Allanach, Phys. Lett. B **415**, 371 (1997).
 15. G. K. Yeghiyan, M. Jurčišin, and D. I. Kazakov, Mod. Phys. Lett. A **14**, 601 (1999); S. Codoban, M. Jurčišin, and D. Kazakov, Phys. Lett. B **477**, 223 (2000).
 16. J. A. Casas, J. R. Espinosa, and H. E. Haber, Nucl. Phys. B **526**, 3 (1998).
 17. B. Brahmachari, Mod. Phys. Lett. A **12**, 1969 (1997).
 18. P. Fayet, Nucl. Phys. B **90**, 104 (1975); M. I. Vysotsky and K. A. Ter-Martirosyan, Zh. Éksp. Teor. Fiz. **90**, 838 (1986) [Sov. Phys. JETP **63**, 489 (1986)].
 19. J. Ellis, J. F. Gunion, H. E. Haber, *et al.*, Phys. Rev. D **39**, 844 (1989).
 20. L. Durand and J. L. Lopes, Phys. Lett. B **217**, 463 (1989); L. Drees, Int. J. Mod. Phys. A **4**, 3635 (1989).
 21. H. P. Nilles, M. Srednicki, and D. Wyler, Phys. Lett. B **120B**, 345 (1983); R. Barbieri, S. Ferrara, and C. Savoy, Phys. Lett. B **119B**, 343 (1982); A. H. Chamseddine, R. Arnowitt, and P. Nath, Phys. Rev. Lett. **49**, 970 (1982).
 22. V. S. Kaplunovsky and J. Louis, Phys. Lett. B **306**, 269 (1993); A. Brignole, L. E. Ibáñez, and C. Muñoz, Nucl. Phys. B **422**, 125 (1994); **436**, 747 (1995); K. Choi, H. B. Kim, and C. Muñoz, Phys. Rev. D **57**, 7521 (1998); A. Lukas, B. A. Ovrut, and D. Waldram, Phys. Rev. D **57**, 7529 (1998); T. Li, Phys. Rev. D **59**, 107902 (1999).
 23. J.-P. Derendinger and C. A. Savoy, Nucl. Phys. B **237**, 307 (1984).
 24. S. F. King and P. L. White, Phys. Rev. D **52**, 4183 (1995).
 25. P. A. Kovalenko, R. B. Nevzorov, and K. A. Ter-Martirosyan, Yad. Fiz. **61**, 898 (1998) [Phys. At. Nucl. **61**, 812 (1998)].
 26. T. Elliott, S. F. King, and P. L. White, Phys. Lett. B **314**, 56 (1993); U. Ellwanger, Phys. Lett. B **303**, 271 (1993); U. Ellwanger and M. Lindner, Phys. Lett. B **301**, 365 (1993); P. N. Pandita, Phys. Lett. B **318**, 338 (1993); Z. Phys. C **59**, 575 (1993); T. Elliott, S. F. King, and P. L. White, Phys. Rev. D **49**, 2435 (1994); S. W. Ham, S. K. Oh, and B. R. Kim, J. Phys. G **22**, 1575 (1996); Phys. Lett. B **414**, 305 (1997); S. W. Ham, S. K. Oh, and H. S. Song, hep-ph/9910461.
 27. I. V. Gaidenko, A. V. Novikov, V. A. Novikov, *et al.*, Pis'ma Zh. Éksp. Teor. Fiz. **67**, 723 (1998) [JETP Lett. **67**, 761 (1998)].
 28. P. Langacker and N. Polonsky, Phys. Rev. D **47**, 4028 (1993); **52**, 3081 (1995).
 29. Particle Data Group (C. Caso *et al.*), Eur. Phys. J. C **3**, 1 (1998).
 30. R. B. Nevzorov and M. A. Trusov, Yad. Fiz. **64**, 1375 (2001) [Phys. At. Nucl. **64**, 1299 (2001)].
 31. R. B. Nevzorov and M. A. Trusov, Yad. Fiz. **64**, 1589 (2001) [Phys. At. Nucl. **64**, 1513 (2001)].
 32. P. Binetruy and C. A. Savoy, Phys. Lett. B **277**, 453 (1992).
 33. B. C. Allanach and S. F. King, Phys. Lett. B **407**, 124 (1997); I. Jack and D. R. T. Jones, Phys. Lett. B **443**, 177 (1998).
 34. B. Schrempp and F. Schrempp, Phys. Lett. B **299**, 321 (1993).
 35. G. K. Yeghiyan, hep-ph/9904488; U. Ellwanger and C. Hugonie, hep-ph/9909260.
 36. M. Masip, R. Muñoz-Tapia, and A. Pomarol, Phys. Rev. D **57**, R5340 (1998).
 37. S. A. Abel, S. Sarkar, and P. L. White, Nucl. Phys. B **454**, 663 (1995).
 38. R. B. Nevzorov and M. A. Trusov, Zh. Éksp. Teor. Fiz. **118**, 1251 (2000) [JETP **91**, 1079 (2000)].
 39. G. F. Giudice and A. Masiero, Phys. Lett. B **206**, 480 (1988).
 40. J. A. Casas and C. Muñoz, Phys. Lett. B **306**, 288 (1993).
 41. J. E. Kim and H. P. Nilles, Phys. Lett. B **138B**, 150 (1984); **263**, 79 (1991); E. J. Chun, J. E. Kim, and H. P. Nilles, Nucl. Phys. B **370**, 105 (1992).
 42. R. Tarrach, Nucl. Phys. B **183**, 384 (1981); S. Narison, Phys. Lett. B **197**, 405 (1987); N. Gray, D. J. Broadhurst, W. Grafe, and K. Schilcher, Z. Phys. C **48**, 673 (1990).

43. L. Demortier *et al.* (the Top Averaging Group for the CDF and D0 Collab.), Fermilab-TM-2084 (1999).
44. J. R. Espinosa and M. Quiros, Phys. Lett. B **279**, 92 (1992); T. Moroi and Y. Okada, Phys. Lett. B **295**, 73 (1992); G. L. Kane, C. Kolda, and J. D. Wells, Phys. Rev. Lett. **70**, 2686 (1993); J. R. Espinosa and M. Quiros, Phys. Lett. B **302**, 51 (1993); J. R. Espinosa, Phys. Lett. B **353**, 243 (1995); D. Comelli and J. R. Espinosa, Phys. Lett. B **388**, 793 (1996); Y. Sakamura, Mod. Phys. Lett. A **14**, 721 (1999).
45. J. R. Espinosa and M. Quiros, Phys. Rev. Lett. **81**, 516 (1998).
46. M. Masip, Phys. Lett. B **444**, 352 (1998).
47. S. K. Kang, Phys. Rev. D **54**, 7077 (1996); S. K. Kang and G. T. Park, Mod. Phys. Lett. A **12**, 553 (1997); D. Dooling, K. Kang, and S. K. Kang, Int. J. Mod. Phys. A **14**, 1605 (1999); Phys. Rev. D **60**, 017701 (1999).

**Conference on Physics of Fundamental Interactions
Theory**

Hadronic Production of Doubly Charmed Baryons and Intrinsic Charm in the Proton

D. A. Gunter and V. A. Saleev*

Samara State University, ul. Akademika Pavlova 1, Samara, 443011 Russia

Received March 7, 2001

Abstract—The production of baryons involving two charmed quarks (Ξ_{cc}^* or Ξ_{cc}) in hadron interactions at high energies and high transverse momenta is considered. It is assumed that a Ξ_{cc} baryon is formed in the nonperturbative fragmentation of a (cc) diquark produced in the hard partonic process of the scattering of charmed quarks from colliding hadrons: $c + c \rightarrow (cc) + g$. It is shown that, upon the inclusion of this mechanism, the cross section for the production of doubly charmed baryons becomes approximately twice as large as that which is expected at the Tevatron and LHC colliders according to the predictions based on the model of gluon–gluon production of a (cc) diquark and obtained in the leading order of perturbative QCD. © 2002 MAIK “Nauka/Interperiodica”.

1. INTRODUCTION

Doubly heavy baryons stand out among baryons containing heavy quarks. The presence of two heavy quarks determines a pronounced quark–diquark structure of doubly heavy baryons, whose wave functions are dominated by configurations involving a compact doubly heavy (QQ) diquark. In many respects, the regularities observed in the mass spectrum of doubly heavy baryons appear to be similar to those in the case of mesons containing one heavy quark [1–4]. The mechanisms of production of (QQq) baryons and $(Q\bar{q})$ mesons also have common features. For the former, the production of a compact heavy (QQ) diquark at the first stage is followed by its nonperturbative fragmentation into a (QQq) baryon through the pickup of a light quark. Presently, the cross sections for the production of doubly heavy baryons in ep and pp interactions have been calculated both within the model of heavy-quark hard fragmentation into a doubly heavy diquark [5–7] and within a model based on an exact calculation of the cross section for the gluon–gluon production of a diquark and two heavy antiquarks in the leading order of perturbative QCD [8–10].

The mechanism that is responsible for the production of hadrons involving charmed quarks and which is based on studying hard partonic subprocesses featuring one c quark in the initial state was considered previously in [11–13]. It was shown that, in the region of high momentum transfers ($Q^2 \gg m_c^2$), the concept of intrinsic charm in hadrons is compatible with the

parton model and makes it possible to take effectively into account higher order corrections of perturbative QCD to the Born approximation. However, there remains the double-counting problem associated with the fact that part of the Born diagrams for the production of two heavy quarks in gluon–gluon fusion can be interpreted as diagrams describing charm excitation in one of the colliding protons; that is, the same diagrams make the leading contribution in α_s to the perturbative (pointlike) c -quark structure function for the proton. The nonperturbative contribution to the c -quark structure function for the proton [14] is independent of Q^2 and, at $Q^2 \gg m_c^2$, becomes negligibly small in relation to the contribution of the perturbative photon structure function. Experience gained in calculating the cross sections for the production of heavy quarks in gluon–gluon fusion suggests that the next-to-leading contribution of perturbation theory in α_s can be commensurate with the contribution of the Born diagrams. Figure 1 depicts one of 36 Born diagrams of order α_s^4 that describe the production of a (cc) diquark and two charmed antiquarks in gluon–gluon fusion. In the case of the gluonic production of two pairs of heavy quarks, there exist more than 300 diagrams featuring an extra gluon in the final state—that is, α_s^5 diagrams—and it is difficult to calculate them directly at present.

2. SUBPROCESS $c + c \rightarrow (cc) + g$

In considering the production of a (cc) diquark in proton–proton interactions, we rely here on the model where the underlying mechanism is that of intrinsic-charm excitation in a proton. It is assumed that a

*e-mail: saleev@ssu.samara.ru

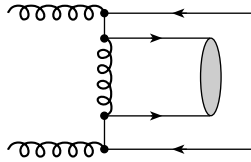


Fig. 1. One of the diagrams for the subprocess $g + g \rightarrow (cc) + c + \bar{c}$.

(cc) diquark is produced in the fusion of c quarks from colliding protons, which is accompanied by the emission of a hard bremsstrahlung gluon—that is, in the partonic process

$$c + c \rightarrow (cc) + g. \quad (1)$$

The Feynman diagrams for the partonic subprocess (1) are shown in Fig. 2, where q_1 and q_2 are the 4-momenta of the primary c quarks, k is the gluon 4-momentum, and p is the diquark 4-momentum shared by the c quarks in equal fractions. In this case, the doubly charmed diquark is considered as a nonrelativistic bound state of two c quarks in the color-antitriplet spin-1 state. If i and j are the color indices of the primary quarks and if m is the color index of the diquark, the amplitude for the production of a (cc) diquark, $M_{ijm}(c + c \rightarrow (cc) + g)$, is related to the amplitude for the production of two c quarks whose 4-momenta are $p_1 = p_2 = p/2$. Specifically, we have

$$M_{ijm}(c + c \rightarrow (cc) + g, p) \quad (2)$$

$$= K_0 \frac{\varepsilon^{nmk}}{\sqrt{2}} M_{ijnk} \left(c + c \rightarrow c + c + g, p_1 = p_2 = \frac{p}{2} \right),$$

where $\varepsilon^{nmk}/\sqrt{2}$ is the color part of the diquark wave function and $K_0 = \sqrt{2/m_{cc}}\Psi_{cc}(0)$, with $m_{cc} = 2m_c$ and $\Psi_{cc}(0)$ being, respectively, the diquark mass and wave function at the origin. As to the spin degrees of freedom of the quarks and the diquark, there is a correspondence between their production amplitudes (the color indices and the common factor K_0 are omitted here):

$$M(c + c \rightarrow (cc) + g, s_z = +1) \quad (3)$$

$$\sim M(c + c \rightarrow c + c + g, s_{1z} = +\frac{1}{2}, s_{2z} = +\frac{1}{2}),$$

$$M(c + c \rightarrow (cc) + g, s_z = -1) \quad (4)$$

$$\sim M(c + c \rightarrow c + c + g, s_{1z} = -\frac{1}{2}, s_{2z} = -\frac{1}{2}),$$

$$M(c + c \rightarrow (cc) + g, s_z = 0) \quad (5)$$

$$\sim \frac{1}{\sqrt{2}} \left[M(c + c \rightarrow c + c + g, \right.$$

$$\left. s_{1z} = +\frac{1}{2}, s_{2z} = -\frac{1}{2} \right)$$

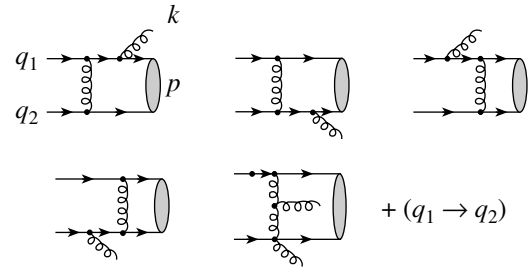


Fig. 2. Diagrams for the subprocess $c + c \rightarrow (cc) + g$.

$$+ M(c + c \rightarrow c + c + g, s_{1z} = -\frac{1}{2}, s_{2z} = +\frac{1}{2}) \Big].$$

Since the wave function of the (cc) diquark is antisymmetric in color and symmetric in the remaining indices, the production of a scalar (cc) diquark is forbidden; that is,

$$M \left(c + c \rightarrow c + c + g, s_{1z} = +\frac{1}{2}, s_{2z} = -\frac{1}{2} \right) \quad (6)$$

$$- M \left(c + c \rightarrow c + c + g, s_{1z} = -\frac{1}{2}, s_{2z} = +\frac{1}{2} \right) = 0.$$

Omitting color factors, we present immediately below the amplitudes $M_1 - M_5$ that correspond to the first five diagrams in Fig. 2 and which describe the partonic process $c + c \rightarrow c + c + g$, where the final c quarks are in the color-antitriplet state. We note that the amplitudes $M_6 - M_{10}$ can be obtained by interchanging the primary quarks ($q_1 \leftrightarrow q_2$) in the amplitudes $M_1 - M_5$ and by reversing their sign, whereby the antisymmetry of the initial state of two identical c -quarks is taken into account. Specifically, we have

$$M_1 = g_s^3 \varepsilon_\mu(k) \bar{U}(p_1) \gamma^\mu (\hat{p}_1 + \hat{k} + m_c) \gamma^\nu U(q_1) \quad (7)$$

$$\times \bar{U}(p_2) \gamma_\nu U(q_2) / ((p_1 + k)^2 - m_c^2)(p_2 - q_2)^2,$$

$$M_2 = g_s^3 \varepsilon_\mu(k) \bar{U}(p_1) \gamma^\nu U(q_1) \bar{U}(p_2) \gamma^\mu (\hat{p}_2 + \hat{k} + m_c) \gamma_\nu U(q_2) / ((p_2 + k)^2 - m_c^2)(q_1 - p_1)^2, \quad (8)$$

$$M_3 = g_s^3 \varepsilon_\mu(k) \bar{U}(p_1) \gamma^\nu (\hat{q}_1 - \hat{k} + m_c) \gamma^\mu U(q_1) \quad (9)$$

$$\times \bar{U}(p_2) \gamma_\nu U(q_2) / ((q_1 - k)^2 - m_c^2)(p_2 - q_2)^2,$$

$$M_4 = g_s^3 \varepsilon_\mu(k) \bar{U}(p_1) \gamma^\nu U(q_1) \bar{U}(p_2) \gamma^\nu (\hat{q}_2 - \hat{k} + m_c) \gamma_\mu U(q_2) / ((q_2 - k)^2 - m_c^2)(q_1 - p_1)^2, \quad (10)$$

$$M_5 = g_s^3 \varepsilon_\mu(k) \bar{U}(p_1) \gamma^\nu U(q_1) \bar{U}(p_2) \gamma^\lambda U(q_2) \quad (11)$$

$$\times G_{\lambda\mu\nu}(p_2 - q_2, k, p_1 - q_1) / (q_1 - p_1)^2 (p_2 - q_2)^2,$$

where $g_s = \sqrt{4\pi\alpha_s}$, $G_{\lambda\mu\nu}(p, k, q) = (p - k)_\nu g_{\lambda\mu} + (k - q)_\lambda g_{\nu\mu} + (q - p)_\mu g_{\nu\lambda}$, and $\varepsilon_\mu(k)$ is the gluon polarization 4-vector. The color factors corresponding

to the diagrams for M_1-M_{10} are given by

$$C_1 = \frac{\varepsilon^{nmk}}{\sqrt{2}}(T_{nl}^c T_{li}^b)(T_{kj}^b), \quad C_6 = \frac{\varepsilon^{nmk}}{\sqrt{2}}(T_{nl}^c T_{lj}^b)(T_{ki}^b), \quad (12)$$

$$C_2 = \frac{\varepsilon^{nmk}}{\sqrt{2}}(T_{ni}^b)(T_{kl}^c T_{lj}^b), \quad C_7 = \frac{\varepsilon^{nmk}}{\sqrt{2}}(T_{nj}^c)(T_{kl}^c T_{li}^b),$$

$$C_3 = \frac{\varepsilon^{nmk}}{\sqrt{2}}(T_{nl}^b T_{li}^c)(T_{kj}^b), \quad C_8 = \frac{\varepsilon^{nmk}}{\sqrt{2}}(T_{nl}^b T_{lj}^c)(T_{ki}^b),$$

$$C_4 = \frac{\varepsilon^{nmk}}{\sqrt{2}}(T_{ni}^b)(T_{kl}^b T_{lj}^c), \quad C_9 = \frac{\varepsilon^{nmk}}{\sqrt{2}}(T_{nj}^b)(T_{kl}^b T_{li}^c),$$

$$C_5 = \frac{i\varepsilon^{nmk}}{\sqrt{2}}(T_{ni}^b)(T_{kj}^a) f^{bac},$$

$$C_{10} = \frac{i\varepsilon^{nmk}}{\sqrt{2}}(T_{nj}^b)(T_{ki}^a) f^{bac}.$$

By using Eqs. (7)–(12), one can straightforwardly verify that, at $p_1 = p_2$, the following relations hold:

$$C_1 M_1 = C_7 M_7, \quad C_2 M_2 = C_6 M_6,$$

$$C_3 M_3 = C_9 M_9,$$

$$C_4 M_4 = C_8 M_8, \quad C_5 M_5 = C_{10} M_{10}.$$

The method that we use to calculate the amplitudes for the production of the bound states of non-relativistic quarks in a pure spin and orbital state is based on the projection-operator formalism [15]. By using the properties of the charge-conjugation matrix $C = i\gamma_2\gamma_0$, we can express the amplitude for quark–quark scattering in terms of the amplitude for antiquark–quark scattering; for example, we have

$$\begin{aligned} M_1 &= g_s^3 \varepsilon_\mu(k) \bar{U}(p_1) \gamma^\mu (\hat{p}_1 + \hat{k} + m_c) \gamma^\nu U(q_1) \quad (13) \\ &\times \bar{U}(p_2) \gamma_\nu U(q_2) / ((p_1 + k)^2 - m_c^2)(p_2 - q_2)^2 \\ &= g_s^3 \varepsilon_\mu(k) \bar{V}(q_1) \gamma^\nu (-\hat{p}_1 - \hat{k} + m_c) \gamma^\mu V(p_1) \\ &\times \bar{U}(p_2) \gamma_\nu U(q_2) / ((p_1 + k)^2 - m_c^2)(p_2 - q_2)^2. \end{aligned}$$

For $p_1 = p_2 = p/2$, it can be shown that

$$\begin{aligned} V(p_1, s_{1z} = -\frac{1}{2}) \bar{U}(p_2, s_{2z} = +\frac{1}{2}) \quad (14) \\ \sim \hat{\varepsilon}(p, s_z = +1)(\hat{p} + m_{cc}), \end{aligned}$$

$$\begin{aligned} V(p_1, s_{1z} = +\frac{1}{2}) \bar{U}(p_2, s_{2z} = -\frac{1}{2}) \\ \sim \hat{\varepsilon}(p, s_z = -1)(\hat{p} + m_{cc}), \end{aligned}$$

$$\begin{aligned} \frac{1}{\sqrt{2}} \left[V(p_1, s_{1z} = -\frac{1}{2}) \bar{U}(p_2, s_{2z} = +\frac{1}{2}) \right. \\ \left. + V(p_1, s_{1z} = +\frac{1}{2}) \bar{U}(p_2, s_{2z} = -\frac{1}{2}) \right] \end{aligned}$$

$$\sim \hat{\varepsilon}(p, s_z = 0)(\hat{p} + m_{cc}),$$

where $\hat{\varepsilon}(p) = \varepsilon^\mu \gamma_\mu$ and $\varepsilon^\mu(p)$ is the diquark polarization 4-vector. Upon the substitution

$$V(p_1) \bar{U}(p_2) \rightarrow K \hat{\varepsilon}(p)(\hat{p} + m_{cc}), \quad (15)$$

where $K = \Psi(0)/2\sqrt{m_{cc}}$, the amplitudes M_i , the color factors C_i apart, describe the production of a (cc) diquark. The squared modulus of the amplitude for the process in question can be written in the form

$$\begin{aligned} |\overline{\mathcal{M}}|^2 &= \frac{1}{72} K^2 \sum_{i,j=1}^{10} \sum_{\text{spin}} M_i(p_1 = p_2 = \frac{p}{2}) \quad (16) \\ &\times M_j^*(p_1 = p_2 = \frac{p}{2}) C_{i,j}, \end{aligned}$$

where the factor $1/72 = (1/2)^2(1/3)^2(1/2)$ takes into account averaging over the spin and color states of the primary quarks and the identity of the final c quarks. Summation over the polarizations of the vector diquark is performed with the aid of the standard formula

$$\sum_{\text{spin}} \varepsilon^\mu(p) \varepsilon^{*\nu}(p) = -g^{\mu\nu} + \frac{p^\mu p^\nu}{m_{cc}^2}. \quad (17)$$

By considering that the fully antisymmetric rank-3 tensor possesses the well-known property

$$\varepsilon_{n'mk'} \varepsilon^{nmk} = \delta_{n'}^n \delta_{k'}^k - \delta_{n'}^k \delta_{k'}^n,$$

it is straightforward to evaluate the following form of the color factors: $C_{i,j} = \sum_{\text{color}} C_i C_j^*$. The results are given in the Appendix A. The quantity

$$F = \sum_{i,j} \sum_{\text{spin}} (M_i M_j^*) \cdot C_{i,j}$$

is computed by using the FeynCalc package for analytic calculations [16]. The analytic expression for F is presented in Appendix B as a function of the standard Mandelstam variables \hat{s} and \hat{t} .

3. RESULTS OF THE CALCULATIONS

In the parton model, the cross section for the production of a (cc) diquark in pp interactions can be represented in the form

$$\begin{aligned} \frac{d\sigma}{dp_\perp} (pp \rightarrow (cc) + X) \quad (18) \\ = 2p_\perp \int_{y_{\min}}^{y_{\max}} dy \int_{x_{1\min}}^1 dx_1 C_p(x_1, Q^2) C_p(x_2, Q^2) \\ \times \frac{|\overline{\mathcal{M}}|^2}{16\pi(s(s - m_{cc}^2))^{1/2}} \frac{1}{x_1 s - \sqrt{s} m_\perp e^y}, \end{aligned}$$

where

$$\begin{aligned} x_2 &= \frac{x_1 \sqrt{s} m_\perp e^{-y} - \frac{3}{2} m_{cc}^2}{x_1 s - \sqrt{s} m_\perp e^y}, \\ x_{1\min} &= \frac{\sqrt{s} m_\perp e^y - \frac{3}{2} m_{cc}^2}{s - \sqrt{s} m_\perp e^{-y}}, \end{aligned}$$

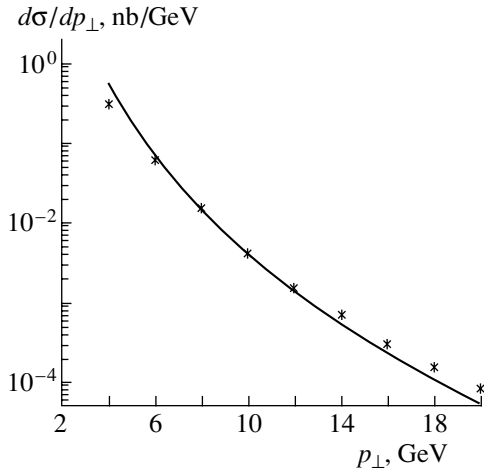


Fig. 3. Cross section for the production of Ξ_{cc} baryons at $\sqrt{s} = 1.8$ TeV and $|y| < 1$. Points (*) represent the results from [10], while the curve corresponds to the results our calculations within the model of intrinsic-charm excitation in colliding protons.

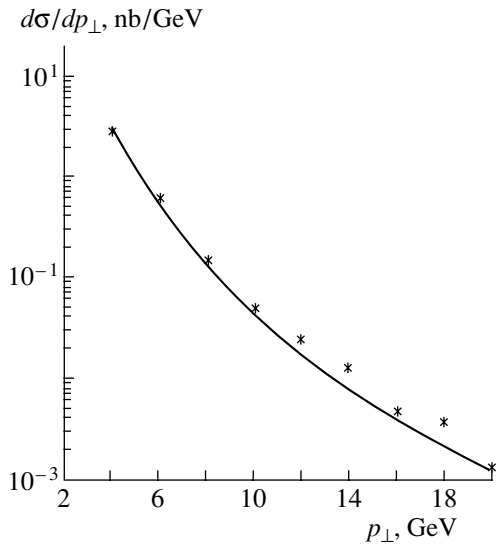


Fig. 4. Cross section for the production of Ξ_{cc} baryons at $\sqrt{s} = 14$ TeV and $|y| < 1$. Points (*) represent the results from [10], while the curve corresponds to the results our calculations within the model of intrinsic-charm excitation in colliding protons.

$C_p(x, Q^2)$ is the distribution of c quarks in the proton at $Q^2 = m_{\perp}^2 = m_{cc}^2 + p_{\perp}^2$; p_{\perp} is the transverse momentum of the (cc) diquark; y is the rapidity of the diquark in the c.m. frame of colliding protons; and s is the square of the total energy in the c.m. frame of colliding protons,

$$\hat{s} = (q_1 + q_2)^2 = x_1 x_2 s + \frac{m_{cc}^2}{2}, \quad (19)$$

$$\begin{aligned} \hat{t} &= (q_1 - p)^2 = \frac{3}{2} m_{cc}^2 - x_1 \sqrt{s} m_{\perp} e^{-y}, \\ \hat{u} &= (q_2 - p)^2 = \frac{3}{2} m_{cc}^2 - x_2 \sqrt{s} m_{\perp} e^y. \end{aligned}$$

Within the nonperturbative-fragmentation model, the cross section for the production of Ξ_{cc} baryons is related to the cross section for the production of (cc) diquarks by the equation

$$\begin{aligned} &\frac{d\sigma}{dp_{\perp}}(pp \rightarrow \Xi_{cc} + X) \quad (20) \\ &= \int_0^1 \frac{dz}{z} \frac{d\sigma}{dp'_{\perp}}(pp \rightarrow (cc)X, p'_{\perp} = \frac{p_{\perp}}{z}) \\ &\quad \times D_{(cc) \rightarrow \Xi_{cc}}(z, Q^2), \end{aligned}$$

where $D_{(cc) \rightarrow \Xi_{cc}}(z, Q^2)$ is the phenomenological fragmentation function normalized to a unit probability for the transition of a (cc) diquark into the final doubly charmed baryon. At $Q_0^2 = m_{cc}^2$, the fragmentation function is chosen in the standard form [17]

$$D_{(cc) \rightarrow \Xi_{cc}}(z, Q_0^2) = \frac{D_0}{z \left(m_{cc}^2 - \frac{m_{\Xi}^2}{z} - \frac{m_q^2}{1-z} \right)^2}, \quad (21)$$

where $m_{\Xi} = m_{cc} + m_q$ is the mass of the Ξ_{cc} baryon, m_q is the mass of the light constituent quark, and D_0 is the normalization constant. At $Q^2 > Q_0^2$, the fragmentation function $D_{(cc) \rightarrow \Xi_{cc}}(z, Q^2)$ can be obtained by numerically solving the QCD evolution equation [18].

Following [10], we performed here our numerical calculations with the parameter values of $m_{cc} = 3.4$ GeV, $\alpha_s = 0.2$, $|\Psi_{cc}(0)|^2 = 0.03$ GeV³, and $m_q = 0.3$ GeV. For the distribution of c quarks in the proton, $C_p(x, Q^2)$, we used the CTEQ5 parametrization [19]. The curves in Figs. 3 and 4 represent the results of our calculations for the p_{\perp} spectra ($|y| < 1$) of the Ξ_{cc} baryons at $\sqrt{s} = 1.8$ and 14 TeV, respectively, while the points correspond to the results obtained in [10] by calculating the contribution of the gluon-gluon production of Ξ_{cc} baryons in the Born approximation. Thus, our calculations demonstrate that, owing to the contribution of the partonic process $c + c \rightarrow (cc) + g$, the observed total cross section for the production of Ξ_{cc} baryons at the Tevatron and LHC colliders can be approximately twice as large as those predicted in [8, 10].

ACKNOWLEDGMENTS

We are grateful to S.P. Baranov, V.V. Kiselev, and A.K. Likhoded for the interest in this study and stimulating discussions.

This work was supported in part by the program Universities of Russia: Basic Research (project no. 02.01.03).

APPENDIX A

$$\begin{aligned}
C_{1,1} &= \frac{7}{9}, & C_{2,3} &= \frac{10}{9}, & C_{3,6} &= -\frac{10}{9}, \\
C_{4,10} &= -2, & C_{6,10} &= 1, \\
C_{1,2} &= \frac{1}{9}, & C_{2,4} &= -\frac{2}{9}, \\
C_{3,7} &= \frac{2}{9}, & C_{5,5} &= 3, & C_{7,7} &= \frac{7}{9}, \\
C_{1,3} &= -\frac{2}{9}, & C_{2,5} &= 1, & C_{3,8} &= \frac{8}{9}, \\
C_{5,6} &= -1, & C_{7,8} &= \frac{10}{9}, \\
C_{1,4} &= \frac{10}{9}, & C_{2,6} &= -\frac{7}{9}, & C_{3,9} &= -\frac{16}{9}, \\
C_{5,7} &= 1, & C_{7,9} &= -\frac{2}{9}, \\
C_{1,5} &= -1, & C_{2,7} &= -\frac{1}{9}, & C_{3,10} &= 2, \\
C_{5,8} &= 2, & C_{7,10} &= 1, \\
C_{1,6} &= -\frac{1}{9}, & C_{2,8} &= \frac{2}{9}, & C_{4,4} &= \frac{16}{9}, \\
C_{5,9} &= -2, & C_{8,8} &= \frac{16}{9}, \\
C_{1,7} &= -\frac{7}{9}, & C_{2,9} &= -\frac{10}{9}, & C_{4,5} &= -2, \\
C_{5,10} &= 3, & C_{8,9} &= -\frac{8}{9}, \\
C_{1,8} &= -\frac{10}{9}, & C_{2,10} &= 1, & C_{4,6} &= \frac{2}{9}, \\
C_{6,6} &= \frac{7}{9}, & C_{8,10} &= 2, \\
C_{1,9} &= \frac{2}{9}, & C_{3,3} &= \frac{16}{9}, & C_{4,7} &= -\frac{10}{9}, \\
C_{6,7} &= \frac{1}{9}, & C_{9,9} &= \frac{16}{9}, \\
C_{1,10} &= -1, & C_{3,4} &= -\frac{8}{9}, & C_{4,8} &= -\frac{16}{9}, \\
C_{6,8} &= -\frac{2}{9}, & C_{9,10} &= -2, \\
C_{2,2} &= \frac{7}{9}, & C_{3,5} &= 2, & C_{4,9} &= \frac{8}{9},
\end{aligned}$$

$$C_{6,9} = \frac{10}{9}, \quad C_{10,10} = 3.$$

APPENDIX B

$$\begin{aligned}
F &= -(4\pi\alpha_s)^3 \frac{512F_N}{9F_D}; \quad (\text{A.1}) \\
F_N &= 26361M^{18} - 6M^{16} \left(20513s + 67472t \right) \\
&\quad + 16M^{14} \left(14621s^2 + 100076st - 86020t^2 \right) \\
&\quad - 16M^{12} \left(14873s^3 + 122408s^2t \right. \\
&\quad \quad \left. - 657280st^2 - 382560t^3 \right) \quad (\text{A.2}) \\
&\quad + 64M^{10} \left(2101s^4 - 658s^3t - 509652s^2t^2 \right. \\
&\quad \quad \left. - 468736st^3 - 170408t^4 \right) \\
&\quad + 65536st^2 \left(s+t \right)^2 \left(9s^4 + 11s^3t + 13s^2t^2 \right. \\
&\quad \quad \quad \left. + 4st^3 + 2t^4 \right) \\
&\quad - 256M^8 \left(120s^5 - 8749s^4t - 201737s^3t^2 \right. \\
&\quad \quad \left. - 255896s^2t^3 - 149332st^4 - 44640t^5 \right) \\
&\quad - 1024M^6 \left(7s^6 + 2180s^5t + 44390s^4t^2 \right. \\
&\quad \quad \left. + 74060s^3t^3 + 57876s^2t^4 + 28176st^5 + 7184t^6 \right) \\
&\quad - 16384M^2t \left(10s^7 + 353s^6t + 924s^5t^2 \right. \\
&\quad \quad \left. + 1151s^4t^3 + 898s^3t^4 + 460s^2t^5 + 160st^6 + 28t^7 \right) \\
&\quad + 4096M^4 \left(s^7 + 235s^6t + 5484s^5t^2 + 11610s^4t^3 \right. \\
&\quad \quad \left. + 11609s^3t^4 + 7368s^2t^5 + 3056st^6 + 672t^7 \right); \\
F_D &= \left(M^2 - s \right)^2 \left(M^2 - 4t \right)^4 \left(5M^2 - 4(s+t) \right)^4. \quad (\text{A.3})
\end{aligned}$$

REFERENCES

1. S. Fleck and J. Richard, *Prog. Theor. Phys.* **82**, 760 (1989).
2. E. Bagan *et al.*, *Z. Phys. C* **64**, 57 (1994).
3. V. V. Kiselev *et al.*, *Phys. Lett. B* **332**, 411 (1994).
4. D. Ebert *et al.*, *Z. Phys. C* **76**, 111 (1997).
5. A. F. Falk *et al.*, *Phys. Rev. D* **49**, 555 (1994).
6. A. P. Martynenko and V. A. Saleev, *Phys. Lett. B* **385**, 297 (1996).
7. V. A. Saleev, *Phys. Lett. B* **426**, 384 (1998).

8. A. V. Berezhnoy *et al.*, *Yad. Fiz.* **59**, 909 (1996) [*Phys. At. Nucl.* **59**, 870 (1996)].
9. S. P. Baranov, *Phys. Rev. D* **54**, 3228 (1996).
10. A. V. Berezhnoy *et al.*, *Phys. Rev. D* **57**, 4385 (1998).
11. V. A. Saleev, *Mod. Phys. Lett. A* **9**, 1083 (1994).
12. A. P. Martynenko and V. A. Saleev, *Phys. Lett. B* **343**, 381 (1995).
13. S. P. Baranov, *Phys. Rev. D* **56**, 3046 (1997).
14. S. J. Brodsky and R. Vogt, *Nucl. Phys. B* **478**, 311 (1996).
15. B. Guberina *et al.*, *Nucl. Phys. B* **174**, 317 (1980).
16. R. Mertig, *The FeynCalc Book* (Mertig Research and Consulting, 1999).
17. C. Peterson, *Phys. Rev. D* **27**, 105 (1983).
18. V. N. Gribov and L. N. Lipatov, *Yad. Fiz.* **15**, 781 (1972) [*Sov. J. Nucl. Phys.* **15**, 438 (1972)]; Yu. A. Dokshitser, *Zh. Éksp. Teor. Fiz.* **73**, 1216 (1977) [*Sov. Phys. JETP* **46**, 641 (1977)]; G. Altarelli and G. Parisi, *Nucl. Phys. B* **126**, 298 (1977).
19. CTEQ Collab. (H. L. Lai *et al.*), hep-ph/9903282.

Translated by A. Isaakyan

Conference on Physics of Fundamental Interactions Theory

Multiargument Renormalization of a Gluon Field*

V. V. Vladimírsky

*Institute of Theoretical and Experimental Physics, Bol'shaya
Cheremushkinskaya ul. 25, Moscow, 117218 Russia*

Received March 7, 2001

Abstract—An extension of traditional renormalization methods that assigns each element of Feynman diagrams an individual evolution parameter is considered. It is shown that conditions necessary for such an extension to be valid are satisfied in quantum gluodynamics. © 2002 MAIK “Nauka/Interperiodica”.

A multiplicative renormalization of operators and coupling constants is widely used in contemporary field theory. In the traditional approach, all renormalization factors Z_k are functions of one scaling variable λ that determines the scaling transformation of all momenta, $p_i \rightarrow \lambda p_i$. It can also be said that the factors Z_k are determined by one momentum scale. However, this mathematically irreproachable formulation does not always fit the physics of problems that the theory has to address. For example, there are two momentum scales in hadron–hadron scattering—one that governs the relative motion of the hadrons involved and the other that characterizes the internal motion of the quarks in a hadron—with the result that, in solving specific problems, one has to invoke additional model assumptions.

As a matter of fact, the application of the renormalization-group approach to gluodynamics must be based on the classical Yang–Mills equations with a running coupling constant that depends on one argument, the evolution parameter t . In the one-loop approximation, t is proportional to the logarithm of the squared momentum, $t \sim \ln(p^2/\Lambda^2)$, where Λ is a new dimensional constant arising from a dimensional transmutation. In dealing with states characterized by a few momentum scales, there arises the question of whether it is possible to construct an effective action that would allow both for the main consequences of renormalization, including asymptotic freedom, and for the dependence of renormalization on all momenta. To tackle this question, we consider a conventional scheme of multiplicative renormalization.

In the Feynman gauge, the original Yang–Mills Lagrangian involving ghost fields has the form

$$L = -\frac{1}{4}F_{\mu\nu}^a F_{\mu\nu}^a - \frac{1}{2}\partial_\mu \Phi^+ D_\mu \Phi - \frac{1}{2}\partial_\lambda V_\lambda D_\mu V_\mu, \quad (1)$$

where

$$F_{\mu\nu}^a = \partial_\mu V_\nu^a - \partial_\nu V_\mu^a + g c^{abc} V_\mu^b V_\nu^c, \quad (2)$$

$$D_\mu^{ac} = \partial_\mu \delta^{ac} + g c^{abc} V_\mu^b \quad (3)$$

[all fields transform according to the adjoint representation of the $SU(3)$ group].

Upon a multiplicative renormalization of the fields, $V_\mu^a \rightarrow Z_3^{1/2} V_\mu^a$, $\Phi^{+a} \rightarrow \bar{Z}_3^{1/2} \Phi^a$, and $\Phi^{+a} \rightarrow \bar{Z}_3^{1/2} \Phi^a$, and of the coupling constant g , the Lagrangian takes the form

$$\begin{aligned} L = & -(1/4Z_3)(\partial_\mu V_\nu^a - \partial_\nu V_\mu^a)^2 \quad (4) \\ & - (g/Z_1)c^{abc}(\partial_\mu V_\nu^a)(V_\mu^b V_\nu^c) \\ & - (g^2/Z_4)c^{abc}c^{ade}V_\mu^b V_\nu^c V_\mu^d V_\nu^e \\ & + (1/\bar{Z}_3)(\partial_\mu \Phi^{+a})(\partial_\mu \Phi^a) \\ & + (g/\bar{Z}_1)c^{abc}(\partial_\mu \Phi^{+a})V_\mu^b \Phi^c \\ & - (1/2Z_3)(\partial_\mu V_\mu^a)^2. \end{aligned}$$

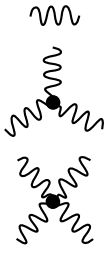
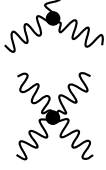

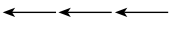
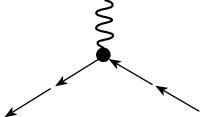

The renormalization factors diverge logarithmically as the parameter of the cutoff in the squared momentum, M^2 , tends to infinity. In the one-loop approximation, they are given by the general formula

$$Z_l - 1 = b_l(g^2/16\pi^2) \ln(M^2/p^2), \quad (5)$$

where p^2 is the square of the spacelike momentum and b_l stands for numerical factors computed in the leading order of perturbation theory. Here, we adopt the traditional notation for the renormalization factors [1]: Z_3 is associated with the renormalization of the vector-field propagator, although it would be more convenient to use $Z_V = \sqrt{Z_3}$ (renormalization of the field), as was proposed in [2].

*This article is a part of the talk “Search for Self-Consistent Vacuum States of a Gluon Field” presented at the Conference on the Physics of Fundamental Interactions (Institute of Theoretical and Experimental Physics, Moscow, November 28, 2000).

Table 1

Z	n_V	n_Φ	n_c	b_l	
Z_3	2	0	0	5	
Z_1	3	0	1	2	
Z_4	4	0	2	-1	
\bar{Z}_3	0	2	0	3/2	
\bar{Z}_1	1	2	1	-3/2	
$\beta(g^2)$	0	0	2	11	

In the case of propagators, renormalization that depends on many arguments presents no special problems because each propagator involves only one momentum variable, which can be used as an argument of the respective renormalization factor. It is somewhat more difficult to renormalize vertices involving two or three independent momenta. This problem can be solved on the basis of the natural assumption that the renormalization factor for a vertex is the product of the renormalization factors for the fields involved and the renormalization factor for the coupling constant, the momentum corresponding to each field and the momentum transfer to the gluon field being taken, respectively, for the argument of the renormalization factor for this field and for the argument of the renormalization factor for the coupling constant. This assignment of the arguments is nothing but a natural assumption, whereas the consistency of the above factorization scheme can be verified by straightforwardly computing all factors Z_l in the one-loop approximation of perturbation theory with allowance for the Ward identities

$$\frac{Z_3}{Z_1} = \frac{\bar{Z}_3}{\bar{Z}_1} = \frac{Z_3^{1/2}}{Z_4^{1/2}}, \quad (6)$$

which reduce the number of independent factors from five to three. At $|Z_l - 1| \ll 1$, it follows from (6) that

$$b_3 - b_1 = \bar{b}_3 - \bar{b}_1 = \frac{1}{2}(b_3 - b_4). \quad (7)$$

For the renormalization of the fields in propagators and vertices to be identical and for the above scheme of the factorization of vertices to be valid, the coefficients b_l must be linear functions of three integer-valued variables: the number of free legs of the vector

field (it is equal to the number of creation or annihilation operators), n_V ; the analogous number for the ghost fields, n_Φ ; and the exponent of the coupling constant in the respective elementary diagram (see Table 1), n_c . For the square of the coupling constant and five renormalized terms in the Lagrangian, these topological features are given in Table 1. The coefficients b_l are evaluated in the one-loop approximation for $SU(3)$ theory in the Feynman gauge. They satisfy the relation

$$b = \frac{5}{2}n_V + \frac{3}{4}n_\Phi - \frac{11}{2}n_c \quad (8)$$

[by definition, $\beta(g^2)$ differs from Z_l by the sign of b_l].

Under some plausible assumptions, a multiplicative formula for the factors Z_l follows from the additive relation between b_l . Since the quark fields are not included in the Lagrangian, the theory involves no dimensional parameters other than Λ_{QCD} that emerges from a dimensional transmutation. In view of this, it may be assumed, as is always done in the renormalization-group approach, that the running coupling constant is the only parameter that determines renormalization of all quantities $Z_l = f_l(g^2)$.

Replacing the renormalization factors of the propagators by the renormalization factors of the fields,

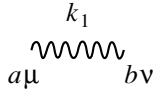
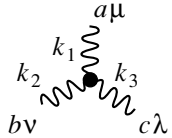
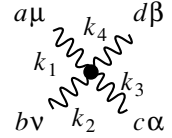
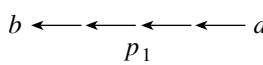
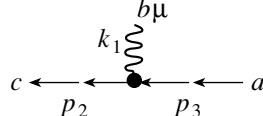
$$Z_3 = Z_V^2, \quad \bar{Z}_3 = Z_\Phi^2, \quad (9)$$

and expressing the coupling constant in terms of the evolution parameter as

$$g^2 = t^{-1}, \quad (10)$$

we can formulate Feynman rules for renormalized diagrams, assigning each renormalization factor an individual momentum argument (see Table 2). Relation

Table 2. Feynman rules for renormalized diagrams

	$-Z_{V1}^2 \frac{i}{k_1^2 + i0} \delta^{ab} \eta_{\mu\nu}$
	$-Z_{V1}^{-1} Z_{V2}^{-1} Z_{V3}^{-1} c^{abc} \left[(k_{1\lambda} \eta_{\mu\nu} - k_{1\nu} \eta_{\mu\lambda}) t_1^{-1/2} + (k_{2\mu} \eta_{\nu\lambda} - k_{2\lambda} \eta_{\mu\nu}) t_2^{-1/2} + (k_{3\nu} \eta_{\mu\lambda} - k_{3\mu} \eta_{\nu\lambda}) t_3^{-1/2} \right]$
	$-i Z_{V1}^{-1} Z_{V2}^{-1} Z_{V3}^{-1} Z_{V4}^{-1} \left[c^{abe} c^{cde} (\eta_{\mu\alpha} \eta_{\nu\beta} - \eta_{\mu\beta} \eta_{\nu\alpha}) t_{12}^{-1} + c^{ace} c^{bde} (\eta_{\mu\nu} \eta_{\alpha\beta} - \eta_{\mu\beta} \eta_{\nu\alpha}) t_{13}^{-1} + c^{ade} c^{cbe} (\eta_{\mu\alpha} \eta_{\nu\beta} - \eta_{\mu\nu} \eta_{\alpha\beta}) t_{14}^{-1} \right]$
	$Z_{\Phi 1}^2 \frac{i \delta^{ab}}{p_1^2 + i0}$
	$Z_{V1}^{-1} Z_{\Phi 2}^{-1} Z_{\Phi 3}^{-1} c^{abc} p_{2\mu} t_1^{-1/2}$

(10) corresponds to the value of $g^2 = 1$ at the normalization point $p^2 = e\Lambda^2$ in the one-loop approximation. Upon adopting this definition, only in the one-loop approximation is there a simple relation between the variable t and the squared momentum,

$$t = \frac{b_l}{16\pi^2} \ln \frac{|p^2|}{\Lambda^2}. \quad (11)$$

With allowance for higher loop corrections, the relation between t and $\ln |p^2|$ becomes more intricate, the renormalization-group method yielding $\ln |p^2|$ as a function of t (or g^2). Despite this, we can treat momentum as a primary argument and g^2 as a function of this argument. We use the following conventions for the arguments: $Z_{V1} = Z_V(p_1^2)$, $t_2 = t(p_2^2)$, $Z_{\Phi 3} = Z_\Phi(p_3^2)$, $t_{12} = t((p_1 + p_2)^2)$, and so on. The momentum-conservation law is taken into account in all formulas. In comparing renormalized Feynman rules with the coefficients b_l presented in Table 1, it should be recalled that, by definition, the renormalized propagator D incorporating quantum corrections is related to the bare propagator $D^{(0)}$ by the formula $D = Z_3 D^{(0)}$; the respective relation between the renormalized and bare vertices has the form $\Gamma = Z_1^{-1} \Gamma^{(0)}$, and there are analogous relations for ghost fields.

If $|Z_l - 1| \ll 1$ (in which case perturbation theory is applicable), the renormalization factors for the fields are related to the evolution parameter by the equations

$$Z_V = t^{5/22}, \quad Z_\Phi = t^{3/44}. \quad (12)$$

In general, the dependence of Z_V and Z_Φ on g^2 and t can be more complicated.

For vacuum diagrams, the field renormalization factors Z_V and Z_Φ cancel, and there remain only the renormalization factors for the coupling constants $g = t^{-1/2}$ and $g^2 = t^{-1}$. The reason is that the renormalization factors Z_3 and \bar{Z}_3 for the propagators appear in the numerator of the integrand, while the renormalization factors Z_1 , Z_4 , and \bar{Z}_1 for the vertices enter into the denominator. The arguments of the vertices are identical to the arguments of the propagators because of the momentum-conservation law. For arbitrary diagrams, one must renormalize only the propagators associated with external lines. Since there are no external lines corresponding to ghost fields, we can always set $Z_\Phi = 1$. Although there are no free gluons in nature, the external lines of gluon fields occur in diagrams that describe the static interaction of colored particles. For this reason, there is the problem of correctly renormalizing external gluon lines, and it must be solved both at high and at low momenta.

The proposed method is rather general—in particular, it can be applied to theories having no rigorous classical limit, including QCD, where the classical approach is inconsistent because of a running coupling constant and also because of the absence of stable solutions with constant fields [3]. In view of the latter, quantum corrections cannot be computed on the basis of the Legendre transformation. Multiargument renormalization does not solve the most

intricate problems of QCD, but it creates preconditions for seeking self-consistent quantum solutions.

REFERENCES

1. M. B. Voloshin and K. A. Ter-Martirosyan, *Theory of Gauge Interactions of Elementary Particles* (Énergoatomizdat, Moscow, 1984).
2. A. N. Vasil'ev, *Quantum Field Renormalization Group in the Theory of Critical Behavior and Stochastic Dynamics* (Peterb. Inst. Yad. Fiz., St. Petersburg, 1998).
3. T. N. Tudron, Phys. Rev. D **22**, 2566 (1980); A. V. Yung, Yad. Fiz. **41**, 1324 (1985) [Sov. J. Nucl. Phys. **41**, 842 (1985)].

Translated by R. Rogalyov

**Conference on Physics of Fundamental Interactions
Theory**

Fluctuations and Correlations of Soft Gluons at the Nonperturbative Stage of Evolution of QCD Jets

V. I. Kuvshinov* and V. A. Shaparau**

Institute of Physics, Belarussian Academy of Sciences, pr. Frantsiask Skorina 70, Minsk, 220072 Belarus

Received March 7, 2001; in final form, August 6, 2001

Abstract—At the nonperturbative stage of jet evolution, fluctuations of soft gluons are less than those for coherent states under specific conditions. This fact suggests that there can arise squeezed gluon states. The angular and rapidity dependences of the gluon correlation function are investigated at this stage of jet evolution. It is shown that these new states of soft gluons can display sub-Poissonian or super-Poissonian statistics corresponding to, respectively, antibunching and bunching of gluons, by analogy with squeezed photon states. © 2002 MAIK “Nauka/Interperiodica”.

1. INTRODUCTION

Many experiments at e^+e^- , $p\bar{p}$, and ep colliders are devoted to the physics of hadron jets, since a detailed investigation of interjet and intrajet features is of great importance for testing perturbative and nonperturbative QCD.

Although the nature of jets is of a universal character, e^+e^- annihilation stands out among hard processes, since jet events admit a straightforward and clear-cut separation in this process. In the reaction $e^+e^- \rightarrow \text{hadrons}$, there are four phases corresponding to various time and space scales. These are (i) the production of a quark–antiquark pairs, $e^+e^- \rightarrow q\bar{q}$; (ii) the emission of gluons and quarks from primary partons (perturbative evolution of the quark–gluon cascade); (iii) the nonperturbative evolution and the hadronization of quarks and gluons; and (iv) the decays of unstable particles.

The second phase of e^+e^- annihilation has been well understood, and rather accurate predictions for it have been obtained within perturbation theory [1, 2]. At the same time, the third phase is usually taken into account either through a constant factor that relates partonic features through hadronic ones (within local parton–hadron duality) or through the application of various phenomenological models of hadronization. As a consequence, theoretical predictions both for intrajet and for interjet features remain unsatisfactory. For example, the width of the distribution in the number of particles according to the predictions of perturbative QCD is larger than the experimental one. The discrepancies between theoretical calculations and

experimental data suggest that, following the perturbative stage, the quark–gluon cascade undergoes nonperturbative evolution, whereupon hadronization effects come into play. New gluon states generated at the nonperturbative stage contribute to various features of jets. For example, such a contribution to the distribution in the number of particles can result in the formation of a sub-Poissonian distribution [3, 4]. Because of this, the distribution width obtained within perturbation theory must become smaller upon taking into account nonperturbative evolution and hadronization effects.

Calculations performed within perturbative QCD show [5, 6] that, at the end of the evolution of the quark–gluon cascade, the distribution in the number of gluons near the completion of the development of a quark–gluon cascade is close to a negative binomial distribution. At the same time, this distribution can be represented as a combination of Poisson distributions [7] and associate a coherent state with each such distribution. Studying a further evolution of gluon states at the nonperturbative stage of jet evolution, we obtain new gluon states that are squeezed states under specific conditions. These states are formed as the result of the nonlinear self-interaction of gluons in a way similar to that in which squeezed photon states arise in quantum optics as the result of interaction with a nonlinear medium [8–11]. Such squeezed states possess some unusual properties—they display a characteristic of factorial and cumulant moments [12] and can have sub-Poissonian or super-Poissonian statistics corresponding to particle antibunching or bunching. At the same time, the distribution in the number of photons in a squeezed state can exhibit oscillations [8, 9], in contrast to Poisson and negative binomial distributions.

* e-mail: kuvshino@dragon.bas-net.by

** e-mail: shaparov@dragon.bas-net.by

2. SQUEEZED GLUON STATES IN A JET

Let us consider the Hamiltonian for gluon-field self-interaction. We have

$$\begin{aligned} V = & -g \int f_{abc} \mathbf{E}_a \cdot \mathbf{A}_b A_c^0 d^3x \quad (1) \\ & + \frac{g}{2} \int f_{abc} \mathbf{B}_a \cdot [\mathbf{A}_b \times \mathbf{A}_c] d^3x \\ & + \frac{g^2}{2} \int (f_{abc} \mathbf{A}_b A_c^0)^2 d^3x \\ & + \frac{g^2}{8} \int (f_{abc} [\mathbf{A}_b \times \mathbf{A}_c])^2 d^3x, \end{aligned}$$

where $\mathbf{E}_a = -\nabla A_a^0 - \partial_0 \mathbf{A}_a$, $\mathbf{B}_a = [\nabla \times \mathbf{A}_a]$, and A_a^μ is the potential of the gluon field ($\mu = \overline{0, 4}$, $a = \overline{1, 8}$). In the momentum representation, this potential for the jet ring of thickness $d\theta$ can be represented in the form [13, 14]

$$\begin{aligned} V = & \frac{k_0^4}{4(2\pi)^3} \left(1 - \frac{q_0^2}{k_0^2}\right)^{3/2} g^2 \pi f_{abc} f_{adf} \quad (2) \\ & \times \left\{ \left(2 - \frac{q_0^2}{k_0^2}\right) [a_{1212}^{bcdf} + a_{1313}^{bcdf}] + a_{2323}^{bcdf} \right. \\ & \quad \left. + \frac{\sin^2 \theta}{2} \left(1 - \frac{q_0^2}{k_0^2}\right) \right\} \\ & \times [2a_{2323}^{bcdf} - a_{1212}^{bcdf} - a_{1313}^{bcdf}] \sin \theta d\theta, \end{aligned}$$

where $a_{lm}^{bcdf} = a_l^{b+} a_m^{c+} a_l^d a_m^f + a_l^{b+} a_m^c a_l^{d+} a_m^f + a_l^b a_m^{c+} a_l^{d+} a_m^f + h.c.$, a_l^b (a_l^{b+}) is the operator annihilating (creating) a gluon of color b and vector component l , q_0^2 is the gluon virtuality at the end of the perturbative cascade, k_0 is the gluon energy at the end of the perturbative cascade, g is the coupling constant, f_{abc} stands for the structure constants of the $SU(3)$ group, and θ is the angle between the jet axis and the momentum \mathbf{k} ($0 \leq \theta \leq \theta_{\max}$, θ_{\max} is half of the opening angle of the jet cone).

The Hamiltonian for gluon self-interaction (2) in the jet ring¹⁾ includes the squares of the creation and annihilation operators for gluons with specific color and vector indices. As is known from quantum mechanics and quantum optics, the presence of such structures in the Hamiltonian and, consequently, in the evolution operator is a necessary condition for

¹⁾By performing integration with respect to θ , it is easy to obtain the gluon Hamiltonian for the whole jet; this Hamiltonian differs from the original one in (2) only by a factor. Hence, all of the further conclusions about the existence of squeezed states remain valid in this case.

emergence of squeezed states [10], since the squeezing operator involves quadratic combinations of the creation and annihilation operators:

$$S(z) = \exp \left\{ \frac{z^*}{2} a^2 - \frac{z}{2} (a^+)^2 \right\}. \quad (3)$$

In order to verify whether the final soft-gluon state vector describes the squeezed state, it is necessary to introduce the phase-sensitive Hermitian operators $(X_l^b)_1 = [a_l^b + a_l^{b+}]/2$ and $(X_l^b)_2 = [a_l^b - a_l^{b+}]/2i$ by analogy with quantum optics and to establish conditions under which the variance of one of them can be less than the variance of a coherent state.

Mathematically, the condition of squeezing is expressed in the form of the inequalities [11]

$$\langle (\Delta(X_l^b)_1)^2 \rangle = \langle N (\Delta(X_l^b)_1)^2 \rangle + \frac{1}{4} < \frac{1}{4}$$

or

$$\langle N (\Delta(X_l^b)_1)^2 \rangle < 0. \quad (4)$$

Here, N is the normal-ordering operator and

$$\begin{aligned} \langle N (\Delta(X_l^b)_1)^2 \rangle = & \frac{1}{4} \left\{ \pm \left[\langle (a_l^b)^2 \rangle - \langle a_l^b \rangle^2 \right] \right. \\ & \pm \left[\langle (a_l^{b+})^2 \rangle - \langle a_l^{b+} \rangle^2 \right] \\ & \left. + 2 \left[\langle a_l^{b+} a_l^b \rangle - \langle a_l^{b+} \rangle \langle a_l^b \rangle \right] \right\}. \quad (5) \end{aligned}$$

The expectation values of the creation and annihilation operators for gluons having specific color and vector components are taken for the vector $\prod_{c=1}^8 \prod_{l=1}^3 |\alpha_l^c(t)\rangle$, which arises as the result of evolution within a small interval of time t :

$$\begin{aligned} \prod_{c=1}^8 \prod_{l=1}^3 |\alpha_l^c(t)\rangle \simeq & \prod_{c=1}^8 \prod_{l=1}^3 |\alpha_l^c(0)\rangle \quad (6) \\ & - itV \prod_{c=1}^8 \prod_{l=1}^3 |\alpha_l^c(0)\rangle. \end{aligned}$$

Here, the time is reckoned from the beginning of the nonperturbative stage, the vector $\prod_{c=1}^8 \prod_{l=1}^3 |\alpha_l^c(0)\rangle$ describes the initial coherent soft-gluon state prepared by the perturbative stage,²⁾ and the potential V is determined by formula (2).

²⁾In general, we are dealing with a superposition of coherent states that have specific weights. However, this circumstance does not lead to qualitative changes in the subsequent conclusions.

Let us consider the specific case where the color index is $b = 1$ and where the vector index l is arbitrary. We then have

$$\begin{aligned} & \left\langle N \left(\Delta(X_l^1)_2 \right)^2 \right\rangle = \pm 4\pi u_2 t d\theta \quad (7) \\ & \times \left\{ (1 + u_1) \sin \theta \left[\delta_{l1} (Z_{33} + Z_{22}) + (1 - \delta_{l1}) Z_{11} \right] \right. \\ & \quad + (1 - \delta_{l1}) \sin \theta \left[\delta_{l2} Z_{33} + \delta_{l3} Z_{22} \right] \\ & \quad + u_1 \sin^3 \theta \left[-\frac{1}{2} \delta_{l1} (Z_{22} + Z_{33}) \right. \\ & \quad \left. \left. + \delta_{l2} \left(Z_{33} - \frac{1}{2} Z_{11} \right) + \delta_{l3} \left(Z_{22} - \frac{1}{2} Z_{11} \right) \right] \right\} \neq 0, \end{aligned}$$

where

$$\begin{aligned} Z_{mn} &= \sum_{k=2}^7 \langle (X_m^k)_1 \rangle \langle (X_n^k)_2 \rangle \quad (m, n = 1, 2, 3), \\ \sum_{k=2}^7 \langle () \rangle &= \sum_{k=2}^3 \langle () \rangle + \frac{1}{4} \sum_{k=4}^7 \langle () \rangle, \\ u_1 &= \left(1 - \frac{q_0^2}{k_0^2} \right), \quad u_2 = \frac{k_0^4}{4(2\pi)^3} \frac{g^2}{2} \sqrt{u_1^3}. \end{aligned}$$

In the final state being considered, fluctuations of one of the squared components of the gluon field, $\Delta(X_l^1)_2$, are weaker than those in the initial coherent state under the following conditions: $\langle (X_m^k)_1 \rangle < 0$ and $\langle (X_m^k)_2 \rangle < 0$ or $\langle (X_m^k)_1 \rangle > 0$ and $\langle (X_m^k)_2 \rangle > 0$ ($k \neq 1, m \neq l$). In this case, we have phase-squeezed gluon states by analogy with quantum optics [9, 10]. If the conditions $\langle (X_m^k)_1 \rangle > 0$ and $\langle (X_m^k)_2 \rangle < 0$ or $\langle (X_m^k)_1 \rangle < 0$ and $\langle (X_m^k)_2 \rangle > 0$ ($k \neq 1, m \neq l$) are satisfied, fluctuations in another squared component of the gluon field, $\Delta(X_l^1)_1$, will be weaker in the final state $\prod_{c=1}^8 \prod_{l=1}^3 |\alpha_l^c(t)\rangle$ than in the coherent state, in which case we arrive at the amplitude-squeezed states (as in the case of photons [9, 10]). Similar conclusions will also be valid for a gluon field featuring other color indices.

Thus, the vector $\prod_{c=1}^8 \prod_{l=1}^3 |\alpha_l^c(t)\rangle$ describes the squeezed state of soft gluons that is produced at the nonperturbative stage of jet evolution within a small interval of time t . Here, the corresponding fluctuations of the squared components of the gluon field will be weaker, under the conditions specified above, than those in the case of the initial coherent state.

3. CORRELATION FUNCTIONS FOR SQUEEZED GLUON STATES

The behavior of a correlation function can provide a criterion of the existence of squeezed gluon states. It is common to define the normalized second-order correlation function as [15]

$$K_{(2)}(\theta_1, \theta_2) = \frac{C_{(2)}(\theta_1, \theta_2)}{\rho_1(\theta_1)\rho_1(\theta_2)}, \quad (8)$$

where $C_{(2)}(\theta_1, \theta_2) = \rho_2(\theta_1, \theta_2) - \rho_1(\theta_1)\rho_1(\theta_2)$, with $\rho_2(\theta_1, \theta_2)$ ($\rho_1(\theta)$) being the two-particle (single-particle) inclusive distribution. For gluons involving color b with a vector component l , we can therefore write

$$K_{l(2)}^b(\theta_1, \theta_2) = \frac{\rho_{l(2)}^b(\theta_1, \theta_2)}{\rho_{l(1)}^b(\theta_1)\rho_{l(1)}^b(\theta_2)} - 1. \quad (9)$$

At the same time, we have

$$\begin{aligned} \int_{\Omega} \rho_1(\theta) d\theta &= \langle n \rangle = \langle a^+ a \rangle \quad (10) \\ &= \int_{\Omega} \langle f(\theta, t) | a^+ a | f(\theta, t) \rangle d\theta, \end{aligned}$$

where $|f(\theta, t)\rangle$ is the final state vector. From (10), we find that the single- and two-particle inclusive distributions can be represented as

$$\begin{aligned} \rho_1(\theta) &= \langle f(\theta, t) | a^+ a | f(\theta, t) \rangle, \quad (11) \\ \rho_2(\theta_1, \theta_2) &= \langle f(\theta_2, t), f(\theta_1, t) | a^+ a^+ a a | f(\theta_1, t), f(\theta_2, t) \rangle. \end{aligned}$$

By taking the expectation values over the vector $\prod_{c=1}^8 \prod_{l=1}^3 |\alpha_l^c(\theta_1, t), \alpha_l^c(\theta_2, t)\rangle$,³⁾ we obtain the explicit form of the normalized second-order correlation function for squeezed gluon states:

$$\begin{aligned} K_{l(2)}^b(\theta_1, \theta_2) &= -M_1(\theta_1, \theta_2) / \{ |\alpha_l^b|^4 \\ &\quad - 2 |\alpha_l^b|^2 M_1(\theta_1, \theta_2) + M_2(\theta_1, \theta_2) \}. \end{aligned} \quad (12)$$

For the color index $b = 1$ and an arbitrary vector component l , we have here

$$\begin{aligned} M_1(\theta_1, \theta_2) &= 24tu_2\pi |\alpha|^2 |\beta|^2 \sin\left(\delta + \frac{\pi}{2}\right) \quad (13) \\ &\times \left\{ (1 + \delta_{l1})(2 + u_1 - \delta_{l1})(\sin\theta_1 + \sin\theta_2) \right. \\ &\quad \left. - \frac{1}{2}u_1(3\delta_{l1} - 1)(\sin^3\theta_1 + \sin^3\theta_2) \right\}, \\ M_2(\theta_1, \theta_2) &= 80tu_2\pi |\alpha|^3 |\beta|^3 \sin\left(\frac{\delta}{2} + \frac{\pi}{4}\right) \quad (14) \end{aligned}$$

³⁾That this vector also describes squeezed gluon states can be proven by verifying the squeezing conditions (4).

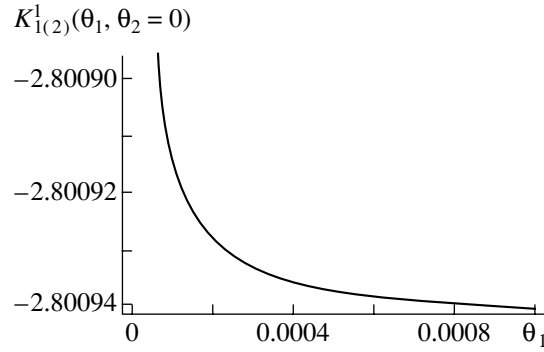


Fig. 1. Angular dependence of the correlation function of squeezed gluons at $|\alpha|^2 = 1$, $|\beta|^2 = 1$, and $\delta = 0$.

$$\times \left\{ (1 + \delta_{l1})(2 + u_1 - \delta_{l1})(\sin \theta_1 + \sin \theta_2) - \frac{1}{2}u_1(3\delta_{l1} - 1)(\sin^3 \theta_1 + \sin^3 \theta_2) \right\}.$$

In deriving these formulas, we assumed, for the sake of simplicity, that $\alpha_l^1 = |\alpha|e^{i\gamma_1}$ for arbitrary l and $\alpha_l^b = |\beta|e^{i\gamma_2}$ for $b \neq 1$ and arbitrary l , where $\gamma_1 - \gamma_2 = \delta/2 + \pi/4$ (the phase δ specifies the direction of squeezing [10]).

Let us perform a comparative analysis of the correlation function (12) for squeezed gluon states and the corresponding function for squeezed photon states, which was thoroughly studied in quantum optics.

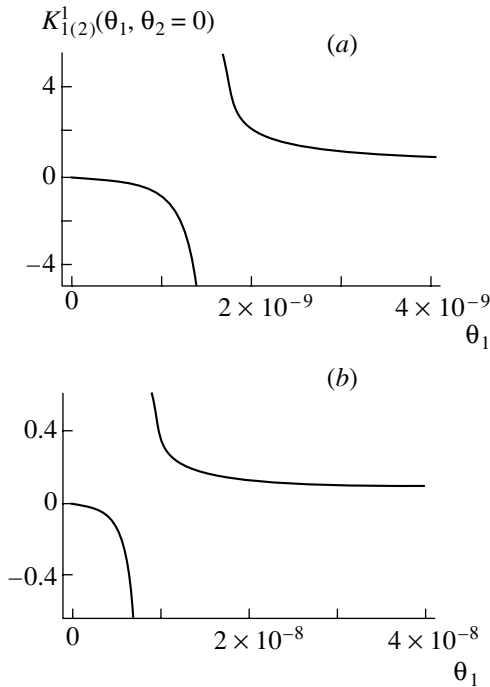


Fig. 2. As in Fig. 1, but for (a) $|\alpha|^2 = 3$ and $|\beta|^2 = 1$ and (b) $|\alpha|^2 = 10$ and $|\beta|^2 = 1$.

In quantum optics, the normalized second-order correlation function is defined as [11]

$$K_{l(2)} = g_l^{(2)} - 1 = \frac{\langle a_l^+ a_l^+ a_l a_l \rangle}{\langle a_l^+ a_l \rangle^2} - 1, \quad (15)$$

where the expectation values are taken over the final state vector at the instant t . If the correlation function being considered is positive, there occurs photon bunching (super-Poissonian distribution); otherwise ($K_{l(2)} < 0$), we have photon antibunching (sub-Poissonian distribution) [9, 11]. For a coherent field obeying Poisson statistics, the normalized second-order correlation function vanishes ($K_{l(2)} = 0$).

For squeezed photon states whose state vector is defined as $|\alpha, z\rangle = S(z)|\alpha\rangle$, the corresponding correlation function has the form (at small values of the squeezing parameter r_l)

$$K_{l(2)} = -\frac{r_l[\alpha_l^2 e^{-i\delta} + (\alpha_l^*)^2 e^{i\delta}]}{|\alpha_l|^4 - 2r_l|\alpha_l|^2[\alpha_l^2 e^{-i\delta} + (\alpha_l^*)^2 e^{i\delta}]}. \quad (16)$$

In contrast to the correlation function for squeezed photon states, $K_{l(2)}$, the corresponding function for the squeezed gluon states, $K_{l(2)}^b(\theta_1, \theta_2)$, includes, as follows from (12), the function $M_2(\theta_1, \theta_2)$, which appears because the Hamiltonian (2) of the gluon field involves a nonlinear combination of the creation and annihilation operators for gluons featuring different color components.

The angular dependence of the correlation function for squeezed gluon states (of color $b = 1$) that are formed at the nonperturbative stage after a lapse of $t = 0.001$ is investigated graphically at the following parameter values: $\theta_2 = 0$, $q_0^2 = 1 \text{ GeV}^2$ (gluon virtuality at the beginning of the nonperturbative stage), $k_0 = \sqrt{s}/2\langle n_{\text{gluon}} \rangle$ (gluon energy in the case of dijet events), $\sqrt{s} = 91 \text{ GeV}$, and $\langle n_{\text{gluon}} \rangle = |\alpha|^2 + 7|\beta|^2$.

If the amplitude $|\alpha|$ of the gluon field being considered is equal to the amplitudes $|\beta|$ of the gluon fields having different colors and vector components,

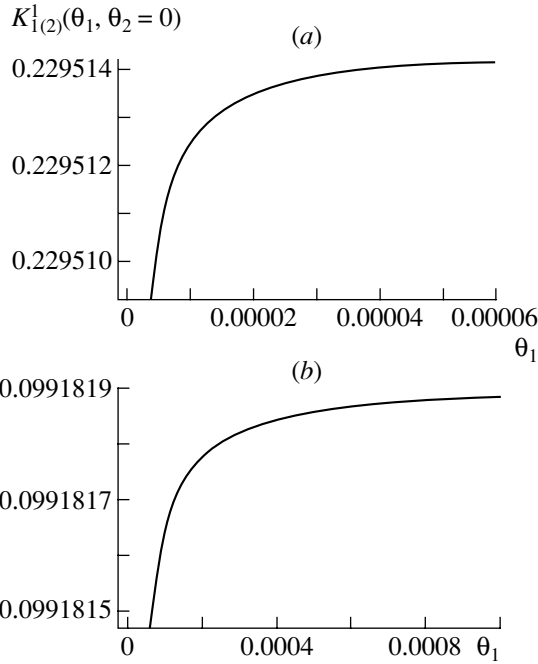


Fig. 3. Angular dependence of the correlation function for antiphased squeezed gluons ($\delta = \pi$): (a) $|\alpha|^2 = 1$ and $|\beta|^2 = 1$ and (b) $|\alpha|^2 = 3$ and $|\beta|^2 = 1$.

the values of the correlation function are negative (Fig. 1), and there occurs the antibunching of gluons with the corresponding sub-Poissonian distribution. In this case, the correlation function tends to a constant as the angle θ_1 increases: $K_{1(2)}^1(\theta_1, \theta_2 = 0) = -2.80094$. This behavior of the angular correlations of the cophased squeezed gluon states ($\delta = 0$) is similar to correlations of the analogous photon states at small values of the squeezing parameter [8].

In the case where the amplitude of the gluon field of specific color—for example, $b = 1$ —begins to dominate in relation to the amplitudes of other color fields ($b \neq 1$), the correlation function involves a singularity (in Fig. 2, $\theta_1 \approx 1.518928762 \times 10^{-9}$ at $|\alpha|^2 = 3$ for $|\beta|^2 = 1$ and $\theta_1 \approx 7.8873381715 \times 10^{-9}$ at $|\alpha|^2 = 10$ for $|\beta|^2 = 1$).

For antiphased squeezed states of soft gluons ($\delta = \pi$), angular correlations fall within the region of positive values, and there occurs gluon bunching with the corresponding super-Poissonian distribution. In this case, the correlation function grows fast at small angles θ_1 and tends to a constant irrespective of the values of the amplitudes $|\alpha|$ and $|\beta|$ (Fig. 3).

By using the transformation

$$\sin \theta = \sqrt{1 - \frac{\tanh^2 y}{u_1}}, \quad (17)$$

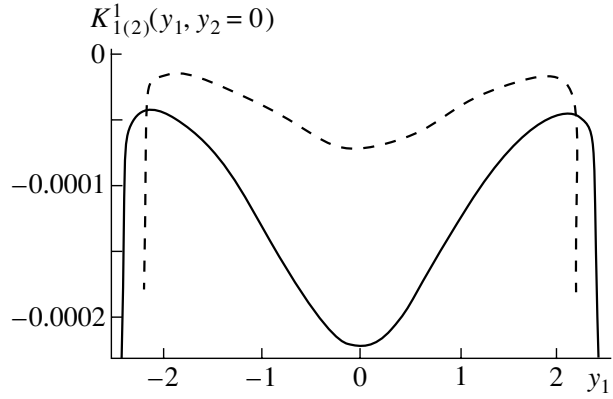


Fig. 4. Squeezed-gluon correlation function versus rapidity at $y_2 = 0$: (solid curve) $|\alpha|^2 = 1$ and $|\beta|^2 = 1$ and (dashed curve) $|\alpha|^2 = 3$ and $|\beta|^2 = 1$.

$$d\theta = -\frac{dy}{\cosh^2 y \sqrt{u_1 - \tanh^2 y}},$$

we can rewrite the correlation function for squeezed gluon states in terms of rapidities; that is,

$$K_{l(2)}^b(\theta_1, \theta_2) = -M_1(y_1, y_2) / \{|\alpha_l^b|^4 - 2|\alpha_l^b|^2 M_1(y_1, y_2) + M_2(y_1, y_2)\}. \quad (18)$$

Rapidity correlations of cophased squeezed gluon states (Fig. 4) fall within the region of negative values and have a minimum at the center ($y_1 = y_2 = 0$) and two peripheral maxima. For $|\alpha| > |\beta|$, the correlation function $K_{l(2)}^b(\theta_1, \theta_2 = 0)$ has a less pronounced minimum at the center. Thus, the behavior of rapidity correlations for the gluon states under investigation suggests that, at the nonperturbative stage of evolution of a QCD jet, there exists the effect of antibunching with the corresponding sub-Poissonian statistics.

4. CONCLUSION

Our investigation of soft-gluon fluctuations at the nonperturbative stage of jet evolution within a small time interval has revealed that squeezed states of gluons are formed under specific conditions. The emergence of such remarkable states becomes possible owing to the self-interaction of gluons having different color indices.

In order to reveal the effect of squeezing for gluons, we have analyzed the behavior of angular and rapidity correlations. Additionally, we have compared our results with the corresponding correlation function for squeezed photon states, which was comprehensively investigated in quantum optics. The form of the normalized correlation function $K_{l(2)}^b(\theta_1, \theta_2)$ for cophased squeezed states suggests the effect of gluon

antibunching if the amplitudes of all gluon fields (featuring various color and vector components) are equal to one another. Such behavior of angular correlations is analogous to the behavior of corresponding correlations of squeezed photon states at small values of the squeezing parameter. At the same time, there is distinction between them: in contrast to the normalized correlation function known in quantum optics, the squeezed-gluon correlation function investigated here displays a singularity if the amplitude for the fixed-color gluon field being studied is much greater than the amplitudes for gluon fields featuring other color components. The correlations of cophased squeezed states suggest the presence of a gluon-antibunching effect; on the contrary, gluon bunching occurs for antiphased squeezed states. Hence, the parton distribution that is prepared by the perturbative stage of jet evolution receives a contribution from the nonperturbative evolution of gluons, this contribution coming in the form of a sub-Poissonian (cophased squeezed states) or a super-Poissonian (antiphased squeezed states) distribution.

Thus, the behavior of two-particle angular and rapidity correlations can serve as one of the criteria of the existence of squeezed gluon states. At the same time, it is obvious that, for a comparison of our results with experimental data, we must take into account the contribution of the perturbative stage of jet evolution and hadronization effects. This can be done by using the Monte Carlo method and will be the subject of our further investigations.

REFERENCES

1. Yu. L. Dokshitzer *et al.*, *Rev. Mod. Phys.* **60**, 373 (1988).
2. Yu. L. Dokshitzer, V. A. Khoze, A. H. Mueller, and S. I. Troyan, *Basics of Perturbative QCD* (Editions Frontières, 1991).
3. V. I. Kuvshinov, *Acta Phys. Pol. B* **10**, 19 (1979).
4. E. S. Kokouline and V. I. Kuvshinov, *Acta Phys. Pol. B* **13**, 553 (1982).
5. E. Malasa and B. Webber, *Nucl. Phys. B* **267**, 702 (1986).
6. I. M. Dremin and R. C. Hwa, *Phys. Rev. D* **49**, 5805 (1994).
7. S. Lupia, W. Ochs, and J. Wosiek, *Nucl. Phys. B* **540**, 405 (1999).
8. O. Hirota, *Squeezed Light* (Elsevier, Amsterdam, 1992).
9. D. F. Walls and G. J. Milburn, *Quantum Optics* (Springer-Verlag, New York, 1995).
10. M. O. Scully and M. S. Zubairy, *Quantum Optics* (Cambridge Univ. Press, 1997).
11. S. Ya. Kilin, *Quantum Optics: Fields and Their Detection* (Nauka i Tekhnika, Minsk, 1990).
12. I. M. Dremin, *Phys. Lett. A* **193**, 209 (1994).
13. V. I. Kuvshinov and V. A. Shaparau, *Acta Phys. Pol. B* **30**, 59 (1999).
14. V. I. Kuvshinov and V. A. Shaporov, *Nonlinear Phenomena in Complex Systems* **3**, 28 (2000).
15. E. A. De Wolf, I. M. Dremin, and W. Kittel, *Phys. Rep.* **270**, 1 (1996).

Translated by A. Isaakyan

**Conference on Physics of Fundamental Interactions
Theory**

QCD Quark Distributions in Mesons*

B. L. Ioffe and A. G. Oganesian*****

*Institute of Theoretical and Experimental Physics, Bol'shaya
Cheremushkinskaya ul. 25, Moscow, 117218 Russia*

Received January 30, 2001

Abstract—The valence-quark distributions in the π meson and in transversely and longitudinally polarized ρ mesons in the region of intermediate x are obtained on the basis of generalized QCD sum rules. Power-law corrections up to $d = 6$ are taken into account. The quark distributions in the pion agree with those found from the data on Drell–Yan processes. A comparison of the results for the π and ρ mesons show that polarization effects are very significant and that the distribution functions do not have $SU(6)$ symmetry.

© 2002 MAIK “Nauka/Interperiodica”.

1. INTRODUCTION

One of the most significant characteristics of the inner structure of hadrons is quark (and gluon) distribution functions. Unfortunately, it is possible to calculate directly only the evolution of the distribution functions in QCD, so that it is necessary to know the distribution functions at some starting normalization point (initial conditions). Usually, these initial conditions are extracted from experimental data by some fitting procedure (see, e.g., [1–4] for the nucleon and [5–7] for the pion). In the case of hadrons, for which there are no experimental results, one should use some models or additional suppositions about the inner structure of hadrons. That is why a determination of quark distribution functions in a model-independent way in QCD sum rules based only on QCD and an operator-product expansion (OPE) seems a very important task, especially for such particles as the ρ meson, where there are no experimental results.

A method for calculating valence-quark distributions at intermediate x was suggested in [8] and developed in [9–11]. The idea was to consider the imaginary part (in the s channel) of a four-point correlation function corresponding to the forward scattering of a virtual photon on a current with the quantum numbers of the hadron of interest. The virtualities of the photon and hadronic current (q^2 and p^2 , respectively) are supposed to be large and negative, $|q^2| \gg |p^2| \gg R_c^{-2}$, where R_c is the confinement radius. The crucial point is that, as was shown in [8, 9], the imaginary part in the s channel [$s = (p + q)^2$]

of the forward-scattering amplitude at intermediate x is dominated by short-distance contributions. Therefore, an operator-product expansion is applicable in this x region. Comparing the dispersion representation of the forward-scattering amplitude in terms of physical states with that calculated in OPE and using the Borel transformation to suppress higher resonance contributions, one can then find quark distribution functions at intermediate x . The fact that this method for calculating the quark distributions in hadrons is invalid at $x \ll 1$ and at $(1 - x) \ll 1$ follows immediately from the theory: OPE diverges in these two domains. Therefore, calculating higher order terms of OPE makes it possible to estimate the numerical values of x up to which the theory is reliable in the domains of small and large x in each particular case. In the way described above, valence-quark distributions in the nucleon were calculated in [9, 11]. However, the accuracy of the calculation was not sufficiently high, especially for d quarks [9]. Moreover, it was found to be impossible to calculate quark distributions in the π and ρ mesons in this way. The reason is that the sum rules in the form used in [9, 11] have a serious drawback.

This drawback comes from the fact that, in the case of a four-point function that corresponds to a forward-scattering amplitude with equal initial and final hadron (h) momenta, the contributions of excited states (h^*) of the form

$$\langle 0 | j^h | h^* \rangle \langle h^* | j^{\text{el}}(x) j^{\text{el}}(0) | h \rangle \langle h | j^h | 0 \rangle \quad (1)$$

are not suppressed directly after the Borel transformation in relation to the matrix element of interest,

$$\langle 0 | j^h | h \rangle \langle h | j^{\text{el}}(x) j^{\text{el}}(0) | h \rangle \langle h | j^h | 0 \rangle, \quad (2)$$

which is proportional to the hadron structure function. In order to eliminate the background matrix

*This article was submitted by the authors in English.

** e-mail: ioffe@vitep5.itep.ru

*** e-mail: armen@vitep5.itep.ru

elements (1), it was necessary to differentiate the sum rule with respect to the Borel parameter. But, as is well known, differentiation of an approximate relation may seriously spoil the accuracy of the results. In QCD sum rules, such a differentiation increases contributions of higher order terms of OPE and excited states in the physical spectrum, so that the sum rules become much poorer or even fail (as for the π and ρ mesons). The situation for the pion is especially bad because a direct calculation shows that the leading term in the OPE (the bare loop diagram) corresponds just to the off-diagonal matrix element, not to the pion structure function.

Recently, a modified method for calculating the hadron structure functions (quark distributions in hadrons) where this problem was eliminated was proposed in [12], and valence-quark distributions in the pion were calculated. This method was also used in [13] to calculate the valence-quark distributions in the ρ meson, separately for longitudinally and for transversely (with respect to the virtual-photon beam) polarized ρ mesons. Since the quark distributions in the ρ meson cannot be measured, a general way to obtain them is to assume $SU(6)$ symmetry, where the π and ρ mesons belong to the same multiplet. Then, the quark distributions in the ρ meson should be similar to those in the pion and are independent of ρ polarization. On the other hand, the pion plays a specific role in the theory—it is a Goldstone boson. From this point of view, it has nothing in common with the ρ meson, and there are no reasons to expect that the quark distributions in the π and the ρ meson are similar. This problem will be resolved, and it will be shown that the valence-quark distributions in the pion and in longitudinally and transversely polarized ρ mesons are quite different.

For the reader's convenience, the method proposed in [12] is briefly surveyed in Section 2. In Section 3, the quark distribution in the pion is considered. In Section 4, the results for the valence-quark distribution in longitudinally and transversely polarized ρ mesons are presented. By using the Regge behavior at small x and quark-counting rules at large x , the first and second moments of the quark distributions are found.

2. DESCRIPTION OF THE METHOD

Let us consider the nonforward four-point correlation function

$$\begin{aligned} & \Pi(p_1, p_2; q, q') \quad (3) \\ &= -i \int d^4x d^4y d^4z \exp(ip_1x + iqy - ip_2z) \\ & \times \langle 0 | T \{ j^h(x), j^{\text{el}}(y), j^{\text{el}}(0), j^h(z) \} | 0 \rangle. \end{aligned}$$

Here, p_1 and p_2 are, respectively, the initial and final momenta carried by the hadronic current j^h ; q and $q' = q + p_1 - p_2$ are, respectively, the initial and final momenta carried by virtual photons; and Lorentz indices are omitted. It will be very important for us to consider unequal p_1 and p_2 and to treat p_1^2 and p_2^2 as two independent variables. However, we may set $q^2 = q'^2$ and $t = (p_1 - p_2)^2 = 0$. The general form of the double dispersion relation (in p_1^2, p_2^2) for the imaginary part of $\Pi(p_1^2, p_2^2, q^2, s)$ in the s channel has the form

$$\begin{aligned} & \text{Im} \Pi(p_1^2, p_2^2, q^2, s) = a(q^2, s) \quad (4) \\ & + \int_0^\infty \frac{\varphi(q^2, s, u)}{u - p_1^2} du + \int_0^\infty \frac{\varphi(q^2, s, u)}{u - p_2^2} du \\ & + \int_0^\infty du_1 \int_0^\infty du_2 \frac{\rho(q^2, s, u_1, u_2)}{(u_1 - p_1^2)(u_2 - p_2^2)}. \end{aligned}$$

The double Borel transformation of (4) in p_1^2 and p_2^2 eliminates the first three terms, and we have

$$\begin{aligned} & \mathcal{B}_{M_1^2} \mathcal{B}_{M_2^2} \text{Im} \Pi(p_1^2, p_2^2, q^2, s) \quad (5) \\ &= \int_0^\infty du_1 \int_0^\infty du_2 \rho(q^2, s, u_1, u_2) \exp \left[-\frac{u_1}{M_1^2} - \frac{u_2}{M_2^2} \right], \end{aligned}$$

where M_1^2 and M_2^2 are the squared Borel masses. The region of integration with respect to u_1 and u_2 may be broken down into four areas:

- I. $u_1 < s_0, \quad u_2 < s_0;$
- II. $u_1 < s_0, \quad u_2 > s_0;$
- III. $u_1 > s_0, \quad u_2 < s_0;$
- IV. $u_1 > s_0, \quad u_2 > s_0.$

Here, s_0 is the continuum threshold in the standard QCD-sum-rule model of the hadronic spectrum featuring one lowest resonance and a continuum. Area I obviously corresponds to the resonance contribution, and the spectral density in this area can be written as

$$\begin{aligned} & \rho(u_1, u_2, x, Q^2) \quad (6) \\ &= g_h^2 \cdot 2\pi F_2(x, Q^2) \delta(u_1 - m_h^2) \delta(u_2 - m_h^2), \end{aligned}$$

where g_h is defined as

$$\langle 0 | j_h | h \rangle = g_h. \quad (7)$$

(For the sake of simplicity, we consider the case of the Lorentz scalar hadronic current. The necessary modifications for the π and ρ mesons will be presented below.) If the structure proportional to $P_\mu P_\nu$ [$P_\mu = (p_1 + p_2)_\mu / 2$] is considered in $\text{Im} \Pi(p_1, p_2, q, q')$, then, in the lowest twist approximation, $F_2(x, Q^2)$ is the structure function we are interested in.

In area IV, where both variables u_1 and u_2 are far from the resonance region, nonperturbative effects can be neglected and, as is usual in sum rules, the spectral function for a hadron state is described by the bare loop spectral function ρ^0 in the same region:

$$\rho(u_1, u_2, x) = \rho^0(u_1, u_2, x). \quad (8)$$

In areas II and III, one of the variables is far from the resonance region, while the other is in the resonance region, and the spectral function in this region is some unknown function $\rho = \psi(u_1, u_2, x)$ that corresponds to $h \rightarrow$ continuum transitions.

Taking all these facts into account, we can recast the physical side of the sum rule (5) into the form

$$\begin{aligned} \hat{B}_1 \hat{B}_2 [\text{Im } \Pi] &= 2\pi F_2(x, Q^2) g_h^2 \quad (9) \\ &\times \exp \left[-m_h^2 \left(\frac{1}{M_1^2} + \frac{1}{M_2^2} \right) \right] \\ &+ \int_0^{s_0} du_1 \int_{s_0}^{\infty} du_2 \psi(u_1, u_2, x) \\ &\times \exp \left[- \left(\frac{u_1}{M_1^2} + \frac{u_2}{M_2^2} \right) \right] \\ &+ \int_{s_0}^{\infty} du_1 \int_0^{s_0} du_2 \psi(u_1, u_2, x) \\ &\times \exp \left[- \left(\frac{u_1}{M_1^2} + \frac{u_2}{M_2^2} \right) \right] \\ &+ \int_{s_0}^{\infty} \int_{s_0}^{\infty} du_1 du_2 \rho^0(u_1, u_2, x) \\ &\times \exp \left[- \left(\frac{u_1}{M_1^2} + \frac{u_2}{M_2^2} \right) \right]. \end{aligned}$$

In what follows, we set $M_1^2 = M_2^2 \equiv 2M^2$. (As was shown in [14], the values of the Borel parameters M_1^2 and M_2^2 in the double Borel transformation are about twice as large as those in the ordinary ones.)

One of the advantages of this method is that, after the double Borel transformation, the unknown contributions of areas II and III [the second and the third term in (9)] are exponentially suppressed. Therefore—and we would like to emphasize this—we do not need any additional artificial procedure such as differentiation with respect to the Borel mass. Using standard duality arguments, we estimate the contribution of the entire nonresonance region (i.e., areas II, III, IV) as the contribution of the bare loop in the same region and require their value to be small (less than 30%). Finally, equating the physical and QCD representations of Π , one can write the sum rules

$$\text{Im } \Pi_{\text{QCD}}^0 + \text{Power-law correction} \quad (10)$$

$$\begin{aligned} &= 2\pi F_2(x, Q^2) g_h^2 \exp \left[-m_h^2 \left(\frac{1}{M_1^2} + \frac{1}{M_2^2} \right) \right], \\ \text{Im } \Pi_{\text{QCD}}^0 &= \int_0^{s_0} \int_0^{s_0} \rho^0(u_1, u_2, x) \times \exp \left[-\frac{u_1 + u_2}{2M^2} \right]. \end{aligned}$$

It is worth mentioning that, if we considered the forward-scattering amplitude from the very beginning (i.e., if we set $p_1 = p_2 = p$ as in [8–11]) and performed the Borel transformation in p^2 , then the contributions of the second and third terms in (4), in contrast to (9), would not be suppressed in relation to the lowest resonance contribution we are interested in. They correspond to the off-diagonal transition matrix elements discussed in the Introduction.

3. QUARK DISTRIBUTIONS IN THE PION

To find the pion structure function by the method described in the preceding section, one should consider the imaginary part of four-point correlation function (3) with two axial and two electromagnetic currents. Since $\bar{d}(x) = u(x)$, it is sufficient to find the distribution of the valence u quark in π^+ . The most suitable choice of the axial current is

$$j_{\mu 5} = \bar{u} \gamma_\mu \gamma_5 d. \quad (11)$$

In order to find the u -quark distribution, the electromagnetic current is chosen as the u -quark current with a unit charge,

$$j_\mu^{\text{el}} = \bar{u} \gamma_\mu u. \quad (12)$$

The most convenient tensor structure, which is chosen to construct the sum rule, is a structure proportional to $P_\mu P_\nu P_\lambda P_\sigma / \nu$. The reasons are the following. As is known, the results of QCD-sum-rule calculations are more reliable if the invariant amplitude at the kinematical structure with the maximal dimension is used. Different $p_1 \neq p_2$ values are important for us only in denominators, where they allow one to separate the terms in dispersion relations. In numerators, one may restrict the consideration to the terms proportional to the 4-vector P_μ and ignore the terms of order r_μ [$r = (p_1 - p_2)$, $r^2 = 0$]. Then, the factor $P_\mu P_\nu$ provides the contribution of the structure function $F_2(x)$, and the factor $P_\lambda P_\sigma$ corresponds to the contribution of zero-spin states. (The factor $1/\nu$ is the scaling factor: $w_2 = F_2/\nu$.)

Let us use the notation

$$\Pi_{\mu\nu\lambda\sigma} = (P_\mu P_\nu P_\lambda P_\sigma / \nu) \Pi(p_1^2, p_2^2, x) + \dots \quad (13)$$

Then, the bare loop contribution to $\text{Im } \Pi(p_1^2, p_2^2, x)$ is [12]

$$\text{Im } \Pi(p_1^2, p_2^2, x) = \frac{3}{\pi} x^2 (1-x) \int_0^\infty du_1 \quad (14)$$

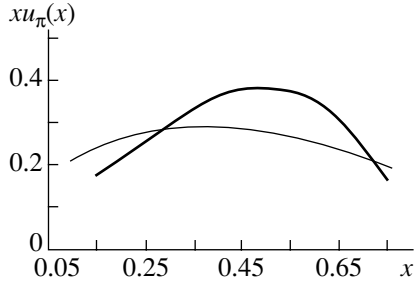


Fig. 1. Quark distribution in the pion (thick curve) and fit from [6] (thin curve).

$$\times \int_0^\infty du_2 \frac{\delta(u_1 - u_2)}{(u_1 - p_1^2)(u_2 - p_2^2)}.$$

The matrix element of the axial current between the vacuum and pion states is well known,

$$\langle 0 | j_{\mu 5} | \pi \rangle = i p_\mu f_\pi, \quad (15)$$

where $f_\pi = 131$ MeV. The use of Eqs. (10), (14), and (15) leads to the sum rule for the valence u -quark distribution in the pion in the bare loop approximation [12],

$$u_\pi(x) = \frac{3}{2\pi^2} \frac{M^2}{f_\pi^2} x(1-x) \quad (16)$$

$$\times (1 - e^{-s_0/M^2}) e^{m_\pi^2/M^2},$$

where s_0 is the continuum threshold. In [12], the following corrections to Eq. (16) were taken into account:

(i) leading-order (LO) perturbative corrections proportional to $\ln(Q^2/\mu^2)$, where μ^2 is the normalization point (in what follows, the normalization point will be chosen to be equal to the Borel parameter $\mu^2 = M^2$);

(ii) power-law corrections—that is, higher order terms of OPE (among them, the dimension-4 correction, which is proportional to the gluon condensate

$$\langle 0 | (\alpha_s/\pi) G_{\mu\nu}^n G_{\mu\nu}^n | 0 \rangle,$$

was first taken into account, but it was found that the gluon-condensate contribution to the sum rule vanishes after double borelization). There are two types of vacuum expectation values of dimension 6, one involving only gluonic fields,

$$\frac{g_s}{\pi} \alpha_s f^{abc} \langle 0 | G_{\mu\nu}^a G_{\nu\lambda}^b G_{\lambda\mu}^c | 0 \rangle, \quad (17)$$

and the other proportional to the 4-quark operators

$$\langle 0 | \bar{\psi} \Gamma \psi \cdot \bar{\psi} \Gamma \psi | 0 \rangle. \quad (18)$$

It was shown in [12] that terms of the first type cancel in the sum rule and that only terms of the second type survive. For the latter, one may use the factorization

hypothesis, which reduces all terms of this type to the square of the quark condensate.

The following comment is in order here. As was mentioned in the Introduction, the present approach is invalid at small and large x . No-loop 4-quark condensate contributions are proportional to $\delta(1-x)$ and, being outside of the applicability domain of the approach, cannot be taken into account. In the same way, the diagrams that can be considered as radiative corrections to those proportional to $\delta(1-x)$ must also be omitted.

All dimension-6 power-law corrections to the sum rule were calculated in [12], and the final result is given by (the pion mass is neglected)

$$x u_\pi(x) = \frac{3}{2\pi^2} \frac{M^2}{f_\pi^2} x^2 (1-x) \quad (19)$$

$$\times \left[\left(1 + \frac{\alpha_s(M^2) \ln(Q_0^2/M^2)}{3\pi} \right) \times \left(\frac{1 + 4x \ln(1-x)}{x} - \frac{2(1-2x) \ln x}{1-x} \right) \right]$$

$$\times (1 - e^{-s_0/M^2}) - \frac{4\pi\alpha_s(M^2) \cdot 4\pi\alpha_s a^2}{2^6 \cdot 3^7 (2\pi)^4 M^6} \frac{\omega(x)}{x^3 (1-x)^3},$$

where $\omega(x)$ is the fourth-degree polynomial in x ,

$$a = -(2\pi)^2 \langle 0 | \bar{\psi} \psi | 0 \rangle, \quad (20)$$

$$\omega(x) = \left(-5784x^4 - 1140x^3 - 20196x^2 \right. \quad (21)$$

$$\left. + 20628x - 8292 \right) \ln 2 + 4740x^4 + 8847x^3$$

$$+ 2066x^2 - 2553x + 1416.$$

The function $u_\pi(x)$ can be used as an initial condition at $Q^2 = Q_0^2$ for a solution to the QCD evolution equations (Dokshitzer–Gribov–Lipatov–Altarelli–Parisi equations).¹⁾

In the numerical calculations, we choose the effective $\Lambda_{\text{QCD}}^{\text{LO}} = 200$ MeV, $Q_0^2 = 2$ GeV², and $\alpha_s a^2(1 \text{ GeV}^2) = 0.13 \text{ GeV}^6$ [12]. The continuum threshold was varied in the interval $0.8 < s_0 < 1.2 \text{ GeV}^2$, and it was found that the results depend only slightly on its variation. The analysis of the sum rule (19) shows that it is fulfilled in the region $0.15 < x < 0.7$; the power-law corrections are less than 30%, and the continuum contribution is small (<25%). The stability in the dependence on the Borel mass parameter M^2 in the region $0.4 < M^2 < 0.6 \text{ GeV}^2$

¹⁾There was a misprint in Eq. (40) in [12]: instead of $\alpha_s(M^2)$, $\alpha_s(Q_0^2)$ was in the last term. In the numerical calculations, the correct value $\alpha_s(M^2)$ was taken.

is good. The result of our calculation of the valence quark distribution $xu_\pi(x, Q_0^2)$ in the pion is shown in Fig. 1.

Let us assume that $u_\pi(x) \sim 1/\sqrt{x}$ at small $x \lesssim 0.15$ according to the Regge behavior and that $u_\pi(x) \sim (1-x)^2$ at large $x \gtrsim 0.7$ according to quark-counting rules. Then, matching these functions with (19), one may find the numerical values of the first and the second moment of the u -quark distribution,

$$\mathcal{M}_1 = \int_0^1 u_\pi(x) dx \approx 0.84 \text{ (0.85)}, \quad (22)$$

$$\mathcal{M}_2 = \int_0^1 xu_\pi(x) dx \approx 0.21 \text{ (0.23)}, \quad (23)$$

where the values in parentheses correspond to behavior $u_\pi(x) \sim (1-x)$ at large x . The results depend only slightly on the points of matching (not more than 5% when the lower and the upper matching point are varied in the regions 0.15–0.2 and 0.65–0.75, respectively). The moment \mathcal{M}_1 has the meaning of the number of u quarks in π^+ , and it should be $\mathcal{M}_1 = 1$. The deviation of (22) from unity characterizes the accuracy of our calculation. The moment \mathcal{M}_2 has the meaning of the pion-momentum fraction carried by the valence u quark. Therefore, the valence u and \bar{d} quarks carry about 40% of the total momentum. In Fig. 1, we also plot the valence u -quark distribution found in [6] by fitting the data on the production of $\mu^+\mu^-$ and e^+e^- pairs in pion-nucleon collisions (Drell–Yan process). In a comparison with the distribution found here, it should be recalled that the accuracy of our curve is on order of 10–20% (see discussion in Section 5). The u -quark distribution found from experimental data is also not free from uncertainties (at least 10–20%, see [5–7]). In particular, what is measured in the Drell–Yan process is the quark fragmentation function into the pion defined at $q^2 > 0$. In order to get the quark distribution in the pion defined at $q^2 < 0$, the analytic continuation is used, which may introduce some uncertainties, especially at the low normalization point, e.g., $Q_0^2 = 2 \text{ GeV}^2$, to which the data in Fig. 1 refer. For all these reasons, we consider the agreement of the two curves as being good. The valence u -quark distribution in the pion was calculated recently in the instanton model [15]. At intermediate x , the values of $xu_\pi(x)$ found in [15] are about 20% higher than our results. Recently, the pion valence quark momentum distribution was also calculated [16] by using a model based on the Dyson–Schwinger equation. Our results are in reasonable agreement with the results of [16]. One should note that, within this accuracy, our

estimate (23) of the second moments of the quark distribution in the π meson is in good agreement with that obtained in [16]. Our estimation (23) of the second moment of the valence quark distribution can also be compared with calculation of the second moment of the total (valence plus sea) quark distribution in the pion [17]. The value obtained in [17] is 0.6 for the total momentum carried by all quarks (valence plus sea) with the accuracy of about 10%. Considering that sea quarks are usually supposed to carry 15% of the total momentum, one can find from the result of [17] that the second moment of one-valence-quark distribution should be about 20–22%, which is in good agreement with our result (23). The quark distribution in the pion was also calculated in [18] by using sum rules with nonlocal condensates. Unfortunately, it is impossible to perform a comparison directly because the quark distribution was calculated in [18] only at a very low normalization point. But, comparing his result with different models, the author of that study arrived at the conclusion that the result is in agreement with experimental data at $Q^2 = 20 \text{ GeV}^2$ within the accuracy about 20%. Our result is also close to an experimental fit, so that we can believe that our results are in agreement with those of [18].

4. QUARK DISTRIBUTIONS IN THE ρ MESON

Let us calculate the valence u -quark distribution in the ρ^+ meson. The choice of hadronic current is evident:

$$j_\mu^\rho = \bar{u}\gamma_\mu d. \quad (24)$$

The matrix element $\langle \rho^+ | j_\mu^\rho | 0 \rangle$ is given by

$$\langle \rho^+ | j_\mu^\rho | 0 \rangle = \frac{m_\rho^2}{g_\rho} e_\mu, \quad (25)$$

where m_ρ is the ρ -meson mass, g_ρ is the ρ – γ coupling constant, $g_\rho^2/4\pi = 1.27$, and e_μ is the ρ -meson polarization vector. We consider the coordinate system where a collision of the ρ meson with momentum p and a virtual photon with a momentum q proceeds along the z axis. Averaging over ρ polarizations is given by the formulas

$$e_\mu^L e_\nu^L = \left(q_\mu - \frac{\nu p_\mu}{m_\rho^2} \right) \left(q_\nu - \frac{\nu p_\nu}{m_\rho^2} \right) \frac{m_\rho^2}{\nu^2 - q^2 m_\rho^2} \quad (26)$$

for longitudinally polarized ρ and

$$\begin{aligned} \sum_{r=1,2} e_\mu^r e_\nu^r &= - \left(\delta_{\mu\nu} - \frac{p_\mu p_\nu}{m_\rho^2} \right) \quad (27) \\ &- \frac{m_\rho^2}{\nu^2 - q^2 m_\rho^2} \left(q_\mu - \frac{\nu p_\mu}{m_\rho^2} \right) \left(q_\nu - \frac{\nu p_\nu}{m_\rho^2} \right) \end{aligned}$$

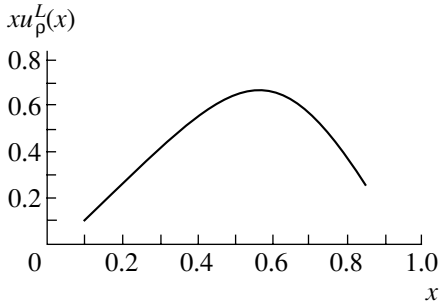


Fig. 2. Quark distribution function for longitudinally polarized ρ meson.

for transversely polarized ρ .

The imaginary part $W_{\mu\nu\lambda\sigma}$ of the amplitude for forward $\rho\gamma$ scattering (before multiplication by ρ polarizations) satisfies the equations $W_{\mu\nu\lambda\sigma}q_\mu = W_{\mu\nu\lambda\sigma}q_\nu = W_{\mu\nu\lambda\sigma}p_\lambda = W_{\mu\nu\lambda\sigma}p_\sigma = 0$, which follow from current conservation. The indices μ and ν refer to the initial and the final photon; λ and σ refer to the initial and the final ρ meson. The general form of $W_{\mu\nu\lambda\sigma}$ is

$$\begin{aligned}
 W_{\mu\nu\lambda\sigma} = & \left[\left(\delta_{\mu\nu} - \frac{q_\mu q_\nu}{q^2} \right) \left(\delta_{\lambda\sigma} - \frac{p_\lambda p_\sigma}{m_\rho^2} \right) A \right. \\
 & - \left(\delta_{\mu\nu} - \frac{q_\mu q_\nu}{q^2} \right) \left(q_\lambda - \frac{\nu p_\lambda}{m_\rho^2} \right) \left(q_\sigma - \frac{\nu p_\sigma}{m_\rho^2} \right) B \\
 & - \left(p_\mu - \frac{\nu q_\mu}{q^2} \right) \left(p_\nu - \frac{\nu q_\nu}{q^2} \right) \left(\delta_{\lambda\sigma} - \frac{p_\lambda p_\sigma}{m_\rho^2} \right) C \\
 & + \left(p_\mu - \frac{\nu q_\mu}{q^2} \right) \left(p_\nu - \frac{\nu q_\nu}{q^2} \right) \\
 & \left. \times \left(q_\lambda - \frac{\nu p_\lambda}{m_\rho^2} \right) \left(q_\sigma - \frac{\nu p_\sigma}{m_\rho^2} \right) D \right], \quad (28)
 \end{aligned}$$

where A , B , C , and D are invariant functions. By averaging Eq. (28) over polarizations for longitudinal and transverse ρ mesons, one can find that the structure function $F_2(x)$ proportional to $p_\mu p_\nu$ is given in the scaling limit ($\nu^2 \gg |q^2| m_\rho^2$) by the contribution of the invariants $C + (\nu^2/m_\rho^2)D$ and C in the cases of a longitudinally polarized and a transversely polarized ρ meson, respectively. This means that, in the forward-scattering amplitude $W_{\mu\nu\lambda\sigma}$ (28), one must separate the structure proportional to $p_\mu p_\nu p_\lambda p_\sigma$ in the first case and the structure proportional to $p_\mu p_\nu \delta_{\lambda\sigma}$ in the second case.

Let us now consider the nonforward four-point correlation function

$$\Pi_{\mu\nu\lambda\sigma}(p_1, p_2; q, q') \quad (29)$$

$$\begin{aligned}
 &= -i \int d^4x d^4y d^4z \exp(ip_1x + iqy - ip_2z) \\
 &\quad \times \langle 0 | T \{ j_\lambda^\rho(x), j_\mu^{\text{el}}(y), j_\nu^{\text{el}}(0), j_\sigma^\rho(z) \} | 0 \rangle,
 \end{aligned}$$

where the currents $j_\mu^{\text{el}}(x)$ and $j_\lambda^\rho(x)$ are given by Eqs. (12) and (25). It is evident from the consideration that, in the nonforward amplitude, the most suitable tensor structure for determining the u -quark distribution in the longitudinal ρ meson is that proportional to $P_\mu P_\nu P_\sigma P_\lambda$, while the u -quark distribution in the transverse ρ meson can be found by considering the invariant function at the structure $(-P_\mu P_\nu \delta_{\lambda\sigma})$.

In the case of a longitudinal ρ meson, the tensor structure that is separated is the same as that in the case of the pion. Since bare loop contributions for vector and axial hadronic currents are equal at $m_q = 0$, the only difference from the pion case is the normalization. It can be shown that the u -quark distribution in the longitudinal ρ meson can be found from Eq. (19) by means of the substitutions $m_\pi \rightarrow m_\rho$ and $f_\pi \rightarrow m_\rho/g_\rho$; therefore, one can easily write down sum rules for this distribution,

$$\begin{aligned}
 x u_\rho^L(x) = & \frac{3}{2\pi^2} M^2 \frac{g_\rho^2}{m_\rho^2} e^{m_\rho^2/M^2} x^2 (1-x) \quad (30) \\
 & \times \left[\left(1 + \frac{\alpha_s(M^2) \ln(Q_0^2/M^2)}{3\pi} \right) \right. \\
 & \times \left(\frac{1 + 4x \ln(1-x)}{x} - \frac{2(1-2x) \ln x}{1-x} \right) \\
 & \left. \times \left(1 - e^{-s_0/M^2} \right) - \frac{\alpha_s(M^2) \alpha_s a^2}{2^6 \cdot 3^7 \pi^2 M^6} \frac{\omega(x)}{x^3 (1-x)^3} \right],
 \end{aligned}$$

where a and $\omega(x)$ are given by Eqs. (20) and (21), respectively. The sum rules for $u_\rho^L(x)$ are satisfied in a wide x region: $0.1 < x < 0.85$. The dependence on the Borel mass M^2 is weak in the entire range of x , with the exception of $x \leq 0.15$ and $x \geq 0.7$. As was discussed in the Introduction, the reason for a stronger M^2 dependence at small and large x is related to the fact that our approach is invalid at small x and at x close to unity. This is manifested in the blowup of the dimension-6 correction for $x \rightarrow 0$ and $x \rightarrow 1$ in Eq. (30). Thus, the applicability domain of the sum rule can be found immediately from the sum rule. Figure 2 presents $x u_\rho^L(x)$ as a function of x . The values $M^2 = 1 \text{ GeV}^2$, $s_0 = 1.5 \text{ GeV}^2$, and $Q_0^2 = 4 \text{ GeV}^2$ were chosen, while the parameters $\Lambda_{\text{QCD}}^{\text{LO}}$ and $\alpha_s a^2$ were identical to those in the calculation of $x u_\pi(x)$.

Let us now consider the case of a transversely polarized ρ meson—i.e., the term proportional to the

structure $P_\mu P_\nu \delta_{\lambda\sigma}$. We first calculate the bare loop contribution

$$\begin{aligned} \text{Im } \Pi_{\mu\nu\lambda\sigma}^{(0)} &\equiv -\frac{1}{\nu} P_\mu P_\nu \delta_{\lambda\sigma} \text{Im } \Pi_T^{(0)} \quad (31) \\ &= -\frac{3}{2\pi} \frac{1}{\nu} P_\mu P_\nu \delta_{\lambda\sigma} x \left[\frac{1}{2} - x(1-x) \right] \\ &\quad \times \int \frac{udu}{(u-p_1^2)(u-p_2^2)}. \end{aligned}$$

After borelization, we get the following expression for the u -quark distribution in a transversely polarized ρ meson in bare loop approximation:

$$\begin{aligned} u_\rho^T(x) &= \frac{3}{(2\pi)^2} g_\rho^2 \frac{M^4}{m_\rho^4} e^{m_\rho^2/M^2} \quad (32) \\ &\quad \times E_1\left(\frac{s_0}{M^2}\right) \left[\frac{1}{2} - x(1-x) \right], \end{aligned}$$

where

$$E_1(z) = 1 - (1+z)e^{-z}. \quad (33)$$

We take into account the leading-order perturbative correction proportional to $\ln(Q^2/\mu^2)$ and choose $Q^2 = Q_0^2$ for the point where we calculate our sum rules. The result is (the second term in the square brackets corresponds to the perturbative correction)

$$\begin{aligned} u^T(x) &= \frac{3}{8\pi^2} \frac{g_\rho^2}{m_\rho^4} \times e^{m_\rho^2/M^2} M^4 E_1\left(\frac{s_0}{M^2}\right) \varphi_0(x) \quad (34) \\ &\quad \times \left[1 + \frac{\alpha_s(\mu^2) \ln(Q_0^2/\mu^2)}{3\pi} \left((4x-1)/\varphi_0(x) \right. \right. \\ &\quad \left. \left. + 4 \ln(1-x) - \frac{2(1-2x+4x^2) \ln x}{\varphi_0(x)} \right) \right], \end{aligned}$$

where

$$\varphi_0(x) = 1 - 2x(1-x). \quad (35)$$

We now consider the power-law-correction contribution to the sum rules. The power-law correction of the lowest dimension is proportional to the gluon condensate $\langle G_{\mu\nu}^q G_{\mu\nu}^q \rangle$ with $d = 4$. The $\langle G_{\mu\nu}^q G_{\mu\nu}^q \rangle$ correction was calculated in the standard way in the Fock–Schwinger gauge $x_\mu A_\mu = 0$ [19].

The quark propagator $iS(x, y) = \langle \psi(x)\psi(y) \rangle$ in the external field A_μ has the well-known form [9, 14, 19, 20]. In contrast to the pion case, the $\langle G_{\mu\nu}^a G_{\mu\nu}^a \rangle$ correction for transversely polarized ρ (ρ_T) does not vanish,

$$\text{Im } \Pi_T^{(d=4)} \cdot M^4 = -\frac{\pi}{8x} \langle 0 | \frac{\alpha_s}{\pi} G_{\mu\nu}^2 | 0 \rangle. \quad (36)$$

Hereafter, all diagrams are calculated by using the REDUCE system for analytic calculations. Let us

recall that we should not take into account nonloop diagrams and diagrams that can be treated as their evolution. There are a large number of loop diagrams for the $d = 6$ correction. It is convenient to divide them into two types and discuss these types separately. Type-I diagrams are those in which only the interaction with the external gluon field is taken into account, while type-II diagrams are those in which the expansion of the quark field is also taken into account.

Let us briefly discuss the special features of a calculation of diagrams of these two types. Type-I diagrams are obviously proportional to $\langle 0 | g^3 f^{abc} G_{\mu\nu}^a G_{\alpha\beta}^b G_{\rho\sigma}^c | 0 \rangle$, $\langle 0 | D_\rho G_{\mu\nu}^a D_\tau G_{\alpha\beta}^a | 0 \rangle$, and $\langle 0 | G_{\mu\nu}^a D_\rho D_\tau G_{\alpha\beta}^a | 0 \rangle$.

One can demonstrate [21] that these tensor structures are proportional to two vacuum expectation values,

$$\langle 0 | g^2 j_\mu^2 | 0 \rangle \quad \text{and} \quad \langle 0 | g^3 G_{\mu\nu}^a G_{\nu\rho}^b G_{\rho\mu}^c f^{abc} | 0 \rangle.$$

By using the factorization hypothesis, the first of them $\langle 0 | g^2 j_\mu^2 | 0 \rangle$ can easily be reduced to $\langle g\bar{\psi}\psi \rangle^2$, which is well known:

$$\langle 0 | g^2 j_\mu^2 | 0 \rangle = -(4/3) [\langle 0 | g\bar{\psi}\psi | 0 \rangle]^2. \quad (37)$$

But $\langle 0 | g^3 G_{\mu\nu}^a G_{\nu\rho}^b G_{\rho\mu}^c f^{abc} | 0 \rangle$ is not well known; there are only some estimates based on the instanton model [22, 23]. In contrast to the π - and ρ_L -meson cases, the terms proportional to $\langle 0 | g^3 f^{abc} G_{\mu\nu}^a G_{\nu\rho}^b G_{\rho\mu}^c | 0 \rangle$ do not cancel for ρ_T , and one should estimate it. The estimation based on the instanton model [22] gives

$$-\langle g^3 f^{abc} G_{\mu\nu}^a G_{\nu\rho}^b G_{\rho\mu}^c \rangle = \frac{48\pi^2}{5} \frac{1}{\rho_c^2} \langle 0 | \frac{\alpha_s}{\pi} G_{\mu\nu}^2 | 0 \rangle, \quad (38)$$

where ρ_c is the effective instanton radius.

Among type-II diagrams, only those in which the interaction with the vacuum occurs inside the loop are considered. Such diagrams cannot be treated as the evolution of any nonloop diagrams and are pure power-law corrections of dimension 6.

The total number of $d = 6$ diagrams is enormous, about 500. Collecting the results, we finally obtain the following sum rules for the valence u -quark distribution in a transversely polarized ρ meson:

$$\begin{aligned} x u_\rho^T(x) &= \frac{3}{8\pi^2} g_\rho^2 e^{m_\rho^2/M^2} \quad (39) \\ &\quad \times \frac{M^4}{m_\rho^4} x \left\{ \varphi_0(x) E_1\left(\frac{s_0}{M^2}\right) \right. \\ &\quad \left. \times \left[1 + \frac{\alpha_s(M^2) \ln(Q_0^2/M^2)}{3\pi} \left(\frac{4x-1}{\varphi_0(x)} \right) \right] \right\} \end{aligned}$$

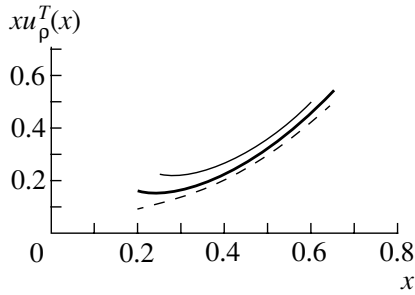


Fig. 3. Quark distribution function for transversely polarized ρ meson at three choices of instanton radius, $\rho_c = 0.4, 0.5,$ and 0.6 fm (curves from top to bottom, respectively).

$$\left. \begin{aligned} &+ 4 \ln(1-x) - \frac{2(1-2x+4x^2) \ln x}{\varphi_0(x)} \Bigg] \\ &- \frac{\pi^2}{6} \frac{\langle 0 | (\alpha_s/\pi) G^2 | 0 \rangle}{M^4 x^2} + \frac{1}{2^8 \cdot 3^5 M^6 x^3 (1-x)^3} \\ &\quad \times \langle 0 | g^3 f^{abc} G_{\mu\nu}^a G_{\nu\lambda}^b G_{\lambda\mu}^c | 0 \rangle \xi(x) \\ &\quad + \frac{\alpha_s(M^2) \alpha_s a^2}{2^5 \cdot 3^8 \pi^2 M^6 x^3 (1-x)^3} \chi(x) \Bigg\}, \end{aligned} \right\}$$

where

$$\xi(x) = -1639 + 8039x - 15233x^2 + 10055x^3 - 624x^4 - 974x^5, \quad (40)$$

$$\begin{aligned} \chi(x) &= 8513 - 41692x + 64589x^2 - 60154x^3 + 99948x^4 - 112516x^5 + 45792x^6 \\ &+ (-180 - 8604x + 53532x^2 - 75492x^3 - 28872x^4 + 109296x^5 - 55440x^6) \ln 2. \end{aligned} \quad (41)$$

The standard value of the gluon condensate, $\langle 0 | (\alpha_s/\pi) G^2 | 0 \rangle = 0.012 \text{ GeV}^4$, was taken in numerical calculations. Equation (38) was used, and the effective instanton radius ρ_c was chosen to be $\rho_c = 0.5$ fm. This value is between the estimates in [22] ($\rho_c = 1$ fm) and [23] ($\rho_c = 0.33$ fm). (In [24], it was argued that the liquid–gas instanton model overestimates higher order gluon condensates, and larger values of ρ_c than in [23] should be used in order to correct this effect.) The Borel mass dependence of $xu_\rho^T(x)$ in the interval $0.2 < x < 0.65$ is weak for $0.8 < M^2 < 1.2 \text{ GeV}^2$. Figure 3 shows $xu_\rho^T(x)$ at $M^2 = 1 \text{ GeV}^2$ and $Q_0^2 = 4 \text{ GeV}^2$. The dashed and thin solid curves demonstrate the influence of the variation in ρ_c on the final result: the lower curve corresponds to $\rho_c = 0.6$ fm, and the upper corresponds to $\rho_c = 0.4$ fm. Our results are reliable for $0.25 < x < 0.65$, where $d = 4$ and $d = 6$ power-law

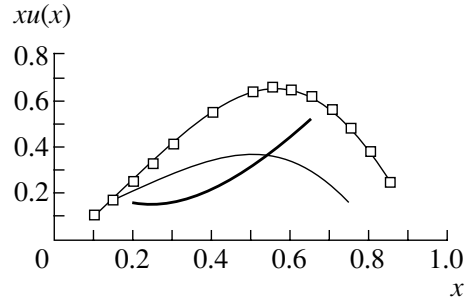


Fig. 4. Valence u -quark distributions for (thick curve) ρ^T , (curve with squares) ρ^L , and (thin curve) the π meson.

corrections each comprise less than 30% of the bare loop contribution. (The contributions $\langle 0 | (\alpha_s/\pi) G^2 | 0 \rangle$ and $\langle 0 | g^3 f^{abc} G_{\mu\nu}^a G_{\nu\lambda}^b G_{\lambda\mu}^c | 0 \rangle$ are of opposite signs and compensate one another; the $\alpha_s(M^2) \alpha_s a^2$ contribution is negligible.) At $\rho_c = 0.4$ fm, the applicability domain shrinks to $0.3 < x < 0.6$.

The moments of the quark distributions in a longitudinally polarized ρ meson are calculated in the same way as this was done in the case of the pion: by matching with the Regge behavior $u(x) \sim 1/\sqrt{x}$ at low x and with the quark-counting rule $u(x) \sim (1-x)^2$ at large x . The matching points were chosen to be $x = 0.10$ at low x and $x = 0.80$ at large x . The numerical values of the moments for a longitudinally polarized ρ are

$$\begin{aligned} \mathcal{M}_1^L &= \int_0^1 dx u_\rho^L(x) = 1.06 (1.05), \quad (42) \\ \mathcal{M}_2^L &= \int_0^1 x dx u_\rho^L(x) = 0.39 (0.37). \end{aligned}$$

The values of the moments obtained by assuming that $u_\rho(x) \sim (1-x)$ at large x are given in parentheses.

A reliable calculation of moments for the case of transversely polarized ρ meson is impossible because of a narrow applicability domain in x and expected double-hump shape of the u -quark distribution, which does not allow soft matching with the expected behavior $xu_\rho^T(x)$ at small and large x .

Let us now discuss the case of an unpolarized ρ meson. In this case, the quark distribution function $u(x)$ is

$$u_\rho(x) = (u_\rho^L(x) + 2u_\rho^T(x))/3$$

and we can determine $u(x)$ only in the region where sum rules for $u_\rho^L(x)$ and $u_\rho^T(x)$ are satisfied, i.e., in the range $0.2 \lesssim x \leq 0.65$. In this region, $u_\rho(x)$ is found

to be very close to $u_\pi(x)$ [the difference in the whole range of x is no more than 10–15%].

5. SUMMARY AND DISCUSSION

Figure 4 gives a comparison of the valence u -quark distributions in the pion and in a longitudinally and a transversely polarized ρ meson. The shapes of the curves are quite different, especially of $xu_\rho^T(x)$ in relation to $xu_\rho^L(x)$ and $xu_\pi(x)$. Strongly different are also the second moments in the pion and a longitudinal ρ meson: the momentum fraction carried by valence quarks and antiquarks $-(u + \bar{d})$ in the longitudinal ρ meson is about 0.8, while, in the pion, it is much less—about 0.4–0.5. All these distinctions are very large and many times larger than the estimated uncertainties of our results. In the case of the u -quark distribution in the pion, the main source of them is the value of the renormalization-invariant quantity $(2\pi)^4 \alpha_s \langle 0 | \bar{\psi} \psi | 0 \rangle^2$. In our calculations, we took it to be equal to 0.13 GeV^6 . In fact, however, it is uncertain by a factor of 2. (The determination of this quantity in [25] from τ -decay data indicates that it may be two times larger.) The perturbative corrections also introduce some uncertainties, especially at large x ($x > 0.6$), where the LO correction, which is taken into account, is large. The estimation of both effects shows that they may result in a 10–20% variation (an increase at $x < 0.3$ and a decrease at $x > 0.3$) of $xu_\pi(x)$.

For the u -quark distribution in a longitudinally polarized ρ meson, the uncertainties in $\alpha_s \langle 0 | \bar{\psi} \psi | 0 \rangle^2$ do not play any role because of higher M^2 values, so that the expected accuracy is even better.

The accuracy of our results for the u -quark distribution in a transversely polarized ρ meson is lower because of a large role of the contributions of the $d = 4$ and $d = 6$ gluon condensates. For the latter, as was discussed before, there are only estimations based on the instanton model, and the gluon condensate $\langle 0 | (\alpha_s/\pi) G^2 | 0 \rangle$ is also uncertain by a factor 1.5. Estimations show that they result in no more than 30–40% variation in xu_ρ^T at $x \approx 0.3$ –0.4 but in much less variation at $x \approx 0.5$ –0.6. (The leading-order perturbative corrections are no more than 20% at small x and negligible at large x .) Thus, one can see that the difference obtained in the quark distribution in the pion and a longitudinally and a transversely polarized ρ meson is in fact much larger than any possible uncertainties of the results.

In summary, the main physical conclusions are the following:

(1) The quark distributions in the pion and in the ρ meson have little in common. The specific properties

of the pion as a Goldstone boson manifest themselves in the quark distributions, which are different from those in the ρ meson. $SU(6)$ symmetry may probably take place for the static properties of π and ρ but not for their internal structure. We cannot explain why the u -quark distributions in the pion and the unpolarized ρ meson at $0.2 < x < 0.65$ are close to each other—we do not know whether this is purely accidental or whether there are some deep reasons for this.

(2) The quark distribution in a polarized ρ meson is significantly dependent on polarization: it is single-humped and double-humped for a longitudinally and for a transversely polarized ρ meson, respectively.

ACKNOWLEDGMENTS

This study was supported in part by Award no. RP2-2247 of the U.S. Civilian Research and Development Foundation for the Independent States of the Former Soviet Union (CRDF) and by the Russian Foundation for Basic Research (project no. 00-02-17808).

REFERENCES

1. A. M. Cooper-Sarkar, R. C. E. Davenish, and A. De Roeck, *Int. J. Mod. Phys. A* **13**, 3385 (1998).
2. CTEQ Collab. (H. L. Lai *et al.*), *Eur. Phys. J. C* **12**, 375 (2000).
3. A. D. Martin, R. G. Roberts, W. J. Stirling, and R. S. Thorne, *Eur. Phys. J. C* **4**, 463 (1998).
4. M. Glück, E. Reya, and A. Vogt, *Eur. Phys. J. C* **5**, 461 (1998).
5. P. Aurenche *et al.*, *Phys. Lett. B* **233**, 517 (1989).
6. M. Glück, E. Reya, and A. Vogt, *Z. Phys. C* **53**, 651 (1992).
7. P. J. Sutton, A. D. Martin, B. G. Roberts, and W. J. Stirling, *Phys. Rev. D* **45**, 2349 (1992).
8. B. L. Ioffe, *Pis'ma Zh. Éksp. Teor. Fiz.* **42**, 266 (1985) [*JETP Lett.* **42**, 327 (1985)].
9. V. M. Belyaev and B. L. Ioffe, *Nucl. Phys. B* **310**, 548 (1988).
10. A. S. Gorsky, B. L. Ioffe, A. Yu. Khodjamirian, and A. G. Oganesian, *Z. Phys. C* **44**, 523 (1989).
11. B. L. Ioffe and A. Yu. Khodjamirian, *Phys. Rev. D* **51**, 3373 (1995).
12. B. L. Ioffe and A. G. Oganesian, *Eur. Phys. J. C* **13**, 485 (2000).
13. B. L. Ioffe and A. G. Oganesian, hep-ph/0011348.
14. B. L. Ioffe and A. V. Smilga, *Nucl. Phys. B* **216**, 373 (1983).
15. A. E. Dorokhov and L. Tomio, *Phys. Rev. D* **62**, 014016 (2000).
16. M. B. Hecht, C. D. Roberts, and S. M. Schmidt, *Phys. Lett. B* **495**, 136 (2000).
17. V. M. Belyaev and B. Yu. Block, *Yad. Fiz.* **43**, 706 (1986) [*Sov. J. Nucl. Phys.* **43**, 450 (1986)].
18. A. Belitsky, *Phys. Lett. B* **386**, 359 (1996).

19. A. V. Smilga, *Yad. Fiz.* **35**, 473 (1982) [*Sov. J. Nucl. Phys.* **35**, 271 (1982)].
20. V. A. Novikov, M. A. Shifman, A. I. Vainshtein, and V. I. Zakharov, *Fortschr. Phys.* **32**, 585 (1984).
21. S. N. Nikolaev and A. V. Radyushkin, *Nucl. Phys. B* **213**, 189 (1983).
22. V. A. Novikov, M. A. Shifman, A. I. Vainshtein, and V. I. Zakharov, *Phys. Lett. B* **86B**, 347 (1979).
23. T. Schäfer and E. V. Shuryak, *Rev. Mod. Phys.* **70**, 323 (1998).
24. B. L. Ioffe and A. V. Samsonov, *Yad. Fiz.* **63**, 1527 (2000) [*Phys. At. Nucl.* **63**, 1448 (2000)].
25. B. L. Ioffe and K. N. Zyblyuk, hep-ph/0010089.

**Conference on Physics of Fundamental Interactions
Theory**

Suppression of Charmonium Production in PbPb Collisions at 158 GeV/c per Nucleon and Quark–Gluon Deconfinement

**A. B. Kurepin
(NA50 Collaboration)**

*Institute for Nuclear Research, Russian Academy of Sciences,
ul. Shestidesyatletiya Oktyabrya 7a, Moscow, 117312 Russia*

Received March 21, 2001

Abstract—An anomalous suppression of the charmonium yield in central collisions was observed in studying charmonium production in collisions of Pb nuclei accelerated to a momentum of 158 GeV/c per nucleon with Pb target nuclei. It is shown that, in peripheral collisions, the ratio of the cross section for J/ψ production to the cross section for the Drell–Yan process decreases exponentially (as in the case of collisions of lighter nuclei) owing to the ordinary absorption of J/ψ in nuclear matter. The observed threshold effect of the anomalous suppression of charmonium production agrees well with the predictions based on the assumption of Debye color screening in the formation of quark–gluon plasma.

© 2002 MAIK “Nauka/Interperiodica”.

1. INTRODUCTION

Although the existence of quark–gluon deconfinement (quark–gluon plasma) is predicted by nonperturbative lattice calculations [1], only an experimental observation of this new state of matter can yield actual values of the critical temperature and energy density at the phase-transition point. In recent years, a few experiments performed at CERN have given some pieces of evidence for the formation of quark–gluon plasma in high-energy nucleus–nucleus collisions.

In particular, the NA50 experiment studied the production of charmonium in collisions of Pb nuclei. Previously, the NA38 experiment explored the analogous process in collisions of protons and light nuclei. A physical motivation of the NA50 experiment is based on the predictions in [2] that, because of Debye color screening, charmonium production in heavy-ion collisions can be suppressed upon the formation of quark–gluon plasma.

A comparison of the cross sections for charmonium production for various incident and target nuclei can be performed with respect to the cross sections for the Drell–Yan process. It was found that the production cross sections for the Drell–Yan process are proportional to the product of the atomic numbers of colliding nuclei, $\sigma(\text{DY}) \sim A \cdot B$. Therefore, we can assume that, in nucleus–nucleus collisions, the Drell–Yan process proceeds through nucleon–nucleon interactions.

In the NA38 experiment, which employed incident light ions, the cross section for J/ψ production was found to deviate from the $A \cdot B$ dependence. A decrease in the cross section for charmonium production in relation to the cross section for the Drell–Yan process for heavier colliding nuclei is explained by the nuclear absorption of $c\bar{c}$ pairs prior to the formation of a J/ψ state [3]. This ordinary nuclear absorption can be described by one parameter, the absorption cross section $\sigma_{\text{abs}} = 6.1 \pm 0.7$ mb [4].

The first experimental data on PbPb collisions—they were obtained in the NA50 experiment of 1995—revealed a strong deviation from a smooth behavior. The cross section for J/ψ production in PbPb collisions appeared to be 0.77 ± 0.04 times smaller than the value obtained by extrapolating, with allowance for conventional nuclear absorption, the experimental cross sections for J/ψ production that were obtained for pA to SU interactions. This effect of the anomalous suppression of charmonium production becomes more pronounced with increasing degree of collision centrality. The degree of collision centrality was determined by measuring the transverse energy E_T of neutral particles with an electromagnetic calorimeter. Collisions characterized by the highest degree of collision centrality correspond to $E_T > 100$ GeV.

The new measurements of 1996 with a thicker target yielded vaster statistics [5]. This made it possible to explore in detail the dependence on the degree of collision centrality; as a result, it was shown that, at

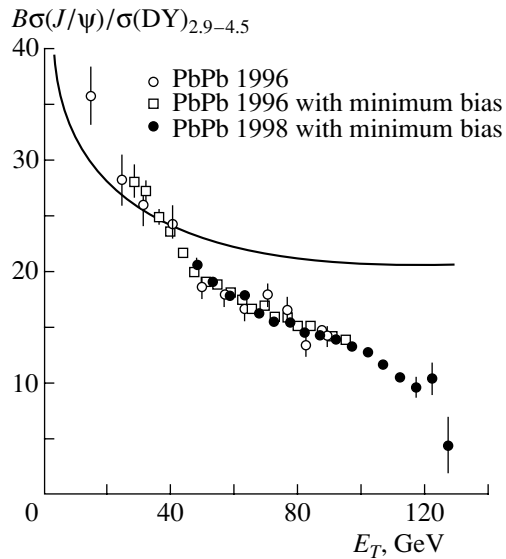


Fig. 1. Ratio $\sigma(J/\psi)/\sigma(DY)$ as a function of transverse energy according to a standard analysis and an analysis that employs data for the minimum bias from the measurement runs of 1996 and 1998.

low E_T —that is, for the most peripheral collisions—the behavior of the cross sections for charmonium production can be described by ordinary nuclear absorption. The statistical accuracy of experimental results was significantly improved by using, for the collision-centrality-independent process of the production of the minimum number of particles in the interaction, the so-called minimum-bias process to calculate the cross sections for the Drell–Yan process.

Events characterized by the minimum bias were analyzed by using the procedure that was comprehensively described in [5]. The data obtained in 1996 show that the cross section for J/ψ production in PbPb collisions changes abruptly at $E_T \sim 40$ GeV, which corresponds to the impact-parameter value of about 8 fm.

However, a comparison of the high- E_T results obtained with a thin target in 1995 and with a thick target in 1996 reveals that the cross section is larger somewhat in the last case. This deviation can be explained by the rescatterings of spectator fragments in the thick target, whose thickness is approximately 30% of the interaction length. Some secondary peripheral collisions characterized by large cross-section ratios can be erroneously taken to be more central collisions free from rescatterings. For this reason, an experiment with a single thin target was performed in 1998 [6]. The results comply well with the data of 1995. The review of data on charmonium suppression in PbPb collisions from three measurement runs is presented in this study.

2. EXPERIMENTAL FACILITY

In the NA50 facility, a dimuon spectrometer equipped with tracking wire chambers, scintillation trigger detectors, a carbon hadron absorber, and a BeO preabsorber [5] was used as the main detector. Additional detectors, including a beam hodoscope and a number of antihalo detectors, were constructed that are able to operate under the conditions of a high radiation, a high multiplicity, and a high background level generated by incident Pb ions. Quartz detectors arranged near each target were used to determine the interaction vertex in a segmented target and to reject events in which a spectator fragment induces a secondary interaction in one of the subsequent targets.

The degree of collision centrality was determined with the aid of an electromagnetic calorimeter, a multiplicity detector, and a zero-angle calorimeter (in all, by three detectors).

In extracting the yields of J/ψ and ψ' from the invariant-mass distribution of dimuons, we also took into account the contributions of other processes, including open-charm production and the Drell–Yan process, as well as the contribution of the combinatorial background that arises because of the uncorrelated decays of pions and kaons.

3. RESULTS OF THE NA50 EXPERIMENT

The main objective of the NA50 experiment was to investigate in detail the anomalous suppression of charmonium production in PbPb collisions. The results obtained to date are presented in Figs. 1–3. In Fig. 1, the ratio of the measured cross sections for J/ψ production and the Drell–Yan process is shown as a function of the transverse energy E_T of neutral particles. The results that are characterized by vaster statistics and which were processed with a larger number of bins in E_T were obtained in calculating the cross sections for the Drell–Yan process from the minimum-bias data within the Glauber model. These ratios were normalized to the results of the standard analysis in the E_T interval between 50 and 75 GeV. The data of 1996 for the most central events having $E_T > 100$ GeV were distorted because of the effect of rescatterings in the thick target and are therefore not shown in the figure. The solid curve in Fig. 1 corresponds to the extrapolation of the exponential obtained by the NA38 and NA51 collaborations [7] for ordinary nuclear absorption in proton–nucleus collisions and in collisions of lighter nuclei. While data for $E_T < 40$ GeV are consistent with the exponential dependence within the errors, near $E_T = 40$ GeV and above this value, there is a sharp deviation from the solid curve. An anomalous threshold effect that was first discovered by the NA50 collaboration in 1995,

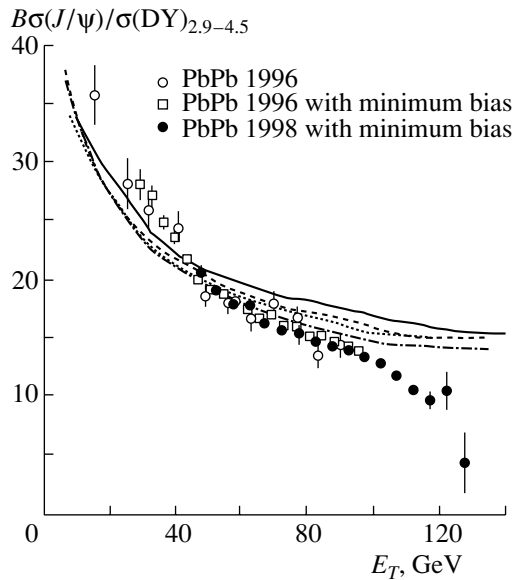


Fig. 2. Experimental data along with the results of theoretical calculations within some hadron models taking into account subsequent rescatterings. The data were borrowed from (solid curve) [8], (dashed curve) [9], (dotted curve) [10], and (dash-dotted curve) [11].

was confirmed by the data of 1996 that have vaster statistics. Hadron models of subsequent rescatterings cannot reproduce this threshold effect arising as the degree of collision centrality becomes higher.

The data from the measurement run of 1998 are shown in Fig. 1 for $E_T > 40$ GeV, since, for lower values of E_T , the contribution of rescatterings of Pb ions in air is rather high. In a dedicated investigation with an empty target, it was found that this contribution is negligibly small for $E_T > 40$ GeV. In the data of 1998, there appeared a second drop in the suppression of J/ψ production at $E_T \sim 90$ GeV.

As the degree of collision centrality becomes higher, the ratio of the cross section for J/ψ production to the cross section for the Drell–Yan process decreases abruptly. Such a dependence on the degree of collision centrality is at odds with the predictions of some hadron models that assume the absorption of charmonium in its interactions with accompanying hadrons [8–11]. All these models predict a smooth reduction of the cross section for J/ψ production in going over from pp to PbPb collisions, with the suppression of the J/ψ yield showing a tendency toward saturation for the most central interactions. A comparison of experimental data with the results of the calculations is illustrated in Fig. 2.

According to the measurements in the NA50 experiment, the dependence of the anomalous suppression of the J/ψ yield on the degree of collision centrality corresponds to the behavior expected in the

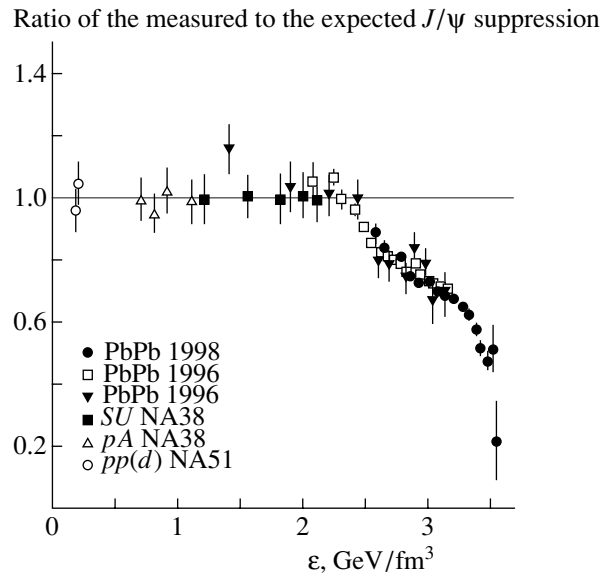


Fig. 3. Measured J/ψ -meson yield normalized to the yield value expected under the assumption that ordinary nuclear absorption is the only source of yield suppression. The results are presented versus the energy density ϵ achieved in a collision event.

case of quark–gluon deconfinement and the formation of quark–gluon plasma [12]. The threshold effect and the anomalous suppression of the charmonium yields are illustrated in Fig. 3, where the ratio of the measured J/ψ yield to that which is expected in the presence of ordinary nuclear absorption alone is shown as a function of the energy density achieved in the nucleus–nucleus collision being considered. The data obtained in the NA38, NA50, and NA51 experiments for various interacting systems are compared in this figure. The energy density was calculated on the basis of the Bjorken model [13]. It amounts to 3.5 GeV/fm^3 for PbPb collisions characterized by the highest degree of centrality and is consistent with other experimental data and with the results of the calculations within the cascade model. In Fig. 3, two inflection points that were observed in the cross section for charmonium production correspond to energy-density values of about 2.3 and 3.1 GeV/fm^3 and can be explained by the disintegration first of the looser bound state χ_c and then of the J/ψ state. The fraction of the J/ψ states formed as the result of χ_c decay is not known for nucleus–nucleus interactions. For proton–nucleus collisions, it is approximately 30 to 40%.

4. CONCLUSION

A global analysis of the results of the NA38 and NA50 experiments suggests that, at high energy densities, charmonium production is suppressed in two

steps without a visible saturation for the most central events. These results contradict the available models of J/ψ suppression, which are based on the interaction of charmonium with accompanying hadrons in ordinary nuclear matter. The threshold behavior of the suppression of charmonium production on the degree of collision centrality is readily explained as the result of Debye color screening upon the phase transition of nuclear matter into quark–gluon plasma in heavy-ion collisions. Thus, the investigation of the suppression of the charmonium yield in the NA50 experiment furnishes evidence for quark–gluon deconfinement in central PbPb collisions at the energies of the SPS accelerator at CERN.

ACKNOWLEDGMENTS

This work was supported in part by the Russian Foundation for Basic Research (project no. 99-02-16003).

REFERENCES

1. G. Boyd *et al.*, Nucl. Phys. B **469**, 419 (1996).
2. T. Matsui and H. Satz, Phys. Lett. B **178**, 416 (1986).
3. C. Gerschel and J. Hufner, Z. Phys. C **56**, 171 (1992).
4. NA50 Collab. (M. C. Abreu *et al.*), Phys. Lett. B **410**, 337 (1997).
5. NA50 Collab. (M. C. Abreu *et al.*), Phys. Lett. B **450**, 456 (1999).
6. NA50 Collab. (M. C. Abreu *et al.*), Phys. Lett. B **477**, 28 (2000).
7. NA38 Collab. (M. C. Abreu *et al.*), Phys. Lett. B **444**, 516 (1998); **449**, 128 (1999).
8. J. Geiss *et al.*, Phys. Lett. B **447**, 31 (1999).
9. C. Spieles *et al.*, Phys. Rev. C **60**, 054901 (1999).
10. D. E. Kahana and S. H. Kahana, nucl-th/9908063.
11. N. Armesto, A. Capella, and E. G. Ferreira, Phys. Rev. C **59**, 395 (1999).
12. H. Satz, Nucl. Phys. A **661**, 104c (1999).
13. J. D. Bjorken, Phys. Rev. D **27**, 140 (1983).

Translated by A. Isaakyan

Conference on Physics of Fundamental Interactions
Theory

Generators of Nuclear Collisions at the LHC Energy*

S. M. Kiselev

Institute of Theoretical and Experimental Physics, Bol'shaya Cheremushkinskaya ul. 25, Moscow, 117218 Russia

Received March 23, 2001

Abstract—Current versions of the most popular generators of ultrarelativistic heavy-ion collisions are used to simulate central ($b < 3$ fm) Pb + Pb collisions at the LHC energy, $\sqrt{s} = 6A$ TeV. The charged-particle density predicted by the generators for the mid-rapidity range, $dN_{\text{ch}}/d\eta$, varies in a wide range, from about 2000 to about 6000. Moreover, even for a given generator, it depends strongly on model parameters and can vary from 10 to 100%. © 2002 MAIK “Nauka/Interperiodica”.

1. INTRODUCTION

There are many codes for simulating high-energy heavy-ion collisions [1]. Five years ago, a detailed comparison of predictions of different generators was performed for Pb + Pb collisions at the LHC energy [2]. In particular, it was shown that the charged-particle density in the mid-rapidity region varies strongly from one prediction to another. Namely, for the VENUS4.12, HIJING1.31, DPMJET-II, and SFM (without and with fusion) codes, the density $dN_{\text{ch}}/d\eta$ at $\eta = 0$ was found to be 7000, 5200, 3700, 3400, and 1400, respectively. Now, there are updated versions of the generators, and we will consider their predictions.

2. SIMULATIONS

The latest version of the HIJING [3] code, HIJING1.36, was taken from the author's home page <http://www-nsdth.lbl.gov/~xnwang/hijing>. Twenty-five central ($b < 3$ fm) Pb + Pb events were simulated with and without jet quenching at a beam energy of 3 TeV per nucleon. The entire body of information (the code itself, files with events in the ROOT [4] format, plots with results, etc.) can be found in the area [/afs/cern.ch/alice/offline/data/evtgen/hijing](http://afs/cern.ch/alice/offline/data/evtgen/hijing).

The current version of the DPMJET [5] generator, DPMJET-II.5 [6], was used by the author, J. Ranft, to simulate 50 central ($b < 3$ fm) Pb + Pb events with and without baryon stopping at a beam energy of 3 TeV per nucleon. Files with events, code and physics of baryon stopping, manuals, and some plots with results are in the area [/afs/cern.ch/alice/offline/data/evtgen/dpmjet/dpmjet25](http://afs/cern.ch/alice/offline/data/evtgen/dpmjet/dpmjet25).

The last version of the SFM [7] code, PSM-1.0 [8], was used by one of the coauthors, N. Armesto,

to generate 50 central ($b < 3$ fm) Pb + Pb events with and without string fusion. Although rescattering of secondaries and spectators is included as a possibility, these simulations did not take into account rescattering. A description of the code, along with events and some results can be found in the area [/afs/cern.ch/alice/offline/data/evtgen/sfm](http://afs/cern.ch/alice/offline/data/evtgen/sfm).

The latest version of the NEXUS [9] code, NEXUS2.0 (NEXUS is the VENUS [10] successor), was taken from the NEXUS site <http://www.subatech.in2p3.fr/theo/nexus/>. Unfortunately, there are problems in running the code with the rescattering mode, and we will use below the results for one central event without rescattering.

The last versions of the RQMD, VNI, and VNIB generators taken from the OSCAR site [1] were also used. Although these codes work at the RHIC energy [11], they give error messages during a run. The authors should adopt their codes to the LHC energy scale.

3. RESULTS

In Fig. 1, the multiplicities of various species, the pseudorapidity and transverse momentum distributions of charged particles, and the net baryon pseudorapidity plot are shown for HIJING. The GEANT codes of particles used in the first plot of the figure are presented in Table 1. One can see that switching on the energy loss of a gluon jet inside excited nuclear matter, jet quenching, leads to approximately two times higher multiplicity in the mid-rapidity region and to a steeper transverse momentum spectrum. Moreover, the pseudorapidity distribution demonstrates a characteristic bump in the region $|\eta| < 3$.

The same plots obtained for the DPMJET-II code are shown in Fig. 2. The baryon-stopping mechanism

*This article was submitted by the author in English.

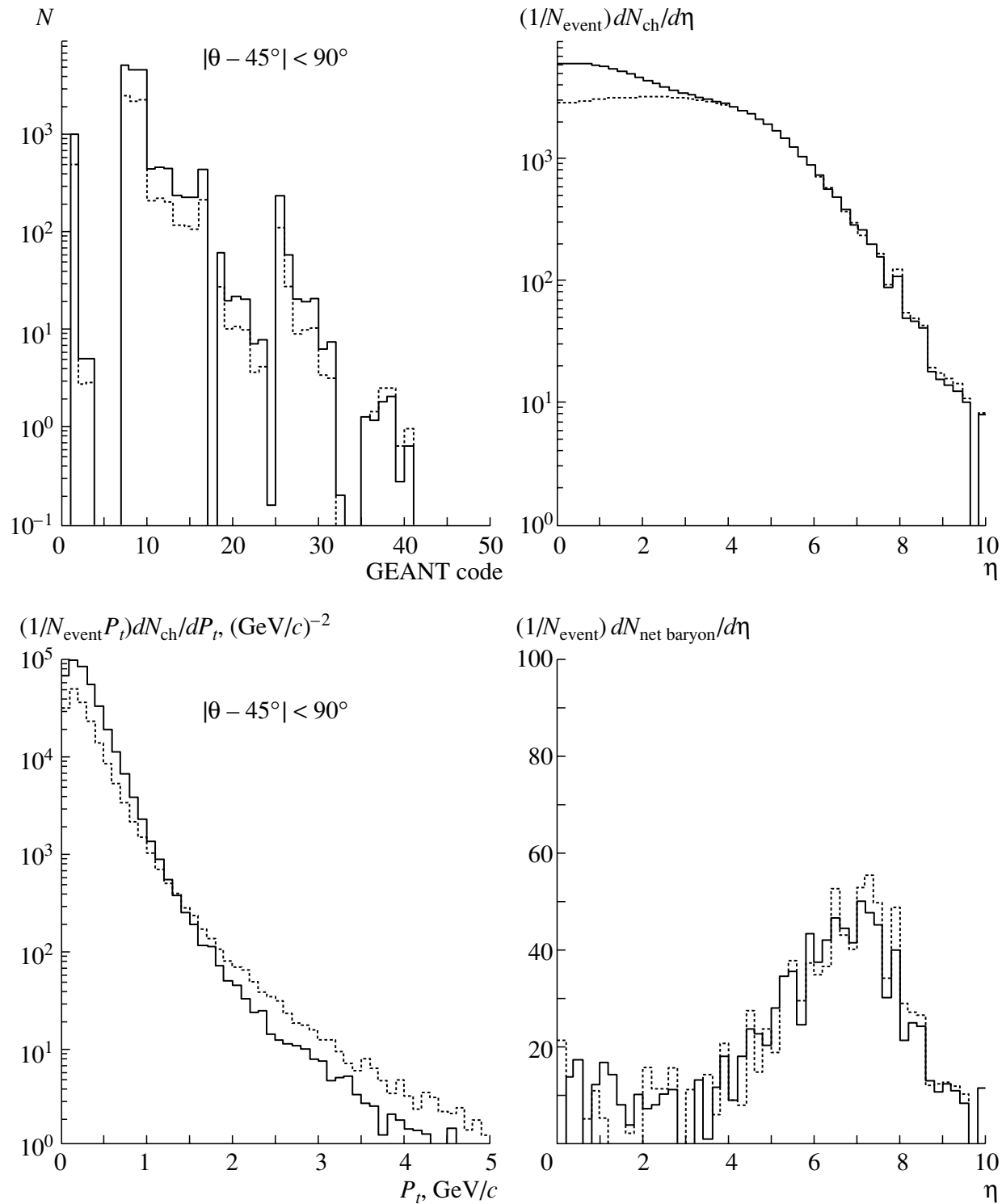


Fig. 1. HIJING1.36: Twenty-five central ($b < 3$ fm) Pb + Pb events at a beam energy of 3 TeV per nucleon. The solid-line (dashed-line) histograms represent results obtained with (without) quenching.

increases the multiplicity by about 15% and changes significantly the net baryon distribution.

Figure 3 demonstrates the same dependences obtained with the aid of the SFM generator. The

inclusion of string fusion leads to an about 10% lower multiplicity and does not change the transverse-momentum spectrum.

Some parameters of the charged-particle multi-

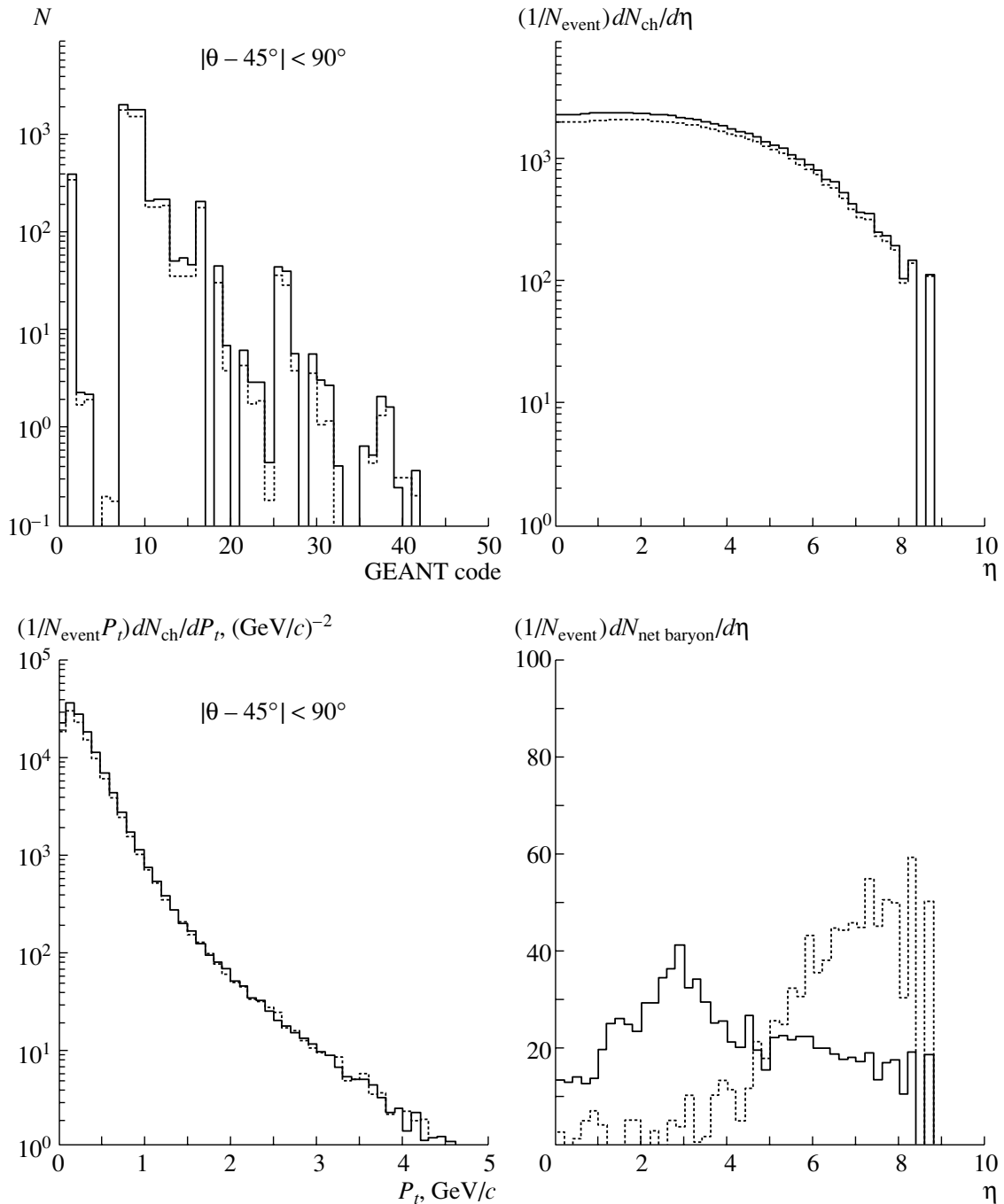


Fig. 2. DPMJET-II.5: Fifty central ($b < 3$ fm) Pb + Pb events at a beam energy of 3 TeV per nucleon. The solid-line (dashed-line) histograms represent results obtained with (without) the baryon-stopping mechanism.

plicity for various generators are presented in Table 2. In the last column, the old value for $dN_{\text{ch}}/d\eta$ is taken from [2].

4. CONCLUSION

The most popular generators of ultrarelativistic heavy-ion collisions were tested at the LHC energy

scale. Half of the tested codes (VNI, VNIb, RQMD, NEXUS) do not work in the LHC regime probably for technical reasons. With the help of the other ones (HIJING, DPMJET, SFM), central Pb + Pb events have been simulated at the energy of $\sqrt{s} = 6A$ TeV. The charged-particle density $dN_{\text{ch}}/d\eta$ predicted by these generators varies in a wide range, from about 2000 (SFM) to about 6000 (HIJING). More-

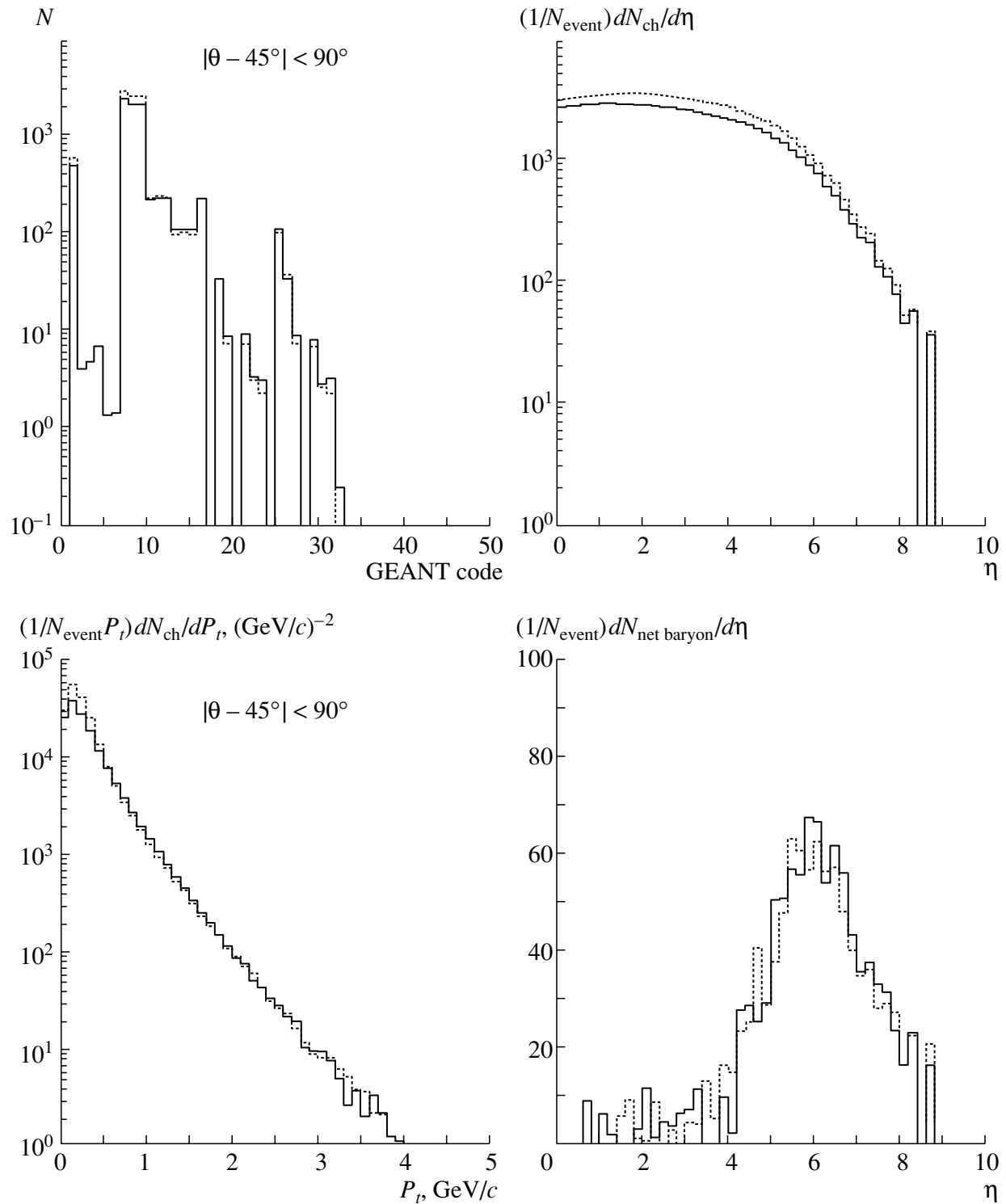


Fig. 3. SFM: Twenty-five central ($b < 3$ fm) Pb + Pb events at a beam energy of 3 TeV per nucleon without rescattering. The solid-line (dashed-line) histograms represent results obtained with (without) fusion.

over, even for a given generator, the density depends strongly on model mechanisms and has an uncertainty of about 10% (SFM with or without fusion) to about 100% (HIJING with or without quenching).

One can hope that the first [12] and forthcoming RHIC data on the charged-particle multiplicity will help to choose model parameters more correctly and reduce uncertainties.

Table 1. GEANT codes of particles

Code	Particle	Code	Particle	Code	Particle	Code	Particle
1	γ	13	n	25	\bar{n}	37	D^0
2	e^+	14	p	26	$\bar{\Lambda}$	38	\bar{D}^0
3	e^-	15	\bar{p}	27	$\bar{\Sigma}^-$	39	D_s^+
4	ν	16	K_S^0	28	$\bar{\Sigma}^0$	40	D_s^-
5	μ^+	17	η	29	$\bar{\Sigma}^+$	41	Λ_c^+
6	μ^-	18	Λ	30	Ξ^0	42	ρ^+
7	π^0	19	Σ^+	31	Ξ^+	43	ρ^-
8	π^+	20	Σ^0	32	$\bar{\Omega}^+$	44	ρ^0
9	π^-	21	Σ^-	33	ω	45	d
10	K_L^0	22	Ξ^0	34	ϕ	46	t
11	K^+	23	Ξ^-	35	D^+	47	α
12	K^-	24	Ω^-	36	D^-	48	Geantino

Table 2. Some parameters of the charge-particle multiplicity for various generators

Generator	Comments	$dN_{\text{ch}}/d\eta$ at $\eta = 0$	N_{ch} for $ \theta - 90^\circ < 45^\circ$	Event time (machine)	New/old for $dN_{\text{ch}}/d\eta$
HIJING1.36	With quenching	$\simeq 6200$	$\simeq 10800$	3 min (HP-UX ion)	$\simeq 1.2$
	Without quenching	$\simeq 2900$	$\simeq 5200$	2.6 min (HP-UX ion)	
DPMJET-II.5	With baryon stopping	$\simeq 2300$	$\simeq 4000$	15 s (PC 350 MHz)	
	Without baryon stopping	$\simeq 2000$	$\simeq 3500$	15 s (PC 350 MHz)	$\simeq 0.5$
SFM	With fusion	$\simeq 2700$	$\simeq 4700$	5 min (PC 500 MHz)	$\simeq 2.1$
	Without fusion	$\simeq 3100$	$\simeq 5500$	4 min (PC 500 MHz)	$\simeq 0.9$
NEXUS-2	With rescattering				
	Without rescattering	$\simeq 1100$		1 h 20 min (HP-UX ion)	

REFERENCES

1. Open Standard Code and Routines (OSCAR), 1997; <http://nt3.phys.columbia.edu/OSCAR>.
2. N. van Eijndhoven *et al.*, Internal Note AL-ICE/GEN 95-32; http://consult.cern.ch/alice/Internal_Notes/1995/32/abstract
3. X. N. Wang and M. Gyulassy, Phys. Rev. D **44**, 3501 (1991); M. Gyulassy and X. N. Wang, Comput. Phys. Commun. **83**, 307 (1994); <http://www-nsdth.lbl.gov/xnwang/hijing/>
4. R. Brun *et al.*, <http://root.cern.ch>
5. J. Ranft, Phys. Rev. D **51**, 64 (1995).

6. J. Ranft, hep-ph/9911213; hep-ph/9911232; hep-ph/0002137.
7. N. S. Amelin, M. A. Braun, and C. Pajares, Phys. Lett. B **306**, 312 (1993); Z. Phys. C **63**, 507 (1994).
8. N. S. Amelin, N. Armesto, C. Pajares, and D. Sousa, in preparation; N. Armesto and C. Pajares, Int. J. Mod. Phys. A **15**, 2019 (2000); E. G. Ferreira, C. Pajares, and D. Sousa, Phys. Lett. B **422**, 314 (1998); N. Armesto, M. A. Braun, E. G. Ferreira, and C. Pajares, Phys. Lett. B **344**, 301 (1995); N. S. Amelin *et al.*, Phys. Rev. C **52**, 362 (1995).
9. H. J. Drescher, M. Hladik, S. Ostapchenko, and K. Werner, hep-ph/9903296.
10. K. Werner, Phys. Rep. **232**, 87 (1993).
11. S. A. Bass *et al.*, Nucl. Phys. A **661**, 205 (1999).
12. PHOBOS Collab. (B. B. Back *et al.*), Phys. Rev. Lett. **85**, 3100 (2000); hep-ex/0007036; PHENIX Collab. (K. Adcox *et al.*), nucl-ex/0012008.

Conference on Physics of Fundamental Interactions
Theory

Quasifixed-Point Scenario in a Modified Nonminimal Supersymmetric Standard Model

R. B. Nevzorov and **M. A. Trusov***

*Institute of Theoretical and Experimental Physics, Bol'shaya
Cheremushkinskaya ul. 25, Moscow, 117218 Russia*

Received February 12, 2001; in final form, May 29, 2001

Abstract—The modified next-to-minimal supersymmetric standard model is the simplest model that is obtained as an extension of the minimal supersymmetric standard model and which is compatible with the LEP II experimental constraint on the mass of the lightest Higgs boson at $\tan \beta \sim 1$. The renormalization of Yukawa coupling constants and of the parameters of a soft breakdown of supersymmetry is investigated within this model. The possibility of unifying the Yukawa coupling constants for the b quark and the τ lepton at the Grand Unification scale M_X is studied. The spectrum of particles is analyzed in the vicinity of a quasifixed point where solutions to the renormalization-group equations are concentrated at the electroweak scale. © 2002 MAIK “Nauka/Interperiodica”.

1. INTRODUCTION

A rapid development of experimental high-energy physics over the last decades of the 20th century gave impetus to intensive investigations of various extensions of the Standard Model. Its supersymmetric generalization known as the minimal supersymmetric (SUSY) standard model (MSSM) is one of the most popular extensions of the Standard Model. The Higgs sector of the MSSM includes two doublets of Higgs fields, H_1 and H_2 . Upon a spontaneous breakdown of gauge symmetry, each of these develops a vacuum expectation value; we denote the corresponding vacuum expectation values by v_1 and v_2 . The sum of the squares of the vacuum expectation values of the Higgs fields is $v^2 = (246 \text{ GeV})^2$, the ratio of the expectation values being determined by the angle β . By definition, $\beta = \arctan(v_2/v_1)$. The value of $\tan \beta$ is not fixed experimentally. It is varied within a wide interval, from 1.3–1.8 to 50–60. Within SUSY models, the upper and lower limits on $\tan \beta$ arise under the assumption that perturbation theory is applicable up to the scale at which gauge coupling constants are unified, $M_X = 3 \times 10^{16} \text{ GeV}$ —that is, under the assumption that there is no Landau pole in solutions to relevant renormalization-group equations.

The spectrum of the Higgs sector of the MSSM contains four massive states. Two of these are CP-even, one is CP-odd, and one is charged. The presence of a light Higgs boson in the CP-even sector is

an important distinguishing feature of SUSY models. Its mass is constrained from above as

$$m_h \leq \sqrt{M_Z^2 \cos^2 2\beta + \Delta}, \quad (1)$$

where M_Z is the Z -boson mass ($M_Z \approx 91.2 \text{ GeV}$) and Δ stands for the contribution of loop corrections. The magnitude of these corrections is proportional to m_t^4 (m_t is the running mass of the t quark), depends logarithmically on the supersymmetry-breakdown scale M_S , and is virtually independent of the choice of $\tan \beta$. An upper limit on the mass of the light CP-even Higgs boson within the MSSM grows with increasing $\tan \beta$ and, for $\tan \beta \gg 1$, reaches 125–128 GeV in realistic SUSY models with $M_S \leq 1000 \text{ GeV}$.

At the same time, it is known from [1] that, for $\tan \beta \ll 50$ –60, solutions to the renormalization-group equations for the t -quark Yukawa coupling constant $h_t(t)$ are concentrated in the vicinity of the quasifixed point

$$Y_{\text{QFP}}(t_0) = E(t_0)/6F(t_0), \quad (2)$$

where

$$E(t) = \left[\frac{\tilde{\alpha}_3(t)}{\tilde{\alpha}(0)} \right]^{16/9} \left[\frac{\tilde{\alpha}_2(t)}{\tilde{\alpha}(0)} \right]^{-3} \left[\frac{\tilde{\alpha}_1(t)}{\tilde{\alpha}(0)} \right]^{-13/99},$$

$$F(t) = \int_0^t E(t') dt',$$

$$Y_t(t) = \frac{h_t^2(t)}{(4\pi)^2}, \quad \tilde{\alpha}_i(t) = \frac{g_i^2(t)}{(4\pi)^2},$$

*e-mail: trusov@heron.itep.ru

with g_i being the gauge constants of the Standard Model group. The variable t is defined in the standard way: $t = \ln(M_X^2/q^2)$. Its value at the electroweak scale is $t_0 = 2\ln(M_X/M_t^{\text{pole}})$, where $M_t^{\text{pole}} \approx 174.3 \pm 5.1$ GeV is the pole mass of the t quark. Along with the t -quark Yukawa coupling constant, solutions to the renormalization-group equations for the corresponding trilinear coupling constant A_t characterizing the interaction of scalar fields and for the combination $\mathfrak{M}_t^2 = m_Q^2 + m_U^2 + m_2^2$ of the scalar-particle masses also approach the infrared quasifixed point. The properties of solutions to the renormalization-group equations within the MSSM and the spectrum of particles in the infrared-quasifixed-point regime at $\tan\beta \sim 1$ were investigated in [2, 3].

A reduction of the number of independent parameters in the vicinity of the infrared quasifixed point considerably increased the predictive power of the theory. On the basis of the equation relating the Yukawa coupling constant for the t quark to its mass at the electroweak scale,

$$m_t(M_t^{\text{pole}}) = \frac{h_t(M_t^{\text{pole}})}{\sqrt{2}} v \sin\beta, \quad (3)$$

and the value calculated for the running mass of the t quark within the \overline{MS} scheme [$m_t(M_t^{\text{pole}}) = 165 \pm 5$ GeV], it was shown in [3–5] that, for a broad class of solutions satisfying the renormalization-group equations within the MSSM and corresponding to the infrared-quasifixed-point regime, $\tan\beta$ takes values in the interval between 1.3 and 1.8. These comparatively small values of $\tan\beta$ lead to much more stringent constraints on the mass of the lightest Higgs boson. A detailed theoretical analysis performed in [3, 4] revealed that, in the case being considered, its mass does not exceed 94 ± 5 GeV, which is 25–30 GeV below the absolute upper limit in the minimal SUSY model. It should be noted that the LEP II constraints on the mass of the lightest Higgs boson [6] are such that a considerable fraction of solutions approaching a quasifixed point at $\tan\beta \sim 1$ have already been ruled out by existing experimental data.

All the aforesaid furnishes a sufficient motivation for studying the Higgs sector in more complicated SUSY models, as well as renormalization-group equations and solutions to these equations therein. The present article is devoted to an analysis of coupling-constant renormalization within a modified next-to-minimal SUSY model, where the mass of the lightest Higgs boson can be as large as 120–130 GeV even at comparatively small values of $\tan\beta \sim 2$. In addition, the spectrum of superpartners of observable particles and of Higgs bosons is studied in the

vicinity of the quasifixed point of the renormalization-group equations within the modified next-to-minimal SUSY model.

2. MODIFIED NEXT-TO-MINIMAL SUPERSYMMETRIC STANDARD MODEL

The next-to-minimal supersymmetric standard model (NMSSM) [7–9] is the simplest extension of the MSSM. Historically, the NMSSM arose as one of the possible solutions to the problem of the μ term in supergravity (SUGRA) models [7]. Along with observable superfields, SUGRA theories contain a hidden sector that includes the dilaton and moduli fields (S and T_m , respectively), which are singlet in gauge interactions. The total superpotential in SUGRA models is usually represented as an expansion in the superfields of the observable sector; that is,

$$W = W_0(S, T_m) + \mu(S, T_m)(\hat{H}_1 \hat{H}_2) + h_t(S, T_m)(\hat{Q} \hat{H}_2) \hat{U}_R^c + \dots, \quad (4)$$

where $W_0(S, T_m)$ is the superpotential of the hidden sector. The expansion in (4) presumes that the parameter μ appearing in front of the bilinear term $(\hat{H}_1 \hat{H}_2)$ must be about the Planck mass, since this scale is the only dimensional parameter characterizing the hidden sector of the theory. In this case, however, the Higgs bosons H_1 and H_2 acquire an enormous mass ($m_{H_1, H_2}^2 \simeq \mu^2 \simeq M_{\text{Pl}}^2$) and $SU(2) \otimes U(1)$ symmetry remains unbroken.

In the NMSSM, an additional singlet superfield \hat{Y} is introduced, while the term $\mu(\hat{H}_1 \hat{H}_2)$ is replaced by $\lambda \hat{Y}(\hat{H}_1 \hat{H}_2) + (\kappa/3)\hat{Y}^3$. A spontaneous breakdown of gauge symmetry leads to the emergence of the vacuum expectation value $\langle Y \rangle = y/\sqrt{2}$ of the field Y and to the generation of an effective μ term ($\mu = \lambda \langle Y \rangle$). The resulting superpotential of the next-to-minimal SUSY model is invariant under discrete transformations of the Z_3 group [8]. The Z_3 symmetry of the superpotential of the observable sector naturally arises in string models, where all observable fields are massless in the limit of exact supersymmetry.

Upon the introduction of the neutral field Y in the superpotential of the NMSSM, there arises the corresponding F term in the potential of interaction of Higgs fields. As a result, an upper limit on the mass of the lightest Higgs boson becomes higher than that in the MSSM:

$$m_h \leq \sqrt{\frac{\lambda^2}{2} v^2 \sin^2 2\beta + M_Z^2 \cos^2 2\beta + \Delta}. \quad (5)$$

In the tree approximation ($\Delta = 0$), relation (5) was obtained in [9]. For $\lambda \rightarrow 0$, the expressions for the

upper limit in the MSSM and in the NMSSM coincide after the substitution of $\lambda y/\sqrt{2}$ for μ . The Higgs sector of the next-to-minimal SUSY model and one-loop corrections to it were studied in [10, 11]. In [12], the upper limit on the mass m_h of the lightest Higgs boson within the NMSSM was contrasted against the analogous limits in the minimal standard and the minimal SUSY model.

From relation (5), it follows that the upper limit on m_h grows with increasing $\lambda(t_0)$. It should be noted that only in the region of small values of $\tan\beta$ does it differ significantly from the analogous limit in the MSSM. As to the small- $\tan\beta$ scenario, it is realized in the case of sufficiently large values of $h_t(t_0)$. The growth of the Yukawa coupling constants at the electroweak scale is accompanied by an increase in $h_t(0)$ and $\lambda(0)$ at the Grand Unification scale; therefore, the upper limit on the mass of the lightest Higgs boson in the nonminimal SUSY model attains a maximum value in the limit of strong Yukawa coupling, in which case both $h_t^2(0)$ and $\lambda^2(0)$ are much greater than $g_i^2(0)$.

Unfortunately, we were unable to obtain a self-consistent solution in the regime of strong Yukawa coupling within the NMSSM featuring the minimal set of fundamental parameters. Moreover, Z_3 symmetry, which makes it possible to avoid the problem of the μ term in the next-to-minimal SUSY model, leads to the emergence of three degenerate vacua in the theory. Immediately following the phase transition at the electroweak scale, the Universe is filled with three degenerate phases that must be separated by domain walls. However, the hypothesis of a domain structure of the vacuum is at odds with data from astrophysical observations. An attempt at destroying Z_3 symmetry and the domain structure of the vacuum by introducing nonrenormalizable operators in the NMSSM Lagrangian leads to the appearance of quadratic divergences—that is, to the hierarchy problem [13].

In order to avoid the domain structure of the vacuum and to obtain a self-consistent solution in the regime of strong Yukawa coupling, it is necessary to modify the next-to-minimal SUSY model. The simplest way to modify the NMSSM is to introduce additional terms in the superpotential of the Higgs sector, $\mu(\hat{H}_1\hat{H}_2)$ and $\mu'\hat{Y}^2$ [14], that are not forbidden by gauge symmetry. The additional bilinear terms in the NMSSM superpotential destroy Z_3 symmetry, and domain walls are not formed in such a theory. Upon the introduction of the parameter μ , it becomes possible to obtain the spectrum of SUSY particles in the modified model; for a specific choice of μ' , the mass m_h of the lightest Higgs boson reaches its upper limit, taking the largest value at $\kappa = 0$. In analyzing

the modified next-to-minimal supersymmetric standard model (MNSSM), it is therefore reasonable to set the coupling constant for the self-interaction of neutral superfields \hat{Y} to zero.

The MNSSM superpotential involves a large number of Yukawa coupling constants. At $\tan\beta \sim 1$, they are all negligibly small, however, with the exception of the t -quark Yukawa coupling constant h_t and the coupling constant λ , which is responsible for the interaction of the superfield \hat{Y} with the doublets \hat{H}_1 and \hat{H}_2 . Thus, the total superpotential of the modified next-to-minimal supersymmetric standard model can be represented in the form

$$W_{\text{MNSSM}} = \mu(\hat{H}_1\hat{H}_2) + \mu'\hat{Y}^2 + \lambda\hat{Y}(\hat{H}_1\hat{H}_2) + h_t(\hat{Q}\hat{H}_2)\hat{U}_R^c. \quad (6)$$

Within SUGRA models, the terms in the superpotential (6) that are bilinear in the superfields can be generated owing to the term $(Z(H_1H_2) + Z'Y^2 + \text{h.c.})$ in the Kähler potential [15, 16] or owing to the nonrenormalized interaction of fields from the observable and the hidden sector (this interaction may be due to nonperturbative effects) [16, 17].

Along with the parameters μ and μ' , the masses of scalar fields, m_i^2 , and the gaugino masses M_i are also generated upon a soft breakdown of supersymmetry. Moreover, a trilinear coupling constant A_i for the interaction of scalar fields is associated in the total Lagrangian of the theory with each Yukawa coupling constant, while a bilinear coupling constant B (B') is associated there with the parameter μ (μ'). The hypothesis of universality of these constants at the scale M_X makes it possible to reduce their number to four: the scalar-particle mass m_0 , the trilinear coupling constant A and the bilinear coupling constant B_0 for the interaction of scalar fields, and the gaugino mass $M_{1/2}$.

3. ANALYSIS OF THE EVOLUTION OF YUKAWA COUPLING CONSTANTS AND DETERMINATION OF A QUASIFIXED POINT

The MNSSM parameters

$$\lambda, h_t, \mu, \mu', m_0, A, B_0, M_{1/2}$$

specified at the Grand Unification scale evolve down to the electroweak scale or the scale of supersymmetry breakdown. Their renormalization is determined by the set of renormalization-group equations, these equations for the coupling constants λ , h_t , A_i , m_i^2 , and M_i being coincident with the corresponding renormalization-group equations within the nonminimal supersymmetric standard model (see, for example, [11]) if one sets $\kappa = 0$ in them. The equations

describing the evolution of μ , μ' , B , and B' within the modified nonminimal supersymmetric standard model were obtained in [14].

Even in the one-loop approximation, the full system of renormalization-group equations is nonlinear, so that it is hardly possible to solve it analytically. This set of equations can be broken down into two subsets. The first subset includes equations that describe the evolution of gauge and Yukawa coupling constants and of the parameters μ and μ' . The second subset comprises equations for the parameters of a soft breakdown of supersymmetry.

In studying the evolution of the Yukawa coupling constants, it is convenient to introduce, instead of the constants h_t , λ , and g_i , the ratios

$$\begin{aligned}\rho_t(t) &= \frac{Y_t(t)}{\tilde{\alpha}_3(t)}, & \rho_\lambda(t) &= \frac{Y_\lambda(t)}{\tilde{\alpha}_3(t)}, \\ \rho_1(t) &= \frac{\tilde{\alpha}_1(t)}{\tilde{\alpha}_3(t)}, & \rho_2(t) &= \frac{\tilde{\alpha}_2(t)}{\tilde{\alpha}_3(t)},\end{aligned}$$

where $Y_\lambda(t) = \lambda^2(t)/(4\pi)^2$. The region of admissible values of the Yukawa coupling constants at the electroweak scale is bounded by the quasifixed (or Hill) line. Beyond this region, solutions to the renormalization-group equations for $Y_i(t)$ develop a Landau pole below the scale M_X , so that perturbation theory becomes inapplicable for $q^2 \sim M_X^2$. The results of our numerical calculations are presented in Fig. 1, whence one can see that, in the regime of strong Yukawa coupling, all solutions for $Y_i(t)$ are attracted to the Hill line, which intersects the ρ_t axis at the point whose coordinates $(\rho_\lambda(t_0), \rho_t(t_0)) = (0, 0.87)$ correspond to the quasifixed point in the minimal supersymmetric standard model.

In analyzing the results of the numerical calculations (see Fig. 1), attention is captured by a pronounced nonuniformity in the distribution of solutions to the renormalization-group equations along the quasifixed line. The main reason behind this is that, in the regime of strong Yukawa coupling, solutions are attracted not only to the quasifixed but also to the infrared fixed (or invariant) line. The latter connects two fixed points. Of these, one is the stable infrared fixed point for the set of renormalization-group equations within the modified nonminimal supersymmetric standard model ($\rho_t = 7/18, \rho_\lambda = 0, \rho_1 = 0, \rho_2 = 0$) [18]. As the invariant line approaches this point, $\rho_\lambda \sim (\rho_t - 7/18)^{25/14}$. The other fixed point [$(\rho_\lambda/\rho_t) = 1$] corresponds to large values of the Yukawa coupling constants, $Y_t, Y_\lambda \gg \tilde{\alpha}_i$, in which case the gauge coupling constants can be disregarded [19]. In the limiting case of $\rho_\lambda, \rho_t \gg 1$, the asymptotic behavior of the curve being studied is given by

$$\rho_\lambda = \rho_t - \frac{8}{15} - \frac{2}{75}\rho_1. \quad (7)$$

The infrared fixed lines and their properties in the minimal standard and the minimal supersymmetric model were studied in detail elsewhere [20].

With increasing initial values of the Yukawa coupling constants $Y_t(0)$ and $Y_\lambda(0)$ at the Grand Unification scale, the region where solutions are concentrated at the electroweak scale shrinks abruptly and all solutions to the renormalization-group equations within the modified nonminimal supersymmetric standard model are focused near the point of intersection of the invariant and the quasifixed line:

$$\rho_t^{\text{QFP}}(t_0) = 0.803, \quad \rho_\lambda^{\text{QFP}}(t_0) = 0.224. \quad (8)$$

This point can be considered as the quasifixed point for the set of renormalization-group equations for the modified nonminimal supersymmetric standard model [21].

Among subsidiary constraints that are frequently imposed in studying supersymmetric models, we would like to mention the unification of the Yukawa coupling constants for the b quark and for τ lepton at the scale M_X ; this usually occurs in minimal schemes for unifying gauge interactions—for example, in those that are based on the $SU(5)$, the E_6 , or the $SO(10)$ group. The unification of h_b and h_τ within the modified nonminimal standard supersymmetric model is realized only in the case where the constants satisfy a specific relation between Y_t and Y_λ . Integrating the renormalization-group equations and substituting $R_{b\tau}(t_0) = m_b(t_0)/m_\tau(t_0) = 1.61$, which corresponds to $m_\tau(t_0) = 1.78$ GeV and $m_b(t_0) = 2.86$ GeV, we obtain

$$\begin{aligned}\frac{Y_t(0)}{Y_t(t_0)} &= \left[\frac{1}{R_{b\tau}(t_0)} \right]^{21/2} \left[\frac{\alpha_3(t_0)}{\alpha_3(0)} \right]^{68/9} \\ &\times \left[\frac{\alpha_2(t_0)}{\alpha_2(0)} \right]^{9/4} \left[\frac{\alpha_1(t_0)}{\alpha_1(0)} \right]^{463/396} \\ &\times \left[\frac{Y_\lambda(0)}{Y_\lambda(t_0)} \right]^{1/4} \approx 3.67 \left[\frac{Y_\lambda(0)}{Y_\lambda(t_0)} \right]^{1/4}.\end{aligned} \quad (9)$$

The results obtained here indicate that b - τ unification is possible under the condition that $Y_t(0) \gg Y_t(t_0)$, which is realized only in the regime of strong Yukawa coupling. By varying the running mass $m_b(m_b)$ of the b quark from 4.1 to 4.4 GeV, we found that the equality of the Yukawa coupling constants at the Grand Unification scale can be achieved only at $\tan \beta \leq 2$.

The possibility of unifying the Yukawa coupling constants within the nonminimal supersymmetric standard model was comprehensively studied in [21, 22]. The condition $Y_b(0) = Y_\tau(0)$ imposes stringent constraints on the parameter space of the model being studied. Since h_b and h_τ are small in magnitude at $\tan \beta \sim 1$, they can be generated, however, owing

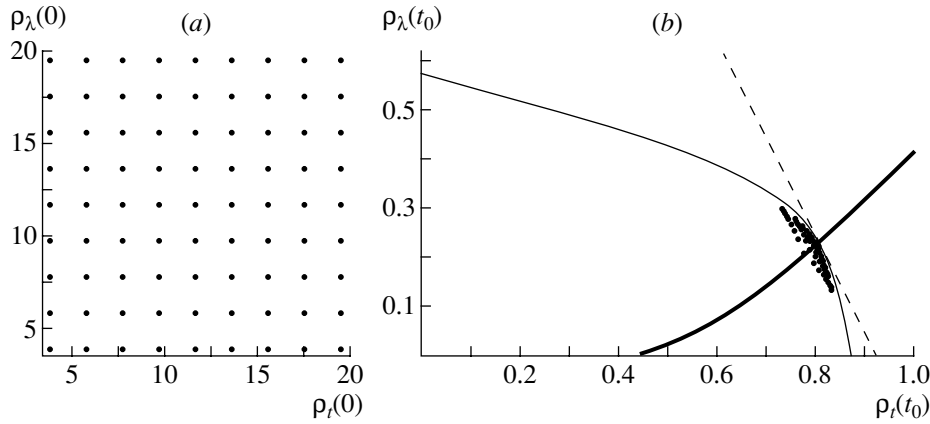


Fig. 1. (a) Boundary conditions specified for the renormalization-group equations within the modified nonminimal supersymmetric standard model at the scale $q = M_X$ for $2 \leq h_i^2(0), \lambda^2(0) \leq 10$ and uniformly distributed over the (ρ_t, ρ_λ) plane and (b) corresponding values of the Yukawa coupling constants at the electroweak scale. In Fig. 1b, the thick and the thin solid curve correspond to the invariant and the Hill line, respectively, while the dashed straight line represents the results of a fit to the values $(\rho_t(t_0), \rho_\lambda(t_0))$ for $20 \leq h_i^2(0), \lambda^2(0) \leq 100$.

to nonrenormalizable operators upon a spontaneous breakdown of symmetry at the Grand Unification scale. In this case, h_b and h_τ may be different. In studying the spectrum of superpartners below, we will not therefore assume that $R_{b\tau}(0) = 1$.

4. RENORMALIZATION OF THE PARAMETERS OF A SOFT BREAKDOWN OF SUPERSYMMETRY

If the evolution of gauge and Yukawa coupling constants is known, the remaining subset of renormalization-group equations within the modified nonminimal supersymmetric standard model can be treated as a set of linear differential equations for the parameters of a soft breakdown of supersymmetry. For universal boundary conditions, a general solution for the trilinear coupling constants $A_i(t)$ for the interaction of scalar fields and their masses $m_i^2(t)$ has the form

$$\begin{aligned}
 A_i(t) &= e_i(t)A + f_i(t)M_{1/2}, \\
 m_i^2(t) &= a_i(t)m_0^2 + b_i(t)M_{1/2}^2 \\
 &\quad + c_i(t)AM_{1/2} + d_i(t)A^2.
 \end{aligned}
 \tag{10}$$

The functions $e_i(t)$, $f_i(t)$, $a_i(t)$, $b_i(t)$, $c_i(t)$, and $d_i(t)$, which determine the evolution of $A_i(t)$ and $m_i^2(t)$, remain unknown. The results of our numerical calculations reveal that these functions greatly depend on the choice of Yukawa coupling constants at the scale M_X .

In analyzing the behavior of solutions to the renormalization-group equations in the regime of strong Yukawa coupling, it is more convenient to

consider, instead of the squares of the scalar-particle masses, their linear combinations

$$\begin{aligned}
 \mathfrak{M}_t^2(t) &= m_2^2(t) + m_Q^2(t) + m_U^2(t), \\
 \mathfrak{M}_\lambda^2(t) &= m_1^2(t) + m_2^2(t) + m_y^2(t).
 \end{aligned}
 \tag{11}$$

For the universal boundary conditions, solutions to the differential equations for $\mathfrak{M}_i^2(t)$ can be represented in the same form as the solutions for $m_i^2(t)$ [see Eqs. (10)]; that is,

$$\begin{aligned}
 \mathfrak{M}_i^2(t) &= 3\tilde{a}_i(t)m_0^2 + \tilde{b}_i(t)M_{1/2}^2 \\
 &\quad + \tilde{c}_i(t)AM_{1/2} + \tilde{d}_i(t)A^2.
 \end{aligned}
 \tag{12}$$

Since the homogeneous equations for $A_i(t)$ and $\mathfrak{M}_i^2(t)$ have the same form, the functions $\tilde{a}_i(t)$ and $e_i(t)$ coincide.

With increasing $Y_i(0)$, the functions $e_i(t_0)$, $c_i(t_0)$, and $d_i(t_0)$ decrease and tend to zero in the limit $Y_i(0) \rightarrow \infty$. Concurrently, $A_t(t)$, $A_\lambda(t)$, $\mathfrak{M}_t^2(t)$, and $\mathfrak{M}_\lambda^2(t)$ become independent of A and m_0^2 , while relations (10) and (12) are significantly simplified. This behavior of the solutions in question implies that, as the solutions to the renormalization-group equations for the Yukawa coupling constants approach quasi-fixed points, the corresponding solutions for $A_i(t)$ and $\mathfrak{M}_i^2(t)$ also approach quasifixed points whose coordinates are [23]

$$\begin{aligned}
 \rho_{A_t}^{\text{QFP}}(t_0) &\approx 1.77, & \rho_{\mathfrak{M}_t^2}^{\text{QFP}}(t_0) &\approx 6.09, \\
 \rho_{A_\lambda}^{\text{QFP}}(t_0) &\approx -0.42, & \rho_{\mathfrak{M}_\lambda^2}^{\text{QFP}}(t_0) &\approx -2.28,
 \end{aligned}
 \tag{13}$$

where $\rho_{A_i}(t) = A_i(t)/M_{1/2}$ and $\rho_{\mathfrak{M}_i^2}(t) = \mathfrak{M}_i^2(t)/M_{1/2}^2$. At the same time, the functions $a_i(t)$

approach some constants independent of t and $Y_i(0)$:

$$\begin{aligned} a_y(t) &\rightarrow 1/7, & a_1(t) &\rightarrow 4/7, & a_2(t) &\rightarrow -5/7, \\ a_u(t) &\rightarrow 1/7, & a_q(t) &\rightarrow 4/7. \end{aligned} \quad (14)$$

In the case of nonuniversal boundary conditions at $Y_t(0) \simeq Y_\lambda(0)$, the required solution to the renormalization-group equations for $A_i(t)$ and $\mathfrak{M}_i^2(t)$ can be represented as [23]

$$\begin{aligned} \begin{pmatrix} A_t(t) \\ A_\lambda(t) \end{pmatrix} &= \alpha_1 \begin{pmatrix} v_{11}(t) \\ v_{21}(t) \end{pmatrix} (\varepsilon_t(t))^{\lambda_1} \\ &+ \alpha_2 \begin{pmatrix} v_{12}(t) \\ -3v_{22}(t) \end{pmatrix} (\varepsilon_t(t))^{\lambda_2} + \dots, \\ \begin{pmatrix} \mathfrak{M}_t^2(t) \\ \mathfrak{M}_\lambda^2(t) \end{pmatrix} &= \beta_1 \begin{pmatrix} v_{11}(t) \\ v_{21}(t) \end{pmatrix} (\varepsilon_t(t))^{\lambda_1} \\ &+ \beta_2 \begin{pmatrix} v_{12}(t) \\ -3v_{22}(t) \end{pmatrix} (\varepsilon_t(t))^{\lambda_2} + \dots, \end{aligned} \quad (15)$$

where α_i and β_i are constants of integration that can be expressed in terms of $A_t(0)$, $A_\lambda(0)$, $\mathfrak{M}_t^2(0)$, and $\mathfrak{M}_\lambda^2(0)$; $\varepsilon_t(t) = Y_t(t)/Y_t(0)$; $\lambda_1 = 1$; and $\lambda_2 = 3/7$. The functions $v_{ij}(t)$ are weakly dependent on the Yukawa coupling constants at the scale M_X , and $v_{ij}(0) = 1$. In Eqs. (15), we have omitted terms proportional to $M_{1/2}$, $M_{1/2}^2$, $A_i(0)M_{1/2}$, and $A_i(0)A_j(0)$.

With increasing $Y_t(0) \simeq Y_\lambda(0)$, the dependence of $A_i(t_0)$ and $\mathfrak{M}_i^2(t_0)$ on α_1 and β_1 quickly becomes weaker. The results of our numerical analysis that are displayed in Fig. 2 indicate that, for $h_t^2(0) = \lambda^2(0) = 20$ and boundary conditions uniformly distributed in the (A_t, A_λ) and the $(\mathfrak{M}_t^2, \mathfrak{M}_\lambda^2)$ plane, the solutions to the renormalization-group equations for the parameters of a soft breakdown of supersymmetry in the vicinity of the quasifixed point are concentrated near some straight lines. The equations of these straight lines can be obtained by setting $A_\lambda(0) = -3A_t(0)$ and $\mathfrak{M}_\lambda^2(0) = -3\mathfrak{M}_t^2(0)$ (that is, $\alpha_1 = \beta_1 = 0$) at the Grand Unification scale. As a result, we find that, at the electroweak scale, the parameters of a soft breakdown of supersymmetry satisfy the relations

$$\begin{aligned} A_t + 0.137(0.147)A_\lambda &= 1.70M_{1/2}, \\ \mathfrak{M}_t^2 + 0.137(0.147)\mathfrak{M}_\lambda^2 &= 5.76M_{1/2}^2. \end{aligned} \quad (16)$$

The equation for \mathfrak{M}_i^2 has been obtained for all $A_i(0)$ set to zero. In relations (16), the coefficients obtained by fitting the results of our numerical calculations (see Fig. 2) are indicated parenthetically. As the Yukawa coupling constants approach quasifixed points, the two sets of coefficients in (16) fast approach each other and, at $Y_i(0) \sim 1$, become virtually coincident.

5. SPECTRUM OF SUPERSYMMETRIC PARTICLES AND HIGGS BOSONS

Let us now proceed to study the spectrum of the superpartners of observable particles and Higgs bosons in the vicinity of the quasifixed point within the modified nonminimal supersymmetric standard model. The Yukawa coupling constants h_t and λ are determined here by relations (8). The value of $\tan \beta$ can be calculated by formula (3). In the regime of the infrared quasifixed point at $m_t(M_t^{\text{pole}}) = 165$ GeV, the result is $\tan \beta \approx 1.88$.

The remaining fundamental parameters of the modified nonminimal supersymmetric standard model must be chosen in such a way that a spontaneous breakdown of $SU(2) \otimes U(1)$ gauge symmetry would occur at the electroweak scale. The position of the physical minimum of the potential representing the interaction of Higgs fields is determined by solving the set of nonlinear algebraic equations

$$\begin{aligned} \frac{\partial V(v_1, v_2, y)}{\partial v_1} &= 0, & \frac{\partial V(v_1, v_2, y)}{\partial v_2} &= 0, \\ \frac{\partial V(v_1, v_2, y)}{\partial y} &= 0, \end{aligned} \quad (17)$$

where $V(v_1, v_2, y)$ is the effective potential of interaction of Higgs fields within the modified nonminimal supersymmetric standard model [14].

Since the vacuum expectation value v and $\tan \beta$ are known, the set of Eqs. (17) can be used to determine the parameters μ and B_0 and to compute the vacuum expectation value $\langle Y \rangle$. Instead of μ , it is convenient to introduce here $\mu_{\text{eff}} = \mu + \lambda y/\sqrt{2}$. The sign of μ_{eff} is not fixed in solving the set of Eqs. (17); it must be considered as a free parameter of the theory. The results obtained in this way for the vacuum expectation value y , the parameters μ_{eff} and B_0 , and the spectrum of particles within the modified nonminimal supersymmetric standard model depend on the choice of A , m_0 , $M_{1/2}$, and μ' .

It is of particular interest to analyze the spectrum of particles in that region of the parameter space of the modified nonminimal supersymmetric standard model where the mass of the lightest Higgs boson is close to its theoretical upper limit, since the remaining part of the parameter space is virtually ruled out by the existing experimental data. For each individual set of the parameters A , m_0 , and $M_{1/2}$, the mass of the lightest Higgs boson reaches the upper bound on it at a specific choice of μ' . It is precisely at these values of the parameter μ' that we have calculated the particle spectrum presented in Tables 1 and 2. On the basis of our numerical results given there, one can assess the effect of the fundamental constants A , m_0 , and $M_{1/2}$ on the spectrum of the superpartners

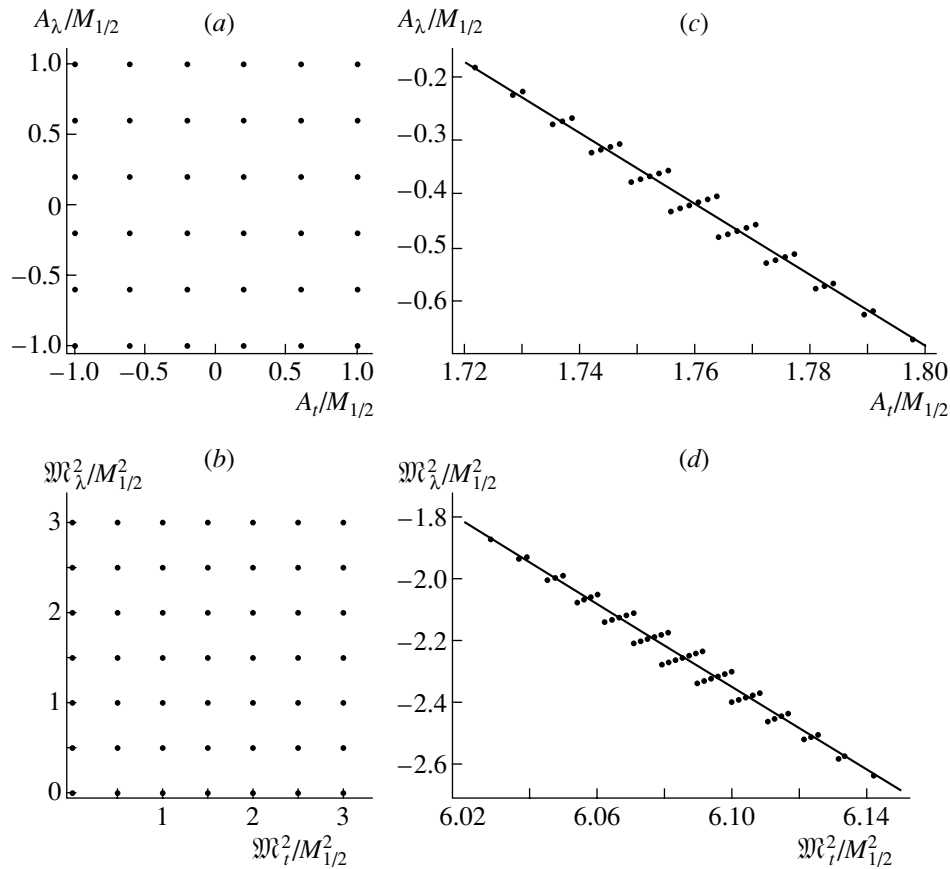


Fig. 2. Boundary conditions specified for the renormalization-group equations within the modified nonminimal supersymmetric standard model and uniformly distributed in the (a) $(A_t/M_{1/2}, A_\lambda/M_{1/2})$ and the (b) $(\mathfrak{M}_t^2/M_{1/2}^2, \mathfrak{M}_\lambda^2/M_{1/2}^2)$ plane and (c, d) corresponding values of the parameters at the electroweak scale for $h_t^2(0) = \lambda^2(0) = 20$. The quantities $\mathfrak{M}_t^2(t_0)$ and $\mathfrak{M}_\lambda^2(t_0)$ were computed at $A_t(0) = A_\lambda(0) = 0$. The straight lines in Figs. 2c and 2d represent the results of a fit to the values $(A_t(t_0), A_\lambda(t_0))$ and $(\mathfrak{M}_t^2(t_0), \mathfrak{M}_\lambda^2(t_0))$.

of the t quark ($m_{\tilde{t}_{1,2}}$), the gluino (M_3), the neutralino ($m_{\tilde{\chi}_{1,\dots,5}}$), the chargino ($m_{\tilde{\chi}_{1,2}^\pm}$), and the Higgs bosons ($m_h, m_H, m_S, m_{A_{1,2}}$). For each set of the aforementioned parameters, we quote the mass of the lightest Higgs boson according to the calculations in the one- and the two-loop approximation, along with the corresponding values of μ_{eff}, B_0, y , and μ' . As can be seen from the data displayed in Tables 1 and 2, the qualitative pattern of the spectrum within the modified nonminimal supersymmetric standard model undergoes no changes in response to variations of the parameters A and m_0 within reasonable limits.

The CP -even Higgs boson (m_S), which corresponds to the neutral field Y , is the heaviest particle in the spectrum of the modified nonminimal supersymmetric standard model, while the neutralino (m_{χ_5}) is the heaviest fermion there, the main contribution to its wave function coming from the superpartner of the field Y . With increasing m_0^2 , the masses of the squarks, the Higgs bosons, and the heavy charginos

and neutralinos grow, whereas the spectrum of extremely light particles remains unchanged. Since the dependence of the parameters of a soft breakdown of supersymmetry on A disappears at the electroweak scale in the regime of strong Yukawa coupling, the parameters μ_{eff}, B , and μ' , together with the spectrum of the superpartners of observable particles and the mass of the lightest Higgs boson, undergo only slight changes in response to a variation of the trilinear coupling constant for the interaction of scalar fields from $-M_{1/2}$ to $M_{1/2}$. Despite this, the A dependence of the masses of one of the CP -even (m_S) and of two CP -odd ($m_{A_{1,2}}$) Higgs bosons survives. It is due primarily to the fact that the bilinear coupling constant B' for the interaction of neutral scalar fields is proportional to A . It should be noted in addition that, for a specific choice of fundamental parameters (in particular, of the parameter A), the mass of the lightest CP -odd Higgs boson may prove to be about 100 GeV or less. However, this Higgs boson takes

Table 1. Spectrum of particles in the vicinity of the quasifixed point within the modified nonminimal supersymmetric standard model at $m_t(M_t^{\text{pole}}) = 165$ GeV, $\tan \beta \approx 1.883$, and $\mu_{\text{eff}} > 0$ for various choices of the fundamental parameters A , m_0 , and $M_{1/2}$ (all the parameters and masses are given in GeV)

m_0^2	0	$M_{1/2}^2$	0	0	0	0
A	0	0	$-M_{1/2}$	$0.5M_{1/2}$	0	0
$M_{1/2}$	-392.8	-392.8	-392.8	-392.8	-785.5	-196.4
μ_{eff}	728.6	841.7	726.8	730.1	1361.2	380.4
B_0	-1629.1	-1935.4	-1260.0	-1813.2	-3064.4	-861.8
y	-0.00037	-0.00021	-0.00043	-0.00035	-0.00006	-0.00233
$\mu'(t_0)$	-1899.8	-2176.7	-1905.9	-1898.3	-3544.6	-993.1
$m_h(t_0)$	125.0	125.1	125.0	125.0	134.9	114.8
(1-loop)						
$m_h(t_0)$	118.4	118.5	118.4	118.4	123.2	111.9
(2-loop)						
$M_3(1 \text{ TeV})$	1000	1000	1000	1000	2000	500
$m_{\tilde{t}_1}(1 \text{ TeV})$	840.6	889.7	841.1	840.3	1652.0	447.4
$m_{\tilde{t}_2}(1 \text{ TeV})$	695.1	713.6	696.6	694.3	1366.2	371.6
$m_H(1 \text{ TeV})$	898.5	1080.5	895.4	900.3	1691.0	468.8
$m_S(1 \text{ TeV})$	2623.4	3034.3	2452.2	2706.0	4901.7	1378.0
$m_{A_1}(1 \text{ TeV})$	953.9	1113.8	1245.7	925.2	1722.6	538.2
$m_{A_2}(1 \text{ TeV})$	704.3	762.7	872.0	318.2	1366.2	302.2
$m_{\tilde{\chi}_1}(t_0)$	164.6	164.4	164.6	164.6	326.9	84.3
$m_{\tilde{\chi}_2}(t_0)$	327.8	327.6	327.8	327.8	649.4	170.1
$m_{\tilde{\chi}_3}(1 \text{ TeV})$	755.1	870.8	753.3	756.7	1404.2	400.9
$ m_{\tilde{\chi}_4}(1 \text{ TeV}) $	755.9	872.6	755.1	758.4	1405.0	404.3
$ m_{\tilde{\chi}_5}(1 \text{ TeV}) $	1931.8	2212.3	1938	1930.3	3599.0	1015.4
$m_{\tilde{\chi}_1^\pm}(t_0)$	327.8	327.6	327.8	327.8	649.4	169.9
$m_{\tilde{\chi}_2^\pm}(1 \text{ TeV})$	757.0	872.6	755.2	758.5	1405.2	404.5

virtually no part in electroweak interaction, since the main contribution to its wave function comes from the CP -odd component of the field Y . Therefore, attempts at experimentally detecting it run into problems.

Loop corrections play an important role in calculating the mass of the lightest Higgs boson. Their inclusion results in that the mass of the lightest Higgs boson proves to be greater for $\mu_{\text{eff}} < 0$ than for $\mu_{\text{eff}} > 0$. This is because m_h grows as the mixing in the sector of the superpartners of the t quark (\tilde{t}_R and \tilde{t}_L) becomes stronger. The point is that the mixing of \tilde{t}_R and \tilde{t}_L is determined by the quantity $X_t = A_t + \mu_{\text{eff}}/\tan \beta$ and is therefore greater in magnitude for

$\mu_{\text{eff}} < 0$ since $A_t < 0$. It should also be noted that the inclusion of two-loop corrections leads to a reduction of m_h by approximately 10 GeV. The mass of the lightest Higgs boson depends only slightly on A and m_0 , because the squark masses depend slightly on the corresponding fundamental parameters (see Tables 1 and 2). The value of m_h is determined primarily by the supersymmetry-breaking scale M_S —that is, by the quantity M_3 . From our numerical results quoted in Tables 1 and 2, one can see that, at $m_t(M_t^{\text{pole}}) = 165$ GeV and $M_3 \leq 2$ TeV, the mass of the lightest Higgs boson does not exceed 127 GeV.

Table 2. Spectrum of particles in the vicinity of the quasifixed point within the modified nonminimal supersymmetric standard model at $m_t(M_t^{\text{pole}}) = 165$ GeV, $\tan \beta \approx 1.883$, and $\mu_{\text{eff}} < 0$ for various choices of the fundamental parameters A , m_0 , and $M_{1/2}$ (all the parameters and masses are given in GeV)

m_0^2	0	$M_{1/2}^2$	0	0	0	0
A	0	0	$-M_{1/2}$	$M_{1/2}$	0	0
$M_{1/2}$	-392.8	-392.8	-392.8	-392.8	-785.5	-196.4
μ_{eff}	-727.8	-840.9	-726.0	-731.2	-1360.7	-378.9
B_0	1008	1320.3	1366.7	647.9	2050.4	495.8
y	-0.00149	-0.001	-0.00128	-0.00177	-0.00020	-0.0112
$\mu'(t_0)$	1671.5	1950.6	1656.8	1690.3	3172.7	857.8
$m_h(t_0)$	134.1	134.9	134.0	134.2	143.1	124.1
(1-loop)						
$m_h(t_0)$	124.4	124.8	124.3	124.5	127.2	119.6
(2-loop)						
$M_3(1 \text{ TeV})$	1000	1000	1000	1000	2000	500
$m_{\tilde{t}_1}(1 \text{ TeV})$	890.2	935.6	890.5	889.8	1682.8	507.9
$m_{\tilde{t}_2}(1 \text{ TeV})$	630.3	652.2	632.2	628.0	1328.1	283.5
$m_H(1 \text{ TeV})$	896.2	1078.5	893.5	899.3	1689.9	464.4
$m_S(1 \text{ TeV})$	2147.4	2565.9	2309.2	1972.3	4126.5	1097.7
$m_{A_1}(1 \text{ TeV})$	1123.2	1219.3	931.0	1437.9	1984.8	623.1
$m_{A_2}(1 \text{ TeV})$	857.6	1017.8	545.0	886.9	1657.5	412.8
$m_{\tilde{\chi}_1}(t_0)$	160.0	160.5	160.0	160.0	324.4	74.9
$m_{\tilde{\chi}_2}(t_0)$	311.1	313.7	311.0	311.2	639.9	141.4
$ m_{\tilde{\chi}_3}(1 \text{ TeV}) $	753.7	896.6	751.9	757.2	1403.4	398.5
$m_{\tilde{\chi}_4}(1 \text{ TeV})$	764.7	878.1	763.0	768.1	1410.0	416.7
$m_{\tilde{\chi}_5}(1 \text{ TeV})$	1700.7	1983.2	1685.8	1719.6	3221.8	879.1
$m_{\tilde{\chi}_1^\pm}(t_0)$	310.7	313.4	310.7	310.8	639.8	139.4
$m_{\tilde{\chi}_2^\pm}(1 \text{ TeV})$	763.3	877.0	761.6	766.7	1409.1	414.5

6. CONCLUSION

We have studied coupling-constant renormalization and the spectrum of particles within the modified nonminimal supersymmetric standard model. We have shown that, in the regime of strong Yukawa coupling, solutions to the renormalization-group equations for $Y_i(t)$ are attracted to the Hill line and that, under specific conditions, $b-\tau$ unification is realized at the scale M_X . In the limit $Y_i(0) \rightarrow \infty$, all solutions for the Yukawa coupling constants are concentrated in the vicinity of the quasifixed point that is formed in the space of the Yukawa coupling constants as the result of intersection of the invariant and the Hill line.

As the Yukawa coupling constants approach the quasifixed point, the corresponding trilinear coupling constants and combinations (11) of the scalar-particle masses cease to depend on the boundary conditions at the scale M_X . In the case of nonuniversal boundary conditions, $A_i(t)$ and $\mathfrak{M}_i^2(t)$ are attracted to straight lines in the space spanned by the parameters of a soft breakdown of supersymmetry and, with increasing $Y_i(0)$, approach the quasifixed points, moving along these straight lines.

We have analyzed the spectrum of particles in the infrared-quasifixed-point regime of the modified nonminimal supersymmetric standard model. The CP -even Higgs boson, which corresponds to the neutral

field Y , is the heaviest particle in this spectrum. At reasonable values of the parameters of the model being studied, the gluinos, the squarks, and the heavy Higgs bosons are much heavier than the lightest Higgs boson and than the lightest chargino and the lightest neutralino as well. This is not so only for one of the CP -odd Higgs bosons whose mass changes within a wide range in response to variations in the fundamental parameters of the modified nonminimal supersymmetric standard model. In the vicinity of the quasifixed point at $m_t(M_t^{\text{pole}}) = 165$ GeV, the mass of the lightest Higgs boson does not exceed 127 GeV.

ACKNOWLEDGMENTS

We are grateful to M.I. Vysotsky, D.I. Kazakov, L.B. Okun, and K.A. Ter-Martirosyan for stimulating questions and enlightening discussions and comments.

This work was supported by the Russian Foundation for Basic Research (project nos. 00-15-96562 and 00-15-96786).

REFERENCES

1. C. T. Hill, Phys. Rev. D **24**, 691 (1981); C. T. Hill, C. N. Leung, and S. Rao, Nucl. Phys. B **262**, 517 (1985).
2. V. Barger, M. S. Berger, P. Ohmann, and R. J. N. Phillips, Phys. Lett. B **314**, 351 (1993); M. Carena, M. Olechowski, S. Pokorski, and C. E. M. Wagner, Nucl. Phys. B **419**, 213 (1994); W. A. Bardeen, M. Carena, S. Pokorski, and C. E. M. Wagner, Phys. Lett. B **320**, 110 (1994); M. Carena and C. E. M. Wagner, Nucl. Phys. B **452**, 45 (1995); S. A. Abel and B. C. Allanach, Phys. Lett. B **415**, 371 (1997); **431**, 339 (1998).
3. G. K. Yeghiyan, M. Jurčišin, and D. I. Kazakov, Mod. Phys. Lett. A **14**, 601 (1999); S. Codoban, M. Jurčišin, and D. Kazakov, hep-ph/9912504.
4. J. A. Casas, J. R. Espinosa, and H. E. Haber, Nucl. Phys. B **526**, 3 (1998).
5. B. Brahmachari, Mod. Phys. Lett. A **12**, 1969 (1997).
6. P. Igo-Kemenes, in *Proceedings of XXX International Conference on High-Energy Physics, Osaka, 2000* (in press).
7. P. Fayet, Nucl. Phys. B **90**, 104 (1975); M. I. Vysotskiĭ and K. A. Ter-Martirosyan, Zh. Éksp. Teor. Fiz. **90**, 838 (1986) [Sov. Phys. JETP **63**, 489 (1986)].
8. J. Ellis, J. F. Gunion, H. E. Haber, *et al.*, Phys. Rev. D **39**, 844 (1989).
9. L. Durand and J. L. Lopes, Phys. Lett. B **217**, 463 (1989); L. Drees, Int. J. Mod. Phys. A **4**, 3635 (1989).
10. T. Elliott, S. F. King, and P. L. White, Phys. Lett. B **314**, 56 (1993); U. Ellwanger, Phys. Lett. B **303**, 271 (1993); U. Ellwanger and M. Lindner, Phys. Lett. B **301**, 365 (1993); P. N. Pandita, Phys. Lett. B **318**, 338 (1993); P. N. Pandita, Z. Phys. C **59**, 575 (1993); T. Elliott, S. F. King, and P. L. White, Phys. Rev. D **49**, 2435 (1994); S. W. Ham, S. K. Oh, and B. R. Kim, J. Phys. G **22**, 1575 (1996); Phys. Lett. B **414**, 305 (1997); P. A. Kovalenko, R. B. Nevzorov, and K. A. Ter-Martirosyan, Yad. Fiz. **61**, 898 (1998) [Phys. At. Nucl. **61**, 812 (1998)]; S. W. Ham, S. K. Oh, and H. S. Song, hep-ph/9910461.
11. S. F. King and P. L. White, Phys. Rev. D **52**, 4183 (1995).
12. M. A. Diaz, T. A. Ter Veldius, and T. J. Weiler, Phys. Rev. D **54**, 5855 (1996).
13. S. A. Abel, S. Sarkar, and P. L. White, Nucl. Phys. B **454**, 663 (1995).
14. R. B. Nevzorov and M. A. Trusov, Zh. Éksp. Teor. Fiz. **118**, 1251 (2000) [JETP **91**, 1079 (2000)].
15. G. F. Giudice and A. Masiero, Phys. Lett. B **206**, 480 (1988).
16. J. A. Casas and C. Muñoz, Phys. Lett. B **306**, 288 (1993).
17. J. E. Kim and H. P. Nilles, Phys. Lett. B **138B**, 150 (1984); **263**, 79 (1991); E. J. Chun, J. E. Kim, and H. P. Nilles, Nucl. Phys. B **370**, 105 (1992).
18. B. C. Allanach and S. F. King, Phys. Lett. B **407**, 124 (1997); I. Jack and D. R. T. Jones, Phys. Lett. B **443**, 177 (1998).
19. P. Binetruy and C. A. Savoy, Phys. Lett. B **277**, 453 (1992).
20. B. Schrempp and F. Schrempp, Phys. Lett. B **299**, 321 (1993); B. Schrempp, Phys. Lett. B **344**, 193 (1995); B. Schrempp and M. Wimmer, Prog. Part. Nucl. Phys. **37**, 1 (1996).
21. R. B. Nevzorov and M. A. Trusov, Yad. Fiz. **64**, 1375 (2001) [Phys. At. Nucl. **64**, 1299 (2001)].
22. B. C. Allanach and S. F. King, Phys. Lett. B **328**, 360 (1994).
23. R. B. Nevzorov and M. A. Trusov, Yad. Fiz. **64**, 1589 (2001) [Phys. At. Nucl. **64**, 1513 (2001)].

Translated by A. Isaakyan

Conference on Physics of Fundamental Interactions Theory

NN Correlations in a Multinucleon System

M. G. Schepkin, I. V. Seluzhenkov¹⁾, and H. Clement²⁾

Institute of Theoretical and Experimental Physics, Bol'shaya Cheremushkinskaya ul. 25, Moscow, 117218 Russia

Received March 21, 2001

Abstract—Cross sections for processes involving three or more identical nucleons in the final state are expected to be strongly suppressed near the threshold because of the Pauli exclusion principle. It is shown that the Migdal–Watson effect (final-state interaction between nucleons) removes this suppression.

© 2002 MAIK “Nauka/Interperiodica”.

1. INTRODUCTION

In this study, we examine reactions involving more than two identical fermions (nucleons) in the final state. The features of such reactions induced by pions and photons are measured at numerous research centers worldwide, such as TRIUMF (π^+ $^4\text{He} \rightarrow \pi^- pppp$, π^- $^3\text{He} \rightarrow \pi^+ nnn$), PSI [single-charge-exchange reactions (π^+ , π^0) on ^3He and ^4He], and TJNAF (γ^* $^3\text{He} \rightarrow \pi^+ nnn$).

The cross sections for such reactions are expected to be strongly suppressed (especially near the threshold) because of the Pauli exclusion principle (see [1–7] and references therein). However, this expectation is not corroborated experimentally. In particular, the low-energy cross sections for the single-charge-exchange reactions π^+ $^3\text{He} \rightarrow \pi^0 ppp$ and $\pi^+ d \rightarrow \pi^0 pp$ are on the same order of magnitude [8]. According to naive estimates, the cross section for the reaction π^+ $^3\text{He} \rightarrow \pi^0 ppp$ at incident pion energies in the range $T_\pi \sim 40$ – 70 MeV is two orders of magnitude smaller than the cross section for the single-charge-exchange reaction $\pi^+ d \rightarrow \pi^0 pp$ on a deuteron. In this study, we show that final-state nucleon–nucleon interaction removes the suppression induced by the Pauli exclusion principle.

The Pauli exclusion principle and final-state *NN* interaction are discussed in almost all articles devoted to studying low-energy processes that lead to the production of more than two identical nucleons in the final state and which include double-charge-exchange reactions on helium isotopes [1–7]. Nevertheless, it seems reasonable to analyze such reactions

more comprehensively in order to clarify the specific role of the final-state interaction between nucleons. In what follows, questions associated with taking into account the Pauli exclusion principle and final-state nucleon–nucleon interaction are discussed for the example of the reaction π^+ $^3\text{He} \rightarrow \pi^0 ppp$.

2. ESTIMATING THE SUPPRESSION OF CROSS SECTIONS

We consider the single-charge-exchange reactions π^+ $^3\text{He} \rightarrow \pi^0 ppp$ and π^- $^3\text{He} \rightarrow \pi^0 nnp$. Assuming that these processes are governed by identical mechanisms (see Fig. 1a), we can easily show that the amplitude of the reaction π^+ $^3\text{He} \rightarrow \pi^0 ppp$ must involve an additional factor $\langle v \rangle$, where $\langle v \rangle$ is the characteristic velocity of a final nucleon. For an incident pion energy of $T_\pi \sim 50$ MeV, the characteristic velocity of particles is $\langle v \rangle \sim 0.1$; therefore, the cross sections for these two reactions must differ by two orders of magnitude.³⁾

The appearance of the additional factor $\langle v \rangle$ (or its powers) in the reaction amplitude is due to antisymmetrization with respect to final-state nucleons. The amplitude of the single-charge-exchange reaction π^+ $^3\text{He} \rightarrow \pi^0 ppp$ can be written in the invariant form

$$M \sim \sum_{ijk} \epsilon_{ijk} (\bar{u}_i (A + B\hat{q}) U) (\bar{u}_j C \gamma_5 \bar{u}_k^T), \quad (1)$$

where the subscripts *i*, *j*, and *k* label the final nucleons; u_i and U are the bispinors corresponding to the *i*th nucleon and ^3He , respectively; C is the

¹⁾Institute of Theoretical and Experimental Physics, Bol'shaya Cheremushkinskaya ul. 25, Moscow, 117218 Russia, and Moscow State Engineering Physics Institute (Technical University), Kashirskoe sh. 31, Moscow, 115409 Russia.

²⁾Institut für Theoretische Physik, Universität Tübingen, Auf der Morgenstelle 14, D-72076 Tübingen, Germany.

³⁾In a similar way, it can be shown that, because the process where a positive pion undergoes double charge exchange on ^4He involves four identical nucleons in the final state, the corresponding suppression must be proportional to $\langle v \rangle^4$ (see, for example, the relevant discussion in [6]).

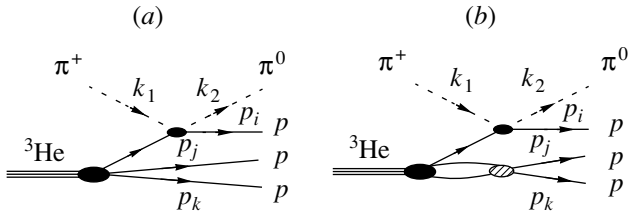


Fig. 1. Diagrams for the reaction where a pion undergoes single charge exchange on ${}^3\text{He}$ (a) without and (b) with allowance for final-state nucleon–nucleon interaction.

charge-conjugation matrix; and $q = k_1 - k_2$ is the momentum transfer, where $k_{1,2}$ are the momenta of initial and final pions, respectively. In expression (1), we omitted trivial isotopic factors, but they can easily be recovered.

In a realistic amplitude corresponding to the process depicted in Fig. 1a, the factors A and B

are smooth functions of kinematic variables. These functions can be determined explicitly from the πN -scattering amplitudes [9] with the phase shifts from [10]. In order to solve the main problem of this study, it is sufficient, however, to use a simplified amplitude where A and B are set to constants.

For further calculations, it is convenient to express the reaction amplitude M in terms of the two-component spinors φ_i and ϕ associated with the i th nucleon and ${}^3\text{He}$, respectively. In the laboratory frame, where ${}^3\text{He}$ is at rest and where the i th nucleon has a momentum \mathbf{p}_i and an energy E_i , we have

$$u_i = \begin{pmatrix} \varphi_i \\ (\boldsymbol{\sigma} \cdot \mathbf{p}_i) \varphi_i \\ E_i + m \end{pmatrix}, \quad U = \begin{pmatrix} \phi \\ 0 \end{pmatrix}.$$

Substituting this expression into Eq. (1), we obtain

$$M \sim \sum_{ijk} \epsilon_{ijk} \left(\varphi_j^\dagger \left\{ 1 + i\boldsymbol{\sigma} \frac{[\mathbf{p}_j \times \mathbf{p}_k]}{(E_j + m)(E_k + m)} \right\} \sigma_2 \varphi_k^* \right) \left(\varphi_i^\dagger \left\{ A + q_0 B - iB\boldsymbol{\sigma} \frac{[\mathbf{p}_i \times \mathbf{q}]}{E_i + m} \right\} \phi \right). \quad (2)$$

From the equality

$$\sum_{ijk} \epsilon_{ijk} \left(\varphi_j^\dagger \sigma_2 \varphi_k^* \right) \left(\varphi_i^\dagger \phi \right) = 0,$$

it is obvious that, upon antisymmetrization in each term of the sum over i , j , and k , the leading contributions cancel. The remaining terms have a simple physical meaning: the term proportional to A corresponds to the transfer of even orbital angular momenta from the pion to the nucleon subsystem, whereas the term proportional to B corresponds to the transfer of odd orbital angular momenta from the p wave, which is the lowest wave allowed by the Pauli exclusion principle. This interpretation is quite clear and is independent of the specific form of the functions A and B . However, the inclusion of the final-state nucleon–nucleon interaction considerably changes this situation.

3. NUCLEON–NUCLEON CORRELATIONS

It is well known that the final-state NN interaction is the most important in the case where a pair of nucleons has low relative invariant mass and where these nucleons are in the relative s wave [11, 12]. For two identical nucleons, this is the 1S_0 ($J^P = 0^+$) state. In the case of three identical nucleons, only two of them can be in the relative s wave. One can demonstrate that the $(\bar{u}_i(A + B\hat{q})U)(\bar{u}_j C \gamma_5 \bar{u}_k^T)$ term

in amplitude (1) corresponds to the case where the j th and the k th nucleon form a 0^+ state, whereas the i th nucleon has a higher orbital angular momentum than the jk pair.

The final-state interaction is represented by the diagram involving the rescattering of two nucleons (Fig. 1b). The contribution of this diagram is proportional to the scattering amplitude f_{jk} for a pair of nucleons in the 1S_0 states. In order to take into account the interaction between final nucleons, we must therefore multiply each term that appears in Eq. (1) and which involves the factor $(\bar{u}_j C \gamma_5 \bar{u}_k^T)$ by $(1 + R^{-1} \cdot f_{jk})$, where R is about the ${}^3\text{He}$ radius and f_{jk} depends on the relative momentum $|\mathbf{p}_{jk}| = \sqrt{m_{jk}^2/4 - m^2}$ (m_{jk} is the invariant mass of the jk nucleon pair) of j th and k th nucleons in their c.m. frame.

With allowance for the final-state nucleon–nucleon interaction, the amplitude of the reaction $\pi^+ {}^3\text{He} \rightarrow \pi^0 ppp$ can therefore be represented as

$$M_{\text{FSI}} \sim \sum_{ijk} \epsilon_{ijk} (\bar{u}_i(A + B\hat{q})U)(\bar{u}_j C \gamma_5 \bar{u}_k^T) \times (1 + R^{-1} \cdot f_{jk}). \quad (3)$$

This amplitude is antisymmetric with respect to permutations of identical fermions, thereby satisfying the Pauli exclusion principle. In contrast to what occurs

in Eq. (2), however, antisymmetrization does not lead in this case to a complete cancellation of the leading terms:

$$\sum_{ijk} \epsilon_{ijk} \left(\varphi_j^+ \sigma_2 \varphi_k^* \right) \left(\varphi_i^+ \phi \right) f_{jk} \neq 0.$$

This is because there is a singularity in the NN -interaction amplitude at low relative momenta of nucleons. This is the region where the nucleon–nucleon interaction is especially strong.

In mathematical terms, the difference between the two cases is the following: the low-energy amplitude determined without taking into account the nucleon–nucleon interaction can be expanded in a power series in low nucleon velocities, but there is no such expansion for the amplitude including this interaction.

Physically, this means that higher orbital angular momenta of each of the nucleons in the 1S_0 state with respect to the third nucleon are no longer suppressed.

4. CONCLUSION

If the final state of a reaction involves three or more identical nucleons of low invariant mass, the Migdal–Watson effect (final-state nucleon–nucleon interaction) removes the suppression of cross sections that is associated with the Pauli exclusion principle. This result has been obtained here for the example of the reaction $\pi^+{}^3\text{He} \rightarrow \pi^0 ppp$, whose amplitude is very sensitive to the details of the nucleon–nucleon interaction, in contrast to, for example, the reaction $\pi^-{}^3\text{He} \rightarrow \pi^0 nnp$, where there is no suppression by the Pauli exclusion principle.

ACKNOWLEDGMENTS

This work was supported by the Russian Foundation for Basic Research (project no. 00-15-96562); by the DAAD (German Academic Exchange Service), “Euler Scholarship” program; and by the DFG (German Science Foundation, Graduiertenkolleg).

REFERENCES

1. I. M. Barbour and A. C. Phillips, *Phys. Rev. Lett.* **19**, 1388 (1967).
2. A. C. Phillips, *Phys. Lett. B* **33B**, 260 (1970).
3. F. Becker and C. Schmit, *Nucl. Phys. B* **18**, 607 (1970).
4. J. F. Germond and C. Wilkin, *Lett. Nuovo Cimento* **13**, 605 (1975).
5. H. Brückmann, W. Kluge, H. Matthäy, *et al.*, *Phys. Lett. B* **30B**, 460 (1969).
6. W. R. Gibbs, B. F. Gibson, A. T. Hess, and G. J. Stephenson, Jr., *Phys. Rev. C* **15**, 1384 (1977).
7. R. I. Jibuti and R. Y. A. Kezerashvili, *Nucl. Phys. A* **437**, 687 (1985).
8. LADS Collab. (A. Lehmann *et al.*), *Phys. Rev. C* **60**, 024603 (1999).
9. G. Höhler, in *Landolt-Börnstein: Numerical Data and Functional Relationships in Science and Technology* (Springer-Verlag, Berlin, 1983), Group I, Vol. 9.
10. A. A. Ebrahim and R. J. Peterson, *Phys. Rev. C* **54**, 2499 (1996).
11. K. M. Watson, *Phys. Rev.* **88**, 1163 (1952).
12. A. B. Migdal, *Zh. Éksp. Teor. Fiz.* **28**, 3 (1955) [*Sov. Phys. JETP* **1**, 2 (1955)].

Translated by R. Tyapaeu

Conference on Physics of Fundamental Interactions Theory

Correlations between Pions of Low Relative Momenta

A. D. Andryakov, O. V. Bulekov^{1)*}, V. S. Demidov, V. A. Okorokov¹⁾,
I. A. Polenkevich¹⁾, A. K. Ponosov¹⁾, I. A. Rubinsky¹⁾, and F. M. Sergeev¹⁾

*Institute of Theoretical and Experimental Physics, Bol'shaya
Cheremushkinskaya ul. 25, Moscow, 117218 Russia*

Received February 21, 2001; in final form, May 31, 2001

Abstract—Two-particle pion correlations in exclusive πp and pp interactions at $\sqrt{s} = 2.9\text{--}4$ GeV are studied in the region of low relative 4-momenta. Relevant correlation functions are obtained with allowance for the results of calculations based on the model of quark–gluon strings and the FRITIOF model. Positive correlations that make it possible to estimate the spatial size of the pion source are observed for pairs of identical pions. No correlations are observed for pairs featuring one charged and one neutral pion.

© 2002 MAIK “Nauka/Interperiodica”.

Investigation of correlations between hadrons of low relative momentum makes it possible to measure the spacetime features of the hadron-generation region. This is of importance for obtaining deeper insights into the quark-hadronization mechanism and is of interest in connection with developing methods for seeking quark–gluon plasma. The first experimental data on correlations between identical pions were obtained as far back as 1959 [1]. Later on, these data gave impetus to the new line of investigations that is known as pion interferometry [2, 3].

Different effects are possible in systems of non-identical pions in the region of low relative momenta. In particular, systems consisting of a neutral and a charged pion can develop correlations associated with the Fermi statistics of quarks [4, 5].

In this article, we report on an investigation of the reactions presented in Table 1. The experimental data used come from the 2-m hydrogen bubble chambers installed at the Institute of Theoretical and Experimental Physics (ITEP, Moscow) and at CERN. The total sample consisted of 120 000 interactions. The features of neutral pions were determined in each individual event from kinematical balance.

In our data analysis, we used the two-particle correlation function defined as

$$C_2(p_1, p_2) = \frac{N_2(p_1, p_2)}{N_1(p_1)N_1(p_2)}, \quad (1)$$

where p_1 and p_2 are the particle 4-momenta, while N_1 and N_2 are, respectively, the single- and two-particle distribution density.

We studied the dependence of the correlation function C_2 on the invariant variable $Q^2 = -(p_1 - p_2)^2$. This variable combines the properties of a three-dimensional analysis with reduced requirements on the volume of the data sample, which are typical of one-dimensional problems [6].

The model of independent emission from single-particle sources whose spacetime distribution over the volume of a static sphere obeys the Gaussian law leads to the Goldhaber parametrization [7]

$$C_2(Q) = (1 + \lambda \exp(-R^2 Q^2))(\alpha + \beta Q + \gamma Q^2), \quad (2)$$

where $(\alpha + \beta Q + \gamma Q^2)$ is an additional factor introduced to take into account kinematical correlations off the interference peak, λ is the coherence parameter, and R is a parameter that is proportional to the mean-square radius of a spherically symmetric source in the dipion rest frame ($R^2 = \langle r^2 \rangle / 3$).

In order to take into account the final-state Coulomb interaction in the product charged-pion pair, we used the Gamow factor

$$G = \frac{2\pi\eta}{e^{2\pi\eta} - 1}, \quad \eta = \frac{Z_1 Z_2 m_\pi \alpha}{Q}, \quad (3)$$

where α is the fine-structure constant and Z_1 and Z_2 are the pion charges.

The choice of background is a key problem in studying interference correlations. For a background, use is usually made either of pairs of oppositely charged pions from the same experiment, or of pairs of particles from different events, or of model calculations. Each method has drawbacks inherent in it. In order to estimate the background effect on the shape of the correlation function, we preliminarily studied

¹⁾Moscow State Engineering Physics Institute (Technical University), Kashirskoe sh. 31, Moscow, 115409 Russia.

*e-mail: bulekov@pc4k07.exp.mephi.ru

Table 1. Reactions under study

Reaction number	Reaction	$p_{\text{beam}}, \text{ GeV}/c$	Number of events
1	$\pi^- p \rightarrow p\pi^+\pi^-\pi^-$	3.9	35972
2	$\pi^- p \rightarrow p\pi^+\pi^-\pi^-\pi^0$	3.9	38371
3	$\pi^- p \rightarrow n\pi^+\pi^+\pi^-\pi^-$	3.9	16189
4	$\pi^+ p \rightarrow p\pi^+\pi^+\pi^-\pi^0$	4.2	18567
5	$pp \rightarrow np\pi^+\pi^+\pi^-$	8	6924
6	$pp \rightarrow pp\pi^+\pi^-\pi^0$	8	4046

Table 2. Fitted values of the parameters in the parametrization (2) of the distributions $C_2(Q)$ for reactions 1–5 in the interval $0 \leq Q \leq 0.5 \text{ GeV}$

Reaction number	$N^{\text{data}}/N^{\text{BG}}$	λ	$R, \text{ fm}$	χ^2/NDF
1	N^{--}/N^{+-}	0.33 ± 0.09	0.80 ± 0.23	0.53
2	N^{--}/N^{+-}	0.78 ± 0.11	1.14 ± 0.09	1.98
2*	N^{--}/N^{+-}	0.54 ± 0.09	0.92 ± 0.11	1.18
3	$N^{\pm\pm}/N^{+-}$	0.67 ± 0.11	1.14 ± 0.13	0.53
4	N^{++}/N^{+-}	0.84 ± 0.19	1.31 ± 0.16	2.3
4*	N^{++}/N^{+-}	0.82 ± 0.21	1.31 ± 0.19	1.83
5	N^{++}/N^{+-}	0.64 ± 0.44	1.84 ± 0.63	0.91

the correlations between pairs of identical pions for the above three types of background distributions.

The observed interference correlations may be affected by intermediate resonance states, Coulomb and strong interactions in the final state, and leading-particle effects. In [8], the effect of these factors on the correlations between identical pions was studied for the example where the background was formed by pairs of oppositely charged pions and pairs consisting of one charged and one neutral pion. It was shown that narrow meson resonances affect the shape of the correlation function in the region of low relative 4-momenta, resulting in the enhancement of spatial dimensions. The leading-particle effect reduces the amplitude of correlations without changing their width. The introduction of the Gamow factor cannot take completely into account final-state Coulomb interaction.

Table 2 displays the results obtained by the correlation function for identical pions from reactions 1–5 (see Table 1) in terms of the function in (2). For the background distributions, we chose the corresponding dependences for oppositely charged pions. An asterisk on the reaction number in the table means that the fitting procedure rejected events where the three-pion effective mass $M_{\text{eff}}(\pi^+\pi^-\pi^0)$ fell within the intervals corresponding to the η and ω resonances (537–561 MeV and 757–813 MeV for reaction 2 and

531–567 MeV and 739–835 MeV for reaction 4). These intervals correspond to the condition $M_{\text{eff}} \in [M_{\eta,\omega} \pm 2\sigma]$, where $M_{\eta,\omega}$ and σ are the mean values and the standard deviation obtained for the η and the ω meson by fitting the effective-mass distribution of the three-pion system $\pi^+\pi^-\pi^0$ in terms of the sum of a Gaussian and a smooth function.

Figure 1 displays the dependences $C_2(Q)$ for identical particles from reactions 2 and 4 for the background distributions constructed from identical-pion pairs simulated on the basis of the FRITIOF model [9] or the model of quark–gluon strings (MSDM) [10]. The curves correspond to the approximation (2) of the correlation function. It is clear that, off the interference peak, the correlation function depends only slightly on Q .

Figure 2 shows the distributions analogous to those in Fig. 1, but the background was obtained here by the mixing method. It is clear that this method requires an additional correction for the “violation” of the energy–conservation law in background events. This correction can be introduced by dividing $C_2(Q)$ by the correlation function obtained with the aid of the same mixing method but, this time, applied to simulated events (open symbols in Fig. 2). To a high precision, the correlation function is close to unity off the interference peak.

Table 3. Fitted values of the parameters in the parametrization (2) of the distributions $C_2(Q)$ for reactions 2 and 4 in the interval $0 \leq Q \leq 1$ GeV

Reaction number	$N^{\text{data}}/N^{\text{BG}}$	λ	R , fm	χ^2/NDF
2*	$N^{--}/N_{\text{FRITIOF}}^{--}$	1.77 ± 0.38	1.19 ± 0.06	1.42
2*	$N^{--}/N_{\text{MSDM}}^{--}$	1.25 ± 0.19	1.13 ± 0.07	0.81
2*	$N^{--}/N_{\text{mix}}^{--}$	0.72 ± 0.14	0.73 ± 0.05	1.29
2*	$\frac{(N^{--}/N_{\text{mix}}^{--})^{\text{data}}}{(N^{--}/N_{\text{mix}}^{--})^{\text{FRITIOF}}}$	2.07 ± 0.31	1.11 ± 0.06	1.48
2*	$\frac{(N^{--}/N_{\text{mix}}^{--})^{\text{data}}}{(N^{--}/N_{\text{mix}}^{--})^{\text{MSDM}}}$	0.61 ± 0.12	0.92 ± 0.09	0.87
4*	$N^{++}/N_{\text{FRITIOF}}^{++}$	1.3 ± 0.4	1.35 ± 0.11	1.48
4*	$N^{++}/N_{\text{MSDM}}^{++}$	0.72 ± 0.24	1.31 ± 0.15	1.52
4*	$N^{++}/N_{\text{mix}}^{++}$	0.52 ± 0.22	1.25 ± 0.19	1.26
4*	$\frac{(N^{++}/N_{\text{mix}}^{++})^{\text{data}}}{(N^{++}/N_{\text{mix}}^{++})^{\text{FRITIOF}}}$	1.62 ± 0.34	1.37 ± 0.11	1.46
4*	$\frac{(N^{++}/N_{\text{mix}}^{++})^{\text{data}}}{(N^{++}/N_{\text{mix}}^{++})^{\text{MSDM}}}$	0.55 ± 0.23	1.28 ± 0.19	1.51

The results obtained on the basis of fits to the correlation functions in Figs. 1 and 2 are quoted in Table 3. The resulting values of the parameter R do not differ significantly from those obtained for the case

where the background consists of oppositely charged pions. The coherence parameter λ derived with the aid of the FRITIOF model is systematically overestimated.

The data in Tables 2 and 3 enable us to estimate the root-mean-square radius of the source within the model used. For the background constructed by the mixing method and improved by the MSDM, the root-mean-square radii in reactions 2 and 4 are 1.6 ± 0.2 and 2.2 ± 0.3 fm, respectively. These values agree with those measured by the Dubna group for πp interactions in inclusive reactions (1.9 ± 0.3 fm) [11].

Figure 3 displays the correlation functions $C_2(Q)$ for pairs consisting of one charged and one neutral pion from reaction 2. For the background formed by similar pion pairs simulated on the basis of the FRITIOF and MSDM, there is no dependence on the difference of the 4-momenta, the scatter of experimental points being within the statistical fluctuations (see Fig. 3a). For the background constructed by mixing (asterisks in Fig. 3b), the observed dependence of C_2 on Q is determined by kinematics. The dependence on Q disappears completely upon dividing the correlation function by that for simulated events (open symbols in Fig. 3b). A similar result was obtained for events from reactions 4 and 6.

In the system consisting of a charged and a neutral pion, featuring no Coulomb interaction, there are no interference correlations. Therefore, this system can be used to construct the background distribution. Table 4 displays the relevant results for reactions 2 and 4. Within statistical errors, the parameters agree with the values obtained here by other methods.

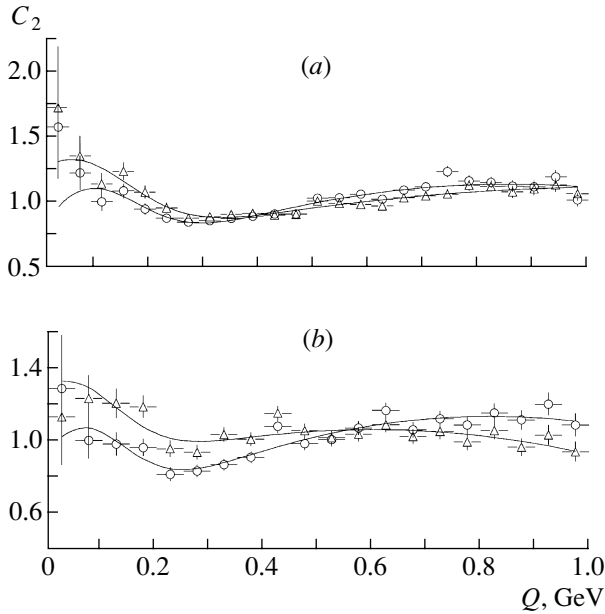


Fig. 1. Correlation function $C_2(Q)$ for identical pions versus the difference Q of the 4-momenta in (a) reaction 2 and (b) reaction 4 (see Table 1). Events satisfying the condition $M_{\text{eff}}(\pi^+\pi^-\pi^0) \in [M_{\eta,\omega} \pm 2\sigma]$ were rejected. The background was constructed from pion pairs generated on the basis of (o) FRITIOF and (Δ) MSDM. The solid curve represents the approximation by the function (2).

Table 4. Fitted values of the parameters in the parametrization (2) of the distributions $C_2(Q)$ for reactions 2 and 4 in the region $0 \leq Q \leq 0.5$ GeV

Reaction number	$N^{\text{data}}/N^{\text{BG}}$	λ	R , fm	χ^2/NDF
2	N^{--}/N^{0-}	0.77 ± 0.13	1.21 ± 0.11	0.43
2*	N^{--}/N^{0-}	0.75 ± 0.13	1.05 ± 0.13	0.66
4	N^{++}/N^{0+}	0.54 ± 0.18	1.45 ± 0.24	0.96
4*	N^{++}/N^{0+}	0.59 ± 0.19	1.32 ± 0.25	0.39

In summary, the main results of our study are the following.

For exclusive hadron interactions, we have analyzed two-particle correlations at low relative momenta in pairs of identical and oppositely charged pions, as well as in pairs consisting of one charged and one neutral pion. We have determined the size of the pion generation region for identical pions.

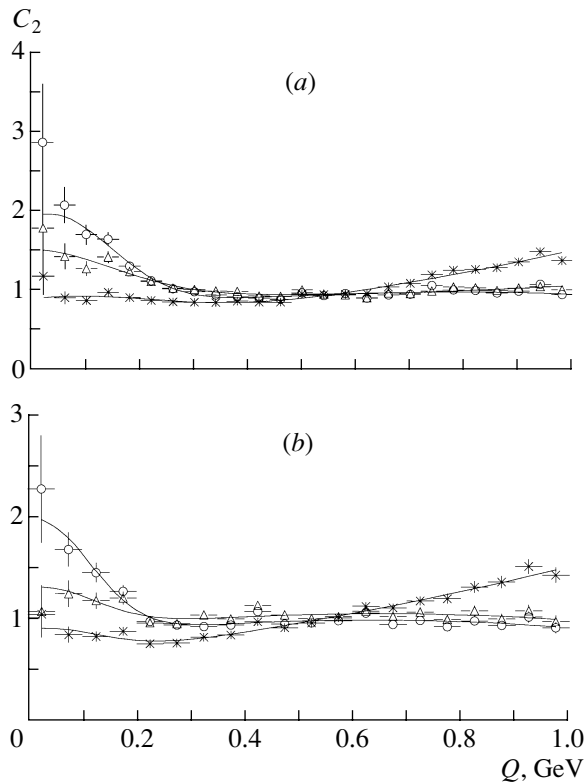


Fig. 2. Correlation function $C_2(Q)$ for identical pions versus the difference Q of the 4-momenta in (a) reaction 1 and (b) reaction 2. Events satisfying the condition $M_{\text{eff}}(\pi^+\pi^-\pi^0) \in [M_{\eta,\omega} \pm 2\sigma]$ were rejected. The background was constructed from pion pairs obtained by mixing (*). The correlation function $C_2(Q)$ was divided by the analogous correlation function obtained on the basis of (o) FRITIOF and (Δ) MSDM calculations. The solid curves represent the approximation by the function (2).

It has been shown that, among the methods used here to construct the background distributions, the best one is that which relies on mixing and which takes into account kinematical correlations through model calculations.

The analysis of the distributions for $\pi^+\pi^0$ ($\pi^-\pi^0$) pairs has revealed that, at the current level of accuracy, there are no effects determined by quark statistics in the system consisting of one charged and one neutral pion.

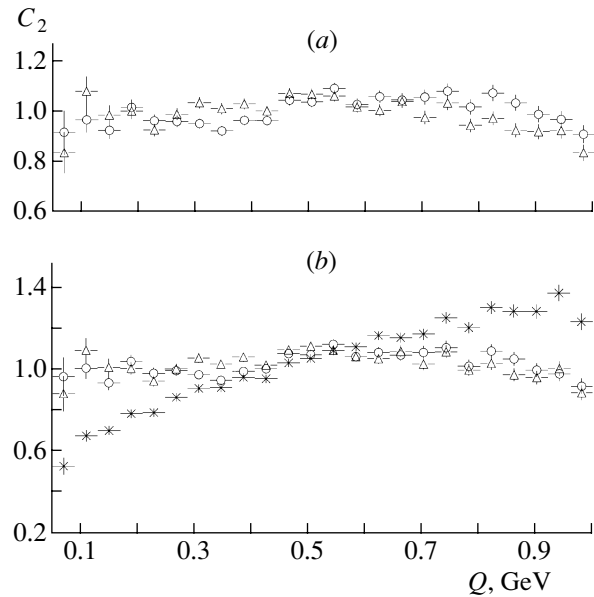


Fig. 3. Correlation function $C_2(Q)$ for pairs consisting of a neutral and a charged pion versus the difference Q of the 4-momenta in reaction 2. Events satisfying the condition $M_{\text{eff}}(\pi^+\pi^-\pi^0) \in [M_{\eta,\omega} \pm 2\sigma]$ were rejected. The background was constructed (a) from pion pairs simulated on the basis of (o) FRITIOF and (Δ) MSDM or (b) by mixing (*). The function $C_2(Q)$ in Fig. 3b obtained by mixing was divided by the analogous correlation function for model events generated by (o) FRITIOF and (Δ) MSDM.

ACKNOWLEDGMENTS

This work was supported by the Federal Program Integration (project A0100) and the Program Universities of Russia—Basic Research (project 02.01.12).

REFERENCES

1. G. Goldhaber *et al.*, Phys. Rev. Lett. **3**, 181 (1959); Phys. Rev. **120**, 300 (1960).
2. M. I. Podgoretskiĭ, Fiz. Élem. Chastits At. Yadra **20**, 628 (1989) [Sov. J. Part. Nucl. **20**, 266 (1989)].
3. E. A. De Wolf, L. M. Dremine, and W. Kittel, Phys. Rep. **270**, 1 (1996).
4. V. V. Vladimirovsky, Preprint No. 20-78, ITÉF (Inst. of Theoretical and Experimental Physics, Moscow, 1978).
5. A. D. Andryakov and Yu. V. Trebukhovskii, Yad. Fiz. **53**, 423 (1991) [Sov. J. Nucl. Phys. **53**, 263 (1991)].
6. N. M. Agababyan *et al.*, Z. Phys. C **59**, 405 (1993).
7. G. Goldhaber, in *Proceedings of Workshop on Local Equilibrium in Strong Interaction Physics (LESIPI)*, Bad Honnef, Germany, 1984, Ed. by D. K. Scott and R. M. Weiner (World Sci., Singapore, 1985), p. 115.
8. A. D. Andryakov, O. V. Bulekov, V. S. Demidov, *et al.*, Preprint No. 42-99, ITÉF (Inst. of Theoretical and Experimental Physics, Moscow, 1999).
9. Hong Pi, LU-TP 91-28.
10. N. S. Amelin, K. K. Gudima, S. Yu. Sivoklokov, and V. D. Toneev, Yad. Fiz. **52**, 272 (1990) [Sov. J. Nucl. Phys. **52**, 172 (1990)].
11. N. Angelov, N. O. Akhababyan, O. Balea, *et al.*, Yad. Fiz. **33**, 1257 (1981) [Sov. J. Nucl. Phys. **33**, 671 (1981)].

Translated by M. Kobrinsky

Conference on Physics of Fundamental Interactions Theory

Phase Transition in Gauge Theories and Multiple-Point Model*

L. V. Laperashvili**, H. B. Nielsen¹⁾,***, and D. A. Ryzhikh****

*Institute of Theoretical and Experimental Physics, Bol'shaya
Cheremushkinskaya ul. 25, Moscow, 117218 Russia*

Received March 21, 2001; in final form August 7, 2001

Abstract—The phase transition in the regularized $U(1)$ gauge theory is investigated by using the dual Abelian Higgs model of scalar monopoles. The corresponding-renormalization-group-improved effective potential, analogous to the Coleman–Weinberg one, is considered in the two-loop approximation for β functions, and the phase-transition (critical) dual and nondual couplings are calculated in the $U(1)$ gauge theory. It is shown that the critical value of the renormalized electric fine-structure constant, $\alpha_{\text{crit}} \approx 0.208$, obtained in this study agrees with the lattice result for compact QED: $\alpha_{\text{crit}}^{\text{lat}} \approx 0.20 \pm 0.015$. This result and the behavior of α in the vicinity of the phase-transition point are compared with the multiple-point-model prediction for the values of α near the Planck scale. Such a comparison is very encouraging for the multiple point model assuming the existence of the multiple critical point at the Planck scale.

© 2002 MAIK “Nauka/Interperiodica”.

1. INTRODUCTION

The philosophy of the multiple-point model (MPM) suggested in [1] and developed in [2–4] leads to the need for investigating the phase transition in various gauge theories. According to the MPM, there is a special point, the multiple critical point (MCP), on the phase diagram of the fundamental regularized gauge theory G —that is, a point where the vacua of all fields existing in nature are degenerate having the same vacuum energy density. Such a phase diagram has axes given by all coupling constants considered in theory. The MPM assumes the existence of an MCP at the Planck scale.

A lattice model of gauge theories is the most convenient formalism for implementing MPM ideas. In the simplest case, we can imagine our spacetime as a regular hypercubic $(3 + 1)$ lattice with the parameter a equal to the fundamental (Planck) scale: $a = \lambda_{\text{Pl}} = 1/M_{\text{Pl}}$, where

$$M_{\text{Pl}} = 1.22 \times 10^{19} \text{ GeV}. \quad (1)$$

Lattice gauge theories, first introduced by Wilson [5] for studying the problem of confinement, are described by the simplest action

$$S = -\frac{\beta}{N} \sum_p \text{Re}(\text{tr} \mathcal{U}_p), \quad (2)$$

where the sum runs over all plaquettes of a hypercubic lattice, \mathcal{U}_p is the product around the plaquette p of the link variables in the N -dimensional fundamental representation of the gauge group G , $\beta = 1/g_0^2$ is the lattice constant, and g_0 is the bare coupling constant in the gauge theory considered. Monte Carlo simulations of these simple Wilson lattice theories in the four dimensions showed a (or an almost) second-order deconfining phase transition for $U(1)$ [6, 7], a crossover behavior for $SU(2)$ and $SU(3)$ [8, 9], and a first-order phase transition for $SU(N)$ with $N \geq 4$ [10]. Bhanot and Creutz [11, 12] generalized the simple Wilson action, introducing two parameters in the action

$$S = \sum_p \left[-\frac{\beta_f}{N} \text{Re}(\text{tr} \mathcal{U}_p) - \frac{\beta_A}{N^2 - 1} \text{Re}(\text{tr}_A \mathcal{U}_p) \right], \quad (3)$$

where β_f (β_A) and tr (tr_A) are, respectively, the lattice constants and traces in the fundamental (adjoint) representation of $SU(N)$ considered in this action for \mathcal{U}_p . The phase diagrams obtained for the generalized lattice $SU(2)$ and $SU(3)$ theories (3) by Monte Carlo methods in [11, 12] showed the existence of a triple point that is a boundary point of three first-order phase transitions: the “Coulomb-like” and the confining $SU(N)/Z_N$ and Z_N phases meet together at this point. Three phase border lines that separate the corresponding phases emanate from the triple point. The Z_N phase transition is a “discreteness” transition occurring when lattice plaquettes jump from the identity to nearby elements in the group. The $SU(N)/Z_N$ phase transition is due to a condensation

*This article was submitted by the authors in English.

¹⁾ Niels Bohr Institute, Copenhagen, Denmark.

** e-mail: laper@heron.itep.ru

*** e-mail: hbech@alf.nbi.dk

**** e-mail: ryzhikh@heron.itep.ru

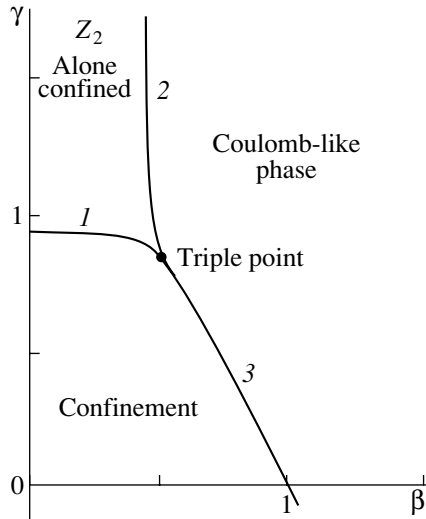


Fig. 1. Phase diagram for $U(1)$ where the two-parameter lattice action is used. This type of action makes it possible to provoke the Z_2 (or Z_3) confinement alone. The diagram shows the existence of a triple (critical) point. Three phase borders emanate from this triple point: the phase border 1 separates the totally confining phase from the phase where only the discrete subgroup Z_2 is confined; the phase border 2 separates the latter phase from the totally Coulomb-like phase; and the phase border 3 separates the totally confining and totally Coulomb-like phases.

of monopoles (a consequence the nontrivial Π_1 of the group).

Monte Carlo simulations of the $U(1)$ gauge theory described by the two-parameter lattice action [13, 14]

$$S = \sum_p [\beta^{\text{lat}} \cos \Theta_p + \gamma^{\text{lat}} \cos 2\Theta_p], \quad (4)$$

$$\text{where } \mathcal{U}_p = e^{i\Theta_p},$$

also indicate the existence of a triple point on the corresponding phase diagram (see Fig. 1): Coulomb-like, totally confining, and Z_2 confining phases come together at the triple point shown in Fig. 1.

Monte Carlo simulations of the lattice $U(1)$ gauge theory described by the simple Wilson action corresponding to the case of $\gamma^{\text{lat}} = 0$ in Eq. (4) yield [14]

$$\alpha_{\text{crit}}^{\text{lat}} \approx 0.20 \pm 0.015, \quad \tilde{\alpha}_{\text{crit}}^{\text{lat}} \approx 1.25 \pm 0.10, \quad (5)$$

where $\alpha = e^2/4\pi$ and $\tilde{\alpha} = g^2/4\pi$ are the electric and the magnetic fine-structure constant containing the electric charge e and the magnetic charge g , respectively. The lattice artifact monopoles are responsible for the confinement mechanism in lattice gauge theories, which is confirmed by many numerical and theoretical investigations (see the reviews articles in [15] and the original studies in [16]). The simplest

effective dynamics describing the confinement mechanism in pure gauge lattice $U(1)$ theory is the dual Abelian Higgs model of scalar monopoles [17].

In [1–3], the calculations of the $U(1)$ phase-transition (critical) coupling constant were connected with the existence of artifact monopoles in lattice gauge theory and also in the Wilson loop action model [3]. Here, we consider the Higgs monopole model (HMM) approximating the lattice artifact monopoles as fundamental pointlike particles described by the Higgs scalar field. The phase border separating the Coulomb-like and confinement phases is investigated by the method developed in the MPM, where degenerate vacua are considered. The phase-transition Coulomb confinement is given by the condition where the first local minimum of the effective potential is degenerate with its second minimum. Considering the renormalization-group improvement of the effective Coleman–Weinberg potential [18, 19] written for the dual sector of scalar electrodynamics in the two-loop approximation, we have calculated the $U(1)$ critical values of the magnetic fine-structure constant $\tilde{\alpha}_{\text{crit}} = g_{\text{crit}}^2/4\pi \approx 1.20$ and electric fine-structure constant $\alpha_{\text{crit}} = \pi/g_{\text{crit}}^2 \approx 0.208$ (by the Dirac relation). These values agree with the lattice result in (5).

Investigating the phase transition in the HMM, we have pursued two objectives. On one hand, we aimed at explaining lattice results. But we also had another aim.

According to the MPM, at the Planck scale, there exists a MCP, which is a boundary point of the phase transitions in $U(1)$, $SU(2)$, and $SU(3)$ sectors of the fundamental regularized gauge theory G . The idea of [1] was that the corresponding critical couplings coincide with the lattice ones. Our calculations in the HMM indicate that the Higgs scalar monopole fields are responsible for the phase-transition Coulomb confinement, giving the same lattice values of critical couplings. For this reason, the results of the present study are very encouraging for the antigrand unified theory (AGUT) [20–25], which was developed previously as a realistic alternative to SUSY Grand Unified Theories (GUTs). In this article, we also discuss the problems of AGUT, which is used in conjunction with the MPM.

2. THE COLEMAN–WEINBERG EFFECTIVE POTENTIAL FOR THE HIGGS MONOPOLE MODEL

As was mentioned in the Introduction, the dual Abelian Higgs model of scalar monopoles (abbreviated as HMM) describes the dynamics of confinement in lattice theories. This model, first suggested in [17], considers the Lagrangian

$$L = -\frac{1}{4g^2} F_{\mu\nu}^2(B) + \frac{1}{2} |(\partial_\mu - iB_\mu)\Phi|^2 - U(\Phi), \quad (6)$$

where

$$U(\Phi) = \frac{1}{2}\mu^2|\Phi|^2 + \frac{\lambda}{4}|\Phi|^4$$

is the Higgs potential of scalar monopoles with magnetic charge g and B_μ is the dual gauge (photon) field interacting with the scalar monopole field Φ . In this model, λ is the self-interaction constant for scalar fields and the mass parameter μ^2 is negative. In Eq. (6), the complex scalar field Φ contains the Higgs (ϕ) and Goldstone (χ) boson fields:

$$\Phi = \phi + i\chi. \tag{7}$$

The effective potential in Higgs scalar electrodynamics (HSED) was first calculated by Coleman and Weinberg [18] in the one-loop approximation. The general method for calculating it is given in the review article of Sher [19]. Using this method, we can construct the effective potential for the HMM. In this case, the total field system of the gauge (B_μ) and magnetically charged (Φ) fields is described by the partition function that, in Euclidean space, has the form

$$Z = \int [DB][D\Phi][D\Phi^+] e^{-S}, \tag{8}$$

where the action $S = \int d^4x L(x) + S_{\text{gf}}$ contains Lagrangian (6) written in Euclidean space and the gauge-fixing action S_{gf} . Let us now consider the shift

$$\Phi(x) = \Phi_b + \hat{\Phi}(x) \tag{9}$$

with Φ_b as a background field and calculate the following expression for the partition function in the one-loop approximation:

$$\begin{aligned} Z &= \int [DB][D\hat{\Phi}][D\hat{\Phi}^+] \tag{10} \\ &\times \exp \left\{ -S(B, \Phi_b) - \int d^4x \left[\frac{\delta S(\Phi)}{\delta \Phi(x)} \right]_{\Phi=\Phi_b} \right. \\ &\left. \times \hat{\Phi}(x) + \text{h.c.} \right\} = \exp \{-F(\Phi_b, g^2, \mu^2, \lambda)\}. \end{aligned}$$

Using representation (7), we obtain the effective potential

$$V_{\text{eff}} = F(\phi_b, g^2, \mu^2, \lambda) \tag{11}$$

given by the function F of Eq. (10) for the constant background field $\Phi_b = \phi_b = \text{const}$. In this case, the one-loop effective potential for monopoles coincides with the expression for the effective potential calculated by the authors of [18] for HSED and extended to the massive theory (see review [19]),

$$\begin{aligned} V_{\text{eff}}(\phi_b^2) &= \frac{\mu^2}{2}\phi_b^2 + \frac{\lambda}{4}\phi_b^4 \tag{12} \\ &+ \frac{1}{64\pi^2} \left[3g^4\phi_b^4 \log \frac{\phi_b^2}{M^2} \right. \end{aligned}$$

$$\begin{aligned} &+ (\mu^2 + 3\lambda\phi_b^2)^2 \log \frac{\mu^2 + 3\lambda\phi_b^2}{M^2} \\ &\left. + (\mu^2 + \lambda\phi_b^2)^2 \log \frac{\mu^2 + \lambda\phi_b^2}{M^2} \right] + C, \end{aligned}$$

where M is the cutoff scale and C is a constant independent of ϕ_b^2 .

The effective potential (11) has several minima. Their positions depend on g^2, μ^2 , and λ . If the first local minimum occurs at $\phi_b = 0$ and $V_{\text{eff}}(0) = 0$, it corresponds to the so-called symmetric phase, which is the Coulomb-like phase in our description. It is then easy to determine the constant C in Eq. (12),

$$C = -\frac{\mu^4}{16\pi^2} \log \frac{\mu}{M}, \tag{13}$$

and we have the effective potential for the HMM described by the expression

$$\begin{aligned} V_{\text{eff}}(\phi_b^2) &= \frac{\mu_{\text{run}}^2}{2}\phi_b^2 + \frac{\lambda_{\text{run}}}{4}\phi_b^4 \tag{14} \\ &+ \frac{\mu^4}{64\pi^2} \log \frac{(\mu^2 + 3\lambda\phi_b^2)(\mu^2 + \lambda\phi_b^2)}{\mu^4}. \end{aligned}$$

Here, λ_{run} is the running self-interaction constant given by Eq. (12):

$$\begin{aligned} \lambda_{\text{run}}(\phi_b^2) &= \lambda + \frac{1}{16\pi^2} \left[3g^4 \log \frac{\phi_b^2}{M^2} \tag{15} \right. \\ &\left. + 9\lambda^2 \log \frac{\mu^2 + 3\lambda\phi_b^2}{M^2} + \lambda^2 \log \frac{\mu^2 + \lambda\phi_b^2}{M^2} \right]. \end{aligned}$$

The running squared mass of the Higgs scalar monopoles also follows from Eq. (12):

$$\begin{aligned} \mu_{\text{run}}^2(\phi_b^2) &= \mu^2 + \frac{\lambda\mu^2}{16\pi^2} \tag{16} \\ &\times \left[3 \log \frac{\mu^2 + 3\lambda\phi_b^2}{M^2} + \log \frac{\mu^2 + \lambda\phi_b^2}{M^2} \right]. \end{aligned}$$

3. RENORMALIZATION-GROUP EQUATIONS IN THE HIGGS MONOPOLE MODEL

The renormalization-group equations (RGE) for the effective potential mean that the potential cannot depend on a change in an arbitrary parameter—renormalization scale M ; i.e., $dV_{\text{eff}}/dM = 0$. The effects of changing it are absorbed into changes in the coupling constants, masses, and fields giving so-called running quantities.

Considering the renormalization-group (RG) improvement of the effective potential [18, 19] and choosing the evolution variable as

$$t = \log(\phi^2/M^2), \tag{17}$$

we have the following RGE for the improved $V_{\text{eff}}(\phi^2)$ with $\phi^2 \equiv \phi_b^2$ [26]:

$$\left(M^2 \frac{\partial}{\partial M^2} + \beta_\lambda \frac{\partial}{\partial \lambda} + \beta_g \frac{\partial}{\partial g^2} + \beta_{(\mu^2)} \mu^2 \frac{\partial}{\partial \mu^2} - \gamma \phi^2 \frac{\partial}{\partial \phi^2} \right) V_{\text{eff}}(\phi^2) = 0. \quad (18)$$

Here, γ is the anomalous dimension, and $\beta_{(\mu^2)}$, β_λ , and β_g are the RG β functions for mass, scalar, and gauge couplings, respectively. The renormalization-group Eq. (18) leads to the following form of the improved effective potential [18]:

$$V_{\text{eff}} = \frac{1}{2} \mu_{\text{run}}^2(t) G^2(t) \phi^2 + \frac{1}{4} \lambda_{\text{run}}(t) G^4(t) \phi^4. \quad (19)$$

In our case,

$$G(t) = \exp \left[-\frac{1}{2} \int_0^t dt' \gamma(g_{\text{run}}(t'), \lambda_{\text{run}}(t')) \right]. \quad (20)$$

A set of ordinary differential equations (RGE) corresponds to Eq. (18):

$$\frac{d\lambda_{\text{run}}}{dt} = \beta_\lambda(g_{\text{run}}(t), \lambda_{\text{run}}(t)), \quad (21)$$

$$\frac{d\mu_{\text{run}}^2}{dt} = \mu_{\text{run}}^2(t) \beta_{(\mu^2)}(g_{\text{run}}(t), \lambda_{\text{run}}(t)), \quad (22)$$

$$\frac{dg_{\text{run}}^2}{dt} = \beta_g(g_{\text{run}}(t), \lambda_{\text{run}}(t)). \quad (23)$$

So far as the mathematical structure of HMM is equivalent to HSED, we can use all results of the scalar electrodynamics in our calculations, replacing the electric charge e and the photon field A_μ by the magnetic charge g and the dual gauge field B_μ , respectively.

The one-loop results for β_λ , $\beta_{(\mu^2)}$, β_g , and γ are given in [18, 19] for a scalar field with electric charge e . Using these results, we obtain, for monopoles with charge $g = g_{\text{run}}$, the following expressions in the one-loop approximation:

$$\frac{d\lambda_{\text{run}}}{dt} \approx \beta_\lambda^{(1)} \quad (24)$$

$$= \frac{1}{16\pi^2} (3g_{\text{run}}^4 + 10\lambda_{\text{run}}^2 - 6\lambda_{\text{run}}g_{\text{run}}^2),$$

$$\frac{d\mu_{\text{run}}^2}{dt} \approx \beta_{(\mu^2)}^{(1)} = \frac{\mu_{\text{run}}^2}{16\pi^2} (4\lambda_{\text{run}} - 3g_{\text{run}}^2), \quad (25)$$

$$\frac{dg_{\text{run}}^2}{dt} \approx \beta_g^{(1)} = \frac{g_{\text{run}}^4}{48\pi^2}, \quad (26)$$

$$\gamma^{(1)} = -\frac{3g_{\text{run}}^2}{16\pi^2}. \quad (27)$$

The RG β functions for various renormalizable gauge theories based on a semisimple group were calculated in the two-loop approximation [27–32] and even beyond it [33]. But in this study, we use the results of [27] and [30] to calculate β functions and the anomalous dimension in the two-loop approximation for the HMM with scalar monopole fields.

In the two-loop approximation, we find for all β functions that

$$\beta = \beta^{(1)} + \beta^{(2)}, \quad (28)$$

where

$$\beta_\lambda^{(2)} = \frac{1}{(16\pi^2)^2} \left(-25\lambda^3 \quad (29) \right.$$

$$\left. + \frac{15}{2}g^2\lambda^2 - \frac{229}{12}g^4\lambda - \frac{59}{6}g^6 \right),$$

$$\beta_{(\mu^2)}^{(2)} = \frac{1}{(16\pi^2)^2} \left(\frac{31}{12}g^4 + 3\lambda^2 \right). \quad (30)$$

The gauge coupling $\beta_g^{(2)}$ function is given by [27]

$$\beta_g^{(2)} = \frac{g^6}{(16\pi^2)^2}. \quad (31)$$

The anomalous dimension follows from the calculations made in [30]:

$$\gamma^{(2)} = \frac{1}{(16\pi^2)^2} \frac{31}{12}g^4. \quad (32)$$

In Eqs. (28)–(32) and below, we have used, for the sake of simplicity, the following notation: $\lambda \equiv \lambda_{\text{run}}$, $g \equiv g_{\text{run}}$, and $\mu \equiv \mu_{\text{run}}$.

4. THE PHASE DIAGRAM IN THE HIGGS MONOPOLE MODEL

Now, we want to apply the effective-potential calculation as a technique for obtaining phase-diagram information about the condensation of monopoles in HMM. As was mentioned in Section 2, the effective potential (19) can have several minima. Their positions depend on g^2 , μ^2 , and λ . If the first local minimum occurs at $\phi = 0$ and $V_{\text{eff}}(0) = 0$, it corresponds to the Coulomb-like phase. In the case where the effective potential has the second local minimum at $\phi = \phi_{\text{min}} \neq 0$ with $V_{\text{eff}}^{\text{min}}(\phi_{\text{min}}^2) < 0$, we have the confinement phase. The phase transition between the Coulomb-like and confinement phases is given by the condition where the first local minimum at $\phi = 0$ is degenerate with the second minimum at $\phi = \phi_0$. These degenerate minima are shown in Fig. 2 by curve 1. They correspond to the different vacua arising in this model. The dashed curve 2 describes the appearance of two minima corresponding to the

confinement phases (for more details, see the next section).

The conditions of the existence of degenerate vacua are given by the equations

$$V_{\text{eff}}(0) = V_{\text{eff}}(\phi_0^2) = 0, \quad (33)$$

$$\left. \frac{\partial V_{\text{eff}}}{\partial \phi} \right|_{\phi=0} = \left. \frac{\partial V_{\text{eff}}}{\partial \phi} \right|_{\phi=\phi_0} = 0, \quad (34)$$

or

$$V'_{\text{eff}}(\phi_0^2) \equiv \left. \frac{\partial V_{\text{eff}}}{\partial \phi^2} \right|_{\phi=\phi_0} = 0,$$

and inequalities

$$\left. \frac{\partial^2 V_{\text{eff}}}{\partial \phi^2} \right|_{\phi=0} > 0, \quad \left. \frac{\partial^2 V_{\text{eff}}}{\partial \phi^2} \right|_{\phi=\phi_0} > 0. \quad (35)$$

Equation (33) applied to Eq. (19) yields

$$\mu_{\text{run}}^2 = -\frac{1}{2} \lambda_{\text{run}}(t_0) \phi_0^2 G^2(t_0), \quad t_0 = \log(\phi_0^2/M^2). \quad (36)$$

Calculating the first derivative of V_{eff} given by Eq. (34), we obtain the following expression:

$$\begin{aligned} V'_{\text{eff}}(\phi^2) &= \frac{V_{\text{eff}}(\phi^2)}{\phi^2} \\ &\times \left(1 + 2 \frac{d \log G}{dt} \right) + \frac{1}{2} \frac{d \mu_{\text{run}}^2}{dt} G^2(t) \\ &+ \frac{1}{4} \left(\lambda_{\text{run}}(t) + \frac{d \lambda_{\text{run}}}{dt} + 2 \lambda_{\text{run}} \frac{d \log G}{dt} \right) G^4(t) \phi^2. \end{aligned} \quad (37)$$

From Eq. (20), we have

$$\frac{d \log G}{dt} = -\frac{1}{2} \gamma. \quad (38)$$

It is easy to find the joint solution of equations

$$V_{\text{eff}}(\phi_0^2) = V'_{\text{eff}}(\phi_0^2) = 0. \quad (39)$$

Using RGE (21), (22), and Eqs. (36)–(38), we obtain

$$\begin{aligned} V'_{\text{eff}}(\phi_0^2) &= \frac{1}{4} (-\lambda_{\text{run}} \beta(\mu^2)) \\ &+ \lambda_{\text{run}} + \beta_\lambda - \gamma \lambda_{\text{run}}) G^4(t_0) \phi_0^2 = 0, \end{aligned} \quad (40)$$

or

$$\beta_\lambda + \lambda_{\text{run}}(1 - \gamma - \beta(\mu^2)) = 0. \quad (41)$$

Substituting, into Eq. (41), the functions $\beta_\lambda^{(1)}$, $\beta(\mu^2)^{(1)}$, and $\gamma^{(1)}$ given by Eqs. (24), (25), and (27), we obtain, in the one-loop approximation, the following equation for the phase-transition border:

$$g_{\text{PT}}^4 = -2 \lambda_{\text{run}} \left(\frac{8\pi^2}{3} + \lambda_{\text{run}} \right). \quad (42)$$

Equation (42) is represented on the $(\lambda_{\text{run}}; g_{\text{run}}^2)$ phase diagram in Fig. 3 by curve 1, which describes the border between the Coulomb-like phase with $V_{\text{eff}} \geq$

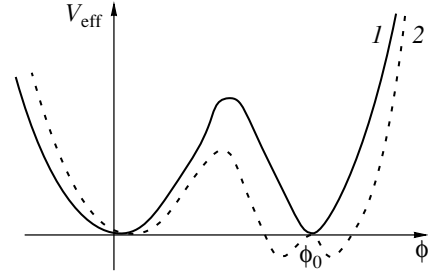


Fig. 2. Effective potential V_{eff} : curve 1 corresponds to the Coulomb confinement phase transition, and curve 2 describes the existence of two minima corresponding to the confinement phases.

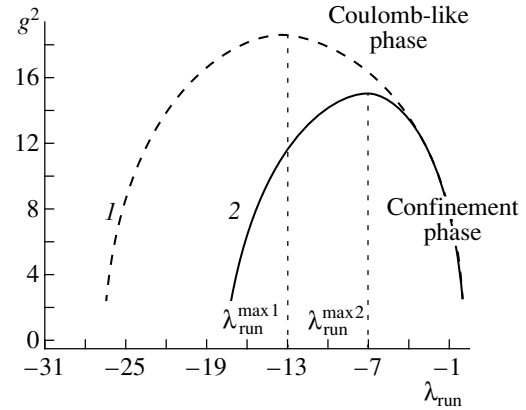


Fig. 3. Phase diagram in the dual Abelian Higgs model of scalar monopoles in the (curve 1) one-loop and (curve 2) two-loop approximation at $\lambda_{\text{run}}^{\text{max}1} = -13.1595$, $g_{\text{max}1}^2 = 18.6103$, $\lambda_{\text{run}}^{\text{max}2} = -7.1307$, and $g_{\text{max}2}^2 = 15.1106$.

0 and the confinement phase with $V_{\text{eff}}^{\text{min}} < 0$. This border corresponds to the one-loop approximation.

Using Eqs. (24), (25), (27)–(30), and (32), we are able to construct the phase-transition border in the two-loop approximation. Substituting these equations into Eq. (41), we obtain the following equation for the phase-transition border in the two-loop approximation:

$$\begin{aligned} 3y^2 - 16\pi^2 + 6x^2 + \frac{1}{16\pi^2} \left(28x^3 \right. \\ \left. + \frac{15}{2}x^2y + \frac{97}{4}xy^2 - \frac{59}{6}y^3 \right) = 0, \end{aligned} \quad (43)$$

where $x = -\lambda_{\text{PT}}$ and $y = g_{\text{PT}}^2$ are the phase-transition values of $-\lambda_{\text{run}}$ and g_{run}^2 . Choosing the physical branch corresponding to $g^2 \geq 0$ and $g^2 \rightarrow 0$, when $\lambda \rightarrow 0$, we have obtained curve 2 on the phase diagram $(\lambda_{\text{run}}; g_{\text{run}}^2)$ shown in Fig. 3. This curve corresponds to the two-loop approximation and can be compared with curve 1 in Fig. 3, which describes

the same phase border calculated in the one-loop approximation. It is easy to see from a comparison of curves 1 and 2 that the accuracy of the one-loop approximation is not excellent, errors being on the order of 30%.

According to the phase diagram shown in Fig. 3, the confinement phase begins at $g^2 = g_{\text{max}}^2$ and exists under the phase-transition borderline in the region $g^2 \leq g_{\text{max}}^2$, where e^2 is large, $e^2 \geq (2\pi/g_{\text{max}})^2$, due to the Dirac relation (see below). Therefore, we have

$$g_{\text{crit}}^2 = g_{\text{max1}}^2 \approx 18.61 \quad (44)$$

in the one-loop approximation and

$$g_{\text{crit}}^2 = g_{\text{max2}}^2 \approx 15.11$$

in the two-loop approximation.

Comparing these results, we obtain the accuracy of deviation between them on the order of 20%.

The results in (44) yield

$$\tilde{\alpha}_{\text{crit}} = \frac{g_{\text{crit}}^2}{4\pi} \approx 1.48 \quad (45)$$

in the one-loop approximation and

$$\tilde{\alpha}_{\text{crit}} = \frac{g_{\text{crit}}^2}{4\pi} \approx 1.20$$

in the two-loop approximation.

Using the Dirac relation for elementary charges,

$$eg = 2\pi \quad \text{or} \quad \alpha\tilde{\alpha} = 1/4, \quad (46)$$

we obtain the following values for the critical electric fine-structure constant:

$$\alpha_{\text{crit}} = \frac{1}{4\tilde{\alpha}_{\text{crit}}} \approx 0.17 \quad (47)$$

in the one-loop approximation and

$$\alpha_{\text{crit}} = \frac{1}{4\tilde{\alpha}_{\text{crit}}} \approx 0.208$$

in the two-loop approximation.

The last result agrees with the lattice values (5) obtained for the compact QED by the Monte Carlo method [14].

Writing Eq. (23) with β_g function given by Eqs. (26), (28), and (31), we have the following RGE for the monopole charge in the two-loop approximation:

$$\frac{dg_{\text{run}}^2}{dt} \approx \frac{g_{\text{run}}^4}{48\pi^2} + \frac{g_{\text{run}}^6}{(16\pi^2)^2} \quad (48)$$

or

$$\frac{d \log \tilde{\alpha}}{dt} \approx \frac{\tilde{\alpha}}{12\pi} \left(1 + 3 \frac{\tilde{\alpha}}{4\pi} \right). \quad (49)$$

The values in (44) for $g_{\text{crit}}^2 = g_{\text{max1,2}}^2$ indicate that the contribution of two loops described by the second term of Eq. (48) or Eq. (49) is about 0.3, which confirms the validity of perturbation theory.

In general, we are able to estimate the validity of the two-loop approximation for all β functions by calculating the corresponding ratios of two-loop contributions to one-loop contributions at the maximum of curve 2, where

$$\lambda_{\text{crit}} = \lambda_{\text{run}}^{\text{max2}} \approx -7.13, \quad g_{\text{crit}}^2 = g_{\text{max2}}^2 \approx 15.11. \quad (50)$$

We have the results

$$\frac{\beta_{(\mu^2)}^{(2)}}{\beta_{(\mu^2)}^{(1)}} \approx -0.0637, \quad \frac{\beta_{\lambda}^{(2)}}{\beta_{\lambda}^{(1)}} \approx 0.0412, \quad (51)$$

$$\frac{\beta_g^{(2)}}{\beta_g^{(1)}} \approx 0.2871.$$

Here, we see that all ratios are sufficiently small, i.e., all two-loop contributions are small in relation to one-loop contributions, confirming the validity of perturbation theory in the two-loop approximation considered in this model. The accuracy of deviation is poorer ($\sim 30\%$) for the β_g function. But it is necessary to emphasize that, in calculating the border curves 1 and 2 of Fig. 3, we have not used RGE (23) for the monopole charge: there is no β_g function in Eq. (41). Therefore, the calculation of g_{crit}^2 according to Eq. (43) does not depend on the approximation of the β_g function. The above-mentioned β_g function appears only in the second-order derivative of V_{eff} , which is related to the monopole mass m (see the next section).

Equations (5) and (47) yield

$$\alpha_{\text{crit}}^{-1} \approx 5. \quad (52)$$

This value is important for the phase transition at the Planck scale predicted by the MPM.

5. TRIPLE POINT

In this section, we demonstrate the existence of the triple point on the phase diagram of the HMM.

Considering the second derivative of the effective potential,

$$V_{\text{eff}}''(\phi_0^2) \equiv \frac{\partial^2 V_{\text{eff}}}{\partial(\phi^2)^2}, \quad (53)$$

we can calculate it for the RG-improved effective potential (19)

$$\begin{aligned} V_{\text{eff}}''(\phi^2) = & \frac{V_{\text{eff}}'(\phi^2)}{\phi^2} + \left(-\frac{1}{2}\mu_{\text{run}}^2 \right. \\ & + \frac{1}{2} \frac{d^2 \mu_{\text{run}}^2}{dt^2} + 2 \frac{d\mu_{\text{run}}^2}{dt} \frac{d \log G}{dt} \\ & \left. + \mu_{\text{run}}^2 \frac{d^2 \log G}{dt^2} + 2\mu_{\text{run}}^2 \left(\frac{d \log G}{dt} \right)^2 \right) \frac{G^2}{\phi^2} \end{aligned} \quad (54)$$

$$\begin{aligned}
 &+ \left(\frac{1}{2} \frac{d\lambda_{\text{run}}}{dt} + \frac{1}{4} \frac{d^2\lambda_{\text{run}}}{dt^2} + 2 \frac{d\lambda_{\text{run}}}{dt} \frac{d \log G}{dt} \right. \\
 &+ 2\lambda_{\text{run}} \frac{d \log G}{dt} + \lambda_{\text{run}} \frac{d^2 \log G}{dt^2} \\
 &\left. + 4\lambda_{\text{run}} \left(\frac{d \log G}{dt} \right)^2 \right) G^4(t).
 \end{aligned}$$

Let us now consider the case where this second derivative changes sign, giving a maximum of V_{eff} instead of the minimum at $\phi^2 = \phi_0^2$. Such a possibility is shown in Fig. 2 by curve 2. Now, two additional minima at $\phi^2 = \phi_1^2$ and $\phi^2 = \phi_2^2$ appear in our theory. They correspond to two different confinement phases for the confinement of electrically charged particles if they exist in the system. When these two minima are degenerate, we have the requirements

$$\begin{aligned}
 V_{\text{eff}}(\phi_1^2) &= V_{\text{eff}}(\phi_2^2) < 0, \\
 V'_{\text{eff}}(\phi_1^2) &= V'_{\text{eff}}(\phi_2^2) = 0,
 \end{aligned} \tag{55}$$

which describe the border between the confinement phases conf. 1 and conf. 2 presented in Fig. 4. This border is given as a curve 3 at the phase diagram $(\lambda_{\text{run}}; g_{\text{run}}^4)$ drawn in Fig. 4. Curve 3 meets curve 1 at the triple point A. According to the illustration shown in Fig. 2, it is obvious that this triple point A is given by the following requirements:

$$V_{\text{eff}}(\phi_0^2) = V'_{\text{eff}}(\phi_0^2) = V''_{\text{eff}}(\phi_0^2) = 0. \tag{56}$$

In contrast to the requirements

$$V_{\text{eff}}(\phi_0^2) = V'_{\text{eff}}(\phi_0^2) = 0 \tag{57}$$

giving curve 1, let us now consider the joint solution to the equations

$$V_{\text{eff}}(\phi_0^2) = V''_{\text{eff}}(\phi_0^2) = 0. \tag{58}$$

For the sake of simplicity, we have considered the one-loop approximation. It is easy to obtain the solution to Eq. (58) in the one-loop approximation by using Eqs. (54), (36), (38), and (24)–(27):

$$\mathcal{F}(\lambda_{\text{run}}, g_{\text{run}}^2) = 0, \tag{59}$$

where

$$\begin{aligned}
 \mathcal{F}(\lambda_{\text{run}}, g_{\text{run}}^2) &= 5g_{\text{run}}^6 + 24\pi^2 g_{\text{run}}^4 + 12\lambda_{\text{run}} g_{\text{run}}^4 \\
 &- 9\lambda_{\text{run}}^2 g_{\text{run}}^2 + 36\lambda_{\text{run}}^3 + 80\pi^2 \lambda_{\text{run}}^2 + 64\pi^4 \lambda_{\text{run}}.
 \end{aligned} \tag{60}$$

The dashed curve 2 in Fig. 4 represents the solution to Eq. (59), which is equivalent to Eqs. (58). Curve 2 goes very close to the maximum of curve 1. Assuming that the position of the triple point A coincides with this maximum, we consider the border between the phase conf. 1 having the first minimum at nonzero ϕ_1 with $V_{\text{eff}}^{\text{min}}(\phi_1^2) = c_1 < 0$ and the phase conf. 2 which reveals two minima with the second minimum being the deeper one and having $V_{\text{eff}}^{\text{min}}(\phi_2^2) = c_2 < 0$. This border (described by curve 3 in Fig. 4) was calculated in the vicinity of the triple point A by means of

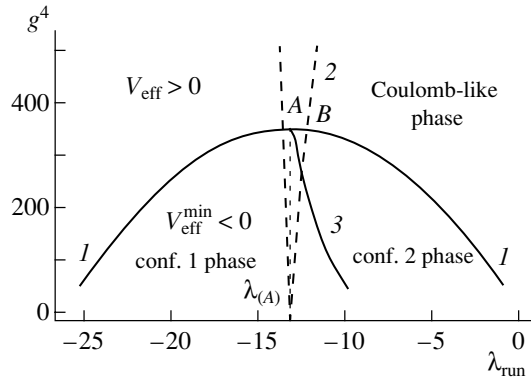


Fig. 4. Phase diagram $(\lambda_{\text{run}}, g^4 \equiv g_{\text{run}}^4)$ corresponding to the HMM in the one-loop approximation. It shows the existence of a triple point $A(\lambda_{(A)} \approx -13.2; g_{(A)}^2 \approx 18.6)$. This triple point is the boundary point of three phase transitions: the Coulomb-like phase and two confinement phases (conf. 1 and conf. 2) meet together at the triple point A. The dashed curve 2 represents the requirement $V_{\text{eff}}(\phi_0^2) = V''_{\text{eff}}(\phi_0^2) = 0$. Monopole condensation leads to the confinement of the electric charges: Abrikosov–Nielsen–Olesen electric vortices are created in the confinement phases conf. 1 and conf. 2.

Eqs. (55) with ϕ_1 and ϕ_2 represented as $\phi_{1,2} = \phi_0 \pm \epsilon$ with $\epsilon \ll \phi_0$. The result of such calculations yields the following expression for curve 3:

$$g_{\text{PT},3}^4 = \frac{5}{2}(5\lambda_{\text{run}} + 8\pi^2)\lambda_{\text{run}} + 8\pi^4. \tag{61}$$

Curve 3 meets curve 1 at the triple point A. The piece of curve 1 to the left of the point A describes the border between the Coulomb-like phase and phase conf. 1. In the vicinity of the triple point A, the second derivative $V''_{\text{eff}}(\phi_0^2)$ changes sign, which leads to the existence of the maximum at $\phi^2 = \phi_0^2$, in correspondence with dashed curve 2 in Fig. 2. For this reason, curve 1 in Fig. 4 does not describe a phase-transition border from the point A to the point B where curve 2 again intersects curve 1 at $\lambda_{(B)} \approx -12.24$. This intersection (again giving $V''_{\text{eff}}(\phi_0^2) > 0$) occurs surprisingly fast. The right piece of curve 1 to the right of the point B separates the Coulomb-like phase and the phase conf. 2. But between the points A and B, the phase-transition border goes slightly above curve 1. This deviation is very small and cannot be distinguished in Fig. 4.

It is necessary to note that only $V''_{\text{eff}}(\phi^2)$ contains the derivative dg_{run}^2/dt . The joint solution to Eqs. (56) leads to the joint solution of Eqs. (42) and (59). This solution was obtained numerically and gave the following triple-point values of λ_{run} and g_{run}^2 :

$$\lambda_{(A)} \approx -13.4073, \quad g_{(A)}^2 \approx 18.6070. \tag{62}$$

The solution in (62) demonstrates that the triple point A exists in the very neighborhood of the maximum of the curve given by (42). The position of this maximum is determined by the following analytic expressions, together with their approximate values:

$$\lambda_{(A)} \approx -\frac{4\pi^2}{3} \approx -13.2, \quad (63)$$

$$g_{(A)}^2 = g_{\text{crit}}^2 |_{\lambda_{\text{run}}=\lambda_{(A)}} \approx \frac{4\sqrt{2}}{3}\pi^2 \approx 18.6. \quad (64)$$

Finally, we can conclude that the phase diagram shown in Fig. 4 gives such a description: there exist three phases in the dual sector of the HSED—the Coulomb-like phase and confinement phases conf. 1 and conf. 2.

The border 1 , which is described by the curve given by (42), separates the Coulomb-like phase (with $V_{\text{eff}} \geq 0$) and confinement phases (with $V_{\text{eff}}^{\text{min}}(\phi_0^2) < 0$). Curve 1 corresponds to the joint solution to the equations $V_{\text{eff}}(\phi_0^2) = V'_{\text{eff}}(\phi_0^2) = 0$. The dashed curve 2 represents the solution to the equations $V_{\text{eff}}(\phi_0^2) = V''_{\text{eff}}(\phi_0^2) = 0$. The phase border 3 in Fig. 4 separates two confinement phases. The following requirements take place for this border:

$$\begin{aligned} V_{\text{eff}}(\phi_{1,2}^2) < 0, \quad V_{\text{eff}}(\phi_1^2) = V_{\text{eff}}(\phi_2^2), \quad (65) \\ V'_{\text{eff}}(\phi_1^2) = V'_{\text{eff}}(\phi_2^2) = 0, \quad V''_{\text{eff}}(\phi_1^2) > 0, \quad V''_{\text{eff}}(\phi_2^2) > 0. \end{aligned}$$

The triple point A is the boundary point of all three phase transitions shown in the phase diagram in Fig. 4. For $g^2 < g_{(A)}^2$, the field system described by our model exists in the confinement phase, where all electric charges have to be confined.

Considering that monopole mass m is given by the expression

$$V''_{\text{eff}}(\phi_0^2) = \frac{1}{4\phi_0^2} \frac{d^2 V_{\text{eff}}}{d\phi^2} |_{\phi=\phi_0} = \frac{m^2}{4\phi_0^2}, \quad (66)$$

we see that monopoles acquire zero mass in the vicinity of the triple point A :

$$V''_{\text{eff}}(\phi_{0A}^2) = \frac{m_{(A)}^2}{4\phi_{0A}^2} = 0. \quad (67)$$

This result is in agreement with the result of compact QED [34]: $m^2 \rightarrow 0$ in the vicinity of the critical point.

6. ABRIKOSOV–NIELSEN–OLESEN STRINGS, OR THE VORTEX DESCRIPTION OF THE CONFINEMENT PHASES

As was shown in the preceding section, two regions between curves $1, 3$ and $3, 1$ given by the phase diagram in Fig. 4 correspond to the existence of the two confinement phases, different in the sense that the phase conf. 1 is produced by the second minimum, while the phase conf. 2 corresponds to the third minimum of the effective potential. It is obvious that, in our case, both phases have nonzero monopole condensate at the minima of the effective potential, where $V_{\text{eff}}^{\text{min}}(\phi_{1,2} \neq 0) < 0$. For this reason, the Abrikosov–Nielsen–Olesen (ANO) electric vortices (see [35, 36]) may be created in both these phases. Only closed strings exist in the confinement phases of the HMM. The properties of ANO strings in $U(1)$ gauge theory were investigated in [37].

7. MULTIPLE-POINT MODEL AND CRITICAL VALUES OF THE $U(1)$ AND $SU(N)$ FINE-STRUCTURE CONSTANTS

7.1. Antigrand Unified Theory

Grand Unified Theories were constructed with the aim of extending the Standard Model (SM). The supersymmetric extension of the SM consists in taking the SM and adding the corresponding supersymmetric partners [38]. The minimal supersymmetric standard model (MSSM) shows the possibility of the existence of the Grand Unification point at $\mu_{\text{GUT}} \sim 10^{16}$ GeV [39]. Unfortunately, experimental data do not presently indicate any manifestation of supersymmetry. In this connection, AGUT was developed in [20–25] as a realistic alternative to SUSY GUTs. According to this theory, supersymmetry does not come into existence up to the Planck energy scale (1).

The SM is based on the group

$$SMG = SU(3)_c \times SU(2)_L \times U(1)_Y. \quad (68)$$

Antigrand unified theory suggests that, at the scale $\mu_G \sim \mu_{\text{Pl}} = M_{\text{Pl}}$, there exists the more fundamental group G containing N_{gen} copies of the SM group (SMG), that is,

$$G = SMG_1 \times SMG_2 \quad (69)$$

$$\dots \times SMG_{N_{\text{gen}}} \equiv (SMG)^{N_{\text{gen}}},$$

where N_{gen} denotes the number of quark and lepton generations.

If $N_{\text{gen}} = 3$ (as AGUT predicts), then the fundamental gauge group G is

$$\begin{aligned} G = (SMG)^3 = SMG_{1\text{st gen}} \quad (70) \\ \times SMG_{2\text{nd gen}} \times SMG_{3\text{rd gen}} \end{aligned}$$

or the generalized one

$$G_f = (SMG)^3 \times U(1)_f, \quad (71)$$

which was suggested by the fitting the SM fermion masses (see [22]).

Recently, a new generalization of AGUT was suggested in [24],

$$G_{\text{ext}} = (SMG \times U(1)_{B-L})^3. \quad (72)$$

It takes into account the seesaw mechanism with right-handed neutrinos, also gives a reasonable fit to the SM fermion masses, and describes all neutrino experiments known today.

The group G_f contains the following gauge fields: $3 \times 8 = 24$ gluons, $3 \times 3 = 9$ W bosons, and $3 \times 1 + 1 = 4$ Abelian gauge bosons.

At first glance, this $(SMG)^3 \otimes U(1)_f$ group with its 37 generators seems to be just one among many possible SM gauge group extensions. However, it is not such an arbitrary choice. There are reasonable requirements (postulates) on the gauge group G (or G_f , or G_{ext}) that unambiguously specify this group. It should obey the following postulates [the first two are also valid for $SU(5)$ GUT]:

(1) G or G_f should only contain transformations converting the known 45 Weyl fermions (three generations of 15 Weyl particles each) counted as left-handed ones, say, into each other unitarily, so that G (or G_f) must be a subgroup of $U(45)$: $G \subseteq U(45)$.

(2) No anomalies, neither gauge nor mixed, occur; AGUT assumes that only straightforward anomaly cancellation takes place and forbids the Green–Schwarz-type anomaly cancellation [40].

(3) AGUT should not unify the irreducible representations under the SM gauge group called here SMG [see Eq. (68)].

(4) G is the maximal group satisfying the above-mentioned postulates.

There are five Higgs fields in the extended AGUT with the symmetry group G_f [22]. These fields break AGUT to the SM, which means that their vacuum expectation values (VEVs) are active. The extended AGUT with the symmetry group G_{ext} given by Eq. (72) was suggested in [24] with the aim of explaining the neutrino oscillations. Introducing the right-handed neutrino in the model, the authors of this theory replaced postulate (1) and considered $U(48)$ group instead of $U(45)$, so that G_{ext} is a subgroup of $U(48)$: $G_{\text{ext}} \subseteq U(48)$. This group ends up having seven Higgs fields (for details, see [24]). A typical fit to the masses and mixing angles for the SM leptons and quarks within G_{ext} theory showed that, in contrast to the old extended AGUT with the symmetry group G_f , new results are more encouraging.

7.2. AGUT–MPM Prediction for the Planck Scale Values of the $U(1)$, $SU(2)$, and $SU(3)$ Fine-Structure Constants

As was mentioned in the Introduction, the AGUT approach is used in conjunction with the MPM [1–4], which assumes the existence of the MCP at the Planck scale.

The usual definition of the SM coupling constants,

$$\alpha_1 = \frac{5}{3} \frac{\alpha}{\cos^2 \theta_{\overline{MS}}}, \quad \alpha_2 = \frac{\alpha}{\sin^2 \theta_{\overline{MS}}}, \quad (73)$$

$$\alpha_3 \equiv \alpha_s = \frac{g_s^2}{4\pi},$$

where α and α_s are the electromagnetic and $SU(3)$ fine-structure constants, respectively, is given in the modified minimal subtraction scheme (\overline{MS}). Here, $\theta_{\overline{MS}}$ is the Weinberg weak angle in the \overline{MS} scheme. With the aid of RGE with experimentally established parameters, it is possible to extrapolate the experimental values of three inverse running constants $\alpha_i^{-1}(\mu)$ [here, μ is an energy scale and $i = 1, 2, 3$ correspond to $U(1)$, $SU(2)$, and $SU(3)$ groups of the SM] from the electroweak scale to the Planck scale. The precision of the LEP data allows one to make this extrapolation with small errors (see [39]). Assuming that these RGE for $\alpha_i^{-1}(\mu)$ contain only the contributions of the SM particles up to $\mu \approx \mu_{\text{Pl}}$ and performing an extrapolation with one Higgs doublet under the assumption of a “desert,” one can obtain the following results for the inverses $\alpha_{Y,2,3}^{-1}$ (here, $\alpha_Y \equiv (3/5) \alpha_1$) [1] (compare with [39]):

$$\alpha_Y^{-1}(\mu_{\text{Pl}}) \approx 55.5, \quad \alpha_2^{-1}(\mu_{\text{Pl}}) \approx 49.5, \quad (74)$$

$$\alpha_3^{-1}(\mu_{\text{Pl}}) \approx 54.0.$$

The extrapolation of $\alpha_{Y,2,3}^{-1}(\mu)$ up to the point $\mu = \mu_{\text{Pl}}$ is shown in Fig. 5.

According to the AGUT, the fundamental group G (or G_f , or G_{ext}) undergoes, at some point $\mu = \mu_G < \mu_{\text{Pl}}$ (but near μ_{Pl}), a spontaneous breakdown to the diagonal subgroup,

$$G \longrightarrow G_{\text{diag.subgr}} = \{g, g, g | g \in SMG\}, \quad (75)$$

which is identified with the usual (low-energy) group SMG . The point $\mu_G \sim 10^{18}$ GeV is also shown in Fig. 5, together with the region of G theory where the AGUT works.

The AGUT prediction of the values of $\alpha_i(\mu)$ at $\mu = \mu_{\text{Pl}}$ is based on the MPM assumption about the existence of the phase-transition boundary MCP at the Planck scale and gives these values in terms of the corresponding critical couplings $\alpha_{i,\text{crit}}$ [1, 20, 21]:

$$\alpha_i(\mu_{\text{Pl}}) = \frac{\alpha_{i,\text{crit}}}{N_{\text{gen}}} = \frac{\alpha_{i,\text{crit}}}{3} \quad \text{for } i = 2, 3, \quad (76)$$

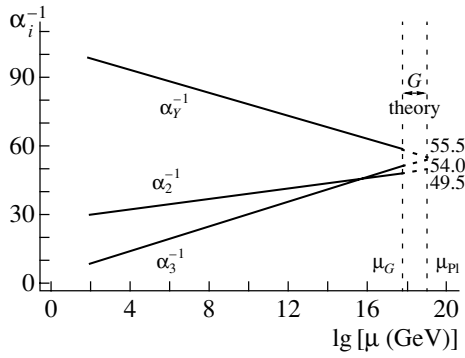


Fig. 5. Evolution of three inverse running constants $\alpha_i^{-1}(\mu)$, where $i = 1, 2, 3$ correspond to $U(1)$, $SU(2)$, and $SU(3)$ groups of the SM. The extrapolation of their experimental values from the electroweak scale to the Planck scale was obtained by using the RGE with one Higgs doublet under the assumption of a “desert.” The precision of the LEP data allows us to make this extrapolation with small errors (see [39]). AGUT works in the region $\mu_G \leq \mu \leq \mu_{PI}$.

and

$$\alpha_1(\mu_{PI}) = \frac{2\alpha_{1,crit}}{N_{gen}(N_{gen} + 1)} = \frac{\alpha_{1,crit}}{6} \quad (77)$$

for $U(1)$.

There exists a simple explanation of relations (76) and (77). As was mentioned above, the group G breaks down at $\mu = \mu_G$. It should be said that, at the very high energies $\mu_G \leq \mu \leq \mu_{PI}$ (see Fig. 5), each generation has its own gluons, own W bosons, etc. The breaking makes only a linear combination of a certain color combination of gluons which exists below $\mu = \mu_G$ and down to low energies. We can say that the phenomenological gluon is a linear combination (with amplitude $1/\sqrt{3}$ for $N_{gen} = 3$) for each of the AGUT gluons of the same color combination. This means that the coupling constant for the phenomenological gluon has a strength that is $\sqrt{3}$ times smaller if, as we effectively assume, three AGUT $SU(3)$ couplings are equal to each other. Then, we have the following formula relating the fine-structure constants of G theory (e.g., AGUT) to low-energy surviving diagonal subgroup $G_{diag.subg} \subseteq (SMG)^3$ given by Eq. (75):

$$\alpha_{diag,i}^{-1} = \alpha_{1st\ gen,i}^{-1} + \alpha_{2nd\ gen,i}^{-1} + \alpha_{3rd\ gen,i}^{-1}. \quad (78)$$

Here, $i = U(1), SU(2), SU(3)$, and $i = 3$ means that we talk about the gluon couplings. For non-Abelian theories, we immediately obtain Eq. (76) from Eq. (78) at the critical point (MCP).

In contrast to non-Abelian theories, in which the gauge invariance forbids the mixed (in generations)

terms in the Lagrangian of G theory, the $U(1)$ sector of AGUT contains such mixed terms:

$$\frac{1}{g^2} \sum_{p,q} F_{\mu\nu,p} F_q^{\mu\nu} = \frac{1}{g_{11}^2} F_{\mu\nu,1} F_1^{\mu\nu} \quad (79)$$

$$+ \frac{1}{g_{12}^2} F_{\mu\nu,1} F_2^{\mu\nu} + \dots + \frac{1}{g_{23}^2} F_{\mu\nu,2} F_3^{\mu\nu} + \frac{1}{g_{33}^2} F_{\mu\nu,3} F_3^{\mu\nu},$$

where $p, q = 1, 2, 3$ are the indices of three generations of the AGUT group $(SMG)^3$. Equation (79) explains the difference between expressions (76) and (77).

It was assumed in [1] that the MCP values $\alpha_{i,crit}$ in Eqs. (76) and (77) coincide with (or are very close to) the triple-point values of the effective fine-structure constants given by the generalized lattice $SU(3)$, $SU(2)$, and $U(1)$ gauge theories [11–14] described by Eqs. (3) and (4). Also, the authors of [1] used the assumption that the effective α_{crit} does not change (at least too much) along the entire borderline \mathcal{B} of Fig. 1 for the phase-transition Coulomb confinement (for details, see in [1]).

7.3. Multiple-Point Model and Behavior of the Electric Fine-Structure Constant near the Phase-Transition Point

The authors of [11–14] were not able to obtain the lattice triple-point values of $\alpha_{i,crit}$ by the Monte Carlo simulation method. Only the critical value of the electric fine-structure constant α was obtained in [14] in compact QED described by the simple Wilson action corresponding to the case of $\gamma^{lat} = 0$ in Eq. (4). The result of [14] for the behavior of $\alpha(\beta)$ in the vicinity of the phase-transition point β_T is shown in Fig. 6a for the Wilson and Villain lattice actions. Here, $\beta \equiv \beta^{lat} = 1/e_0^2$, and e_0 is the bare electric charge. The Villain lattice action has the form

$$S_V = (\beta/2) \sum_p (\Theta_p - 2\pi k)^2, \quad k \in Z. \quad (80)$$

Figure 6b demonstrates a comparison of the functions $\alpha(\beta)$ obtained by the Monte Carlo method for the Wilson lattice action and by theoretical calculation of the same quantity. The theoretical (dashed) curve was calculated by the so-called Parisi improvement formula [41]

$$\alpha(\beta) = [4\pi\beta W_p]^{-1}. \quad (81)$$

Here, $W_p = \langle \cos \Theta_p \rangle$ is the mean value of the plaquette energy. The corresponding values of W_p were taken from [13].

According to Fig. 6b, we have

$$\alpha_{crit,theor}^{-1} \approx 8. \quad (82)$$

This result does not agree with the lattice and the HMM result (52). The deviation of the theoretical

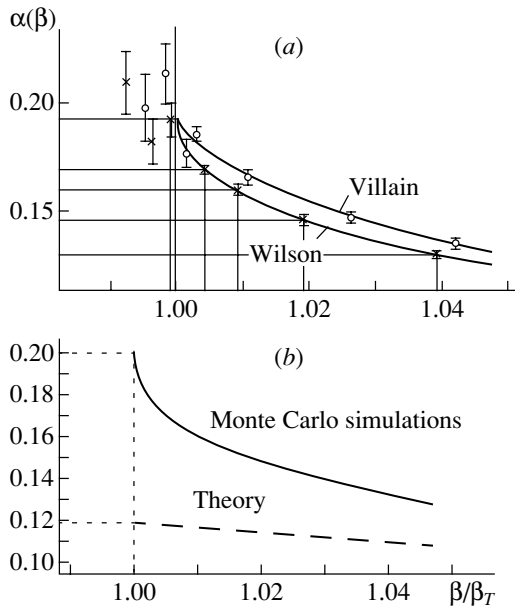


Fig. 6. (a) Renormalized electric fine-structure constant plotted versus β/β_T for the (circles) Villain action and (crosses) Wilson action. The points were obtained in [14] by the Monte Carlo simulation method for compact QED. (b) Behavior of the effective electric fine-structure constant in the vicinity of the phase-transition point for the case of the lattice Wilson action. The dashed curve corresponds to the theoretical calculations by the Parisi improvement formula [41].

calculations from the lattice ones has the following explanation. The Parisi improvement formula (81) is valid in the Coulomb phase, where the mass of artifact monopoles is infinitely large and where the photon is massless. But in the vicinity of the phase-transition (critical) point, the monopole mass m tends to zero and the photon acquires a nonzero mass ($m_0 \neq 0$). This phenomenon leads to the “freezing” of α at the phase-transition point: the effective electric fine-structure constant is nearly constant in the confinement phase and approaches its maximal value $\alpha = \alpha_{\max}$. The authors of [42] predicted $\alpha_{\max} = \pi/12 \approx 0.26$ due to the Casimir effect (see also [3]). The analogous freezing of α_s was considered in [43] in QCD. We also see that Fig. 6a demonstrates the tendency toward the freezing of α .

Let us now consider $\alpha_Y^{-1} (\approx \alpha^{-1})$ at the point $\mu = \mu_G$ shown in Fig. 5. If the point $\mu = \mu_G$ is very close to the Planck scale $\mu = \mu_{Pl}$, then, according to Eqs. (74) and (77), we have

$$\alpha_{1st\ gen}^{-1} \approx \alpha_{2nd\ gen}^{-1} \approx \alpha_{3rd\ gen}^{-1} \approx \frac{\alpha_Y^{-1}(\mu_G)}{6} \approx 9, \quad (83)$$

which is very close to the value in (82). This means (see Fig. 6b) that, in the $U(1)$ sector of G theory, we have α near the critical point; therefore, we can expect

the existence of a MCP at the Planck scale. As a consequence of such a prediction, we have to expect a change in the evolution of $\alpha_i^{-1}(\mu)$ in the region $\mu > \mu_G$ shown in Fig. 5 by dashed lines. Instead of these dashed lines, we have to see a decrease in $\alpha_i^{-1}(\mu)$ approaching the MCP at the Planck scale, where α_{crit} is close to the value in (52) obtained in the present study. But this is an aim of our future investigations based on the idea that the MCP governs the evolution of all fine-structure constants in the SM and beyond it.

8. CONCLUSION

In the present study, we have considered the dual Abelian Higgs model of scalar monopoles reproducing a confinement mechanism in the lattice gauge theories. Using the Coleman–Weinberg idea of the RG improvement of the effective potential [18], we have considered this potential with β functions calculated in the two-loop approximation. The phase transition between the Coulomb-like and confinement phases has been investigated in $U(1)$ gauge theory by the method developed in the MPM, where degenerate vacua are considered. A comparison of the results $\alpha_{\text{crit}} \approx 0.17$ and $\tilde{\alpha}_{\text{crit}} \approx 1.48$ obtained in the one-loop approximation with the results $\alpha_{\text{crit}} \approx 0.208$ and $\tilde{\alpha}_{\text{crit}} \approx 1.20$ obtained in the two-loop approximation demonstrates that the critical values of the electric and magnetic fine-structure constants calculated in the two-loop approximation of the HMM agree with the lattice result [14]: $\alpha_{\text{crit}}^{\text{lat}} \approx 0.20 \pm 0.015$ and $\tilde{\alpha}_{\text{crit}}^{\text{lat}} \approx 1.25 \pm 0.10$. Comparing the one-loop and two-loop contributions to the β functions, we have also demonstrated the validity of perturbation theory in solving the phase-transition problem in $U(1)$ gauge theory.

In the second part of our article, we have compared the prediction of AGUT and the MPM for the Planck scale values of $\alpha_i^{-1}(\mu)$ with the lattice and HMM results. Such a comparison is very encouraging for the MPM.

REFERENCES

1. D. L. Bennett and H. B. Nielsen, *Int. J. Mod. Phys. A* **9**, 5155 (1994); **14**, 3313 (1999).
2. L. V. Laperashvili, *Yad. Fiz.* **57**, 501 (1994) [*Phys. At. Nucl.* **57**, 471 (1994)]; *Yad. Fiz.* **59**, 172 (1996) [*Phys. At. Nucl.* **59**, 162 (1996)].
3. L. V. Laperashvili and H. B. Nielsen, *Mod. Phys. Lett. A* **12**, 73 (1997).
4. L. V. Laperashvili and H. B. Nielsen, in *Proceedings of the International Workshop on What Comes Beyond the Standard Model, Bled, Slovenia, 1998* (Ljubljana, 1999), p. 15.
5. K. Wilson, *Phys. Rev. D* **10**, 2445 (1974).

6. M. Creutz, I. Jacobs, and C. Rebbi, Phys. Rev. D **20**, 1915 (1979).
7. B. Lautrup and M. Nauenberg, Phys. Lett. B **95B**, 63 (1980).
8. M. Creutz, Phys. Rev. D **21**, 2308 (1980); Phys. Rev. Lett. **45**, 313 (1980).
9. B. Lautrup and M. Nauenberg, Phys. Rev. Lett. **45B**, 1755 (1980).
10. M. Creutz, Phys. Rev. Lett. **46**, 1441 (1981).
11. G. Bhanot and M. Creutz, Phys. Rev. D **24**, 3212 (1981).
12. G. Bhanot, Phys. Lett. B **108B**, 337 (1982).
13. G. Bhanot, Nucl. Phys. B **205**, 168 (1982); Phys. Rev. D **24**, 461 (1981); Nucl. Phys. B **378**, 633 (1992).
14. J. Jersak, T. Neuhaus, and P. M. Zerwas, Phys. Lett. B **133B**, 103 (1983); Nucl. Phys. B **251**, 299 (1985).
15. T. Suzuki, Nucl. Phys. B (Proc. Suppl.) **30**, 176 (1993); R. W. Haymaker, Phys. Rep. **315**, 153 (1999).
16. M. N. Chernodub and M. I. Polikarpov, in *Confinement, Duality and Non-perturbative Aspects of QCD*, Ed. by Pierre van Baal (Plenum, New York, 1998), p. 387; hep-th/9710205; M. N. Chernodub, F. V. Gubarev, M. I. Polikarpov, and A. I. Veselov, Prog. Theor. Phys. Suppl. **131**, 309 (1998); hep-lat/9802036; M. N. Chernodub, F. V. Gubarev, M. I. Polikarpov, and V. I. Zakharov, hep-th/0007135.
17. T. Suzuki, Prog. Theor. Phys. **80**, 929 (1988); S. Maedan and T. Suzuki, Prog. Theor. Phys. **81**, 229 (1989).
18. S. Coleman and E. Weinberg, Phys. Rev. D **7**, 1888 (1973); S. Coleman, in *Laws of Hadronic Matter*, Ed. by A. Zichichi (Academic, New York, 1975).
19. M. Sher, Phys. Rep. **179**, 274 (1989).
20. H. B. Nielsen, in *Proceedings of the XVII Scottish University Summer School in Physics, St. Andrews, 1976*, p. 528; D. L. Bennett, H. B. Nielsen, and I. Picek, Phys. Lett. B **208**, 275 (1988); H. B. Nielsen and N. Brene, Phys. Lett. B **233**, 399 (1989).
21. C. D. Froggatt and H. B. Nielsen, *Origin of Symmetries* (World Sci., Singapore, 1991).
22. C. D. Froggatt, G. Lowe, and H. B. Nielsen, Phys. Lett. B **311**, 163 (1993); Nucl. Phys. B **414**, 579 (1994); **420**, 3 (1994); C. D. Froggatt, H. B. Nielsen, and D. J. Smith, Phys. Lett. B **385**, 150 (1996); C. D. Froggatt, M. Gibson, H. B. Nielsen, and D. J. Smith, Int. J. Mod. Phys. A **13**, 5037 (1998).
23. C. D. Froggatt, L. V. Laperashvili, and H. B. Nielsen, in *SUSY'98, Oxford, 1998*; hepnts1.rl.ac.uk/susy98/.
24. H. B. Nielsen and Y. Takanishi, Nucl. Phys. B **588**, 281 (2000); **604**, 405 (2001); Phys. Lett. B **507**, 241 (2001); hep-ph/0011168; hep-ph/0101181; hep-ph/0101307.
25. L. V. Laperashvili, in *Proceedings of the 4th International Symposium Frontiers of Fundamental Physics, Hyderabad, India, 2000*.
26. C. G. Callan, Phys. Rev. D **2**, 1541 (1970); K. Symanzik, in *Fundamental Interactions at High Energies*, Ed. by A. Perlmutter (Gordon and Breach, New York, 1970).
27. D. R. T. Jones, Nucl. Phys. B **75**, 531 (1974); Phys. Rev. D **25**, 581 (1982).
28. M. Fischler and C. T. Hill, Nucl. Phys. B **193**, 53 (1981).
29. I. Jack and H. Osborn, J. Phys. A **16**, 1101 (1983).
30. M. E. Machacek and M. T. Vaughn, Nucl. Phys. B **222**, 83 (1983); **249**, 70 (1985).
31. H. Alhendi, Phys. Rev. D **37**, 3749 (1988).
32. H. Arason, D. J. Castano, B. Kesthelyi, *et al.*, Phys. Rev. D **46**, 3945 (1992).
33. O. V. Tarasov, A. A. Vladimirov, and A. Yu. Zharkov, Phys. Lett. B **93B**, 429 (1980); S. Larin, T. Ritberg, and J. Vermaseren, Phys. Lett. B **400**, 379 (1997).
34. J. Jersak, T. Neuhaus, and H. Pfeiffer, Phys. Rev. D **60**, 054502 (1999).
35. A. A. Abrikosov, Zh. Éksp. Teor. Fiz. **32**, 1442 (1957) [Sov. Phys. JETP **5**, 1174 (1957)].
36. H. B. Nielsen and P. Olesen, Nucl. Phys. B **61**, 45 (1973).
37. L. V. Laperashvili and H. B. Nielsen, Int. J. Mod. Phys. A **16**, 2365 (2001).
38. H. P. Nilles, Phys. Rep. **110**, 1 (1984).
39. P. Langacker and N. Polonsky, Phys. Rev. D **47**, 4028 (1993); **49**, 1454 (1994); **52**, 3081 (1995).
40. M. B. Green and J. Schwarz, Phys. Lett. B **149B**, 117 (1984).
41. G. Parisi, R. Petronzio, and F. Rapuano, Phys. Lett. B **128B**, 418 (1983); E. Marinari, M. Guagnelli, M. P. Lombardo, *et al.*, in *Lattice 91: Proceedings of the International Symposium on Lattice, Tsukuba, 1991*, p. 278. Nucl. Phys. B (Proc. Suppl.) **26**, 278 (1992).
42. M. Lüscher, K. Symanzik, and P. Weisz, Nucl. Phys. B **173**, 365 (1980).
43. Yu. A. Simonov, Yad. Fiz. **58**, 113 (1995) [Phys. At. Nucl. **58**, 107 (1995)]; A. M. Badalian and Yu. A. Simonov, Yad. Fiz. **60**, 714 (1997) [Phys. At. Nucl. **60**, 630 (1997)]; A. M. Badalian and D. S. Kuzmenko, hep-ph/0104097.

Analysis of Isomeric Ratios in (γ, n) and (γ, p) Reactions around Giant-Resonance Energies

N. A. Demekhina, A. S. Danagulyan¹⁾, and G. S. Karapetyan¹⁾

Yerevan Physics Institute, ul. Brat'ev Alikhanian 2, Yerevan, 375036 Armenia

Received June 28, 2000; in final form, April 5, 2001

Abstract—Isomeric ratios are investigated in simple photonuclear reactions occurring on targets in the mass range 90–180 amu that are irradiated with 20- to 40-MeV photons. The results of measurements are compared with estimates based on the statistical model of deexcitation of compound nuclei. The isomeric ratios in question are calculated with allowance for special features of photonuclear reactions induced by bremsstrahlung photons and for the properties of nuclear transitions in residual products. The results of these calculations, involving no free parameters, agree satisfactorily with experimental data.

© 2002 MAIK “Nauka/Interperiodica”.

1. INTRODUCTION

The probability of formation of high-spin nuclear states in the interaction of accelerated particles with nuclei is extremely sensitive to the energy and spin features of excited nuclei and to the mechanism of their deexcitation.

Investigation of such processes provides the possibility of exploring the properties of intermediate nuclear states and determining parameters characterizing them (spin–parities, moments of inertia, excitation energies, distributions of nuclear-level density).

In reactions involving the emission of a small number of particles, it is easier to obtain reliable information of this kind.

Photonuclear reactions are characterized by pure electromagnetic interaction and by resonance photoabsorption at energies below 50 MeV [1, 2]. In contrast to charged particles, photons interacting with nuclei do not have to overcome a Coulomb barrier, so that the excitation of a nucleus formed is completely determined by the energy of the absorbed photon. Investigation of absorption processes at such energies that is usually based on the long-wave approximation and on a partial-wave analysis [1, 2] makes it possible to determine the features of the compound system formed. This simplifies the reaction pattern by imposing constraints on the spin and energy features of excited nuclear systems. In the energy range 10–40 MeV, simple processes involving the emission of not more than three particles are dominant channels of photon interaction with light and medium-mass

nuclei. In this energy range, the properties of reaction products are usually interpreted on the basis of the statistical model and the compound-nucleus formalism [1, 3–5].

Experimental inquiries into this region include investigation of the probability of formation of long-lived high-spin nuclear states. The ratio of the yields of high-spin and low-spin states (isomeric ratio) is controlled by the following factors: the spin of the target nucleus; the energy and spin distributions of the density of excited states; the number, the type, and the energy of particles emitted from the compound nucleus; and the spin and the energy features of the isomeric and the ground state. Calculations based on the statistical model and a comparison with experimental results make it possible to assess the potential of the model approximations used and to obtain information about the character of spin distributions of nuclear levels [3, 5, 6].

Here, the precision of experimental information guarantees the reliability of the results of such an analysis. Unfortunately, the experimental data published so far in the literature are sometimes contradictory because the contribution of radioactive predecessors was either disregarded or taken into account incompletely. In the future, the experimental database may also prove to be somewhat “outdated” because the sensitivity of detecting facilities is being improved and because the spectroscopic features of nuclei are being refined.

The use of precise calculated or experimental values of isomeric ratios plays a substantial role for a number of applied problems as well.

¹⁾Yerevan State University, ul. A. Manukyana 1, Yerevan, 375049 Armenia.

Table 1

Target	Isotopic composition	Reaction type
Zr	Natural	$^{90}\text{Zr}(\gamma, n)$
Ag	»	$^{107}\text{Ag}(\gamma, n)$
^{113}In	»	$^{113}\text{In}(\gamma, n)$
^{124}Sn	Enriched	$^{124}\text{Sn}(\gamma, n)$
^{112}Sn	»	$^{112}\text{Sn}(\gamma, p)$
^{118}Sn	»	$^{118}\text{Sn}(\gamma, p)$
^{120}Sn	»	$^{120}\text{Sn}(\gamma, p)$
Hf	Natural	$^{179}\text{Hf}(\gamma, p)$
W	»	$^{180}\text{W}(\gamma, n)$
Cd	»	$^{116}\text{Cd}(\gamma, n)$

2. EXPERIMENTAL PROCEDURE

The irradiations were carried out at the linear electron accelerator-injector of the Yerevan synchrotron at accelerated-electron energies of 20, 30, and 40 MeV. For targets, we used a set of elements of natural and enriched isotopic composition (Table 1).

The thicknesses of the targets used did not exceed 0.1 r.l. The gamma radiation from radioactive products was measured by a semiconductor detector from ultrapure germanium, its resolution being about 0.25% at an energy of 1330 keV (^{60}Co line). As a reference reaction, we chose $^{65}\text{Cu}(\gamma, n)^{64}\text{Cu}$ [7] and measured its yield. In processing the results of measurements, we employed the most recent spectroscopic data quoted on the Internet (Nuclide Information, Nuclear Wallet Card).

The isomeric ratios were calculated by formulas involving the ratio of the areas under the peaks of measured γ transitions and taking into account, if necessary, the contribution of the isomeric state as the radioactive predecessor [8, 9]:

$$\frac{\sigma_m}{\sigma_g} = \left[\frac{\lambda_g(1 - e^{-\lambda_m t_1})e^{-\lambda_m t_2}(1 - e^{-\lambda_m t_3})}{\lambda_m(1 - e^{-\lambda_g t_1})e^{-\lambda_g t_2}(1 - e^{-\lambda_g t_3})} \right]^{-1} \times \left(\frac{k_m N_g \eta_m \varepsilon_m}{k_g N_m \eta_g \varepsilon_g} - p \frac{\lambda_g}{\lambda_g - \lambda_m} \right) + p \frac{\lambda_m}{\lambda_g - \lambda_m} \quad (1)$$

Here, N is the area under the photopeak, t_1 is the time of irradiation, t_2 is the time of exposure between the end of irradiation and the beginning of measurements, t_3 is the time of measurements, λ is the decay constant, η is the relative intensity of the γ transitions with allowance for the effect of internal conversion, k is the coefficient of photon absorption in target and detector materials, ε is the efficiency of measurements of the energies for recorded γ transitions, and p is the

contribution of the isomeric state. The subscripts m and g label quantities referring to the isomeric and the ground state, respectively.

The formula becomes more cumbersome if it is necessary to take into account the parent contribution from the radioactive predecessor to the formation of both the isomeric and the ground state.

Below, we present the results of a data treatment and of a comparison with those known from the literature:

(i) In the reaction $^{90}\text{Zr}(\gamma, n)^{89m,g}\text{Zr}$ (the contribution of the metastable state to the ground state amounts to 94%), the isomeric ratio agrees with the results of measurements published in [6, 10–12].

(ii) In the reaction $^{107}\text{Ag}(\gamma, n)^{106m,g}\text{Ag}$ (the yields of the metastable and the ground state were considered to be independent), the agreement with data from the literature [11] is attained within the statistical errors.

(iii) In the reaction $^{112}\text{Sn}(\gamma, p)^{111m,g}\text{In}$ (the parent contribution from ^{111}Sn to the formation of the metastable state is 0.2%, while that to the formation of the ground state is 99.8%; the isomeric state is converted completely into the ground state, and the isomeric ratio was calculated by a complicated formula that takes into account the contribution of both parents), the data differ substantially from the results presented in [11, 13, 14]; this difference can be explained by the contribution from ^{111}Sn , whose yield is approximately an order of magnitude higher than that from the reaction under investigation.

(iv) In the reaction $^{113}\text{In}(\gamma, n)^{112m,g}\text{In}$ (the contribution from the metastable state to the ground state amounts to 100%), the result agrees with data from [6, 10, 11].

(v) In the reaction $^{116}\text{Cd}(\gamma, n)^{115m,g}\text{Cd}$ (the contribution from the radioactive predecessor ^{115g}Ag to the ground-state yield amounts to 94.2%, while that to the metastable-state yield is 5.8%), the value of the isomeric ratio agrees with data from [10, 11].

(vi) In the reaction $^{118}\text{Sn}(\gamma, p)^{117m,g}\text{In}$ (the contribution from the metastable state to the ground state amounts to 47.1%), the value of the isomeric ratio agrees within the two statistical errors with data from [9] and differs from the values quoted in [11, 15], where the contribution from the isomeric state seems to be disregarded.

(vii) In the reaction $^{120}\text{Sn}(\gamma, p)^{119m,g}\text{In}$ (the contribution from the metastable level to the ground state amounts to 5.6%), the isomeric ratio differs from the data presented by Gangrsky *et al.* [15], who disregarded the parent contribution of the isomeric state.

Table 2. Isomeric ratios

Target nucleus	Product nucleus	Isomeric ratio, MeV		
		20	30	40
$^{120}\text{Sn}(0^+)(\gamma, p)$	$^{119}\text{In } m(1/2^-)$	0.49**	0.65**	0.7**
	$g(9/2^+)$	0.53 ± 0.05	0.68 ± 0.07	0.68 ± 0.07
$^{118}\text{Sn}(0^+)(\gamma, p)$	$^{117}\text{In } m(1/2^-)$	0.44	0.63**	0.82**
	$g(9/2^+)$		0.66 ± 0.07	0.85 ± 0.08
$^{112}\text{Sn}(0^+)(\gamma, p)$	$^{111}\text{In } m(1/2^-)$	1.26*	1.84	1.9
	$g(9/2^+)$		≤ 2	
$^{179}\text{Hf}(9/2^+)(\gamma, p)$	$^{178}\text{Lu } m(9^-)$	0.34	0.38**	0.44
	$g(1^+)$	0.36 ± 0.04		
$^{90}\text{Zr}(0^+)(\gamma, n)$	$^{89}\text{Zr } m(1/2^-)$	0.57**	0.575**	0.6**
	$g(9/2^+)$			0.85 ± 0.04
$^{107}\text{Ag}(1/2^-)(\gamma, n)$	$^{106}\text{Ag } m(6^+)$	0.0147**	0.016**	0.0197**
	$g(1^+)$	0.015 ± 0.0045	0.010 ± 0.002	
$^{113}\text{In}(9/2^+)(\gamma, n)$	$^{112}\text{I } m(4^+)$	1.9**	2.37**	2.5**
	$g(1^+)$		2.21 ± 0.20	
$^{124}\text{Sn}(0^+)(\gamma, n)$	$^{123}\text{Sn } m(3/2^+)$	0.2	0.32**	0.5
	$g(11/2^-)$		0.33 ± 0.10	0.49 ± 0.30
$^{180}\text{W}(0^+)(\gamma, n)$	$^{179}\text{W } m(1/2^-)$	1.45**	1.72**	1.82**
	$g(7/2^-)$		1.93 ± 0.20	
$^{85}\text{Rb}(7/2^-)(\gamma, n)^*$	$^{84}\text{Rb } m(6^+)$	0.23**	0.3	0.352
	$g(2^+)$	0.31 ± 0.04	0.34 ± 0.06	0.44 ± 0.08
$^{116}\text{Cd}(0^+)(\gamma, n)$	$^{115}\text{Cd } m(11/2^-)$	0.13**	0.178**	0.179**
	$g(1/2^+)$	0.148 ± 0.020		
$^{130}\text{Te}(0^+)(\gamma, n)^*$	$^{129}\text{Te } m(11/2^-)$	0.43**	0.56**	0.58**
	$g(3/2^+)$	0.43 ± 0.06	0.48 ± 0.02	0.55 ± 0.11

* Data from [16].

** Data calculated with the aid of photon strength functions [17].

(viii) In the reaction $^{124}\text{Sn}(\gamma, n)^{123m,g}\text{Sn}$ (the contributions from the metastable and the ground state were considered to be independent), the isomeric ratio agrees with the results of measurements reported in [11].

(ix) In the reaction $^{179}\text{Hf}(\gamma, p)^{178m,g}\text{Lu}$, the isomeric and the ground state are considered to be independent; the data agree satisfactory with those from [6].

(x) For the reaction $^{180}\text{W}(\gamma, n)^{179m,g}\text{W}$ (the contribution from the metastable state to the ground state is 99.7%), there are no corresponding experimental data.

From the results of our measurements (Table 2) and also from data reported previously in [16], it can be seen that, in the range 20–40 MeV, the isomeric ratio increases somewhat with incident-photon energy.

The dependence of this type means that, with increasing endpoint bremsstrahlung energy, the yields of high-spin states grow faster than the yield of low-spin states.

3. CALCULATION OF ISOMERIC RATIOS

A method that can be used to analyze the ratio of the cross sections for the formation of isomeric pairs

in nuclear reactions was proposed by Huizenga and Vandenbosch [3] and is based on the use of the statistical model and the concept of a compound nucleus. By considering, within this model, the probability of emission of one or two nucleons with the subsequent cascade of photons, one can reproduce the interaction pattern and estimate the possibility of population of high-spin states. The density of the spin distribution of nuclear levels and its variation during the reaction form a key element of the calculations. Huizenga and Vandenbosch introduced a number of free parameters associated with the properties of cascade γ transitions, nuclear levels, and the spin distributions of intermediate states. In more recent studies, the applicability range of this formalism was considerably extended and the computational method was standardized by introducing the effect of parity, the pairing of nucleons, and the admixture of higher multipoles in the formation and deexcitation of the compound nucleus and by taking into account the effect of the features of nuclear states in that section of the discrete spectrum where the last transitions occur [17, 18].

In this study, we have calculated isomeric states on the basis of the method proposed in [18]. In consistently applying the statistical model, we relied on the recursion relation for calculating the probability of population of intermediate nuclear levels, took into account the specific properties of nuclear γ transitions at the final stage of the reaction, and eliminated free parameters. Investigation of photonuclear reactions induced by bremsstrahlung photons presumes an additional procedure for calculating the excitation of the compound nucleus.

The mean excitation energy of the compound nucleus was calculated with allowance for the magnitude, the shape, and the position of the giant-resonance function describing the photoabsorption cross section [1, 4] and also for the continuous energy spectrum of incident photons. Under the assumption of dipole photon absorption, the absorption cross section was taken in the form of the Lorentzian function; that is,

$$\sigma(E_\gamma) = C \frac{[E_m^2 + \frac{1}{4}\Gamma^2]}{(E_\gamma - E_m)^2 + \frac{1}{4}\Gamma^2}, \quad (2a)$$

where C is a constant involving some constant factors. The position of the maximum of the curve was determined within the hydrodynamic model ($E_m = 82A^{-1/3}$), while the FWHM was approximated by a mean value of $\Gamma \sim 5$ MeV. Our results proved to be weakly sensitive to variations in the position of the resonance maximum and width within 1 to 2 MeV. In

calculating the mean excitation energy

$$\bar{E}^* = \frac{\int_{E_{\text{thr}}}^{E_\gamma^{\text{max}}} E_\gamma \sigma(E_\gamma) N(E_\gamma, E_\gamma^{\text{max}}) dE_\gamma}{\int_{E_{\text{thr}}}^{E_\gamma^{\text{max}}} \sigma(E_\gamma) N(E_\gamma, E_\gamma^{\text{max}}) dE_\gamma}, \quad (2b)$$

where E_{thr} is the energy threshold of the reaction, the energy distribution of photons in the bremsstrahlung spectrum was approximated as $N(E_\gamma, E_\gamma^{\text{max}}) \sim \text{const} \cdot (1/E_\gamma)$, the endpoint energy being set to $E_\gamma^{\text{max}} = 20, 30, \text{ or } 40$ MeV. In response to a variation of the endpoint bremsstrahlung energy in the range 20–40 MeV, the excitation energy of nuclei increased by 2 to 3 MeV, on average.

The spin and the parity of the compound nucleus were determined by the multipolarity of the absorbed photon; in the case of dipole photon absorption, the spins of product nuclei take the values of $J_c = J, J \pm 1$. In the calculations, we used the normalized (to unity) spin distribution of compound nuclei instead of the absolute values of the absorption cross sections.

Nucleon emission is accompanied by a change in the energy and the spin distribution of compound nuclei. In the case of (γ, n) reactions, the effective excitation energy that corresponds to the beginning of photon emission was determined with allowance for the threshold energy (E_{thr}) of the reaction and the mean energy (ϵ_n) of an evaporated neutron: $E_{\text{eff}}^* = \bar{E}^* - E_{\text{thr}} - \epsilon_n$.

According to the evaporation model, neutrons are emitted by an excited nucleus with a mean energy ϵ_n equal to $2t$, where t is the nuclear temperature satisfying the equation $at^2 - 4t = E_{\text{eff}}^*$ [19], with a being the level-density parameter determined directly in terms of the density of single-particle states at the Fermi surface; in our calculations, we used the values of $a = A/8, A/9, \text{ and } A/10$. The results of the calculations changed insignificantly in response to a variation in the parameter a within the above range, and the mean energy of the neutrons was about 1 MeV. The calculations of the transmission coefficients revealed that, in the reactions under investigation, the neutrons are emitted predominantly in the S -wave state; the relative probability of the emission of neutrons in the P - and D -wave state is much less.

In determining the mean energy of emitted protons, we took additionally into account the effect of the Coulomb barrier; as a result, there arose a non-negligible probability of the emission of protons in the P - and the D -wave state in relation to that in the S -wave state [19]. In this case, the calculation of the effective excitation energy of a nucleus must also take into account the centrifugal energy.

The parity of the nucleus at the onset of deexcitation was determined with allowance for internal nucleon parity.

At the stage of the process involving the cascade of γ transitions eventually leading to the metastable or the ground state, the density of the spin distribution of nuclear levels is the most substantial factor determining the probability of population of intermediate nuclear states. In the calculations, we used the spin part of the Bethe–Bloch formula,

$$\rho(J) = \rho(0)(2J + 1) \exp \left[-\frac{(J + 1/2)^2}{2\sigma^2} \right], \quad (3)$$

where σ is the spin-cutoff parameter given by $\sigma^2 = 0.00889 \sqrt{aE_{\text{eff}}^*} A^{2/3}$.

For the population of intermediate states, we further used the recursion relation proposed by Arifov *et al.* [18], who analyzed data on proton–nucleus reactions. In addition to the conditions of the calculations in [18], we took into account the change in the excitation energy and in the parameters associated with it at each stage of the γ cascade.

The basic points of the calculations can be formulated as follows:

(a) All γ transitions, including the last “crucial” one, are of the $E1$ type.

(b) The transition probabilities are determined by the spin part of the density of the distribution of levels.

(c) The total multiplicity of photons is calculated on the basis of data including the excitation energy of the compound nucleus and the mean energy of the emitted photon:

$$\bar{N}_\gamma = \frac{\sqrt{aE_{\text{eff}}^*}}{2} \quad (4)$$

{in this case, we consider various assumptions on the mean energy \bar{E} of emitted photons: $\bar{E} = 4(E_{\text{eff}}^*/a - 5/a^2)^{1/2}$ and $\bar{E} = [4(E_{\text{eff}}^* - 1)]^{1/2}$ }.}

(d) The excitation energy E_{eff}^* and, accordingly, the energy \bar{E} of emitted photons are determined at each stage of the cascade.

(e) The last “crucial” level from which the population of the ground or the isomeric state occurs is characterized by an excitation energy E_{eff}^* not higher than 2 MeV and by a change of $(-1)^{N_\gamma - 1}$ in parity upon photon emission.

(f) At the last stage of population, we take into account the known experimental fact that the $E1$ transitions from lower levels are suppressed in relation to $E2$ transitions and the spectroscopic features of specific nuclear levels from Tables 1 and 2 and from the Internet. The relative probability of radiative

transitions was estimated by means of the strength functions in the form [17]

$$\begin{aligned} S_\gamma^{E1} &= 4 \times 10^{-9} A^{2/3} \text{ MeV}^{-3}, \\ S_\gamma^{E2} &= 2 \times 10^{-14} A^{4/3} \text{ MeV}^{-5}, \\ S_\gamma^{M1} &= 10^{-8} A^{2/3} \text{ MeV}^{-3}. \end{aligned} \quad (5)$$

The results of the calculations (Table 2) agree satisfactorily with experimental data. With increasing incident-photon energy (from 20 to 40 MeV), the isomeric ratios somewhat grow, which is also observed in experimental data. Usually, the energy dependence of yields in reactions induced by bremsstrahlung photons is less pronounced.

As can be seen from a comparison of the calculated and experimental data, the deexcitation of compound nuclei can be described satisfactorily within the assumptions adopted here. It should be emphasized that the agreement is attained without introducing free parameters. However, we admitted some uncertainty in choosing the mean number of γ transitions (within $\bar{N}_\gamma \pm 1$), because it can prove to be fractional according to relation (4).

On average, the spin-cutoff parameter σ characterizing the spin distributions of excited nuclei changed from 3 to 4 for $a = A/8, A/9, A/10$.

The parameter σ is related to the moment of inertia of the nucleus involved by the equation

$$I = \frac{2\pi\sigma^2 t}{h^2}. \quad (6)$$

On the basis of the values found here for the parameter σ , we have calculated the moments of inertia for nuclei in the excited state. On average, the results did not exceed $0.71I_{\text{rb}}$, where $I_{\text{rb}} = (2/5)MAR^2$ is the rigid-body moment of inertia for a spherical nucleus of mass number A and radius $R = 1.2r_0A^{1/3}$, M being the nucleon mass.

The conclusions drawn from our analysis performed are compatible with data obtained by investigating the isomeric ratios in other processes proceeding through a compound nucleus [20, 21].

ACKNOWLEDGMENTS

We are grateful to I.S. Amirkhanova and N.R. Boyadzhyan for assistance in processing experimental data and to the personnel of the accelerator for providing the required beam parameters during irradiation.

This work was supported by the International Science and Technological Center.

REFERENCES

1. B. S. Ishkhanov and I. M. Kapitonov, *Interaction of Electromagnetic Radiation with Nuclei* (Mosk. Gos. Univ., Moscow, 1979).
2. J. S. Levinger, *Nuclear Photo-Disintegration* (Oxford Univ. Press, London, 1960; translated under the title *Fotoyadernye reaktsii* by Inostrannaya Literatura, Moscow, 1962).
3. J. R. Huizenga and R. Vandenbosch, *Phys. Rev.* **120**, 1305 (1960).
4. Yu. P. Gangrskii, A. P. Tonchev, and N. P. Balabanov, *Fiz. Élem. Chastits At. Yadra* **27**, 1043 (1996) [*Phys. Part. Nucl.* **27**, 428 (1996)].
5. E. A. Skakun, A. P. Klyucharev, Yu. N. Rakivnenko, and I. A. Romanin, *Izv. Akad. Nauk SSSR, Ser. Fiz.* **39**, 193 (1975).
6. D. Kolev, *Appl. Radiat. Isot.* **49**, 989 (1998).
7. K. Masumoto and T. Kato, *Nucl. Instrum. Methods Phys. Res.* **157**, 567 (1978).
8. R. Vanska and R. Rieppo, *Nucl. Instrum. Methods Phys. Res.* **179**, 525 (1981).
9. D. Kolev, E. Dobрева, N. Nenov, and V. Todorov, *Nucl. Instrum. Methods Phys. Res.* **356**, 390 (1995).
10. A. D. Antonov, N. P. Balabanov, A. G. Belov, *et al.*, in *Proceedings of the 41st Conference on Nuclear Spectroscopy and Nuclear Structure, Minsk, 1991*, p. 286.
11. M. G. Davydov, V. G. Magera, and A. V. Trukhov, *At. Énerg.* **62**, 236 (1987).
12. Zui Khien Fam, Kuang Zui Ngo, and Tak An Nguen, *Yad. Fiz.* **35**, 257 (1982) [*Sov. J. Nucl. Phys.* **35**, 145 (1982)].
13. R. D. Babadzhanov, S. R. Palvanov, G. Yu. Tadzhibaev, *et al.*, in *Proceedings of the 41st Conference on Nuclear Spectroscopy and Nuclear Structure, Minsk, 1991*, p. 288.
14. M. G. Davydov, F. Sh. Khamraev, and É. M. Shomurodov, in *Proceedings of the 37th Conference on Nuclear Spectroscopy and Nuclear Structure, Yurmala, 1987*, p. 377.
15. Yu. P. Gangrsky, P. Zuzaan, N. N. Kolesnikov, *et al.*, Preprint No. R15-98-37, OIYaI (Joint Inst. for Nuclear Research, Dubna, 1998).
16. A. S. Danagulyan and N. A. Demekhina, *Yad. Fiz.* **60**, 2117 (1997) [*Phys. At. Nucl.* **60**, 1937 (1997)].
17. L. Z. Dzhilavyan, V. L. Kauts, V. I. Furman, and A. Yu. Chuprikov, *Yad. Fiz.* **51**, 336 (1990) [*Sov. J. Nucl. Phys.* **51**, 215 (1990)].
18. L. Ya. Arifov, B. S. Mazitov, and V. G. Ulanov, *Yad. Fiz.* **34**, 1028 (1981) [*Sov. J. Nucl. Phys.* **34**, 572 (1981)].
19. J. M. Blatt and V. F. Weisskopf, *Theoretical Nuclear Physics* (Wiley, New York, 1952; Inostrannaya Literatura, Moscow, 1954).
20. E. A. Skakun, A. P. Klyucharev, Yu. N. Rakivnenko, *et al.*, *Izv. Akad. Nauk SSSR, Ser. Fiz.* **39**, 31 (1975).
21. E. A. Skakun, A. P. Klyucharev, Yu. N. Rakivnenko, and I. A. Romanin, *Yad. Fiz.* **14**, 261 (1971) [*Sov. J. Nucl. Phys.* **14**, 147 (1972)].

Translated by V. Bukhanov

$T \rightarrow d + n$ Vertex Function and Its Correlation with the Triton Binding Energy and with the Doublet nd Scattering Length

Yu. V. Orlov, Yu. P. Orevkov, and L. I. Nikitina

Institute of Nuclear Physics, Moscow State University, Vorob'evy gory, Moscow, 119992 Russia

Received August 2, 2000; in final form, November 22, 2000

Abstract—The asymptotic normalization constant C_T^2 for the triton is calculated within a two-body model for potentials characterized by a Yukawa-type short-distance behavior and the long-distance asymptotic behavior $V(r) \rightarrow \text{const} \times r^{-\nu} \exp(-\mu r)$, where $\nu = 0, 1, 2$. It is shown that C_T^2 decreases monotonically with increasing ν and that it smoothly decreases with increasing $a_2\kappa$, where a_2 is the doublet scattering length and κ is the triton wave number. This behavior is consistent with effective-range theory taking into account the pole of $k \cot \delta$ and with the general trend of Faddeev calculations. It is established, however, that some calculations reported previously and performed on the basis of the N/D method yield, on the contrary, a sharp growth of C_T^2 . The results of the calculation of the form factor for the $T \rightarrow d + n$ vertex are compared with the results of the well-known three-body calculation.

© 2002 MAIK “Nauka/Interperiodica”.

1. INTRODUCTION

Information about the $T \rightarrow d + n$ vertex function can be obtained by solving Faddeev equations for the three-body problem as formulated for the bound-state triton T . However, the results of three-body calculations with a realistic NN interaction poorly reproduce even the triton binding energy ε_T . These results greatly depend on input data. The doublet nd scattering length a_2 is an especially sensitive quantity—it can change not only in magnitude but also in sign. In view of this, it is of interest to calculate the $T \rightarrow d + n$ vertex function on the basis of some model that would provide correct values (compatible with experimental data) for the triton binding energy ε_T and for the doublet nd scattering length a_2 . This is of paramount importance in applications where the cross sections for nuclear reactions are calculated with the aid of Feynman diagrams involving this vertex function.

As was shown in investigations performed in recent years, the low-energy properties of the doublet nd system are successfully described on the basis of the two-body potential model proposed for the first time by Petrov [1] and by Tomio *et al.* [2].

Petrov [1] considered the Hulthén potential

$$V(r) = -V_0/[\exp(\mu r) - 1] \quad (1)$$

and calculated the nuclear structure constant G_T^2 . He showed that the model in question reproduces fairly well the trend of variations in the results of Faddeev calculations for the vertex functions at various values of a_2 and ε_T , which were used to fit the potential parameters. Later on, it was shown [3] that, at

the experimental values of $a_2 = 0.65$ fm and $\varepsilon_T = 8.48$ MeV, the model value of G_T^2 for the Hulthén potential complies well with the result produced by generalized effective-range theory [4] taking into account the pole of $k \cot \delta$ and employing data from a partial-wave analysis of nd scattering. In [3, 5], it was shown that, within the same model, other low-energy features of the doublet nd system can also be described satisfactorily without additionally fitting the parameters involved. These features include the position of the virtual pole (the binding energy ε_{T^*} of the virtual triton T^*) and the corresponding nuclear vertex constant ($G_{T^*}^2$) [5], as well as the position of the pole of $k \cot \delta$ —that is, the position of the zero of the s -wave partial scattering amplitude $f(k)$ [3].

Two potentials were proposed in [2]; of these, one (version B) has the form

$$V(r) = -V_0(R/r)^2[\sin(r/R)]^2 \exp(-\mu r). \quad (2)$$

The potential (2) involves three parameters (V_0 , R , and μ), which were fitted in [2] to three experimental values, those of a_2 and ε_T and that of the binding energy of the ${}^3\text{He}$ nucleus. Tomio *et al.* [2] aimed at obtaining a theoretical estimate of the “nuclear” doublet pd scattering length. Following [6], they supplemented the potential with the factor $1/r^2$, which leads to a long-range interaction when $\mu \rightarrow 0$. The oscillating factor in (2) ensures that the potential is regular at the origin of coordinates. In our opinion, the oscillations of the potential in (2) does not seem natural. An acceptable behavior of $V(r)$ at the origin

can be obtained, for example, with the aid of the factor $[1 - \exp(-r/R)]$, which is used in the present study.

In [3], we calculated all of the aforementioned quantities for the Yukawa potential

$$V(r) = -V_0(\mu r)^{-1} \exp(-\mu r) \quad (3)$$

and also achieved a fairly good agreement both with experimental data and with the results of the calculations with the Hulthén potential. In [7], we computed all these features of the doublet nd system using the potential (2) and refitted the parameters of this potential to the experimental values of a_2 and ε_T . The results of the calculations with the potentials (1)–(3) were compared over a broad range of values of the interaction-strength parameter $g = K_0^2/\mu^2$, where $K_0^2 = (2m_{12}/\hbar^2)V_0$ and m_{12} is the reduced mass of the system (for the nd system, $m_{12} = (2/3)m$, with m being the nucleon mass). In order to perform a systematic analysis of the models featuring the potentials (1)–(3) at the same level (that is, with two parameters), μR was fixed in [7] at the value of 0.2646, as in [2]. It turned out that C_T^2 takes nearly the same values for the case of the Hulthén potential (1) and for the case of the potential (2). On this basis, we concluded in [7] that the quality of description of C_T^2 is not affected significantly by taking into account the Faddeev character of the asymptotic behavior of the potential; therefore, this is not very advantageous. The Hulthén potential (1) and the Yukawa potential (3) belong to the class of potentials featuring screened Coulomb interaction, since their behavior at the origin ($V(r) \sim 1/r$) is analogous to the Coulomb behavior; on the contrary, the potential (2) is finite at the origin. With the aim of singling out effects of long-range interaction, we consider here the potential

$$V(r) = -(V_0/\beta\mu r^2)[1 - \exp(-\beta r)] \exp(-\mu r), \quad (4)$$

which is free from oscillations. The potential (4) has a correct Faddeev asymptotic behavior, but, in contrast to what we have for the potential in (2), its behavior at the origin is characteristic of screened Coulomb potentials. By analogy with the potential in (2), we fixed, for the potential (4), the value of $M/R \cong 3.5$ ($M = 1/\mu$, $R = 1/\beta$).

The possibility of using a model that involves only two adjustable parameter is closely related to the existence of correlations between the low-energy features of the doublet nd system. Investigation of such correlations has a long history, which includes, in particular, the Phillips graph [8] for the dependence of the triton binding energy ε_T on the doublet scattering length a_2 . This dependence, which is nearly linear, is based on the results of numerous Faddeev calculations. Another example is provided by the Girard–Fuda graph [9] for the analogous a_2 dependence of the position of the pole in the energy of the virtual triton

T^* . Correlations between a_2 and the asymptotic normalization parameter C^2 (or the vertex constant G^2) for T and T^* were considered in a number of studies. For the triton, this was done in [9, 10] by using the N/D method. The a_2 dependence of C_T^2 was analyzed in [9] at the fixed experimental value of ε_T , and the analogous dependence of the nuclear vertex constant G_T^2 was considered in [10].

In the present study, we continue exploring the correlation between C_T^2 and the product $a_2\kappa_1$, where $\kappa_1 = \sqrt{(4/3)(m/\hbar^2)(\varepsilon_T - \varepsilon_d)}$, with ε_d being the deuteron binding energy. For the aforementioned potentials (1)–(4), which possess the scaling property, it is natural to investigate the function $C_T^2(a_2\kappa_1)$, since the quantities C_T^2 and $a_2\kappa_1$ are invariant under the scaling transformation $r \rightarrow \gamma r$, $p \rightarrow \gamma^{-1}p$ of the coordinates r and momenta p (see [3]). This property of the potentials makes it possible to consider combinations of physical quantities (they can include potential parameters) that are invariant under scaling transformations and which depend only on the scaling parameter g of the excitation strength.

Specifically, we calculate the scaling-invariant quantities

$$a\kappa_1, \kappa_1/\mu, \kappa_2/\mu, \kappa_0/\mu, C_T, C_\nu. \quad (5)$$

In addition to the asymptotic normalization coefficients C_T and C_ν , these include quantities proportional to $\kappa_n = (2m_{12}\varepsilon_n)^{1/2}/\hbar$ and $\kappa_0 = (2m_{12}E_0)^{1/2}/\hbar$, where ε_1 and ε_2 are the binding energies for, respectively, the ground (real) and the first excited (virtual in the case being considered) state (the corresponding principal quantum numbers are $n = 1$ and 2) and $-E_0$ is the position of the pole of the function $k \cot \delta$ in the complex plane of the energy E , with E and $k = (2m_{12}E)^{1/2}/\hbar$ being the energy and the momentum of the relative motion of d and n . The two-body energy E is related to the three-body energy E_3 by the obvious equation $E_3 = E - \varepsilon_d$. The positions of the poles of the scattering amplitude at $E = -\varepsilon_n$ for the bound ($B_T = \varepsilon_1 = \varepsilon_T - \varepsilon_d$) and the virtual ($B_\nu = \varepsilon_2 = \varepsilon_\nu - \varepsilon_d$) state and the position of the pole ($-E_0$) of the function $k \cot \delta$ are reckoned from the threshold for the nd -scattering channel at $E_3 = -\varepsilon_d$. In order to avoid encumbering the presentation, the subscript that indicates, in the scattering length a_2 , the spin-doublet character ($= 1/2$) of the nd state being considered is suppressed in (5) and in some other places; also, the subscript T^* is replaced by ν .

By eliminating the parameter g , one can derive a relation between the aforementioned scaling invariant physical variables—for example, between C_T and $a\kappa_1$ —which do not involve explicitly the potential

parameters. The procedure of fitting the potential parameters on the basis of preset values of a_2 and κ_1 is considerably simplified by taking into account scaling invariance. The parameters in question were determined in the order specified by the following chain:

$$a\kappa_1 \rightarrow g \rightarrow \kappa_1/\mu \rightarrow \mu \rightarrow R \rightarrow V_0. \quad (6)$$

As a matter of fact, scaling invariance makes it possible to reduce the two-parameter problem in question to a single-parameter problem, whereby the fitting of the parameters and a comparison of the results of the calculations with the different potentials are simplified. For the $a\kappa_1$ dependences of C_T^2 that correspond to all four potentials, it is of interest to perform a comparison over a broad range of interaction that covers the case of extremely light systems bound by nuclear forces [deuteron d , hypertriton ${}^3_\Lambda\text{H}$, and triton $T({}^3\text{H})$], because such a comparison would not explicitly involve the parameters of the potentials and because this would make it possible to explore the role of effects that are associated with different types of behavior of the potentials at infinity and at the origin of coordinates.

The dependence of C_T^2 on $a\kappa_1$ is a special form of correlation between three physical observables: the asymptotic normalization factor for the triton radial wave function, the triton binding energy, and the doublet nd scattering length. This dependence can also be derived from other approaches to describing the doublet nd system. Below, we will discuss some results obtained within generalized effective-range theory [4] and within the N/D method [9–12]. Simenog *et al.* [4] presented explicit expressions for the scattering-length (a_2) dependence of the parameters appearing in the formula that effective-range theory yields for $k \cot \delta$. On this basis, we find here the corresponding dependence of C_T^2 on $a\kappa_1$.

In the present study, we show for the first time that the functions $C_T^2(a\kappa_1)$ obtained in [9, 10] by using the N/D method (see the tables in [9, 10]) differ qualitatively from all others: they grow with increasing $a\kappa_1$. Below, we will discuss the possible reasons behind this discrepancy. It should be noted, however, that, at the experimental value of $a\kappa_1$, the results obtained in [9, 10] for C_T^2 are close to the results of corresponding Faddeev calculations. In the literature, this was considered as a success of the model based on the N/D method.

The present study pursues the following basic objectives:

(i) a comparison of the results obtained for the function $C_T^2(a\kappa_1)$ within the two-body model by using some effective nd potentials (this is done in order to reveal the sensitivity of this function to the form

of potential—in particular, to effects of long-range interaction);

(ii) a comparison of the results obtained upon implementing item (i) with the results produced by other approaches—specifically, (a) approaches employing Faddeev equations for various nucleon–nucleon interactions and (b) approaches relying on effective-range theory featuring a pole of the function $k \cot \delta$;

(iii) a comparison of the results of the investigations listed in items (i) and (ii) with results following from the application of the N/D method;

(iv) a calculation of the form factor for the $T \rightarrow d + n$ vertex within the two-body potential model, an estimation of its sensitivity to the form of the effective nd potential, and a comparison with the results of the calculations based on Faddeev equations.

In the calculations performed on the basis of the two-body potential model, use is made of the Lippmann–Schwinger equation and of the Schrödinger equation in the momentum representation. The method employed in these calculations is described in detail elsewhere [7]. We consider energies at which it is sufficient to take into account only the s wave. As a rule, we perform our analysis in the system of units where $\hbar = c = 1$.

2. TWO-BODY POTENTIAL MODEL

Let us briefly recall the analytic properties of the s -wave amplitude $f(k)$ for elastic nd scattering (for more details, see [7]). The important role of the Feynman pole diagram corresponding to proton exchange between the deuteron and the neutron involved and featuring a singularity in the momentum-transfer variable at a point that is close to the physical region is a theoretical argument in favor of the two-body potential model. The corresponding dynamical singularities of $f(k)$ occur at $k = \pm ik_1/2$, where $k_1 = (2/3)\sqrt{m\varepsilon_d} = 0.154$ fm, or at $E_1 = -\varepsilon_d/3 \cong -0.74$ MeV on the energy scale. This character of singularity can be simulated with the aid of a potential that belongs to the Yukawa type and which has the following asymptotic behavior:

$$V(r) \rightarrow C(r)r^{-\nu} \exp(-\mu r). \quad (7)$$

Here, $C(r) \leq \text{const}$; the exponent ν takes the value of $\nu = 0$ for the Hulthén potential (1), the value of $\nu = 1$ for the Yukawa potential (3), and the value of $\nu = 2$ for the potentials given by (2) and (4). The corresponding dynamical singularities of $f(k)$ are situated at $k = \pm i\mu/2$ (see, for example, [13]). Setting $\mu = 2k_1$, we obtain a value of about 3 fm for the radius $M = 1/\mu$.

The properties of the scattering amplitude that are being discussed at this point follow from the analytic structure of the kernel of the Faddeev integral

equation (see, for example, [14]). A $1/r^2$ long-range interaction, which arises when the scattering length for the pair subsystem tends to infinity, is one of the consequences of this. Long-range interactions of this type lead to the Efimov effect [15] (accumulation of levels near the threshold). The corresponding character of the behavior of $V(r)$ is indeed of importance if the physical system being studied is close to a state where the Efimov effect is realized—that is, if $\mu \rightarrow 0$. However, the parameters of nucleon–nucleon interaction are such that the doublet nd system has only one bound state, the triton. For this reason, the value of the exponent ν in (7) is expected to be immaterial, provided that an exponential decay of the potential at infinity is ensured. Thus, all of the aforementioned potentials (1)–(4) can in principle be used to construct a model description of the doublet nd system.

In analyzing the results of relevant numerical calculations, we use some well-known statements from quantum scattering theory, including the symmetry theorem [16] for bound and virtual levels and its consequence presented in [17]. For potentials belonging to the Yukawa type and having the asymptotic behavior as given by (7) ($\nu \leq 2$), it was shown in [16] that the points at which the trajectories of the poles of the function $f(k)$ intersect the lines of dynamical singularities possess a mirror symmetry with respect to the zero-momentum axis. In [17], it was also shown that the above symmetry points also belong to the trajectories of the zeros of $f(k)$. The virtual triton T^* differs from the triton only by the value of the principal quantum number. Therefore, its features are determined by the same set of parameters as the features of the triton. This means that, simultaneously with κ_1 and C_T^2 , one determines the quantities κ_2 and κ_0 (or ε_2 and E_0 on the energy scale), as well as C_{T^*} . The features of T^* were evaluated with the aid of integral equations continued analytically to an unphysical sheet of energy (see, for example, [14, 18]).

3. GENERALIZED EFFECTIVE-RANGE THEORY

The important role of the pole of $k \cot \delta$ at negative energy near the threshold in doublet nd scattering—for the first time, this pole was introduced in [19, 20]—has long since been known and has often been discussed in the literature (see, for example, [17]). Instead of the usual effective-range approximation

$$k \cot \delta = -1/a + r_0 k^2, \quad (8)$$

it was proposed to use the modified formula of effective-range theory:

$$k \operatorname{ctg} \delta = (1 + k^2/\kappa_0^2)^{-1}(-1/a + C_2 k^2 + C_4 k^4). \quad (9)$$

The modified formula at $C_4 = 0$ was considered in [21]. From (9), one can easily obtain (see [3, 12]) the asymptotic normalization constant in the form

$$C_T^2 = (1 - \kappa_1^2/\kappa_0^2)/(1 - 2C_2\kappa_1 - 3\kappa_1^2/\kappa_0^2 + 4C_4\kappa_1^3). \quad (10)$$

We recall that $\kappa_1 = [(4/3)m(\varepsilon_T - \varepsilon_d)]^{1/2}$.

Simenog *et al.* [4] used the formula

$$k \cot \delta = [a + (c_0 + c'a)k^2]^{-1} \quad (11)$$

$$\times [-1 + (c_1 - c' + c_2a)k^2 + (c_3 + c_4a)k^4],$$

which is analogous to (9) and which involves the a dependence of the parameters of formula (10) in an explicit form:

$$\kappa_0^2 = a/(c_0 + c'a); \quad (12)$$

$$C_2 = (c_1 - c' + c_2a)/a; \quad C_4 = (c_3 + c_4a)/a.$$

It is obvious that, for $a \rightarrow 0$, there are no problems in calculating C_T^2 [it is only necessary to recast Eq. (9) into the form (11) with the coefficients aC_2 and aC_4]. From (12), it follows that the parameters in expressions (9) and (10) cannot be considered to be independent of the doublet scattering length a_2 , an important conclusion indeed. In (12), the first relation is directly associated with the definitions of κ_0^2 and a_2 , because it is obvious that $\kappa_0^2 = 0$ when the scattering length a_2 is zero. Since, in the one-channel problem, the s -wave partial scattering amplitude is given by

$$f(k) = (k \cot \delta - ik)^{-1}, \quad (13)$$

the pole of $k \cot \delta$ corresponds to the zero of $f(k)$.

Formula (11) was obtained in [4] on the basis of the following considerations. From an analysis of the Faddeev equations for the scattering problem in the case of a separable nucleon–nucleon potential, the dependence of the effective range r_0 [see Eq. (8)] on the scattering length a was found in the form of the expansion of the so-called slope parameter of the scattering amplitude ($a^2 r_0/2$) in powers of a :

$$a^2 r_0/2 = c_0 + c_1 a + c_2 a^2. \quad (14)$$

The best approximation of three-body calculations with some separable nucleon–nucleon potentials was obtained in [4] for the following sets of values of the coefficients in Eq. (14) ($\alpha = 0.2316 \text{ fm}^{-1}$ is the wave number corresponding to the deuteron binding energy):

$$c_0 = 1.67/\alpha^3, \quad c_1 = -2.30/\alpha^2, \quad c_2 = 1.05/\alpha; \quad (15)$$

$$c' = 0.230/\alpha^2, \quad c_3 = 0.273/\alpha^4, \quad c_4 = 0.168/\alpha^3. \quad (16)$$

The set of values in (16) was obtained from an analysis of relation (11) between the scattering length a and the wave number κ_1 with allowance for the experimental values of ε_T and a_2 . For further details, the reader is referred to [4].

4. APPLICATION OF THE N/D METHOD TO DESCRIBING THE DOUBLET nd SYSTEM

The scattering amplitude is written as

$$f(k) = N(k^2)/D(k^2), \tag{17}$$

where the numerator $N(k^2)$ has dynamical singularities on the left, negative, semiaxis of the complex plane of energy, while the denominator $D(k^2)$ has only a right unitary cut along the positive real axis of energy (the unitarity of the S matrix is ensured). The zeros of $D(k^2)$ determine the positions of the poles of $f(k)$ that correspond to the bound, virtual, or resonance states of the system. The dispersion integral equations of the N/D method that are known from the literature relate the functions $N(k^2)$ and $D(k^2)$. At the points $k = \pm i\kappa_0$, where $f(k) = 0$, the equality $N(-\kappa_0^2) = 0$ holds, since the function $D(k^2)$ does not have poles in a finite part of the complex plane of k .

A number of studies devoted to calculating the features of the doublet nd system by the N/D method have been reported in the literature. The values of C_T^2 (or G_T^2) for various values of the scattering length a_2 at a fixed experimental value of κ_T were presented in [9, 10]. The strategies adopted in these two studies are close—the discontinuity of the scattering amplitude on the left-hand cut is determined there from the Feynman diagram corresponding to one-proton exchange in nd scattering. Like the potential model, the N/D method involves adjustable parameters. For these, Safronov [10] took ε_T and G_T^2 and calculated a_2 , while Girard and Fuda [9] took ε_T and a_2 and calculated C_T^2 . It seems preferable to choose a_2 for an adjustable parameter, since the doublet nd scattering length a_2 was determined from experimental data more reliably than G_T^2 or C_T^2 . It is well known that the nuclear vertex constant G^2 and the asymptotic normalization factor C are related by the equation (see, for example, [5]; $\nu \equiv T^*$)

$$(G_{T,\nu})^2 = 3\pi(3/2)^2(\hbar/mc)^2\kappa_{1,2}(C_{T,\nu})^2. \tag{18}$$

Baryshnikov [12] considered a simple two-pole model,

$$N(k^2) = \frac{\lambda_1}{k^2 + \gamma_1^2} + \frac{\lambda_2}{k^2 + \gamma_2^2}, \tag{19}$$

where the set of equations of the N/D method can be solved analytically. The resulting expression for the function $D(k^2)$ is

$$D(k^2) = 1 - \frac{\lambda_1}{\gamma_1 - ik} - \frac{\lambda_2}{\gamma_2 - ik}. \tag{20}$$

It is remarkable that the model based on Eqs. (19) and (20) leads to expression (10) for C_T^2 . The scattering amplitude $f(k)$ involves four parameters, which can be found by specifying the values of four physical

quantities. For example, one can specify κ_1, κ_2 (wave numbers for the triton and the virtual triton), and the position $i\kappa_0$ of the zero of $f(k)$ from experiments (or from a version of Faddeev calculations that yields results that are close to experimental data) and obtain the dependence of the parameters $\lambda_1, \lambda_2, \gamma_1$, and γ_2 on a_2 by solving the set of equations

$$\begin{aligned} f(0) &= -a_2; & N(-\kappa_0^2) &= 0; \\ D(-\kappa_1^2) &= 0; & D(-\kappa_2^2) &= 0 \end{aligned} \tag{21}$$

with allowance for relations (17), (19), and (20). At a preset value of a_2 , one can then calculate the coefficients C_2 and C_4 in expression (9) and find $C_T^2(a_2\kappa_1)$ with the aid of Eq. (10). In [12], it was found that the quantities κ_0^2, a_2, C_2 , and C_4 can be analytically expressed in terms of the parameters $\lambda_1, \lambda_2, \gamma_1$, and γ_2 as

$$\begin{aligned} a_2 &= d/[\gamma_1\gamma_2(\lambda_1\gamma_2 + \lambda_2\gamma_1 - \gamma_1\gamma_2)]; \\ \kappa_0^2 &= (\lambda_1 + \lambda_2)/d; \end{aligned} \tag{22}$$

$$C_2 = [\gamma_1^2 + \gamma_2^2 - \lambda_1\gamma_1 - \lambda_2\gamma_2]/d; \quad C_4 = 1/d,$$

where $d = \lambda_1\gamma_2^2 + \lambda_2\gamma_1^2$.

5. RESULTS OF THE CALCULATIONS

5.1. Two-Body Potential Model

For the sets of parameters from Table 1, which were fitted to the experimental values of ε_T and a_2 , Fig. 1 displays all the potentials being discussed. The function $rV(r)$, which is finite at the origin of coordinates, considered here for the convenience of comparison. We can clearly see a sharp distinction between the potential (2), on one hand, and the group of potentials that feature no oscillations and which are similar to one another within this group, on the other hand. For this potential, the values obtained in [7] for the parameters R and M are close to the parameter values quoted in [2]. Table 1 indicates the position of the closest singularity on the energy scale [$E_1 = -(3/4)\kappa_1^2/m$]. For the position of the dynamical singularity, the two-body model employing the Yukawa potential yields a result that is close to the singularity of this diagram. In the case of the Hulthén potential [$\nu = 0$ in Eq. (7)], this singularity is a spurious pole; on the energy scale, its position is twice as far as that for the Yukawa potential. As to the case of the potential (2), the singularity is one order of magnitude closer to the physical region. So strong a distinction is caused by the concerted effect of two factors: a distinction of the exponent of the radius in the denominator ($\nu = 2$) and the presence of an oscillating factor in the potential (2). Both these factors reduce the attracting properties of the potential, but this is compensated by an increase in its radius (M) and its depth (V_0). For the potential (4),

Table 1. Parameters of the potentials (1)–(4), adjustable quantities, and position (E_1) of the closest dynamical singularity of the scattering amplitude

Parameter	Potential			
	Hulthén (1)	Yukawa (3)	Our study, (4)	Tomio <i>et al.</i> (2)
V_0 , MeV	22.11	17.95	11.38	40.50
$M = 1/\mu$, fm	1.976	2.73	5.012	6.64
R , fm	–	–	1.432	1.7565
$\varepsilon_T - \varepsilon_d$, MeV	6.26	6.26	6.256	6.260
a_2 , fm	0.65	0.65	0.651	0.650
$-E_1$, MeV	2.00	1.04	0.311	0.177

Note: The parameters that we refined in [7] are presented for the potential of Tomio *et al.* and used in the calculations. The values of V_0 and M for the Yukawa potential were obtained in the calculations performed with a higher precision (by making $N = 400$ steps in evaluating relevant integrals) and are somewhat different from the parameters presented previously in [3, 7]. In Table 3 of [7], it is necessary to interchange the values of E_1 that were obtained for the Yukawa and the Hulthén potential. The Feynman diagram for the one-proton exchange has a singularity at $E_1 = -0.738$ MeV.

the dynamical singularity is closer to the singularity of the Feynman diagram being discussed than for the potential (2) (see Table 1).

For the potentials (1)–(4) with the parameters set to the values from Table 1, the calculated features of the nd system are quoted in Table 2. The value of the vertex constant G_T^2 for the potential (2) is close to the result for the Hulthén potential and the

result produced by generalized effective-range theory ($C_4 \neq 0$). However, the value of $E_0 = 0.063$ MeV, which specifies the position ($-E_0$) of the pole of the function $k \cot \delta$ for the potential (2) at the experimental value of $a\kappa_1$, is strongly underestimated in relation to the corresponding results for the Hulthén and the Yukawa potential as well as in relation to the “experimental” value of $E_0 = 0.15$ MeV [4]. For the potential (4), the resulting value of $E_0 = 0.125$ MeV is in fairly good agreement with experimental data.

The value of the potential radius ($M = 1/\mu$) is of crucial importance for correctly describing the position of the virtual triton level. The symmetry theorem [16] for bound and virtual states imposes a constraint (see [7]) on the position of the virtual level: $\kappa_\nu \leq \mu/2$ [$\cong 0.075$ and 0.10 fm $^{-1}$ for the potentials (2) and (4), respectively]. On the energy scale, we accordingly have $B_\nu \leq 0.176$ MeV for the potential (2); this is approximately one-third as large as the well-known estimate $B_\nu \cong 0.5$ MeV, which was obtained both from experimental data and from calculations based on Faddeev equations (see, for example, [9, 14, 18]). For the potential (4), we have $B_\nu \leq 0.31$ MeV, which is approximately two times lower than the required value. From the “experimental” value of $B_\nu \cong 0.5$ MeV, it follows that the potential radius is constrained as $M \leq 3.7$ fm. In view of this, we do not consider the virtual triton level for the potentials (2) and (4), in which case the values of M go beyond the above limit. The parameters of the potentials (1), (3), and (4) do not differ very strongly, monotonically changing with the exponent ν in the asymptotic expression (7). The difference in the behavior of the potentials (1), (3), and (4) can easily be explained: an increase in the exponent ν in expression (7) leads to a faster decay of the potential at large distances,

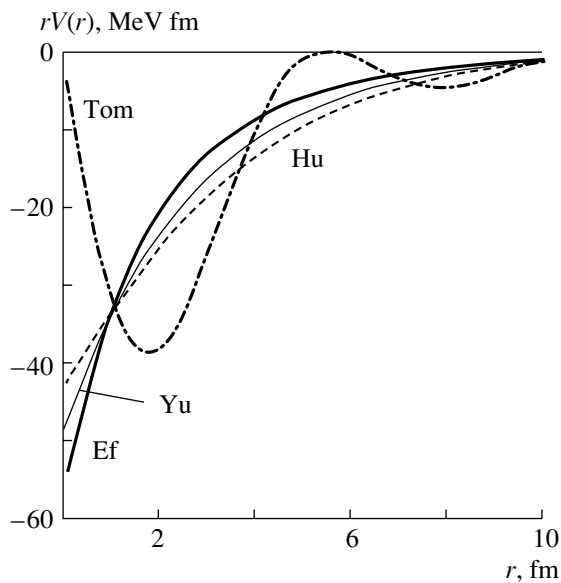


Fig. 1. Comparison of the potentials $V(r)$ (1)–(4) at the parameter values (see Table 1) fitted to the experimental values of $\varepsilon_T = 8.48$ MeV and $a_2 = 0.65$ fm. The thick solid curve (Ef), the thin solid curve (Yu), the dashed curve (Hu), and the dash-dotted curve displaying oscillations (Tom) represent, respectively, the potential (4), the Yukawa potential (3), the Hulthén potential (1), and the potential (2) of Tomio *et al.*

Table 2. Features of the doublet nd system

Model, reference	Physical quantities			
	$C_T^2 (G_T^2, \text{fm})$	B_ν, MeV	$-C_\nu^2 (-G_\nu^2, \text{fm})$	E_0, MeV
Effective-range theory:				
[4, 3], $C_4 \neq 0$	3.50(1.48)	0.530	0.017(0.007)	0.150
[21], $C_4 = 0$	0.77(0.33)	0.482	0.019(0.008)	0.047
N/D method:				
[9]	3.31(1.39)	0.48	0.051(0.006)	–
[10]	3.50(1.48)	0.48	0.051(0.006)	–
[12]*	3.66(1.54)	0.53*	0.052(0.006)	0.15*
Potential:				
Hulthén [3, 5], (1)	3.50(1.48)	0.75	0.043(0.018)	0.24**
Yukawa [3], (3)	2.74(1.16)	0.61	0.059(0.025)	0.18
Tomio <i>et al.</i> [2], (2)	3.48(1.47)	0.176	–	0.063
Our study, (4)	2.17(0.91)	≤ 0.31	–	0.125

* The calculations were performed by formulas (19)–(22) at the experimental values of ε_T , ε_{T^*} , and a_2 for $\kappa_0^2 = 4.737 \times 10^{-3} \text{fm}^{-2}$ (the value of κ_0^2 was borrowed from [4]) (see main body of the text).

but this is compensated by a moderate increase in the potential depth. From Table 2, it is obvious that within the group of potentials that is being presently discussed, the dependence of C_T^2 on ν is quite natural: the asymptotic normalization constant C_T^2 decreases monotonically with increasing ν .

The trajectories for the bound and for the virtual level, as well as for the pole of $k \cot \delta$, are displayed in Fig. 2 in the form of the dependence of the corresponding scaling quantities in (5) on the potential strength. The quantity $\rho = \sqrt{g/g_{\text{cr}}}$, where $g = (4/3)mV_0M^2$ and g_{cr} is the value of g at which the ground state becomes bound [$g_{\text{cr}} = 1.422$ for the potential (2) and 4.038 for the potential (4)], was taken for the argument. In order to avoid encumbering the figure, the results of the calculations for the aforementioned trajectories, as well as for the function $a\kappa_1(\rho)$, are displayed only for two potentials [those that are given by (2) and (4)]. Here, we are interested in a comparison of the results for the potentials (2) and (4), which have a Faddeev-like asymptotic form. The results for other potentials are described elsewhere [3, 7]. They have the same qualitative character as those shown in Fig. 2. One can notice only one distinction: for the potentials (2) and (4), the ρ dependence of κ_1M is close to a linear one; as to the Yukawa and the Hulthén potential, there is a linear dependence for them between κ_1M and g , which is approximate for the former and exact for the latter (see [1, 3]). For the potentials (2) and (4), the dependences of κ_1M

on ρ are rather close to each other. As a matter of fact, the distinctions for the quantities $a\kappa_1$ and κ_0/μ amount to a renormalization of the scale of the argument ρ . For all of the potentials considered here, the trajectories of the pole of $k \cot \delta$ [zero of $f(k)$] have a similar character: they intersect the abscissa (zero-momentum axis) at a right angle (that is, the derivative is infinite at the point of intersection) and quickly move away from the physical region. This is one of the reasons why it is difficult to discover experimentally the pole of $k \cot \delta$. As the interaction strength g is reduced, the trajectory of κ_0/μ approaches asymptotically the line of the closest dynamical singularity of the partial-wave scattering amplitude.

The results of the calculations for the function $C_T^2(a_2\kappa_1)$ are shown in Fig. 3. The graphs for the two-body model employing the potentials (1)–(4) are qualitatively similar. From Fig. 3 and from Table 2, it can be seen that the asymptotic normalization constant for the triton decreases with increasing ν . This is the point where the effect of long-range interaction manifests itself in the two-body potential model for the doublet nd system. From a comparison of the results obtained for the quantity C_T^2 by using the potentials (2) and (4), it follows, in addition, that, for the physical system being considered, the behavior at the origin of coordinates is even more important than the asymptotic behavior of the potential. This means that the doublet nd system is indeed far from the situation where the Efimov effect must occur.

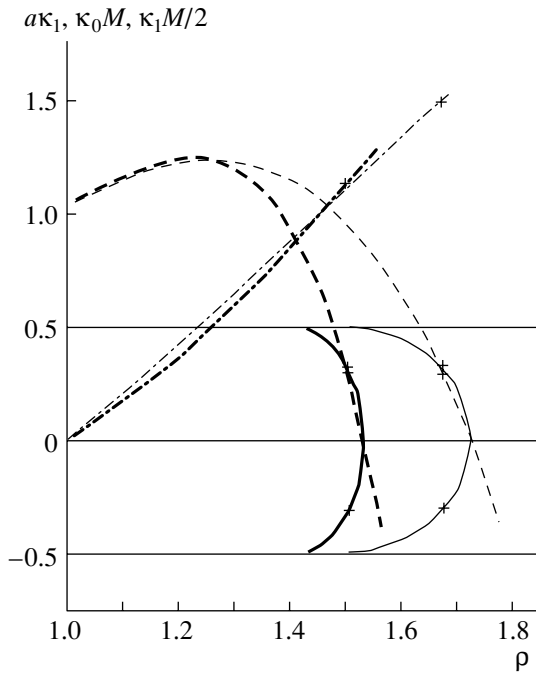


Fig. 2. Scaling quantities $a\kappa_1$, κ_0M , and $\kappa_1M/2$ according to the calculations with the potential (2) from the study of Tomio *et al.* [2] and with the potential (4) (our present study) versus the scaling parameter $\rho = \sqrt{g/g_{cr}}$. The crosses indicate those points on the curves that correspond to the experimental value of $a\kappa_1 = 0.292$ for the doublet nd system. The thick and the thin curves represent the result obtained for, respectively, the potential (4) and the potential (2): (dash-dotted curves) $\kappa_1M/2$, (dashed curves) $a\kappa_1$, and (solid curves) κ_0M . Also shown in the figure are the abscissa ($kM = 0$) and the lines of dynamical singularities ($kM = \pm i0.5$).

Unfortunately, the uncertainties in currently available experimental data on the nuclear vertex constant G_T^2 (and, accordingly, on C_T^2) are so great that it is impossible at present to make a definitive choice between the potentials considered here. The scatter of the C_T^2 values calculated on the basis of the two-body model with the different potentials and displayed in Fig. 3 is commensurate with the uncertainty in the analysis of experimental data on G_T^2 and, in particular, with the estimate presented for the relevant error in [23] ($C_T^2 = 2.78 \pm 1.09$).

5.2. Generalized Effective-Range Theory

Table 2 also presents the results obtained from an analysis of experimental data on the doublet nd system [4] according to formula (11) of effective-range theory for the function $k \cot \delta$, which has a pole at $k = \pm i\kappa_0$. It should be emphasized that, in effective-range theory, G_T^2 takes sharply different

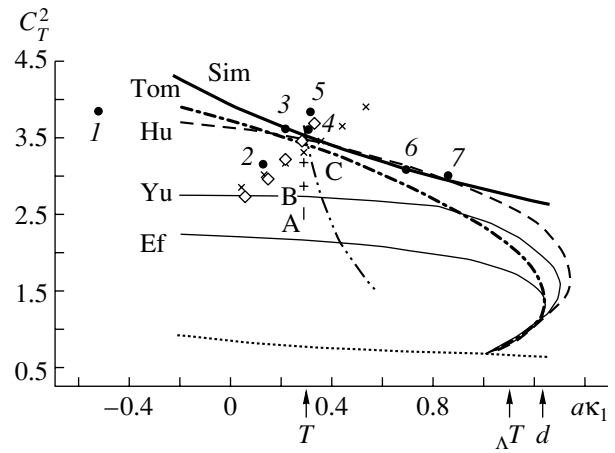


Fig. 3. Asymptotic normalization factor C_T^2 for the triton radial wave function (ground bound state) as a function of the product $a_2\kappa_1$ according to calculations within various approaches and experimental data derived from an analysis of nuclear reactions. The results derived on the basis of the two-body model are shown by the dashed curve (Hu) for the Hulthén potential (1), the solid curve (Yu) for the Yukawa potential (3), the dash-dotted curve (Tom) for the potential (2), and the solid curve (Ef) for the potential (4). Closed circles represent the results of Faddeev calculations (for references, see [1]) with the (1) Yamaguchi separable, (2) quark-bag-method, (3, 4) square-well, (5) Malfliet–Tjon, and (6, 7) soft-core Reid nucleon–nucleon potentials. The results produced by effective-range theory are depicted by the thick solid curve (Sim), taken from [4], and the dotted curve, taken from [11, 21]. The results derived by the N/D method are illustrated by the crosses (\times) [9]; diamonds (\diamond) [10]; and the dash-and-double-dot curve, which was computed with allowance for the dependence of κ_0^2 on a_2 (see main body of the text and [12]). The experimental data are represented by the vertical straight-line segment (\uparrow) A [22] and by the straight crosses ($+$) B [23] and C [24]. The arrows indicate the values of $a\kappa_1$ for the triton T ($= 0.292$), the hypertriton ${}_{\Lambda}T$ ($= 1.088$), and the deuteron d ($= 1.256$).

values at $C_4 = 0$ and at $C_4 \neq 0$. It is worth noting that the position of the dynamical singularity of $f(k)$ in generalized effective-range theory ($E_1 = -1.02$ MeV) [4] is close to the position of the singularity of $f(k)$ for the case where the calculation is based on the one-nucleon-exchange Feynman diagram ($E_1 = -0.738$ MeV).

The function $C_T^2(a_2\kappa_1)$ calculated by formulas (10) and (12) with the constants set to values presented in (15) and (16) is displayed in Fig. 3. It can be seen that the corresponding curve (Sim), which descends smoothly, complies well with the results of Faddeev calculations and with the graphs corresponding to the potentials (1) and (2).

5.3. N/D Method

That the character of the $a\kappa_1$ dependence of C_T^2 within the versions of the N/D method that were considered in [9, 10] is sharply different from the entire body of other results (see Fig. 3) is, we believe, the most interesting result obtained in the present study, because it is quite unexpected. This result seems all the more strange if we consider that the physical concepts underlying the two-body potential model and the N/D method (namely, the importance of the one-proton-exchange Feynman diagram) are close. The corresponding functions $C_T^2(a\kappa_1)$ are qualitatively similar—they grow sharply with increasing $a\kappa_1$, yielding close results at the experimental value of $a\kappa_1$, which are in good agreement with the result presented in [4] for the triton. Since we did not reproduce the calculations from [9, 10], the latter circumstance is of paramount importance for being confident that the discrepancy discovered here does indeed occur.

In [11], where the approximate formulas derived within the N/D method correspond to expression (9) at $C_4 = 0$ (this expression is identical to that for $k \cot \delta$ from [21]), it was also pointed out that the value of G_T^2 is strongly underestimated in relation to the results of Faddeev calculations from [9]. According to [11], this means that it is necessary to take into account the three-body cut of the S matrix. In [7], it was indicated that the reason behind this discrepancy is simpler: Adhikari [11] and Adhikari and Torreaõ [21] and did not retain the required number of terms in the expansion of the partial-wave scattering amplitude $f(k)$ (or the function $k \cot \delta$) in powers of k . We have calculated the function $C_T^2(a\kappa_1)$ corresponding to the results from [11, 21]. From Fig. 3, it can be seen that, in contrast to what was obtained in [9, 10], the relevant (dotted) curve has a correct descending character, but it lies overly low because of the small value of C_T^2 for the triton. We recall that, in [11], the analytic formula for $f(k)$ was obtained within the N/D method by using the pole approximation for the discontinuity at the dynamical left-hand cut and that a linear relation between κ_0^2 and a_2 was taken in doing this.

The set of parameters appearing in expressions (19)–(22) that corresponds to the values of $\varepsilon_T = 9.2$ MeV and $a_2 = 0.333$ fm, which were found from Faddeev calculations with a separable potential, is quoted in [12], where it was found, for this case, that $\kappa_0^2 = 2.306 \times 10^{-3} \text{fm}^{-2}$. In the present study, we have found the set of parameters that, at $\kappa_0^2 = 4.737 \times 10^{-3} \text{fm}^{-2}$, corresponds to the experimental values of ε_T , ε_{T^*} , and a_2 . The position of the pole of $k \cot \delta$ [zero of $f(k)$] was taken from [4]. The corresponding

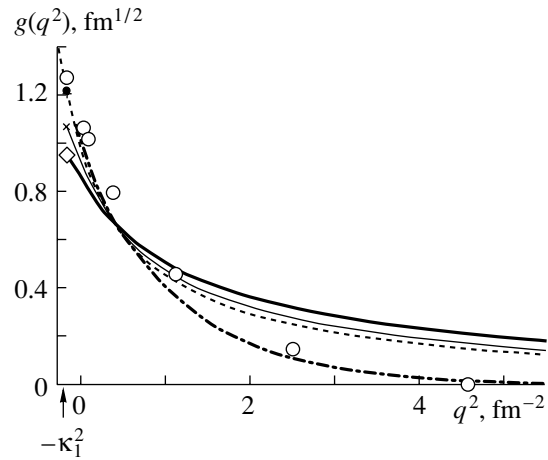


Fig. 4. Calculated nuclear form factor $g(q^2)$ [and the quantity $g(-\kappa_1^2)$] for the $T \rightarrow d + n$ vertex. The calculations on the basis of the two-body model were performed for (dash-dotted curve, +) the potential (2) (Tom) from [2], (dashed curve, •) the Hulthén potential, (thin solid curve, x) the Yukawa potential, and (thick solid curve, ◊) the potential (4). The presentation of the curves corresponds to that in Fig. 1. The results of the Faddeev calculations from [25, 26] with the Malliet–Tjon potential are represented by open circles.

values calculated for C_T^2 are presented in Table 2. Figure 3 also displays the function $C_T^2(a_2\kappa_T)$ computed at the experimental values of κ_T and κ_{T^*} {data on κ_{T^*} can be obtained from Faddeev calculations (see, for example, [9, 14, 18])} for κ_0^2 proportional to the scattering length,

$$\kappa_0^2 = 7.288 \times 10^{-3} a_2. \tag{23}$$

In contrast to the curves that were obtained from the tables presented in [9, 10] and which are displayed in the same figure, this function has a sharply descending character. We note that, if the relevant experimental value is taken instead of the quantity κ_0^2 proportional to the scattering length a_2 , the corresponding function $C_T^2(a_2\kappa_1)$ appears to be sharply growing with increasing $a_2\kappa_1$. In the range of a_2 being considered, the simple dependence in (23) shows virtually no difference from the more complicated function presented in (12) for the parameter values from (15) and (16).

5.4. Nuclear Form Factor for the $T \rightarrow d + n$ Vertex

Figure 4 displays the calculated nuclear form factor $g(q^2)$ for the $T \rightarrow d + n$ vertex. It can be seen that, at low momentum transfers, this function depends only moderately on the choice of potential for the two-body model. The range of its variation does not exceed the scatter of values of the vertex constant $G_T^2 =$

$g(-\kappa_1^2)$. With increasing q^2 , this range shrinks, virtually vanishing in the interval $0.3\text{--}0.5\text{ fm}^{-2}$. As q^2 increases further, the distinctions between the functions corresponding to the different potentials become more pronounced, the relevant curves occurring in the order inverse to their order near the origin. The curve calculated for the potential (2), which involves oscillations, proves to be the closest to the results for the Faddeev calculations from [25, 26] for the Malfliet–Tjon nucleon–nucleon potential (see also [27]), while the curve for the potential (4), which exhibits a Faddeev-like asymptotic behavior without oscillations, is the farthest from it. Obviously, the function $g(q^2)$ is more sensitive to the periphery of the potential at low momentum transfers ($q^2 < 0.3\text{ fm}^{-2}$) and to the short-distance behavior of the potential at high momentum transfers ($q^2 > 0.5\text{ fm}^{-2}$). The observed distinctions between the vertex functions $g(q^2)$ and the constants C_T^2 for the different potentials and the fact that the results for the potential (2) from the study of Tomio *et al.* [2] stand out admit a rather simple explanation. In the potential (2), the attraction is severely reduced in the central region because of oscillations in relation to potentials belonging to the type of screened Coulomb potentials. As a result, the triton radial wave function for this potential is the most peripheral (which corresponds to the greatest value of C_T^2) for the potentials considered in the present study. It can be stated that, upon solving the corresponding Faddeev equations, one arrives at the same character of the structure of the wave function (see Fig. 4). Low momenta, where the proton-exchange Feynman diagram plays an important role, correspond to long distances. Because of the indistinguishability of nucleons, this exchange process does not disturb the original $d + n$ configuration of the bound triton. In a sense, the Faddeev solution proves to be even more peripheral than that in the two-body potential model, since, in this model, one has to introduce an ad hoc reduction of the attraction in the central region in order to obtain the vertex form factor $g(q^2)$ that is consistent with the three-body result. Within the three-body approach, the vertex constants G_T^2 and $G_{T^*}^2$ were computed in a number of publications for some nucleon–nucleon potentials, including local potentials (for the first time, in [25, 26]).

6. CONCLUSION

From a comparison of the results obtained with potentials showing different types of asymptotic behavior, one can draw the conclusion that effects of long-range interaction are quite sizable in the calculations of C_T^2 (or G_T^2) for the virtual decay $T \rightarrow$

$d + n$, but that these effects are less pronounced in the results for the position of the pole of $k \cot \delta$ [zero of $f(k)$]. The quantities C_T^2 and E_0 have been found to decrease upon going over to a correct asymptotic behavior [that which corresponds to $\nu = 2$ in Eq. (7)]. The resulting distinctions between the quantities C_T^2 and G_T^2 are even more pronounced than the distinctions between the potentials (1), (3), and (4) themselves. These quantities undergo still stronger variations upon going over from the screened Coulomb potential (4) to the potential (2), which is finite at the origin of coordinates. It is well known that the residue of the scattering amplitude at the pole corresponding to the bound state (this residue is directly related to the quantities C_T^2 and G_T^2) plays an important role in solving the inverse problem of reconstructing the potential from the phase shifts. In the present study, we have revealed the effect of the behavior of the potential at the coordinate origin and of its asymptotic behavior on low-energy parameters in the direct problem. It would be highly desirable to improve the accuracy in determining the nuclear vertex constant G_T^2 from an analysis of experimental data, because this would provide a firmer basis for choosing between the various potentials in the two-body model for describing the doublet nd system at low energies. This would be of importance for specific applications as well, especially in the theory of direct reactions treated in terms of Feynman diagrams involving the $T \rightarrow d + n$ vertex. Taking into account uncertainties in experimental data on the vertex constant G_T^2 , we can state that, presently, the two-body model employing the Hulthén potential provides a fairly good description of the low-energy properties of the doublet nd system. This model can be used to perform specific calculations in the theory of nuclear reactions, especially as an analytic solution to the problem in the s wave is known. This choice is also supported by results obtained with the aid of Faddeev equations. As can be seen from Fig. 3, the results for C_T^2 that are obtained from Faddeev calculations are largely grouped in the vicinity of the result for the Hulthén potential. In order to assess the applicability of the two-body potential model, one could in principle invoke a comparison with the results of accurate three-body calculations. It would be of interest to analyze, from this point of view, modern three-nucleon calculations yielding correct values for the triton binding energy and the doublet nd scattering length.

A qualitative distinction between the functions $C_T^2(a\kappa_1)$ that we have calculated here with the aid of the tables quoted in [9, 10], where the authors used the N/D method, on one hand, and all other results, on the other hand, is a new and unexpected

result of the present study. The latter include the function $C_T^2(a\kappa_1)$ found with the aid of the formulas of generalized effective-range theory [4] and the results obtained from calculations on the basis of Faddeev equations and displayed in Fig. 3. For the possible reason behind this discrepancy, we can indicate the dependence of the parameters of the N/D method, which are used in a fit to experimental data, on the doublet nd scattering length a_2 . In all probability, the correct a_2 dependence of the coefficients in the expansion of the function $k \cot \delta$ in powers of k^2 was obtained in [4]. We note that the function $C_T^2(a\kappa_1)$ computed by using the formula for $k \cot \delta$ from [11, 21] also has a correct descending character (see Fig. 3), but that it is greatly underestimated in absolute value. In the immediate vicinity of the experimental value of $a\kappa_1$, the asymptotic normalization constants C_T^2 obtained from calculations on the basis of Faddeev equations and shown in Fig. 3 also grow with increasing $a\kappa_1$, as the results from [9, 10] do.

One of the conclusions drawn in the present study is that, in applying the N/D method, one should be very careful in analyzing correlations between the low-energy features of the doublet nd system, since the parameters of the model can be dependent on the scattering length a_2 .

Finally, a comparison of the results obtained by calculating the form factor $g(q^2)$ for the $T \rightarrow d + n$ vertex within the two-body potential model with the results of Faddeev calculations indicates that the structure of the triton wave function has a peripheral character and that the $(d + n)$ cluster configuration plays an important role in the triton.

REFERENCES

1. N. M. Petrov, *Yad. Fiz.* **48**, 50 (1988) [*Sov. J. Nucl. Phys.* **48**, 31 (1988)].
2. L. Tomio, A. Delfino, and S. K. Adhikari, *Phys. Rev. C* **35**, 441 (1987).
3. Yu. V. Orlov, Yu. P. Orevkov, and L. I. Nikitina, *Izv. Akad. Nauk, Ser. Fiz.* **60** (11), 152 (1996).
4. I. V. Simenog, A. I. Sitnichenko, and D. V. Shapoval, *Yad. Fiz.* **45**, 60 (1987) [*Sov. J. Nucl. Phys.* **45**, 37 (1987)].
5. Yu. V. Orlov, N. M. Petrov, and G. N. Teneva, *Yad. Fiz.* **55**, 38 (1992) [*Sov. J. Nucl. Phys.* **55**, 23 (1992)].

6. V. Efimov, *Nucl. Phys. A* **362**, 45 (1981).
7. Yu. V. Orlov, Yu. P. Orevkov, and L. I. Nikitina, *Yad. Fiz.* **63**, 394 (2000) [*Phys. At. Nucl.* **63**, 328 (2000)].
8. A. C. Phillips, *Nucl. Phys. A* **107**, 209 (1968).
9. B. A. Girard and M. G. Fuda, *Phys. Rev. C* **19**, 579 (1979); **19**, 583 (1979).
10. A. N. Safronov, *Yad. Fiz.* **50**, 951 (1989) [*Sov. J. Nucl. Phys.* **50**, 593 (1989)].
11. S. K. Adhikari, *Phys. Rev. C* **30**, 31 (1984).
12. A. G. Baryshnikov, Candidate's Dissertation in Physics and Mathematics (Nauchn. Issled. Inst. Yad. Fiz. Mosk. Gos. Univ., Moscow, 1975).
13. R. G. Newton, *Scattering Theory of Waves and Particles* (McGraw-Hill, New York, 1966; Mir, Moscow, 1969).
14. Yu. V. Orlov and V. V. Turovtsev, *Zh. Éksp. Teor. Fiz.* **86**, 1600 (1984) [*Sov. Phys. JETP* **59**, 934 (1984)].
15. V. Efimov, *Yad. Fiz.* **12**, 1080 (1970) [*Sov. J. Nucl. Phys.* **12**, 589 (1971)].
16. Yu. V. Orlov, *Phys. Lett. B* **163B**, 25 (1985).
17. Yu. V. Orlov and L. I. Nikitina, *Yad. Fiz.* **61**, 833 (1998) [*Phys. At. Nucl.* **61**, 750 (1998)].
18. K. Moller and Yu. V. Orlov, *Fiz. Élem. Chastits At. Yadra* **20**, 1341 (1989) [*Sov. J. Part. Nucl.* **20**, 569 (1989)].
19. L. M. Delves, *Phys. Rev.* **118**, 1318 (1960).
20. W. T. H. Van Oers and J. D. Seagrave, *Phys. Lett. B* **24B**, 562 (1967).
21. S. K. Adhikari and J. R. A. Torreão, *Phys. Lett. B* **132B**, 257 (1983).
22. L. D. Blokhintsev, I. Borbely, and É. I. Dolinskii, *Fiz. Élem. Chastits At. Yadra* **8**, 1189 (1977) [*Sov. J. Part. Nucl.* **8**, 485 (1977)].
23. A. I. Sattarov, M. K. Ubajdullaeva, and R. Ya. Yarmukhamedov, *Yad. Fiz.* **60**, 1221 (1997) [*Phys. At. Nucl.* **60**, 1096 (1997)].
24. L. D. Blokhintsev, A. M. Mukhamedzhanov, and A. N. Safronov, *Fiz. Élem. Chastits At. Yadra* **15**, 1296 (1984) [*Sov. J. Part. Nucl.* **15**, 580 (1984)].
25. V. B. Belyaev, B. F. Irgaziev, and Yu. V. Orlov, Preprint No. R4-8158, OIYaI (Joint Inst. for Nuclear Research, Dubna, 1974).
26. V. B. Belyaev, B. F. Irgaziev, and Yu. V. Orlov, *Yad. Fiz.* **24**, 44 (1976) [*Sov. J. Nucl. Phys.* **24**, 22 (1976)].
27. Yu. V. Orlov and N. M. Petrov, in *Microscopic Methods in Theory of Few-Body Systems* (Kalinin, 1988), p. 16.

Translated by A. Isaakyan

ELEMENTARY PARTICLES AND FIELDS
Theory

Monochromatic Neutrinos from the Annihilation of Fourth-Generation Massive Stable Neutrinos in the Sun and in the Earth

K. M. Belotsky^{1),2),3)}, M. Yu. Khlopov^{1),2),3)}, and K. I. Shibaev^{1),3)}

Received June 21, 2000; in final form, October 20, 2000

Abstract—The accumulation of relic fourth-generation heavy neutrinos (of mass 50 GeV) in the Earth and the Sun, which is followed by their annihilation, is considered. The most conservative estimates of the fluxes of monochromatic electron, muon, and tau neutrinos and antineutrinos of energy 50 GeV from the annihilation of heavy neutrinos are $4.1 \times 10^{-6} \text{ cm}^{-2} \text{ s}^{-1}$ from Earth's core and $1.1 \times 10^{-7} \text{ cm}^{-2} \text{ s}^{-1}$ from Sun's core, whence it follows that an analysis of data from underground neutrino observatories may furnish additional information about the existence of fourth-generation neutrinos. It is shown that, because of kinetic equilibrium between the arrival of cosmic neutrinos and their annihilation, the existence of new $U(1)$ gauge interaction of fourth-generation neutrinos has virtually no effect on the estimates of the annihilation fluxes of electron, muon, and tau neutrinos. © 2002 MAIK "Nauka/Interperiodica".

1. INTRODUCTION

Searches for the fourth fermion generation are among the hottest problems of high-energy physics. The most important tools for such searches are provided not only by accelerator experiments but also by cosmological and astrophysical data, where one seeks, in particular, manifestations of the new generation with special emphasis on the existence of a new neutrino (ν_4) as the lightest and, possibly, stable weakly interacting neutral particle of fourth generation. It has been known for a long time [1] that a neutrino of mass about a few GeV may be a candidate for a particle providing cold dark matter in the Universe. The up-to-date experimental constraint on the mass of the new neutrino follows from experimental data on the Z -boson width: the ν_4 mass must be greater than $m_Z/2 \approx 45$ GeV, where m_Z is the Z -boson mass. An analysis of virtual processes featuring fourth-generation particles leads to results that are compatible with the mass of the new neutrino in the region around 50 GeV [2]. Recent results from an underground experiment devoted to a direct search for a weakly interacting massive particle (WIMP) at the DAMA facility do not rule out a WIMP of mass around 50 GeV, which is consistent with the accelerator constraint on the mass of the new

neutrino. If neutrinos of this mass do indeed exist, the pairs of such neutrinos and their antineutrinos must have been in equilibrium in the early Universe and, upon the quenching of their concentration, must be preserved in the present-day Universe in the form of a relic background whose mean relative density is $\Omega \sim 10^{-4}$ [3]. It follows that relic fourth-generation neutrinos cannot dominate dark matter; this implies that a cosmological test of their existence requires considering subtler astrophysical effects whose analysis must be performed under the assumption that there is hidden mass of a different origin. The possible manifestations of a new heavy stable neutrino, should it exist, were studied in experiments at LEP [4, 5] and on the basis of astrophysical observations [4, 6, 7]. Just like any other form of nonrelativistic dark matter, heavy neutrinos must be concentrated in galaxies. Under the assumption of charge symmetry, galaxies must contain an equal number of their antineutrinos, so that there occur effects associated with neutrino–antineutrino annihilation. It was shown in [7] that neutrino–antineutrino annihilation in the halo of the Milky Way Galaxy may account for the galactic diffuse gamma background, which was recently discovered by the EGRET collaboration. An attempt at explaining this gamma background in terms of the annihilation of neutralinos that are predicted in supersymmetric models and which are known to be popular candidates for WIMP runs into difficulties associated with the Majorana nature of the neutralino. On the Earth, fluxes of products originating from the annihilation of heavy neutrinos were recorded in [4, 5]. In this connection, it should be mentioned that the fluxes of positrons, antiprotons,

¹⁾Moscow State Engineering Physics Institute (Technical University), Kashirskoe sh. 31, Moscow, 115409 Russia.

²⁾Keldysh Institute for Applied Mathematics, Russian Academy of Sciences, Miusskaya pl. 4, Moscow, 125047 Russia.

³⁾Cosmion Centre for Cosmoparticle Physics, Miusskaya pl. 4, Moscow, 125047 Russia.

and photons suggest the most sensitive experimental test of the existence of ν_4 neutrinos in the Milky Way Galaxy. It is also of interest to consider other possible astrophysical effects associated with the existence of fourth-generation neutrinos.

Many authors (see, for example, [8–10]) consider the accumulation of WIMPs (neutralinos, neutrinos) in the Earth and in the Sun and their subsequent annihilation producing fluxes that are formed by neutrinos of conventional flavors and which can be recorded by underground neutrino detectors. In the present study, we analyze similar processes for the specific example of fourth-generation neutrinos of mass 50 GeV. We briefly consider the possibility that the heavy neutrino features a new type of interaction (a property that may be peculiar to the fourth generation as a whole). In realistic versions of superstring theory, an additional interaction (or even a few of them) appears in the low-energy limit. We also assess the impact of this new interaction on effects associated with the annihilation of heavy neutrinos.

2. CAPTURE OF GALACTIC MASSIVE NEUTRINOS IN THE EARTH AND IN THE SUN

The concentration of massive neutrinos (which are henceforth referred to as merely neutrinos) that are not disturbed by the gravitational fields of the Earth and the Sun (for the sake of generality, they will be called a gravitating body) will be estimated here under the assumption that the distribution of the neutrino concentration in the Milky Way Galaxy has the form

$$n = \xi(r)\langle n \rangle = \frac{\kappa}{1 + r^2/r_0^2}\langle n \rangle,$$

where $\langle n \rangle \approx 10^{-11} \frac{\Omega}{10^{-4}} \text{ cm}^{-3}$ is the mean concentration of neutrinos in the Universe at the Hubble constant value of $h = 0.65$, $\kappa = \frac{n(r=0)}{\langle n \rangle}$, r is the distance from the center of the galaxy, and r_0 is the characteristic range of the distribution. It was shown in [11] that, for weakly interacting nonrelativistic matter, the ratio κ of the concentration of neutrinos at the center of the Milky Way Galaxy to their mean concentration in the Universe is related to the analogous ratio of concentrations for baryons (B) and dark matter (DM), which contains antineutrinos as well (however, their weight is small there):

$$\kappa \equiv \frac{n(r=0)}{\langle n \rangle} = \left(\frac{\rho_B(r=0)}{\langle \rho_{B+DM} \rangle} \right)^{3/4} \approx 10^6.$$

We set r_0 to 1.2 kpc and r to $r_C = 8.5$ kpc for the Solar System; for the neutrino concentration undisturbed by the gravitational fields of the Sun and the

Earth (this will be indicated by labeling the relevant quantities with the subscript ∞), we obtain

$$n_\infty = \xi_C \langle n \rangle \approx 2 \times 10^4 \langle n \rangle \approx 2 \times 10^{-7} \text{ cm}^{-3}.$$

We set the mean velocity of neutrinos in the Milky Way Galaxy to $v_\infty = 300$ km/s, the corresponding kinetic energy of neutrinos being $T_\infty = 25$ keV. It can be shown that, for a neutrino of fixed energy in a potential field, the following relation holds:

$$n/v = \text{const.} \tag{1}$$

The number of neutrinos captured by the gravitating body per unit time is

$$\dot{N}_{\text{capt}} = \sum_A \int n \sigma v w_1 n_A dV, \tag{2}$$

where n and n_A are the concentrations of, respectively, incident neutrinos and the nuclei of Earth's or Sun's matter⁴⁾ [summation over these nuclei is performed in (2), and the subscript ν on the neutrino concentration is omitted there]; σ is the cross section for neutrino–nucleus interaction; v is the neutrino velocity;⁵⁾ w_1 is the probability that, in one collision event, a neutrino loses an amount of energy such that it can be captured, after this event, by the gravitational field of the gravitating body; and integration is performed over the volume of the gravitating body. The concentration and the velocity of incident neutrinos are assumed to be disturbed by the gravitational field of the gravitating body [in accordance with (1)], but the change in these features of the neutrino flux because of its interaction with matter is disregarded. The latter is obviously justified for weakly interacting particles, and the validity of this approximation will be demonstrated below. With the aid of Eq. (1), expression (2) can be recast into the form

$$\dot{N}_{\text{capt}} = \sum_A \frac{n_\infty}{v_\infty} \int \sigma v^2 w_1 n_A dV. \tag{3}$$

The distribution of density in Earth's matter will be assumed to be uniform; other, more realistic, distributions complicate the situation considerably, but this changes the result only slightly. For a uniform distribution, the escape velocity as a function of the dimensionless radius $x = R/R_0$, where R_0 is the radius of the gravitating body, within the Earth has the form

$$v_{\text{escE}}^2(x) = v_{\text{escE}}^2 \frac{3 - x^2}{2}, \tag{4}$$

⁴⁾The interaction of neutrinos with electrons is much weaker; therefore, we consider only their interaction with nuclei.

⁵⁾In the calculations, we use the system of units where $\hbar = c = 1$. For the velocities denoted by v , we employ dimensional units (km/s, cm/s).

where $v_{\text{escE}} \equiv v_{\text{escE}}(1) = 11.2$ km/s is the escape velocity at Earth's surface (second cosmic velocity). Obviously, the gravitational field of the Earth has virtually no effect either on the neutrino concentration or on the neutrino velocity; it plays an important role only in determining the factor w_1 . The gravitational field of the Sun near the Earth is also immaterial. In the present study, we disregard the possibility indicated in [10], where it is argued that there can exist a "slow" neutrino component. According to [10], this population of neutrinos that rotate about the Sun along orbits that intersect Earth's orbit arises as the result of "weak" collisions between background neutrinos and nuclei in the Sun. This population can contribute significantly to processes of neutrino accumulation in the Earth owing to a large value of the factor w_1 ; the reason for the latter is that the speed of these neutrinos (which is about the orbital speed of the Earth) is much less than the speed of neutrinos in the Milky Way Galaxy. The role of the slow component in the effects of ν_4 accumulation and annihilation in the Earth will be considered elsewhere.

The radial distribution of the solar-matter density (we denote by x the relevant radial coordinate) as obtained on the basis of the standard solar model [12] can be approximated by the function

$$\rho_C(x) = 148 (1 - x^2) \exp\left(-\frac{9.04x^2}{0.17 + x^{1.52}}\right) \text{ (g/cm}^3\text{)}. \quad (5)$$

The resulting dependence for the squared velocity $v_{\text{escS}}^2(x)$ is closely approximated as

$$v_{\text{escS}}^2(x) = v_{\text{escS}}^2 \left(4.011 \frac{1 - x^{1.868}}{1 + 8.05x^{1.868}} + 1\right), \quad (6)$$

where $v_{\text{escS}} \equiv v_{\text{escS}}(1) = 618$ km/s. We will now present the values of the escape and the total (maximal) velocity for a neutrino at the center of the Sun and of the corresponding kinetic energies: $v_{\text{escS}}(0) = 1383$ km/s, $v_S(0) = \sqrt{v_\infty^2 + v_{\text{escS}}^2(0)} = 1416$ km/s, $T_{\text{escS}}(0) = 531$ keV, and $T_S(0) = T_\infty + T_{\text{escS}}(0) = 556$ keV.

Let us now consider the cross sections for massive-neutrino interactions with nuclei.

The wavelength of neutrinos having a mass of 50 GeV and velocities in the range 300–1416 km/s takes values in the range $\lambda = (3.9\text{--}0.84) \times 10^{-13}$ cm, which are commensurate with nuclear sizes. Therefore, it is necessary to consider that nuclei are nonpointlike particles. For all nuclei whose numbers in the Sun and in the Earth are significant, the lowest excitation energies, which are greater than 0.8 MeV, exceed the neutrino kinetic energies, which are less than 0.56 MeV. In view of this, neutrino–nucleus

scattering will be considered here as an elastic process occurring on a nucleus as a discrete unit. In this case, the amplitude for neutrino (antineutrino) scattering on a nucleus is determined by the coherent contribution of the isoscalar vector neutral weak current and, in the nonrelativistic limit, is given by [13]

$$M = \frac{G_F}{2\sqrt{2}} F_V F(q^2).$$

Here, G_F is the Fermi constant; $F_V = 2Z - A - 4Z \times \sin^2 \theta_W = -(A - 1.074Z)$, where A and Z are, respectively, the atomic number and the charge of the nucleus involved and θ_W is the Weinberg angle; and $F(q^2)$ is a form factor through which it is considered that the nucleus is nonpointlike. The cross section in question has the form

$$\sigma = \frac{G_F^2 \mu^2}{8\pi} F_V^2 \eta(T) = \sigma_0 \eta(T), \quad (7)$$

where $\mu = m_\nu m_A / (m_\nu + m_A)$ is the reduced mass of the system formed by the neutrino of mass m_ν and the nucleus of mass m_A , while $\eta(T)$ is a factor that takes into account the finite size of the nucleus and which is dependent on the neutrino kinetic energy (velocity). For the proton, we have $F_V \approx 0$, so that its interaction with the neutrino is dominated by the axial weak current. In the nonrelativistic limit, the cross section for proton–neutrino interaction assumes the form

$$\sigma = \frac{G_F^2 \mu^2}{8\pi} (3F_A^2 + F_V^2) \eta(T) = \sigma_0 \eta(T).$$

Both for the proton and for the neutron, we have $F_A \approx 1.25$.

For all nuclei, the q^2 dependence of the form factor will be determined on the basis of the Fermi gas model for nucleons, but this is not quite correct in general for extremely light nuclei. Since the neutrino energies are insufficient for exciting a nucleus, the Fermi gas of nucleons is assumed to be fully degenerate. In this case, we have

$$F(q^2) = 3(\sin y - y \cos y)/y^3, \quad y = qa,$$

where q is the absolute value of the 3-momentum transfer from the neutrino to the nucleus involved. The factor $\eta(T)$ is given by

$$\begin{aligned} \eta &= \frac{9}{4}(-1 + \cos 2y_{\text{max}} - 2y_{\text{max}}^2 \\ &+ 2y_{\text{max}} \sin 2y_{\text{max}} + 2y_{\text{max}}^4)/y_{\text{max}}^6, \\ y_{\text{max}} &= q_{\text{max}} a = 2\mu\beta a \equiv v/v_{\text{nonpoint}}. \end{aligned} \quad (8)$$

In two limiting cases, it becomes

$$\begin{aligned} \eta &\approx 1 \quad \text{for } y_{\text{max}}^2 \ll 1 \quad (\text{or } v^2 \ll v_{\text{nonpoint}}^2), \\ \eta &\approx \frac{9}{2y_{\text{max}}^2} \quad \text{for } y_{\text{max}}^2 \gg 1 \quad (\text{or } v^2 \gg v_{\text{nonpoint}}^2). \end{aligned}$$

In the above expressions, $\beta = v/c$ is the neutrino speed (we everywhere disregard the speed of the nucleus), c being the speed of light, while $v_{\text{nonpoint}} = c/(2\mu a)$ is the characteristic speed above which the nucleus cannot be treated as a pointlike object. The size of the nucleus is $a = 1.25 \text{ fm} \times A^{1/3} = A^{1/3}/(158 \text{ MeV})$.

At this point, we would like to emphasize the important role of heavy nuclei in the capture of massive neutrinos. First, the cross section in question grows sharply with A —specifically, in proportion to A^4 for $m_A \ll m_\nu$ and $v^2 \ll v_{\text{nonpoint}}^2$. Second, it can be shown that, for nuclei of mass around 50 GeV, the probability that a neutrino loses a large amount of energy in a single collision event grows for kinematical reasons; accordingly, the probability w_1 of neutrino capture per collision event becomes higher for these nuclei—the amount of energy that a neutrino must release in order to undergo capture is $T_\infty = 25 \text{ keV}$ in this case. The value of w_1 is determined by the probability distribution with respect to the neutrino kinetic energy transferred to the nucleus involved. The shape of this distribution depends on the extension of the nucleus: it is stepwise in the case of a pointlike nucleus and descends toward high energy transfers (where the finite dimensions of the nucleus has the most pronounced effect). In general, the probability w_1 can be represented in the form

$$w_1 = 1 - \frac{f(y_\infty)}{f(y_{\text{max}})}, \tag{9}$$

where $y_\infty = \sqrt{m_\nu m_A} \beta_\infty a$ and $\beta_\infty = v_\infty/c$. The function $f(y)$ appears in the expression for η [see Eq. (8)] and is given by

$$f(y) = \frac{-1 + \cos 2y - 2y^2 + 2y \sin 2y + 2y^4}{2y^4}. \tag{10}$$

In two limiting cases, it becomes

$$\begin{aligned} f(y) &\approx 2y^2/9 \quad \text{for } y \ll 1 \\ f(y) &\approx 1 - 1/y^2 \quad \text{for } y \gg 1 \end{aligned}$$

(the small term $1/y^2$ is of importance in the case where $y_{\text{max}} \gg 1$ and $y_\infty \gg 1$). The quantity w_1 is meaningful for $y_\infty < y_{\text{max}}$ or

$$v > \gamma v_\infty, \quad \gamma = \frac{m_\nu + m_A}{2\sqrt{m_\nu m_A}} \tag{11}$$

($v = \sqrt{v_\infty^2 + v_{\text{esc}}^2(x)}$). In the Earth, a neutrino can be captured only upon a collision with nuclei whose masses are close to 50 GeV (between 46 and 54 GeV). Fortunately, this mass interval includes the iron nucleus, which is abundant in the Earth, the relevant capture probability being $w_1 \sim 10^{-3}$. In the case of the Sun, the inequality in (11) holds for all nuclei, with the exception of that of hydrogen.

The probability w_1 for the hydrogen nucleus (proton) is positive only in the interior of the Sun for $x \in [0; 0.29]$.

With the aid of expressions (8) and (9) for η and w_1 , respectively, we can recast Eq. (3) into the form

$$\begin{aligned} \dot{N}_{\text{capt}} &= \sum_A \frac{n_\infty}{v_\infty} \sigma_0 N_{A \text{ tot}} \tag{12} \\ &\times \frac{\int v^2 \frac{9}{2y_{\text{max}}^2} (f(y_{\text{max}}) - f(y_\infty)) n_A dV}{N_{A \text{ tot}}}, \end{aligned}$$

where $N_{A \text{ tot}} = \frac{\langle \alpha_A \rangle M}{A} N_A$ is the total number of A nuclei in the gravitating body, $\langle \alpha_A \rangle$ is the mass fraction of the A element in the entire gravitating body of mass M , N_A is Avogadro's number, and $n_A = \frac{\alpha_A \rho}{A} N_A$ is the concentration of the A element. In limiting cases, expression (12) can be simplified. For example, we have

$$\begin{aligned} \dot{N}_{\text{capt}} &\cong \sum_A \frac{n_\infty}{v_\infty} \sigma_0 N_{A \text{ tot}} (\langle v_{\text{esc}}^2 \rangle - \delta^2 v_\infty^2) \tag{13} \\ &\text{for } v^2 \ll v_{\text{nonpoint}}^2, \quad \delta^2 \equiv \gamma^2 - 1. \end{aligned}$$

In expression (13), $\langle v_{\text{esc}}^2 \rangle$ stands for the quantity obtained by averaging the square of the escape velocity over the density (concentration) of A nuclei in the Earth or in the Sun. If the relative content of the A element is uniform over the volume of the gravitating body—that is, if $\alpha_A = \text{const} = \langle \alpha_A \rangle$ — $\langle v_{\text{esc}}^2 \rangle$ reduces to the square of the escape velocity averaged over the total matter density:

$$\langle v_{\text{esc}}^2 \rangle = \int v_{\text{esc}}^2(x) \rho dV / M.$$

For the chosen distribution of Earth's density, we have $\langle v_{\text{escE}}^2 \rangle = 1.2 v_{\text{escE}}^2$. For the Sun, the corresponding result is $\langle v_{\text{escS}}^2 \rangle \approx 3.3 v_{\text{escS}}^2$.

In the opposite limiting case, expression (12) takes the form

$$\dot{N}_{\text{capt}} \cong \sum_A \frac{n_\infty}{v_\infty} \sigma_0 N_{A \text{ tot}} \frac{9}{2} v_{\text{nonpoint}}^2 (1 - f(y_\infty)) \tag{14}$$

$$\text{for } v^2 \gg v_{\text{nonpoint}}^2.$$

There are virtually no data on the chemical composition of the interior of the Earth (we are interested above all in the abundance of iron there). It is only known that, in all probability, Earth's core is dominated by iron and that there are considerable amounts of iron in the mantle of the Earth. We set the mass fraction of iron in the Earth to $\langle \alpha_{\text{Fe}} \rangle = 20\%$ and assume that its distribution over the volume of the Earth is uniform. The result would slightly increase upon

taking into account an increase in the concentration of iron toward the center of the Earth.

For the sake of simplicity, the chemical composition of the Sun will also be assumed to be uniform over its volume and to be consistent to the composition of Sun's atmosphere, the latter being known from observations. Calculations based on the standard solar model reveal that, in general, the relative concentration of helium increases toward the center of the Sun, that of hydrogen decreases, and so on. Upon taking into account this nonuniformity of the chemical composition, the result would slightly increase, owing primarily to a higher concentration of helium. Data on the chemical composition of Sun's atmosphere were borrowed from [14]. The relevant atomic mass will everywhere be set to the atomic mass of the most abundant isotope of the element being considered.

3. ACCUMULATION AND ANNIHILATION OF MASSIVE NEUTRINOS IN THE EARTH AND IN THE SUN

Let us now consider processes of neutrino accumulation and annihilation.

In calculating the rate of neutrino capture in the Earth with allowance for the relations $n \approx n_\infty$ and $v \approx v_\infty$, it is convenient to make use of expression (3) and to take everything there outside of the integral sign, with the exception of w_1 , whereupon this formula becomes similar to that in (13), but it features the additional factor η (8); as a result, we obtain

$$\eta \approx 0.86, \quad (15a)$$

$$\langle w_1 \rangle = 1.2 \frac{v_{\text{escE}}^2}{v_\infty^2} - \delta^2 \approx 1.3 \times 10^{-3}, \quad (15b)$$

$$\dot{N}_{\text{capt}} = n_\infty v_\infty \sigma_0 \eta N_{\text{Fe tot}} \langle w_1 \rangle \approx 1.0 \times 10^{14} \text{ s}^{-1}. \quad (15c)$$

Estimates show that the contribution of multiple collisions to neutrino capture does not exceed 10%. The correction that is associated with taking into account the velocity distribution of neutrinos is also insignificant. Under the assumption that neutrinos obey the Maxwell \bar{v}_e velocity distribution at a mean velocity of 300 km/s, the result will increase by a factor of 1.3. If we take additionally into account, in this distribution, the motion of the Solar System (about the center of the Milky Way Galaxy) at a velocity of 200 km/s, the result will increase by at least 10%. There are no grounds to expect that the correction associated with the velocity distribution of neutrinos will be significant for the Sun either.

Over a time interval of about a year, which is obviously much less than the age of the Earth, the

kinetic energy of neutrinos that are captured by its field reduces to energies of thermal motion of nuclei, with the result that the neutrinos settle in the central part of the Earth. In the following, we will refer to this process as the thermalization of neutrinos and to its characteristic time as the thermalization time. In order to estimate the number of neutrinos accumulated in the Earth, we assume, for the sake of simplicity, that the concentration of thermalized neutrinos is distributed uniformly (is constant) within a sphere of radius x_{thermal} . This radius is defined as the limiting distance within which a particle of total energy $T_{\text{therm}} + U(0)$, where T_{therm} and $U(0)$ are, respectively, the thermal energy of particles (molecules) and the potential energy of neutrinos at the center of the Earth, can occur in its potential field. A precise value of the temperature at the center of the Earth is unknown and is assumed to be within the range 3000–10000 K. Setting $T_{\text{therm}} = 1$ eV, taking into account (4), and using the equality

$$T_{\text{therm}} - \frac{3}{2} T_{\text{escE}} = -T_{\text{escE}} \frac{(3 - x_{\text{thermal}}^2)}{2},$$

($T_{\text{escE}} \equiv m_\nu v_{\text{escE}}^2/2 = 35$ eV), we obtain $x_{\text{thermal}} \approx 0.24$. The accumulation of neutrinos within the Earth (an increase in the concentration of thermalized neutrinos) terminates as soon as the rate of their annihilation becomes equal to the capture rate ($\dot{N}_{\text{ann. equil}} = \dot{N}_{\text{capt}}$), in which case the energy release in annihilation is 0.84×10^{13} erg/s (this corresponds to 0.5×10^{-12} of the total energy flux incident on the Earth from the Sun). We note that, in studying the actual thermodynamic distribution of thermalized neutrinos, it is necessary to consider evaporation (escape from the Earth). It was shown in [9], however, that, for neutrino masses in excess of 10 GeV, the rate of annihilation is much higher than the rate of evaporation. The cross section for ν_4 annihilation is determined by the weak interaction of neutrinos in the vicinity of the Z -boson resonance. In the nonrelativistic approximation, the cross section for such an annihilation process through the channel involving the production of a neutrino–antineutrino pair of specific flavor is

$$\sigma_{\nu_e \bar{\nu}_e} \cong \frac{\bar{g}^4}{2^8 \pi} \frac{m_\nu^2}{(4m_\nu^2 - m_Z^2)^2} \frac{1}{\beta^*} \approx \frac{1.28 \times 10^{-34} \text{ cm}^2}{\beta^*}.$$

The total annihilation cross section is

$$\sigma_{\text{ann}} = \frac{\sigma_{\nu_e \bar{\nu}_e}}{\text{Br}(Z \rightarrow \nu_e \bar{\nu}_e)} \approx \frac{1.93 \times 10^{-33} \text{ cm}^2}{\beta^*}. \quad (16)$$

In the above expressions, $\bar{g} = \sqrt{4\sqrt{2}G_F m_Z^2}$ is the dimensionless weak-interaction constant; G_F is the Fermi constant; m_Z is the Z -boson mass; $\beta^* = v^*/c$, v^* being the ν_4 velocity in the c.m. frame; and $\text{Br}(Z \rightarrow \nu_e \bar{\nu}_e) \approx 6.67\%$ is the branching fraction for

Z -boson decay into a pair formed by a neutrino and an antineutrino of the same flavor. The equilibrium concentration n_{equil} and the corresponding total number N_{equil} of thermalized neutrinos are [$\dot{N}_{\text{ann, equil}} = 0.25n_{\text{equil}}^2\sigma_{\text{ann}}v_{\text{rel}}V_{\text{therm}}$, where $v_{\text{rel}} = \sqrt{2}v^*$ is the mean relative velocity of the neutrinos and $V_{\text{thermal}} = \frac{4}{3}\pi(R_E x_{\text{thermal}})^3 \approx 1.5 \times 10^{25} \text{ cm}^3$] $n_{\text{equil}} \approx 0.58 \times 10^6 \text{ cm}^{-3}$ and $N_{\text{equil}} = n_{\text{equil}}V_{\text{thermal}} \approx 0.88 \times 10^{31}$ (this corresponds to a mass of 780 t). The time it takes for this equilibrium state to be established is

$$t_{\text{equil}} = \frac{N_{\text{equil}}}{\dot{N}_{\text{capt}}} \approx 2.6 \times 10^9 \text{ yr.}$$

The value that we obtained for this time is commensurate with the age of the Earth (the former is one-half as great as the latter); therefore, the current number N of neutrinos (that is, the number of these accumulated over the time period equal to the age of the Earth) may be different from N_{equil} . Solving equation $\dot{N} = \dot{N}_{\text{capt}} - \dot{N}_{\text{ann}}$ with respect to N , we obtain

$$N = N_{\text{equil}} \tanh(t_E/t_{\text{equil}}) = 0.964N_{\text{equil}},$$

where t_E is the present-day age of the Earth. Accordingly, \dot{N}_{ann} is given by

$$\dot{N}_{\text{ann}} = 0.964^2 \dot{N}_{\text{capt}} = 0.93 \dot{N}_{\text{capt}}.$$

Taking into account the degree of precision to which this result was obtained, we can set $N \approx N_{\text{equil}}$ and $\dot{N}_{\text{ann}} \approx \dot{N}_{\text{capt}}$.

In the case where the annihilation process proceeds through an intermediate Z boson, 20% of annihilated ν_4 are converted into pairs of monochromatic neutrinos of known species ($\nu_e\bar{\nu}_e$, $\nu_\mu\bar{\nu}_\mu$, $\nu_\tau\bar{\nu}_\tau$), their energies being 50 GeV. Their flux at Earth's surface is

$$I = \frac{0.2\dot{N}_{\text{ann}}}{4\pi R_E^2} \approx 4.1 \times 10^{-6} \text{ cm}^{-2} \text{ s}^{-1}.$$

For each neutrino (neutrino + antineutrino) flavor individually, the flux is one-third as great as that.

For the Sun, the number of captured neutrinos per unit time upon the interaction with a specific nuclear species, $\dot{N}_{A \text{ capt}}$, is given in Table 1, where the elements are arranged in order of decrease in their concentration in the Sun. The total number of ν_4 captured in the Sun per unit time is

$$\dot{N}_{\text{capt}} \approx 2.2 \times 10^{21} \text{ s}^{-1}.$$

The total flux of ν_4 through the entire surface of the Sun is $n\sigma_S v = \frac{n_\infty}{v_\infty} v^2 \pi R_S^2 \approx 4.8 \times 10^{23} \text{ s}^{-1}$, where n and v are, respectively, the neutrino concentration and the neutrino velocity at the level of Sun's surface ($v = 687 \text{ km/s}$) and $\sigma_S = \pi R_S^2$ is the cross-sectional

area of the Sun. The flux of arriving neutrinos is much greater than \dot{N}_{capt} . Therefore, the approximation where the interaction with matter is assumed to induce only negligible changes in the concentration of incident neutrinos is justified. We also note that the relationship between \dot{N}_{capt} and the arriving flux is independent of n_∞ , and so therefore is the applicability of this approximation.

The time of thermalization of neutrinos captured in the Sun (it is also about a year) is much less than the age of the Sun. The kinetic energy of the neutrinos at the center of the Sun is $T_{\text{therm}} = 1.9 \text{ keV}$, while the potential energy is obtained by multiplying expression (6) by $-m_\nu/2$. We then have $x_{\text{thermal}} \approx 0.017$; $V_{\text{thermal}} \approx 0.69 \times 10^{28} \text{ cm}^3$; $n_{\text{equil}} \approx 1.3 \times 10^8 \text{ cm}^{-3}$; $N_{\text{equil}} \approx 0.87 \times 10^{36}$, which corresponds to a mass of $0.78 \times 10^{14} \text{ g}$; and $t_{\text{equil}} \approx 1.2 \times 10^7 \text{ yr}$ —that is, $N = N_{\text{equil}}$ and $\dot{N}_{\text{ann}} = \dot{N}_{\text{capt}}$. The energy release from ν_4 annihilation is $1.8 \times 10^{20} \text{ erg/s} = 4.7 \times 10^{-14} L_C$, where L_C is Sun's luminosity.

Neutrinos of known species from the annihilation of 50-GeV ν_4 are partly absorbed in the Sun. The cross sections for the interaction of 50-GeV neutrinos and antineutrinos of known species with a nucleon are different [15]: they are 5.1×10^{-37} and $2.6 \times 10^{-37} \text{ cm}^2$, respectively. We note that the distinctions between the cross sections for neutrinos of different flavors are insignificant at the energies being considered. The fractions of neutrinos and antineutrinos that escaped from the Sun are 0.63 and 0.79, respectively. The fluxes of monochromatic neutrinos and antineutrinos and their total (neutrino + antineutrino) flux from ν_4 annihilation is

$$\begin{aligned} I_\nu &\approx 0.50 \times 10^{-7} \text{ cm}^{-2} \text{ s}^{-1}, \\ I_{\bar{\nu}} &\approx 0.63 \times 10^{-7} \text{ cm}^{-2} \text{ s}^{-1}, \\ I_{\nu\bar{\nu}} &\approx 1.1 \times 10^{-7} \text{ cm}^{-2} \text{ s}^{-1}. \end{aligned}$$

For each flavor individually, the fluxes are smaller by a factor of 3.

Among the parameters that affect eventual results, the neutrino concentration n_∞ , which is proportional to $\xi_C \Omega$, is characterized by the highest degree of uncertainty. The concentration n_∞ affects not only \dot{N}_{capt} and I but also the equilibration time t_{equil} . The $\xi_C \Omega$ values at which t_{equil} is equal to the present-day age of the Earth and the present-day age of the Sun are 0.5 and 1.2×10^{-5} , respectively. Taking these values into account, we can generalize the neutrino fluxes from Earth's and Sun's center to the case of arbitrary $\xi_C \Omega$. The result for the Sun is

$$I \approx 1.1 \times 10^{-7} \frac{\xi_C \Omega}{2}$$

Table 1. Rates of neutrino capture by nuclei of specific elements in the Sun

Element	$\dot{N}_{A \text{ capt}}, 10^{20} \text{ s}^{-1}$	Element	$\dot{N}_{A \text{ capt}}, 10^{20} \text{ s}^{-1}$	Element	$\dot{N}_{A \text{ capt}}, 10^{20} \text{ s}^{-1}$
^1H	0.94	^{26}Fe	3.34	^{17}Cl	0.02
^2He	4.60	^{16}S	0.75	^{15}P	0.01
^8O	5.89	^{18}Ar	0.29	$^{25}\text{Mn}^*$	0.03
^6C	1.26	^{13}Al	0.11	^{19}K	0.01
^{10}Ne	1.94	^{20}Ca	0.15	^{22}Ti	0.01
^7N	0.53	^{11}Na	0.05	^{27}Co	0.01
^{12}Mg	0.97	^{28}Ni	0.18		
^{14}Si	1.27	^{24}Cr	0.05		

* The lowest excited level of the $^{25}\text{Mn}^{55}$ nucleus is that at 126 keV. In the interaction of neutrinos having energies (within the Sun) in the range 131–556 keV, there can occur inelastic scattering, which is not coherent. In calculating the interaction-cross-section values quoted in the table, we relied on formula (7), which is valid for elastic interaction, so that the possible effects of inelastic scattering were disregarded.

$$\times \tanh^2 \sqrt{\frac{\xi_C \Omega}{1.2 \times 10^{-5}}} \text{ (cm}^{-2} \text{ s}^{-1}\text{)}.$$

Upon a generalization to the case of an arbitrary mass fraction of iron, we find for the Earth that

$$I \approx 4.1 \times 10^{-6} \frac{\xi_C \Omega}{2} \frac{\alpha_{Fe}}{20\%} \times \tanh^2 \sqrt{\frac{\xi_C \Omega}{0.5} \frac{\alpha_{Fe}}{20\%}} \text{ (cm}^{-2} \text{ s}^{-1}\text{)},$$

where $\xi_C \Omega = 2$ corresponds to the value used here ($\xi_C \Omega = 2 \times 10^4 \times 10^{-4} = 2$, $n_\infty = 2 \times 10^{-7} \text{ cm}^{-3}$) and $\tanh x \approx 1$ for $x > 1$.

The solid angle of the annihilation-neutrino flux from Earth's center is about 1 sr; for the Sun, the analogous solid angle is determined by the angular resolution of the detector. The fluxes of atmospheric neutrinos are direction-dependent (this dependence is especially strong for high-energy electron neutrinos [16]): a flux in the horizontal direction is greater than the analogous flux in the vertical direction. For various neutrino flavors, the data in Table 2 illustrate, at various energies, a comparison of the fluxes of monochromatic annihilation neutrinos and of upward going atmospheric neutrinos of the same flavor. In the first column, the ratios of these fluxes

Table 2. Ratios of the fluxes of monochromatic annihilation neutrinos of specific flavor from Earth's center to the flux of upward going atmospheric neutrinos of the same flavor for various neutrino flavors at various energies

	50 GeV	>50 GeV	>1 GeV
$\nu_\mu \bar{\nu}_\mu$	3	0.14	0.6×10^{-4}
$\nu_e \bar{\nu}_e$	50	2.4	2×10^{-4}

are given for atmospheric neutrinos in the energy region (chosen by convention) around 1 GeV. The ratios in the remaining columns were taken for the integrated fluxes of atmospheric neutrinos. Similar ratios for atmospheric-neutrino fluxes averaged over directions are considerably smaller. We note once again that these ratios were obtained at $\xi_C \Omega = 2$ and $\alpha_{Fe} = 20\%$.

It is important to note that the presence of electron, muon, and tau neutrinos (in equal amounts) from ν_4 annihilation is a feature that distinguishes the case at hand from the analogous case where the accumulation and annihilation at Sun's and Earth's center are considered for neutralinos, another popular candidate for a WIMP. Because of its Majorana nature, the neutralino cannot directly annihilate into a neutrino. Neutrinos are produced in the decays of neutralino-annihilation products and in the interactions of these products with surrounding matter; as a result, their spectrum becomes softer (in this way, there arise many muon neutrinos and only a few tau neutrinos). There is a similar soft section of the spectrum of electron, muon, and tau neutrinos in ν_4 annihilation as well.

Let us now estimate the local concentration of heavy neutrinos at the level of Earth's surface. The total neutrino concentration near the surface of the Earth receives contributions not only from galactic neutrinos themselves, whose concentration near the Earth is approximately equal to n_∞ , and the slow component, but also from neutrinos captured by the Earth (both from nonthermalized and from thermalized ones). The group of nonthermalized neutrinos consists of captured neutrinos, which, upon the first collision with a nucleus, execute oscillatory motion of amplitude greater than Earth's radius, forming a

neutrino atmosphere around the Earth. The neutrino atmosphere of the Earth also involves thermalized neutrinos, since the actual distribution of their concentration can go beyond Earth's surface. These neutrinos have a velocity of about 1 km/s, which is two orders of magnitude less than the velocity of galactic neutrinos and one order of magnitude less than the velocity of neutrinos from the slow component; in view of this, they can hardly be discovered with present-day underground facilities intended for direct WIMP searches. In order to estimate the concentration of this ultraslow component of heavy neutrinos, we assume that thermalized neutrinos obey the Boltzmann distribution

$$n(x) = n_0 \exp\left(-\frac{U'(x)}{kT}\right),$$

where n_0 is the concentration of neutrinos at Earth's center, $U'(x)$ is the neutrino potential energy reckoned from Earth's center [at the surface of the Earth, it is $U'(1) = T_{\text{esc}E}/2 \approx 18$ eV], and $kT = (2/3)T_{\text{therm}} \approx 0.6$ eV is the temperature of thermalized neutrinos. At the surface of the Earth, the concentration is $n(1) \approx 10^{-13}n_0 \approx 5 \times 10^{-8} \text{ cm}^{-3} \approx 0.3n_\infty$; in order to obtain this estimate, we set the concentration at Earth's center to $n_0 = n_{\text{equil}} \approx 0.58 \times 10^6 \text{ cm}^{-3}$. Upon taking into account an increase in the density of Earth's matter toward the center, $U'(1)$ will increase, with the result that the concentration of thermalized neutrinos at Earth's surface will become a few orders of magnitude smaller. Thus, the number of thermalized neutrinos at Earth's surface is negligibly small in relation to the number of galactic neutrinos. In order to assess the concentration of nonthermalized neutrinos, we assume that the neutrinos being discussed move along orbits whose eccentricity is $e = 1$ —that is, along straight-line trajectories—and consider neutrinos only after the first collision with a nucleus; in other words, we disregard the contribution from neutrinos that suffered two or more collisions with nuclei of Earth's matter. For a single neutrino of total energy E ($E < 0$), the amplitude of oscillations can then be represented as $a = GM_E m_\nu / |E| = R_E T_{\text{esc}E} / |E|$. We interested in neutrinos for which $a > R_E$; in this case, the distribution of the concentration of neutrinos with respect to the radius r is given by

$$n_1 = \frac{1}{2\pi^2 a r^{3/2} \sqrt{a-r}}, \quad r < a.$$

The rate ($d\dot{N}_+/dE$) at which this neutrino population is replenished in the energy range E to $E + dE$ is obtained by dividing expression (15c), where the factor $w_{\text{esc}} = v_{\text{esc}E}^2/v_\infty^2 - \delta^2$ is substituted for $\langle w_1 \rangle$ (15b), by $T_{\text{esc}E}$. In contrast to $\langle w_1 \rangle$, the factor w_{esc} is independent of the form of the density distribution in the

Earth. In order to demonstrate this explicitly, we note that, at a point where the potential energy $U(x)$ takes any value satisfying the condition $|U(x)| \ll T_\infty$ and depending on the density distribution in the Earth, the probability that a neutrino is scattered by an iron nucleus into an orbit whose size a is greater than R_E is determined by the final-total-energy interval $-T_{\text{esc}E} < E < 0$, which is independent of $U(x)$ and, hence, of the density distribution. This explains why, in w_{esc} , there is not the factor of 1.2, which arose in $\langle w_1 \rangle$ (15b) from averaging over the entire volume of the Earth. Neutrinos of energy E that belong to this population exist (are thermalized) within the time period $t(E) = T_{1/2}/w$, where $T_{1/2} = \frac{\pi a^{3/2}}{v_{\text{esc}E} \sqrt{R_E}}$ is the oscillation half-period and $w \approx 2R_E \langle n_{\text{Fe}} \rangle \sigma_0$ is the probability for a neutrino to undergo a collision with an iron nucleus in traversing the Earth. The distribution of the thermalized-neutrino concentration n is determined by a balance between its replenishment via the capture of new neutrinos and their departure via thermalization. The corresponding balance equation can be represented as

$$\frac{d\dot{N}_+}{dE} n_1(E) = \frac{dn}{dE} \frac{1}{t(E)}.$$

Upon the substitution of all relevant quantities and integration over the region covering all possible neutrino energies, we find from this equation that the concentration $n(x)$, $x > 1$, can be represented as

$$n(x) = \frac{2}{3} \eta \frac{v_\infty}{v_{\text{IE}}} w_{\text{II}} \frac{n_\infty}{x^{5/2}},$$

where η given by (15a). We note that this result will also be valid for WIMPs of mass 50 GeV that are of a different nature, since it is virtually independent of the properties of the particles involved and of the properties of Earth's matter. This is because the rate of capture of new galactic neutrinos and the thermalization rate depend identically on these properties (in particular, on the transparency of the Earth). In accordance with the expression obtained for the concentration of nonthermalized neutrinos, its value at the surface of the Earth is $n(1) \approx 1.6 \times 10^{-2} n_\infty$. Thus, the neutrino atmosphere does not make a significant contribution to the neutrino background near the surface of the Earth, nor does it accordingly produce noticeable effects from annihilation.

4. EFFECTS OF NEW LONG-RANGE INTERACTION IN THE ANNIHILATION OF FOURTH-INTERACTION NEUTRINOS

The existence of fourth-generation fermions, including ν_4 , can be theoretically justified within superstring theory. In the low-energy limit of its realistic

versions, there arises $U(1)$ gauge symmetry (or even a few of them) [17] that is not contained in the Standard Model and which may be associated only with the fourth generation of fermions, not involving fermions of the three known generations. The corresponding new gauge interaction may be similar to electromagnetic interaction. For the sake of definiteness, we denote its coupling constant by α_y and refer to the massless boson mediating it as a y photon. The impact of the new interaction on phenomena associated with the existence of ν_4 was considered elsewhere [18]. Here, we will briefly consider the effect of the new interaction of ν_4 on its accumulation and annihilation in the Earth and in the Sun.

The new interaction leads to the new annihilation channel $\nu_4\bar{\nu}_4 \rightarrow yy$. The cross section for this process is analogous to the cross section for electron-positron annihilation into two photons and, in the nonrelativistic approximation ($\alpha_y \ll \beta^* \ll 1$), has the form [19]

$$\sigma_{y\text{-ann}} \cong \frac{\pi\alpha_y^2}{2m_\nu^2} \frac{1}{\beta^*} \approx \frac{1.30 \times 10^{-35} \text{ cm}^2}{\beta^*} \left(\frac{\alpha_y}{\alpha}\right)^2,$$

where $\alpha = 1/137$ is the coupling constant for electromagnetic interaction (fine-structure constant). At $\alpha_y = \alpha$, this cross section is more than two orders of magnitude smaller than the cross section (16) for annihilation through a Z boson. For α_y about α , the dominant channel of neutrino annihilation is that through an intermediate Z boson. Of greater importance is the following fact also associated with the new interaction: the presence of the long-range interaction between neutrinos whose velocities β^* are less than $2\pi\alpha_y$, which is similar to Coulomb interaction, leads to an increase in interaction cross sections (Sakharov's enhancement), including the cross section for annihilation through a Z boson, that is expressed in terms of the Coulomb factor [20]

$$C(\beta^*) = \frac{2\pi\alpha_y/\beta^*}{1 - \exp(-2\pi\alpha_y/\beta^*)}.$$

At a speed of 300 km/s, a maximal speed of thermalized neutrinos that correspond to T_{therm} in the Earth, and a maximal speed of thermalized neutrinos that correspond to T_{therm} in the Sun, the Coulomb factor $C(\beta^*)$ at $\alpha_y = \alpha$ takes the values of 46, 7300, and 166, respectively. If we assume that the dynamics of capture and thermalization, together with the adopted approximations on the distribution of the thermalized-neutrino concentration, undergoes no changes, the quantities n_{equil} , N_{equil} , and t_{equil} decrease in proportion to the square root of the Coulomb factor—that is, in proportion to 85 for the Earth and in proportion to 13 for the Sun. The fluxes of neutrinos of known flavors from ν_4 annihilation correspond to the equilibrium case of $\dot{N}_{\text{ann, equil}} = \dot{N}_{\text{capt}}$ and remain

unchanged; since $t_{\text{equil}} \gg t_{\text{thermal}}$ as before, ν_4 have time to be accumulated at the center prior to the commencement of annihilation. Hence, we can conclude that, because of kinetic equilibrium, the presence of the new long-range interaction and the enhancement of the annihilation cross section because of this interaction have virtually no effect on the estimates of the fluxes of neutrinos from annihilation.

5. CONCLUSION

The present article reports on a continuation of investigations into observable effects that could be associated with the existence of the fourth-generation neutrino ν_4 [3–7]. Some of such effects make it possible to single out manifestations of the new neutrino against the background of other candidates for a WIMP and may serve as a tool for studying the composition of multicomponent dark matter in the Milky Way Galaxy. For example, the annihilation of ν_4 in the halo leads to the emergence of a characteristic outlier at an energy of about m_ν in the spectrum of cosmic-ray positrons [4, 5]. The prediction of fluxes of strictly monochromatic neutrinos of energy precisely equal to m_ν that belong to the known species, including tau neutrinos, is an important distinguishing feature in dealing with ν_4 annihilation in the Earth and in the Sun. By using the soft continuous section that is present in the spectrum of annihilation neutrinos and which is associated with other channels of ν_4 annihilation, it is more difficult to distinguish ν_4 from other WIMP candidates, especially as this section of the spectrum has a comparatively low spectral density because of a comparatively low density of relic ν_4 . In searches for manifestations of ν_4 from the Sun, a difference of about 25% between the fluxes of monochromatic neutrinos and antineutrinos, which is due to a stronger absorption of escaping neutrinos in Sun's matter, may be of considerable interest.

ACKNOWLEDGMENTS

This work was performed in the framework of the Project Cosmoparticle Physics and was supported in part by the Kosmion–ETHZ and EPCOS–AMS collaborations and by the Russian Foundation for Basic Research (project no. 00-15-96699).

REFERENCES

1. S. S. Gershtein and Ya. B. Zel'dovich, Pis'ma Zh. Éksp. Teor. Fiz. **4**, 174 (1966) [JETP Lett. **4**, 120 (1966)]; B. W. Lee and S. Weinberg, Phys. Rev. Lett. **39**, 165 (1977); M. I. Vysotskiĭ, A. D. Dolgov, and Ya. B. Zel'dovich, Pis'ma Zh. Éksp. Teor. Fiz. **26**, 200 (1977) [JETP Lett. **26**, 188 (1977)]; A. D. Dolgov and Ya. B. Zeldovich, Rev. Mod. Phys. **53**, 1 (1981).

2. M. Maltoni and M. I. Vysotsky, Phys. Lett. B **463**, 230 (1999); M. Maltoni, V. A. Novikov, A. N. Rozanov, and M. I. Vysotsky, Phys. Lett. B **476**, 107 (2000); hep-ph/9911535; V. A. Ilyin, M. Maltoni, V. A. Novikov, *et al.*, hep-ph/0006324.
3. D. Fargion, M. Yu. Khlopov, R. V. Konoplich, and R. Mignani, Pis'ma Zh. Éksp. Teor. Fiz. **68**, 657 (1998) [JETP Lett. **68**, 685 (1998)].
4. Yu. A. Golubkov and R. V. Konoplich, Yad. Fiz. **61**, 675 (1998) [Phys. At. Nucl. **61**, 602 (1998)].
5. D. Fargion, Yu. A. Golubkov, R. V. Konoplich, and R. Mignani, astro-ph/9903086.
6. D. Fargion, M. Yu. Khlopov, R. V. Konoplich, and R. Mignani, Phys. Rev. D **54**, 4684 (1996).
7. D. Fargion, M. Grossi, M. Yu. Khlopov, and R. V. Konoplich, Preprint No. 1220, Rome University "La Sapienza" (1998); astro-ph/9809260.
8. W. H. Press and D. H. Spergel, Astrophys. J. **296**, 679 (1985); L. Krauss, Preprint HUTP-85/A008A (Harvard, 1985); J. Silk, K. Olive, and M. Srednicki, Phys. Rev. Lett. **55**, 257 (1985); K. Griest and S. Seckel, Nucl. Phys. B **283**, 681 (1987); A. Gould, Astrophys. J. **321**, 571 (1987); A. Bottino *et al.*, Phys. Lett. B **265**, 57 (1991).
9. L. Krauss, M. Srednicki, and F. Wilczek, Phys. Rev. D **33**, 2079 (1986); T. Gaisser, G. Steigman, and S. Tilav, Phys. Rev. D **34**, 2206 (1986).
10. T. Damour and L. Krauss, Phys. Rev. Lett. **81**, 5726 (1998); astro-ph/9806165; L. Bergstrom *et al.*, hep-ph/9905446.
11. Ya. B. Zel'dovich, A. A. Klypin, M. Yu. Khlopov, and V. M. Chechetkin, Yad. Fiz. **31**, 1286 (1980) [Sov. J. Nucl. Phys. **31**, 664 (1980)].
12. J. N. Bahcal, *Neutrino Astrophysics* (Cambridge Univ. Press, Cambridge, 1989; Mir, Moscow, 1993).
13. M. W. Goodman and E. Witten, Phys. Rev. D **31**, 3059 (1985).
14. L. S. Lyubimkov, *Chemical Composition of Stars: Method and Results of Analysis* (Astroprint, Odessa, 1995).
15. R. Gandhi, C. Quigg, and M. H. Reno, FERMILAB-PUB-95/221-T; hep-ph/9512364.
16. A. V. Butkevich, L. G. Dedenko, and I. M. Zheleznykh, Yad. Fiz. **50**, 142 (1989) [Sov. J. Nucl. Phys. **50**, 90 (1989)].
17. M. B. Green, J. H. Schwarz, and E. Witten, *Superstring Theory* (Cambridge Univ. Press, Cambridge, 1987; Mir, Moscow, 1990), Vol. 2, Sect. 16.3.1.
18. K. M. Belotsky, M. Yu. Khlopov, and K. I. Shibaev, Gravitation and Cosmology Suppl. **6**, 140 (2000).
19. V. B. Berestetskii, E. M. Lifshitz, and L. P. Pitaevskii, *Quantum Electrodynamics* (Nauka, Moscow, 1989; Pergamon, Oxford, 1982), Vol. 4.
20. A. D. Sakharov, Zh. Éksp. Teor. Fiz. **18**, 631 (1948).

Translated by A. Isaakyan